DCU

Ollscoil Chathair
Bhaile Átha Cliath
Dublin City University

Synthesis and spectroscopy of novel charge-transfer triplet sensitizers and fluorescent probes for sensing applications

Ruben Arturo Arellano Reyes B. Sc. (hons), M. Sc.

A thesis submitted to Dublin City University for the award of PhD.

School of Chemical Sciences

Dublin City University

March 2024

Supervisor: Prof. Tia E. Keyes

Declaration

I hereby certify that this material, which I now submit for assessment on the programme of study leading to the award of PhD is entirely my own work, and that I have exercised reasonable care to ensure that the work is original, and does not to the best of my knowledge breach any law of copyright, and has not been taken from the work of others save and to the extent that such work has been cited and acknowledged within the text of my work.

Signed:

Ruben Arturo Arellano Reyes

Student ID No: 19212183

Date: 28/03/2024

Sections

This thesis is dedicated to the memory of a great researcher and human being, Professor Héctor Jaime Salgado Zamora. Doc, thanks for seeing in me what I still cannot see.

Acknowledgments

I would like to express my deep gratitude to my supervisor Professor Tia E. Keyes for her constant support, help and time. Tia, thanks for being the best at making me realise that my concerns are never as big as I think they are. Thanks for helping me understand the way scientific knowledge is made. Thanks for encouraging me to go out of my learning comfort zone. And thanks for trusting me and giving me the opportunity to have students at my charge, I have now a tiny glimpse into everything you have to do.

I would like to thank Dr. Amrutha Prabhakaran for her contribution to the up-conversion experiments and for her invaluable friendship. Amru, Thanks for explaining to me everything in the simplest terms so I can understand. Thanks for comforting me when I've been desperate and couldn't see the answer. I'm a better scientist and person thanks to you.

Thanks to David Cullinane, for being a wonderful friend, thanks for being so kind and so smart. Dave, thanks for being an excellent conversation and party partner. And thanks for telling me all those four stories that later became one thousand.

I would like to thank the rest of the Keyes group members past and present, Nirod, Chris, Ryan, Karmel, Lorcan, Rhianne, Colm and Philip, thanks for your advice, the chats, the science and the fun.

I would like to thank Justine, Marta, and Mariana. Thanks for listening to me and for giving me support when I most needed it. Thanks for making me feel so welcome and loved. Thanks for sharing a bit of your life, the good and bad things with me. Your energy and passion for life and for people inspire me all the time.

Thanks to my lovely Ping and Noemi. Thanks for laughing with me and at me. Thanks for sharing with me your music, your wine, your time. Every moment shared with you makes me love life.

Thanks to my dear Delphine, you are a warrior. Thanks for giving me so much of your time and for listening to me. Thanks for encouraging me to write, to learn and to be.

Thanks to Victoria, for sharing the joys and difficulties of doing the PhD and the pleasures and struggles of being human beings trying to find their place in the world.

Thanks to my most beloved Tony. Thanks for putting up with me all this long. Thanks for being always so undoubtfully kind. I admire you and love you so much. My life has been better thanks to you all these years.

Thanks to Roberta, for being so clever, so strong and so weirdly like me in some respects. Thanks for making me feel I'm not alone and for giving me the strength to finish this. And thanks for believing in my more than I will ever do.

Especial thanks to Carlos, thanks for listening to me all the time and for helping me laugh during the writing of this thesis. Thanks for sharing your life, your food, your friends, and your space with me. Te quiero.

Big thanks to Gustavo, thanks for your love and support even at the distance. Thanks for all the lovely pictures you have always shared with me. Thanks for being so brave and so fun. It's a true honour to have you in my life.

Thanks to José Ángel, Oscar Daniel and Karen. Thanks for sharing your human experiences with me, thanks for the laughs and for the endless conversations.

Thanks to my parents, Oto and Key for giving me all the privileges I've had and above all, the privilege of choosing what I wanted to do and be, even if that sometimes meant not doing or being who you wanted. Thanks for nurturing my curiosity, my hobbies and my desire for knowledge of all kinds. Thanks for never sugar-coating reality and teaching me to work hard, all the early-morning wake ups at the butchery have paid off, I can assure you. This is your achievement as much as it is mine.

List of publications

[1]   R. C. E. Sia, **R. A. Arellano-Reyes**, T. E. Keyes, J. Guthmuller, *Phys. Chem. Chem. Phys.* **2021**, *23*, 26324–26335.

[2]   **R. A. Arellano-Reyes**, A. Prabhakaran, R. C. E. Sia, J. Guthmuller, K. K. Jha, T. Yang, B. Dietzek-Ivanšić, V. McKee, T. E. Keyes, *Chem. Eur. J.* **2023**, *29*, e202300239.

[3]   T. Yang, **R. A. Arellano-Reyes**, R. C. Curley, K. K. Jha, A. Chettri, T. E. Keyes, B. Dietzek-Ivanšić, *Chem. Eur. J.* **2023**, *29*, e202300224.

[4]   K. Kumar Jha, A. Prabhakaran, R. Cane Sia, **R. A. Arellano Reyes**, N. Kumar Sarangi, T. Yang, K. Kumar, S. Kupfer, J. Guthmuller, T. E. Keyes, B. Dietzek-Ivanšić, *ChemPhotoChem* **2023**, *7*, e202300073.

[5]   K. K. Jha, A. Prabhakaran, L. Spantzel, R. C. Sia, I. Pérez, **R. A. Arellano-Reyes**, A. Elmanova, A. Dasgupta, C. Eggeling, M. Börsch, J. Guthmuller, M. Presselt, T. E. Keyes, B. Dietzek-Ivanšić, *ChemPhotoChem* **2023**, *7*, e202300091.

[6]   A. Pieczara, **R. A. Arellano Reyes**, T. E. Keyes, P. Dawiec, M. Baranska, *ACS Sens.* **2024**, acssensors.3c02576.

[7]   Amrutha Prabhakaran, Keshav Kumar Jha, Rengel Cane E. Sia, **Ruben Arturo Arellano Reyes,** Nirod Kumar Sarangi, Mateusz Kogut, Julien Guthmuller, Jacek Czub, Benjamin Dietzek-Ivanšić, and Tia E. Keyes. *ACS Appl. Mater.* Interfaces **2024**, 16, 22, 29324–29337.

Table of Content

Chapter 1 General introduction

Chapter 2 BODIPY-perylene heterochromophores with Mega Stokes shifts as sensitizers for Triplet-triplet annihilation up-conversion

Chapter 3 Synthesis and functionalisation of BODIPY fluorophores

Chapter 4 Spectroscopy and photophysics of BODIPY derivatives

Chapter 5 Membrane, mitochondria, and NO sensors.

Chapter 6 general conclusions and perspectives

Appendices

Supporting information for Chapter 2

Supporting information for Chapter 3

Supporting information for Chapter 4

Supporting information for Chapter 5

Table of figures

Abbreviations

APCI	Atmospheric pressure chemical ionization
Boc	*tert*-Butyloxycarbonyl
DCC	*N,N*-Dicyclohexylcarbodiimide
DCM	Dichloromethane
DMAP	4-Dimethylaminopyridine
DMF	Dimethylformamide
DMSO	Dimethylsulphoxide
dppf	Bis(diphenylphosphino) ferrocene
eq.	Equivalents
ESI	Electrospray Ionisation
EtOAc	Ethyl acetate
FWHM	Full width at half maximum
HR-MS	Hight Resolution Mass spectrometry
mL	Mililitre
µL	Microlitre
MALDI	Matrix-assisted laser desorption/ionisation
MeCN	Acetonitrile
NBS	*N*-Bromosuccinimide
NIS	*N*-Iodosuccinimide
nm	nanometre
NMR	Nuclear Magnetic Resonance
ns	Nanosecond
PEPPSI	Pyridine-enhanced precatalyst preparation stabilization and initiation

ppm   Parts per million

s   Second

TEA   Triethylamine

TFA   Trifluoroacetic acid

TOF   Time of Flight

THF   Tetrahydrofuran

v/v   Volume per volume

Synthesis and spectroscopy of novel charge-transfer triplet sensitizers and fluorescent probes for sensing applications

Ruben Arturo Arellano Reyes

Abstract

Fluorescence spectroscopy has hugely improved our understanding of the eukaryotic cell. Thanks to fluorescence techniques, the composition and dynamic nature of the membrane, cytosol, mitochondria, and other organelles has been elucidated. However, the more we discover the more we realise that there is still much to study. In this thesis a series of fluorescence probes were developed to further improve our understanding of key cellular features.

A few synthetic strategies were developed to prepare non-symmetrically substituted BODIPY-perylene conjugates. The products obtained were characterised using spectroscopic techniques. These molecules were successfully used for two purposes: first, as triplet-triplet annihilation up-conversion sensitisers; a second, as viscosity sensors. The results indicate that the dyes are good sensitisers even in the absence of heavy atoms such as iodine, but the up-conversion process was found to be very solvent-dependent. The viscosity sensitivity experiments determined the molecules that have potential as intensity-based and lifetime-based viscosity sensors. Solid-state spectroscopic studies were conducted on crystalline samples obtained from some BODIPY-perylene conjugates. The results give us some insights into the electronic effects taking place in the crystal structure.

A few different sensors were prepared as part of the LogicLab project. A BODIPY-cholesterol conjugate was designed and tested as a viscosity sensor. The results indicate that this molecule can be used an intensity-based probe. A mitochondrial Raman reporter was prepared and studied in cells. The molecule was found to be better than the commercial standard. Finally, a nitric oxide sensor was synthesized and studied in solution. The molecule reacted with nitric oxide, but the results indicate the challenges associated with sensing this gas using up-conversion systems.

A total of six research articles were published from the results obtained in this work and as the results of the collaboration with other research groups of the LogicLab consortium.

"The ideas formed by the pure intelligence have no more than a logical, a possible truth,
they are arbitrarily chosen. …only experience is a criterion of truth"

— Marcel Proust, Le Temps retrouvé.

"Ignorance makes one more self-confident than knowledge."

— Étienne Klein, Le goût du vrai.

"Be a philosopher; but, amidst all your philosophy, be still a man."

— David Hume, An Enquiry Concerning Human Understanding.

Chapter 1 General introduction

Overview

The first goal of this thesis was to prepare organic sensitizers capable of performing triplet-triplet annihilation up-conversion. The second objective was preparing molecular rotors capable of sensing viscosity in biological environments. The third and final objective was to prepare sensors capable of being incorporated into liposomal vesicles.

In this introductory chapter, the photophysics of the up-conversion process will be described, as well as the relationship between the structure of a molecule and its capacity to act as a sensitizer. The potential of triplet sensitizers to be applied in Photodynamic therapy will also be explained.

Finally, the interest of studying cytoplasmic and membrane viscosity, their relationship with disease and the molecular tools used to study them will be described.

1.1 Introduction to TTA-UC and BODIPY dyes

1.1.1 Radiative processes

Photons and electrons mediate the interaction between matter and light. After a chromophore absorbs light, it can reemit it in the form of fluorescence or phosphorescence depending on the spin multiplicity orientation of the electrons involved in the process, singlet for fluorescence and triplet for phosphorescence. Figure 1. In both cases the light emitted will be of a lower energy (longer wavelength) than the light used to excite the molecule. In contrast, photon up-conversion is an anti-Stokes process. It transforms low energy light to high energy photons. It is a relatively more recent discovery[1] but it has recently been increasingly a focus of research efforts, given that it could help overcome some of the challenges that fluorescence faces such as lack of penetration of visible light in tissues.
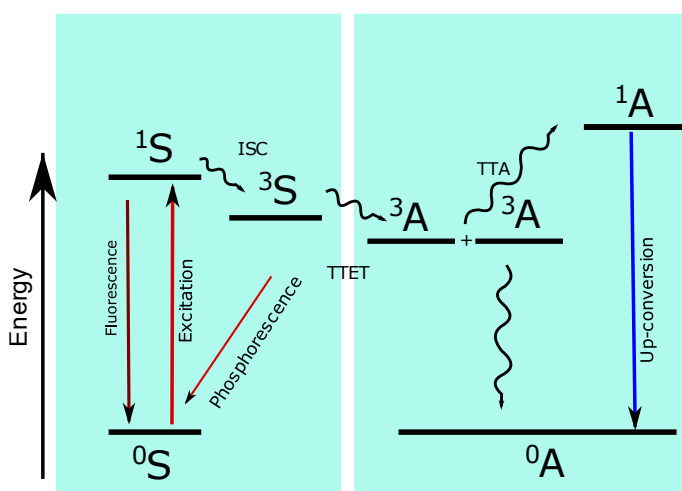
Figure 1 *Jablonski-Perrin diagram of the fluorescence, phosphorescence, and TTA-UC mechanisms. S= sensitizer A= annihilator, 0= ground state 1=singlet state 3= triplet sate, ISC=Intersystem crossing, TTET= triplet-triplet energy transfer, TTA= triplet-triplet annihilation.*

In triplet-triplet annihilation up-conversion (TTA-UC), low frequency light, e.g., red light, excites the sensitizer to the first singlet excited state, which then undergoes inter-system crossing (ISC) to populate its first triplet excited state. Energy is then transferred from the sensitizer to the annihilator through a Dexter

mechanism generating a triplet state annihilator. The collision of two triplet annihilators generates a ground state and singlet emissive state that produces the up-converted photon through fluorescence.[2] All steps are explained in detail in the following sections. For a visual understanding of the TTA-UC process, see the Jablonski-Perrin diagram in Figure 1.

One of the benefits of up-conversion is its capacity to work with red or even near infrared light. In biological applications most fluorophores absorb in the 200-700 nm. While this light is strongly absorbed and produce high fluorescence, it is sometimes incapable of penetrating tissues.[3,4] UV-Vis light can also cause photobleaching and produce the fluorescence of biomolecules, decreasing the signal-to-noise ration.[5,6] Irradiating with red and near-infrared light could help prevent all these issues.

Parker and Hatchward first reported the TTA-UC process about 50 years ago in mixtures of phenanthrene/naphthalene or proflavine hydrochloride/anthracene.[1]

The generation of triplet states and the energy transfer are two of the pivotal steps in up-conversion. Our understanding of those phenomena is essential to allow chemists to tune and improve the efficiency of TTA-UC.

1.1.2 Photosensitizers and generation of triplet states

Fluorescence is a generally well-understood phenomenon with wide analytical applications. The structural characteristics of molecules predisposed to fluoresce are well understood. However, apart from metal complexes with strong spin-orbit coupling, the structural characteristics of organic species that promote triplet state formation are less well established.[7] There are a few reasons to account for this disparity. First, triplet state population in molecules possessing only light

atoms is relatively rare, generally formed by photo excitation and inter-system crossing.[8] Second, there is a significant difference between relaxation of singlet and triplet states as the latter is formally spin-forbidden in quantum theory. Finally, the rules that govern the generation of triplet states are not well articulated. Historically, much emphasis has been given to the structural and electronic effects that maximize quantum yield,[9] but the manipulation of ISC to generate triplet states has only recently attracted attention due to the potential applications of triplet states in photodynamic therapy (PDT),[10] solar energy harvesting,[11] phosphorescence spectroscopy[12] and triplet-triplet annihilation up-conversion.[13]

One of the best known mechanisms to promote triplet state formation, particularly for metal complexes, is the spin-orbit coupling effect (SOC).[8] SOC can be rationalised considering the electron as a relativistic object.[14] In the frame of reference of the electron, the nucleus will generate an electric field due to its charge and a magnetic field due to its orbital motion.[15] Figure 2.[16] The magnitude of the field depends on the effective nuclear charge and the electric field of the nucleus.[17] In other words, the SOC interaction will be more intense in heavier atoms than in light ones.
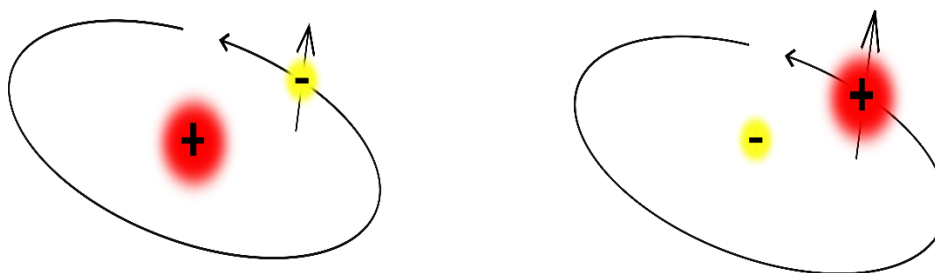
Figure 2 *Spin–orbit coupling. Left, from the nucleus' point of view, there is only an electric interaction between itself and the electron. Right, from the electron's point of view the motion of the nucleus produces a magnetic field.*

The SOC effect facilitates the transition between singlet and triplet states (intersystem crossing). In fact, if we consider this kind of systems as Born-

Oppenheimer ones, there is no essential difference between internal conversion (IC) and ISC in energetic terms.[18] It is worth noting that SOC effect is especially strong in atoms heavier than Cu or Ag,[19,20] and more importantly, ISC competes with fluorescence, when ISC occurs the fluorescence quantum yield decreases.[21]

In the case of molecules possessing only light atoms the most widely accepted concept is that IC is much faster than the ISC (formally forbidden). However, there are some examples suggesting that ISC rates might be higher than previously expected. In a study using Xanthone, it was observed that the triplet state formation was an ultrafast process happening in the timescale of 1.5 ps.[22–24] The formation of triplet states in 1-nitronaphthalene was observed on the timescale of 200 femtoseconds[22–24] For these kinds of system, SOC plays a minor role in terms of promoting ISC. However, it has been observed that, when two electronic states have a different multiplicity but are energetically close, the transition from one state to the other might not require the aid of a heavy atom.[18]

SOC dominates in metallic complexes. These molecules have helped establish the characteristics of a triplet photosensitizer, namely, long-lived triplet states, large Stokes shifts, high extinction coefficient, absorption of visible light, and effective ISC that leads to high triplet state quantum yields.[25–28] These are, as a consequence, the desirable properties of equivalent organic sensitizers. Metal complexes have been extensively used to produce and exploit triplet states in several applications from photodynamic therapy to solar energy harvesting. The most common elements studied for these applications are Ru,[27,29] Pd,[30–32] Pt,[33,34] and Os.[35,36]

However, as effective as they are, metallic complexes have some drawbacks. The most noteworthy are the potential dark toxicity in biological applications[37,38]

and the high cost of using precious metals such as Pt or Ru Au.[39–42] In addition, the quantum yield and lifetimes decrease as the wavelength increases due to the energy gap law.[43] All of this makes some metallic complexes impractical for certain applications.[44]

For fully organic fluorophores, there are other effects that could promote the generation of triple state such as vibrational contributions and even spin-spin coupling.[45] To this day, however, reliably predicting triplet state population during the design phase of a molecule is still challenging because the parameters that dictate efficiency of triplet crossover although long-known are difficult to predict.[13] Research in room temperature phosphorescence of fully organic molecules has provided details on how ISC/ triplet states are formed and how they can be amplified in the absence of metallic atoms. As a consequence, there is an increasing number of reports in the domain of heavy-atom-free sensitizers.[41,44,46,47]

1.1.3 Triplet state generation by charge transfer

One of the most promising approaches to encourage triplet state formation in metal free sensitizers, in absence of SO coupling, is the incorporation of charge transfer (CT) dyads into the structure of a fluorophore. The donor-acceptor array (D-A) can be both inter or intra molecular. In both cases, excited electrons are transferred from one molecule, or part of the molecule, to the other.[48] **Figure 3**.
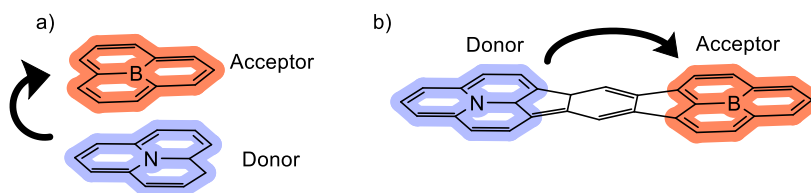
Figure 3 Intermolecular (a) vs intramolecular (b) charge transfer.

Charge transfer is followed by charge recombination (CR) which can occur through fluorescence.[49] Charge recombination is generally spin-selective, and singlet states are formed preferentially over triplet states.[50] It has been observed, however, that charge recombination can, in some cases, help generate triplet states. [51–53]

CR-induced ISC can occur in donor-acceptor dyads separated by a long and rigid linker. The separation helps reduce the electron exchange energy of the electrons in the frontier molecular orbitals significantly reducing the energy gap between singlet and triplet states.[54,55] The charge recombination induces a change in orbital angular momentum overcoming the selection rule. This allows the conservation of angular momentum.[56] Figure 4 (a).
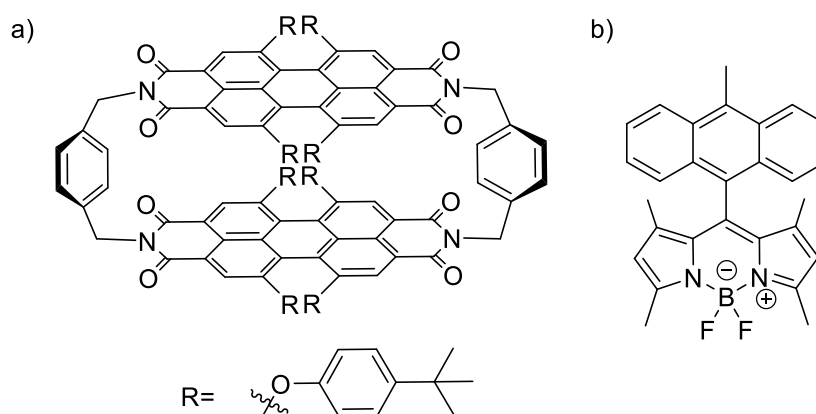
Figure 4 Example of fluorophores capable of generating triplet states via charge recombination (a) or via SOCT-ISC (b).

Triplet states can also be formed from singlet states when there is a radiationless transition that involves a change in the orbital type, the so-called El-Sayed's rule.[57,58] The rule states that the rates of conversion of $^1S(\pi, \pi^*) \rightarrow {}^3T(n, \pi^*)$ are generally higher than the $^1S(\pi, \pi^*) \rightarrow {}^3T(\pi, \pi^*)$ transitions, and that the $^1S(n, \pi^*) \rightarrow {}^3T(\pi, \pi^*)$ conversion is faster than the $^1S(n, \pi^*) \rightarrow {}^3T(n, \pi^*)$ transition.[59] The operation of this mechanism has been observed in BODIPY-polyaromatic

hydrocarbon dyads where the donor and acceptor moieties are very close to each other but orthogonally oriented in such a way that the π-conjugation is limited.[60,61] Figure 4 (b). Photoexcitation into a charge transfer state causes molecular orbital angular momentum changes generating the magnetic torque required to induce spin inversion. The phenomenon is called Spin Orbit Charge Transfer Inter System crossing (SOCT-ISC).[37] In most cases, the relative orientation of the donor/acceptor in the dyad has a significant impact on the spin selectivity of the ISC.[56,62,63] The same change in molecular orbital angular momentum compensates the spin change produced by the ISC so the total angular momentum will remain the same.[62]

The charge recombination process or the SOCT-ISC involving El-Sayed's rule can explain the formation of triplet states in molecules made only of light atoms such as the BODIPY-perylene conjugates prepared in this chapter.

After the formation of an excited triplet state by any of the mechanisms explained above, the next step in the TTA-UC process is the intermolecular energy transfer.

1.1.4 Dexter energy transfer

Energy transfer (ET) from one excited molecule, or molecular unit in a supramolecular system, typically occurs either via FRET or by Dexter mechanisms. Fluorescence or Föster resonance energy transfer (FRET) is a non-radiative energy transfer stimulated through dipole-dipole columbic coupling between the excited donor and the ground state of the acceptor.[64] Figure 5.
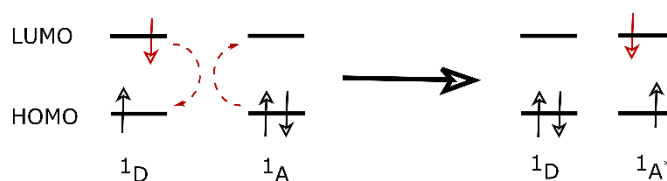
In contrast, the Dexter energy transfer is a non-radiative mechanism involving the concerted exchange of two electrons. The electrons can have the same spin (singlet-singlet)[65] of different spin (singlet-triplet).[66] Figure 6. It is important to notice that the Dexter triplet-triplet ET process generally should not violate the Wigner spin conservation rule.[67]
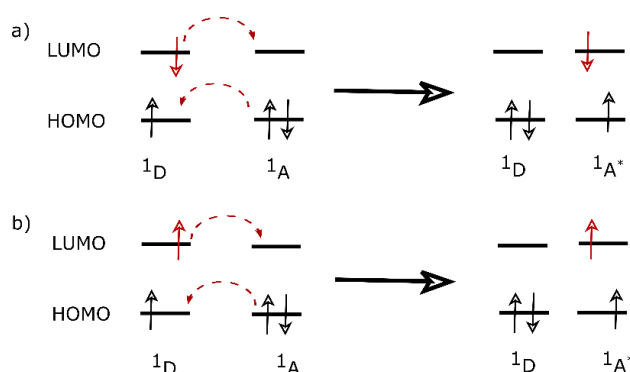
The Dexter mechanism is the energy transfer mechanism behind TTA-UC; it depends on the overlap of electronic wave functions of donor and acceptor so this mechanisms is only effective when the separation between donor and acceptor (D-A) is approximately 1 nm or less.[68] Current research suggests that spin-forbidden electronic triplet states can participate in energy transfer only by a Dexter mechanism. It seems that their low oscillator strengths render the energy transfer by a FRET mechanism inefficient.[69]

1.1.5 Biological applications of TTA-UC

Among the plethora of TTA-UC applications, sensing strategies are of significant potential value. They are, however, not among the most widely studied. Below some of the most interesting examples in the literature are outlined

As previously explained, TTA-UC requires two molecular partners. In molecular sensors, the sensing moiety can be on either sensitizer or annihilator. In this way, the up-conversion can be switch on and off by the presence or absence of the analyte and the annihilator. Figure 7. In this example, Chen and collaborators used up-conversion to detect F^{3+} ions. The sensitizer, whose properties remain nearly constant, can act as an internal reference to quantify the UC signal observed.[70]
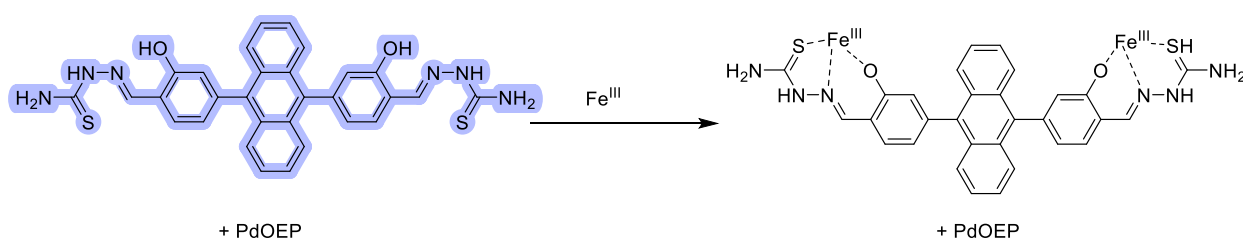
Figure 7 *Up-conversion-based ion sensing. The presence of Fe^{III} ions quenches the UC signal. PdOEP = palladium (II) octaethylporphyrin, the sensitizer.* [70]

Given that TTA-UC is a triplet state-mediated process, it is sensitive to oxygen quenching.[71] In fact, while this may offer a means of detecting oxygen in low oxygen environments, it is one of UC's main limitations in biological applications and researchers are actively trying to solve this problem.[72] A good example of how to put that sensitivity to use is the system developed Huang and coworkers. This system incorporates the glucose oxidase enzyme, which uses oxygen and glucose as part of its catalytic activity. The enzyme removes the oxygen from the solution and allows the TTA-UC to take place. This approach was successfully applied to

sense glucose in solution and in cell cultures. Figure 8. The sensitizer, a palladium porphyrin, and the annihilator, 2,5,8,11-tetra(tert-butyl)perylene were integrated in nanoparticles by the aid of an amphiphilic polymer.[32]
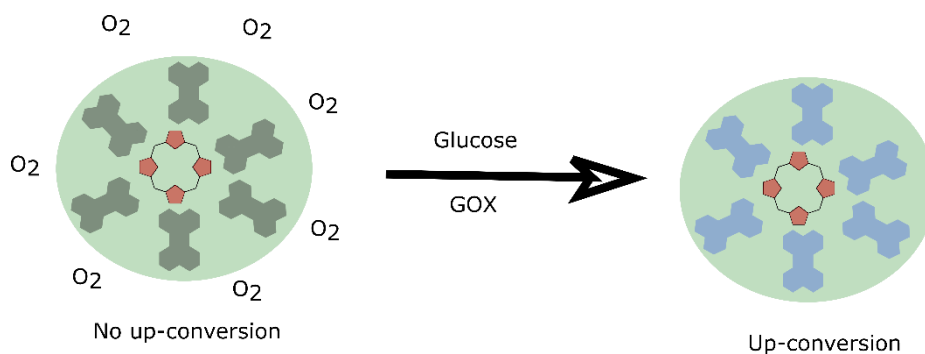
Figure 8 Up-conversion nanoparticles. The UC signals appears as soon as oxygen is consumed by the catalytic activity of glucose oxidase (GOX). [32]

In some rare cases, the sensitizer and the annihilator can be on the same molecule. A remarkable example is the Rhodamine-BODIPY conjugate that produces up-converted fluorescence at 745 nm when excited at 800 nm. The probe also showed a very high selectivity for Hg^+ ions.[73] (Figure 9.) The up-conversion mechanism would be worth studying as Rhodamine derivatives rarely show up-converting activity and could help develop heavy atom-free sensitizers.
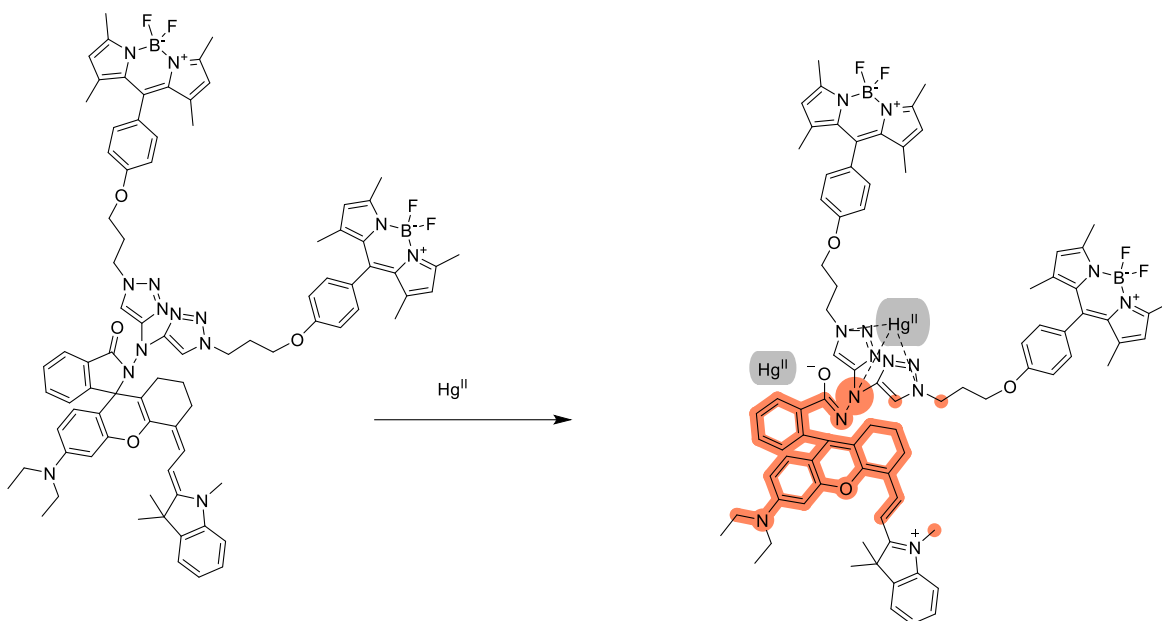
Figure 9 *Heavy atom-free UC-based sensor for Hg^{II} ions. The molecule possesses both sensitizer (BODIPY) and annihilator (rhodamine).* [73]

Up-conversion is a diffusion-controlled process, meaning it works better in solution. Nevertheless, a recent study shows some progress towards the development of a solid-state TTA-UC system by using polymeric sensitizers. (Figure 10). In this instance, the polymeric metallic complex acts as a macromolecular sensitizer that can be embedded in a solid matrix.[74]
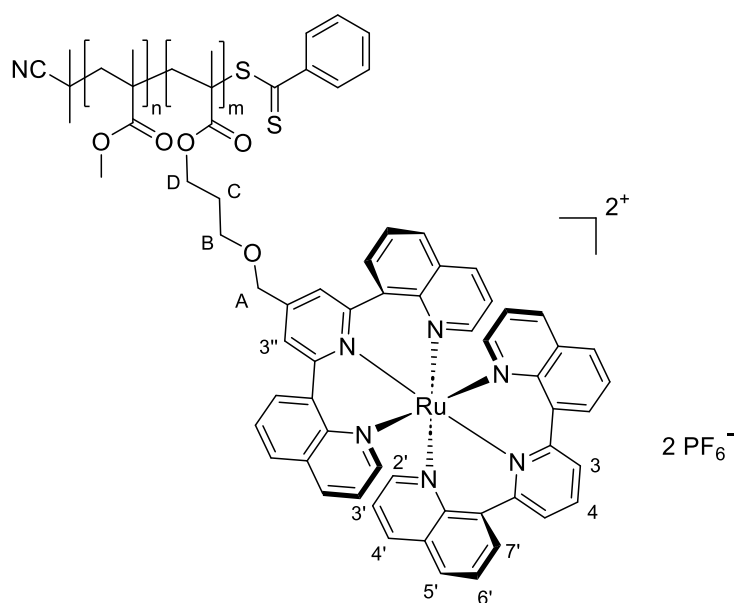
Figure 10 *Polymethyl methacrylate ruthenium-based sensitizer used in TTA-UC systems with diphenylanthracene as annihilator.* [74]

As observed so far, there are a wide variety of molecular structures and sensitizer/annihilator pairs. We will focus now in the extensively studied field of BODIPY dyes, as they constitute a particularly useful kind of chromophores and one of the main foci of this thesis.

1.1.6 Singlet oxygen and its biological applications

One important application of triplet sensitizers is the potential of these molecules to generate singlet oxygen. Such molecules are of great interest because they can be used as photodynamic therapy (PDT) agents. In this section, some of the characteristics of the PDT will be described as well as the characteristics of the PDT agents approved for medical use.

1.1.6.1 Singlet oxygen and photodynamic therapy

Ground state molecular oxygen is one of the few molecules that exist in a triplet electronic state. Singlet oxygen can be generated by chemical and photophysical processes. It is a very reactive molecule found in the upper parts of the atmosphere and as an air pollutant in cities.[75] Singlet oxygen is a very reactive molecule having a number of applications in organic chemistry because of its very strong oxidising capabilities.[76,77] In biology, singlet oxygen is one of several biologically important reactive oxygen species applied in labelling of proteins,[78] DNA cross-linking,[79] but, perhaps more abundantly, in the field of photodynamic therapy (PDT).[80]

PDT is a light activated modality in which a photosensitizer (PS) of low toxicity, on irradiation by light, activates molecular oxygen to produce a cytotoxic effect. Ideally, the exciting wavelength should be visible or, particularly, red due to its better capacity to penetrate tissues. In type I PDT free radicals are generated

(hydroxy, superoxide, peroxynitrite) whereas in type II PDT singlet oxygen is the main responsible for the cell damage. Figure 11.[81]
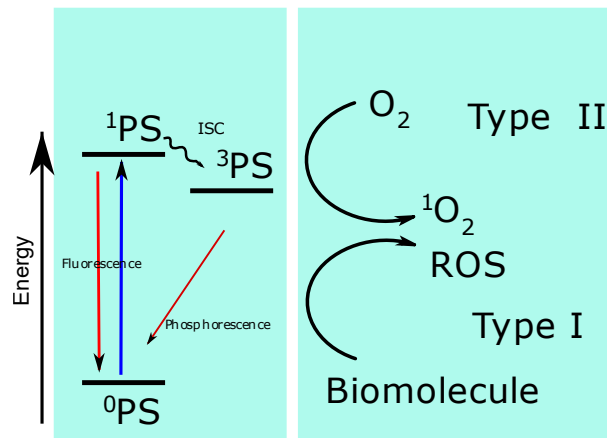
Figure 11 PDT mechanisms, type I generates ROS type II generates singlet oxygen.

PDT mechanisms are not mutually exclusive and a single sensitizer may generate one or more products depending on the molecular structure, the light that reaches the tissue, and oxygen availability.[80,82] In both types, the damage produced by the reactive species generated after photoexcitation provokes cell necrosis or apoptosis.[83]

1.1.6.2 PDT photosensitizers

A good PDT photosensitizer should have good photostability, a high extinction coefficient at red or near infrared wavelengths and, critically, for type II PDT, have a long-lived triplet state energetic enough to transfer that energy to another molecule.[84] As a general rule, PSs with triplet energies in excess of 1 eV have the capacity to excite oxygen to its singlet, more energetic, state. However, when the energy of the triplet state is below 0.95 eV, the molecules can act as oxygen quenchers.[85]

By the end of the 1990's, there were already some porphyrin-based PDT agents commercially available and FDA approved for use treating certain types of lung cancers.[86–88] More recently, PDT agents have been approved for certain types of head, neck, biliary track cancers as well as for some dermatological conditions.[89] Nonetheless, the number of FDA approved PDT agents remains very modest.[90]

Most of the successful PDT agents are based on the porphyrin and phthalocyanine rings. These kinds of molecules present some disadvantages, as some of them have high dark toxicity and poor photostability.[91,92] There has been much interest in developing metallic complexes as potential PDT agents. The capacity of heavy metal centres to generate triplet states has been the main incentive. There are examples in literature with cobalt, ruthenium, platinum, to name a few. However, very few of these molecules have reached clinical trial to date.[93–95]

1.2 Viscosity sensing

One of the main goals of the research proposed in this thesis was to prepare molecules capable of sensing one or more variables in a cellular environment. The cell lines targeted at the beginning of the project were endothelial cells. Sensing viscosity was the first approach given that these parameter plays a key role in the vascular function. In this section, the role that viscosity has on the cytoplasmic and cell membrane will be explained as well as its importance as a disease marker.

1.2.1 Impact of viscosity in the cell function

Viscosity is one of the key factors regulating a eukaryotic cell's microenvironment. The viscosity across cytosol, membranes, and extracellular medium of cells plays a critical role in the regulation of chemical reactions. The viscosity of the membrane, for example, will affect diffusion-based processes

including signalling, raft formation, ion channels, and protein-protein interactions.[96,97] The viscosity of the cell varies enormously across the membrane, the cytosol, and the organelles, it can go from 1 cp (centipoise) to 400 cp.[98] Even if we consider only the viscosity of the membrane, there are significant differences; artificial membrane models show viscosities between 70-120 cp, human epidermis cell membranes have been found to have a viscosity of 30-100 cp and liver cells membranes shoes values between 108-217 cp.[99–101] For comparison, the viscosity of water is 0.890 cp at 25 °C.[102]

The ensemble of effects that controls either cytoplasmic or membrane viscosity is not yet fully understood. Some studies in prokaryotic cells suggest that cytoplasmic viscosity depends on temperature and energy availability. When one of this factors changes, trehalose and glycogen are synthesised to keep stable the diffusion inside the cell in a regulated process called viscoadaptation.[103] In human cells, research suggests that cytoplasmic cell viscosity is conserved at constant levels in most human cells indicating that it is a capital parameter for the cell function.[104,105] When it comes to the cell membrane, the viscosity depends significantly on the way an organism regulates its temperature. In ectothermic organism, membrane viscosity is directly affected by temperature and regulated by modifying the lipid composition of the membrane; saturated lipids are more tightly packed and produce higher viscosities, whereas unsaturated lipids are less orderly packed and are responsible for low viscous membranes.[106,107] In mammals, the effects of temperature are negligible, but the membrane composition and fluidity highly depend on dietary lipid consumption.[108,109] The fact that viscosity of the membrane tends to be constant and that many cellular processes require a constant

viscosity indicates that there are mechanism responsible for the homeostasis of this variable.[110]

Given the importance of the cell membrane, it not surprising that abnormal values of membrane, cytoplasm, or mitochondrial viscosity have been related to diseases. It has been observed that cell viscosity can be a marker for cancer related-inflammation.[111–116] In addition, abnormally high viscosities have been linked to certain insulin-resistant conditions.[117,118] An increased viscosity of the platelets' membrane could represent a higher risk of Alzheimer's.[119] Finally, deregulation of the membrane's viscosity could be involved in the development of cardiovascular diseases such as atherosclerosis.[120,121]

1.2.2 Sensing viscosity by fluorescence spectroscopy

Fluorescence spectroscopy is a powerful tool to study variation in the cell viscosity and its organelles. An important range of fluorescence sensors has been developed to try to understand the cell's microenvironment and its relationships with transport, metabolism, and other intra and extra cellular interactions.[112,122,123] There are reports of molecular probes used to measure viscosity and do imaging of mitochondria and lysosomes in living cells,[98,124] and even in living organisms such as Zebra fish and mice.[125,126]

Organelle targeting can be implemented with judicious selection of the functional group. For example, lysosomal targeting fluorescent probes tend to have a morpholine substituent,[127] whereas mitochondrial targeting molecules tend to be positively charged, e.g., through introduction of a quaternary nitrogen atom or triphenylphosphine.[128] Shown in Figure 12(a) is a viscosity sensor designed to include two morpholine units. It is likely that the molecule will accumulate in the acidic lysosomal regions because morpholine is a weak base. The probe shows a linear relationship between viscosity and fluorescence intensity making this molecule an intensity-based probe. Figure 12(b), the use of an indolium derivative allows the probe to accumulate selectively in mitochondria, and despite the presence of a phenol, the probe seems to be stable across pH values from 4 to 10. The lifetime changes were not reported so it is likely that this molecule is also only and intensity-based sensor. As seen in these examples, fluorescent probes must have an elevated number of degrees of rotational freedom, an essential property for viscosity sensors.[112,125]
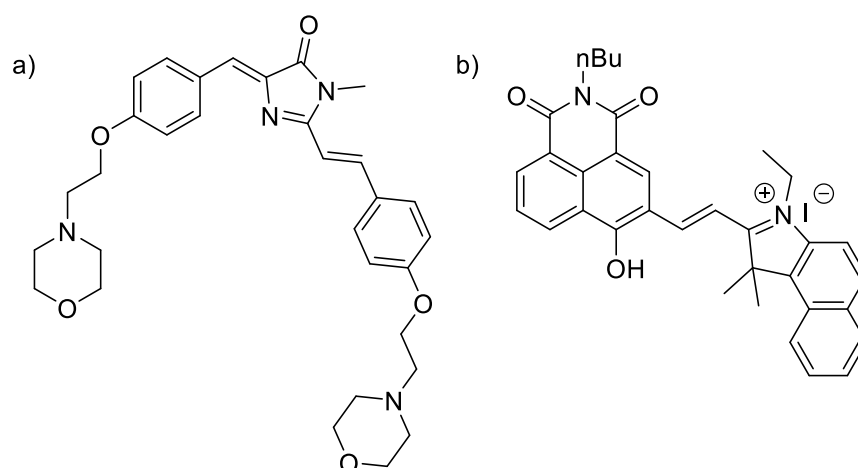
Figure 12 Examples of lysosome- (a) and mitochondria-targeting (b) viscosity sensors. [112,125]

1.2.3 Intensity vs lifetime-based sensors

When it comes to applying molecular rotors to sensing applications, there are generally three kinds of sensors, intensity-based, ratiometric, and lifetime-based sensors. Intensity-based sensors directly link the emission intensity of the probe to a property of the environment such as pH, viscosity, temperature etc. This is very effective in homogenous solution; however, in cellular and subcellular media there is a significant lack of homogeneity. Consequently, uptake of the probe and its distribution depend highly on its physicochemical properties but also in its interactions with intracellular structures. This could make, for example, one dye highly accumulate in a place with low viscosity increasing the fluorescence of that point giving the false impression that there is a high viscosity in that region.[129] A way to overcome this problem is ratiometric probes. For these sensors, changes in fluorescence intensity of the probe are ratioed to a non-viscosity sensitive reference permitting quantification of the response, as a mathematical relationship between fluorescence intensity and viscosity can be determined.[130] The synthesis of this

molecules tends to be more challenging as it is required that some parts of the molecule generate a distinct emission band that remains unchanged.

Another way to remediate the intensity-based problem is using lifetime-based molecular sensors as the emission lifetime of a probe is generally independent of the concentration. However, to act as a good viscosity sensor, the lifetime of a molecule needs to be sensitive to changes in the viscosity (or other property) of the medium. Typically, this is due to the contribution of moiety rotation on the non-radiative decay rate of the molecule. Furthermore, as lifetime imaging is available (Fluorescence Lifetime Imaging Microscopy, FLIM) the distribution of lifetime, e.g., across a cell can be used to understand spatial viscoelastic changes in a cell, and such dyes have wide potential applications.[131] Yet, both methods, ratiometry and lifetime are not mutually exclusive. There are increasing examples that exploit both approaches in areas such as oxygen,[132] viscosity,[133,134] and temperature sensing. Figure 13. [135]
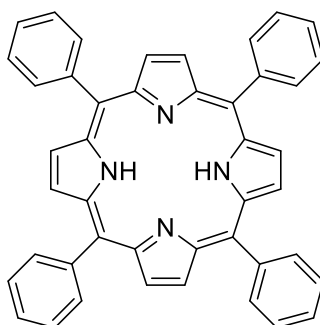
Figure 13 *Tetraphenylporphyrin used as a ratiometric and lifetime-based optical temperature probe.* [135]

1.2.4 Molecular rotors and their sensing mechanism

For a viscosity sensor to work, the fluorescence intensity or lifetime must change proportionally as the viscosity of the medium changes.[112,122] The most widely applied strategy to sense viscosity is to develop molecules that combine two functional groups, moieties or fluorophores by at least one single bond to create a so called molecular rotor. One of the key factors responsible for the viscosity sensitivity is that rotation of the fluorophores around the single bond(s) contributes as a pathway to non-radiative decay, supressing emission and decreasing lifetime in non-viscous media and increasing emission intensity and lifetime in high viscous environments.

Another effect responsible for the viscosity sensitivity is the strong electronic interaction between the two fluorophores. In fact, most rotors reported to date as viscosity sensors have twisted intramolecular charge transfer (TICT) states.[136,137] It is the promotion or quenching of this effect that makes molecular rotors particularly sensitive to changes in polarity and viscosity of the medium.[138] Generally, the molecules of a solvent with a high dielectric constant will be reoriented when surrounding an excited fluorescent dye. Some of the fluorophore's energy will be transferred to these molecules affecting the emission features (bathochromic effect).[138]

Some of the most helpful sensors are off/on probes.[139] These molecules show very low emission intensities in low viscous media but high emission intensity and a larger Stokes shift in viscous media. In some cases, such as the example below, the off/on change is so drastic that visual detection can be used to assess the properties of the tested sample.(Figure 14).[140] This molecule is an intensity-based probe and was used to visually determine the decomposition of food. The

emission bands observed in viscous and non-viscous samples are different enough to distinguish a viscous (spoiled) solution from a non-viscous one (fresh).
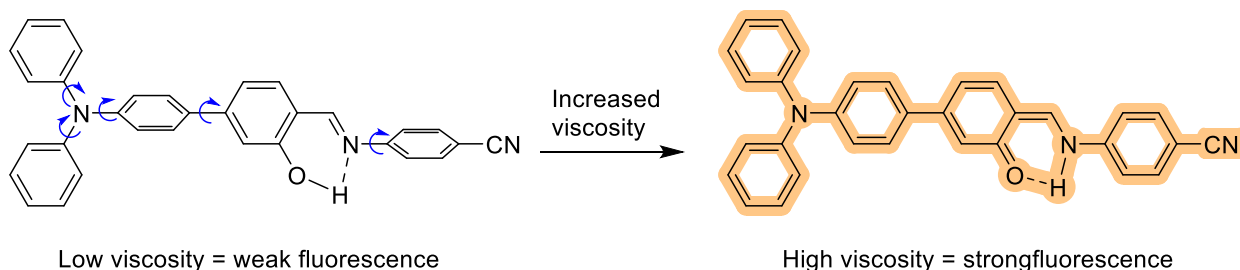
Figure 14 Example of a molecular rotor. The fluorescence intensity is very weak in a low viscosity environment and strong in a high viscosity medium.[140]

1.2.5 BODIPYs as viscosity sensors

BODIPYs have been quite widely explored as molecular rotors and viscosity sensors. In most reports, the BODIPY moiety is typically part of a TICT complex which is, in part, responsible for the viscosity sensitivity. The other features responsible for the viscosity sensitivity are the substituents on the BODIPY and its electronic and steric characteristics.[141,142] For example, highly electron withdrawing groups have been found to increase the viscosity sensitivity of BODIPYs. (Figure 15 a and b). Research suggests that the electron-withdrawing group decreases the energy required for rotation in the excited state and this gives the probe the capacity of sensing solutions with very high viscosities (up to 50 000 cp).[143] When it comes to sterically modulating the viscosity sensitivity, modifying the number of methyl (or phenyl) groups on positions 1 and 7 of the BODIPY core, seems the best option. In fact, the number of bulky groups at these positions is related to the viscosity range in which a BODIPY can act as viscosity sensor. (Figure 15 c).[133]

22
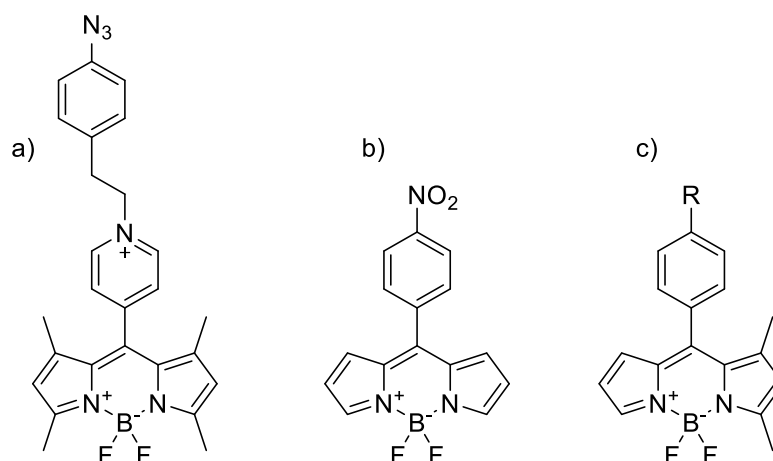
Figure 15 *Examples of BODIPY-based viscosity sensors. Viscosity sensitivity comes from the modification of the aryl group on position 8 (a and b) or the methyl groups at position 1 or 7 (c).*

As explained above, morpholine can act as a lysosome targeting unit. In the example below, introducing morpholine to BODIPY through a simple reductive amination was an effective way to increase the accumulation of the probe in lysosomes (Figure 16).[144]
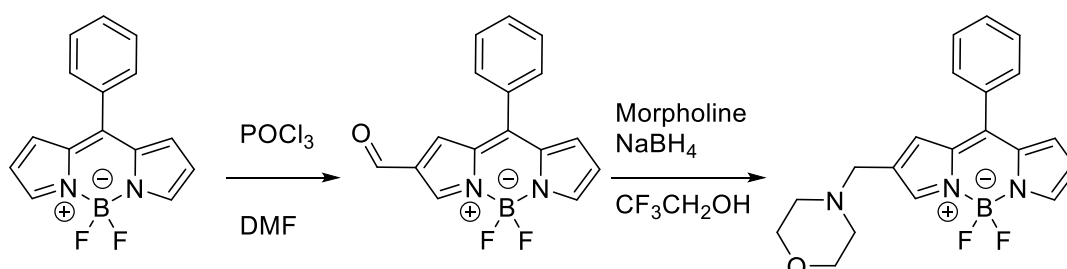
Figure 16 *Functionalisation of a BODIPY with a morpholine substituent, a lysosomal-targeting group.* [144]

Increasing the viscosity sensitivity can be done by modulating the rotational freedom of a molecule. One very common way of achieving this is via the Knoevenagel condensation. The double bond introduced by this reaction increases conjugation and the resulting molecules will have two chromophores separated by a set of single-double-single bonds. The properties of the molecule will depend on the orientation of both chromophores around the main double bond which is a function of the viscosity of the medium.[145,146] (Figure 17 a and b). Extending the

23

conjugation, by functionalising positions 2 and 6 of the BODIPY core, is less common but there are some examples that include the addition of triple bonds through a Sonogashira reaction [147,148] (Figure 17 c) or the addition of a double bond using the same Knoevenagel reaction after a formylation step.[149]
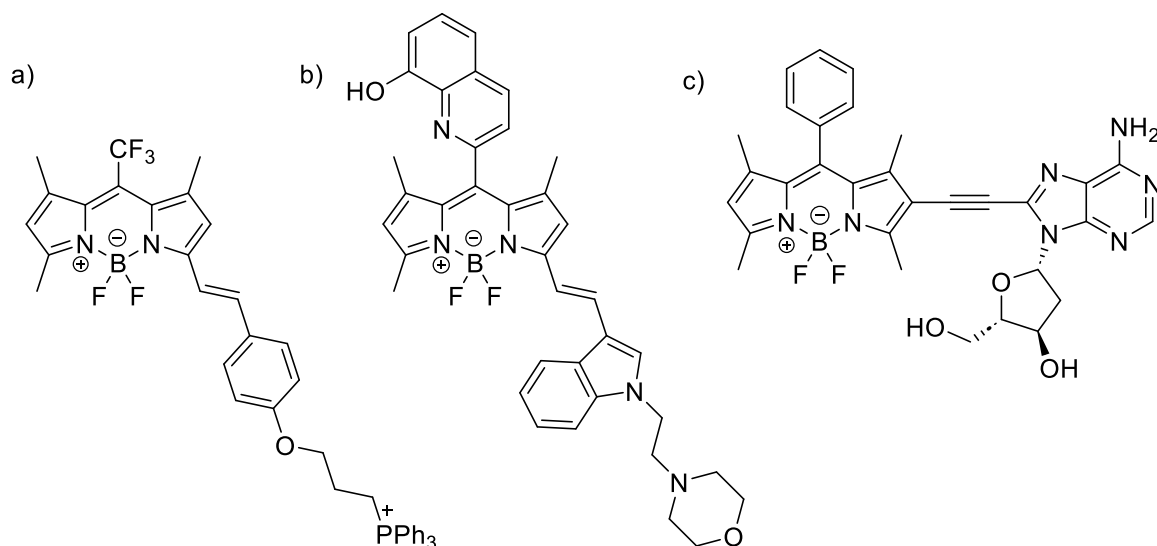
Figure 17 (a and b) BODIPY-based viscosity sensors prepared using the Knoevenagel reaction. They possess mitochondria (a) and lysosome (b) targeting moieties. (c) RNA targeting viscosity sensor.

Although there is a growing number of viscosity sensors reported, some challenges remain. For example, there is a need to develop probes that can track the crowding of proteins and macromolecules inside the cell or measure the viscoelasticity of the cells.[150] The viscosity of the extracellular fluid is also a key factor that remains understudied, but that could have significant consequences in diseases such as cancer.[151] Finally, there are chemical, biological and photophysical properties often hard to predict when designing a sensor. It is difficult to predict the magnitude of the response to viscosity and the systematic behaviour. In addition, there are changes in fluorescence emission that might not be due viscosity but that overlap with the viscosity response, and, there are uptake and toxicity parameters that are important and often not considered when characterising and calibrating a dye only in solution.[152]

1.2 References

[1]   *Proc. R. Soc. Lond. A* **1963**, *276*, 125–135.

[2]   T. N. Singh-Rachford, F. N. Castellano, *Coord. Chem. Rev.* **2010**, *254*, 2560–2573.

[3]   K. Kwon, T. Son, K.-J. Lee, B. Jung, *Lasers. Med. Sci.* **2009**, *24*, 605–615.

[4]   C. Ash, M. Dubec, K. Donne, T. Bashford, *Lasers. Med. Sci.* **2017**, *32*, 1909–1918.

[5]   Q. le Masne de Chermont, C. Chanéac, J. Seguin, F. Pellé, S. Maîtrejean, J.-P. Jolivet, D. Gourier, M. Bessodes, D. Scherman, *Proc. Natl. Acad. Sci. U.S.A.* **2007**, *104*, 9266–9271.

[6]   D. Chatterjee, A. Rufaihah, Y. Zhang, *Biomater.* **2008**, *29*, 937–943.

[7]   X. Xiao, W. Tian, M. Imran, H. Cao, J. Zhao, *Chem. Soc. Rev.* **2021**, *50*, 9686–9714.

[8]   C. Karunakaran, M. Balamurugan, in *Spin Resonance Spectroscopy, Principles and Applications*, Elsevier Inc., Berkeley. **2018**, pp. 215–216.

[9]   Z. Lou, Y. Hou, K. Chen, J. Zhao, S. Ji, F. Zhong, Y. Dede, B. Dick, *J. Phys. Chem. C* **2018**, *122*, 185–193.

[10]   T. Takemura, N. Ohta, S. Nakajima, I. Sakata, *Photochem. Photobiol.* **1989**, *50*, 339–344.

[11]   V. Gray, D. Dzebo, M. Abrahamsson, B. Albinsson, K. Moth-Poulsen, *Phys. Chem. Chem. Phys.* **2014**, *16*, 10345–10352.

[12]   M. E. Díaz-García, A. Fernández-González, R. Badía-Laíño, *App. Spectrosc. Rev.* **2007**, *42*, 605–624.

[13]   S. K. Lower, M. A. El-Sayed, *Chem. Rev.* **1966**, *66*, 199–241.

[14]   P. A. M. Dirac, *Proc. R. S. Lond.* **1928**, *117*, 610–624.

[15]   P. Pyykkö, *Annu. Rev. Phys. Chem.* **2012**, *63*, 45–64.

[16]   M. Chapman, C. S. de Melo, *Nature* **2011**, *471*, 41–42.

[17]   J. MacLaren, in *Magnetic Interactions and Spin Transport* (Eds.: A. Chtchelkanova, S. Wolf, Y. Idzerda), Springer US, Boston, MA, **2003**, pp. 131–184.

[18]   C. M. Marian, *WIREs Comput Mol Sci* **2012**, *2*, 187–203.

[19]   P. Pyykko, *Chem. Rev.* **1988**, *88*, 563–594.

[20]   B. J. R. Cuyacot, J. Novotný, R. J. F. Berger, S. Komorovsky, R. Marek, *Chem. Eur. J.* **2022**, *28*, DOI 10.1002/chem.202200277.

[21]   E. A. Gastilovich, N. V. Korol'kova, V. G. Klimenko, R. N. Nurmukhametov, *Opt. Spectrosc.* **2008**, *104*, 491–494.

[22]   C. Reichardt, R. A. Vogt, C. E. Crespo-Hernández, *J. Chem. Phys.* **2009**, *131*, 224518.

[23]   J. J. Cavaleri, K. Prater, R. M. Bowman, *Chem. Phys. Lett.* **1996**, *259*, 495–502.

[24]   H. Satzger, B. Schmidt, C. Root, W. Zinth, B. Fierz, F. Krieger, T. Kiefhaber, P. Gilch, *J. Phys. Chem. A* **2004**, *108*, 10072–10079.

[25]   J. Zhao, S. Ji, W. Wu, W. Wu, H. Guo, J. Sun, H. Sun, Y. Liu, Q. Li, L. Huang, *RSC Adv.* **2012**, *2*, 1712–1728.

[26]   A. Chettri, H. D. Cole, J. A. Roque III, K. R. A. Schneider, T. Yang, C. G. Cameron, S. A. McFarland, B. Dietzek-Ivanšić, *J. Phys. Chem. A* **2022**, *126*, 1336–1344.

[27]   C. S. Burke, A. Byrne, Tia. E. Keyes, *J. Am. Chem. Soc.* **2018**, *140*, 6945–6955.

[28]   C. S. Burke, T. E. Keyes, *RSC Adv.* **2016**, *6*, 40869–40877.

[29]   M. Lin, S. Zou, X. Liao, Y. Chen, D. Luo, L. Ji, H. Chao, *Chem. Commun.* **2021**, *57*, 4408–4411.

[30]   X.-Q. Zhou, M. Xiao, V. Ramu, J. Hilgendorf, X. Li, P. Papadopoulou, M. A. Siegler, A. Kros, W. Sun, S. Bonnet, *J. Am. Chem. Soc.* **2020**, *142*, 10383–10399.

[31]   F.-R. Dai, Y.-C. Chen, L.-F. Lai, W.-J. Wu, C.-H. Cui, G.-P. Tan, X.-Z. Wang, J.-T. Lin, H. Tian, W.-Y. Wong, *Chem. Asian J.* **2012**, *7*, 1426–1434.

[32]   L. Huang, T. Le, K. Huang, G. Han, *Nat Commun* **2021**, *12*, 1898.

[33]   Y. Wang, X. Shi, H. Fang, Z. Han, H. Yuan, Z. Zhu, L. Dong, Z. Guo, X. Wang, *J. Med. Chem.* **2022**, *65*, 7786–7798.

[34]   G. Li, M. F. Mark, H. Lv, D. W. McCamant, R. Eisenberg, *J. Am. Chem. Soc.* **2018**, *140*, 2575–2586.

[35]   J. A. Roque, P. C. Barrett, H. D. Cole, L. M. Lifshits, G. Shi, S. Monro, D. von Dohlen, S. Kim, N. Russo, G. Deep, C. G. Cameron, M. E. Alberto, S. A. McFarland, *Chem. Sci.* **2020**, *11*, 9784–9806.

[36]   S. Lazic, P. Kaspler, G. Shi, S. Monro, T. Sainuddin, S. Forward, K. Kasimova, R. Hennigar, A. Mandel, S. McFarland, L. Lilge, *Photochem. Photobiol.* **2017**, *93*, 1248–1258.

[37]   K. Chen, I. V. Kurganskii, X. Zhang, A. Elmali, J. Zhao, A. Karatay, M. V. Fedin, *Chem. Eur. J.* **2021**, *27*, 7572–7587.

[38]   S. Monro, K. L. Colón, H. Yin, J. Roque, P. Konda, S. Gujar, R. P. Thummel, L. Lilge, C. G. Cameron, S. A. McFarland, *Chem. Rev.* **2019**, *119*, 797–828.

[39]   S. Goel, F. Chen, W. Cai, *Small* **2014**, *10*, 631–645.

[40]   D. Diaz-Diestra, H. M. Gholipour, M. Bazian, B. Thapa, J. Beltran-Huarac, *Nanoscale Res Lett* **2022**, *17*, 33.

[41]   M. Uji, N. Harada, N. Kimizuka, M. Saigo, K. Miyata, K. Onda, N. Yanai, *J. Mater. Chem. C* **2022**, *10*, 4558–4562.

[42]   N. T. Nassar, *Green Chem.* **2015**, *17*, 2226–2235.

[43]   Z. Murtaza, P. Herman, J. R. Lakowicz, *Biophys. Chem.* **1999**, *80*, 143–151.

[44]   S. R. Pristash, K. L. Corp, E. J. Rabe, C. W. Schlenker, *ACS Appl. Energy Mater.* **2020**, *3*, 19–28.

[45]   C. M. Marian, *Annu. Rev. Phys. Chem.* **2021**, *72*, 617–640.

[46]   S. Ji, J. Ge, D. Escudero, Z. Wang, J. Zhao, D. Jacquemin, *J. Org. Chem.* **2015**, *80*, 5958–5963.

[47]   S. Duman, Y. Cakmak, S. Kolemen, E. U. Akkaya, Y. Dede, *J. Org. Chem.* **2012**, *77*, 4516–4527.

[48]   F.-W. Gao, R.-L. Zhong, H.-L. Xu, Z.-M. Su, *J. Phys. Chem. C* **2017**, *121*, 25472–25478.

[49]   A. Nano, R. Ziessel, P. Stachelek, A. Harriman, *Chem. Eur. J.* **2013**, *19*, 13528–13537.

[50]   S. V. Feskov, V. A. Mikhailova, A. I. Ivanov, *J. Photochem. Photobiol. C.* **2016**, *29*, 48–72.

[51]   T. Kircher, H.-G. Löhmannsröben, *Phys. Chem. Chem. Phys.* **1999**, *1*, 3987–3992.

[52]   D. J. Gibbons, A. Farawar, P. Mazzella, S. Leroy-Lhez, R. M. Williams, *Photochem. Photobiol. Sci.* **2020**, *19*, 136–158.

[53]   Z. E. X. Dance, Q. Mi, D. W. McCamant, M. J. Ahrens, M. A. Ratner, M. R. Wasielewski, *J. Phys. Chem. B* **2006**, *110*, 25163–25173.

[54]   E. A. Weiss, M. A. Ratner, M. R. Wasielewski, *J. Phys. Chem. A* **2003**, *107*, 3639–3647.

[55]   P. Spenst, R. M. Young, M. R. Wasielewski, F. Würthner, *Chem. Sci.* **2016**, *7*, 5428–5434.

[56]   M. Imran, A. A. Sukhanov, Z. Wang, A. Karatay, J. Zhao, Z. Mahmood, A. Elmali, V. K. Voronkova, M. Hayvali, Y. H. Xing, S. Weber, *J. Phys. Chem. C* **2019**, *123*, 7010–7024.

[57]   M. A. El-Sayed, *J. Chem. Phys.* **1974**, *60*, 4502–4507.

[58]   M. A. El-Sayed, *Acc. Chem. Res.* **1968**, *1*, 8–16.

[59]   Y. Beldjoudi, A. Atilgan, J. A. Weber, I. Roy, R. M. Young, J. Yu, P. Deria, A. E. Enciso, M. R. Wasielewski, J. T. Hupp, J. F. Stoddart, *Adv. Mater.* **2020**, *32*, 2001592.

[60]   J. T. Buck, A. M. Boudreau, A. DeCarmine, R. W. Wilson, J. Hampsey, T. Mani, *Chem* **2019**, *5*, 138–155.

[61]   H. van Willigen, G. Jones, M. S. Farahat, *J. Phys. Chem.* **1996**, *100*, 3312–3316.

[62]   Z. E. X. Dance, S. M. Mickley, T. M. Wilson, A. B. Ricks, A. M. Scott, M. A. Ratner, M. R. Wasielewski, *J. Phys. Chem. A* **2008**, *112*, 4194–4201.

[63]   Z. Wang, J. Zhao, *Org. Lett.* **2017**, *19*, 4492–4495.

[64]   J. R. Lakowicz, Ed., in *Principles of Fluorescence Spectroscopy*, Springer US, Boston, MA, **2006**, pp. 443–475.

[65]   D. L. Dexter. *J. Chem. Phys.* **1953**, *21*, 836–850.

[66]   Z.-Q. You, C.-P. Hsu, G. R. Fleming, *The Journal of Chemical Physics* **2006**, *124*, 044506.

[67]   M. W. Schmidt, E. K. C. Lee, *J. Am. Chem. Soc.* **1970**, *92*, 3579–3586.

[68]   S. V. Gaponenko, H. V. Demir, in *Applied Nanophotonics*, Cambridge University Press, Cambridge, **2018**, pp. 210–226.

[69]   A. Köhler, H. Bässler, *Mater. Sci. Eng.: R.* **2009**, *66*, 71–109.

[70]   S. Chen, F. Chen, P. Han, C. Ye, S. Huang, L. Xu, X. Wang, Y. Song, *RSC Adv.* **2019**, *9*, 36410–36415.

[71]   F. Wilkinson, D. J. McGarvey, A. F. Olea, *J. Phys. Chem.* **1994**, *98*, 3762–3769.

[72]   S. H. C. Askes, S. Bonnet, *Nat. Rev. Chem.* **2018**, *2*, 437–452.

[73]   B. Shen, Y. Qian, Z. Qi, C. Lu, Y. Cui, *ChemistrySelect.* **2017**, *2*, 9970–9976.

[74]   K. K. Jha, A. Prabhakaran, C. S. Burke, M. Schulze, U. S. Schubert, T. E. Keyes, M. Jäger, B. D. Ivanšić, *J. Phys. Chem. C* **2022**, *126*, 4057–4066.

[75]   R. P. Wayne, in *Advances in Photochemistry* (Eds.: J.N. Pitts, G.S. Hammond, W.A. Noyes), Wiley, Oxford. **1969**, pp. 311–371.

[76]   C. Ye, Y. Zhang, A. Ding, Y. Hu, H. Guo, *Sci. Rep.* **2018**, *8*, 2205.

[77]   T. Montagnon, D. Kalaitzakis, M. Triantafyllakis, M. Stratakis, G. Vassilikogiannakis, *Chem. Commun.* **2014**, *50*, 15480–15498.

[78]   T.-L. To, K. F. Medzihradszky, A. L. Burlingame, W. F. DeGrado, H. Jo, X. Shu, *Bioorg. Med. Chem. Lett.* **2016**, *26*, 3359–3363.

[79]   N. De Laet, E. M. Llamas, A. Madder, *ChemPhotoChem.* **2018**, *2*, 575–579.

[80]   P. S. Maharjan, H. K. Bhattarai, *J. Oncol.* **2022**, *2022*, 1–20.

[81]   G. Calixto, J. Bernegossi, L. de Freitas, C. Fontana, M. Chorilli, *Molecules* **2016**, *21*, 342.

[82]   A. P. Castano, T. N. Demidova, M. R. Hamblin, *Photodiag. and Photodyn. Ther* **2004**, *1*, 279–293.

[83]   R. R. Allison, K. Moghissi, *Clin Endosc* **2013**, *46*, 24.

[84]   R. Fekrazad, A. Nejat, K. A. M. Kalhori, in *Nanostructures for Antimicrobial Therapy*, Elsevier. Berkeley. **2017**, pp. 237–259.

[85]   F. H. Quina, G. T. M. Silva, *J. Photochem. Photobiol.* **2021**, *7*, 100042.

[86]   K. Furuse, M. Fukuoka, H. Kato, T. Horai, K. Kubota, N. Kodama, Y. Kusunoki, N. Takifuji, T. Okunaka, C. Konaka, *Clin. Oncol.* **1993**, *11*, 1852–1857.

[87]   H. Kato, K. Furukawa, M. Sato, T. Okunaka, Y. Kusunoki, M. Kawahara, M. Fukuoka, T. Miyazawa, T. Yana, K. Matsui, T. Shiraishi, H. Horinouchi, *Lung Cancer* **2003**, *42*, 103–111.

[88]   J. Usuda, H. Kato, T. Okunaka, K. Furukawa, H. Tsutsui, K. Yamada, Y. Suga, H. Honda, Y. Nagatsuka, T. Ohira, M. Tsuboi, T. Hirano, *J. Thor. Oncol.* **2006**, *1*, 489–493.

[89]   P. Babilas, S. Schreml, M. Landthaler, R.-M. Szeimies, *Photodermatol. Photoimmunol. & Photomed.* **2010**, *26*, 118–132.

[90]   R. Baskaran, J. Lee, S.-G. Yang, *Biomater. Res.* **2018**, *22*, 25.

[91]   J. Ostapko, A. Gorski, J. Buczyńska, B. Golec, K. Nawara, A. Kharchenko, A. Listkowski, M. Ceborska, M. Pietrzak, J. Waluk, *Chem. Eur. J.* **2020**, *26*, 16666–16675.

[92]   G. F. Hassan, N. El Hoda Saad, M. Hmadeh, P. Karam, *Dalton Trans.* **2018**, *47*, 15765–15771.

[93]   M. Redrado, V. Fernández-Moreira, M. C. Gimeno, *ChemMedChem* **2021**, *16*, 932–941.

[94]   Y. Wu, S. Li, Y. Chen, W. He, Z. Guo, *Chem. Sci.* **2022**, *13*, 5085–5106.

[95]   C. B. Smith, L. C. Days, D. R. Alajroush, K. Faye, Y. Khodour, S. J. Beebe, A. A. Holder, *Photochem. Photobiol.* **2022**, *98*, 17–41.

[96]   P. Sashi, A. K. Bhuyan, *Biochem.* **2015**, *54*, 4453–4461.

[97]   R. Ghosh, A. Kushwaha, D. Das, *J. Phys. Chem. B* **2017**, *121*, 8786–8794.

[98]   T. Liu, X. Liu, D. R. Spring, X. Qian, J. Cui, Z. Xu, *Sci. Rep.* **2015**, *4*, 5418.

[99]   J. Kapitulnik, E. Weil, R. Rabinowitz, M. M. Krausz, *Hepatology* **1987**, *7*, 55–60.

[100]   M. A. Haidekker, T. Ling, M. Anglo, H. Y. Stevens, J. A. Frangos, E. A. Theodorakis, *Chem. Biol.* **2001**, *8*, 123–131.

[101]   C. E. Kung, J. K. Reed, *Biochem.* **1986**, *25*, 6114–6121.

[102]   P. B. Kelter, M. D. Mosher, A. Scott, *Chemistry: The Practical Science*, Houghton Mifflin, Boston, **2009**.

[103]   L. B. Persson, V. S. Ambati, O. Brandman, *Cell* **2020**, *183*, 1572-1585.e16.

[104]   K. Kwapiszewska, K. Szczepański, T. Kalwarczyk, B. Michalska, P. Patalas-Krawczyk, J. Szymański, T. Andryszewski, M. Iwan, J. Duszyński, R. Hołyst, *J. Phys. Chem. Lett.* **2020**, *11*, 6914–6920.

[105]   K. Szczepański, K. Kwapiszewska, R. Hołyst, *Sci Rep* **2019**, *9*, 16486.

[106]   J. R. Hazel, *Annu. Rev. Physiol.* **1995**, *57*, 19–42.

[107]   R. Ernst, C. S. Ejsing, B. Antonny, *J. Mol. Biol.* **2016**, *428*, 4776–4791.

[108]   J. Cao, K. A. Schwichtenberg, N. Q. Hanson, M. Y. Tsai, *Clin. Chem.* **2006**, *52*, 2265–2272.

[109]   T. V. Oliveira, F. Maniero, M. H. H. Santos, S. P. Bydlowski, R. C. Maranhão, *Nutrition* **2011**, *27*, 713–718.

[110]   K. R. Levental, E. Malmberg, J. L. Symons, Y.-Y. Fan, R. S. Chapkin, R. Ernst, I. Levental, *Nat. Commun.* **2020**, *11*, 1339.

[111]   A. K. Yadav, D. L. Shen, X. Shan, X. He, A. R. Kermode, D. J. Vocadlo, *J. Am. Chem. Soc.* **2015**, *137*, 1181–1189.

[112]   C. Ma, W. Sun, L. Xu, Y. Qian, J. Dai, G. Zhong, Y. Hou, J. Liu, B. Shen, *J. Mater. Chem. B* **2020**, *8*, 9642–9651.

[113]   R. Li, J. Guo, Y. Duan, X. Liu, L. Gui, Y. Xu, X. Kong, Y. Li, H. Chen, Z. Yuan, *Chem. Eng. J.* **2022**, *435*, 135043.

[114]   M. Peng, J. Yin, W. Lin, *New J. Chem.* **2019**, *43*, 16945–16949.

[115]   K. Wang, X. H. Sun, Y. Zhang, T. Zhang, Y. Zheng, Y. C. Wei, P. Zhao, D. Y. Chen, H. A. Wu, W. H. Wang, R. Long, J. B. Wang, J. Chen, *R. Soc. open sci.* **2019**, *6*, 181707.

[116]   J. A. Robson, M. Kubánková, T. Bond, R. A. Hendley, A. J. P. White, M. K. Kuimova, J. D. E. T. Wilton-Ely, *Angew. Chem. Int. Ed.* **2020**, *59*, 21431–21435.

[117]   O. Nadiv, M. Shinitzky, H. Manu, D. Hecht, C. T. Roberts, D. LeRoith, Y. Zick, *Biochem. J.* **1994**, *298*, 443–450.

[118]   C. Watala, H. Witas, L. Olszowska, W. Piasecki, *Int. J. Exp. Pathol.* **1992**, *73*, 655–663.

[119]   G. S. Zubenko, U. Kopp, T. Seto, L. L. Firestone, *Psychopharmacol.* **1999**, *145*, 175–180.

[120]   G. Deliconstantinos, V. Villiotou, J. C. Stavrides, *Biochem. Pharmacol.* **1995**, *49*, 1589–1600.

[121]   A. M. Forsyth, J. Wan, P. D. Owrutsky, M. Abkarian, H. A. Stone, *Proc. Natl. Acad. Sci. U.S.A.* **2011**, *108*, 10986–10991.

[122] S.-C. Lee, J. Heo, H. C. Woo, J.-A. Lee, Y. H. Seo, C.-L. Lee, S. Kim, O.-P. Kwon, *Chem. Eur. J.* **2018**, *24*, 13706–13718.

[123] M. Pittman, A. M. Ali, Y. Chen, *Int. J. Biochem. Cell Biol.* **2022**, *153*, 106329.

[124] B. Chen, C. Li, J. Zhang, J. Kan, T. Jiang, J. Zhou, H. Ma, *Chem. Commun.* **2019**, *55*, 7410–7413.

[125] J. Zhan, C. Geng, X. Hao, W. Song, W. Lin, *New J. Chem.* **2021**, *45*, 3778–3782.

[126] H. Song, W. Zhang, Y. Zhang, C. Yin, F. Huo, *Chem. Eng. J.* **2022**, *445*, 136448.

[127] X. Li, R. Zhao, Y. Wang, C. Huang, *J. Mater. Chem. B* **2018**, *6*, 6592–6598.

[128] L. Zhu, M. Fu, B. Yin, L. Wang, Y. Chen, Q. Zhu, *Dyes and Pigments* **2020**, *172*, 107859.

[129] H. Szmacinski, J. R. Lakowicz, *Sens. Actuators B: Chem.* **1995**, *29*, 16–24.

[130] Th. Förster, G. Hoffmann, *Z. Phys. Chem.* **1971**, *75*, 63–76.

[131] R. Datta, T. M. Heaster, J. T. Sharick, A. A. Gillette, M. C. Skala, *J. Biomed. Opt.* **2020**, *25*, 1.

[132] J. Yang, P. Dai, M. Li, M. Tang, Q. Wu, S. Liu, Q. Zhao, K. Y. Zhang, *Dalton Trans.* **2022**, *51*, 6095–6102.

[133] D. Su, C. Teoh, N. Gao, Q.-H. Xu, Y.-T. Chang, *Sensors* **2016**, *16*, 1397.

[134] X. Peng, Z. Yang, J. Wang, J. Fan, Y. He, F. Song, B. Wang, S. Sun, J. Qu, J. Qi, M. Yan, *J. Am. Chem. Soc.* **2011**, *133*, 6626–6635.

[135] I. E. Kolesnikov, A. A. Kalinichev, M. A. Kurochkin, E. Y. Kolesnikov, E. Lähderanta, *Mater. Des.* **2019**, *184*, 108188.

[136] W. L. Goh, M. Y. Lee, T. L. Joseph, S. T. Quah, C. J. Brown, C. Verma, S. Brenner, F. J. Ghadessy, Y. N. Teo, *J. Am. Chem. Soc.* **2014**, *136*, 6159–6162.

[137] Z. R. Grabowski, K. Rotkiewicz, W. Rettig, *Chem. Rev.* **2003**, *103*, 3899–4032.

[138] M. A. Haidekker, T. P. Brady, D. Lichlyter, E. A. Theodorakis, *Bioorg. Chem.* **2005**, *33*, 415–425.

[139] M. A. Haidekker, E. A. Theodorakis, *Org. Biomol. Chem.* **2007**, *5*, 1669–1678.

[140] L. Xu, K. Wu, R. Han, Y. Sui, C. Huang, W. Huang, L. Liu, *Spectrochim. Acta A.* **2021**, *261*, 120016.

[141] A. Prlj, L. Vannay, C. Corminboeuf, *Helv. Chim. Acta* **2017**, *100*, e1700093.

[142] R. Hu, E. Lager, A. Aguilar-Aguilar, J. Liu, J. W. Y. Lam, H. H. Y. Sung, I. D. Williams, Y. Zhong, K. S. Wong, E. Peña-Cabrera, B. Z. Tang, *J. Phys. Chem. C* **2009**, *113*, 15845–15853.

[143] S. Toliautas, J. Dodonova, A. Žvirblis, I. Čiplys, A. Polita, A. Devižis, S. Tumkevičius, J. Šulskus, A. Vyšniauskas, *Chem. Eur. J.* **2019**, *25*, 10342–10349.

[144] L. Wang, Y. Xiao, W. Tian, L. Deng, *J. Am. Chem. Soc.* **2013**, *135*, 2903–2906.

[145] W.-J. Shi, Y.-F. Wei, J. Yang, H.-Z. Li, Q.-H. Wan, Y. Wang, H. Leng, K. Chen, J. Yan, *Sens. Actuators B: Chem.* **2022**, *359*, 131594.

[146] B. Shen, L. F. Wang, X. Zhi, Y. Qian, *Sens. Actuators B: Chem.* **2020**, *304*, 127271.

[147] W. Miao, C. Yu, E. Hao, L. Jiao, *Front. Chem.* **2019**, *7*, 825.

[148] J. Li, Y. Zhang, H. Zhang, X. Xuan, M. Xie, S. Xia, G. Qu, H. Guo, *Anal. Chem.* **2016**, *88*, 5554–5560.

[149] X. Wang, F. Song, X. Peng, *Dyes and Pigments* **2016**, *125*, 89–94.

[150] S. Lecinski, J. W. Shepherd, K. Bunting, L. Dresser, S. D. Quinn, C. MacDonald, M. C. Leake, *Interface Focus.* **2022**, *12*, 20220042.

[151] K. Bera, A. Kiepas, I. Godet, Y. Li, P. Mehta, B. Ifemembi, C. D. Paul, A. Sen, S. A. Serra, K. Stoletov, J. Tao, G. Shatkin, S. J. Lee, Y. Zhang, A. Boen,

P. Mistriotis, D. M. Gilkes, J. D. Lewis, C.-M. Fan, A. P. Feinberg, M. A. Valverde, S. X. Sun, K. Konstantopoulos, *Nature* **2022**, *611*, 365–373.

[152]   T. Kowada, H. Maeda, K. Kikuchi, *Chem. Soc. Rev.* **2015**, *44*, 4953–4972.

Chapter 2 BODIPY-perylene heterochromophores with Mega Stokes shifts as sensitizers for Triplet-triplet annihilation up-conversion

Overview

Triplet-triplet annihilation up-conversion (TTA-UC) is a bimolecular process involving the transformation of low energy photons into high energy ones. The main advantage of TTA-UC is that it does not require coherent light nor high-power densities to work. For this reason, its applications in areas such as photodynamic therapy and solar energy harvesting are promising.

TTA-UC is a bimolecular process. The energy is harvested by a photosensitizer and then transferred to an emitter or annihilator. The energy transfer is mediated by excited triplet states; as a result, the structural and electronic features that enhance the population and perseverance of triplet states in a molecule will be beneficial for up-conversion.

In this chapter, the design, preparation, and characterisation of photosensitizers for TTA-UC is described. Two chromophores, BODIPY and perylene, were combined to produce charge transfer conjugates with sensitizer properties. BODIPY was chosen because it presents a high quantum yield and good photostability. The low triplet quantum yield of the unsubstituted BODIPY core can be improved by adding certain substituents such as halogen atoms or other fluorophores. Perylene was added to promote a twisted intramolecular charge transfer that subsequently will facilitate the generation of triplet states. Supported by computational techniques to aid interpretation, the absorptive and emissive properties were studied. The presence of triplet states was evidenced by TTA-UC experiments and by transient absorption. The sensitizers were successfully

incorporated into TTA-UC systems in solution and the solvent dependence was described.

2.1 Introduction to BODIPYs
2.1.1 BODIPY dyes synthesis and properties

Boron dipyrridomethenes are one of the most studied fluorophores and their applications range from fluorescence imaging,[75,76], sensing,[77,78] to organic photovoltaics.[79,80] As with most heterocycles, the *de novo* synthesis of BODIPY is generally easier than functionalising the main core as it is not commercially available and it is poorly stable.[81]

The synthesis typically involves the condensation of two equivalents of a pyrrole, indole, or other fused heterocycle, with the same carbon atom coming from an electrophile such as an aldehyde,[82] an acyl chloride,[83] an orthoesteres[84] or even thiophosgene[85] (Figure 18)**Figure 18** Different methodologies to prepare C2-symmetric BODIPYs. In all cases, the synthesis requires two equivalents of pyrrole, and the last step is the chelation with BF3. In purple is the atom that occupies position 8 in the product. The symmetry of the BODIPY is generally C_2 if two equivalents of the same pyrrole are used.
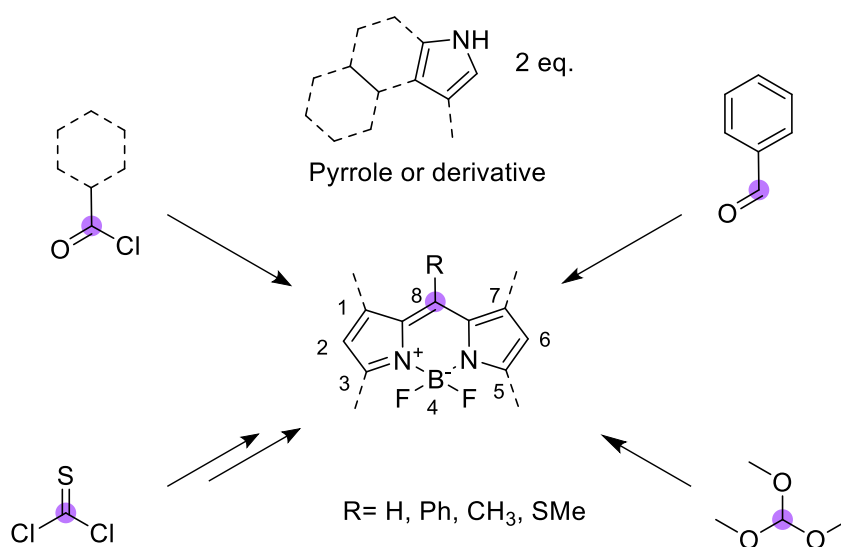
Figure 18 *Different methodologies to prepare C2-symmetric BODIPYs. In all cases, the synthesis requires two equivalents of pyrrole, and the last step is the chelation with BF₃. In purple is the atom that occupies position 8 in the product.*

A very common procedure to prepare symmetric BODIPYs is the three-step one-pot method. The first step is the acid-catalysed condensation of 2 eq. of pyrrole with an aldehyde to form a dipyrridomethane that is oxidised by DDQ (or *p*-chloranil) to a dipyrridomethene that then chelates the boron from BF_3 etherate.[82,86,87]

Non-symmetrically substituted BODIPYs can be prepared in two steps, a first C-C formation reaction involving one equivalent of the first pyrrole (or derivative) produces a ketopyrrole- or pyrrole carboxaldehyde that is later condensed with 1 equivalent of a second pyrrole.[88] The required ketopyrroles are prepared by C-acylation through Friedel-Crafts acylation[89,90] by Vilsmeier-Haack reaction[91,92] and by metalation-acylation with either magnesium[93,94] or lithium,[95] whereas pyrrole- or indolecarboxaldehydes are generally prepared by the well-known Vilsmeier-Haack[96] or Rieche formylations[97] (Figure 19). The condensation with the second equivalent of pyrrole can be catalysed by acid, frequently trifluoroacetic acid,[98] or by POCl3.[88]
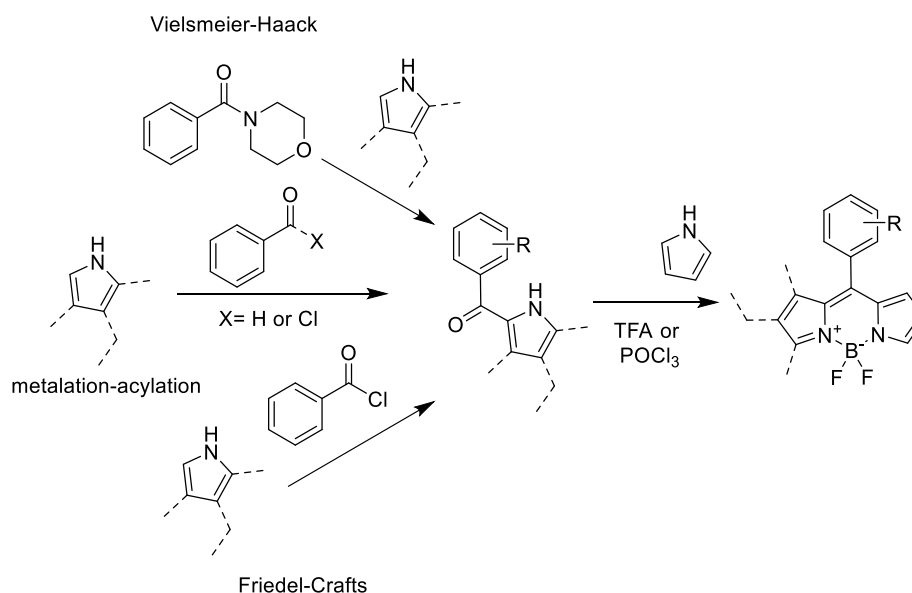
Figure 19 *Common synthesis of non-symmetric BODIPYs (detailed conditions not included).*

Further modifications of the BODIPY include the palladium-catalysed functionalisation of positions 2, 3, 5, or 6, with an intermediate halogenation step.

Some application examples include the Sonogashira,[99] Suzuki-Miyaura[100] and Mizoroki–Heck[101] couplings (Figure 20), or even the direct functionalisation though C-H activation mediated by iridium catalyst.[102] This reactions will be further explained and studied in chapter 3.
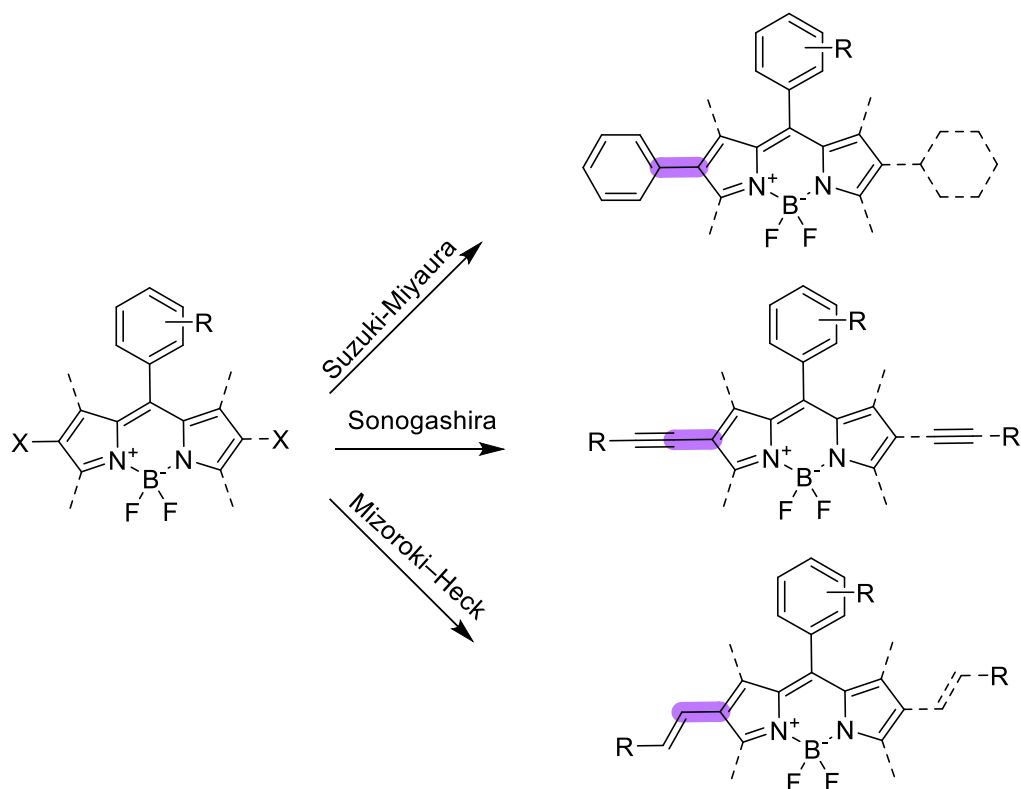
Figure 20 *Typical Palladium-catalysed cross coupling reactions involving BODIPYs. In purple, the new bond formed.*

There is no doubt that BODIPYs are among the best chemical fluorophores in terms of photophysical properties, their synthetic versatility, diversity, and breadth of application.

2.1.2 BODIPY derivatives as sensitizers and annihilators for TTA-UC

Given that the emission and absorption of BODIPY derivatives are relatively easy to modify, they are excellent candidates for up-conversion dyads, and they have been applied as both annihilators and sensitizers.

When it comes to BODIPY sensitizers, a few different mechanisms to generate triplet states have been exploited and studied.[103] The most common example is the 2,6-diiodo BODIPY, a very good sensitizer that has been extensively studied.[104–106] In this case, the presence of two iodine atoms significantly reduces the fluorescence quantum yield by enhancing non radiative ISC leading to triplet formation.[107] Figure 21.
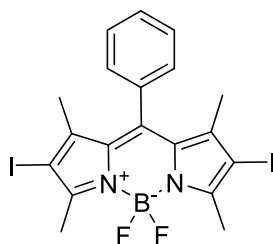
Figure 21 *2-6-diiodo-8-phenyl-BODIPY, one of the most studied metal-free sensitizers.*

BODIPYs in combination with transition metal complexes in the same molecule seem to have an extended lifetime of the triplet state, from nanoseconds in the original metallic complex to milliseconds in the BODIPY-substituted complex.[108]

Special attention should be paid to the twisted BODIPYS dimers in which the mechanism that generates the ISC is still a matter of debate (Figure 22). Among the proposals are doubly excited state,[47] charge transfer,[109,110] singlet fission,[111] and, finally, the balance between two triplet states.[112]
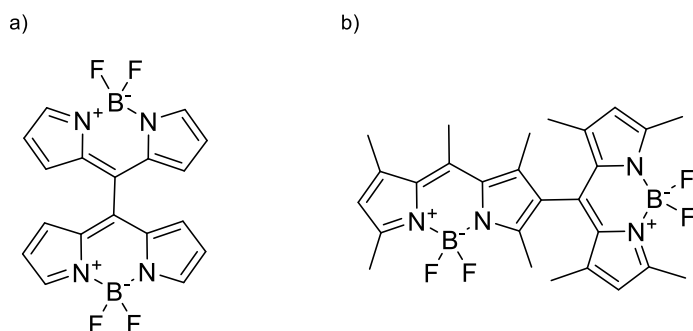
a)   b)

BODIPY has been less commonly used to prepare annihilators. One pertinent example is the *meso*-phenyl perylene substituted BODIPY shown below. This molecule shows better annihilator properties, compared to perylene, and the computational studies suggest that this is due to a triplet state closer in energy to the one of the sensitizer used (a BODIPY dimer), increasing the TTA-UC yield.[113]
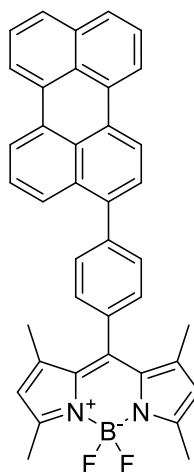
Figure 23 *A BODIPY-perylene fluorophore used as annihilator. This molecule outdoes perylene in certain TTA-UC systems.*

2.1.3 BODIPY-polyaromatic hydrocarbon dyads

Combinations of two or more fluorophores in the same molecule are very frequent. BODIPY has been combined with other chromophores such as dithienylethene,[114] corrole,[115] porphyrin,[116] rhodamine,[117] and naphthalimide,[118] Of special interest are the dyads that include polyaromatic rings such as perylene, pyrene, or even anthracene, because these substituents can improve the triplet yield of BODIPY. In general, the position of the aromatic hydrocarbon has a huge impact on the final product's properties. In a recent example, the triplet states formed by BODIPY-anthracene dyes with anthracene at the *meso*-position were much higher (up to 96%) than the ones obtained when anthracene was at 2-position[63] (Figure 24 a).

Perylene is another polyaromatic hydrocarbon found in UC systems. The energy of its first triplet state was reported back in 1969 and, since then, it has become one of the benchmark annihilators.[119,120] Some synthetic derivatives and modifications allowed the fine-tuning of its properties. Of special attention are all the perylene diimide derivatives widely studied in organocatalysis[121] and up-conversion.[122] In a more pertinent example, the combination of perylene with BODIPY through a triazole linker yielded an efficient sensitizer but failed to produce self-up-conversion[123] (Figure 24 b). This is presumably the result of unfavourable changes in the triplet state energy of perylene due to the substitution with a triazole, a strong electron withdrawing group.
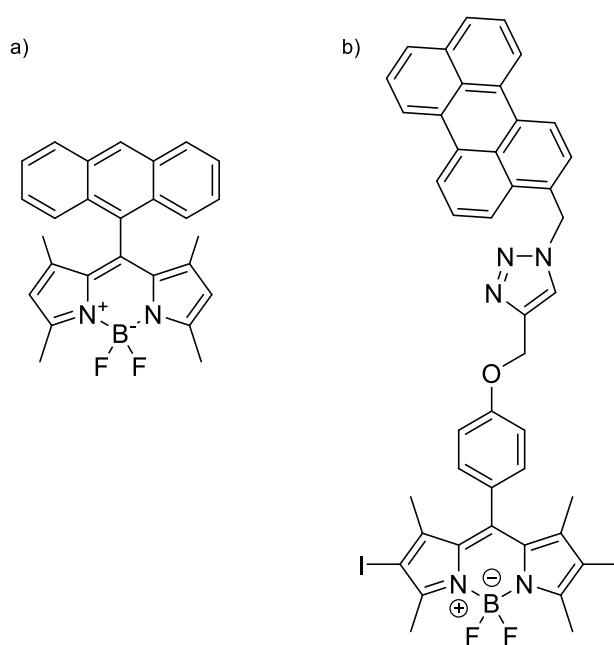
Figure 24 *Previously reported examples of BODIPY dyes with anthracene (a) and perylene (b) as substituents.*

2.2 Results and discussion

2.2.1 Synthesis of BODIPY-perylene conjugates from symmetric BODIPYs

The synthetic methodology began by preparing a symmetric phenyl-BODIPY derivative following the three-step, one pot method[82] (Figure 25). The first step is the condensation of two equivalents of a pyrrole, one with at least one α position free, with an aldehyde, generally an aromatic one. That leads to the formation of dipyrridomethanes, which are rather unstable molecules and only rarely isolated.[124] The next step is the oxidative dehydrogenation by a quinone derivative (DDQ or *p*-chloranil).[125] The dipyrridomethene thus formed is then complexed with an excess of BF$_3$ etherate in the presence of an organic base, generally triethylamine or diisopropylethylamine (DIPEA).

Although simple, for this methodology, the yields rarely exceeded 15%. Isolation of the product is difficult due to the presence of the hydroquinone, which is soluble in both organic and aqueous solvents. Moreover, the multigram scale-up was particularly problematic. The oxidation step was never complete at a 1-gram scale, which only increased the difficulty of isolating the product.
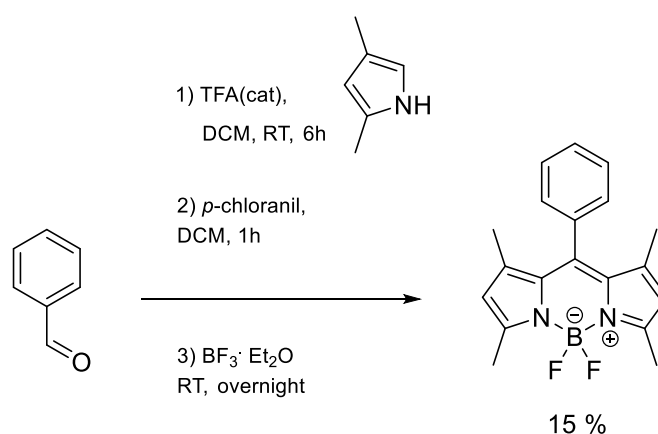
Figure 25 *Synthesis of the symmetric phenyl-BODIPY in the three-step one-pot methodology.*

In addition to the previous procedure in solution, a mechanochemical approach was also evaluated.[86] The product was obtained in a very short time (about 10 minutes), but isolation and scale-up were equally tricky. The workup remained the same and larger amounts of solvents were required to recover the product from the mortar.

The monoiodination of phenyl-BODIPY was carried out with *N*-iodosuccinimide (NIS) (Figure 26). The reaction was carried out at 0 °C to avoid diiodination and NIS was added over a period of 30 minutes. Nevertheless, from the very beginning, a mixture of three different products was formed, the mono, and diiodinated products plus the starting material. On TLC, the retention factors of the three products where very similar, so chromatographic purification was not an option.
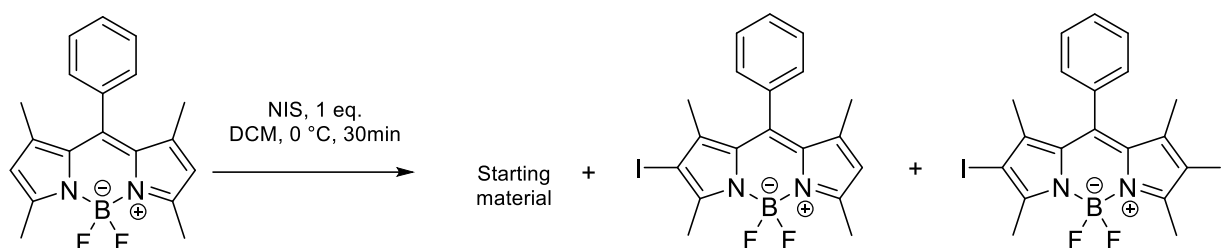
Figure 26 *Iodination of phenyl-BODIPY.*

2.2.2 Synthesis of BODIPY-perylene conjugates from non-symmetric BODIPYs

This strategy was implemented to overcome some of the challenges explained in the previous section. As the key intermediate for the synthesis of BODIPY-perylene derivatives was the monohalogenated BODIPYs, the multistep synthesis was preferred over the three-step one pot strategy. The full pathway is shown in Figure 27. The synthesis includes the acylation of pyrrole, the halogenation of pyrrole's position 4, the condensation with a second equivalent of pyrrole, and, finally, complexation with BF_3 etherate.
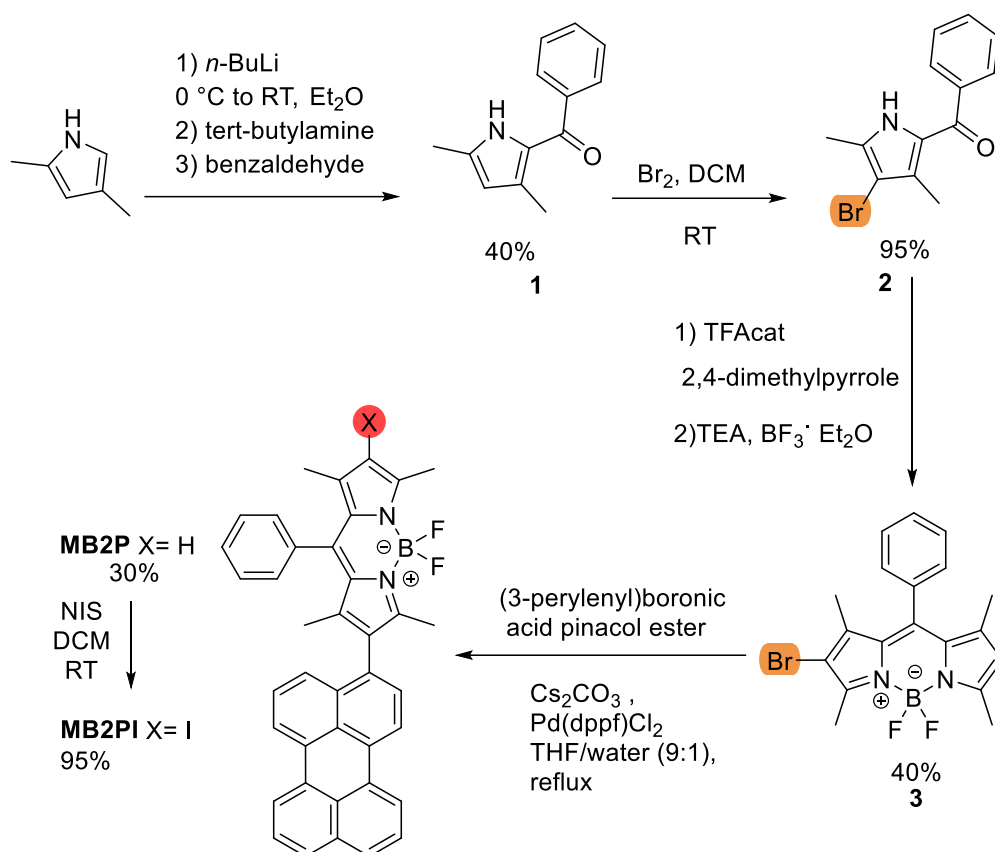
Figure 27 *Synthesis of BODIPY-perylene conjugates starting from non-symmetrically substituted BODIPYs.*

The non-symmetric pathway was commenced by preparing ketopyrroles (2-benzoylpyrroles) following a reported methodology.[95] Figure 28.
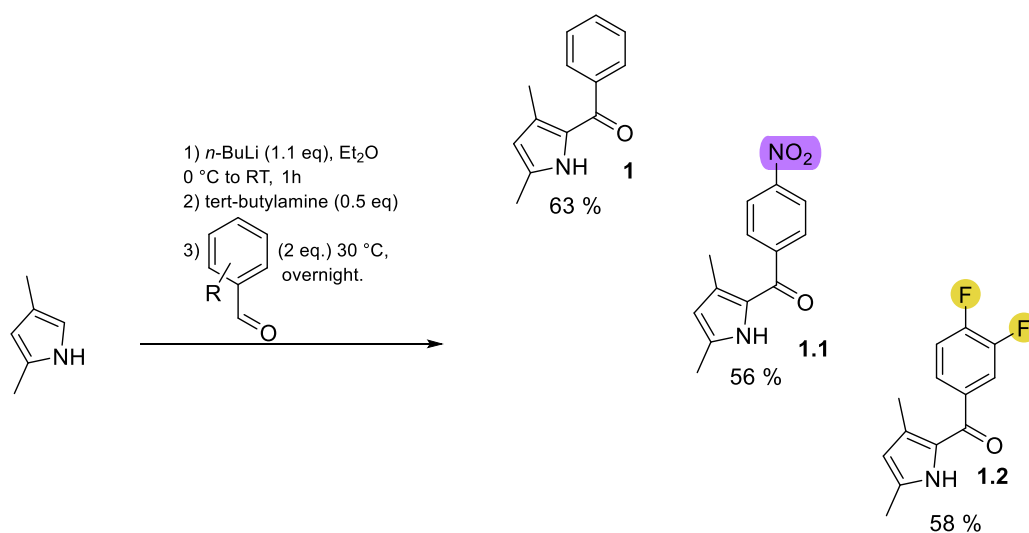
Figure 28 *Synthesis of ketopyrroles by metalation-acylation of pyrrole.*

The reaction mechanism, as reported in literature (Figure 29[95]) suggests that the first step is the metalation of pyrrole with *n*-butyllithium. The most nucleophilic centre of the resulting lithiated pyrrole is the nitrogen atom and N-acylation would be the main product. To avoid N-acylation an additive is required, namely a bulky amine. The original paper reports better results with 2,6-dimethylaniline. As a large amount of the amine was needed, only the first reactions were carried out with 2,6-dimethylaniline and the rest were carried out using *tert*-butylamine, without a significant decrease of the yield. The reason 0.5 equivalents of the amine work as well as 1.0 equivalents in terms of yield, is so far unclear. The formation of organolithium aggregates could explain the reactivity and the requirements for a bulky amine.[95,126]
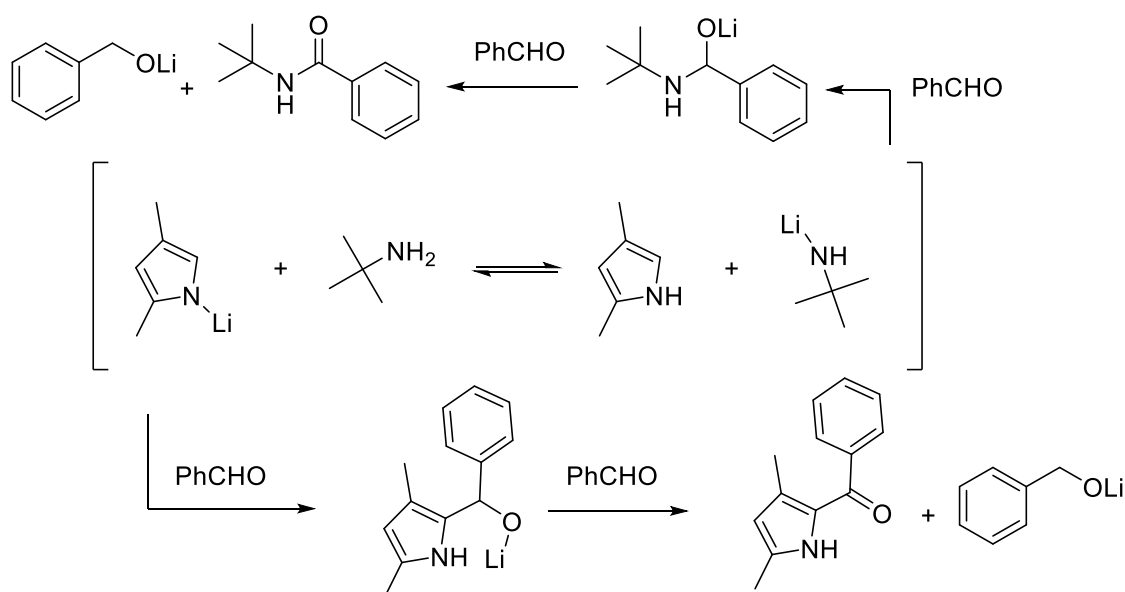
Figure 29 *Proposed mechanisms for the 2-acylation of 2,4-dimethylpyrrole.*

The halogenation of the ketopyrrole was optimised in two different ways (Figure 30). NIS was used first; iodine derivatives being generally the most reactive species in cross-couplings, but the reaction did not proceed at room temperature and required a reflux in acetonitrile. The isolated yield was a meagre 8% and massive degradation was observed. After that, bromine was used and the reaction

yielded the 4-bromoketopyrrole in very good yields (94%).[98] The same strategy, with bromine, was used to halogenate the ketopyrroles 1.1 and 1.2.
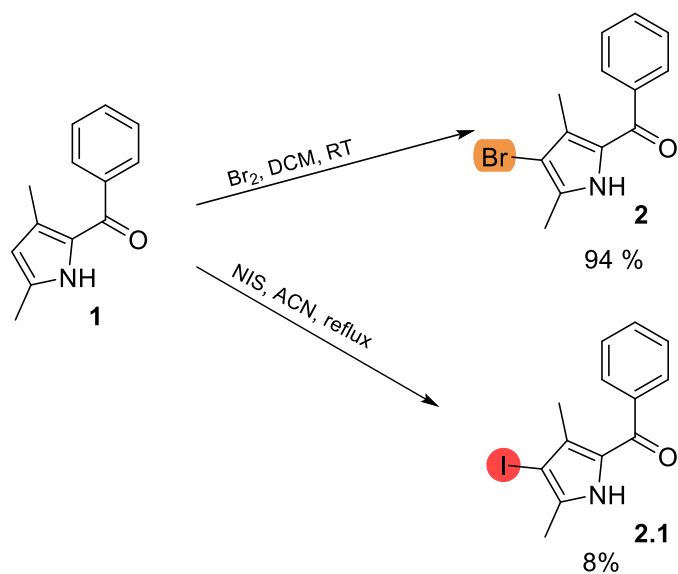
Four different BODIPYs with the 4-bromo and 4-iodobenzoylpyrroles in moderate yields of 40% were prepared. Figure 31. The reaction of ketopyrroles with another equivalent of pyrrole to form a dipyrromethene can be catalysed by phosphorus oxychloride (POCl$_3$)[88] and trifluoroacetic acid (TFA).[98] In this work, the acid method was exclusively used as POCl$_3$ needs to be freshly distilled and it is used in stoichiometric amounts whereas TFA is used in catalytic amounts.
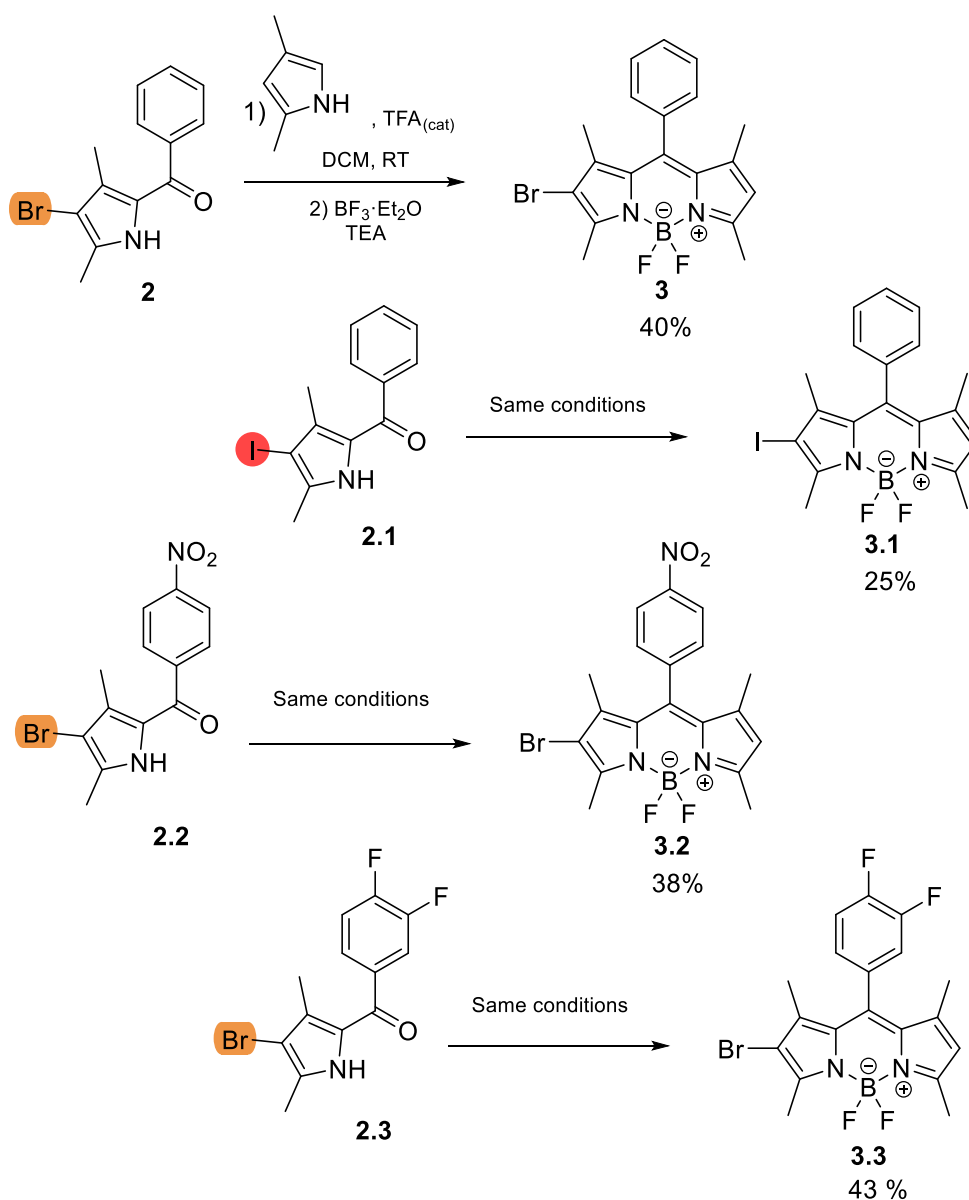
Figure 31 *Monohalogenated BODIPYs prepared as key intermediates in the multistep pathway.*

The complexation was completed with an excess of BF_3 etherate and triethylamine (6-8 eq. of each). BODIPYs **3**, **3.1**, **3.2** and **3.3** were obtained in moderate yields of about 40%. Molecules **3**, **3.2** and **3.3** were stable, but the monoiodinated BODIPY **3.1** was rather unstable and underwent dehalogenation during the chromatographic separation on silica and the non-halogenated phenyl BODIPY was obtained in approx. 10% yield calculated by NMR.

The multi-step synthesis was found to be way better than the three-step one pot method. The longer reaction times for the condensation, 24 h instead of 5 h, are compensated by the higher yields obtain in the multistep synthesis 40 % vs 15 %. In addition, we obtained some of the ketopyrroles pure enough after the first and second steps (acylation and bromination) on a multi-gram scale or we easily purified them by recrystallization without the need for a chromatographic purification.

2.2.2.1 Cross coupling, the boron reagent

Functionalizing perylene proved challenging since some of the reactions gave low yields and some derivatives were observed to be unstable. Electrophilic substitution occurs preferentially on position 3 for "soft" electrophiles.[127] For "hard" electrophiles, substitution can also occur up to 20 % on position 1, formylation[128] or nitration.[129] There are only a few reports concerning the chlorination of perylene,[130] bromination is easily performed with N-bromosuccinimide (NBS),[131] and iodination is never carried out directly, instead it is achieved through a sequence of nitration (that produces 1- and 3-nitroperylene), reduction, and Sandmeyer reaction.[132] For that reason, bromine was the halogen of choice to functionalise perylene. However, the bromination was never quantitative and always produced mixtures of product and starting material in a 1:4 ratio.

The cross coupling of BODIPY to perylene required the formation of a C-C bond. The Suzuki-Miyaura protocol was the first choice, but many of the perylene derivatives required were not commercially available, most certainly because of their lack of stability. For that purpose, perylene boronic acid and its derivatives were prepared from perylene. The first step consisted in functionalising perylene; this was achieved with freshly recrystallized NBS. The reaction was carried out in THF with 1.0 equivalent of NBS.[133] Despite the apparent simplicity of this reaction, the

conversion was never complete even when the reaction time was extended from 24 to 72 h. However, since perylene does not interfere in the next step, there was no need for further purification steps.

Preparing the 3-perylene boronic acid from 3-bromoperylene was unsuccessful following the lithiation-borylation method. The yields were too low (~15%) and the purity of the product was not adequate. For that reason, the Miyaura borylation was used as an alternative approach. This reaction was first carried out at reflux in 1,4-dioxane (101 °C) but the low yields (~25 %) suggested degradation of the product. Reducing the temperature to 70 °C improved the yields (~46%).[134] The perylene boronic acid pinacol ester **4.1** was purified by column chromatography in silica gel using cyclohexane and chloroform (6:4) as the solvent. Figure 32.
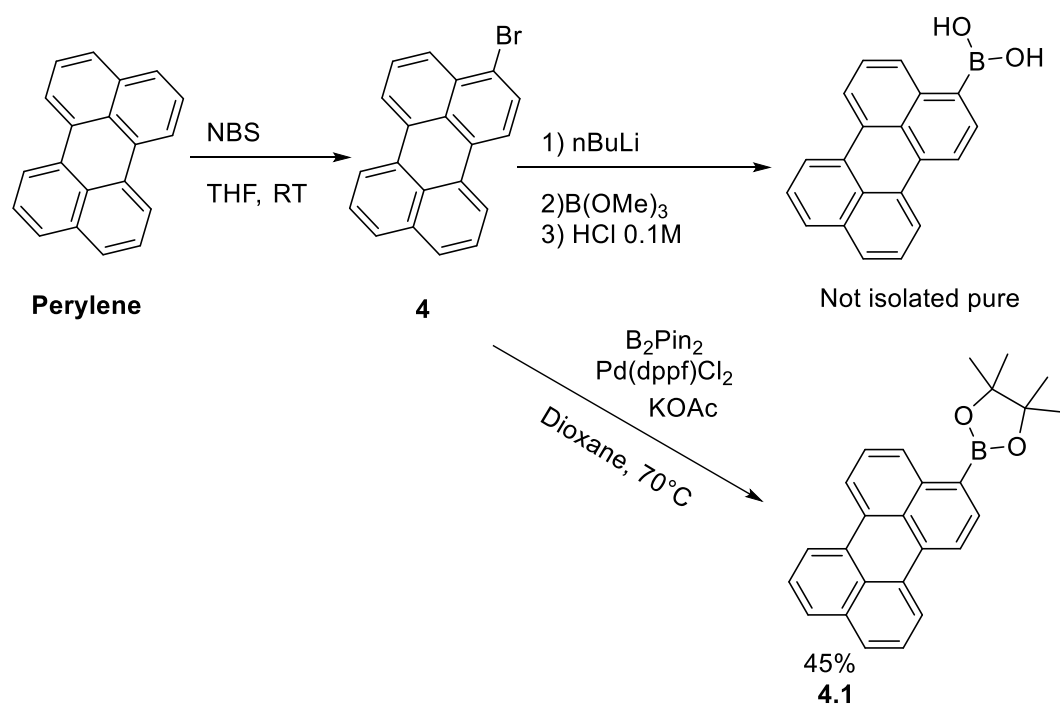
Figure 32 *Synthesis of perylene boronic acid and pinacol boronic ester applied in this thesis.*

All the boron derivatives turned out to be rather unstable. Even at room temperature, the solutions of these compounds change from a bright yellow to a

51

dark brown colour overnight and the effect increases when the solutions are exposed to light. It was later observed that, under common cross-coupling conditions, a large amount of perylene was produced as a byproduct indicating that protodeborylation occurs in these conditions. For those reasons, the pinacol ester was preferred as these derivatives tend to be more stable[135] and the boronic acid was used only rarely in reactions carried out at room temperature (see Chapter 3). In chapter 3, efforts will be made to prepare alternative boron species such as potassium trifluoroborate[136] and diethanolamine[137] to increase both the stability and the reactivity in cross-coupling methodologies.[135]

2.2.2.3 Cross coupling, reaction of monohalogenated BODIPYs with the boron derivative.

Suzuki-Miyaura couplings of BODIPYs **3, 3.1, 3.2** and **3.3** with 3-perylene boronic acid pinacol ester were carried out using Pd(dppf)Cl$_2$ as the catalyst and a 9:1 mixture of THF/ water as the solvent. The best yields were only 30%. Other palladium sources and ligands were tested: Pd (MeCN)$_2$Cl$_2$/S-Phos, Pd (MeCN)$_2$Cl$_2$/X-Phos but, the yield was never higher than 30%.

There are a few explanations for the low yield in the Suzuki-Miyaura reaction.[138–141] The first argument concerns the oxidative addition, the first step in the catalytic cycle. This step is challenging because at any point in time the BODIPY core has a π-excessive aromatic pyrrole. Since Pd(0), the catalytic species, is nucleophilic, the oxidative addition will be more difficult than with electron deficient electrophiles.[139,142]

The second possible origin of the low yield is about the less understood and always tricky transmetalation step. As part of the original plan to prepare BODIPY-perylene conjugates attempts were made to prepare the 2-BODIPY boronic acid

pinacol ester from **3** (Figure 31) as the starting material using the Miyaura protocol. However, across a range of catalysts (Pd(dppf)Cl₂, Pd(MeCN)₂Cl₂/S-Phos, Pd(MeCN)₂Cl₂/X-Phos, Pd(dba)₂/S-Phos) and conditions, no product was obtained. In fact, under harsh conditions (sealed tube, toluene, 120 °C, 16 h) the only product observed were traces of the dehalogenated starting material. These results suggest that oxidative addition during the Miyaura protocol is taking place but that transmetalation might be the limiting step. These observations can be extrapolated to what is observed in the Suzuki-Miyaura reaction.

The third and final potential origin of the low yield of the Suzuki-Miyaura is steric hindrance by the two methyl groups in positions 1 and 3 on the BODIPY and the relatively high bulkiness of the perylenyl boronic ester. The yield of the reaction under the same conditions drops to about 2 % when an anthracene boronic acid is used.
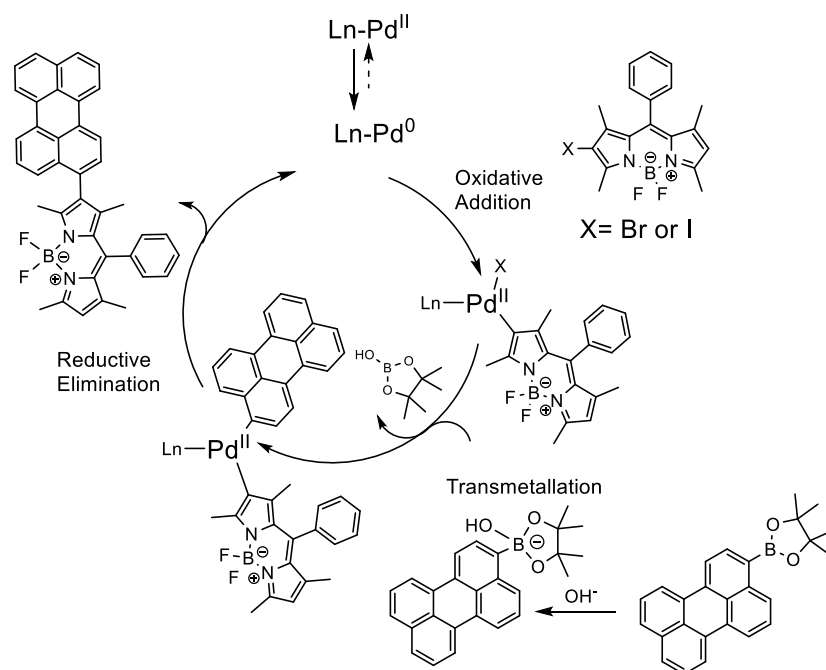
Figure 33 *Proposed reaction mechanism for the Suzuki-Miyaura cross-coupling between monohalogenated BODIPYs and perylene boronic acid pinacol ester.*

53

2.2.2.4 Synthesis of iodinated derivatives

The last iodination step (from B2P to B2PI) was carried out with N-iodosuccinimide. A relatively large amount of iodinating agent (1.5 eq.) was used along with a long reaction time (16 h) to avoid unreacted starting materials interfering with the chromatographic purification and the later photophysical studies.

2.2.2.5 Observations on the stability of BODIPY-perylene conjugates

During the preparation of the perylene conjugates, it was observed that phenyl substituted BODIPYs are the most stable ones (B2P and B2PI). The nitro-B2P and difluoro-B2P were very unstable. In fact, they massively degraded on the column and only a few milligrams of very impure products were isolated. The synthesis of BODIPY-perylene derivatives bearing electron donating substituents (dimethylamino, methoxy) will be discussed in chapter 3.

2.2.3 Photophysical studies

Molecules B2P and B2PI were prepared for three applications, as potential cell imaging probes, potential PDT agents and as sensitizers for TTA-UC. As part of the photophysical characterisation, the emission and absorption spectra of both dyes were explored in different media, namely toluene, 1,4-dioxane, chloroform, ethyl acetate, tetrahydrofuran (THF), dichloromethane, ethanol, methanol, and dimethylsulphoxide (DMSO) (Figure 34). In contrast with literature examples of charge transfer BODIPYs dyads,[143,144] a strong solvatochromism in the absorption spectrum was not observed. The main effect solvent has is on the intensity of the emission, polar solvents inhibit fluorescence whereas non-polar solvents increase it. The solvatochromism, however, is moderate. This behaviour has been observed in other donor-acceptor pairs where experimental and DFT calculations suggest that, for charge transfer compounds, highly polar solvents inhibit fluorescence. This inhibition is due to the stabilisation of the charge-separated state responsible for the fluorescence.[145,146]
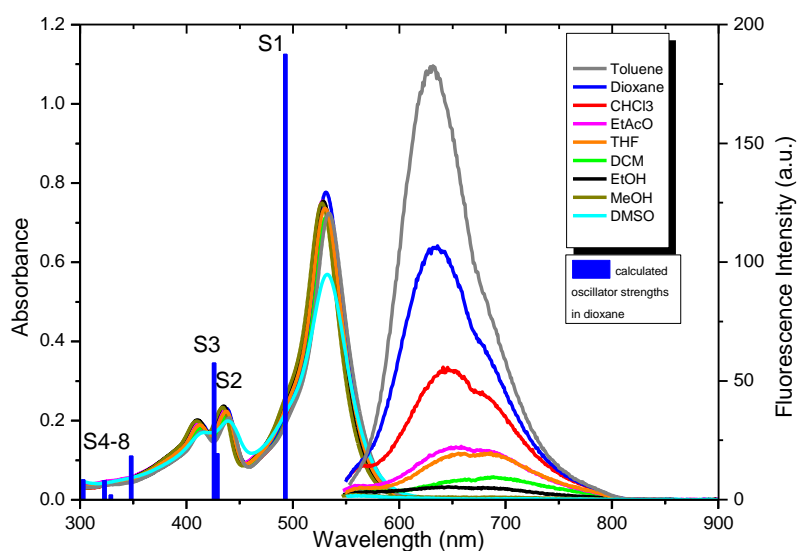
Figure 34 *Solvent effect and calculated oscillator strengths of B2PI in different solvents at 10 µM, excitation at λ_{max} using 5-5 nm slit widths.*

Other interesting features of the perylene substituted BODIPY dyes are the lack of symmetry between the emission and the absorption bands and the Stokes shift of about 3500 cm^{-1}. The emission bands were very broad which is distinct from the sharp emission profile commonly observed in BODIPY fluorescence ~25 nm FWHM for phenyl-BODIPY vs 124 nm for B2PI in chloroform). [145,147,148] This observation suggested a charge transfer is taking place, as it has been reported that energy transfer is highly dependent on the solvent.[105,149] Polar solvents help stabilise the charge-separated states resulting in a decrease of the emission. [149,150]

The bathochromic effect between non-polar solvents with increasing dielectric constants is around ~60 nm (toluene vs DCM). The absoption in methanol and DMSO, although very low, has a maximum at close to 700 nm. The bathochromic effect has been observed in other donor/acceptor BODIPYs where the emission is due to a strong Twisted Intramolecular Charge Transfer (TICT). Examples of those fluorophores are triphenylamine *meso*-substituted BODIPYs. However, in this case there is a bigger bathochromic shift (~120 nm) and a larger difference between solvents with similar dielectric constants e.g. toluene and chloroform. The lipophilic character of some literature examples can result in aggregation in polar solvents which leads to an increase in emission.[143] In contrast, in the literature, donor/acceptor dyads where there is no twisted conformation the bathochromic shift tends to be very small (<10 nm) for similar solvents.[151]

To gain further insight into the photophysical behaviour of the dyes, they were further studied by TCSPC to obtain lifetime data, and the absolute quantum yields were determined, Table 1. Emission from both compounds shows unusual dual exponential decay in dioxane, but monoexponential emission decay in toluene. This could be explained by the formation of different rotamers. There is no evidence for aggregation from concentration dependence studies, i. e. no change was found in the relative amplitude of the two components at different concentrations.[152] Some of the experimental values were compared to those obtained with DFT calculations.

Table 1 Photophysical properties of B2P and B2PI in 1,4-dioxane and toluene [a] Absolute quantum yields were obtained in an integrating sphere and have a ± 2% of error. [b] Lifetimes were recorded in triplicate (deaerated solutions in sup. info). [c] Radiative decay rates calculated using $k_r = \Phi F/\tau$. Non radiative decays calculated using $\Phi = k_r/(k_r+k_{nr})$. [d] At 517 nm. [e] at 532 nm. [g] Theoretical values calculated with MN15/6-311++G (2d, p) level of theory. IW = intensity-weighted average lifetime.

	Abs.λ_{max} (nm), (ε, M^{-1} cm^{-1})	Em. λ_{max}, (nm), ϕ_F[a]	Mol. Bright.	τ_1 (ns)[b]	Amplitude (%)	τ_2 (ns)[b]	Amplitude (%)	IW	k_r[c] (10^{7}s^{-1})	k_{nr}[c] (10^{7}s^{-1})
					Dioxane					
B2P	515, (73291) 483[g]	625, 0.094[d] 585[g]	6889	4.1 ± 0.2	5.3	1.8 ± 0.01	94.7	2.0 ± 0.02	4.6 18[g]	44.4
B2PI	531, (67665) 493[g]	641, 0.025[e] 605[g]	1691	3.8 ± 0.1	94.6	0.6 ± 0.01	5.4	1.4 ± 0.01	1.8 15[g]	68.2
					Toluene					
B2P	518, (80431)	616, 0.209	16810	2.5 ± 0.01	100	---	----	2.5 ± 0.01	8.5	32.1
B2PI	534, (63338)	636, 0.033	2090	2.9 ± 0.1	7.2	0.7 ± 0.01	92.8	1.2 ± 0.02	2.6	78.7

As shown in Table 1, the absorption maximum occurs at approximately 531 nm for B2PI and at 515 nm for B2P in dioxane and, notably, varies minimally in terms of wavelength or extinction coefficient with solvent. Superficially, both absorptions, based on λ_{max}, extinction, and narrow profile appear characteristic of BODIPY localised $^1\pi-\pi^*$ transitions consistent with the lack of solvent sensitivity.

However, the TD-DFT calculations (reflected in the difference electron density plots shown in Figure 35, top) show that this state (S_1) exhibits significant charge transfer character (perylene to BODIPY). This was confirmed experimentally below on the basis of the resonance Raman data (vide infra).

Both compounds also show sharp absorption features between 400 and 430 nm, that are characteristic of perylene (Table A3). The emission spectra for both complexes are characteristic of a charge transfer excited state, ascribed to emission on recombination of charge separated BODIPY radical-anion and perylene radical-cation, formed in the excited state from rapid photoinduced electron transfer from perylene to BODIPY. The emission shows a large Stokes shift of around 3500 cm^{-1} and, characteristic of a charge transfer emission, the spectrum is very broad, compared to conventional BODIPY emission. In contrast, the emission maxima shift modestly, which is unusual in CT systems, and broad features remain constant across all solvent. In other reported BODIPY charge transfer compounds the emission undergoes large shifts in different solvents. The identification of the absorption and emission as CT transitions agree with the TDDFT calculations carried out by Rengel Cane E. Sia and Dr. Julien Guthmuller. Theoretical results suggest an increased charge transfer character for S_1 at its equilibrium geometry (Figure 35, bottom).
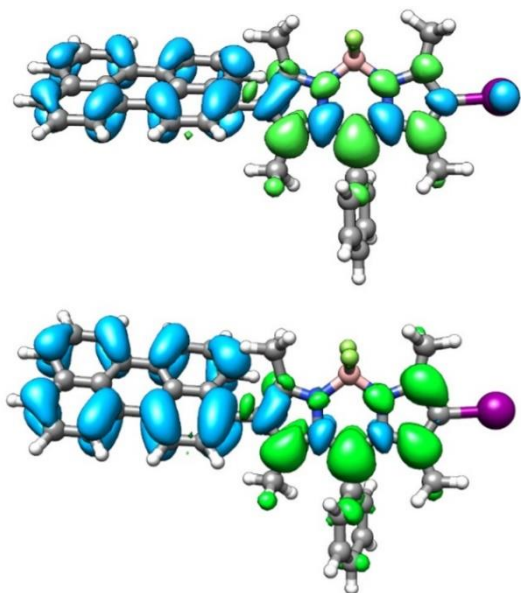
Figure 35 *Isosurface of charge density difference for the S1 excitation in B2PI. Positive (electron) and negative (hole) values are indicated in green and blue colours, respectively. (Top) at the S0 geometry, (Bottom) at the S1 geometry.*

2.2.4 Crystallography

Single crystals of B2P were obtained by slow vapour diffusion (CHCl$_3$/MeOH). The crystal had an asymmetric unit containing two independent, but similar, B2P conformers, molecules A and B. The single-crystal X-ray analysis, carried out by Prof. Vickie McKee, confirmed the structure of the compound. Crystallography showed that the angle between perylene and the mean plane of the BODIPY are 73.54(3)° and 74.512(4)° for molecules A and B, respectively. These values are slightly higher than those obtained by DFT calculations for the S$_0$ geometry (59.7°). This conformation reduces repulsive interactions between the BODIPY methyl groups (C22A and C25A) and perylene. However, despite the fact that the two fluorophores are not strictly orthogonal, the calculations suggest that the S$_1$ conformation the coplanarity of the two moieties increases (41.7°). Figure 36. Similar structures can be found in the Cambridge Structural Database.[153]
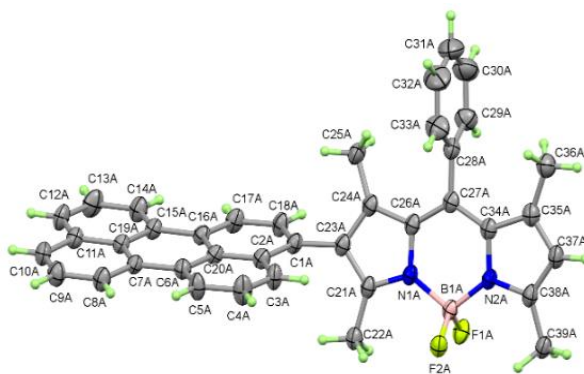
Figure 36 *Perspective view of one of the two independent molecules of B2P (molecule A) showing 50% displacement ellipsoids. Courtesy of Prof. Vickie McKee.*

Other important features are the intense π-π stacking observed for molecule A in opposition to molecule B or some literature examples (pyrene-BODIPY dyes) that show no special π-π stacking.[154] The presence of interactions between aromatic hydrogens and the fluorine is also remarkable, since this type of dipole-dipole interaction has been observed mainly with N-H donors.[155]
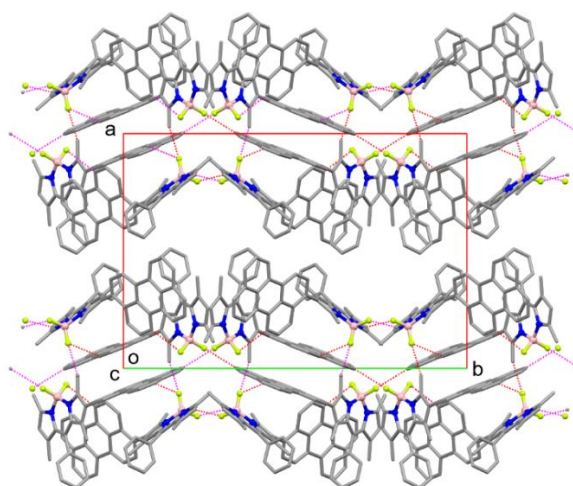
Figure 37 Unit cell packing viewed down the b axis. Dotted lines represent hydrogen bonds.

2.2.5 Resonance Raman

In resonance Raman (RR) spectroscopy, the spectrum of the sample is collected by exciting the sample with a laser that is resonant or closely resonant to the optical transition of interest. This leads to selective signal enhancement, of up to 7 orders of magnitude, of vibrational modes associated with the bonds that undergo distortion in the excited state, i.e. vibrational modes associated with the chromophoric unit in a complex molecule.[156] RR has been used along with DFT to characterise a number of donor-acceptor dyads and charge transfer systems.[157–159]

The resonance Raman spectra of B2P and B2PI were obtained using a 474 nm laser for the excitation, which is pre-resonant with the λ_{max} to resolve the origin of the optical transition, as the absorbance band solvent-independence implied BODIPY centered π-π* but the DFT calculations implied charge transfer. The experimental spectra were compared to the calculated ones obtained using MN15/6-311++G (2d, p)/MWB46, and 1,4-dioxane for the Polarizable Continuum Model (PCM). Figure 38. The resonance enhancement of the vibrational modes of both perylene and BODIPY was observed. That result indicates that both

chromophores contribute to the absorption, as expected from a charge transfer transition. To confirm that hypothesis, the resonance Raman spectra of the isolated BODIPY and perylene were calculated and they did not correspond to the experimental spectra. (Figures A22 and A23). The full band assignment is given in table A8.
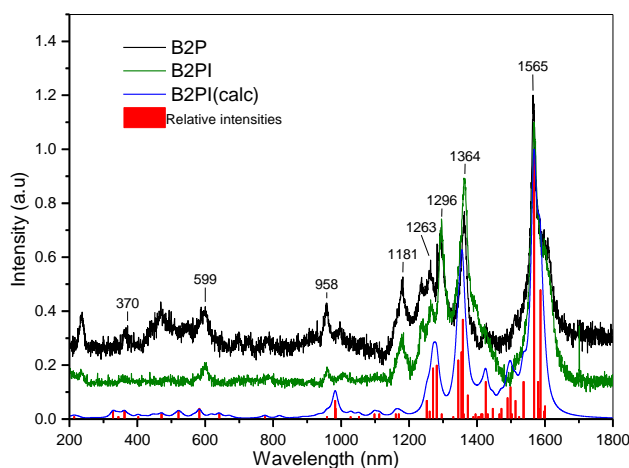
Figure 38 Resonance Raman spectra of B2P (black) and B2PI (green) Excitation at 473 nm in solid KBr. Computed resonance Raman spectrum of B2PI (blue).

The resonance Raman spectra of B2PI showed that the first singlet state has characteristics of a charge transfer with a BODIPY-centred excitation at the Franck-Condon geometry. The most intense features are found at 1565 cm^{-1} and a main band at 1600cm^{-1}. Both bands were attributed to the C-C stretches of the polyaromatic hydrocarbon and in-plane stretches of the aromatic ring of the BODIPY directly connected to it. Other modes of interest occur at 1364 cm^{-1} and 1296 cm^{-1}, and they were attributed to in-plane stretches of perylene coupled to BODIPY stretches and coupled to C-H bending modes of the methyl substituents. The BODIPY-based modes appear at 958 cm^{-1}, 1181 cm^{-1} and as shoulders around 1425 cm^{-1} and 1530 cm^{-1}.

2.2.6 Up-conversion in solution

Finally, the above-described BODIPYs were evaluated as up-conversion sensitizers in solution in collaboration with Amrutha Prabhakaran. In these experiments, perylene was used as the annihilator as it is the benchmark molecule UC systems and it has a triplet energy compatible with the BODIPY perylene dyes studied here.[60,104,160,161] First, it was necessary to determine the optimal ratio of sensitizer: annihilator to maximise UC signal. It was found that a 1/20 molar ration gives the best results for B2P whereas B2PI worked best in a 1/10 ratio. In all experiments, a 532 nm laser was used for excitation and the Anti-Stokes emission bands of perylene at 443 and 473 nm were observed as reported in literature.[162,163] (

Figure **39**).

 Before every TTA-UC experiment, the solution containing the sensitizer-annihilator pair was deaerated, and the control experiment consisted in introducing oxygen to the cuvette and irradiating with the laser again. No emission bands during the control experiment were observed. A second control was carried out using the same experimental conditions but without deaerating at all, and no emission bands were observed in this case either. This is further evidence that the signal observed is up-converted fluorescence coming from the sensitized perylene.
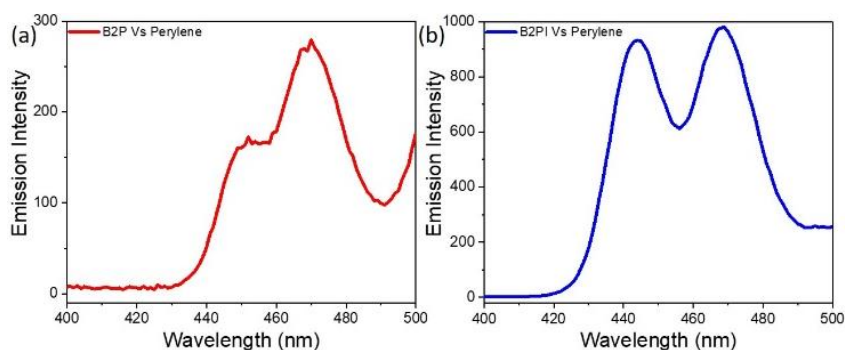
Figure 39 Up-converted emission from (a) 5 µM B2P with 100 µM perylene, and (b) 2.5 µM B2PI with 25 µM perylene in deaerated dioxane at 10 nm slit widths under 532 nm excitation. Courtesy of Dr. Amrutha Prabhakaran.

It was observed that, using the optimised molar ratio, the emission generated by the couple perylene/B2PI is three times more intense than the one generated by perylene/B2P at the same optical densities. In fact, using B2PI the TTA-UC is visible to the naked eye. Figure 40. That demonstrates the profound effect that the iodine atoms have on the sensitizer. As explained in section 1.4, the heavy atom enhances the ISC by SOC effect.

By analysing the TTA-UC spectra, it can be seen that the intensity of the emission bands of perylene varies depending on the sensitizer. This could be the result of either aggregation of perylene in high concentrations or excimer formation.[160]

Figure 40 Digital photograph of Up-converted emission from 5 µM B2PI and 50 µM perylene in deaerated dioxane at 532 nm (power density 1.27 Wcm^{-2}) excitation. Courtesy of Dr. Amrutha Prabhakaran.

The TTA-UC sensitized by B2P and B2PI is strongly solvent-dependent. Using the optimised sensitizer/annihilator ratio, a few solvents with different polarity

64

and dielectric constants were tested, namely acetonitrile, dioxane, THF, cyclohexane, toluene, DMSO, 1-butanol, hexane, ethyl acetate, dioxane/water (3:2), and dichloroethane. Among these solvents, TTA-UC was observed only in dioxane and DMSO, dioxane being the best solvent for the UC. TTA-UC in DMSO is a particularly interesting case. As explained above, polar solvents tend to inhibit fluorescence coming from charge transfers. In our case, UC is still visible in a solvent of high polarity. That behaviour is further evidence that the up-conversion is coming from the energy transfer between dark triplet states. In contrast, the highest fluorescent emission is observed in solvents of low polarity, but no TTA-UC was observed in any of them.

There are some reports in the literature concerning the solvent-dependence of TTA-UC. In a recent example,[104] researchers studied the couple 2,6-diiodo-BODIPY and perylene and found a rather different trend. They observed that dioxane was the best solvent for the system but, in contrast to us, they observed up-converted emission in hexane, heptane, toluene and DMSO, where DMSO had the worst efficiency. In this report, the researchers advanced viscosity differences as the reason for the changes in UC. Moreover, they explained the low UC in DMSO as the product of the detrimental change in the energy of perylene's triplet state produced by the solvent. However, in our system it is the lifetime of the triplet state that dictates TTA-UC efficiency.

2.2.7 Transient absorption

The ultrafast studies using B2P and B2PI were performed in collaboration and reported by Dr. Keshav Kumar Jha.[164] The experiments were performed in degassed dioxane in 5 µM solutions. The formation of triplet states in both molecules were confirmed in the femtosecond studies. The process follows the following

dynamic: excitation and geometrical relaxation occur in ~0.6 ps, the formation of a CT state occurs in the ~4.5 ps time-frame, after CR, the passage to the ground state happens in ~280 ps, whereas CR to triplet state occurs in 685 ps for B2PI and 1785 ps for B2P. [164] (Figure 41).
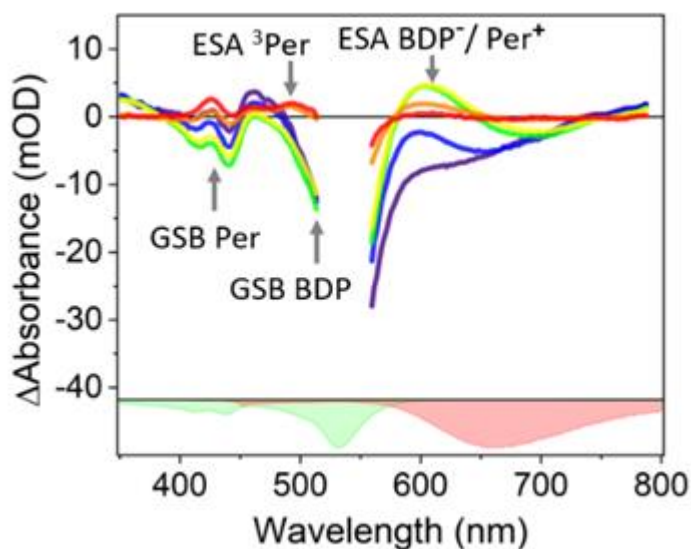
Figure 41 Femtosecond transient absorption spectra of B2PI in dioxane at 5 µM. The excitation wavelength is 532 nm. Per: perylene, BDP: BODIPY. ³Per: perylene-centred triplet. Courtesy of Dr. Keshav Kumar Jha.

Further studies of B2PI were conducted in DMSO and dioxane by Dr. Tinxiang Yang in the femtosecond time frame. In DMSO, the dye is weakly emissive, as seen in Figure 34. Structural and vibrational non emissive relaxation process were found to occur in a shorter time than charge recombination, the former process takes place in less than 4 ps whereas the latter in 43 ps. For comparison, the formation of the triplet state was found to occur in 685 ns in dioxane. In dioxane, the solvent with the lower dielectric constant, the energy of the charge separated (CS) state is higher than the energy of the CS state in DMSO. As a consequence, the energy gap between the CS and the ground state is higher in dioxane than in DMSO. In contrast, DMSO stabilises the CS sate reducing the energy gap between CS and S0 which results in the rapid return to the ground state. After the addition of perylene (50 µM), the lifetimes of the triplet states decrease indicating a quenching by

annihilation. B2PI, the iodinated molecule presented a un up-conversion yield 8.4 times higher than the non-iodinated dyad. [165]

2.3 Conclusions

A new synthetic approach was developed and optimised to prepare non-symmetrically functionalised BODIPYs. The purpose was to create a charge transfer derivative to promote ISC in BODIPY for TTA-UC where a single iodine substituent could be applied to test the impact of heavy atom effect on triplet efficacy. The dyes prepared are functionalised with perylene at position 2 and with or without iodine at position 6. Both compounds are effective sensitizers for TTA-UC with perylene as the annihilator.

B2P and B2PI show solvent-independent absorption with a λ_{max} around about 530 nm. The dyes present a highly solvent dependent emission with a large Stokes shift attributed to relaxation from an intramolecular charge transfer state between BODIPY and perylene excited states. The iodinated compound showed >6-fold reduction in emission quantum yield compared to the B2P, attributed to efficient inter-system crossing due to the heavy atom effect. This behaviour was further reflected in the efficiency of the TTA-UC, which was observed, under optimised conditions to be 3-fold greater for the B2PI sensitized process. For both compounds the TTA was strongly solvent dependent. Intense visible-by-eye TTA-UC was observed, with perylene as the annihilator but only from DMSO and dioxane across a diverse range of solvents explored. In a separate study, this was revealed to be due to the solvent-dependent lifetimes of the charge separated states.

Computational studies indicate that inter-system crossing in both derivatives most likely occurs from S1 charge transfer state to T3 charge transfer state from where TTET to perylene annihilator occurs. The solvent dependence of the process was attributed to solvent modulation of the charge separated state on the lifetime of the T3 of the sensitizer.

2.4 Experimental section

2.4.1 TTA-UC Measurements

A Varian Cary Eclipse fluorescence spectrophotometer was used for TTA-UC measurements with an additional 532 nm excitation laser of 10 mW power with 1 mm beam diameter of 1.27 Wcm^{-2} power density purchased from Edmund optics. The TTA-UC measurements were recorded by blocking the excitation line in bioluminescence measurement mode. The solution measurements were carried out by deaerating the sample by purging N_2 for 30 min in a quartz cuvette of 1 cm path length. The up-converted emission was recorded across the range 400 to 500 nm to avoid the interference from the excitation source.

2.4.2 Synthesis
Synthesis of ketopyrrole **1** (general procedure **A**)

Ketopyrrole **1** was prepared following a modified reported procedure.[95] In a 100 mL round bottom flask 2,4-dimethylpyrrole (2 mL, 19.42 mmol) was dissolved in 30 mL of diethyl ether at 0 °C in an ice/water bath, *n*-BuLi 2.5 M in hexanes was added dropwise (8.5 mL, 21.37 mmol, 1.1 eq.) and the bath was removed. After 1 h, tert-butylamine was added (1.2 mL, 9.71 mmol, 0.5 eq.), after 30 min., 2 equivalents of benzaldehyde were added (3.96 mL, 38.85 mmol) and the reaction was heated and stirred at 30 °C overnight. The solvent was removed under vacuum and 50 mL of hexane were added to precipitate the product. All the solids were collected by filtration under vacuum and washed with 100 mL of water to remove salts. The product was dried under vacuum overnight. The product thus obtained was very pure and was used as such in the next step. Yield 63%. ^{1}H-NMR (CDCl$_3$, 600 MHz): δ (ppm) 9.23 (br, 1H), 7.64-7.61 (m, 2H), 7.51-7.48 (m, 1H), 7.46-7.42 (m, 2H), 5.89-5.84 (m, 1H), 2.29 (s, 3H), 1.92 (s, 3H). ^{13}C-NMR (CDCl$_3$, 150 MHz):

δ (ppm) 185.8, 140.2, 135.8, 131.0, 130.9, 128.4 (2C), 128.3 (2C), 127.9, 113.2, 14.1, 13.3. HR-MS (ESI-TOF) m/z: calculated for $C_{13}H_{14}NO$ 200.1070 found 200.1069

Synthesis of **2**.

1 g of **1** (5.02 mmol) was dissolved in 20 mL of dichloromethane, Br_2 (0.26 mL, 5.1 mmol, 1.2 eq.) was added dropwise and the reaction stirred at RT overnight. The reaction was quenched with water, and the product extracted with DCM (3 x 30 mL), the combined organic phases were dried under vacuum and the product recrystallized from ethanol. The product obtained was highly pure and was used as such in the next step. Yield 95%. ^{1}H-NMR (CDCl$_3$, 600 MHz): δ (ppm) 9.79 (br, 1H), 7.65-7.61 (m, 2H), 7.55-7.51 (m, 1H), 7.48-7.43 (m, 2H), 2.31 (s, 3H), 1.91 (s, 3H). ^{13}C-NMR (CDCl$_3$, 150 MHz): δ (ppm) 185.8, 139.5, 133.9, 131.6, 128.6, 128.51(2C), 128.50(2C), 126.9, 102.5, 13.4, 12.5. HR-MS (ESI-TOF) m/z: calculated for $C_{13}H_{13}BrNO$ 278.0175 found 278.0175.

Synthesis of BODIPY **3**

850 mg of **2** (3.06 mmol) were dissolved in 5 mL of DCM, 0.35 mL of 2,4-dimethylpyrrole (3.36 mmol, 1.1 eq.) and 5 drops of trifluoroacetic acid were added. The reaction was stirred at RT for 24 h. 2.5 mL of triethylamine (18.34 mmol, 6 eq.) and 3.0 mL of BF$_3$ diethyletherate (24.5 mmol, 8 eq.) were added and the reaction proceed at room temperature overnight. Volatiles were removed under vacuum and the crude product was purified by column chromatography (silica gel) using cyclohexane: EtAcO (9:1) as eluent to afford 560 mg of 3 as a dark red solid in 45 % yield. Single crystals of **3** were prepared by slow vapour diffusion and analysed by X-ray diffraction (see Appendix A). ^{1}H-NMR (CDCl$_3$, 600 MHz): δ (ppm) 7.52-7.47 (m, 3H), 7.29-7.24 (m, 2H), 6.04 (s, 1H), 2.60 (s, 3H), 2.58 (s, 3H), 1.39 (s, 3H),

1.37 (s, 3H). ^{13}C-NMR (CDCl$_3$, 150 MHz): δ (ppm) 158.1, 151.5, 145.2, 142.0, 138.9, 134.8, 132.2, 129.9, 129.39, 129.36, 128.0, 122.28, 122.27, 110.71, 110.69, 14.9, 14.6, 13.6, 13.5. HR-MS (ESI-TOF) m/z: calculated for C$_{19}$H$_{18}$BBrF$_2$N$_2$Na 425.0612 found 425.0610.

Synthesis of **B2P**

In a 50 mL round-bottom flask 300 mg of **3** (0.47 mmol), 225.2 mg of 3-(perylenyl) boronic acid pinacol ester (0.56 mmol, 1.2 eq.), 485 mg of caesium carbonate (1.49 mmol, 3 eq.) and 18.15 mg of Pd(dppf)Cl$_2$ were refluxed for 16 h in 10 mL of a 9:1 THF/water solution. The reaction was cooled to room temperature and filtered through a pad of celite using diethyl ether. The filtrate was dried over MgSO$_4$, and the solvents were removed under vacuum. The product was purified by column chromatography (silica gel) using cyclohexane: EtAcO (90:10) to afford 85 mg of B2P, 30% yield. Single crystals of **B2P** were prepared by slow diffusion of vapor and analysed by X-ray diffraction (see sup. info.). ^{1}H-NMR (CDCl$_3$, 600 MHz): δ (ppm) 8.22-8.16 (m, 4H) 7.68(d, ^3J =8.1 Hz) 7.51-7.45 (m, 5H), 7.45-7.41(m, 2H) 7.40-7.36 (m, 1H), 7.35-7.33 (m, 1H), 7.26 (d, ^3J =7.6 Hz), 6.04 (s, 1H), 2.61 (s, 3H), 2.42 (s, 3H), 1.41 (s, 3H), 1.19 (s, 3H). ^{13}C-NMR (CDCl$_3$, 150 MHz): δ (ppm) 156.0, 154.8, 143.7, 142.0, 140.8, 135.2, 134.8, 134.1, 131.94, 131.86, 131.7, 131.34, 131.3, 131.2, 129.3, 129.1, 129.0, 128.7, 128.1, 128.05, 128.0, 126.9, 126.74, 126.73, 126.01, 121.6, 120.52, 120.5, 120.4, 119.9, 14.8, 14.6, 13.5, 13.0. HR-MS (APCI) m/z: calculated for C$_{39}$H$_{29}$BF$_2$N$_2$ 574.2392 found 574.240.

Synthesis of **B2PI**

75 mg of **B2P** (0.13 mmol) were dissolved in 5mL of DCM, 35 mg of NIS were added (0.156 mmol, 1.2 eq.) and the reaction proceeded at room temperature for 2 h. After this time, traces of the starting material were still visible on TLC so 0.6

equivalents of NIS were added (18 mg, 0.078 mmol) and the reaction stirred at RT overnight. Solvents were removed under vacuum and the product was purified by column chromatography (silica gel) using cyclohexane: EtAcO (95:5) to afford 64 mg of **B2PI**. 70% yield. ^{1}H-NMR (CD$_2$Cl$_2$, 600 MHz): δ (ppm) 8.26-8.17(m, 4H), 7.73-7.68 (m, 2H), 7.55-7.47 (m, 5H), 7.47-7.41(m, 2H), 7.41-7.37 (m, 1H), 7.37-7.34 (m, 1H), 7.29 (d, ^3J=7.6 Hz), 2.65 (s, 3H), 2.39 (s, 3H), 1.43 (s, 3H), 1.21 (s, 3H). ^{13}C-NMR (CD$_2$Cl$_2$, 150 MHz): δ (ppm) 157.6, 155.0, 144.0, 143.1, 142.4, 135.2, 135.1, 134.2, 133.3, 132.1, 131.9, 131.6, 131.4, 131.2, 131.0, 129.8, 129.7, 129.3, 128.9, 128.4, 128.39, 128.35, 128.3, 127.3, 127.08, 127.07, 126.1, 120.9, 120.8, 120.7, 120.2, 84.7, 16.9, 16.1, 13.8, 13.3. HR-MS (APCI) m/z: calculated for C$_{39}$H$_{28}$BF$_2$IN$_2$ 700.1358 found 700.136.

2.4.3 Theoretical methods

The quantum chemical calculations were performed by Dr. Julien Guthmuller and Rengel Cane Sia from the Gdańsk University of Technology, Poland using Gaussian 16.[166] Density functional theory (DFT) was employed to calculate the geometry and the harmonic vibrational frequencies of the ground state (S0), while we used time-dependent DFT (TD-DFT) to compute the singlet and triplet excited states properties (i.e. energy, transition dipole moment, geometry). DFT and TD-DFT calculations were done with the MN15[167] exchange-correlation functional in association with the 6-311++G(2d,p) basis set. This combination of functional and basis set proved to be adapted for a previously investigated BODIPY dye.[168]w The effects of the solvent were taken into account (1,4-dioxane, ε=2.2099) by the polarizable continuum model[169] (PCM). A conventional linear response (LR) theory was used for the excited states properties. The vertical absorption energies, oscillator strengths and gradients - employed for the simulation of resonance Raman

(RR) intensities – were calculated using the non-equilibrium procedure of solvation, whereas the equilibrium procedure of solvation was applied to calculate the excited states geometries, transition dipole moments and vertical emission energies.

The radiative rate k_r and associated radiative lifetime ($\tau_r = 1/k_r$) were obtained from the Einstein A_{if} coefficient[168,170]

$$k_r = A_{if} = \frac{\omega_{if}^3}{3\varepsilon_0 \pi \hbar c^3} \left| \vec{\mu}_{if} \right|^2 \tag{1}$$

Within the two-state approximation of Eq. (1), the radiative lifetime was estimated using the vertical emission energy (i.e., $\hbar\omega_{if}$) and the electronic transition dipole moment at the S1 geometry.

The RR intensities of B2PI were obtained with the so-called simplified Φ_e approximation[171],[172] using a local program. The RR spectra were calculated within the Franck-Condon approximation assuming an excitation wavelength of 474nm. The contributions of the S1, S2 and S3 states were included in the simulated RR spectrum. The harmonic frequencies were scaled by a factor of 0.96 to correct for the lack of anharmonicity and the approximate treatment of electron correlation.

The charge density difference (CDD) was calculated with the Multiwfn program[173] in order to characterize the nature of the excited states.

2.4.4 Crystallography.

A) **B2P·[CH₃OH]** $C_{39}H_{29}BF_2N_2$ [CH₃OH]

Experimental

The data were collected at 100(1)K on a Synergy, Dualflex, AtlasS2 diffractometer using Cu*K*α radiation (λ = 1.54184 Å) and the *CrysAlis PRO* suite. Using SHELXLE and Olex2 the structure was solved by dual space methods

(SHELXT) and refined on *F* using all the reflections (SHELXL-2018/3). All the non-hydrogen atoms were refined using anisotropic atomic displacement parameters and hydrogen atoms were inserted at calculated positions using a riding model. Platon SQUEEZE was used to account for some diffuse electron density. The cell contained two voids each of 392 Å containing 78 electrons (Figure A13); the density was assigned to one methanol molecule per formula unit (8 per cell). Crystal parameters, data collection and structure refinement details are summarised in Table A2.

2.5 References

[1]   *Proc. R. Soc. Lond. A* **1963**, *276*, 125–135.

[2]   T. N. Singh-Rachford, F. N. Castellano, *Coord. Chem. Rev.* **2010**, *254*, 2560–2573.

[3]   K. Kwon, T. Son, K.-J. Lee, B. Jung, *Lasers. Med. Sci.* **2009**, *24*, 605–615.

[4]   C. Ash, M. Dubec, K. Donne, T. Bashford, *Lasers. Med. Sci.* **2017**, *32*, 1909–1918.

[5]   Q. le Masne de Chermont, C. Chanéac, J. Seguin, F. Pellé, S. Maîtrejean, J.-P. Jolivet, D. Gourier, M. Bessodes, D. Scherman, *Proc. Natl. Acad. Sci. U.S.A.* **2007**, *104*, 9266–9271.

[6]   D. Chatterjee, A. Rufaihah, Y. Zhang, *Biomater.* **2008**, *29*, 937–943.

[7]   X. Xiao, W. Tian, M. Imran, H. Cao, J. Zhao, *Chem. Soc. Rev.* **2021**, *50*, 9686–9714.

[8]   C. Karunakaran, M. Balamurugan, in *Spin Resonance Spectroscopy, Principles and Applications*, Elsevier Inc., Berkeley. **2018**, pp. 215–216.

[9]   Z. Lou, Y. Hou, K. Chen, J. Zhao, S. Ji, F. Zhong, Y. Dede, B. Dick, *J. Phys. Chem. C* **2018**, *122*, 185–193.

[10]   T. Takemura, N. Ohta, S. Nakajima, I. Sakata, *Photochem. Photobiol.* **1989**, *50*, 339–344.

[11]   V. Gray, D. Dzebo, M. Abrahamsson, B. Albinsson, K. Moth-Poulsen, *Phys. Chem. Chem. Phys.* **2014**, *16*, 10345–10352.

[12]   M. E. Díaz-García, A. Fernández-González, R. Badía-Laíño, *Appl. Spectrosc. Rev.* **2007**, *42*, 605–624.

[13]   S. K. Lower, M. A. El-Sayed, *Chem. Rev.* **1966**, *66*, 199–241.

[14]   P. A. M. Dirac, *Proc. R. S. Lond.* **1928**, *117*, 610–624.

[15]   P. Pyykkö, *Annu. Rev. Phys. Chem.* **2012**, *63*, 45–64.

[16]   M. Chapman, C. S. de Melo, *Nature* **2011**, *471*, 41–42.

[17]   J. MacLaren, in *Magnetic Interactions and Spin Transport* (Eds.: A. Chtchelkanova, S. Wolf, Y. Idzerda), Springer US, Boston, MA, **2003**, pp. 131–184.

[18]   C. M. Marian, *WIREs Comput. Mol. Sci.* **2012**, *2*, 187–203.

[19]   P. Pyykko, *Chem. Rev.* **1988**, *88*, 563–594.

[20]   B. J. R. Cuyacot, J. Novotný, R. J. F. Berger, S. Komorovsky, R. Marek, *Chem. Eur. J.* **2022**, *28*.

[21]   E. A. Gastilovich, N. V. Korol'kova, V. G. Klimenko, R. N. Nurmukhametov, *Opt. Spectrosc.* **2008**, *104*, 491–494.

[22]   C. Reichardt, R. A. Vogt, C. E. Crespo-Hernández, *J. Chem. Phys.* **2009**, *131*, 224518.

[23]   J. J. Cavaleri, K. Prater, R. M. Bowman, *Chem. Phys. Lett.* **1996**, *259*, 495–502.

[24]   H. Satzger, B. Schmidt, C. Root, W. Zinth, B. Fierz, F. Krieger, T. Kiefhaber, P. Gilch, *J. Phys. Chem. A* **2004**, *108*, 10072–10079.

[25]   J. Zhao, S. Ji, W. Wu, W. Wu, H. Guo, J. Sun, H. Sun, Y. Liu, Q. Li, L. Huang, *RSC Adv.* **2012**, *2*, 1712–1728.

[26]   A. Chettri, H. D. Cole, J. A. Roque III, K. R. A. Schneider, T. Yang, C. G. Cameron, S. A. McFarland, B. Dietzek-Ivanšić, *J. Phys. Chem. A* **2022**, *126*, 1336–1344.

[27]   C. S. Burke, A. Byrne, Tia. E. Keyes, *J. Am. Chem. Soc.* **2018**, *140*, 6945–6955.

[28]   C. S. Burke, T. E. Keyes, *RSC Adv.* **2016**, *6*, 40869–40877.

[29]   M. Lin, S. Zou, X. Liao, Y. Chen, D. Luo, L. Ji, H. Chao, *Chem. Commun.* **2021**, *57*, 4408–4411.

[30]   X.-Q. Zhou, M. Xiao, V. Ramu, J. Hilgendorf, X. Li, P. Papadopoulou, M. A. Siegler, A. Kros, W. Sun, S. Bonnet, *J. Am. Chem. Soc.* **2020**, *142*, 10383–10399.

[31]   F.-R. Dai, Y.-C. Chen, L.-F. Lai, W.-J. Wu, C.-H. Cui, G.-P. Tan, X.-Z. Wang, J.-T. Lin, H. Tian, W.-Y. Wong, *Chem. Asian J.* **2012**, *7*, 1426–1434.

[32]   L. Huang, T. Le, K. Huang, G. Han, *Nat. Commun.* **2021**, *12*, 1898.

[33]   Y. Wang, X. Shi, H. Fang, Z. Han, H. Yuan, Z. Zhu, L. Dong, Z. Guo, X. Wang, *J. Med. Chem.* **2022**, *65*, 7786–7798.

[34]   G. Li, M. F. Mark, H. Lv, D. W. McCamant, R. Eisenberg, *J. Am. Chem. Soc.* **2018**, *140*, 2575–2586.

[35]   J. A. Roque, P. C. Barrett, H. D. Cole, L. M. Lifshits, G. Shi, S. Monro, D. von Dohlen, S. Kim, N. Russo, G. Deep, C. G. Cameron, M. E. Alberto, S. A. McFarland, *Chem. Sci.* **2020**, *11*, 9784–9806.

[36]   S. Lazic, P. Kaspler, G. Shi, S. Monro, T. Sainuddin, S. Forward, K. Kasimova, R. Hennigar, A. Mandel, S. McFarland, L. Lilge, *Photochem. Photobiol.* **2017**, *93*, 1248–1258.

[37]   K. Chen, I. V. Kurganskii, X. Zhang, A. Elmali, J. Zhao, A. Karatay, M. V. Fedin, *Chem. Eur. J.* **2021**, *27*, 7572–7587.

[38]   S. Monro, K. L. Colón, H. Yin, J. Roque, P. Konda, S. Gujar, R. P. Thummel, L. Lilge, C. G. Cameron, S. A. McFarland, *Chem. Rev.* **2019**, *119*, 797–828.

[39]   S. Goel, F. Chen, W. Cai, *Small* **2014**, *10*, 631–645.

[40]   D. Diaz-Diestra, H. M. Gholipour, M. Bazian, B. Thapa, J. Beltran-Huarac, *Nanoscale Res. Lett.* **2022**, *17*, 33.

[41]   M. Uji, N. Harada, N. Kimizuka, M. Saigo, K. Miyata, K. Onda, N. Yanai, *J. Mater. Chem. C* **2022**, *10*, 4558–4562.

[42]   N. T. Nassar, *Green Chem.* **2015**, *17*, 2226–2235.

[43]   Z. Murtaza, P. Herman, J. R. Lakowicz, *Biophys. Chem.* **1999**, *80*, 143–151.

[44]   S. R. Pristash, K. L. Corp, E. J. Rabe, C. W. Schlenker, *ACS Appl. Energy Mater.* **2020**, *3*, 19–28.

[45]   C. M. Marian, *Annu. Rev. Phys. Chem.* **2021**, *72*, 617–640.

[46]   S. Ji, J. Ge, D. Escudero, Z. Wang, J. Zhao, D. Jacquemin, *J. Org. Chem.* **2015**, *80*, 5958–5963.

[47]   S. Duman, Y. Cakmak, S. Kolemen, E. U. Akkaya, Y. Dede, *J. Org. Chem.* **2012**, *77*, 4516–4527.

[48]   F.-W. Gao, R.-L. Zhong, H.-L. Xu, Z.-M. Su, *J. Phys. Chem. C* **2017**, *121*, 25472–25478.

[49]   A. Nano, R. Ziessel, P. Stachelek, A. Harriman, *Chem. Eur. J.* **2013**, *19*, 13528–13537.

[50]   S. V. Feskov, V. A. Mikhailova, A. I. Ivanov, *J. Photochem. Photobiol. C.* **2016**, *29*, 48–72.

[51]   T. Kircher, H.-G. Löhmannsröben, *Phys. Chem. Chem. Phys.* **1999**, *1*, 3987–3992.

[52]   D. J. Gibbons, A. Farawar, P. Mazzella, S. Leroy-Lhez, R. M. Williams, *Photochem. Photobiol. Sci.* **2020**, *19*, 136–158.

[53]   Z. E. X. Dance, Q. Mi, D. W. McCamant, M. J. Ahrens, M. A. Ratner, M. R. Wasielewski, *J. Phys. Chem. B* **2006**, *110*, 25163–25173.

[54]   E. A. Weiss, M. A. Ratner, M. R. Wasielewski, *J. Phys. Chem. A* **2003**, *107*, 3639–3647.

[55]   P. Spenst, R. M. Young, M. R. Wasielewski, F. Würthner, *Chem. Sci.* **2016**, *7*, 5428–5434.

[56]   M. Imran, A. A. Sukhanov, Z. Wang, A. Karatay, J. Zhao, Z. Mahmood, A. Elmali, V. K. Voronkova, M. Hayvali, Y. H. Xing, S. Weber, *J. Phys. Chem. C* **2019**, *123*, 7010–7024.

[57]   M. A. El-Sayed, *J. Chem. Phys.* **1974**, *60*, 4502–4507.

[58]   M. A. El-Sayed, *Acc. Chem. Res.* **1968**, *1*, 8–16.

[59]   Y. Beldjoudi, A. Atilgan, J. A. Weber, I. Roy, R. M. Young, J. Yu, P. Deria, A. E. Enciso, M. R. Wasielewski, J. T. Hupp, J. F. Stoddart, *Adv. Mater.* **2020**, *32*, 2001592.

[60]   J. T. Buck, A. M. Boudreau, A. DeCarmine, R. W. Wilson, J. Hampsey, T. Mani, *Chem* **2019**, *5*, 138–155.

[61]   H. van Willigen, G. Jones, M. S. Farahat, *J. Phys. Chem.* **1996**, *100*, 3312–3316.

[62]   Z. E. X. Dance, S. M. Mickley, T. M. Wilson, A. B. Ricks, A. M. Scott, M. A. Ratner, M. R. Wasielewski, *J. Phys. Chem. A* **2008**, *112*, 4194–4201.

[63]   Z. Wang, J. Zhao, *Org. Lett.* **2017**, *19*, 4492–4495.

[64]   J. R. Lakowicz. in *Principles of Fluorescence Spectroscopy*, Springer US, Boston, MA, **2006**. pp. 443-445.

[65]   D. L. Dexter, *J. Chem. Phys.* **1953**, *21*, 836–850.

[66]   Z.-Q. You, C.-P. Hsu, G. R. Fleming. *J. Chem. Phys.* **2006**, *124*, 044506.

[67]   M. W. Schmidt, E. K. C. Lee, *J. Am. Chem. Soc.* **1970**, *92*, 3579–3586.

[68]   S. V. Gaponenko, H. V. Demir, in *Applied Nanophotonics*, Cambridge University Press, Cambridge, **2018**, pp. 210–226.

[69]   A. Köhler, H. Bässler, *Mater. Sci. Eng. R.* **2009**, *66*, 71–109.

[70]   S. Chen, F. Chen, P. Han, C. Ye, S. Huang, L. Xu, X. Wang, Y. Song, *RSC Adv.* **2019**, *9*, 36410–36415.

[71]   F. Wilkinson, D. J. McGarvey, A. F. Olea, *J. Phys. Chem.* **1994**, *98*, 3762–3769.

[72]   S. H. C. Askes, S. Bonnet, *Nat. Rev. Chem.* **2018**, *2*, 437–452.

[73]   B. Shen, Y. Qian, Z. Qi, C. Lu, Y. Cui, *Chem.Select* **2017**, *2*, 9970–9976.

[74]   K. K. Jha, A. Prabhakaran, C. S. Burke, M. Schulze, U. S. Schubert, T. E. Keyes, M. Jäger, B. D. Ivanšić, *J. Phys. Chem. C* **2022**, *126*, 4057–4066.

[75]   D. O' Connor, A. Byrne, T. E. Keyes, *RSC Adv.* **2019**, *9*, 22805–22816.

[76]   Li, Li, Otsuka, Zhang, Takahashi, Yamada, *Materials* **2020**, *13*, 677.

[77]   M. M. Ogle, A. D. Smith McWilliams, M. J. Ware, S. A. Curley, S. J. Corr, A. A. Martí, *J. Phys. Chem. B* **2019**, *123*, 7282–7289.

[78]   H.-C. Xia, X.-H. Xu, Q.-H. Song, *Anal. Chem.* **2017**, *89*, 4192–4197.

[79]   F. Cai, Y. Guo, Y. Fang, C. P. Gros, A. Agrawal, G. D. Sharma, H. Xu, *Solar Energy* **2021**, *227*, 354–364.

[80]   A. M. Poe, A. M. Della Pelle, A. V. Subrahmanyam, W. White, G. Wantz, S. Thayumanavan, *Chem. Commun.* **2014**, *50*, 2913–2915.

[81]   A. Schmitt, B. Hinkeldey, M. Wild, G. Jung, *J. Fluoresc.* **2009**, *19*, 755–758.

[82]   R. W. Wagner, J. S. Lindsey, *Pure App. Chem.* **1996**, *68*, 1373–1380.

[83]   J. Godoy, G. Vives, J. M. Tour, *Org. Lett.* **2010**, *12*, 1464–1467.

[84]   C. B. Reese, H. Yan, *Tetrahedron Lett.* **2001**, *42*, 5545–5547.

[85]   T. V. Goud, A. Tutar, J.-F. Biellmann, *Tetrahedron* **2006**, *62*, 5084–5091.

[86]   L. P. Jameson, S. V. Dzyuba, *Beilstein J. Org. Chem.* **2013**, *9*, 786–790.

[87]   N. Boens, B. Verbelen, M. J. Ortiz, L. Jiao, W. Dehaen, *Coord. Chem. Rev.* **2019**, *399*, 213024.

[88]   C. Tahtaoui, C. Thomas, F. Rohmer, P. Klotz, G. Duportail, Y. Mély, D. Bonnet, M. Hibert, *J. Org. Chem.* **2007**, *72*, 269–272.

[89]   K. O. Jeon, J. H. Jun, J. S. Yu, C. K. Lee, *J. Heterocycl. Chem.* **2003**, *40*, 763–771.

[90]   C.-H. Lee, J. S. Lindsey, *Tetrahedron* **1994**, *50*, 11427–11440.

[91]   S. Massa, R. Ragno, G. C. Porretta, A. Mai, A. Retico, M. Artico, N. Simonetti, *Arch. Pharm. Pharm. Med. Chem.* **1993**, *326*, 539–546.

[92]   D. M. Wallace, S. H. Leung, M. O. Senge, K. M. Smith, *J. Org. Chem.* **1993**, *58*, 7245–7257.

[93]   J. Bergman, L. Venemalm, *Tetrahedron Lett.* **1987**, *28*, 3741–3744.

[94] P. Wang, F. Lu, J. S. Lindsey, *J. Org. Chem.* **2020**, *85*, 702–715.

[95] Z. Guo, X. Wei, Y. Hua, J. Chao, D. Liu, *Tetrahedron Lett.* **2015**, *56*, 3919–3922.

[96] C. F. Candy, R. A. Jones, P. H. Wright, *J. Chem. Soc. C* **1970**, *0*, 2563–2567.

[97] P. D. Magnus, C. Exon, N. L. Sear, *Tetrahedron* **1983**, *39*, 3725–3729.

[98] R. I. Lerrick, T. P. L. Winstanley, K. Haggerty, C. Wills, W. Clegg, R. W. Harrington, P. Bultinck, W. Herrebout, A. C. Benniston, M. J. Hall, *Chem. Commun.* **2014**, *50*, 4714–4716.

[99] C. Xu, Y. Qian, Z. Qi, C. Lu, Y. Cui, *New J. Chem.* **2018**, *42*, 6910–6917.

[100] Z. Zhou, J. Zhou, L. Gai, A. Yuan, Z. Shen, *Chem. Commun.* **2017**, *53*, 6621–6624.

[101] C. Bellomo, D. Zanetti, F. Cardano, S. Sinha, M. Chaari, A. Fin, A. Maranzana, R. Núñez, M. Blangetti, C. Prandi, *Dyes Pigm.* **2021**, *194*, 109644.

[102] J. Chen, M. Mizumura, H. Shinokubo, A. Osuka, *Chem. Eur. J.* **2009**, *15*, 5942–5949.

[103] K. Chen, Y. Dong, X. Zhao, M. Imran, G. Tang, J. Zhao, Q. Liu, *Front. Chem.* **2019**, *7*, 821.

[104] Q. Zhou, M. Zhou, Y. Wei, X. Zhou, S. Liu, S. Zhang, B. Zhang, *Phys. Chem. Chem. Phys.* **2017**, *19*, 1516–1525.

[105] Z. Wang, Y. Xie, K. Xu, J. Zhao, K. D. Glusac, *J. Phys. Chem. A* **2015**, *119*, 6791–6806.

[106] J. Sun, Y. Dai, Y. Hou, Q. Wu, L. Ma, J. Zhao, B. Wang, *J. Phys. Chem. A* **2021**, *125*, 2344–2355.

[107] W. Wu, H. Guo, W. Wu, S. Ji, J. Zhao, *J. Org. Chem.* **2011**, *76*, 7056–7064.

[108] M. Galletta, S. Campagna, M. Quesada, G. Ulrich, R. Ziessel, *Chem. Commun.* **2005**, 4222.

[109] N. Epelde-Elezcano, E. Palao, H. Manzano, A. Prieto-Castañeda, A. R. Agarrabeitia, A. Tabero, A. Villanueva, S. de la Moya, Í. López-Arbeloa, V. Martínez-Martínez, M. J. Ortiz, *Chem. Eur. J.* **2017**, *23*, 4837–4848.

[110] Y. Liu, J. Zhao, A. Iagatti, L. Bussotti, P. Foggi, E. Castellucci, M. Di Donato, K.-L. Han, *J. Phys. Chem. C* **2018**, *122*, 2502–2511.

[111] R. Montero, V. Martínez-Martínez, A. Longarte, N. Epelde-Elezcano, E. Palao, I. Lamas, H. Manzano, A. R. Agarrabeitia, I. López Arbeloa, M. J. Ortiz, I. Garcia-Moreno, *J. Phys. Chem. Lett.* **2018**, *9*, 641–646.

[112] Y. E. Kandrashkin, Z. Wang, A. A. Sukhanov, Y. Hou, X. Zhang, Y. Liu, V. K. Voronkova, J. Zhao, *J. Phys. Chem. Lett.* **2019**, *10*, 4157–4163.

[113] X. Cui, A. Charaf-Eddin, J. Wang, B. Le Guennic, J. Zhao, D. Jacquemin, *J. Org. Chem.* **2014**, *79*, 2038–2048.

[114] F. Schweighöfer, L. Dworak, C. A. Hammer, H. Gustmann, M. Zastrow, K. Rück-Braun, J. Wachtveitl, *Sci Rep* **2016**, *6*, 28638.

[115] B. Basumatary, A. Raja Sekhar, R. V. Ramana Reddy, J. Sankar, *Inorg. Chem.* **2015**, *54*, 4257–4267.

[116] K. Ladomenou, V. Nikolaou, G. Charalambidis, A. Charisiadis, A. G. Coutsolelos, *C. R. Chim.* **2017**, *20*, 314–322.

[117] E. Karakuş, M. Üçüncü, M. Emrullahoğlu, *Chem. Commun.* **2014**, *50*, 1119–1121.

[118] H. Eserci, M. Çetin, F. Aydınoğlu, E. T. Eçik, E. Okutan, *J. Mol. Struct.* **2022**, *1265*, 133440.

[119] R. H. Clarke, R. M. Hochstrasser, *J. Mol. Spectrosc.* **1969**, *32*, 309–319.

[120] T. N. Singh-Rachford, F. N. Castellano, *J. Phys. Chem. Lett.* **2010**, *1*, 195–200.

[121] I. Ghosh, T. Ghosh, J. I. Bardagi, B. König, *Science* **2014**, *346*, 725–728.

[122] K. M. Felter, M. C. Fravventura, E. Koster, R. D. Abellon, T. J. Savenije, F. C. Grozema, *ACS Energy Lett.* **2020**, *5*, 124–129.

[123] X. Cui, A. M. El-Zohry, Z. Wang, J. Zhao, O. F. Mohammed, *J. Phys. Chem. C* **2017**, *121*, 16182–16192.

[124] A. J. F. N. Sobral, N. G. C. L. Rebanda, M. da Silva, S. H. Lampreia, M. Ramos Silva, A. M. Beja, J. A. Paixão, A. M. d'A Rocha Gonsalves, *Tetrahedron Lett.* **2003**, *44*, 3971–3973.

[125] C. Brückner, V. Karunaratne, S. J. Rettig, D. Dolphin, *Can. J. Chem.* **1996**, *74*, 2182–2193.

[126] Z. Guo, Q. Liu, X. Wei, Y. Zhang, H. Tong, J. Chao, J. Guo, D. Liu, *Organometallics* **2013**, *32*, 4677–4683.

[127] R. J. Brea, M. J. Pérez-Alvite, M. Panciera, M. Mosquera, L. Castedo, J. R. Granja, *Chem. Asian J.* **2011**, *6*, 110–121.

[128] K. Xu, J. Zhao, E. G. Moore, *J. Phys. Chem. C* **2017**, *121*, 22665–22679.

[129] H. J. Shine, C. V. Ristagno, *J. Am. Chem. Soc.* **1971**, *93*, 1811–1812.

[130] T. A. Perera, M. Masjedi, P. R. Sharp, *Inorg. Chem.* **2014**, *53*, 7608–7621.

[131] K. Kodama, A. Kobayashi, T. Hirose, *Tetrahedron Lett.* **2013**, *54*, 5514–5517.

[132] M. Inouye, Y. Hyodo, H. Nakazumi, *J. Org. Chem.* **1999**, *64*, 2704–2710.

[133] H. Guo, L. Zhu, C. Dang, J. Zhao, B. Dick, *Phys. Chem. Chem. Phys.* **2018**, *20*, 17504–17516.

[134] Y. Avlasevich, K. Müllen, *J. Org. Chem.* **2007**, *72*, 10243–10246.

[135] A. J. J. Lennox, G. C. Lloyd-Jones, *Chem. Soc. Rev.* **2014**, *43*, 412–443.

[136] A. K. L. Yuen, C. A. Hutton, *Tetrahedron Lett.* **2005**, *46*, 7899–7903.

[137]   P. A. Inglesby, L. R. Agnew, H. L. Carter, O. T. Ring, *Org. Process Res. Dev.* **2020**, *24*, 1683–1689.

[138]   M. C. D'Alterio, È. Casals-Cruañas, N. V. Tzouras, G. Talarico, S. P. Nolan, A. Poater, *Chem. Eur. J.* **2021**, *27*, 13481–13493.

[139]   N. Miyaura, A. Suzuki, *Chem. Rev.* **1995**, *95*, 2457–2483.

[140]   A. A. Thomas, A. F. Zahrt, C. P. Delaney, S. E. Denmark, *J. Am. Chem. Soc.* **2018**, *140*, 4401–4416.

[141]   C. Amatore, A. Jutand, in *Handbook of Organopalladium Chemistry for Organic Synthesis* (Ed.: E. Negishi), John Wiley & Sons, Inc., New York, USA, **2002**, pp. 943–972.

[142]   J. W. Suggs, in *Encyclopedia of Inorganic and Bioinorganic Chemistry* (Ed.: R.A. Scott), John Wiley & Sons, Ltd, Chichester, UK, **2011**, p. eibc0165.

[143]   R. Hu, E. Lager, A. Aguilar-Aguilar, J. Liu, J. W. Y. Lam, H. H. Y. Sung, I. D. Williams, Y. Zhong, K. S. Wong, E. Peña-Cabrera, B. Z. Tang, *J. Phys. Chem. C* **2009**, *113*, 15845–15853.

[144]   Y. Zhao, S. He, J. Yang, H. Sun, X. Shen, X. Han, Z. Ni, *Opt. Mater.* **2018**, *81*, 102–108.

[145]   Y. Oshikawa, A. Ojida, *Chem. Commun.* **2013**, *49*, 11373.

[146]   H. Sunahara, Y. Urano, H. Kojima, T. Nagano, *J. Am. Chem. Soc.* **2007**, *129*, 5597–5604.

[147]   S. Toliautas, J. Dodonova, A. Žvirblis, I. Čiplys, A. Polita, A. Devižis, S. Tumkevičius, J. Šulskus, A. Vyšniauskas, *Chem. Eur. J.* **2019**, *25*, 10342–10349.

[148]   H. Gao, Y. Gao, C. Wang, D. Hu, Z. Xie, L. Liu, B. Yang, Y. Ma, *ACS Appl. Mater. Interfaces* **2018**, *10*, 14956–14965.

[149]   J. Wan, A. Ferreira, W. Xia, C. H. Chow, K. Takechi, P. V. Kamat, G. Jones, V. I. Vullev, *J. Photochem. Photobiol. A.* **2008**, *197*, 364–374.

[150]   F. Gutierrez, J. Trzcionka, R. Deloncle, R. Poteau, N. Chouini-Lalanne, *New J. Chem.* **2005**, *29*, 570.

[151] B. Carlotti, M. Poddar, F. Elisei, A. Spalletti, R. Misra, *J. Phys. Chem. C* **2019**, *123*, 24362–24374.

[152] R. A. Arellano-Reyes, A. Prabhakaran, R. C. E. Sia, J. Guthmuller, K. K. Jha, T. Yang, B. Dietzek-Ivanšić, V. McKee, T. E. Keyes, *Chem. Eur. J.* **2023**, *29*, e202300239.

[153] C. R. Groom, I. J. Bruno, M. P. Lightfoot, S. C. Ward, *Acta Crystallogr. B* **2016**, *72*, 171–179.

[154] R. Ziessel, C. Goze, G. Ulrich, M. Césario, P. Retailleau, A. Harriman, J. P. Rostron, *Chem. Eur. J.* **2005**, *11*, 7366–7378.

[155] J. A. Jacobsen, J. R. Stork, D. Magde, S. M. Cohen, *Dalton Trans.* **2010**, *39*, 957–962.

[156] E. Smith, G. Dent. In *Modern Raman Spectroscopy - A Practical Approach*, John Wiley & Sons, Ltd, Chichester, UK, **2005**, pp. 93–112.

[157] W.-H. Kim, J. I. Mapley, D.-H. Roh, J. S. Kim, S. Y. Yoon, K. C. Gordon, T.-H. Kwon, *Mater. Today Adv.* **2021**, *12*, 100180.

[158] Y. Nishina, T. Kitagawa, K. Shiga, H. Watari, T. Yamano. *J. Biochem.* **1980**, *87*, 831–839.

[159] R. L. Birke, J. R. Lombardi, *Nanomater.* **2021**, *11*, 1491.

[160] C. Ye, V. Gray, K. Kushwaha, S. Kumar Singh, P. Erhart, K. Börjesson, *Phys. Chem. Chem. Phys.* **2020**, *22*, 1715–1720.

[161] Y. Wei, M. Zheng, Q. Zhou, X. Zhou, S. Liu, *Org. Biomol. Chem.* **2018**, *16*, 5598–5608.

[162] K. Chen, W. Yang, Z. Wang, A. Iagatti, L. Bussotti, P. Foggi, W. Ji, J. Zhao, M. Di Donato, *J. Phys. Chem. A* **2017**, *121*, 7550–7564.

[163] S. Dartar, M. Ucuncu, E. Karakus, Y. Hou, J. Zhao, M. Emrullahoglu, *Chem. Commun.* **2021**, *57*, 6039–6042.

[164] K. Kumar Jha, A. Prabhakaran, R. Cane Sia, R. A. Arellano Reyes, N. Kumar Sarangi, T. Yang, K. Kumar, S. Kupfer, J. Guthmuller, T. E. Keyes, B. Dietzek-Ivanšić, *ChemPhotoChem* **2023**, *7*, e202300073.

[165] T. Yang, R. A. Arellano-Reyes, R. C. Curley, K. K. Jha, A. Chettri, T. E. Keyes, B. Dietzek-Ivanšić, *Chem. Eur. J.* **2023**, *29*, e202300224.

[166] M. J. Frisch, G. W. Trucks, H. B. Schlegel, G. E. Scuseria, M. A. Robb, J. R. Cheeseman, G. Scalmani, V. Barone, G. A. Petersson, H. Nakatsuji, X. Li, M. Caricato, A. B. Marenich, J. Bloino, B. G. Janesko, R. Gomperts, B. Mennucci, H. P. Hratchian, J. V. Ortiz, A. F. Izmaylov, J. L. Sonnenberg, D. Williams-Young, F. Ding, F. Lipparini, F. Egidi, J. Goings, B. Peng, A. Petrone, T. Henderson, D. Ranasinghe, V. G. Zakrzewski, J. Gao, N. Rega, G. Zheng, W. Liang, M. Hada, M. Ehara, K. Toyota, R. Fukuda, J. Hasegawa, M. Ishida, T. Nakajima, Y. Honda, O. Kitao, H. Nakai, T. Vreven, K. Throssell, J. A. Montgomery Jr., J. E. Peralta, F. Ogliaro, M. J. Bearpark, J. J. Heyd, E. N. Brothers, K. N. Kudin, V. N. Staroverov, T. A. . Keith, R. Kobayashi, J. Normand, Raghavachari, A. P. Rendell, J. C. Burant, S. S. Iyengar, J. Tomasi, M. Cossi, J. M. Millam, M. Klene, C. Adamo, R. Cammi, J. W. Ochterski, R. L. Martin, K. Morokuma, O. Farkas, J. B. Foresman, D. J. Fox, *Gaussian 16*, Gaussian, Inc., Wallingford CT, **2016**.

[167] H. S. Yu, X. He, S. L. Li, D. G. Truhlar, *Chem. Sci.* **2016**, *7*, 5032–5051.

[168] R. C. E. Sia, R. A. Arellano-Reyes, T. E. Keyes, J. Guthmuller, *Phys. Chem. Chem. Phys.* **2021**, *23*, 26324–26335.

[169] J. Tomasi, B. Mennucci, R. Cammi, *Chem. Rev.* **2005**, *105*, 2999–3093.

[170] D. P. Craig, T. Thirunamachandran, *Molecular Quantum Electrodynamics: An Introduction to Radiation Molecule Interaction*, Dover Publications, Mineola, NY, **1984**.

[171] J. Guthmuller, *J. Chem. Phys.* **2016**, *144*, 064106.

[172] J. Guthmuller, in *Molecular Spectroscopy: A Quantum Chemistry Approach* (Eds.: Y. Ozaki, M.J. Wójcik, J. Popp), Wiley-VCH, **2019**, pp. 497–536.

[173] T. Lu, F. Chen, *J. Comput. Chem.* **2012**, *33*, 580–592.

Chapter 3 Synthesis and functionalisation of BODIPY fluorophores

Overview

In this chapter, to understand further the photophysics of the BODIPY-perylene dyads and the prospects for controlling their properties through modification of the torsion angle between the pair, a series of modified dyads was prepared with varying degrees of steric constraint to the angle between the donor and acceptor units.

A brief introduction to the main reactions involved during the synthesis is presented. This includes selective halogenation, cross-coupling reactions (Stille, Suzuki-Miyaura, Mizoroki-Heck), and the Knoevenagel condensation. The synthetic strategies, the specificities of the methodologies, as well as their application to the functionalisation of BODIPYs are described and justified.

Descriptions of the attempts to change the properties of the dyads by introducing electron donating functional groups is included. The approaches to change the array of the methyl substituents on BODIPY are explained. The improvements in the cross-coupling functionalisation of hindered BODIPY positions are described and rationalised. The extension of the conjugation by addition of double bonds between BODIPY and perylene was studied. Observations concerning the stability and reactivity of BODIPYs in different conditions are included and discussed.

Finally, a basic description of the photophysical properties of the dyes is also included as well as the effect of the solvents on the BODIPYs' properties.

3.1 Functionalisation of BODIPY fluorophores

BODIPYs are synthetically versatile, and the spectroscopical properties can be extensively modified by the introduction of electron donating/withdrawing groups, by the halogenation of the rings or by the extension of the conjugation. In this section, some key modifications used for photophysical/spectroscopic tuning reported in the recent literature will be presented. The reactions included in this introduction will be later applied to the design and modification of a series of BODIPYs-perylene conjugates.

3.1.1 Synthesis and applications of halogenated BODIPYS

Halogenation of the BODIPY highly depends on the substituent the core bears. For the symmetric unsubstituted core, there have been some reports that selectively add 1 to 4 halogen atoms, mainly bromine[1] (Figure 42 a). Another alternative using choline chloride and hexafluoro-2-propanol as the solvent system has also been reported, but this combination was not studied as a step-by-step halogenation.[2]

In the case of substituted and non-symmetric BODIPYs, the substitution patterns and the nature of the substituents determine the electronic distribution and therefore the selectivity of the electrophilic halogenation. To the best of my knowledge, there are no methodologies reported to accomplish the halogenations below in Figure 42 (b).
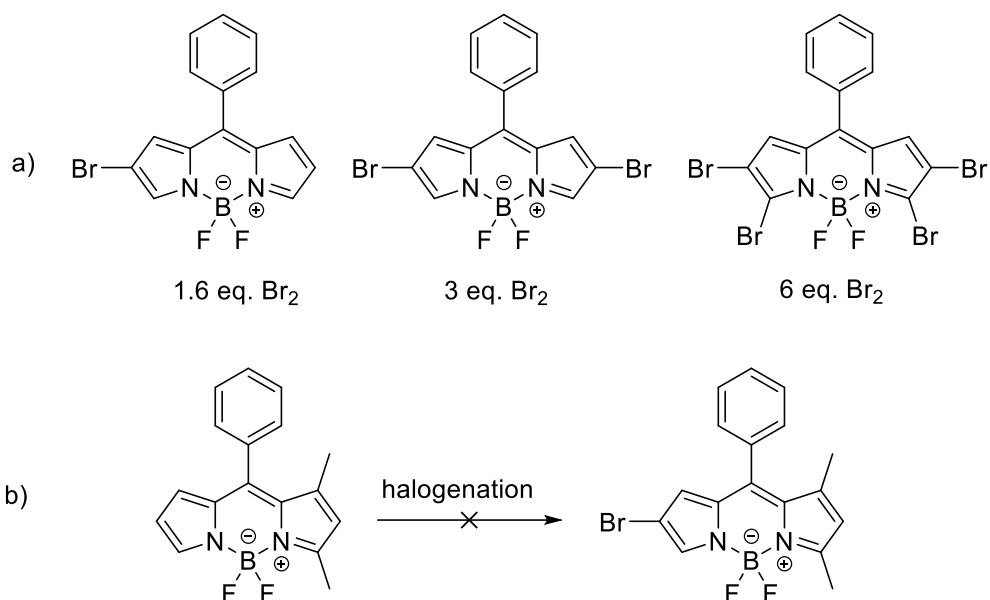
Figure 42 *a) Selective bromination of a symmetric BODIPY.* [1] *(b) No methodology exists to perform this transformation.*

Relatively simple halogenated BODIPYs are worth paying attention to. They have been used for photodynamic therapy and singlet oxygen generation with generally good results.[3–5]

3.1.2 The Stille reaction and its application to the functionalisation of BODIPYs

The Stille reaction is a cross-coupling methodology to form C-C bonds. The reaction involves an organotin compound, called a stannane, as the nucleophilic partner, and a halide or pseudo halide as the electrophilic partner.[6] The reaction has a wide application scope due to the simplicity of its implementation, (generally only the two partners and the palladium catalyst are required), and broad functional group tolerance (no base is typically required, limiting side reactions).[7] The reaction has been widely used in the synthesis of natural products.[7–9] The main drawback of the transformation is the toxicity of the stannanes and tin byproducts.[10,11] Nevertheless, due to the mild conditions of the reaction and its robustness, it has been used in large-scale production of pharmaceutical ingredients.[12]

Applications of the Stille reaction to the functionalisation of the BODIPY core have been very successful and do not require either a complex catalyst or particularly inert conditions. More importantly, the success of the reaction does not seem to be restricted by steric considerations. In fact, positions 8, 3, 5 have all been functionalised in chloro-substituted BODIPYs, positions 2 and 6 have been functionalised in tetramethyl substituted BODIPYS with significant steric hindrance, and unsubstituted BODIPYs have been functionalised using only Pd(PPh3)4 in toluene and the corresponding aryl or heteroaryl stannane.[13–15] Figure 43.
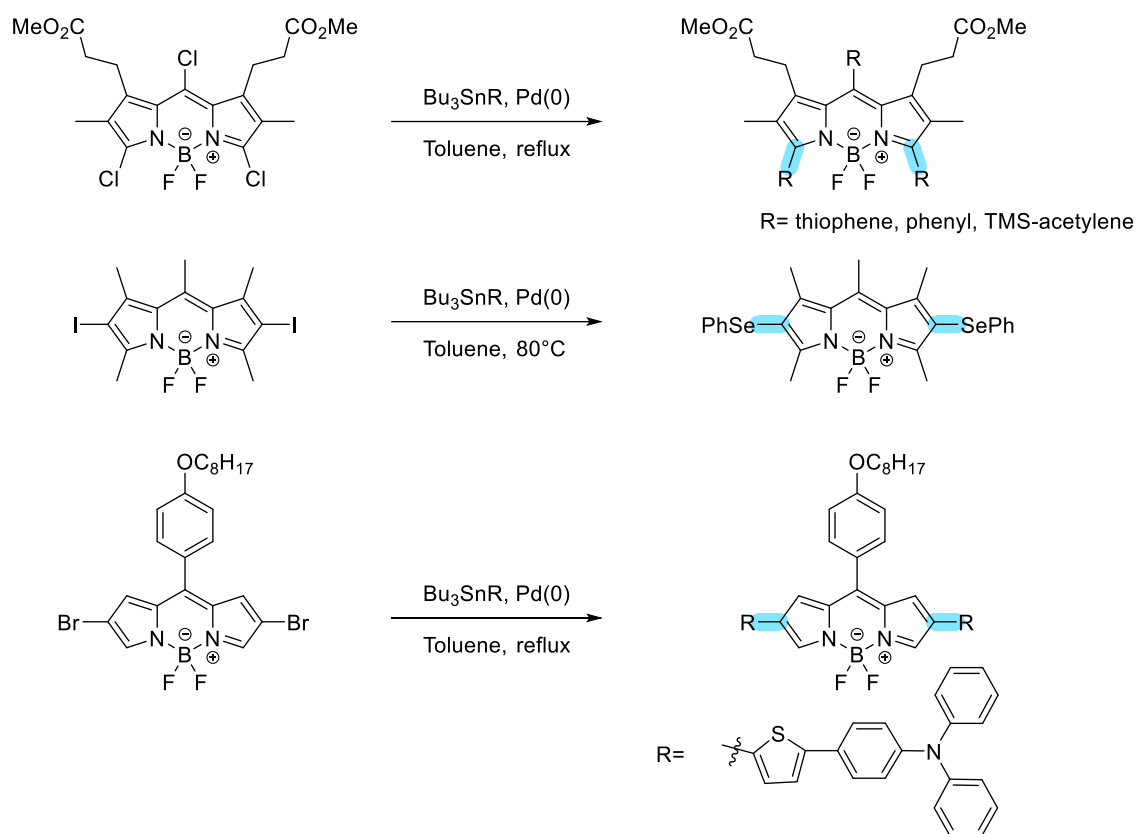
Figure 43 *Examples of the reported use of the Stille reaction to modify halogenated BODIPYs. (The bond formed during the reaction is in colour).* [13–15]

3.2.5 The Suzuki-Miyaura reaction and its application to the functionalisation of BODIPYs

The Suzuki-Miyaura reaction of one of the most widely used cross-coupling methodologies.[16] The large functional group tolerance, the great availability of electrophilic and nucleophilic partners, and the absence of cryogenic or strictly anhydrous reaction conditions are the main advantages of this transformation.[17,18] In the last couple of decades, many catalysts and ligands have been developed to correspond to a wide variety of requirements. Remarkable examples include the development of Pd–NHC (N-heterocyclic carbenes) catalyst by Prof. Organ and coworkers that allows the Suzuki coupling of challenging substrates such as electron-rich electrophiles and electron-deficient nucleophiles.[19,20] Another outstanding example are the four generations of Pd precatalyst developed by Prof. Buchwald and collaborators that allowed the reaction to happen using challenging substrates under very mild Suzuki conditions, and the expansion of palladium-catalysed aminations (Buchwald-Hartwig reaction).[21–23]

In the functionalisation of BODIPYs through Suzuki cross-coupling reaction there are a few notable trends. The electrophiles are exclusively halogenated BODIPYs (-Cl, -Br, -I), and there is an overwhelming preference for tetrakis(triphenylphosphine)palladium(0) as the palladium source,[24–27] a powerful catalyst but strongly oxygen and light sensitive.[28] A much less used catalyst is Pd(dppf)Cl$_2$, which is much more stable.[29,30] The use of PEPPSI, dialkylbiaryl phosphine ligands, as well as the Buchwald precatalyst, that allows milder conditions, remains largely unexplored and only very few reports exist to this date.[31,32] On the side of the electrophile, the use of boronic acids and pinacol esters is the norm. The use of MIDA (methyliminodiacetic acid) and cyclic triol boronates, more stable boron derivatives, also remains rare.[33]

BODIPYs are generally functionalised with polyaromatic hydrocarbons and (hetero)aromatic rings. The resulting molecules have several important properties compared to unsubstituted BODIPYs, typically, from the generation of new charge transfer states that promote triplet state formation and red-shifted absorption and emission.[24–27] The Suzuki-Miyaura protocol has also been found useful for the synthesis of BODIPY oligomers.[32] Examples are shown in Figure 44.
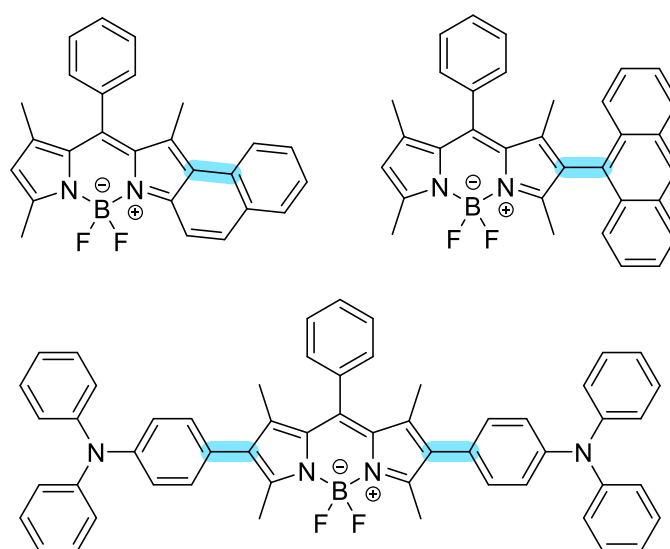
Figure 44 Examples of BODIPYs prepared through a Suzuki reaction in literature. (The bond indicated in blue is the one created during the reaction). [24–27]

3.2.6 The Mizoroki-Heck reaction and its application to the functionalisation of BODIPYs

The Heck reaction is a powerful method to form a C-C bond between an olefin and an aromatic or vinyl halide. The conditions include a palladium catalyst Pd(OAc)$_2$, Pd$_2$(dba)$_3$, Pd(PPh$_3$)$_2$Cl$_2$) and a base, typically an alkali carbonate or triethylamine.[34–36] The Heck reaction is a great tool to prepare double bonds with an *E(trans)* selectivity.[37] The classic conditions for this transformation generally take advantage of simple palladium salts, such as palladium(II) acetate and tetraalkylammonium chlorides or sulphates, the so called Jeffery conditions.[38,39]

The Heck reaction has been successfully used to introduce double bonds to the BODIPY core (Figure 45). In this way, the π-system is extended, and the dyes obtained present appealing spectroscopical properties, namely red-shifted emission and high extinction coefficient. In the case of double functionalisation of symmetric BODIPYs, a few different products can be obtained. Depending on the electronic characteristics of the alkene, the products can include: a) exclusively the ββ isomer;[40,41] b) the ββ isomer plus the αβ;[42] or c) the ββ, αβ, plus the regio-irregular αα isomer.[43]
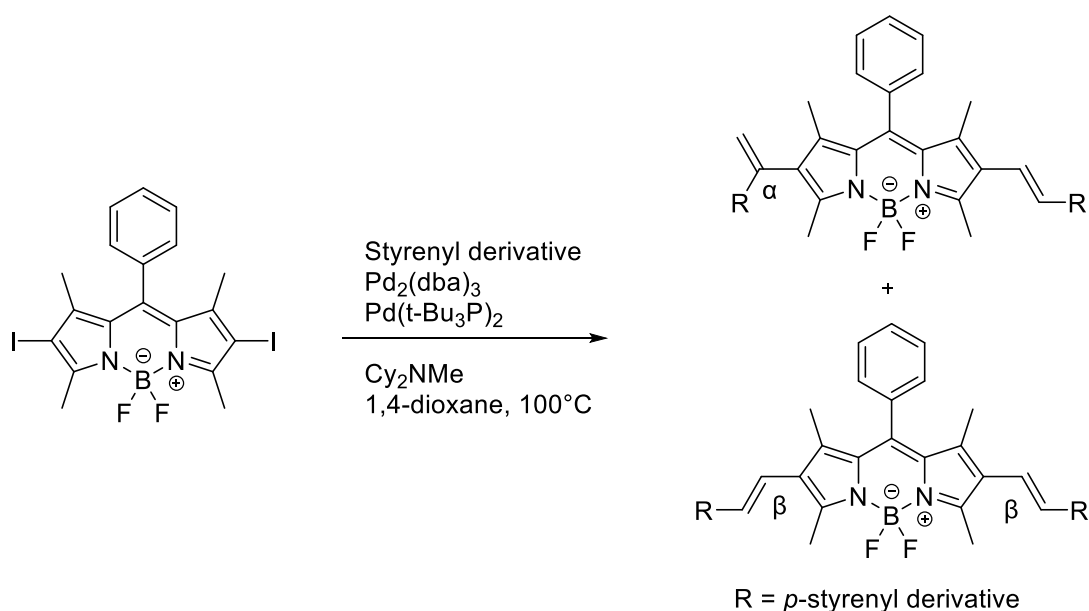
Figure 45 *Literature example of products obtained in the Heck functionalisation of tetramethyl-substituted BODIPYs. Under these specific conditions, no αα isomer was detected.* [42]

3.2.7 Functionalisation of BODIPY through the Knoevenagel condensation

The Knoevenagel condensation is, along with the Heck and Wittig reaction, a very popular method to extend the conjugation of BODIPYs (Figure 46). In general, the products obtained by this method have a significant red-shifted emission and absorption compared to the unmodified BODIPY.[44–46]

The Knoevenagel condensation, as originally described, involves the reaction of an active methylene compound with a non-enolisable aldehyde.[47] In the case of tetramethyl substituted BODIPYs, the most acidic protons are on the methyl groups closest to the nitrogen atoms. Stabilisation by resonance makes them easy to deprotonate with an organic base. Several procedures have been described, including those that allow a level of control on the number of substituents. The general catalytic system is a stoichiometric mixture of acetic acid and piperidine. In all cases, water should be removed from the medium to avoid the reversible reaction.

The impact of the number of substituents on the photophysical properties has also been explored. As a general trend, the emission and absorption gradually shift to the red as the number of aryl substituents increases. Absorption coefficients also increase following the increase in the number of substituents.[45,48]
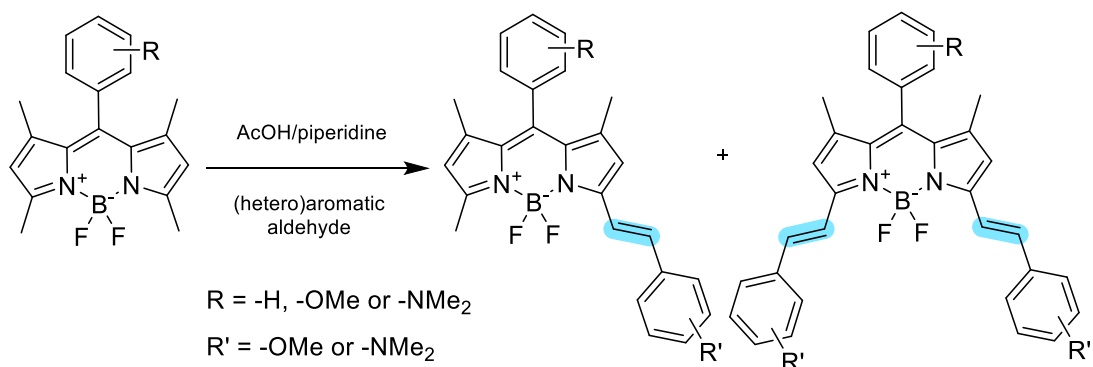
Figure 46 *Common Knoevenagel conditions to extend the conjugation of BODIPY. The products are obtained in different proportions depending on the conditions. (The bonds formed during the reaction are highlighted in colour).*

The bathochromic effect in styryl-substituted BODIPYs is sometimes so intense that the emission falls into the near-infrared region opening the possibility to use those dyes in biological applications without the risk associated with photosensitizers that require shorter wavelengths.[48,49] BODIPY's prepared by this reaction have been used for a number of applications including viscosity sensing in lysosomes,[50] monitoring of the Tau protein aggregation,[51] and pH sensing.[52]

3.2 Results and discussion

3.2.1 Design of potential BODIPY-perylene-based viscosity sensors.

In this Chapter the BODIPY perylene system introduced in Chapter 1 is modified to create a series of potential viscosity sensors/membrane probes that can also function as viscosity dependent sensitizers for TTA-UC. Ultimately, the broader objective is to create a TTA-UC system that reports membrane viscosity.

This Chapter focusses on modifications introduced to change the spectroscopical properties of the BODIPY-perylene heterochromophores described in Chapter 1. Perylene is retained as the main substituent as it has proved efficient to promote twisted intramolecular charge transfer triplet state. A phenyl substituent at *meso* position was introduced to ensure the chemical stability of the dyes. Methyl groups were added or removed to control the degrees of freedom of the molecules and, in some cases, an iodine atom was added to further promote the generation of the triplet state. Figure 47.
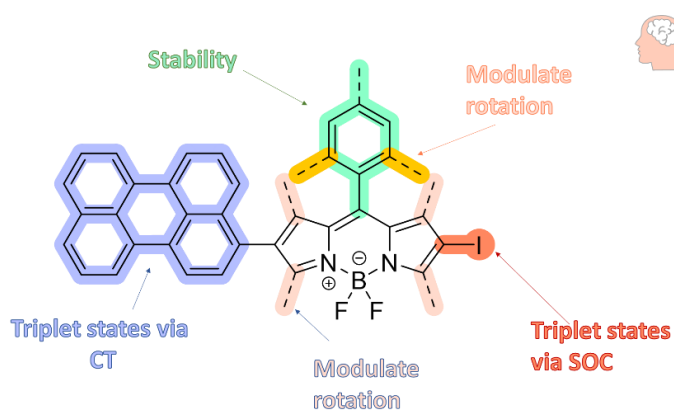
Figure 47 *Graphical representation of the rationale behind the design of BODIPY-perylene conjugates. Stability elements are coloured in green, perylene is in blue, methyl groups modulating rotation are highlighted in pink (BODIPY) and yellow (meso substituent), the iodine atom, present in some molecules appears in red at position 6.*

3.2.2 Synthetic strategy to prepare directly linked BODIPY-perylene conjugates.

Due to the non-symmetric nature of the molecules described in this chapter, the first part of the synthetic strategy focussed on designing mono-halogenated BODIPYs intermediates. Once this step was achieved, the functionalisation of those intermediates followed, mainly by cross-coupling methodologies.

3.2.2.1 Synthesis of 2-benzoylpyrrole derivatives

The ketopyrroles, as reported in Chapter 1, are the key starting point of the synthesis. The synthesis of (3,5-dimethyl-1H-pyrrol-2-yl)(phenyl)methanone (molecule **1**) was successfully achieved by the lithiation of pyrrole and subsequent reaction of this species with 2 equivalents of benzaldehyde as reported by Guo.[53] The same approach was successfully used in this Chapter with other aromatic groups possessing π-electron donating groups. The isolation of the product by column chromatography (silica, cyclohexane/EtAcO) could not always be avoided, but the yields were good enough to prepare the subsequent intermediates. Figure 48.

Substituent		Yield
1.3	R= -OMe	67%
1.4	R= -Br	75%
1.5	R= -NMe$_2$	63%
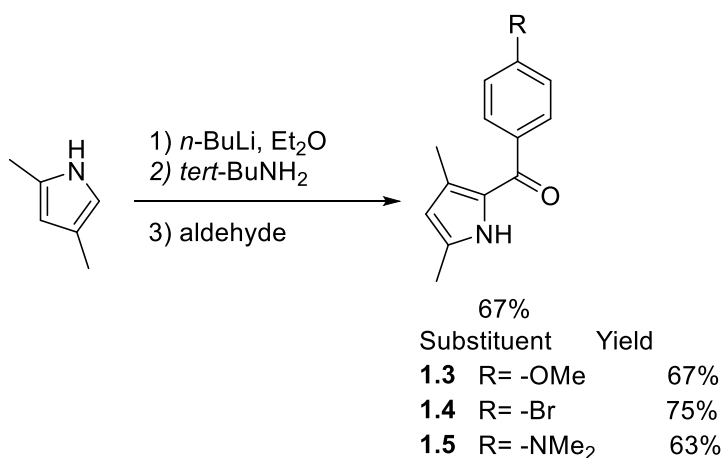
Figure 48 Ketopyrroles prepared by C-H functionalisation with aromatic aldehydes.

In general, the reaction of aromatic aldehydes and 2,4-dimethylpyrrole yielded mainly the corresponding benzylic alcohol as the major impurity. It was observed that, when present, this component did not represent any obstacle to the following bromination step. However, the reaction of unsubstituted pyrrole, consistently produced a significant number of impurities increasing the complexity of the isolation by chromatography. All attempts at crystallisation were unsuccessful. Therefore, a few alternative methods were tested. Figure 49 (a).

The Friedel-Crafts method using unsubstituted NH-pyrrole, anhydrous aluminium chloride, and benzoyl chloride[54,55] produced a rather low yield (~20%). In addition, the use of 2 equivalents of aluminium chloride unnecessarily complicated the workup of the reaction (Figure 49 b). The metalation of pyrrole with Grignard reagents[56,57] and the subsequent reaction with benzoyl chloride produced, as observed in the case of the lithiation, a complex mixture of at least five products difficult to separate by normal column chromatography. Figure 49 (c).

The Vilsmeier-Haack methodology turned out to be a good alternative.[58,59] The starting material is *N*-benzoylmorpholine, obtained very easily by reaction between benzoyl chloride and morpholine without the need of any purification step. The Vilsmeier-Haack procedure is performed using this amide and POCl$_3$ (Figure 49 d). The yields on the 1g scale were moderate (40-60%), but the chromatographic separation was simple due to the large difference in polarity of the unreacted starting material and the unique product.[60] Attempts to scale up the reaction using 2 to 4 grams of *N*-benzoylmorpholine were unsuccessful. In all scale-up attempts, the reaction produced molecule **1.6** in a yield of about 15-20 %. This low yield may be due to the increase of the viscosity in the reaction medium that decreases the reaction rates or the loss of the product during the workup and aqueous washings due to the surfactant effect of morpholine.
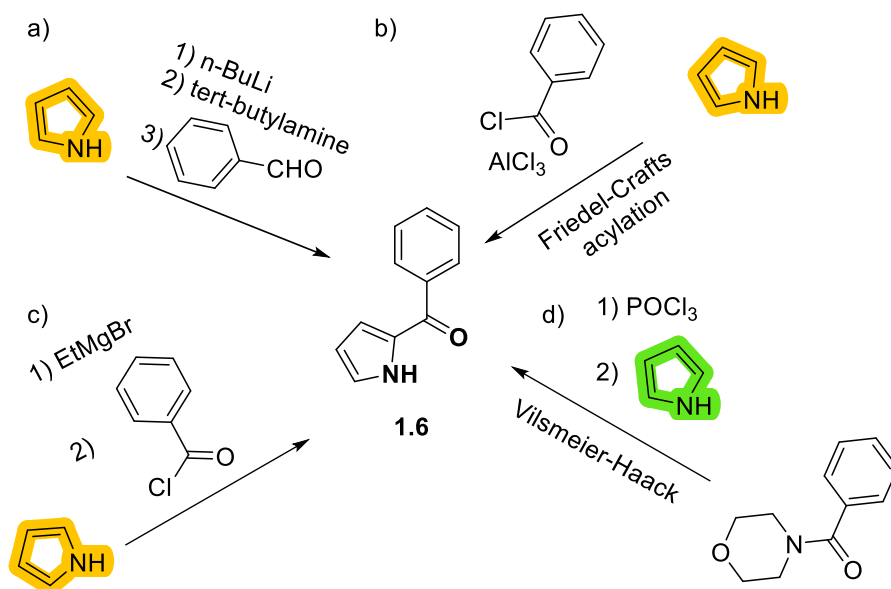
Figure 49 *Different methods to prepare 2-benzoylpyrrole.*

3.2.2.2 Halogenation of ketopyrroles

The monohalogenation of **1.6** yielded two different isomers, namely the 4- and 5- bromo-substituted 2-benzoylpyrrole in a ratio 8:2, respectively (Figure 50). Chromatographic separation was not difficult, but there were no conditions identified that were capable of increasing the proportion of the 4-substituted ketopyrrole.[57]
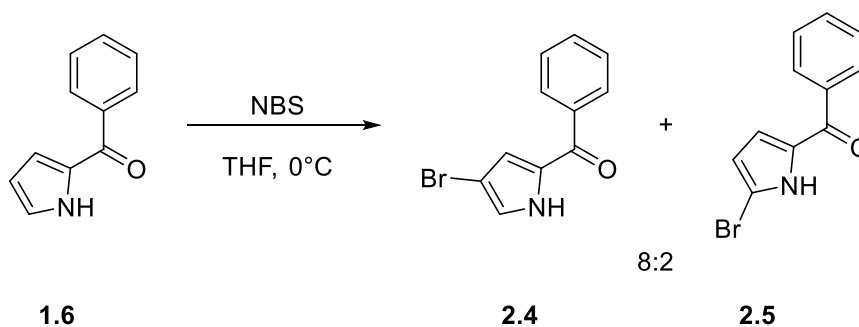
Figure 50 *Bromination of 2-benzoyl pyrrole*

The bromination of -NMe$_2$, -Br and -OMe 3,5-dimethyl substituted pyrroles was performed using bromine and following the procedure reported in Chapter 1 (Figure 51). The iodination of -NMe$_2$ substituted ketopyrrole **1.5** was done using iodine and iodic acid[61–63] (Figure 53).

3.2.2.3 Synthesis of intermediate BODIPYs

Using halogenated ketopyrroles as starting materials, a few intermediate BODIPYs were prepared. Bromo- and methoxy-substituted BODIPYs **3.6** and **3.7** were prepared in a similar fashion to the BODIPYs prepared in Chapter 1 (2,4-dimethylpyrrole + catalytic TFA), but the yields were significantly lower than those obtained with BODIPYs possessing electron-withdrawing groups. Figure 51.
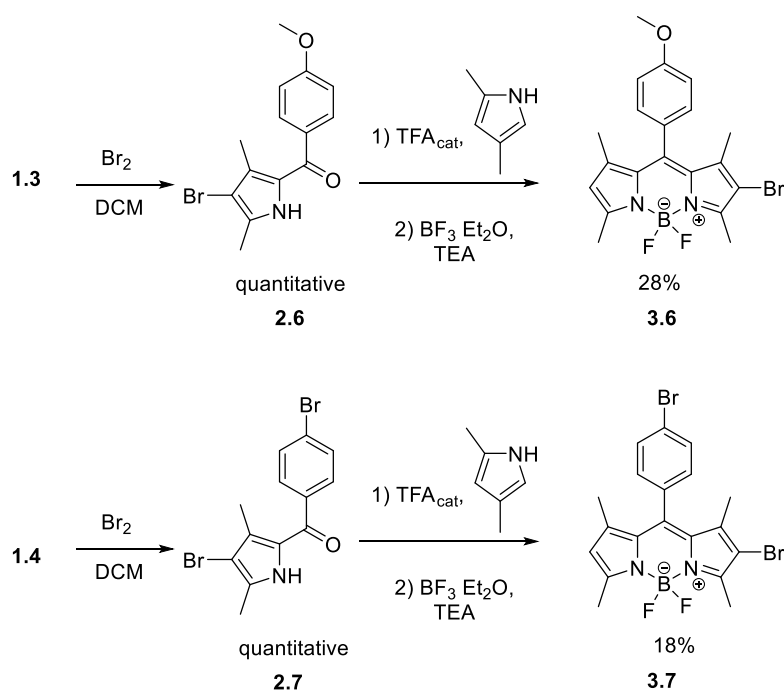
Figure 51 *Halogenation of ketopyrroles and synthesis of some intermediate BODIPYs.*

The reaction mechanism proposed for this transformation could help explain the low yields obtained. Initially, protonation of the ketopyrrole activates the carbonyl centre towards nucleophilic attack. The pyrrole, the nucleophile, is then added to this electrophile to form a dipyrridomethane. The elimination of water is promoted by thermodynamic gains due to the extension of the π-system. The rate of the reaction depends strongly on the electrophilicity of the carbonyl intermediate. Methoxy and bromo substituents are typically π-donors, (halogens do so very poorly) despite their electronegativity, the ketopyrroles possessing these groups are

therefore less activated towards nucleophilic attack.[64] In no case increasing the temperature increased the consumption of the starting material, polymerisation of pyrroles under acidic conditions or their oxidation with atmospheric air, were probably the reason[65,66] (Figure 52).
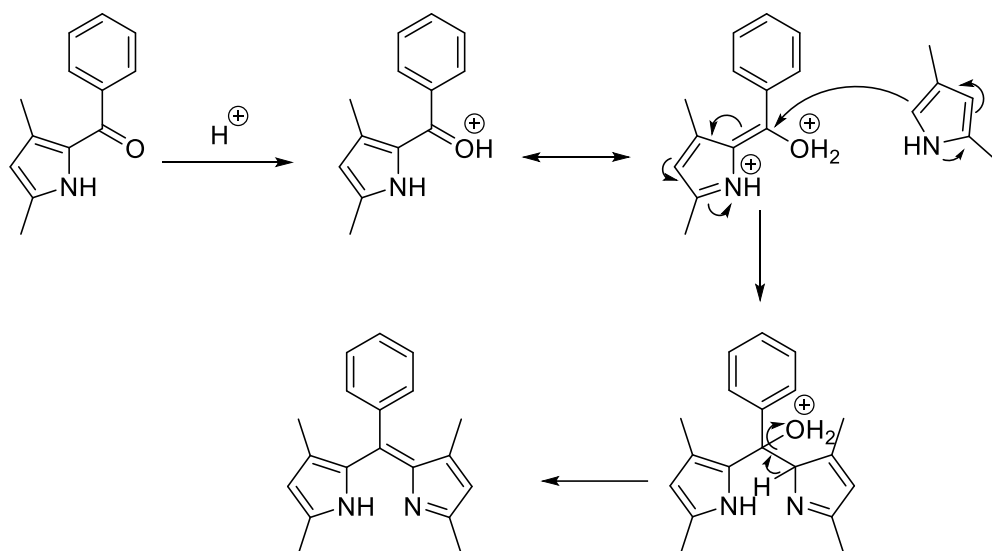
Figure 52 *Proposed mechanism for the acid catalysed condensation of ketopyrroles with pyrrole.*

In the case of the dimethylamino-substituted ketopyrrole (2.8), the π-donating character and the lower electronegativity of the nitrogen atom (compared to oxygen), makes this ketopyrrole a particularly good bidentate ligand. For that reason, the major product of the condensation with 2,4-dimethyl pyrrole was the BF$_2$-complex of the ketopyrrole instead of the dipyrridomethane (Figure 53). The three-step, one-pot methodology using *N,N*-dimethylaminobenzaldehyde as the starting material also yielded the same BF$_2$-complex instead of the BODIPY. This kind of complex has been previously described and presents interesting spectroscopic properties. They tend to show high emission quantum yields with maxima at shorter wavelengths than the ones observed in similar BODIPYs.[67] The spectroscopic characterisation of this molecule in the solid state and in solution is discussed in Chapter 4.
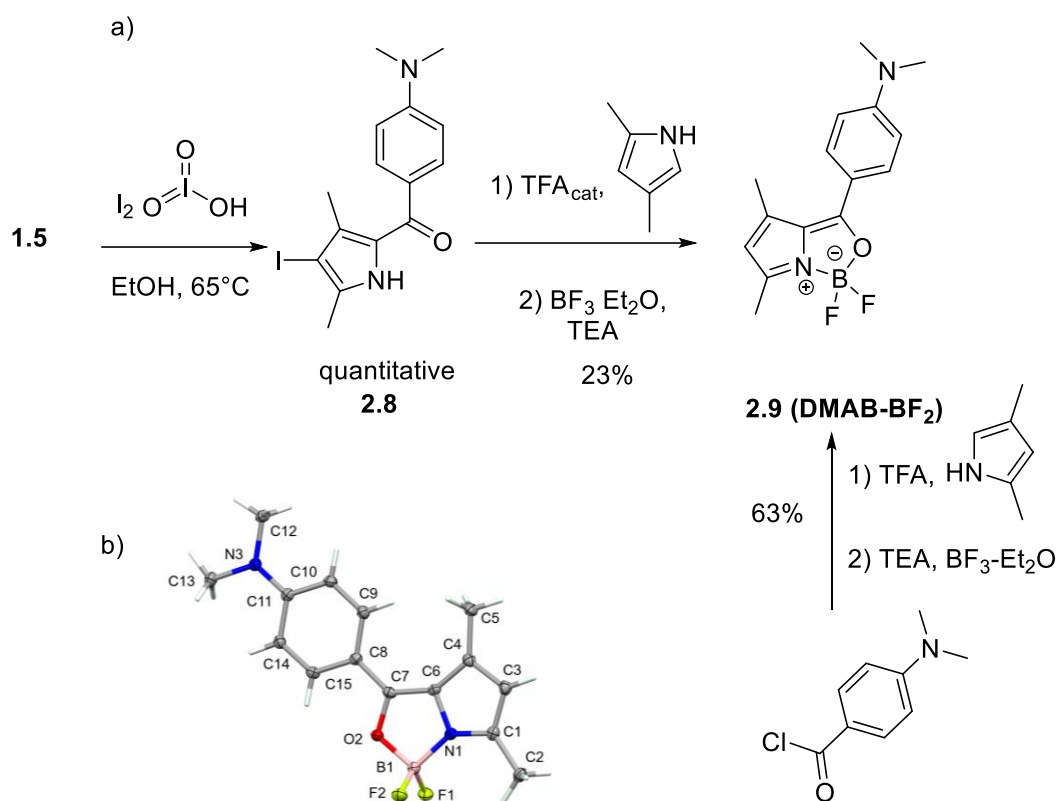
Figure 53 *Iodination of -NMe$_2$ ketopyrrole and its condensation with 2,4-dimethyl pyrrole. The main product obtained during the condensation rection was the BF$_2$ complex. The three-step one-pot condensation of 4-(dimethylamino)benzoyl chloride with 2,4-dimethyl pyrrole yielded the same product. b) Crystal structure of the BF$_2$ complex 2.9.*

In meso phenyl-substituted BODIPYS the nature of the ring can have a huge impact on the spectroscopical properties. The electron donor/acceptor character of the substituent is central but the ease of rotation of the single bond between the main core and the ring also determines a great deal of the dye's properties. In fact, the rotation can be responsible for the charge transfer character and, therefore, for the potential of the dye to be used in sensing applications.[68–73] In consequence, two BODIPY-perylene conjugates were prepared in which the rotation of the ring at meso position was restricted by the presence of two methyl groups.

The mesityl ketopyrrole **1.8**, was prepared using the C-H functionalisation method described above. However, the steric hindrance produced by the methyl groups drastically reduced the yield (18 %). As an alternative, the three-step, one pot method produced the symmetric mesityl BODIPY, and the bromination of this

species with NBS and 0 °C followed by recrystallisation yielded the mono-halogenated intermediate BODIPY **3.8** with good purity.
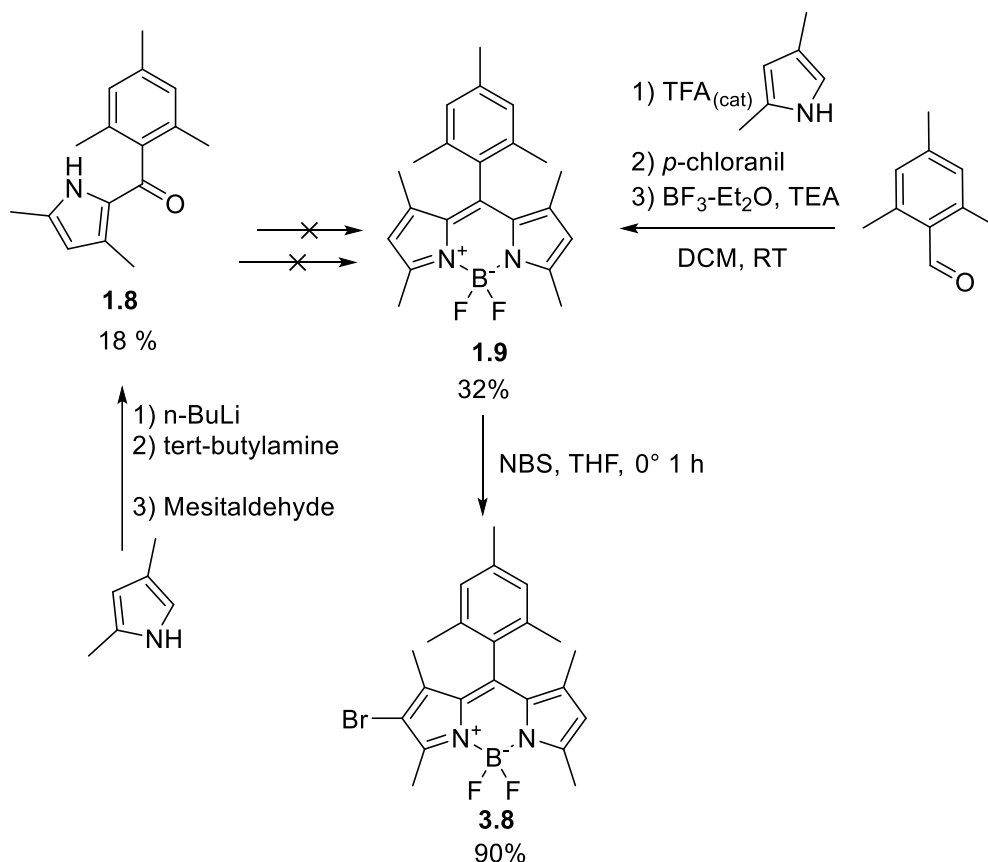
Figure 54 Synthesis of monohalogenated mesityl BODIPY

In the synthesis of BODIPY **1.7**, it was observed that the condensation between the ketopyrrole **1** and unsubstituted pyrrole did not proceed at room temperature nor under reflux in dichloroethane. The product was finally obtained by the TFA-catalysed reaction between 2-benzoyl pyrrole and 2,4-dimethylpyrrole in dichloromethane at room temperature. Several overcondensation products were observed in relatively low amounts and the isolation of the product was achieved with no particular difficulty by column chromatography (silica gel, cyclohexane:EtAcO, 9:1) followed by crystallisation from DCM/cyclohexane (Figure 55).
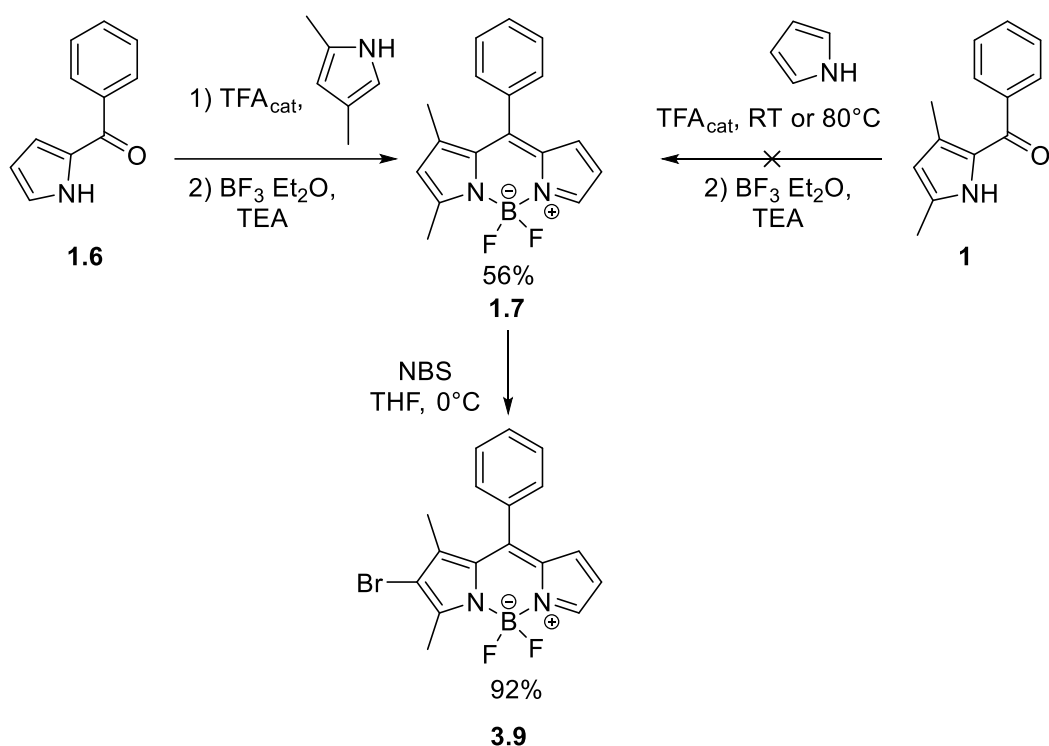
Figure 55 *Synthesis of non-symmetric BODIPY 3.9.*

The condensation to prepare BODIPY **3.4** presented several challenges. The absence of a methyl group or other substituent at the alpha position of bromoketopyrrole **2.4** did not avoid overcondensation. Several colourful by-products were observed in high proportions, the chromatographic separation followed by crystallisation from DCM/cyclohexane yielded the pure product (Figure 56). Overcondensation products can be avoided by addition of a large excess of the pyrrole (40 eq. or more),[74] though this is an impractical solution when the pyrrole is difficult to obtain.
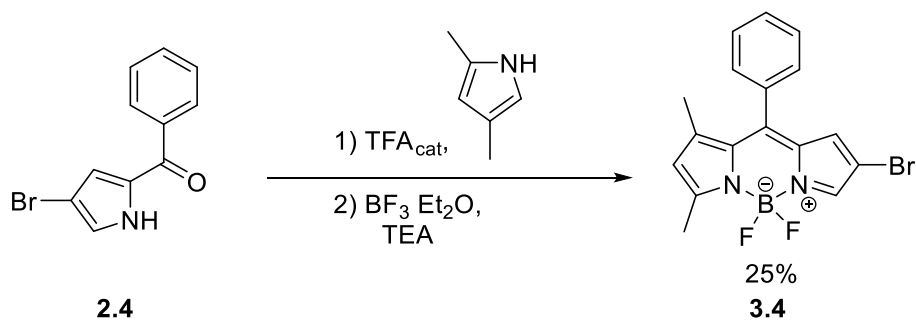
Figure 56 *Synthesis of non-symmetric BODIPY 3.4. The low yield is due to the formation of overcondensation products.*

3.2.2.4 Diphenyl-substituted BODIPY

Tetraphenyl-substituted BODIPYs and aza-BODIPYs present, in some instances, better spectroscopic/photophysical properties than methyl-substituted BODIPYs; particularly appealing is their significant red-shifted absorption.[75,76] Hence, a non-symmetric BODIPY possessing two phenyl groups was one of the synthetic targets in this Chapter.

The first step was the synthesis of 2,4-dipheyl-1H-pyrrole **8**. This was achieved by the nitration of *trans*-chalcone, followed by the Nef reaction and condensation with NH₄AcO.[77] The condensation with a ketopyrrole, however, did not proceed even in relatively strong conditions (Figure 57). Following the results observed so far, it can be concluded that the condensation between a ketopyrrole and a pyrrole works better with nucleophilic pyrroles and electron deficient ketopyrroles.
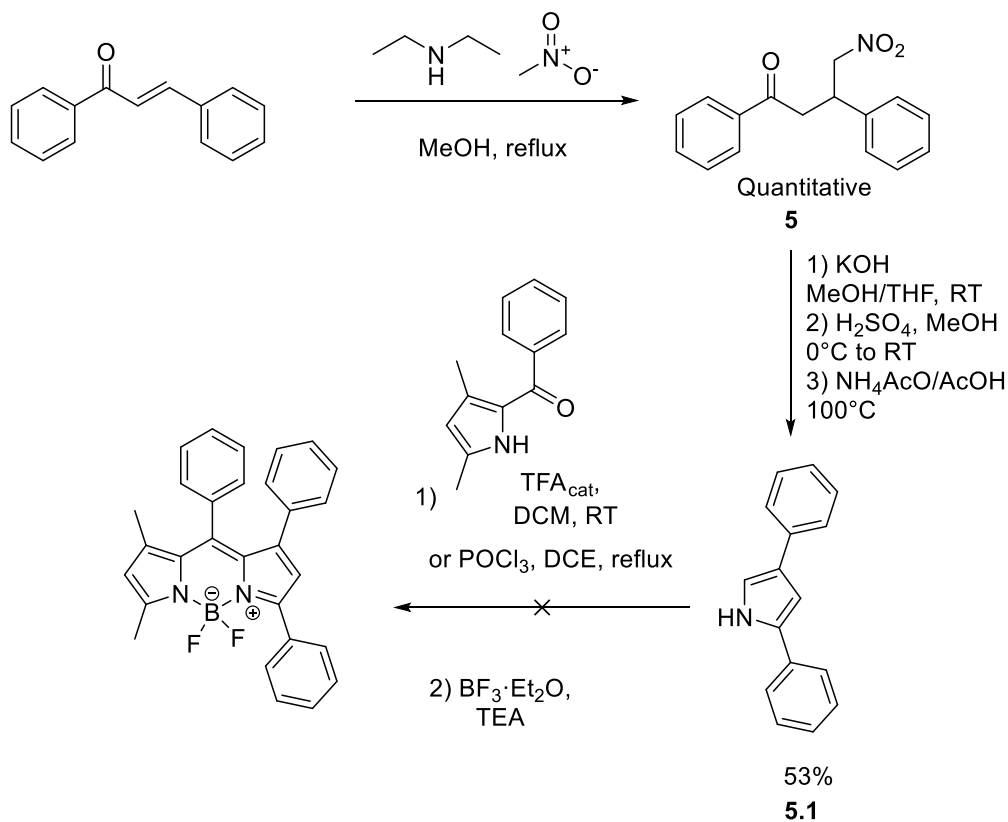
Figure 57 Synthesis of 2,4-diphenylpyrrole and attempted condensations with a ketopyrrole.

3.2.2.5 Improvements in the synthesis of the boron reagent.

The main procedure to prepare 3-perylene boronic acid pinacol ester in Chapter 1 was the Miyaura borylation using potassium acetate as the base, Pd(dppf)Cl$_2$ as the catalyst, dioxane as the solvent and a temperature of 70 °C. However, even if the yields were moderate (~45%), there is a risk that the product is degrading at that temperature. Therefore, other alternatives were studied. In a recent publication, Barroso and coworkers develop a great methodology to perform the Miyaura borylation under very mild conditions (Figure 58). The improvement comes from the fact that the base, potassium 2-ethylhexanoate, is much more soluble in organic solvents than potassium acetate. The use of isopropyl acetate was also beneficial as it allows the temperature to be reduced without changing the yields,[78] i.e., applied to our substrate, the reaction occurred at temperatures as low as 50 °C and the yield was increased to 61% (+15%).
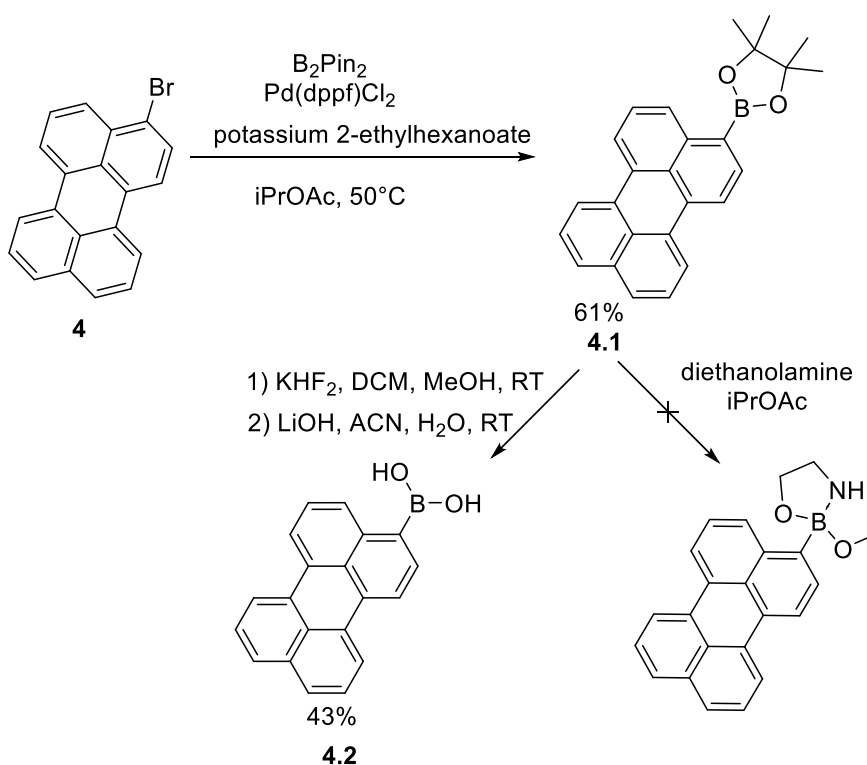
Figure 58 *Synthesis of 3-perylene boronic derivates from 3-bromoperylene.*

3-perylene boronic acid was prepared in from the pinacol ester following a literature procedure via the potassium trifluoroborate.[79] Both steps proceeded smoothly, and the difference in solubility of the final product allowed isolation by filtration. The yields never exceeded 50%.

In an effort to improve the stability of the boron reagent for the Suzuki coupling, alternative boron derivatives were considered. The use of diethanolamine (DEA) boronates has been reported to highly improve the stability of boron species in synthetic applications.[80–82] According to Inglesby and coworkers, DEA boronates can be prepared from boronic acids, pinacol boronates and other open ring esters. The isolation of the DEA boronate is supposed to be simple due to the reduced solubility of this functional group.[83] However, in this case the solubility of the 3-perylene pinacol ester is low in most organic solvents. As such, large amounts of solvents were required to carry out the reaction with DEA, the reaction took place over a longer period (>12 hours) and the isolation of the product did not occur by precipitation. Instead, the solvent was removed under reduced pressure. The final product was even less soluble than the starting material, and so its purity could not be established by NMR.

3.2.2.6 The Suzuki-Miyaura reaction of intermediate BODIPYs with perylene derivatives

The reaction of BODIPY **3.4** with the perylene-BPin **4.1** was unsuccessful under the conditions typically used in the previous chapter (THF/H$_2$O, reflux, Pd(dppf)Cl$_2$, Cs$_2$CO$_3$), in fact, no product was formed after 16 hours. The reaction finally worked with a different catalytic system (THF/H$_2$O, Pd(MeCN)$_2$Cl$_2$, SPhos) and the reaction procced at room temperature with a longer reaction time, 48 h instead of 16 h. The low yield (28%) of this transformation could be explain by the low stability of the product. It was found that the product degraded slightly in the

column, even after neutralisation with triethylamine. The product could only be isolated by precipitation from MeOH/cyclohexane.

2-DMB2 was prepared using the same conditions (THF/H$_2$O, Pd(ACN)$_2$Cl$_2$, SPhos) and the yields were surprisingly high (72%). This product did not show any signs of degradation during the chromatographic separation. Figure 59.

8-DMB2P, R^1 = Me, R^2 = H, 28%

2-DMB2P, R^1 = H, R^2 = Me, 72%
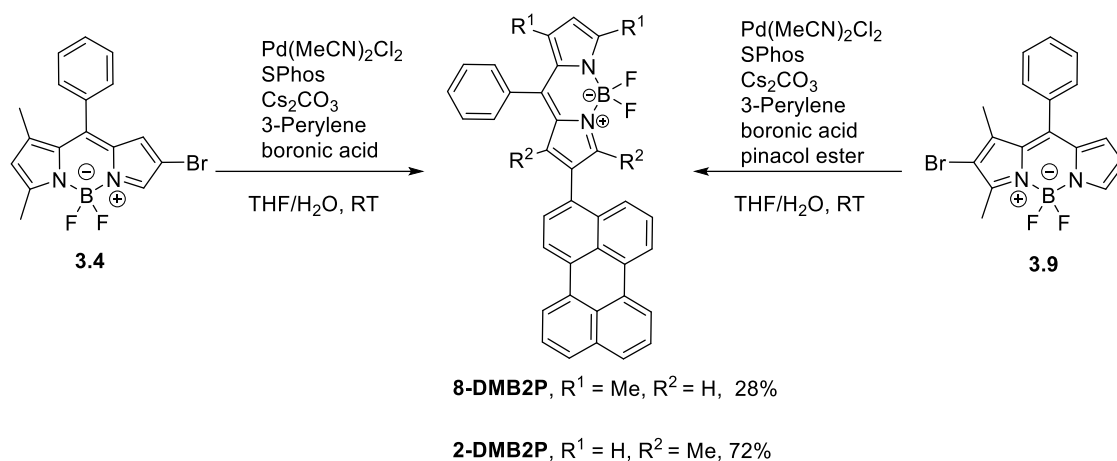
Figure 59 Synthesis of 2-DMB2P and 8-DMB2P.

The synthesis of BODIPY-perylene conjugates using BODIPYs bearing electron donating groups was largely unsuccessful. When using methoxyphenyl BODIPY **3.6** as the starting material the yields were never higher than 5%. To account for this disparity, it is necessary to remember some of the key aspects of the electronic characteristics of electrophiles and nucleophiles in Suzuki reactions. The oxidative addition step depends on the rate of attack of the electrophilic Bromo-BODIPY by the nucleophilic palladium(0) species.[84] Electron rich electrophiles are less reactive towards nucleophilic attack than electron neutral or electron deficient ones.[17,84,85]

BODIPY is an electron rich system, the aromaticity of the rings changes according to the substituents. In a computational study, Menges showed that, when it comes to *meso*-substituted BODIPYs, the aromaticity of the rings increase when

the substituent is an electron donor group and decreases when the substituent is an electron withdrawing group.[86] Yet the pyrrole and the azafulvene rings remain π-rich which makes them unsuitable to participate in oxidative additions.[84,85,87] As explained in Chapter 1, the cross-coupling reactions involving nitrophenyl and difluorophenyl *meso*-substitued BODIPYs worked well, even if the products were not stable. However, when the same conditions were applied to *meso*-phenylmethoxy-substituted BODIPY, the yields were very low. The temperature limitations imposed by the instability of the boron reagent prevent the use of stronger conditions (Figure 60).
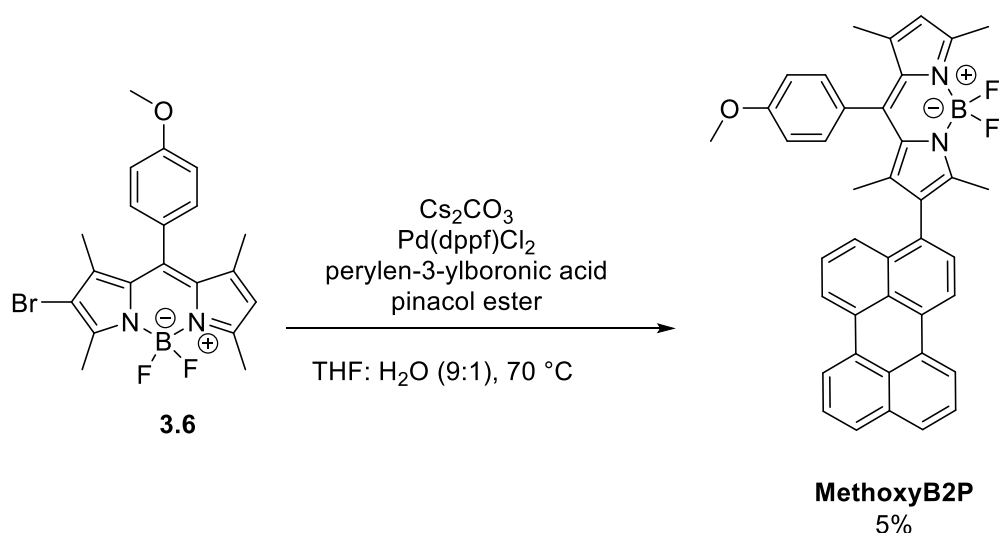
Figure 60 *Suzuki-Miyaura coupling between an electron rich BODIPY and perylene pinacol ester.*

In a final attempt to improve the yields of some of the Suzuki-Miyaura couplings, a reaction including XphosPdG4 as the catalyst was performed. The reaction temperature was decreased to 40 °C to avoid degradation of the boronate. The yields obtained were 63% when BODIPY **3.8** was used as the staring material and 54% when BODIPY **3** was used. These results are significantly higher than any of the yields previously obtained. There is thus no reason to prepare the boronic acids (Figure 61).
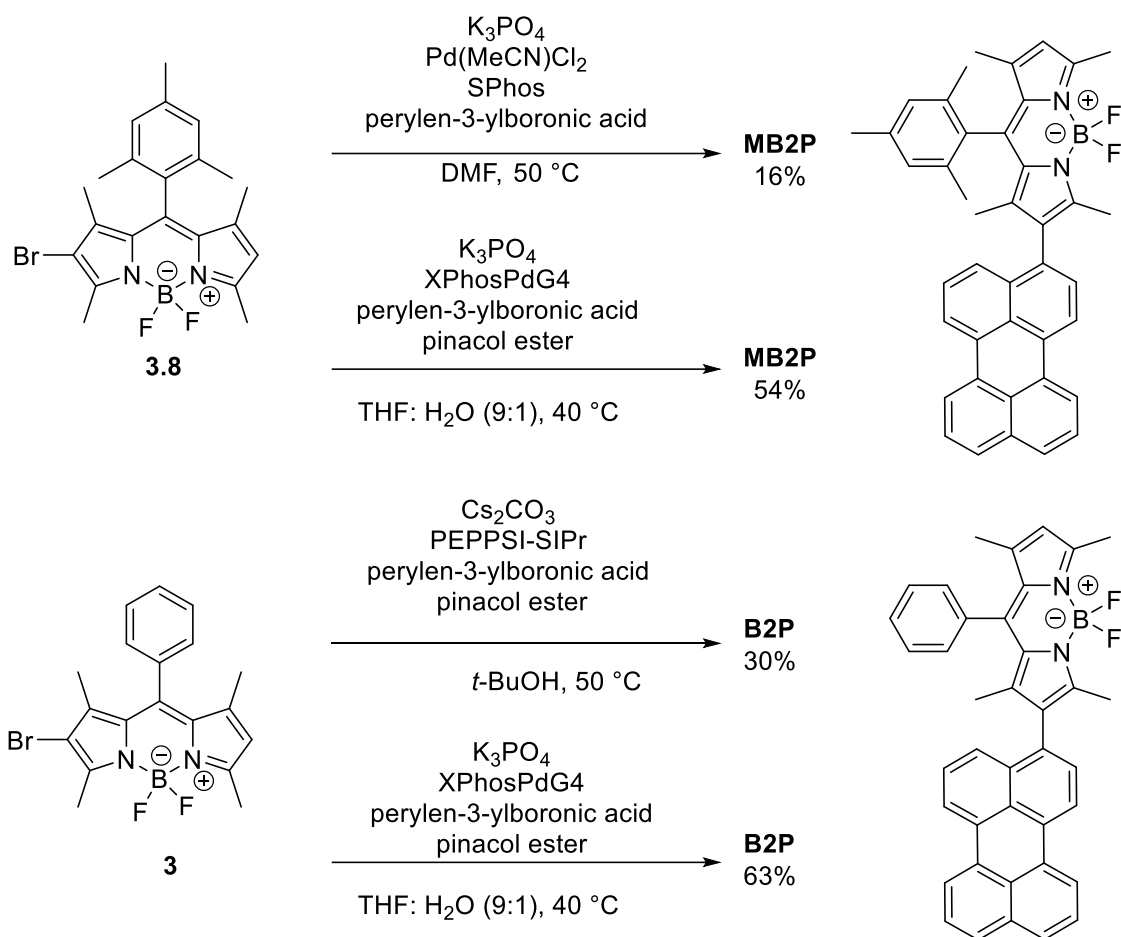
Figure 61 Improvements in the Suzuki-Miyaura cross coupling of BODIPYs with perylene boronic derivatives.

The explanation for the result is the higher reactivity of the catalytic species formed by activation of the precatalyst. After treatment with a base *in situ*, the reductive elimination of *N*-methylcarbazole generates a highly reactive 12-electron palladium complex that is the active catalytic species.[21,88] For comparison, using $Pd(PPh_3)_4$ and $Pd(dppf)Cl_2$ the reactive species is a 14 electron Pd^0L_2 or Pd^0L-L complex[84,89,90] (Figure 62).
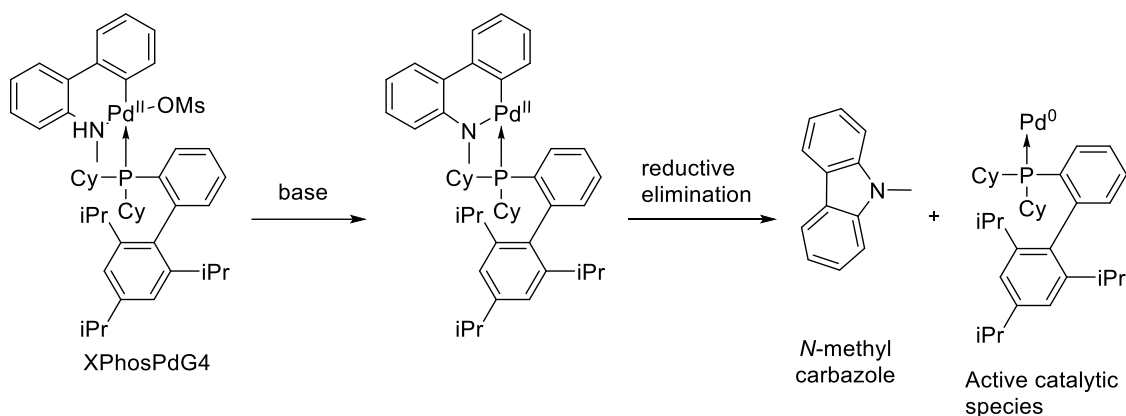
Figure 62 Mechanism of activation of the XPhosPdG4 precatalyst. The active species is a 12 electron Pd complex.

3.2.2.7 Iodination of BODIPY-perylene derivatives

The iodination of 8-DMB2P was unsuccessful. In every repeat, the reaction yielded a mixture of degradation products. As explained before, the stability of BODIPY-perylene conjugates depends on the number of methyl groups and the presence or absence of electron withdrawing groups. Furthermore, some reports suggest that the photostability of BODIPYs decreases with halogenation.[91,92]
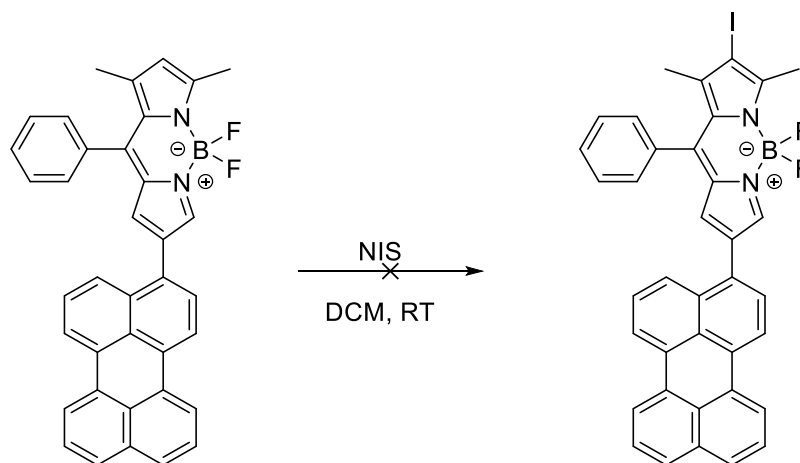
Figure 63 Conditions tested for the iodination of 8-DMB2P. No iodinated product was identified.

The iodination of MB2P proceeded smoothly. The conversion was complete, and the product was stable enough to be isolated by chromatography (Figure 64).
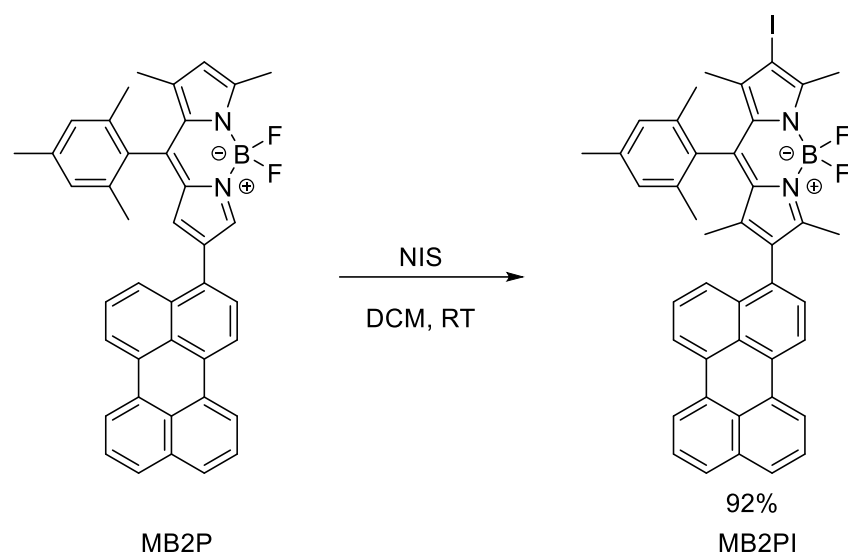
Figure 64 Iodination of MB2P

3.2.2.8 Functionalisation of BODIPYs through the Stille reaction

As explained in Chapter 1, the borylation of tetramethyl substituted bromo-BODIPY **3** was unsuccessful, the transmetalation step being most likely the limiting step. Therefore, to prepare an alternative nucleophilic partner for cross-coupling, the stannylation of the same dye was tested. The reaction, however, did not produce the expected tributyltin-BODIPY. Under the conditions tested, the main product was molecule **6** (Figure 65). The origin of that transformation can be rationalised by the presence of the intermediate BODIPY-stannane which, in the same conditions, during the same reaction and likely at a similar rate, reacts with the starting material to produce the dimer. This kind of dimer has been previously reported, but was prepared by a Lewis acid catalysis, namely with FeCl$_3$, from the non-halogenated 2-phenyl substituted BODIPYs to avoid polymerisation.[93]The method presented here could be a good alternative to prepare such dimers avoiding the formation of oligomers.
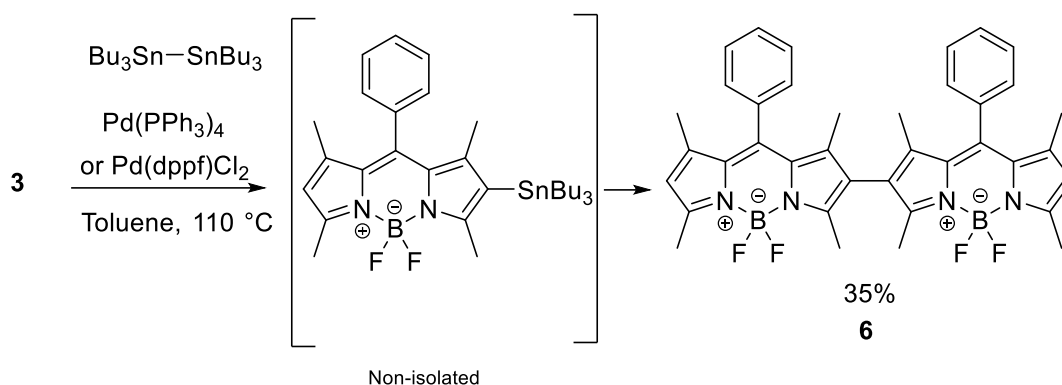
Figure 65 *Stannylation assay of BODIPY 3*

To prepare BODIPY-perylene conjugates linked by a double bond, the alkene was prepared from bromo-BODIPY **3**. The vinylation reaction was promptly achieved using tributyl(vinyl)tin. Figure 66. The conversion was complete, and the isolated yields were high, and the isolation of the product presented no difficulties. This vinyl BODIPY will be used to prepare BODIPY-perylene conjugates in the next section.
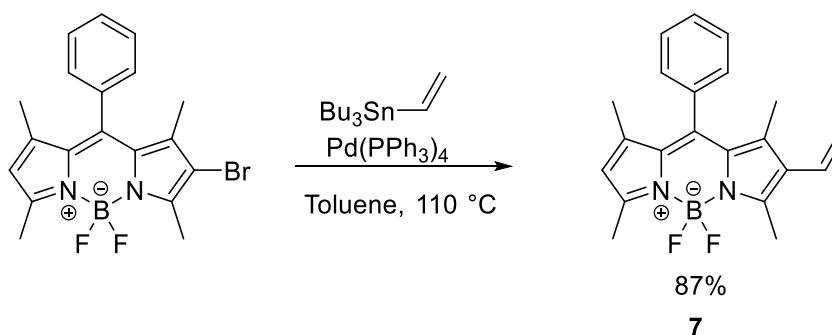
Figure 66 *Synthesis of vinyl BODIPY through the Stille reaction.*

The Stille reaction could provide further insights into the reasons for the low yields observed in the Suzuki-Miyaura protocol. Given the good yield obtained in the reaction between BODIPY and organotin reagents, it seems that the transmetalation works better with tin reagents than with boron derivatives. As explained in Chapter 2, the Miyaura borylation of 2-halo-BODIPYs was totally unsuccessful so it is only logical that the transmetalation involving boron reagents and BODIPYs happens at a much slower rate. [94–96]

3.2.3 Synthetic strategies to extend the conjugation in BODIPY-perylene dyads.

3.2.3.1 Functionalisation of BODIPYs by Mizoroki-Heck reaction

The Heck reaction is a robust methodology to from C-C bond of sp^2 partners. We tested the reaction in a few different conditions[34,37] (Table 2). All the reactions were carried out in dry toluene first at 50 °C but the conversion was not complete after 16h in all three cases. When the temperature was increased to 100 °C the conversion was still incomplete under conditions A and B.

Table 2 Condition of reactions tested for the Heck coupling.

Reaction	Starting materials	Pd source	Base	ligand	Additive	Observations
A	Vinyl-BODIPY **7** + 3-Br-perylene	Pd(PPh$_3$)$_2$Cl$_2$	Et$_3$N	none	none	Incomplete transformation, two main products, multiple by-products observed.
B	Vinyl-BODIPY **7** + 3-Br-perylene	Pd$_2$(dba)$_3$	Na$_2$CO$_3$	PCy$_3$	none	Incomplete transformation, two main products, multiple by-products observed.
C	Vinyl-BODIPY **7** + 3-Br-perylene	Pd(OAc)$_2$	Na$_2$CO$_3$	none	nBu$_4$NCl	Complete conversion, minor by-products observed.

Using the Jeffery conditions (C) the consumption of the vinyl-BODIPY was complete, and only minor by-products were observed. There were two main products, molecules **9**, the alpha product and **9.1** the beta product. The similarity of their retention times made them difficult to separate in normal phase chromatography. According to the literature, *trans* double bonds for similarly substituted compounds can be found at around 7.5 ppm with coupling constants of around 16 Hz whereas geminal double bonds can be found at higher field with constant couplings around 1 Hz. [42,97] In the NMR spectrum of products formed under conditions C, only one of the signals corresponding to the *trans* double bond can be clearly observed (6.95 ppm, d, *J* = 16 Hz) (Figure 67). The signals of the geminal double bond appear at the higher field as expected (5.72 ppm, d, *J* = 2 Hz and 5.47

ppm d, J = 2 Hz). The signals at 6.02 and 5.99 ppm correspond to the protons marked with the * and the x. From the relative integration, it can be concluded that the major component of the mix in the geminal double bond.
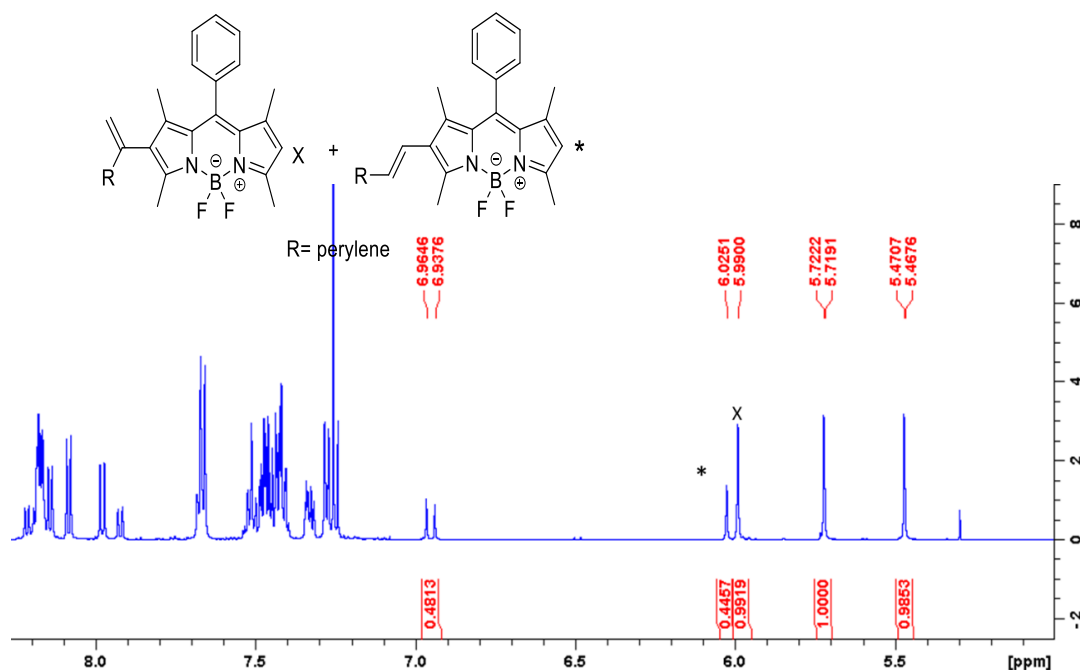
Figure 67 *Extract of the ¹H-NMR in CDCl₃ spectrum obtained from the Heck reaction under Jeffery conditions of products 9 (α) and 9.1 (β) Only the integration corresponding to the double bonds and the protons at position 6 of the BODIPY core are shown.*

Conditions A and B yielded the opposite substitution pattern, (β adduct slightly higher than α adduct), but the transformation was never complete, and several by-products were obtained. In summary, none of the reaction conditions were suitable to obtain exclusively a *trans*-substituted double bond. The Heck reactions were performed in parallel with the Knoevenagel procedure here below, but the overall results did not encourage the research for alternative synthetic methods.

3.2.3.2 Functionalisation of BODIPYs by Knoevenagel condensation

As explained in the introduction of this Chapter, the Knoevenagel condensation is relatively easy to perform. The acetic acid/piperidine is the most convenient catalytic system. From preliminary experiments, it was observed that the

reaction between aromatic aldehydes and symmetric tetraphenyl substituted BODIPYs yielded a variety of products, likely the mono- and bi-substituted adducts. Since the functionalisation with perylene as the substituent was envisaged, it was decided to perform the reaction with non-symmetric BODIPYs possessing only two methyl groups, one of them much more reactive than the other. In this way, the behaviour of the resulting products and its characterisation would be simplified.

To perform this reaction, a few more intermediates were prepared. Thus, 3-perylenecarboxaldehyde was prepared by two methods. The Vilsmeier-Haack reaction yielded the 1- and 3-substituted perylenecarboxaldehydes in an 8:2 ratio. The separation was relatively challenging due to the low solubility of the products. An alternative method, using dichloromethyl methyl ether catalysed by titanium chloride, yielded exclusively the 3-substituted perylenecarboxaldehyde. The product was isolated by precipitation and there was no need for chromatographic separation even though traces of perylene remained in the product (Figure 68). The non-symmetric methoxyphenyl BODIPY **10.3** was prepared as the phenyl analogue following the amidation-Vilsmeier-Haack procedure explained in section 3.2.2.1.
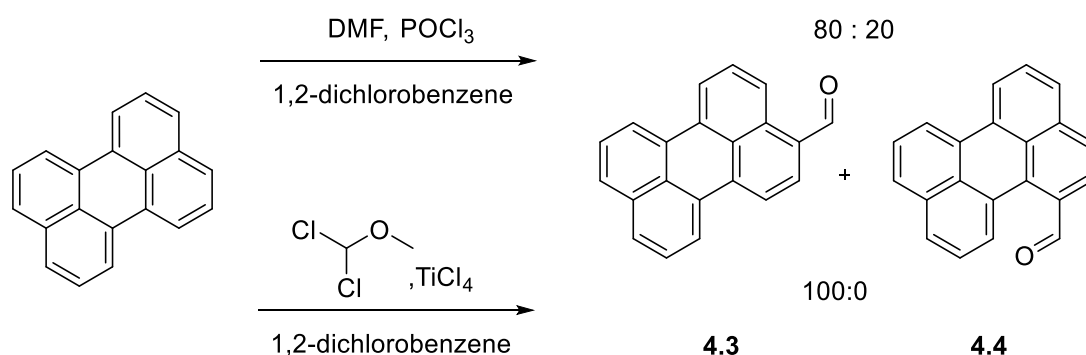
Figure 68 Synthesis of formyl perylene and the selectivity of each reaction.

The Knoevenagel condensations were run in sealed tubes at 110°C using 1,2-dichlorobenzene as the solvent for a period of 16 to 20 hours. 3Å molecular

sieves were used to remove water, with the help of a paper filter a few pellets were attached to the cap of the sealed tube. In that way, water is removed by evaporation and trapped. Very good conversions were observed by TLC, and only traces of both the BODIPY and 3-perylene carboxaldehyde remained at the end of the reaction. The products were dark blue (Figure 69).

1.7   R = -H
10.3   -OMe

1,2-dichlorobenzene
110 °C
sealed tube,
3Å molecular
sieves

AGB3P   R = -H
AGB3PO   -OMe
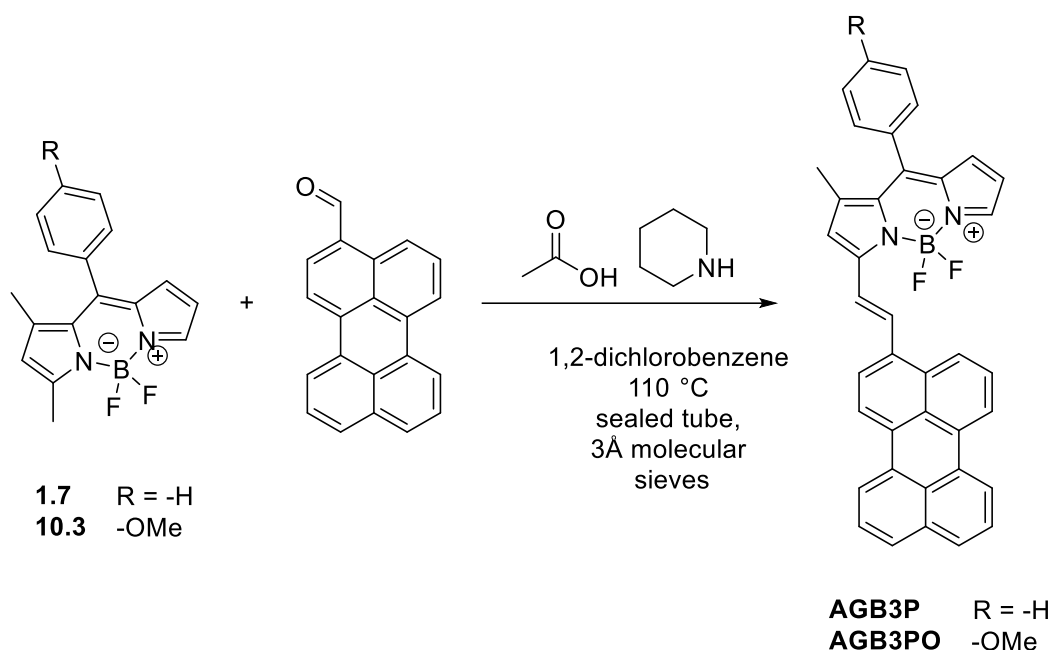
Figure 69 *Knoevenagel condensation between a non-symmetric BODIPY and 3-perylene carboxaldehyde.*

The proposed mechanism for this transformation is as follows. In methyl-substituted BODIPYs, the most activated methyl group is the closest to the nitrogen atom. This methyl group bears the most acidic protons given that the conjugated based is largely stabilised by resonance. The attack of the deprotonated BODIPY on the perylene carboxaldehyde is the step that forms the C-C bond. A subsequent base-promoted elimination of water leads to the formation of the double bond. The *trans* selectivity is due to the need of reducing the repulsion between the substituents, as commonly observed in this kind of reactions. The Knoevenagel reaction fully reversible. The product is a very good Michael acceptor that can readily react with water. It is for these reason that water needs to be removed from the reaction[45,47,98] (Figure 70).
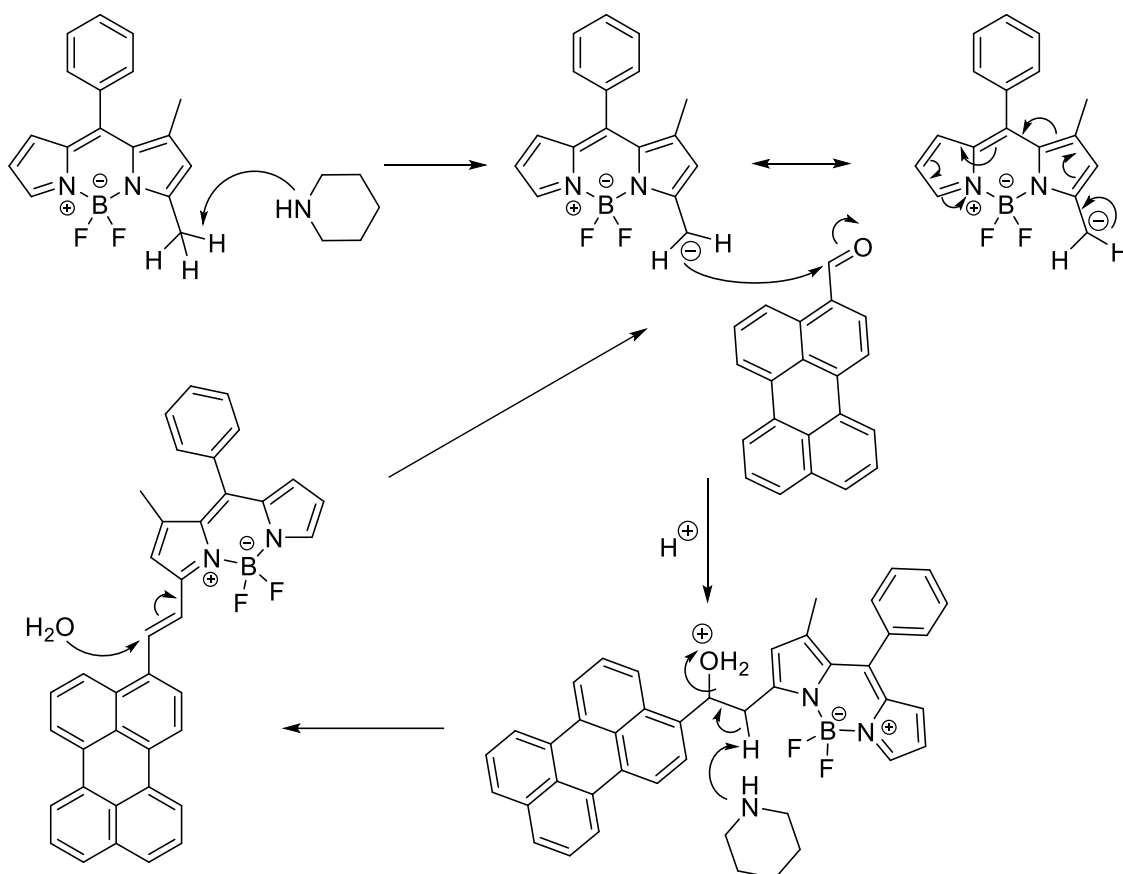
Figure 70 *Proposed mechanism for the Knoevenagel condensation of BODIPYs with an aromatic aldehyde to produce AGB3P.*

The isolation of the products presented several challenges. Their low solubility made them difficult to separate by column chromatography. In several occasions the products crystallised inside the chromatographic column. Yet the main challenge, was the degradation of the products. In fact, way after the elution of unreacted 3-perylene carboxaldehyde, this molecule reappeared on the TLCs tracking the progress of the separation. Even when the polarity of the solvent was doubled, the blue product was not present on the TLC and only the aldehyde was.

It is likely that the acid character of the silica and the use of non-anhydrous solvents for the purification made it possible for water to attack the double bond and regenerate the starting materials. In addition, it has been observed that the BODIPY core has the potential of activating double bonds towards nucleophilic attack. This particular reactivity could explain the apparently high rate of the reversible reaction. Neutralisation the column with triethylamine did not prevent degradation.

Nonetheless, a few milligrams of **AGB3P**, were isolated by crystallisation from DCM/cyclohexane and a basic spectroscopical characterisation can be found at the end of this Chapter.

3.2.4 Crystallography

Dark red crystals of the chloroform solvate MB2P·0.475(CHCl₃) were obtained by vapour diffusion of methanol into a chloroform solution. The single crystal was analysed by Dr James N. McPherson and Professor V. McKee from the Department of Physics, Chemistry and Pharmacy, University of Southern Denmark. The crystals diffracted poorly, and, despite a long collection time (ca. 80 hours), the data set is very weak and also shows significant disorder. Consequently, the precision of the structure determination is reduced but the main features are clear (Figure 71).
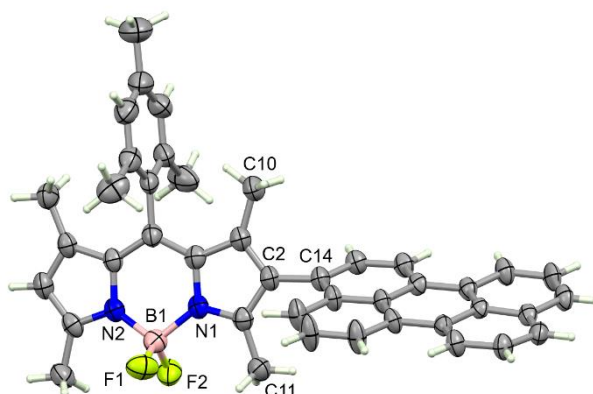
Figure 71 Perspective view of the crystal structure of the major component of MB2P (mol1) showing 50% displacement ellipsoids.

The asymmetric unit contains two independent but similar MB2P molecules (mol1 and mol2), as well as some disordered chloroform solvent. One of the MB2P molecules (mol1) is disordered; the conformation of the major component (74%) is shown in Figure 71. In the minor conformation (26%), the perylene group is rotated by 180° about the C2–C14 bond. There is also a slight displacement of the linked 5-membered ring, so that the two perylene orientations coincide (Figures B2 and B3). The second molecule (mol2) has a very similar conformation to the major component of mol1 (Figures B4 and B5). In the observed conformation, repulsive

interactions between the BODIPY methyl groups (C10 and C11) and the perylene system are reduced. However, the two fluorophores are not strictly orthogonal. The interplanar angles between the BODIPY and perylene moieties are 69.8(1)° and 73.5(3)° for the major and minor components of mol1 and 73.23(6)° for mol2. Comparison with related structures in the Cambridge Structural Database, suggests this geometry is not unusual.[110]

Despite the very similar conformations, the intermolecular interactions differ markedly between the two independent molecules. Mol1 is paired with a symmetry equivalent molecule across a centre of inversion, leading to formation of π-stacked dimers (Figure B6), but this stacking does not extend further through the structure. There are no equivalent π-interactions involving mol2, but there is a set of reasonably convincing (sp^2)C–H$\cdots$F interactions linking the mol2 units into chains (Figure B7).

3.2.3 Photophysical studies

The BODIPY-perylene conjugates that showed enough chemical stability to be purified by common methods were characterised, their absorption, emission, lifetime, extinction coefficient and fluorescence lifetime are reported in Table 2.

The more rigid dyes, MB2P and MB2PI, show higher extinction coefficients than the dyes with more degrees of freedom, around 1.4 times for 2-DMB2P and around 3.5 times for 8-DMB2P. For MB2P and MB2PI the extinction coefficient is not significantly affected by the solvent. In the case of the less rigid molecules the values are 8% (2-DMB2P) and 18% (8-DMB2P), and the values are higher in dioxane than in toluene.

Table 3 Spectroscopical properties of BODIPY-perylene conjugates.

	Solv.	λ_{abs} (nm)	λ_{em} (nm)	ε $(M^{-1}cm^{-1})$	ϕ_{f*}	τ_{1lum} (ns)	τ_{2lum} (ns)	τ_{lum} (ns) (IW)**
MB2P	Tol	517	612	89300	35.8±1.1	2.8±0.0	-----	2.8±0.0
	Diox	515	614	89200	23.8±0.3	3.1±0.1	-----	3.1±0.1
MB2PI	Tol	534	630	72600	8.6±0.7	1.6±0.1	0.7±0.0	0.8±0.0
	Diox	532	635	72900	6.3±0.2	4.0±0.1	0.7±0.0	1.1±0.0
2-DMB2P	Tol	513	654	57900	4.9±0.3	3.2±0.8	0.8±0.0	0.9±0.0
	Diox	504	661	61900	1.9±0.1	3.3±0.1	0.5±0.0	0.8±0.0
8-DMB2P	Tol	541	703	25300	1.7±0.5	2.7±0.0	0.5±0.0	1.7±0.0
	Diox	527	709	29800	2.1±0.2	3.1±0.1	0.8±0.0	2.5±0.1

* Absolute quantum yield **Intensity weighted average lifetime. The errors indicate that the measurement was done in triplicates.

In the solvents tested, MB2P, MB2PI and 2-DMB2P show a mega Stokes shifts of 3000 to 3800 cm^{-1}. MB2P stands out as the brightest molecule (QY = 35% in toluene). The restriction of the rotation due to the mesityl substituent on the BODIPY core removes some of the non-radiative relaxation pathways increasing the emission quantum yield, a phenomenon widely reported in other fluorescent molecular rotors.[99–103]

2-DMB2P and 8-DMB2P show quantum yields of 5% and 2 % in toluene, respectively. The high degrees of rotational freedom between the perylene and BODIPY moieties in these molecules increases the non-radiative relaxation pathways and, therefore, the fluorescence quantum yield decreases.

Iodination significantly decreases the fluorescence in the case of MB2PI (QY= 8.5% in toluene). This was also observed for B2PI versus B2P and is common in halogenated BODIPYs, it is attributed to heavy atom effect that increases the inter system crossing generating triplet and, in turn, decreases the fluorescence.[91,104,105]

Varying solvent, three of the dyes, MB2P, MB2PI and 2-DMB2P show similar absorption and emission properties. The variation in absorption is never greater than 0.14 units (e. g. DMSO vs DCM) and there is no shift in the absorption maxima. At the same concentration, fluorescence intensity massively varies depending on the dielectric constant of the solvent. Fluorescence intensity, is the highest in solvents with low dielectric constant such as dioxane (2.25) and toluene(2.38) whereas the emission is almost completely extinguished in polar solvents, ethanol (24.5) and DMSO (46.7),[106] for instance. A similar effect was described in chapter 1 for B2P and B2PI[105] (Figure 72).
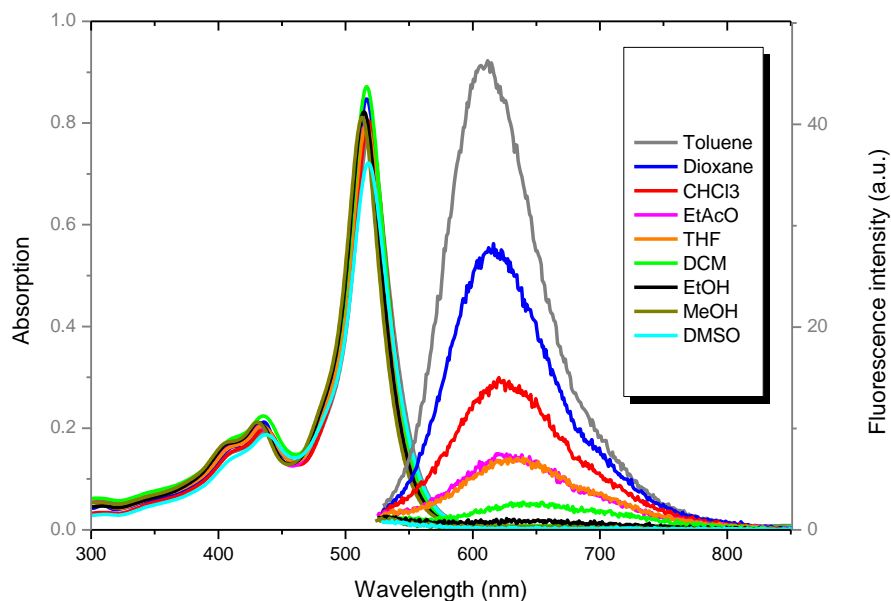
Figure 72 Absorption and emission spectra of MB2P in different solvents at 10 μM. Excitation light 532 nm. Emission recorded with 2.5-2.5 nm slit widths.

MB2P, MB2PI and 2-DMB2P share a structural characteristic that could explain some similarities observed in the emission spectra in different solvents. In the three molecules perylene is at position 2 of the BODIPY core and the rotation between the perylene and BODIPY moieties is hindered by the presence of two methyl groups. In contrast, the emission and absorption spectra of 8-DMB2P show a different behaviour (Figure 73). The absorption spectra have two big maxima at 460 nm and 525 nm. Among different solvents, the absorption changes in intensity to a greater extent than in the previous dyes, but the wavelengths remain constant. There is a single emission band with a small Stokes shift (~ 2150 cm^{-1}) in solvents with dielectric constants >8 MeOH (32.7), EtOH (24.5), DMSO (46.7), DCM (8.93). However, there are two emission features in solvents with dielectric constants <8, THF (7.58), toluene (2.38), chloroform (4.81), and ethyl acetate (6.02). The first emission band is the same as in solvents with higher dielectric constants (~590 nm). The second emission band is around 710 nm. The intensity of the second emission band follows the same response to the dielectric constant of the solvent, that is, it is

more intense in solvents with lower dielectric constants such as toluene. In fact, in this solvent the Stokes shift in toluene is close to 4320 cm^{-1}. This observation suggests that there is a strong solvent dependent charge transfer in 8-DMB2P. As described in the literature, in any CT compound, there is a charge separation state and the solvents likely to stabilise it are those with high dielectric constants. Therefore, a stabilised CT donor-acceptor pair is generally non emissive.[107–109]
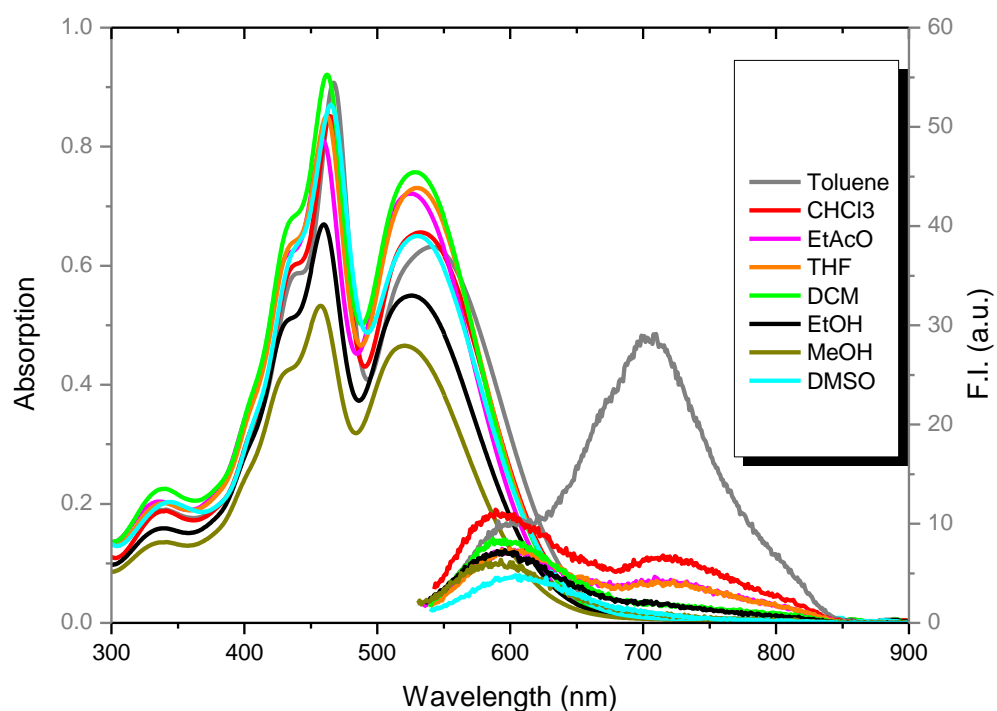
Figure 73 Absorption and emission spectra of 8-DMB2P in different solvents at 10µM. Emission recorded at λmax for each solvent with slit widths of 5-5 nm.

In the case of AGB3P, (Figure 69) the solvent effect is much stronger than in directly linked BODIPY-perylene conjugates (Figure 74). Both absorption and emission are highly solvent dependent. The Stokes shift is much smaller than in the case of 2-perylene BODIPYS, 1024 cm^{-1} for AGB3P vs 3500 cm^{-1} for B2P. The extinction coefficient in toluene (73500 $M^{-1}cm^{-1}$) was within the ranges observed for MB2PI and B2PI. Fluorescence intensity is higher in solvents with low dielectric constant, suggesting a charge transfer process responsible for the emission. In cyclohexane, the solvent with the lowest dielectric constant (2.02) there are two emission features at 640 and 700 nm. This could indicate that both, a π-π* transition and a charge transfer occur in cyclohexane. For the other solvents there is only one emission band that shifts to the red as the dielectric constant of the solvents increases (Figure 74).
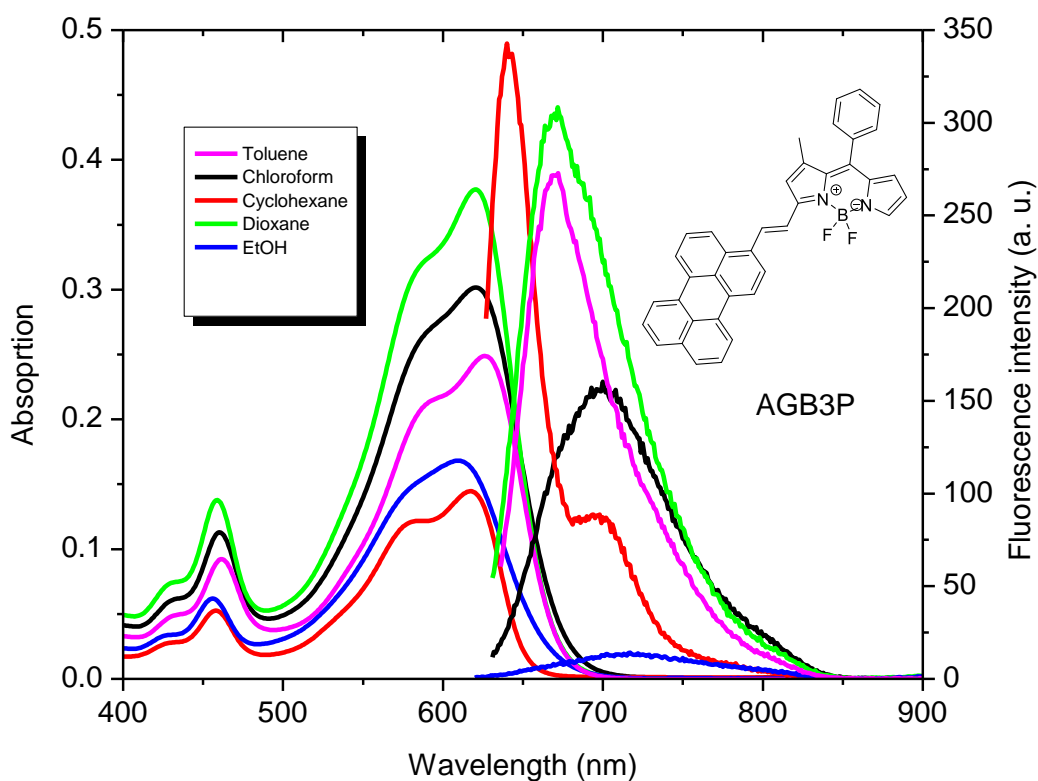
Figure 74 Absorption and emission spectra of AGB3P at 5 μM in different solvents. Excitation at $λ_{max}$ using 2.5-5 nm slit widths.

3.3 Conclusions

Chapter three extended the BODIPY-perylene motif to prepare a series of molecular rotors as viscosity-sensitive TTA-UC sensitizers by substituting the BODIPY moiety. Non-symmetric monohalogenated BODIPYs were synthesised from ketopyrroles. With this intermediate, two sets of BODIPY-perylene conjugates were prepared and characterised. The first comprised a pair where BODIPY core was substituted with a mesityl group to increase the rigidity of the molecules. In the second set, two methyl groups were removed to increase the degrees of freedom of the molecules. Stable molecules were iodinated. Single crystals of some molecules were obtained and characterised by X-Ray diffraction.

The conditions for the Suzuki reaction were optimised, the use of XPhos PdG4 as the catalyst improve the yields from 30% to 60%. The reaction proceeded with the perylene pinacol ester and the use of more unstable boronic acids was avoided.

The Knoevenagel and Heck reactions produced BODIPY-perylene conjugates with a double bond linking both fluorophores. The Heck reaction produced a mixture of α and β adducts that could not be separated. The Knoevenagel reaction produces very unstable molecules and only a few milligrams of one of them were isolated. This product, AGB3P, showed a strongly solvent-dependent emission and absorption properties. The fluorescence intensity is the highest in solvents with low dielectric constants, dioxane and cyclohexane and it is reduced protic polar solvents like ethanol. The Stokes shift was smaller than the one observed on BODIPYs bearing perylene at position 2, 1024 cm^{-1} for AGB3P vs 3500 cm^{-1} for B2P.

Further details into the properties of the dyes, their use as viscosity sensors, singlet oxygen generators, as well as the solid-state spectroscopy are explained in Chapter 4.

3.4 Experimental section

3.4.1 Synthesis

Only the intermediates leading to stable BODIPY-perylene conjugates are described here. Synthetic details and characterisation of the rest of the molecules can be found in appendix B.

Morpholino(phenyl)methanone. In a 250 round-bottom flask, 6.30 mL of triethylamine (45.2 mmol, 1.05 eq.) and 3.79 mL of morpholine (43.9 mmol, 1.02 eq.) were diluted in 50 mL of diethyl ether and cooled to 0 °C in an ice/water bath. Benzoyl chloride (5 mL, 43.04 mmol) was added dropwise. The reaction was stirred at room temperature overnight. Solid triethylammonium chloride was removed by filtration and rinsed with 2 x 30 mL of diethyl ether. The filtrate was concentrated under vacuum and washed first with an aqueous saturated solution of sodium carbonate and then with 1M HCl. The organic phase was separated, dried over $MgSO_4$ and the solvent was evaporated under vacuum. The product was obtained in 96% yield as a transparent oil that solidified overnight. The product was pure enough to be used as such in the next step. ^{1}H-NMR (CDCl$_3$, 600 MHz) δ (ppm) 7.47-7.33 (m, 5H), 3.77 (br, 3H) 3.62 (br, 3H), 3.44 (br, 2H).

Phenyl(1H-pyrrol-2-yl)methanone (1.6) In a 50 mL round-bottom flask, morpholino(phenyl)methanone (2g, 10.46 mmol) was mixed with neat POCl$_3$ (2.05 mL, 20.96 mmol, 2.1 eq.) and heated at 35 °C until the solid was dissolved, the reaction proceeded at room temperature for 5 hours. Pyrrole (0.47 mL, 6.80 mmol, 0.65 eq.) was diluted in 5 mL of dichloroethane and added to the reaction flask. The reaction was stirred at room temperature overnight. Then, 20 mL of a saturated aqueous solution of sodium carbonate was added until the pH was slightly basic (~8). The reaction was transferred to a separating funnel and extracted with

chloroform (3 x 20 mL). The organic phases were combined, dried over magnesium sulphate and evaporated under vacuum. The product was purified by column chromatography on silica gel using cyclohexane and ethyl acetate (8:2). The product was obtained in 60% yield as an off-white solid. ^{1}H-NMR (CDCl$_3$, 600 MHz), δ (ppm) 10.28 (br, 1 H), 7.94-7.90 (m, 2H), 7.59-7.55 (m, 1H), 7.51-7.47 (m, 2H), 7.19-7.16 (m, 1H), 6.92-6.89 (m, 1H), 6.35-6.32 (m, 1H). ^{13}C-NMR (CDCl$_3$, 150 MHz), δ (ppm) 185.1, 138.5, 131.9, 131.2, 129.1, 128.4, 125.6, 119.8, 111.1. HR-MS (ESI-TOF) m/z: Calculated for C$_{11}$H$_9$NNaO (M+Na): 194.0576 found: 194.0579. Calculated for C$_{11}$H$_8$NO (M-1): 170.0610, found: 170.0611.

(4-bromo-1H-pyrrol-2-yl)(phenyl)methanone (2.4) In a 50 mL round-bottom flask, 486 mg of phenyl(1H-pyrrol-2-yl)methanone (2.84 mmol) were dissolved in 10 mL of THF and the solution was cooled to 0 °C. NBS (525 mg, 2.95 mmol, 1.04 eq.) was added and the solution was stirred at room temperature for 1.5 hours. The solvent was evaporated under vacuum and the product was purified on silica gel using hexane:ethyl acetate (9:1). The product was isolated as a white solid in 78% yield. ^{1}H-NMR (CDCl$_3$, 600 MHz) δ (ppm) 9.70 (br, 1H), 7.90-7.86 (m, 2H), 7.61-7.57 (m, 1H), 7.52-7.47 (m, 2H), 7.13 (dd, $J = 3$, 1 Hz), 6.88 (dd, $J = 3$, 1 Hz). ^{13}C-NMR (CDCl$_3$, 150 MHz), δ (ppm) 184.2, 137.6, 132.5, 131.1, 129.0, 128.6, 124.8, 120.4, 98.6. HR-MS (ESI-TOF) m/z: Calculated for C$_{11}$H$_9$BrNO (M+1): 249.9862, found 249.9868. Calculated for C$_{11}$H$_7$BrNO (M-1): 247.9716, found 247.9713.

(4-(dimethylamino)phenyl)(4-iodo-3,5-dimethyl-1H-pyrrol-2-yl)methanone (2.8) In a 100 mL round-bottom flask, 1.97 g of ketopyrrole **1.5** (8.11 mmol) was dissolved in 10 mL of DCM and then 40 mL of ethanol were added. Then, 1.23 g of iodine (4.87 mmol, 0.6 eq.) were added and, immediately after, 428 mg of iodic acid (2.43 mmol, 0.3 eq.) dissolved in 4 mL of water were added. The suspension was

heated and stirred at 65 °C for 1 hour. After that time, 1/3 of the solvent was removed under vacuum and 10 mL of a saturated aqueous solution of sodium sulphide were added. The suspension was filtered under vacuum and the product washed with 30 mL of water/ethanol (50:50). The product was obtained in a quantitative yield as a yellow solid and it was pure enough to be used as such in the next step. ^{1}H-NMR (DMSO-d$_6$, 600 MHz) δ (ppm) 7.54 (d, $J = 9$ Hz), 6.75 (d, $J = 9$ Hz), 3.01 (s, 6H), 2.21 (s, 1H), 1.97 (s, 3H). ^{13}C-NMR (DMSO-d$_6$, 150 MHz), δ (ppm) 183.8, 153.1, 135.1, 131.5, 128.4, 128.2, 126.3, 111.2, 73.2, 40.5, 15.9, 14.1.

DMAB-BF$_2$ (2.9) This product was obtained in two different ways:

1. From iodoketopyrrole **2.8**: In a 50 mL round-bottom flask, 540 mg of the ketopyrrole 2.8 (1.47 mmol) were dissolved in 10 mL of DCM. 0.16 mL of 2,4-dimethylaminopyrrole (1.61 mmol, 1.1 eq.) and 10 drops of TFA were added. The reaction was stirred at room temperature for 24 hours. Triethylamine (1.23 mL, 8.8 mmol, 6 eq.) and BF$_3$-etherate (1.45 mL, 11.73 mmol, 8 eq.) were added and the reaction stirred at room temperature overnight. The solvents were evaporated under vacuum and the product was purified by column chromatography on silica gel using cyclohexane:EtAcO (50:50). The product was obtained as a coral red solid in 23% yield. ^{1}H-NMR (CDCl$_3$, 600 MHz) δ (ppm) 8.00 (d, $J = 9$ Hz, 2H), 6.73 (d, $J = 9$ Hz, 2H), 6.14 (s, 1H), 3.14 (s, 6H), 2.42 (s, 3H), 2.40 (s, 3H). ^{13}C-NMR (CDCl$_3$, 150 MHz), δ (ppm) 174.7, 154.7, 148.7, 134.1, 133.7, 131.4, 121.9, 115.9, 111.4, 111.2, 40.2, 16.0, 13.6. HR-MS (ESI-TOF) m/z: calculated for C$_{15}$H$_{17}$BF$_2$N$_2$NaO (M+Na): 313.1300, found: 313.1308.

2. From 4-(dimethylamino)benzoyl chloride. In a 50 mL round-bottom flask 4-(dimethylamino)benzoyl chloride (1.5 g, 8.17 mmol), was dissolved in 6 mL of DCM, 2,4-dimethylpyrrole (1.8 mL, 17.15 mmol) was added and 10 drops of TFA. The reaction was stirred at room temperature for 48 hours. TEA (6.8 mL, 49.0 mmol,

6 eq.) and BF$_3$-etherate (8 mL, 65 mmol, 8 eq.) were added and the reaction stirred at room temperature overnight. The solvents were evaporated under vacuum and the product was purified by column chromatography on silica gel using cyclohexane/EtAcO (50:50). The product was obtained in 63% yield. ^{1}H-NMR (600 MHz, DMSO-d6) δ (ppm) 7.96 (d, J = 9 Hz, 2H), 6.92 (d, J = 9 Hz, 2H), 6.30 (s, 1H), 3.15 (s, 6H), 2.42 (s, 3H), 2.30 (s, 3H). ^{13}C-NMR (150 MHz, DMSO-d6) δ (ppm) 173.5, 155.4, 147.6, 138.4, 134.3, 133.8, 130.6, 122.3, 114.0, 112.2, 16.0, 13.5. HR-MS (ESI-TOF) m/z: calculated for C$_{15}$H$_{17}$BF$_2$N$_2$NaO (M+Na): 313.1300, found: 313.1308. (This reaction also produced the corresponding BODIPY in about 8% yield).

BODIPY 1.7 In a 50 mL round-bottom flask 169 mg of benzoyl pyrrole 1.6 (0.987 mmol), were dissolved in 10 mL of DCM, 111 μL of 2,4-dimethyl pyrrole (1.09 mmol, 1.1 eq.) and 3 drops of TFA were added. The reaction was stirred at room temperature for 24 hours. Triethylamine (0.825 mL, 5.92 mmol, 6 eq.) and BF$_3$ etherate (0.975 mL, 7.90 mmol, 8 eq.) were added and the reaction was stirred at room temperature overnight. Solvents were removed under vacuum and the product was purified by column chromatography using cyclohexane/ethyl acetate (9:1). The fractions containing the product were evaporated and the product was dissolved in the least possible amount of DCM (~5 mL) and four times more cyclohexane was added, the solution was cooled in an ice/water bath until the product precipitated. The product was filtered under vacuum and rinsed with cyclohexane (30 mL). The product was obtained in 56% yield as a metallic dark red solid. ^{1}H-NMR (CDCl$_3$, 600 MHz) δ (ppm) 7.68 (s, 1H), 7.53-7.45 (m, 3H), 7.37-7.33 (m, 2H), 6-41-6.38 (m, 1H), 6.38-6.35 (m, 1H), 6.13 (s, 1H), 2.62 (s, 3H), 1.53 (s, 3H). ^{13}C-NMR (CDCl$_3$, 150 MHz), δ (ppm) 162.2, 147.2, 143.5, 138.8, 134.9, 134.1, 133.7, 129.5, 128.9, 128.6, 127.2, 123.4, 116.2, 15.3, 15.1. HR-MS (ESI-TOF) m/z: Calculated for C$_{17}$H$_{14}$BF$_2$N$_2$

(M-1): 295.1226, found: 295.1224. Calculated for $C_{17}H_{15}BF_2N_2Na$ (M+Na): 319.1191, found: 319.1191.

BODIPY 1.9 In a 50 mL round-bottom flask, mesitaldehyde (0.5 mL, 3.39 mmol), was dissolved in 2 mL of DCM. 0.73 mL of 2,4-dimethylpyrrole (7.12 mmol, 2.1 eq.) were added along with 5 drops of TFA. The reaction was stirred at room temperature for 6 hours. Then, 10 mL of a DCM solution of *p*-chloranil (917 mg, 3.73 mmol, 1.1 eq.) were added and the reaction stirred for 1 hour at room temperature. Triethylamine (2.84 mL, 20.34 mmol, 6 eq.) and BF_3-etherate (3.35 mL, 27.12 mmol, 8 eq.) were added and the reaction was stirred overnight at room temperature. Solvents were removed under vacuum and the product was purified by column chromatography on silica gel using cyclohexane/ethyl acetate (9:1). The product was isolated as a red solid in 32 % yield. ^{1}H-NMR (CDCl$_3$, 600 MHz) δ (ppm) 6.94 (s, 2H), 5.96 (s, 2H), 2.56 (s, 6H), 2.33 (s, 3H), 2.09 (s, 6H), 1.38 (s, 6H).

BODIPY 3.4 In a 50 mL round-bottom flask, 642 mg of bromoketopyrrole **2.4** were dissolved in 10 mL of DCM, 2,4-dimethylpyrrole (0.290 mL, 2.80 mmol, 1.1 eq.) and 5 drops of TFA were added. The solution was stirred at room temperature for 24 hours. Triethylamine (2.15 ml, 15.40 mmol, 6 eq.0 and BF_3-etherate (2.53 mL, 20.54 mmol, 8 eq.) were added and the reaction stirred at room temperature overnight. Volatiles were removed under vacuum and the product was purified by column chromatography on silica gel using cyclohexane/ethyl acetate (9:1). The solvent of the fractions containing the product were combined and the solvent was evaporated under vacuum until the solution reached the maximum concentration limit, at which point cyclohexane (30 mL) was added and the flask was set into an ice/water bath until the product precipitated. The product was vacuum filtered. BODIPY **3.4** was obtained as dark red crystals in 25 % yield. ^{1}H-NMR (CDCl$_3$, 600 MHz) δ (ppm) 7.54 (s, 1H), 7/52-7.47 (m, 3H), 7.34-7.31 (m, 2H), 6.32 (s, 1H), 6.18 (s, 1H), 2.63 (s,

3H), 1.54 (s, 3H). ^{13}C-NMR (CDCl$_3$, 150 MHz), δ (ppm) 164.6, 148.6, 142.6, 136.9, 134.4, 134.3, 133.4, 129.8, 128.8, 128.7, 126.2, 124.3, 106.3, 15.5, 15.2. HS-MS (ESI-TOF) *m/z*: Calculated for C$_{17}$H$_{14}$BBrF$_2$N$_2$Na (M+Na): 397.0296, found: 397.0297. Calculated for C$_{17}$H$_{13}$BBrF$_2$N$_2$ (M-1): 373.0331, found: 373.0323.

BODIPY 3.8 In a 50 mL round-bottom flask, 393 mg (1.07 mmol) of mesityl BODIPY (1.9) were dissolved in 40mL of DCM. The solution was cooled to 0°C in an ice/water bath. NBS (191 mg, 1.07 mmol, 1 eq.) was added in small portions over 20 minutes, the solution was stirred for 1 hour. Solvents were evaporated under vacuum and the product was recrystallised from methanol. The product was recovered as a red solid in 86% yield, but ^{1}H-NMR analysis showed around 5% of unreacted starting material. ^{1}H-NMR (CDCl$_3$, 600 MHz) δ (ppm) 6.96 (s, 2H), 6.01 (s, 1H), 2.59 (s, 3H), 2.57 (s, 3H), 2.34 (s, 3H), 2.07 (s, 6H), 1.38 (s, 3H), 1.37 (s, 3H). ^{13}C-NMR (CDCl$_3$, 150 MHz), δ (ppm) 157.8, 151.2, 144.5, 142.1, 139.1, 138.1, 135.0, 131.5, 130.9, 129.3, 129.1, 121.9, 110.3, 21.4, 19.6, 14.9, 13.7, 13.6, 12.4. HR-MS (ESI-TOF) *m/z*: Calculated for C$_{22}$H$_{24}$BBrF$_2$N$_2$Na (M+Na): 467.1080, found: 467.1081.

BODIPY 3.9. In a 50 mL round-bottom flask, 168 mg of BODIPY **1.7** were dissolved in 10 mL of DCM and cooled in an ice-brine bath. Then, 101 mg of recrystallised NBS (0.567 mmol, 1 eq.) were added and the reaction was stirred for 1 hour at the same temperature. Solvents was removed under vacuum and the product was recrystallised from methanol. The product was obtained as dark red crystals in 92% yield. No further purification was required. ^{1}H-NMR (CDCl$_3$, 600 MHz) δ (ppm) 7.75 (s, 1H), 7.56-7.47 (m, 3H), 7.36-7.32 (m, 2H), 6.49 (d, *J* = 4 Hz, 1H), 6.41 (dd, *J* = 4, 2 Hz, 1H), 2.67 (s, 3H), 1.51 (s, 3H). ^{13}C-NMR (CDCl3, 150 MHz), δ (ppm) 158.4, 144.1, 142.9, 140.7, 135.0, 133.9, 131.9, 129.8, 129.0, 128.8, 128.7, 117.1, 113.3, 14.4, 14.2. HS-MS (ESI-TOF) *m/z*: calculated for C$_{17}$H$_{13}$BBrF$_2$N$_2$ (M-1): 373.0329,

found: 373.0329. Calculated for $C_{17}H_{14}BBrF_2N_2Na$ (M+Na): 397.0294, found 397.0305.

2-DMB2P. BODIPY 3.9 (100 mg, 0.266 mmol), 3-perylene boronic acid pinacol ester (121 mg, 0.319 mmol, 1.2 eq.), caesium carbonate (87 mg, 0.266 mmol, 1 eq.), Pd(ACN)$_2$Cl$_2$ (6.9 mg, 0.026 mmol, 0.1 eq.) and SPhos (22 mg, 0.053 mmol, 0.2 eq.) were added to a sealed tube. The tube was flushed with argon and stirred at room temperature for 72 hours. Solvents were evaporated and the product was isolated by column chromatography using hexane:EtAcO (85:15), the product was obtained as a dark red solid in 72% yield. ^{1}H-NMR (CDCl$_3$, 600 MHz) δ (ppm) 8.26-8.17 (m, 4H), 7.76 (s, 1H), 7.71 (d, J = 3 Hz, 1H), 7.69 (d, J = 3 Hz, 1H), 7.52-7.48 (m, 5H), 7.48-7.41 (m, 3H), 7.39 (d, J = 8 Hz, 1H), 7.27 (d, J = 8 Hz, 1H), 6.48 (d, J = 4, 1H), 6.43 (dd, J = 4 Hz, 2), 2.48 (s, 3H), 1.36 (s, 3H). ^{13}C-NMR (CDCl$_3$, 150 MHz), δ (ppm) 161.8, 144.3, 143.7, 139.2, 135.2, 134.8, 134.3, 134.2, 133.8, 133.4, 131.9, 131.8, 131.2, 131.0, 130.1, 129.6, 129.18, 129.17, 128.92, 128.90, 128.7, 128.62, 128.60, 128.3, 128.2, 127.5, 127.2, 126.81, 126.76, 125.5, 120.70, 120.65, 120.6, 119.9, 116.4, 14.1, 13.7. HR-MS (ESI-TOF) m/z: calculated for $C_{37}H_{25}BF_2N_2Na$ (M+Na): 569.1971, found: 569.2098. calculated for $C_{37}H_{24}BF_2N_2$ (M-H): 545.2006, found: 545.2059.

8-DMB2P. BODIPY **3.4** (100 mg, 0.266 mmol), 3-perylene boronic acid (103 mg, 0.346 mmol, 1.2 eq.), caesium carbonate (261 mg, 0.8 mmol, 3 eq.), Pd(CAN)$_2$Cl$_2$ (6.92 mg, 0.026 mmol, 0.1 eq.) and SPhos (22 mg, 0.053 mmol, 0.2 eq.) were dissolved in 3 mL of THF and 0.5 mL of water and the reaction was stirred at room temperature for 48 hours. Solvents were evaporated under vacuum and the product was purified by column chromatography using silica gel and cyclohexane/ethyl acetate (8:2). The product was then dissolved in dichloromethane and precipitated with methanol to obtain DMB2P with higher purity as a dark green solid in 41 %

yield. ^{1}H-NMR (CDCl$_3$, 600 MHz): δ (ppm) 8.22-8.10 (m, 4H), 8.01-7.95 (m, 2H), 7.69-7.63 (m, 2H), 7.52-7.48 (m, 2H), 7.48-7.40 (m, 8H), 6.63 (s, 1H), 6.18 (s, 1H), 2.68 (s, 3H), 1.57 (s, 3H). ^{13}C-NMR (CDCl$_3$, 150 MHz): δ (ppm) 162.7, 147.4, 143.3, 138.9, 135.2, 134.8, 134.0, 132.9, 132.3, 131.61, 131.58, 131.4, 130.9, 130.6, 129.7, 129.3, 128.9, 128.8, 128.7, 127.9, 127.8, 127.4, 126.8, 126.75, 126.3, 125.9, 123.6, 120.6, 120.5, 120.2, 120.1, 15.4, 15.2. HR-MS (ESI-TOF) m/z: calculated for C$_{37}$H$_{24}$BF$_2$N$_2$ (M-1): 545.2006, found: 545.2012. calculated for C$_{37}$H$_{25}$BF$_2$N$_2$Na (M+Na): 569.1977, found: 569.1967.

MB2P. BODIPY **3.8** (140 mg, 0.314 mmol), 3-perylene boronic acid pinacol ester (143 mg, 0.377 mmol, 1.2 eq.), K$_3$PO$_4$ (135 mg, 0.629 mmol, 2 eq.) XPhos Pd G4 (13.5 mg, 0.015 mmol, 0.05 eq.) were dissolved in 3 mL of THF/Water (9:1) and stirred at 40 degrees for 72 hours. The product was purified by column chromatography using silica gel and cyclohexane/ethyl acetate (9:1) to afford MB2P as a red solid in a 54 % yield. ^{1}H-NMR (CDCl$_3$, 600 MHz): δ (ppm) 8.24-8.15 (m, 4H), 7.67 (d, $J = 9$), 7.50-7.46 (m, 2H), 7.46-7.39 (m, 2H), 7.29 (d, $J = 9$), 6.95 (s, 2H), 6.03 (s, 1H), 2.62 (s, 3H), 2.43 (s, 3H), 2.31 (s, 3H), 2.21 (s, 3H), 2.19 (s, 3H), 1.43 (s, 3H), 1.22 (s, 3H). ^{13}C-NMR (CDCl$_3$, 150 MHz): δ (ppm) 155.7, 154.5, 142.8, 142.0, 140.0, 138.8, 135.04, 134.98, 134.8, 134.1, 131.7, 131.43, 131.39, 131.24, 131.15, 130.5, 129.4, 129.22, 129.18, 129.1, 128.7, 128.04, 128.0, 126.9, 126.74, 126.73, 126.0, 121.2, 120.51, 120.48, 120.3, 119.9, 21.3, 19.81, 19.77, 14.8, 13.6, 13.5, 11.9. HR-MS (ESI-TOF) m/z: calculated for C$_{42}$H$_{35}$BF$_2$N$_2$ 616.2863 found 616.2872.

MB2PI. MB2P (85 mg, 0.137 mmol) was dissolved in 5 mL of dichloromethane and recrystallized NIS (37.22 mg, 0.165 mmol, 1.2 eq.) was added, and the reaction was stirred at room temperature for 16 hours. The solvent was evaporated under vacuum and the product purified by column chromatography to afford MB2PI as a dark red

solid in 73 % yield. ^{1}H-NMR (CDCl$_3$, 600 MHz): δ (ppm) 8.24-8.17 (m, 4H), 7.69 (d, 2H), 7.71-7-66 (m, 2H), 7.51-7.46 (m, 2H), 7.46-7.42 (m, 1H), 7.39-7.35 (m, 1H), 7.28 (d, J = 8), 6.97 (s, 2H), 2.69 (s, 3H), 2.43 (s, 3H), 2.32 (s, 3H), 2.19 (s, 3H), 2.17 (s, 3H), 1.46 (s, 3H), 1.21 (s, 3H). ^{13}C-NMR (CDCl$_3$, 150 MHz): δ (ppm) 157.0,154.8, 142.9, 142.0, 141.9, 139.1, 135.0, 134.9, 134.8, 134.0, 132.6, 131.8, 131.4, 131.3, 131.2, 131.1, 131.0, 130.8, 130.6, 129.4, 129.35, 129.31, 129.1, 128.7, 128.2, 128.1, 127.0, 126.79, 126.75, 125.7, 120.6, 120.55, 120.47, 119.9, 84.3, 21.3, 19.85, 19.80, 16.0, 15.7, 13.7, 12.2. HR-MS (ESI-TOF) m/z: calculated for C$_{42}$H$_{34}$BF$_2$IN$_2$: 742.1829, found: 742.1819. Calculated for C$_{42}$H$_{33}$BF$_2$IN$_2$ (M-1): 741.1762 found 741.1744.

AGB3P. BODIPY 1.7 (200mg, 0.675 mmol), 3-formylperylene (283 mg, 1.01 mmol, 1.50 eq.), piperidine (10 µL, 51 µmol, 0.15 eq.), acetic acid (6 µL, 51 µmol, 0.15 eq.) and 1 ml of toluene were added to a seal tube. Using a filter paper, a few pellets of 3Å molecular sieves were attached to the inside top of the tube. The tube was placed in an oil bath at 110 °C and stirred for 16 hours. The solution was removed from the oil bath and cooled to room temperature. Solvents were evaporated under vacuum and the product was purified by column chromatography on silica gel. The silica gel was neutralised using hexane: triethylamine (97:3). Hexane and ethyl acetate were used as the mobile phase (97:3). 1% of triethylamine was added to the mobile phase all along. Crystals of AGB3P were isolated from one of the fractions, 4 mg (1.06 %) in total, and that was the product used for characterisation and for spectroscopic studies. The rest of the fractions contained variable amounts of 3-formyl perylene as a decomposition product. ^{1}H-NMR (CD$_2$Cl$_2$, 600 MHz) δ (ppm) 8.34-8.26 (m, 4H), 8.22 (d, J = 16 Hz, 1H), 8.14 (d, J = 8 Hz, 1H), 8.04 (d, J = 8 Hz, 1H), 7.86 (d, J = 16 Hz, 1H), 7.76 (t, J = 8 Hz, 2H), 7.71 (s, 1H), 7.63 (t, J = 8 Hz, 1H), 7.57-7.50 (m, 5H), 7.45-7.41 (m, 2H), 6.96 (s, 1H), 6.46 (d, J = 4 Hz, 1H), 6.44 (dd, J = 4, 2 Hz, 1H), 1.65 (s, 3H). Due to the

low concentration of the sample and the impossibility of adding more product, it was not possible to obtain the ^{13}C-NMR spectrum of AGB3P. HS-MS (ESI-TOF) m/z: $C_{38}H_{26}BF_2N_2$ (M+H): 559.2158, found 559.2149. Calculated for $C_{38}H_{25}BF_2N_2Na$ (M+Na): 581.1977, found: 581.1973.

3.4.2 Spectroscopical measurements

Absorbance spectra were recorded in a Jasco V670 spectrophotometer and all data was manipulated using Jasco Spectra Manager v2 software. Stock solutions of the dyes were prepared in dioxane and diluted into the studied solvents. Samples were analysed in Hellma quartz fluorescence cuvettes, with a path length of 1 cm. Background measurements were carried out at room temperature prior to each measurement. Fluorescence emission spectra were obtained using a Varian Cary Eclipse fluorescence spectrophotometer. The lifetime of the excited state was measured using a PicoQuant FluoTime 100 Compact FLS TCSPC system using a 450 nm pulsed laser source generated from a PicoQuant PDL800-B box. Lifetime decay plots were analysed using PicoQuant TimeHarp software. The goodness of each fit to exponential decay kinetics was assessed from chi-squared values (where $\chi^2 < 1.3$) and visual inspection of residuals. Absolute quantum yields were measured in a SF5 fluorimeter from Edinburgh Instruments using the SF5 SC-30 integrating sphere module.

3.4.3 Crystallography

Diffraction data for **MB2P** were collected on a Synergy, Dualflex, AtlasS2 diffractometer using CuKα radiation (λ = 1.54184 Å). The structure was solved by dual space methods (SHELXT) and refined on F^2 using all the reflections (SHELXL-2018/3.[111] All non-hydrogen atoms were refined using anisotropic atomic displacement parameters, except for the carbon atoms and 5% occupancy chlorine

atoms of overlapping, partial-occupancy chloroform solvate molecules. Hydrogen atoms were inserted at calculated positions using a riding model. Details of the refinement and disorder model are included in the supplementary material.

Crystal Data for $C_{42}H_{35}BF_2N_2 \cdot 0.475(CHCl_3)$**:** ($M$ = 673.23 g/mol): monoclinic, space group P2$_1$/c (no. 14), a = 22.5919(8) Å, b = 12.5812(5) Å, c = 25.2321(9) Å, β = 96.352(3)°, V = 7127.8(5) Å^3, Z = 8, T = 100.01(11) K, μ(Cu $K\alpha$) = 1.584 mm^{-1}, D_{calc} = 1.255 g/cm^3, 52467 reflections measured (7.05° ≤ 2θ ≤ 133.202°), 12557 unique (R_{int} = 0.0886, R_{sigma} = 0.0612) which were used in all calculations. R1 = 0.1039 (I > 2σ(I)); wR2 = 0.3148 (all data). CCDC 2157191 and 2157530 contain the supplementary crystallographic data for this chapter. These data can be found in Appendix B or obtained free of charge from The Cambridge Crystallographic Data Centre via www.ccdc.cam.ac.uk/data_request/cif.

3.5 References

[1]   L. Jiao, W. Pang, J. Zhou, Y. Wei, X. Mu, G. Bai, E. Hao, *J. Org. Chem.* **2011**, *76*, 9988–9996.

[2]   L. Wang, K. Zhu, Q. Chen, M. He, *Dyes and Pigments* **2015**, *112*, 274–279.

[3]   W. Hu, R. Zhang, X.-F. Zhang, J. Liu, L. Luo, *Spectrochim. Acta A.* **2022**, *272*, 120965.

[4]   N. Epelde-Elezcano, V. Martínez-Martínez, E. Peña-Cabrera, C. F. A. Gómez-Durán, I. L. Arbeloa, S. Lacombe, *RSC Adv.* **2016**, *6*, 41991–41998.

[5]   M. Gorbe, A. M. Costero, F. Sancenón, R. Martínez-Máñez, R. Ballesteros-Cillero, L. E. Ochando, K. Chulvi, R. Gotor, S. Gil, *Dyes and Pigments* **2019**, *160*, 198–207.

[6]   C. Cordovilla, C. Bartolomé, J. M. Martínez-Ilarduya, P. Espinet, *ACS Catal.* **2015**, *5*, 3040–3053.

[7]   M. M. Heravi, E. Hashemi, F. Azimian, *Tetrahedron* **2014**, *70*, 7–21.

[8]   Y. Tanabe, E. Sato, N. Nakajima, A. Ohkubo, O. Ohno, K. Suenaga, *Org. Lett.* **2014**, *16*, 2858–2861.

[9]   G. Valot, C. S. Regens, D. P. O'Malley, E. Godineau, H. Takikawa, A. Fürstner, *Angew Chem. Int. Ed. Engl.* **2013**, *125*, 9713–9717.

[10]   A. Pagliarani, S. Nesci, V. Ventrella, *In Vitro Toxicol.* **2013**, *27*, 978–990.

[11]   A. Olushola Sunday, B. Abdullahi Alafara, O. Godwin Oladele, *Chem. Spec. Bioavailab.* **2012**, *24*, 216–226.

[12]   J. A. Ragan, J. W. Raggon, P. D. Hill, B. P. Jones, R. E. McDermott, M. J. Munchhof, M. A. Marx, J. M. Casavant, B. A. Cooper, J. L. Doty, Y. Lu, *Org. Process Res. Dev.* **2003**, *7*, 676–683.

[13]   H. Wang, F. R. Fronczek, M. G. H. Vicente, K. M. Smith, *J. Org. Chem.* **2014**, *79*, 10342–10352.

[14]   B. Xie, L. Yin, C. Liu, J. Fan, X. Wang, Y. Li, *Org. Electron.* **2023**, *122*, 106913.

[15]   E. Palao, T. Slanina, P. Klán, *Chem. Commun.* **2016**, *52*, 11951–11954.

[16]   M. J. Buskes, M.-J. Blanco, *Molecules* **2020**, *25*, 3493.

[17]   D. Blakemore, D., Doyle, P., & Fobian, Y. (2016). Chapter 1 in *Synthetic Methods in Drug Discovery*. RCS. London. **2016** pp. 1–69.

[18]   A. J. J. Lennox, G. C. Lloyd-Jones, *Chem. Soc. Rev.* **2014**, *43*, 412–443.

[19]   C. J. O'Brien, E. A. B. Kantchev, C. Valente, N. Hadei, G. A. Chass, A. Lough, A. C. Hopkinson, M. G. Organ, *Chem. Eur. J.* **2006**, *12*, 4743–4748.

[20]   A.-X. Song, X.-X. Zeng, B.-B. Ma, C. Xu, F.-S. Liu, *Organometallics* **2020**, *39*, 3524–3534.

[21]   S. Wagschal, L. A. Perego, A. Simon, A. Franco-Espejo, C. Tocqueville, J. Albaneze-Walker, A. Jutand, L. Grimaud, *Chem. Eur. J.* **2019**, *25*, 6980–6987.

[22]   Q. Shen, J. F. Hartwig, *Org. Lett.* **2008**, *10*, 4109–4112.

[23]   B. P. Fors, S. L. Buchwald, *J. Am. Chem. Soc.* **2010**, *132*, 15914–15917.

[24]   Z. Wang, J. Zhao, *Org. Lett.* **2017**, *19*, 4492–4495.

[25]   W. Che, G. Li, J. Zhang, Y. Geng, Z. Xie, D. Zhu, Z. Su, *J. Photochem. Photobiol. A.* **2018**, *358*, 274–283.

[26]   V. Nguyen, Y. Yim, S. Kim, B. Ryu, K. M. K. Swamy, G. Kim, N. Kwon, C. Kim, S. Park, J. Yoon, *Angew. Chem. Int. Ed.* **2020**, *59*, 8957–8962.

[27]   Z. Zhou, J. Zhou, L. Gai, A. Yuan, Z. Shen, *Chem. Commun.* **2017**, *53*, 6621–6624.

[28]   R. W. Friesen, E. M. D. Allouche, in *Encyclopedia of Reagents for Organic Synthesis*, John Wiley & Sons, Ltd, Chichester, UK, **2017**, pp. 1–7.

[29]   J. Liao, H. Zhao, Y. Xu, W. Zhou, F. Peng, Y. Wang, Y. Fang, *RSC Adv.* **2017**, *7*, 33975–33985.

[30]   M. Mayländer, T. Quintes, M. Franz, X. Allonas, A. Vargas Jentzsch, S. Richert, *Chem. Sci.* **2023**, *14*, 5361–5368.

[31]   D. Pfeifer, A. Russegger, I. Klimant, S. M. Borisov, *Sens. Actuators B.* **2020**, *304*, 127312.

[32]   Y. Hayashi, S. Yamaguchi, W. Y. Cha, D. Kim, H. Shinokubo, *Org. Lett.* **2011**, *13*, 2992–2995.

[33]   G. Li, Y. Otsuka, T. Matsumiya, T. Suzuki, J. Li, M. Takahashi, K. Yamada, *Materials* **2018**, *11*, 1297.

[34]   A. Dermenci, J. W. Coe, in *Synthetic Methods in Drug Discovery*. RCS. London. **2016** pp**.**, pp. 143–169.

[35]   R. F. Heck, J. P. Nolley, *J. Org. Chem.* **1972**, *37*, 2320–2322.

[36]   T. Mizoroki, K. Mori, A. Ozaki, *BCSJ* **1971**, *44*, 581–581.

[37]   M. Larhed, A. Hallberg, in *Handbook of Organopalladium Chemistry for Organic Synthesis* (Ed.: E. Negishi), John Wiley & Sons, Inc., New York, **2002**, pp. 1133–1178.

[38]   T. Jeffery, *Tetrahedron* **1996**, *52*, 10113–10130.

[39]   B. P. Carrow, John. F. Hartwig, *J. Am. Chem. Soc.* **2010**, *132*, 79–81.

[40]   J. Wang, Q. Wu, Q. Gong, K. Cheng, Q. Liu, C. Yu, E. Hao, L. Jiao, *Adv. Synth. Catal.* **2019**, *361*, 769–777.

[41]   W. Qin, T. Rohand, W. Dehaen, J. N. Clifford, K. Driesen, D. Beljonne, B. Van Averbeke, M. Van der Auweraer, N. Boens, *J. Phys. Chem. A* **2007**, *111*, 8588–8597.

[42]   C. Bellomo, D. Zanetti, F. Cardano, S. Sinha, M. Chaari, A. Fin, A. Maranzana, R. Núñez, M. Blangetti, C. Prandi, *Dyes and Pigments* **2021**, *194*, 109644.

[43]   L. Gai, J. Mack, H. Lu, H. Yamada, D. Kuzuhara, G. Lai, Z. Li, Z. Shen, *Chem. Eur. J.* **2014**, *20*, 1091–1102.

[44]   H. G. Knaus, T. Moshammer, K. Friedrich, H. C. Kang, R. P. Haugland, H. Glossman, *Proc. Natl. Acad. Sci. U.S.A.* **1992**, *89*, 3586–3590.

[45]   S. Zhu, J. Zhang, G. Vegesna, A. Tiwari, F.-T. Luo, M. Zeller, R. Luck, H. Li, S. Green, H. Liu, *RSC Adv.* **2012**, *2*, 404–407.

[46]   G. Biagiotti, E. Purić, I. Urbančič, A. Krišelj, M. Weiss, J. Mravljak, C. Gellini, L. Lay, F. Chiodo, M. Anderluh, S. Cicchi, B. Richichi, *Bioorg. Chem.* **2021**, *109*, 104730.

[47]   K. van Beurden, S. de Koning, D. Molendijk, J. van Schijndel, *Green Chem. Lett. Rev.* **2020**, *13*, 349–364.

[48]   J. Tao, D. Sun, L. Sun, Z. Li, B. Fu, J. Liu, L. Zhang, S. Wang, Y. Fang, H. Xu, *Dyes and Pigments* **2019**, *168*, 166–174.

[49]   M. Li, R. Tian, J. Fan, J. Du, S. Long, X. Peng, *Dyes and Pigments* **2017**, *147*, 99–105.

[50]   B. Shen, L. F. Wang, X. Zhi, Y. Qian, *Sens. Actuators B.* **2020**, *304*, 127271.

[51]   G. Lippens, A. Sillen, I. Landrieu, L. Amniai, N. Sibille, P. Barbier, A. Leroy, X. Hanoulle, J.-M. Wieruszeski, *Prion* **2007**, *1*, 21–25.

[52]   T. Bura, P. Retailleau, G. Ulrich, R. Ziessel, *J. Org. Chem.* **2011**, *76*, 1109–1117.

[53]   Z. Guo, X. Wei, Y. Hua, J. Chao, D. Liu, *Tetrahedron Lett.* **2015**, *56*, 3919–3922.

[54]   K. O. Jeon, J. H. Jun, J. S. Yu, C. K. Lee, *J. Heterocyclic Chem.* **2003**, *40*, 763–771.

[55]   C.-H. Lee, J. S. Lindsey, *Tetrahedron* **1994**, *50*, 11427–11440.

[56]   J. Bergman, L. Venemalm, *Tetrahedron Lett.* **1987**, *28*, 3741–3744.

[57]   P. Wang, F. Lu, J. S. Lindsey, *J. Org. Chem.* **2020**, *85*, 702–715.

[58]   S. Massa, R. Ragno, G. C. Porretta, A. Mai, A. Retico, M. Artico, N. Simonetti, *Arch. Pharm. Pharm. Med. Chem.* **1993**, *326*, 539–546.

[59]   D. M. Wallace, S. H. Leung, M. O. Senge, K. M. Smith, *J. Org. Chem.* **1993**, *58*, 7245–7257.

[60]   J. White, G. McGillivray, *J. Chem. Soc., Perkin Trans. 2* **1982**, 259–261.

[61]   B. R. Patil, S. R. Bhusare, R. P. Pawar, Y. B. Vibhute, *Tetrahedron Lett.* **2005**, *46*, 7179–7181.

[62]   A. T. Shinde, S. B. Zangade, S. B. Chavan, A. Y. Vibhute, Y. S. Nalwar, Y. B. Vibhute, *Synth. Comm.* **2010**, *40*, 3506–3513.

[63]   W. Krzemien, M. Rohlickova, M. Machacek, V. Novakova, J. Piskorz, P. Zimcik, *Molecules* **2021**, *26*, 4194.

[64]   A. P. Phillips, J. G. Murphy, *J. Org. Chem.* **1951**, *16*, 954–962.

[65]   S. J. Hawkins, N. M. Ratcliffe, *J. Mater. Chem.* **2000**, *10*, 2057–2062.

[66]   G. P. Gardini, in *Advances in Heterocyclic Chemistry*, Elsevier, London. **1973**, pp. 67–98.

[67]   J. Chen, A. Burghart, C.-W. Wan, L. Thai, C. Ortiz, J. Reibenspies, K. Burgess, *Tetrahedron Letters* **2000**, *41*, 2303–2307.

[68]   K. Chen, Y. Dong, X. Zhao, M. Imran, G. Tang, J. Zhao, Q. Liu, *Front. Chem.* **2019**, *7*, 821.

[69]   W. Hu, X.-F. Zhang, X. Lu, S. Lan, D. Tian, T. Li, L. Wang, S. Zhao, M. Feng, J. Zhang, *Dyes and Pigments* **2018**, *149*, 306–314.

[70]   W. Miao, C. Yu, E. Hao, L. Jiao, *Front. Chem.* **2019**, *7*, 825.

[71]   G. Zhang, M. Wang, C. Ndung'U, P. Bobadova-Parvanova, F. R. Fronczek, K. M. Smith, M. G. H. Vicente, *J. Porphyr. Phthalocya.* **2020**, *24*, 869–877.

[72]   M. A. Panfilov, T. Yu. Karogodina, Y. Songyin, O. Yu. Karmatskih, A. Yu. Vorob'ev, I. S. Tretyakova, E. M. Glebov, A. E. Moskalensky, *J. Lumin.* **2022**, *246*, 118837.

[73]   S. Toliautas, J. Dodonova, A. Žvirblis, I. Čiplys, A. Polita, A. Devižis, S. Tumkevičius, J. Šulskus, A. Vyšniauskas, *Chem. Eur. J.* **2019**, *25*, 10342–10349.

[74]   R. W. Wagner, J. S. Lindsey, *Pure App. Chem.* **1996**, *68*, 1373–1380.

[75]   S. David, G. Pilet, G. Berginc, C. Andraud, O. Maury, *New J. Chem.* **2020**, *44*, 13125–13130.

[76]   S. T. Salunke, D. S. Shelar, S. T. Manjare, *J. Fluoresc.* **2023**, *33*, 437–444.

[77]   M. J. Hall, S. O. McDonnell, J. Killoran, D. F. O'Shea, *J. Org. Chem.* **2005**, *70*, 5571–5578.

[78]   S. Barroso, M. Joksch, P. Puylaert, S. Tin, S. J. Bell, L. Donnellan, S. Duguid, C. Muir, P. Zhao, V. Farina, D. N. Tran, J. G. de Vries, *J. Org. Chem.* **2021**, *86*, 103–109.

[79]   G. A. Molander, D. L. Sandrock, *Curr. Opin. Drug. Discov. Devel.* **2009**, *12*, 811–823.

[80]   D. R. Fandrick, J. T. Reeves, Z. Tan, H. Lee, J. J. Song, N. K. Yee, C. H. Senanayake, *Org. Lett.* **2009**, *11*, 5458–5461.

[81]   M. Reilly, S. Rychnovsky, *Synlett* **2011**, *2011*, 2392–2396.

[82]   P. Kohler, T. Perrin, G. Schäfer, *Synthesis* **2023**, *55*, 3159–3171.

[83]   P. A. Inglesby, L. R. Agnew, H. L. Carter, O. T. Ring, *Org. Process Res. Dev.* **2020**, *24*, 1683–1689.

[84]   C. Amatore, A. Jutand, in *Handbook of Organopalladium Chemistry for Organic Synthesis* (Ed.: E. Negishi), John Wiley & Sons, Inc., New York. **2002**, pp. 943–972.

[85]   M. C. D'Alterio, È. Casals-Cruañas, N. V. Tzouras, G. Talarico, S. P. Nolan, A. Poater, *Chem. Eur. J.* **2021**, *27*, 13481–13493.

[86]   N. Menges, *Comput. Theor. Chem.* **2015**, *1068*, 117–122.

[87]   M. D. Brooker, S. M. Cooper, D. R. Hodges, R. R. Carter, J. K. Wyatt, *Tetrahedron Lett.* **2010**, *51*, 6748–6752.

[88]   S. J. Firsan, V. Sivakumar, T. J. Colacot, *Chem. Rev.* **2022**, *122*, 16983–17027.

[89]   L. M. Alcazar-Roman, J. F. Hartwig, A. L. Rheingold, L. M. Liable-Sands, I. A. Guzei, *J. Am. Chem. Soc.* **2000**, *122*, 4618–4630.

[90]   T. Hayashi, M. Konishi, M. Kumada, *Tetrahedron Letters* **1979**, *20*, 1871–1874.

[91]   S. Banfi, G. Nasini, S. Zaza, E. Caruso, *Tetrahedron* **2013**, *69*, 4845–4856.

[92]   D. K. Joshi, F. Betancourt, M. Pilkington, H. Yan, *J. Photochem. Photobiol. A.* **2023**, *442*, 114770.

[93]   L. Gai, H. Lu, B. Zou, G. Lai, Z. Shen, Z. Li, *RSC Adv.* **2012**, *2*, 8840.

[94]   A. J. J. Lennox, G. C. Lloyd-Jones, *Angew. Chem. Int. Ed.* **2013**, *52*, 7362–7370.

[95]   M. Busch, M. D. Wodrich, C. Corminboeuf, *ACS Catal.* **2017**, *7*, 5643–5653.

[96]   A. L. Casado, P. Espinet, *J. Am. Chem. Soc.* **1998**, *120*, 8978–8985.

[97]   V. Mani, V. G. Krishnakumar, S. Gupta, S. Mori, I. Gupta, *Sens. Actuators B.* **2017**, *244*, 673–683.

[98]   A. M. Al-Majid, M. S. Islam, A. Barakat, N. J. Al-Qahtani, S. Yousuf, M. Iqbal Choudhary, *Arab. J. Chem.* **2017**, *10*, 185–193.

[99]   T. T. Vu, R. Méallet-Renault, G. Clavier, B. A. Trofimov, M. K. Kuimova, *J. Mater. Chem. C* **2016**, *4*, 2828–2833.

[100]   A. Vyšniauskas, I. López-Duarte, N. Duchemin, T.-T. Vu, Y. Wu, E. M. Budynina, Y. A. Volkova, E. Peña Cabrera, D. E. Ramírez-Ornelas, M. K. Kuimova, *Phys. Chem. Chem. Phys.* **2017**, *19*, 25252–25259.

[101]   D. Su, C. L. Teoh, L. Wang, X. Liu, Y.-T. Chang, *Chem. Soc. Rev.* **2017**, *46*, 4833–4844.

[102]   M. K. Kuimova, *Phys. Chem. Chem. Phys.* **2012**, *14*, 12671.

[103]   M. A. Haidekker, E. A. Theodorakis, *Org. Biomol. Chem.* **2007**, *5*, 1669–1678.

[104] P. Rybczynski, A. Smolarkiewicz-Wyczachowski, J. Piskorz, S. Bocian, M. Ziegler-Borowska, D. Kędziera, A. Kaczmarek-Kędziera, *IJMS* **2021**, *22*, 6735.

[105] R. A. Arellano-Reyes, A. Prabhakaran, R. C. E. Sia, J. Guthmuller, K. K. Jha, T. Yang, B. Dietzek-Ivanšić, V. McKee, T. E. Keyes, *Chem. Eur. J.* **2023**, *29*, e202300239.

[106] A. K. Covington, T. Dickinson, in *Physical Chemistry of Organic Solvent Systems* (Eds.: A.K. Covington, T. Dickinson), Springer US, Boston, **1973**, pp. 1–22.

[107] Z. Wang, M. Ivanov, Y. Gao, L. Bussotti, P. Foggi, H. Zhang, N. Russo, B. Dick, J. Zhao, M. Di Donato, G. Mazzone, L. Luo, M. Fedin, *Chem. Eur. J.* **2020**, *26*, 1091–1102.

[108] T. Ryu, K. Miyata, M. Saigo, Y. Shimoda, Y. Tsuchiya, H. Nakanotani, C. Adachi, K. Onda, *Chem. Phys. Lett.* **2022**, *809*, 140155.

[109] R. Misra, S. P. Bhattacharyya, in *Intramolecular Charge Transfer: Theory and Applications*, Wiley, Weinhein. **2018**.

[110] C. R. Groom, I. J. Bruno, M. P. Lightfoot, S. C. Ward, *Acta Crystallogr. B.* **2016**, *72*, 171–179.

[111] G. M. Sheldrick, *Acta Crystallogr. C.* **2015**, *71*, 3–8.

Chapter 4 Spectroscopy and photophysics of BODIPY derivatives

Overview

In this Chapter, the photophysical properties of the BODIPY-perylene conjugates prepared in Chapters 2 and 3 are described. A key objective was to explore the impact of viscosity on the photophysics of the probes reported in Chapter 2, to understand whether some dyads are potential viscosity sensors. B2P, MB2P, 2-DMB2P and 8-DMB2P, prepared in previous chapters were tested as potential viscosity sensors. To understand the role of viscosity on the photophysics and spectroscopy of the dyads, studies were carried out in both polar and in non-polar solvent combinations, methanol-glycerol and castor oil-toluene, respectively, and the ratio was varied to modulate the solvent viscosity. The non-polar system was chosen because it is similar in polarity and dielectric constant to the cell membrane environments in which highly lipophilic dyads tend to accumulate. The polar system was included to understand whether modulation of charge transfer characteristics of the compounds could be induced in polar and viscous solvents due to evident changes to photophysics described in Chapter 2 in polar solvents. In addition to steady state absorbance and emission, the fluorescence lifetime of the dyes in the non-polar system was studied. The temperature-dependence of the charge transfer emission was also studied in selected examples in viscous media.

As, evidenced from effective TTA-UC sensitization, and discussed in Chapter 2, the BODIPY-perylene dyads undergo intersystem crossing to form triplet excited states and the triplet can undergo Dexter energy transfer with

molecular oxygen. In other words, they are also expected to be ROS (reactive oxygen species) generators. These, selected BODIPY-perylene conjugates, were also explored as singlet oxygen generators. Singlet oxygen was detected by the indirect method using a scavenger. The solvent dependence of singlet oxygen generation in non-polar solvents was studied. Significant differences between iodinated and non-iodinated dyes were found, consistent with ISC promoted due to the heavy atom effect in the latter. Given their propensity for singlet oxygen generation, the capacity of the BODIPY-perylene dyads as photodynamic therapy sensitisers, their uptake, dark and phototoxicity were studied in MCF-7 cells.

Finally, for dyads where crystals were isolated, their solid-state properties were studied including emission and quantum yield. Crystals of one dye were ground and the properties of the resulting sample were studied.

4.1 Introduction

Some of the key properties of BODIPY-perylene in homogeneous solution have been explained in the main introduction and in previous chapters. In this introductory section attention has been paid to the solid-state properties of fluorescence dyes in general and BODIPYs in particular. The potential of BODIPYs as singlet oxygen generation will also be explained.

4.1.1 Solid state spectroscopy of organic fluorophores

The solid-state properties of fluorescent dyes are of interest for several reasons. First, the lipophilic nature of the BODIPY probes may lead to their aggregation in biological environments with high water content. Secondly, the solid state photophysics can vary significantly compared to solution, and BODIPY dyes in the solid state have shown e.g. J-aggregation and other behaviours that can lead to either augmentation or quenching of the fluorescence. In general, for solid-state organic fluorophores, emission is red-shifted compared to the diluted solution,[1] although blue-shifted solid-state emission has been reported.[2,3]

Aggregation induced fluorescence has been used for a wide variety of sensing applications.[4] For instance, a tetraphenylethylene (TPE) derivative (Figure 75) was used to detect charged biomolecules. The isolated probe is barely emissive, but the addition of the biomolecules such as DNA induces the formation of emissive aggregates.[5]
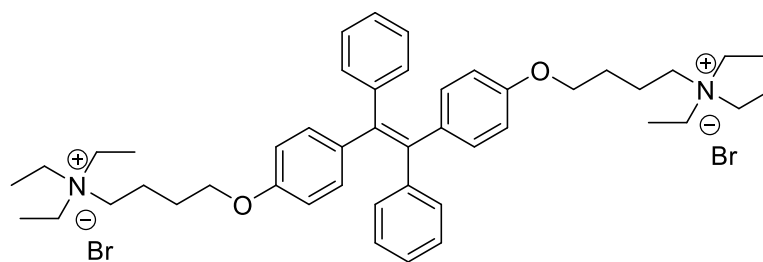
Figure 75 *Tetraphenylethylene derivative with emissive properties in the aggregate state.*

The solid-state properties of a molecule highly depend on the molecular packaging, e.g. the π-π stacking, hydrogen bond and other weak intermolecular interactions.[6–8] In the case of molecular rotors, intramolecular motion is restricted in the solid state and this inhibition is likely to be one of the key factors influencing the solid state photophysical properties.[9] A good example is the use of a quinolinemalonitrile as an organic waveguide. The molecule has a 0.1% fluorescence quantum yield in THF (Figure 76 a) whereas it becomes more and more emissive as the aggregation, induced by addition of water, increases (Figure 76 b).[10] The interaction between the cyano groups and the *N,N*-dimethylamino group in a head-to-tail interaction type are responsible for the formation of J-agregates. The weak CH-π bonds are responsible for the intramolecular interaction and the red-shifted emission in the solid state.

a)

0.1% QY in THF

b)

4.1% QY agregate
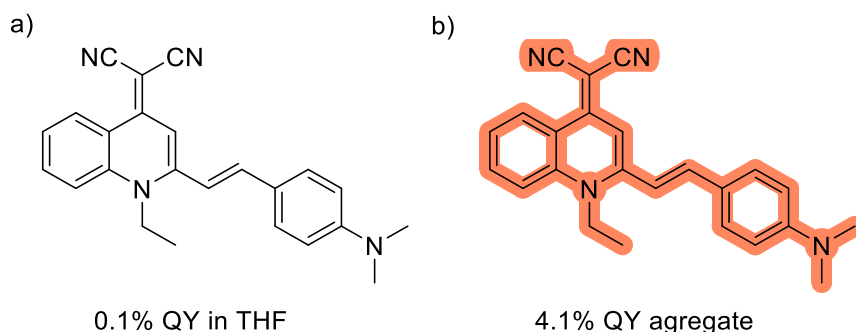
Figure 76 *Quinolinemalonitrile derivative with no emission in solution (a) and 4% QY emission in the aggregate form (b). Aggregates are formed by a head-to-tail interaction between the cyano groups and the N,N-dimethylamino group.*

4.1.2 Solid state properties of BODIPYs

BODIPYS have been used extensively studied solution; however, their solid-state properties are significantly less explored.[11] In the example in Figure 77, the fluorine atoms of a BODIPY dye were replaced by alkoxy groups. This modification produced minor changes in solution photophysics, as the molecules have features similar to -F substituted BODIPYs. Figure 77 (a). However, in the solid state, the O-substituted BODIPYs presented a broad emission that extends across the red and near infrared regions (Figure 77b). The authors attributed the solid-state properties to the disruption in π-π stacking produced by the alkoxy groups which are bulky.[12]
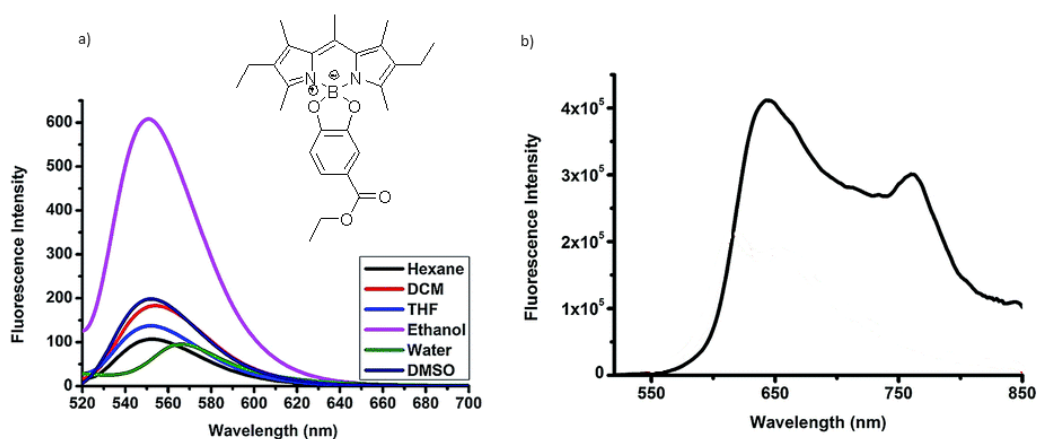
Figure 77 *(a) Emission spectra of an O-substituted BODIPY in solution in different solvents. (b) Emission spectra of the same molecule in the solid state.*

In a study from 2019, researchers prepared crystals of methyl, phenyl, and mesityl *meso* substituted BODIPYs. The solid-state emission of this dyes was red-shifted compared to the solutions by at least 100 nm, from ~515 nm in solution to ~620 nm in the crystalline state. The quantum yields were reported to be much lower in the solid state than in solution (~3-15 times). However, what is most striking is that the red-shifted emission of the crystals was reduced after a gentle

grinding and almost reach the values of the emission in solution after a strong grinding. In this study these observations are restricted to BODIPYs with aromatic rings at the *meso* position. The authors concluded that the red-shifted emission of the crystalline forms was the result of J-aggregation that was disrupted on grinding to form an amorphous structure. Figure 78.[13]
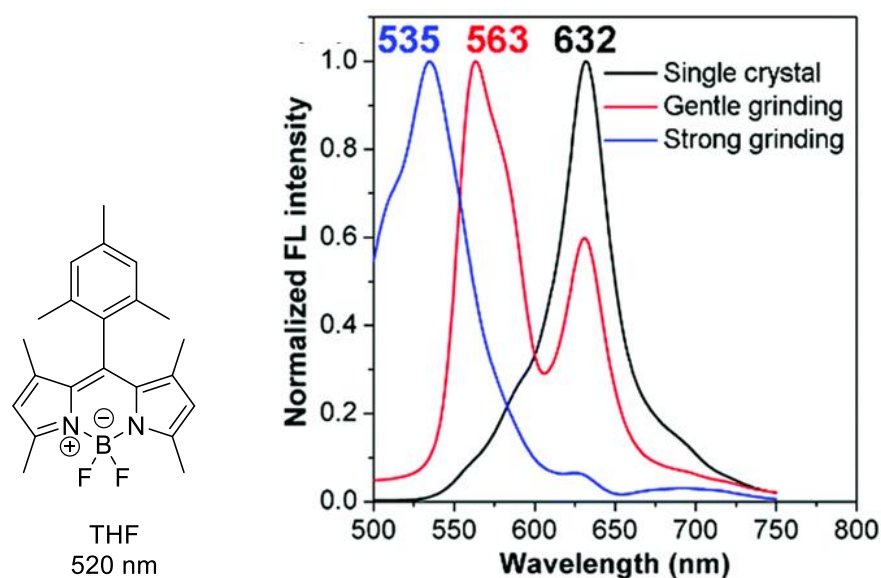
Figure 78 *Mesityl BODIPY and the changes in emission wavelength in the crystalline state and after grinding.*[13]

Integrating BODIPYs into solid polymeric matrixes has given useful insights into the effects of aggregation. For example, combination of styrene and BODIPY in a random polymer produced a shift of over 200 nm of emission compared to the monomer in solution, from 537 to 757 nm. The polymers in solution had similar properties to the monomers due to the absence of aggregation of BODIPY units in the same polymeric chain. The change in the emission wavelength was observed in the solid state where aggregation of BODIPYs in different polymer chains was effective or when the only component of the polymer was the BODIPY and there was no styrene present at all[14] (Figure 79).
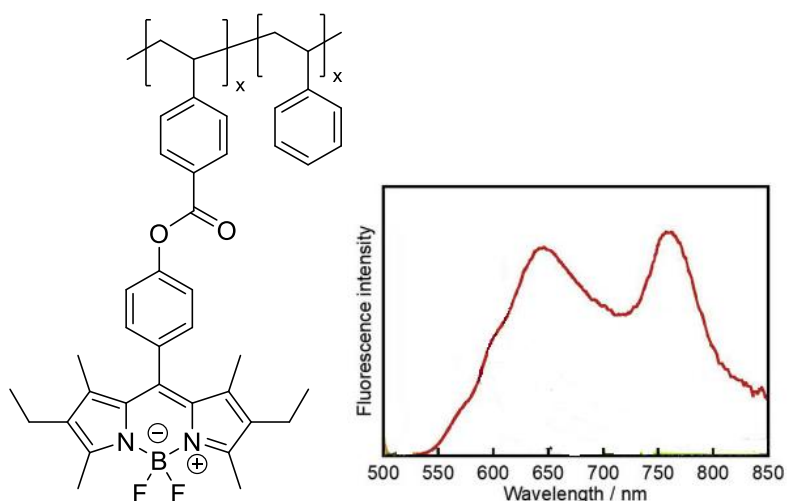
Figure 79 *Left: Polymer presenting red-shifted emission due to aggregation. Right: emission spectrum of the polymer containing only BODIPY units.* [14]

In a contrasting example, another team explicitly designed a BODIPY dye to avoid the formation of aggregates by including adamantly substituents on the BODIPY core. The dye was then added to a polymeric matrix of polymethyl methacrylate (PMMA) in different proportions. Even though aggregation is not completely avoided, researchers found only minor red-shifted emission of the solid polymer and almost the same small Stokes shift than the one observed in solution[15] (Figure 80). This is an indication that, more than the restriction of the rotation, it is the intermolecular interactions that have a key role in determining the properties of a BODIPY in the solid state.
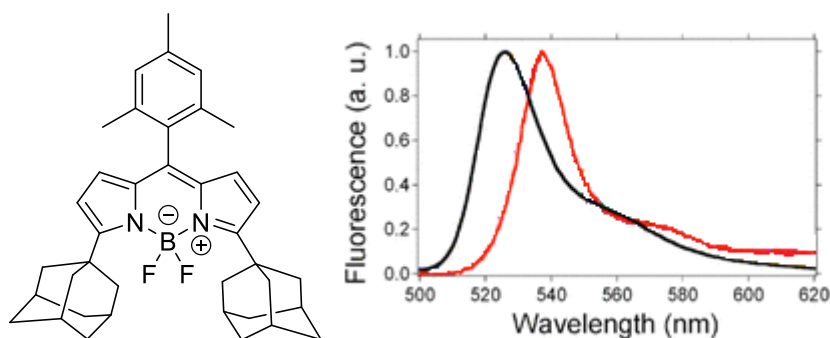
Figure 80 *Left: structure of the BODIPY-adamantane. Right : Normalised emission of the dye dissolved in methyl methacrylate monomer (40%) in toluene (black) and in solid PMMA (red) the lack of aggregation limits the red-shifted emission in the solid state.* [15]

4.2.3 BODIPYs as singlet oxygen generators

At first sight, BODIPY might not be considered a good candidate as a PDT sensitiser. The unsubstituted molecule's absorption and emission are around 500 nm, and, without a heavy atom, the ISC for the simple core is very low (<1%).[16] Yet, the tuneable structure allows to modify both parameters and shift them into the red or near infra-red regions, the biologically-relevant window.[17,18] introduction of heavy atoms such as iodine or the functionalisation with polyaromatic hydrocarbons can dramatically enhance ISC in BODIPY derivatives. In these cases, ISC can be promoted by a TICT or by heavy atom effect.[19–22] Finally, another reason that challenges the application of BODIPY as PDT agents is their solubility. BODIPYs are generally lipophilic, and while that can benefit their lipid membrane association or permeation, they are rarely water soluble which can make them hard to use in certain biological applications. There are a number of ways to improve water solubility, e.g., adding sulfobetaine groups can drastically enhance the water solubility when required.[23]

One common synthetic modification of BODIPY aiming to improve the PDT potential is the introduction of heavy atoms or the synthesis of twisted BODIPY dimers.[24] On one side, the heavy atoms used are generally bromine or iodine and the *meso* substituent is modified to improve the selectivity or solubility of the dyes.[25] Figure 81 (a). Halogenated BODIPYs have shown promising results *in vitro* and *in vivo* and could be good candidates for clinical trials.[24,26–28] On the other hand, making twisted BODIPYs can help decrease the toxicity associated with halogenated molecules[29–32] (Figure 81 b).
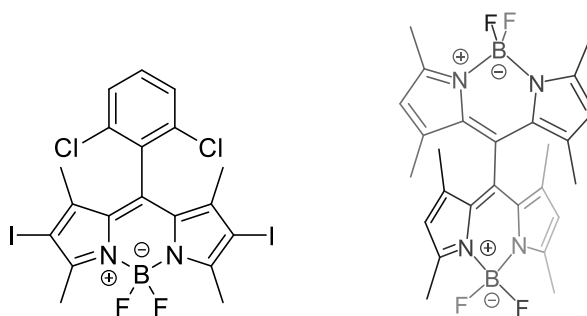
Figure 81 Examples of halogen-BODIPY (a) and heavy atom-free (b) photosensitisers.

Both strategies, heavy atom and twisted conformation, have applied to antimicrobial photodynamic therapy[33,34] and the design of antimicrobial surfaces.[35]

4.2.4 BODIPYs and the challenges of photodynamic therapy

PDT, in its current form, still faces some major challenges. Type II PDT photosensitisers rely on oxygen availability in the medium; however, cancer tumours are often hypoxic.[36] As a general rule, the rapid growth of cancer tumours avoids the proper vascularisation of the tissue provoking a lack of blood irrigation and hence of oxygen. To address this problem, some alternatives have been suggested.

The first approach to overcome hypoxia is fractional PDT, that has been applied to BODIPY.[24] In this method there is a dark interval between each irradiation to allow oxygen replenishment. The intervals are generally two hours long, but the exact time depends on the tissue.[37] The second approach, linked to the first one, is the use of photosensitizers carrying endoperoxides.[38] In this way, a reactive moiety such as anthracene or pyridone carries one equivalent of peroxide and is capable of releasing it under light excitation. It has also been

observed that these molecules can store singlet oxygen and release it back in the

dark phases of fractional PDT. [39] Figure 82.[40]
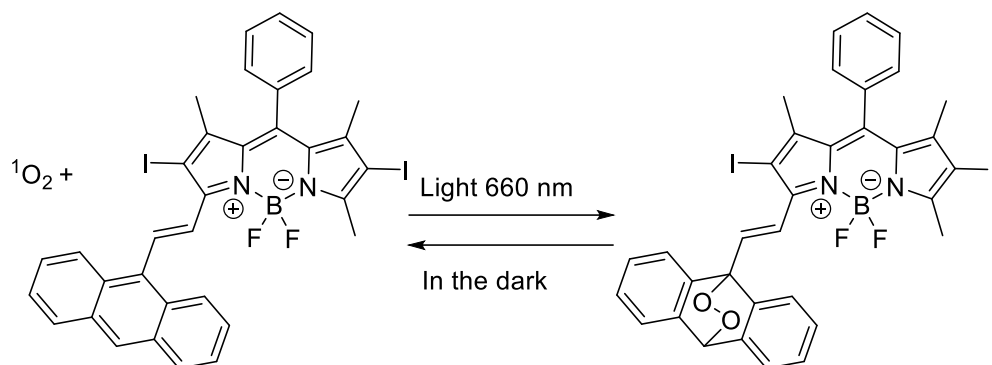
Figure 82 *Example of an endoperoxide. Singlet oxygen is stored under light irradiation and released in the absence of light.*

4.3 Results and discussion
4.3.1 Viscosity sensing in castor oil-toluene

Fluorescent viscosity sensors are most commonly reported in two different system; a mix of castor oil in combination with toluene, or glycerol in combination with methanol.[41–43] The glycerol/methanol system is by far the most reported methodology to assess the potential of a viscosity sensor.[44–46] However, in most cases the molecules tested are electrically neutral and highly lipophilic. Given that such lipophilic dyes will accumulate mainly in the lipidic parts of a cell, it seems counter-intuitive to use a system with an elevated polarity to calibrate the behaviour of lipophilic dyes.[47] In fact, research suggest that only when the polarity of the solvent does not affect the emission, the calibration in methanol/glycerol can be extrapolated to the castor oil/toluene system, but those cases are rare.[48]

The molecules prepared in this thesis are highly lipophilic, both methanol/glycerol and castor oil/toluene systems were tested but only the latter is a good approximation of the cell membrane and other lipid-rich regions of the cell in which lipophilic molecules can accumulate Due to the lipophilic nature of the BODIPY-perylene conjugates, the solubility in the non-polar system is also much higher than in the polar system. Due to their superior quantum yields, study focussed attention mainly on the non-iodinated dyads.

To study the properties of B2P, MB2P, 2-DMB2P, and 8-DMB2P stock solutions of each compound were prepared in dioxane. The dyes were then diluted in class B volumetric flasks in the corresponding toluene fraction. The volume was then made up with castor oil. The absorption and emission data are presented separately for clarity. All the castor oil and glycerol percentages are expressed as volume per volume (v/v).

In the case of B2P, as shown in Figure 83, the absorption presents minimal change as viscosity increases; λ_{max} is at 518 nm in pure toluene and varies by less than 4 nm across solvents of different polarities (see appendix A), remaining the same across all % castor oil (Figure 83 left). Conversely, the emission intensity does vary with the ratio of toluene to castor oil, but the response is complex. The fluorescence intensity decreases with the increasing in viscosity up to 60% castor oil (Figure 83 right). After this point, the fluorescence increases in intensity with a hypsochromic shift of ~20 nm. The fluorescence intensity of the 90% castor oil solution is higher than the fluorescence of the 10% castor oil solution. The dielectric constant of toluene at 25 °C is 2.38 whereas at the same temperature it is 4.47 for castor oil. Therefore, with the increase in viscosity there is a modest increase in dielectric constant. As explained in Chapters 2 and 3, for all BODIPY-perylene conjugates studied here, an increase in the dielectric constant induces a decrease in the fluorescence intensity. This may explain why a decrease in emission is observed up to 60% castor oil as the dielectric constant increases. It is likely that, after this point, the increase in fluorescence intensity that follows, is the effect of viscosity. At 70% castor oil and above, the reduction of non-radiative relaxation pathways, associated with impeded rotational relaxation, surpasses any decrease of fluorescence intensity caused by the higher dielectric constant.
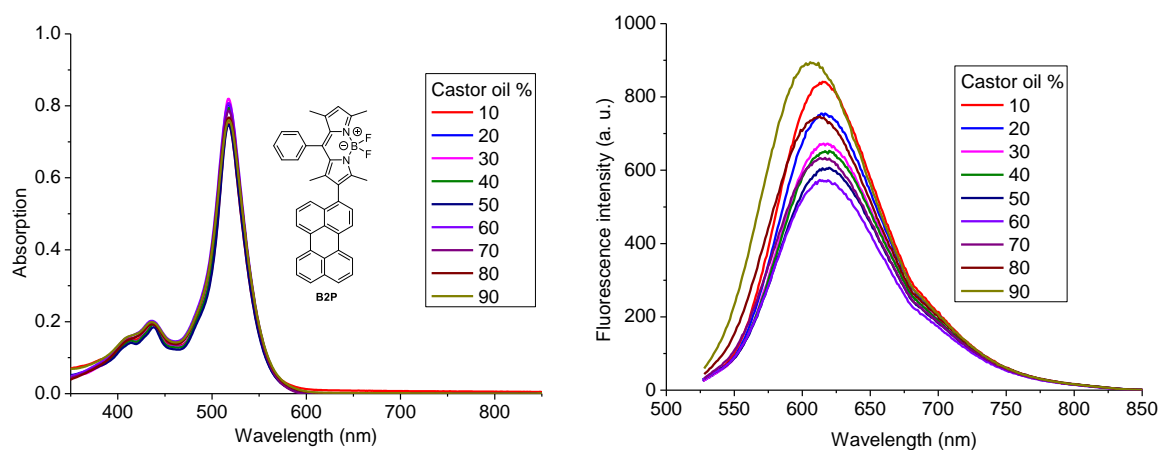
Figure 83 *Absorption (left) and emission (right) spectra of B2P at 10μM in solutions with an increasing percentage of castor oil in toluene. Excitation at 518 nm, emission recorded using 5-5 nm slit widths. Percentage expressed in v/v.*

MB2P is expected to be more rotationally restricted than B2P as the rotation of the aromatic ring at the *meso* position is totally inhibited by the presence of two methyl groups on each side of the BODIPY core. Nonetheless, a similar effect to B2P is observed in the BODIPY-based absorption, with minimal change to the spectrum (Figure 84 left). (The changes in the UV region are due to the increasing proportion of castor oil.) The emission decreases with increasing viscosity up to 50% castor oil. At this point, fluorescence increases again with a minor blue-shift (10 nm), (Figure 84 right). The emission of the 90% castor oil solution is also higher than that of the 10% castor oil solution.

In both B2P and MB2P viscosity experiments the emission maxima correspond to the one observed in solutions of solvents with low dielectric constant, such as pure toluene (~610 nm) and dioxane (~614 nm). These large Stokes shifts indicate that the same charge transfer occurring in pure solvents is taking place in the castor oil/toluene system.

The non-systematic response of B2P and MB2P in castor oil/toluene solutions may, under low viscosity conditions, be associated with solvent dielectric changes but, nonetheless, indicates that the viscosity must be quite high before

increases in emission intensity are systematically observed. This suggests that these molecules are not ideal intensity-based viscosity sensors, as solutions of high viscosity can show similar emission intensities as solutions of low viscosity above a certain threshold, and the Stokes shift is not sufficiently large to unequivocally tell apart a viscous environment from another. In most literature examples of intensity-based sensors, the increase of the fluorescence intensity is consistent with the increase in viscosity across all castor oil percentages.[49–51]
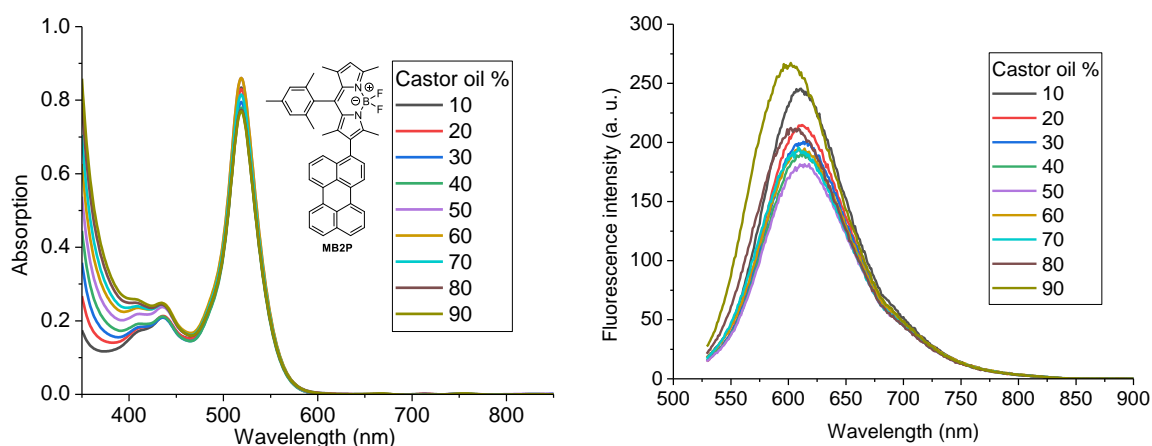
Figure 84 Absorption (left) and emission (right) spectra of MB2P at 10 μM in solutions with an increasing percentage of castor oil in toluene. Excitation at 519 nm, emission recorded using 2.5-5 nm slit widths. Percentage expressed in v/v.

As explained in the introduction of this Chapter, increasing the degrees of rotational freedom of a molecule can improve its potential for use as a viscosity sensor. For that reason, two additional molecules, 2-DMB2P and 8-DMB2P (Chapter 3) were tested in the same castor oil/toluene system. These BODIPYs are positional isomers, as they both have two methyl groups on the BODIPY core, but a perylene substituent at opposite positions. The compound 8-DMB2P has greater rotational freedom given that no methyl groups interact with perylene. In the case of 2-DMB2P, like the previous compounds, only minor changes in absorption were observed; a decrease of 10% absorption was observed for 80% and 90% castor oil solutions compared with the 10% solution. The λ_{max} did not

change at all from one solution to the other and it is equal to 511 nm (Figure 85 left). The only significant changes in the absorption spectra are due to absorption of castor oil below 459 nm. As the absorption cross section does not greatly change with viscosity, we can assume that the variation in emission intensity comes from the changes in viscosity. The emission decreases significantly from 10% to 30% castor oil, but changes between 30% and 60% are minor. After this point the emission increases, and both 80% and 90% solutions show a higher intensity than the 10% solution (Figure 85 right).
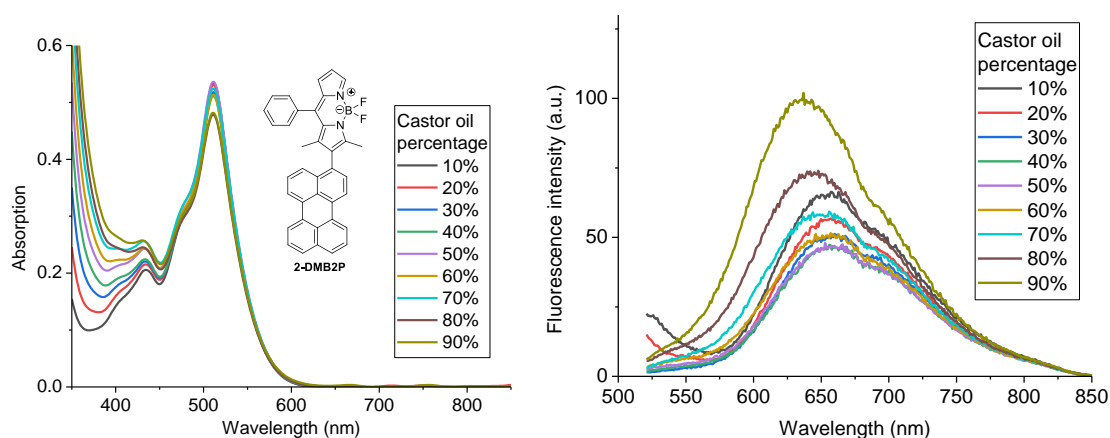
Figure 85 Absorption (left) and emission (right) spectra of 2-DMB2P at 10 μM in solutions with an increasing percentage of castor oil in toluene. Excitation at 511 nm, emission recorded using 5-5 nm slit widths. Percentage expressed in v/v.

The compound 8-DMB2P shows a constant absorption at all viscosities. The emission spectra show two features at ~580 nm and ~700 nm. There is a slight decrease in emission up to 30% castor oil, and then an increase in both bands, but especially pronounced in the 700 nm band (Figure 86).
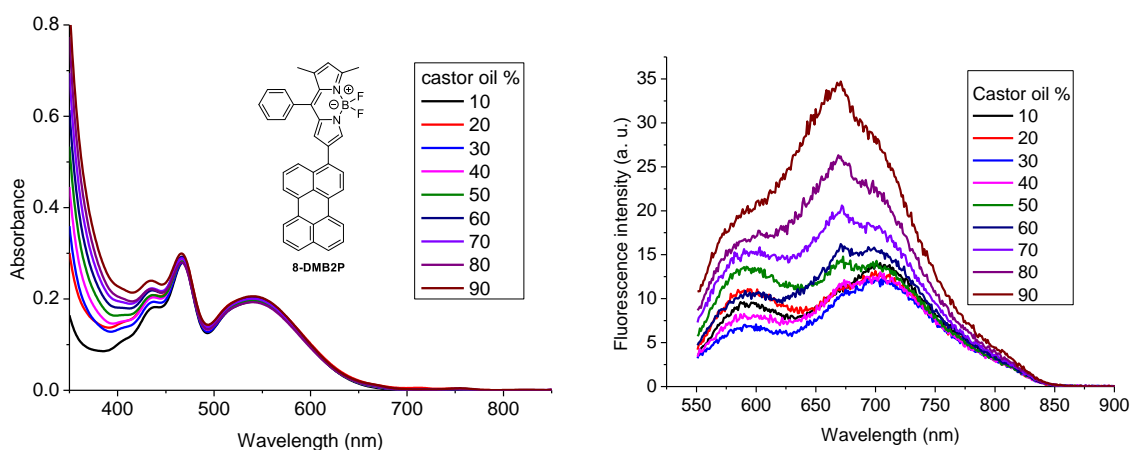
Figure 86 *Absorption (left) and emission (right) spectra of 8-DMB2P at 10µM in solutions with an increasing percentage of castor oil in toluene. Excitation at 540 nm, emission recorded using 5-5 nm slit widths. Percentage expressed in v/v.*

For 8-DMB2P, the relationship between maximum fluorescence intensity and castor oil can be described by an exponential function from 30% and above (Figure 87). From the dyad molecules studied, 8-DMB2P is a prospective intensity-based sensor for non-polar viscous systems.
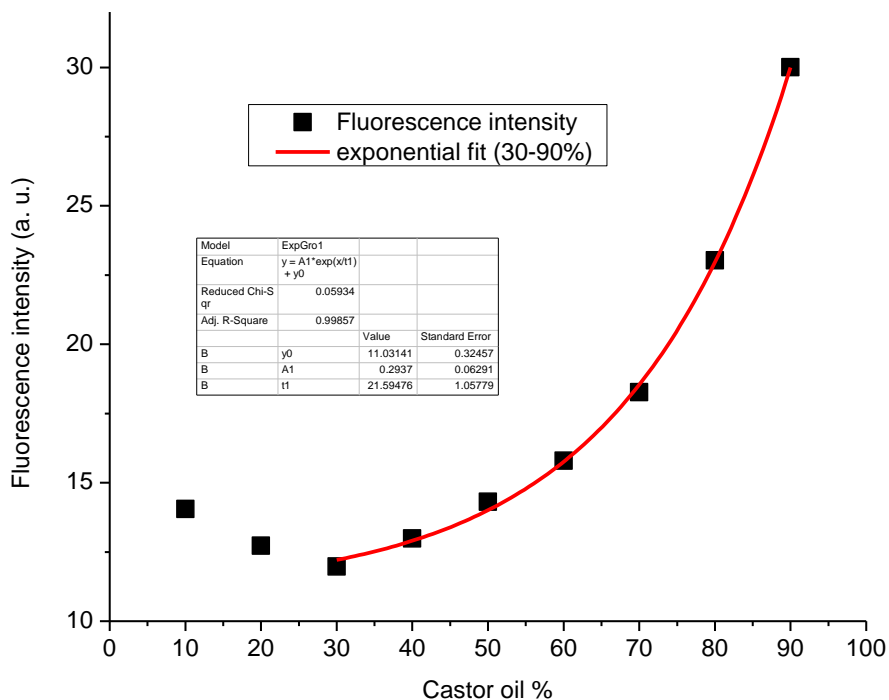
Figure 87 *Maximum fluorescence intensity of 8-DMB2P in solutions of different proportions of toluene and castor oil. y = A1*exp(x/t1) + y0. R^2 = 0.9985.*

4.3.2 Lifetime and viscosity

In order to understand whether any of the BODIPY-perylene conjugates can be used as lifetime-based viscosity sensors, the lifetime of the dyes in solutions of varying viscosity was studied. The lifetime decays of B2P are mono exponential in solutions with 10% to 50% castor oil; τ_1 = 2.3±0.3 ns at 10% castor oil and τ_1 = 2.1±0.2 ns at 50% castor oil. From 60% castor oil onwards, the decays become biexponential. τ_1 is larger than τ_2 although it is not always the component with the largest intensity-based amplitude. The intensity-weighted average lifetime remains around 2.1±0.3 ns across all viscosities (Figure 88). At 60% castor oil, there is an increase in τ_1 (5.3 ns) that slowly reduced to 2.5 ns at 90%. The first component and a second, shorter, component appears.
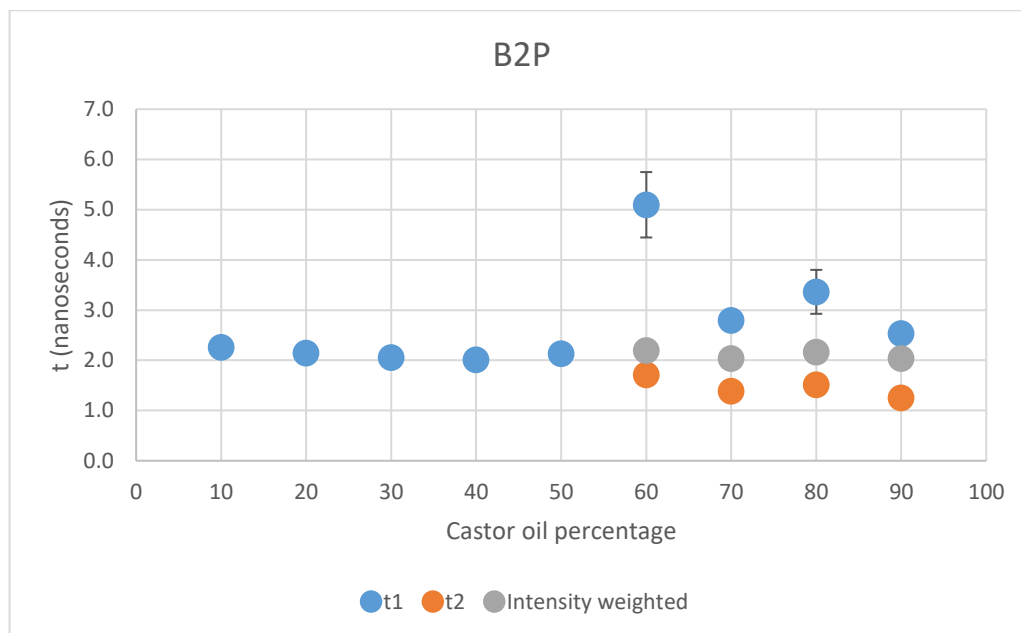
	T_1	AMPLITUDE(%)	T_2	AMPLITUDE(%)	IW
90	2.5±0.1	51	1.3±0.1	49	2.0±0.0
80	3.4±0.4	23	1.5±0.1	77	2.2±0.0
70	2.8±0.0	28	1.4±0.0	72	2.0±0.1
60	5.1±0.7	7	1.4±0.5	93	2.2±0.0
50	2.1±0.2	100	-----	-----	2.1±0.2
40	2.0±0.0	100	-----	-----	2.0±0.0
30	2.1±0.0	100	-----	-----	2.1±0.0
20	2.1±0.0	100	-----	-----	2.1±0.0
10	2.3±0.3	100	-----	-----	2.3±0.0

Figure 88 Top: fluorescence lifetime vs castor oil percentage of B2P. (In some cases, error bars are smaller than the marks). Bottom: table of τ_1 and τ_2 and intensity weighted average (IW) lifetime values of B2P in solutions of toluene and castor oil in different proportions.

A similar behaviour is observed for MB2P; the lifetime decay is monoexponential from 10% castor oil (2.7±0.0 ns) to 30% castor oil (2.5±0.0 ns). The change to a biexponential decay happens at 40% castor oil. From that point on, τ_1 remains almost constant (2.0±0.2 ns) and τ_2 decreases from 4.6±0.9 ns at 40% castor oil to 2.7±0.0 ns at 90% castor oil. When the decay is biexponential τ_1 is the component with the largest amplitude. The intensity-weighted lifetime remains around 2.5 ±0.2 ns across all viscosities (Figure 89). In literature examples, the fluorescence lifetime of good viscosity sensors changes from a few

nanoseconds in low-viscosity solutions to 10-15ns in highly viscous media, i.e. values typically double or treble.[52–55]

Figure 89 *Top: fluorescence lifetime vs castor oil percentage of B2P. (In some cases, error bars are smaller than the marks). Bottom: τ_1 and τ_2 and intensity weighted average (IW) lifetime values of MB2P in solutions of toluene and castor oil in different proportions.*
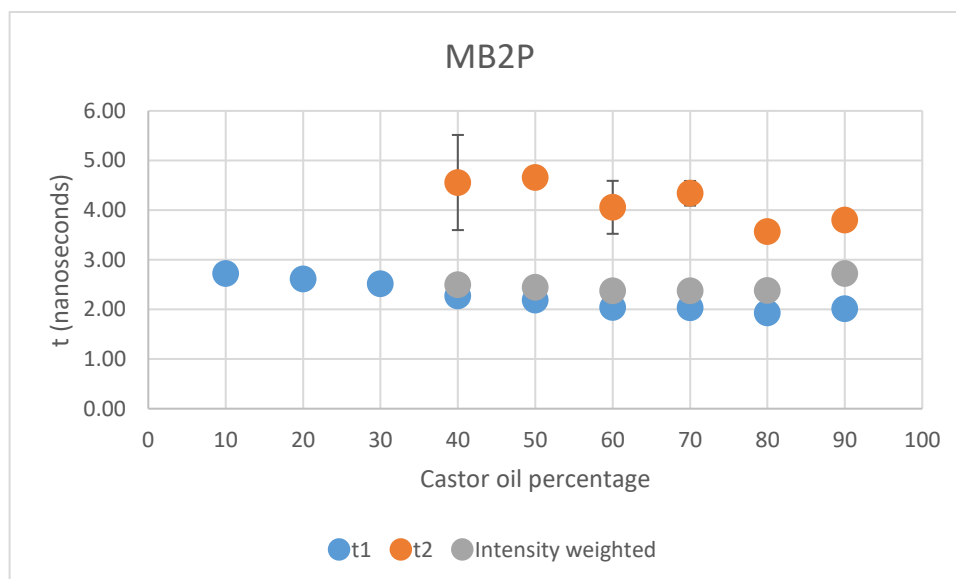
CASTOR OIL %	T_1	AMPLITUDE (%)	T_2	AMPLITUDE (%)	IW
90	2.0±0.0	80	2.7±0.0	20	2.7±0.0
80	1.9±0.1	84	2.6±0.0	16	2.4±0.0
70	2.0±0.0	91	4.3±0.2	9	2.4±0.0
60	2.0±0.1	82	4.1±0.5	16	2.4±0.0
50	2.2±0.0	95	4.7±0.2	5	2.5±0.0
40	2.3±0.0	91	4.6±0.9	9	2.5±0.0
30	2.5±0.0	100	----		2.5±0.0
20	2.6±0.0	100	----		2.6±0.0
10	2.7±0.0	100	----		2.7±0.0

The fluorescence lifetimes of 2-DMB2P decay according to biexponential kinetics in all solutions. τ_1 is the component with the smallest amplitude and it increases from 3.4±0.1 ns at 10% castor oil to 4.3±0.1 ns at 90 % castor oil, although the maximum value can be found at 70 % (4.9±0.1 ns). T_2 is the component with the largest amplitude and it remains constant at 0.6 ns cross all

viscosities. The intensity-weighted lifetime increases from 1.0±0.2 ns at 10%
castor oil to 1.6±0.0 ns at 90% although a few solutions have similar values. This
behaviour is very likely to be due to the greater rotational freedom present in 2-
DMB2P compared with more rigid dyes such as B2P and MB2P. Figure 90.
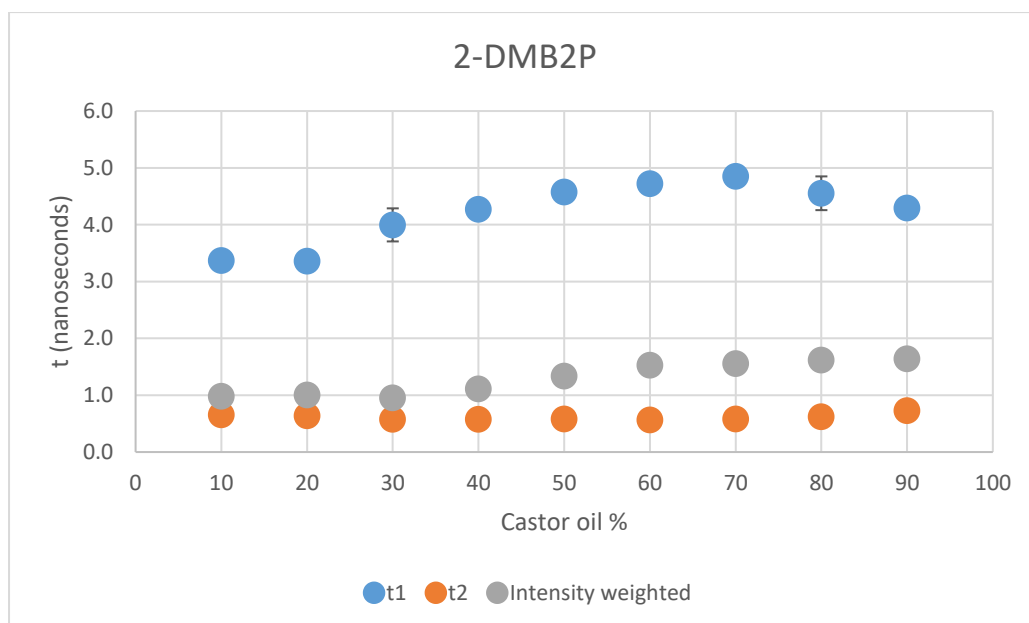
CASTOR OIL %	T_1	AMPLITUDE (%)	T_2	AMPLITUDE (%)	IW
90	4.3±0.1	5.6	0.7±0.0	94.4	1.6±0.0
80	4.6±0.3	5	0.6±0.0	95	1.6±0.0
70	4.9±0.1	3.5	0.6±0.0	96.5	1.6±0.0
60	4.7±0.0	3.5	0.6±0.0	96.5	1.5±0.0
50	4.6±0.1	3	0.6±0.0	97	1.3±0.0
40	4.3±0.1	2.5	0.6±0.0	97.5	1.1±0.1
30	4.0±0.3	1.7	0.6±0.0	98.3	1.0±0.1
20	3.4±0.1	1.8	0.6±0.0	98.2	1.0±0.2
10	3.4±0.1	51.8	0.7±0.0	98.2	1.0±0.2

Figure 90 Top: Fluorescence lifetime of 2-DMB2P in solutions of different viscosity at 10µM. (In some cases, error bars are smaller than the marks). Bottom: τ₁ and τ₂ and intensity weighted average (IW) lifetime values of 2-DMB2P in solutions of toluene and castor oil in different proportions.

In the case of 8-DMB2P, τ_1 consistently increases from 3.2±0.0 ns at 10 %
castor oil to 7.6±0.7 ns at 90% castor oil, although τ_1 is the component with the
smallest amplitude. τ_2 changes significantly, going from 0.5-0.6 ns in solutions from

10% to 30% castor oil to 2.4-2.6 ns in solutions with 40% castor oil or more. At 40% there is a third component that appears and becomes the one with the largest amplitude with almost a constant value of 0.4-0.5 ns. In this case, the intensity-weighted average lifetime changes discreetly. Figure 91.
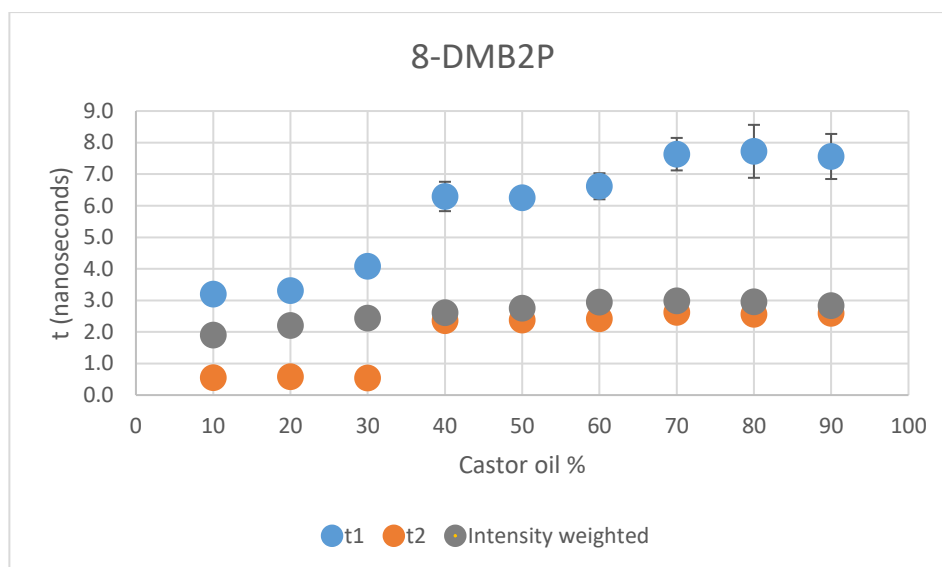
CASTOR OIL %	T_1	AMPLITUDE (%)	T_2	AMPLITUDE (%)	IW
90	7.6±0.7	18	2.6±0.2	82	2.8±0.0
80	7.7±0.8	12.5	2.6±0.2	87.5	3.0±0.1
70	7.6±0.5	11	2.6±0.2	89	3.0±0.1
60	6.6±0.4	22	2.4±0.2	78	2.9±0.1
50	6.3±0.3	17	2.4±0.1	83	2.8±0.1
40	6.3±0.5	18	2.4±0.2	82	2.6±0.1
30	4.1±0.0	13	0.5±0.0	87	2.4±0.0
20	3.3±0.0	20	0.6±0.0	80	2.2±0.0
10	3.2±0.0	15.6	0.6±0.0	84.4	2.9±0.0

Figure 91 Top: Fluorescence lifetime 8-DMB2P in solutions of different viscosity at 10µM. (In some cases, error bars are smaller than the marks). Bottom: τ_1 and τ_2 and intensity weighted average(IW) lifetime values of 8-DMB2P in solutions of toluene and castor oil in different proportions.

From the fluorescence and lifetime data, it seems that B2P, MB2P and 2-DMB2P are not suitable for viscosity lifetime sensing. The changes in fluorescence are likely influenced by other factors such as dielectric constant of the solvent mixture or interaction with the castor oil constituents. Aggregation is most likely

excluded as the dyes are soluble in non-polar solvents and the concentrations used in these experiments were never higher than 10 µM. In the case of B2P, MB2P and 2-DMB2P the variation of lifetime seems not to be enough to discriminate between one viscous castor oil/toluene solution and the other with high precision, the changes in lifetime being too modest. As cell environments are a much more complex medium than a two-component solution, the sensor should not show impact from e.g. dielectric changes and should respond only to viscosity and the changes should be large enough to distinguish on a low resolution spectroscope on a microscope.[56,57] However, 8-DMB2P could be used to sense viscosity in media with equal or higher viscosity than 30% castor oil. The τ_1 component increases with viscosity and so does the intensity-weighted lifetime. The changes are moderate, so the sensing strategy could combine the intensity-based and the lifetime-based approaches when using this molecule.

4.3.3 Viscosity sensing in methanol-glycerol

An interesting effect was observed when the dyes were dissolved in glycerol/methanol solutions. Solutions of all of the dyes were prepared in methanol/glycerol in different proportions. glycerol percentages are expressed as volume per volume (v/v). For all the molecules, B2P, MB2P, 2-DMB2P, and 8-DMB2P, the maximum absorption remains constant in solutions with 70% glycerol or less but decreases in the solutions with the highest viscosities and highest dielectric constant. (MeOH = 33, Glycerol = 46.5 at 20°C). The origin of the decrease could be the change in viscosity or aggregation, as the molecules are highly lipophilic. In all cases, the fluorescence intensity is significantly weaker than in the non-polar system. This was expected, based on the observation that polar solvents dramatically reduce emission quantum yield of this type of charge transfer compounds (Chapters 1 and 2). In the case of B2P, solutions containing 70% glycerol or less show an emission spectrum with a maximum emission band at ~575 nm and the fluorescence intensity remains almost constant in this range of viscosities. In contrast, in solutions containing 80% and 90% glycerol, the emission not only gains in intensity but becomes broader and red-shifted with a maximum emission at 675 nm (Figure 92). The emission maxima in highly viscous solutions are red-shifted (~50 nm) in comparison to what is observed in non-polar solvents such as toluene or dioxane. It is likely that highly viscous solvents promote the formation of the most stable twisted conformation where the twisted charge transfer is promoted.
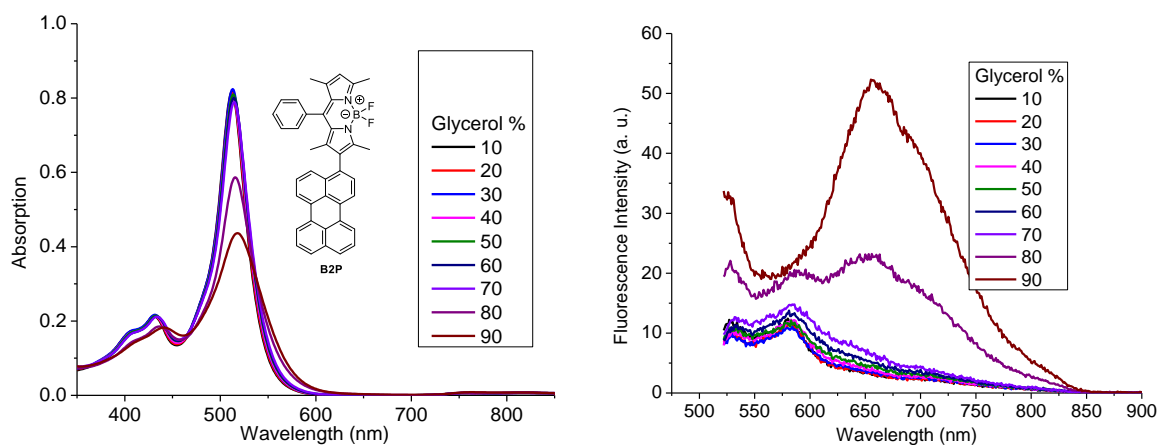
Figure 92 *Absorption (left) and emission(right) spectra B2P at 10µM in mixtures of methanol/glycerol in different proportions. 515 nm excitation wavelength for emission 5-5nm slit widths. Percentage expressed in v/v.*

A similar observation was made for MB2P. The extinction coefficient is constant in solutions with 70% glycerol or less and decreases in the 80% and 90% glycerol solutions. In the range from 10% to 50% the fluorescence intensity shows little variation but, at 60% and 70% glycerol, a band from 600 nm to 650 nm starts to increase modestly. In the most viscous solutions, 80% and 90% glycerol, the emission maxima move from ~535 nm to ~660 nm (Figure 93).
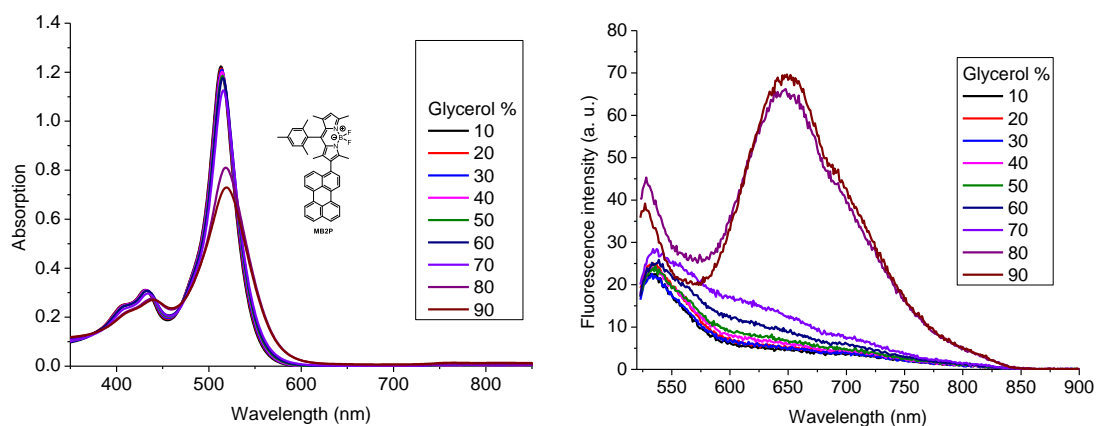
Figure 93 Absorption (left) and emission(right) spectra MB2P at 10µM in mixtures of methanol/glycerol in different proportions. 515 nm excitation wavelength for emission 5-5 nm slit widths. Percentage expressed in v/v.

The spectra of 2-DMB2P in the polar system shows a constant absorption intensity up to 70% glycerol, but there is a reduction in absorption of ~0.5 units at 80% and 90% glycerol corresponding to approx. 40% reduction. In the fluorescence spectra the maxima are observed at ~535 nm for solutions between 10% to 80% glycerol, the increase between solution is very moderate. However, the mission maximum changes drastically at 90% glycerol from 535 nm to 720 nm with a slight increase in intensity. Figure 94.
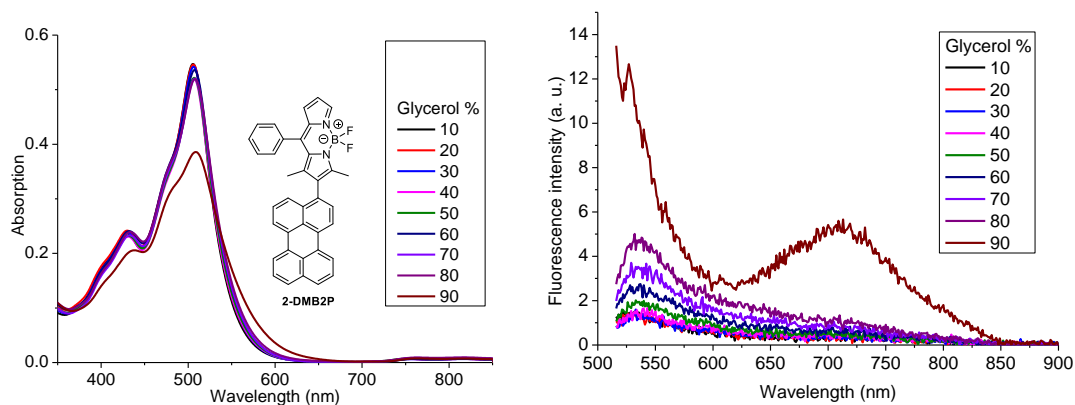
Figure 94 Absorption (left) and emission(right) spectra 2-DMB2P at 10µM in mixtures of methanol/glycerol in different proportions. 511 nm excitation wavelength for emission 5-5nm slit widths. Percentage expressed in v/v.

In the case of 8-DMB2P, the behaviour is less consistent. There are significant changes in absorption between solutions, but the changes are not systematic, and no clear trend can be established. For highly viscous and polar

solutions (70-90% glycerol), the absorption features change, and they might indicate aggregation as explained below (see Polarity effect section). The emission increases slowly with maxima at 575 nm from 10% to 80 % glycerol. The solution at 90% glycerol shows an enormous red-shift in emission maximum from 568 nm for all the solutions below, to 664 nm. Figure 95. This indicates that the emission is switching in low viscosity medium from what appears to be primarily π-π* BODIPY fluorescence to fluorescence from a charge transfer state as explained above.
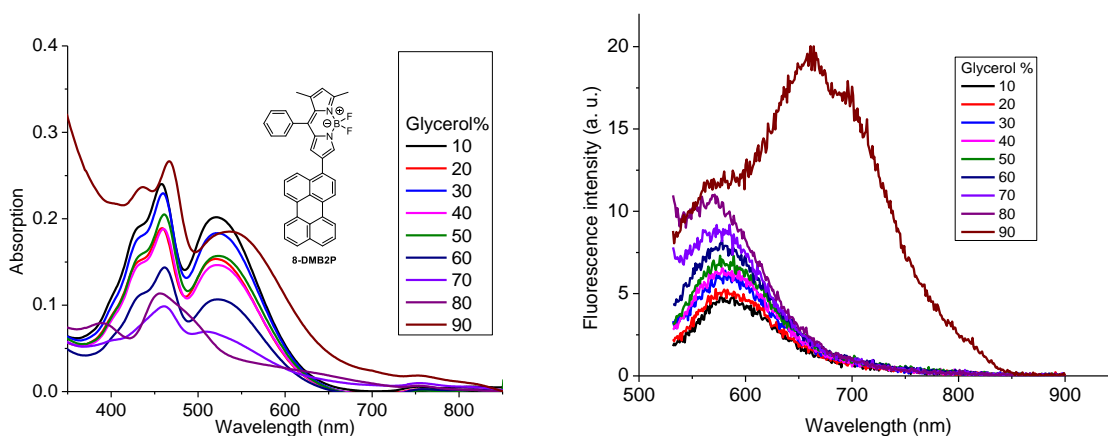
Figure 95 *Absorption (left) and emission(right) spectra 8-DMB2P at 10μM in mixtures of methanol/glycerol in different proportions. 533 nm excitation wavelength for emission 5-5nm slit widths. Percentage expressed in v/v.*

A similar behaviour is seen across all dyes (B2P, MB2P, 2-DMB2P, 8-DMB2P) from 80% or 90% glycerol, indicating that these materials behave as switches rather than viscosity sensors for the polar system methanol/glycerol. As observed in the previous section, the switch is completely absent in the non-polar castor oil/toluene system. In general, the spectroscopic properties of the dyes studied so far in MeOH/glycerol tend to be affected by a combination of viscosity and dielectric constant of the solvent, a behaviour that has been observed in other BODIPYs. Vyšniauskas and coworkers reported a series of *meso*-substituted BODIPYs with simple substitutes such as aliphatic chains and it was observed

that, when other factors are considered, temperature, polarity, even structurally simple BODIPYS show a sensitivity to the environment.[42]

B2P, MB2P, and 2-DMB2P show more constant absorption values than 8-DMB2P and so they may be suitable as polarity sensors. Some examples of BODIPYs from literature with sensitivity to polarity have been using to study the binding of a dye to proteins in solution and in cells.[42,58,59] Most of these dyes are ratiometric probes and their emission spectra show variations in intensity of one of the emission bands. Literature reports of BODIPY polarity sensors do not generally show Stokes shifts as dramatic as the one observed for the BODIPY-perylene conjugates studied here. However, B2P, MB2P, 2-DMB2P, 8-DMB2P, have very specific viscosity switching points and some of these dyes could find application in polymer chemistry, where a few fluorophores have been used to monitor polymerisation process (see chapter 6).[60–62] On the one hand, the fact that the BODIPY-perylene conjugates are sensitive to changes in both polarity and viscosity of the medium could be an advantage when tracking polymerisation process where both properties change. On the other, the switch behaviour is only observed on polar systems where the emission intensity of these dyes is the lowest.

4.3.3.1 Temperature effect on the charge transfer

The fluorescence intensity of selected BODIPY derivatives in MeOH/glycerol solutions were studied in a temperature-controlled experiment to understand more about the influence of solvent viscosity on the switch effect. In the case of 8-DMB2P the solution with 90% glycerol was chosen because it is the one in which the Stokes shift is the largest and it is the most viscous medium. The fluorescence band around 700 nm shows temperature dependence, decreaseing

as temperature decreases. From this behaviour, it is evident that the rotational non-emissive relaxation plays a significant role in decreasing the emission. Non-emissive relaxation is caused by rotation of the substituents and internal bending of the BODIPY core. Molecules with more rotational freedom will have more routes to relax via non-emissive pathways.[63] It is worth noting, however, that even in at 60°C the switch is not observed, and the red emission is observed across all temperatures so the behaviour observed in the lower viscosity solvent mix is not recovered by reducing the viscosity through changes in temperature (Figure 96). The viscosity of pure glycerol goes from 1480 cp at 20°C to 330 cp at 40°C and is further reduced to 102 cp at 60°C. The viscosity at 60°C corresponds to the viscosity observed in a solution with 60% to 70% glycerol in methanol at room 20°C.[52,64] Consequently, the fact that the low-viscosity behaviour is not observed at hight temperatures indicates that, for this dye, the red emission is also caused by the change in dielectric constant and polarity and not only by viscosity.
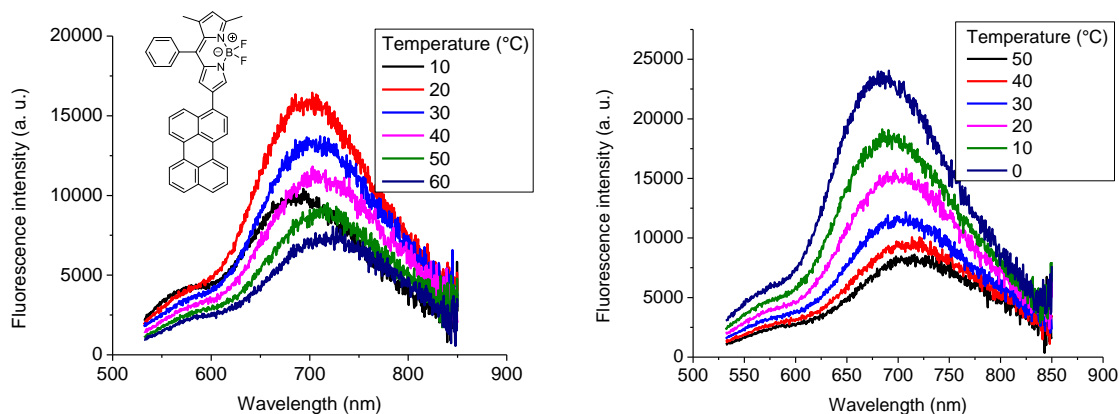
Figure 96 *Temperature effect on the emission of 8-DMB2P at 10 µM in a solution of 90% glycerol in methanol. Excitation at 532 nm, 4-1 nm slit widths. 5 minutes of equilibration time between each temperature. Increasing temperature (left) decreasing temperature (right).*

A similar effect was observed when the experiment was carried out using the 90% glycerol solution of MB2P. The emission increases as the temperature decreases, but at no point does the switch occur, the emission band at 660 nm remains across all temperatures and, by implication, viscosities (Figure 97). In the

case of this compound, the mesityl substituent at the *meso* position cannot be the source of rotational relaxation[65] so it could then be inferred that the rotation of perylene is the major source of non-radiative rotational relaxation.
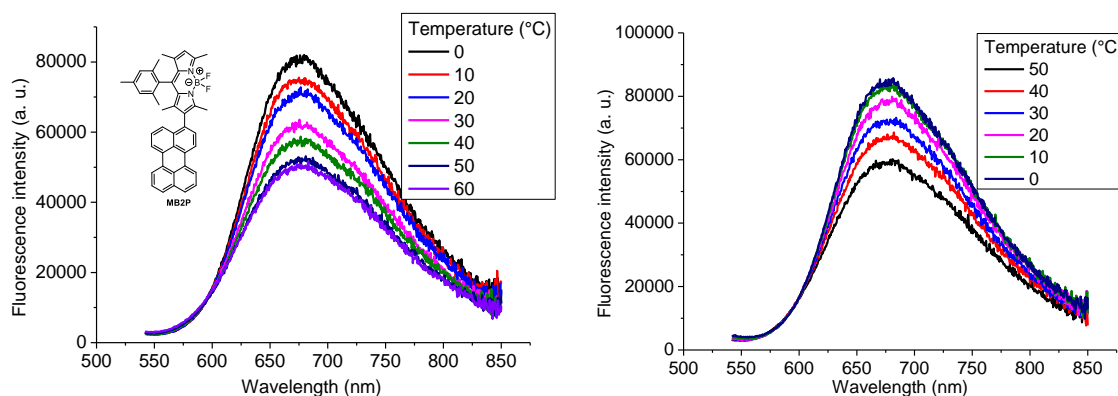
Figure 97 *Temperature effect on the emission of MB2P at 10µM in a solution of 80% glycerol in methanol. Excitation at 532 nm, 4-1 nm slit widths. 5 minutes of equilibration time between each temperature. Increasing temperature (left) decreasing temperature (right).*

In contrast, in the case of B2P (and dyes with higher freedom of rotation), the structural features responsible for the behaviour are much harder to isolate. The emission spectra of B2P show that the intensity of the band at 532 nm decreases with the increase of temperature up to 30°C, but it remains almost constant above that temperature. The band at 700 nm, however, very prominent at 0°C, disappears completely at 50°C and above. In this case, it seems that temperature can completely supress the charge transfer effect responsible for the most red-shifted emission (Figure 98). From this information, it could be proposed that the reduction of the 532 nm band corresponds to the rotation of the phenyl group whereas the changes in the band at 700 nm are due to the rotation of perylene that modulates the formation of emissive charge transfer states.[41,66]
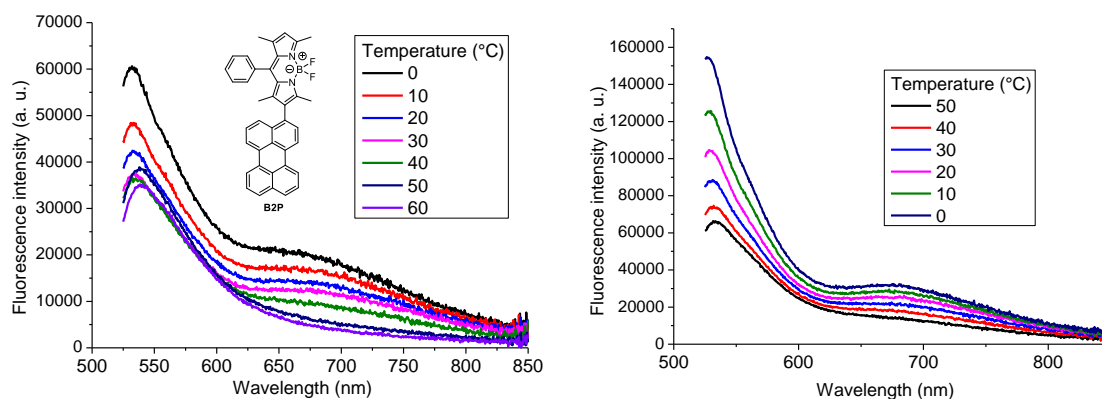
Figure 98 Temperature effect on the emission of B2P at 10 μM in a solution of 80% glycerol in methanol. Excitation at 522 nm, 4-1 nm slit widths. 5 minutes of equilibration time between each temperature. Increasing temperature (left) decreasing temperature (right).

In the case of 2-DMB2P, both bands, at 535 nm and 750 nm, decrease when temperature increases. At 60°C, there is barely any distinguishable emission feature (Figure 99). Thie behaviour indicates, for this molecule, that the red-shifted band observed at 90% glycerol is due to a high viscosity and a high dielectric constant.

It is worth noting that within the BODIPY-perylene conjugates studied so far, there is not a clear relationship between rotational freedom and emission intensity when the temperature changes. On one hand, the most rigid molecule, MB2P shows a behaviour similar to the molecule with the highest rotational freedom, 8-DMB2P. Both molecules exhibit a band at about 700 nm whose intensity is temperature dependent in solutions with 90% glycerol, and yet this band does not switch to a low-viscosity behaviour when the temperature increases. The increase of temperature also causes the reduction of the dielectric constant, but no low-dielectric constant behaviour is observed. On the other hand, molecules with an intermediate number of rotational freedom, B2P and 2-DMB2P, show one or more emission bands that can be completely supressed by the increase in the rotational relaxation induced by temperature. For the four

176

molecules, the changes observed by variation of the temperature are fully reversible.
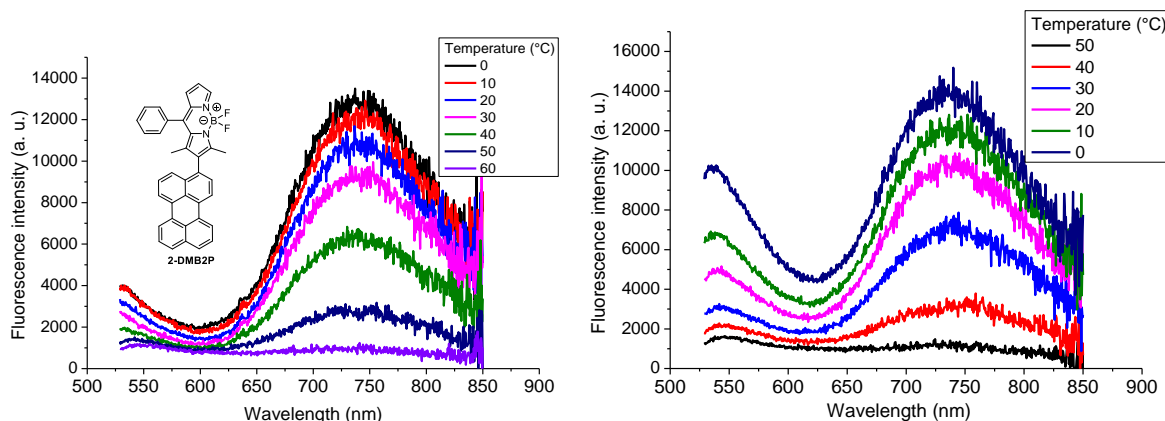
Figure 99 Temperature effect on the emission of 2-DMB2P at 10 µM in a solution of 80% glycerol in methanol. Excitation at 519 nm, 4-1 nm slit widths. 5 minutes of equilibration time between each temperature. Increasing temperature (left) decreasing temperature (right). Percentage expressed in v/v.

4.3.4 Polarity effect

The effect of the polarity of the solvent on BODIPY-perylene conjugates has been discussed in Chapters 2 and 3. Nonetheless, to test the effect of an increasing dielectric constant MB2P and 8-DMB2P, the dye most rigid dye and the one with more rotational freedom, respectively, were dissolved in solutions with different proportions of dioxane and water to observe and identify the effects of aggregation, expected to occur in polar solvents, on the spectroscopic properties. BODIPY aggregates can have significantly different properties and have been extensively studied.[67–69] In cell environments the dyes will most likely distribute in structures and organelles with a high lipidic content; however, in high concentrations aggregation is not excluded.

For MB2P, the absorption remains constant up to 60% water (v/v) and starts to decrease from that point on. Fluorescence changes mainly in intensity, but the emission maxima remain at around 625 nm (Figure 100). The emission decreases up to 40% water (v/v). After this point, it increases again, with a

maximum value at 60% water (v/v). The emission decreases again in 80% and 90% water solutions but, in both cases, it remains higher than in 10% water solutions. This behaviour is different from other BODIPY charge transfer compounds reported in the literature for which addition of water induced aggregation and those aggregates can have a larger Stokes shifts (~120 nm) than the compound in solution.[70]
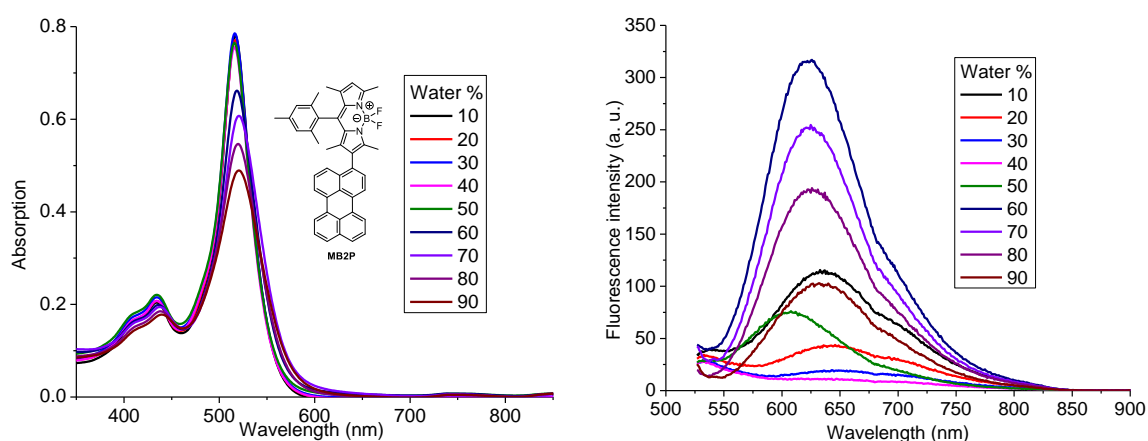
Figure 100 *Absorption (left) and emission (right) spectra of MB2P at 10 µM in solutions with an increasing percentage of water in dioxane. Excitation at 519 nm, emission recorded using 5-5 nm slit widths. Percentage expressed in v/v.*

For 8-DMB2P, the absorption coefficient starts to decrease at 50% water, losing some of the feature's characteristic of the molecule in solution. At 60% and 70% water, the absorption spectra regain intensity, but they have completely lost the absorption bands characteristic of the dye in homogeneous solution. This effect suggests the formation of aggregates. At 80 and 90% water, the absorption becomes more intense, and the absorption bands look similar to those of the dye in homogeneous solution. The emission consistently decreases as the water percentage increases. The highest emission can be found at 10% water and starts to decrease from that point on (Figure 101), although solutions of similar water percentages (20%, 30%, 40%, and 50%) have similar emission values 8-DMB2P could be used as an intensity-based polarity sensor. This type of fluorescent

sensor has been used to study the changes in polarity associated with the folding of proteins and DNA.[71–73] The solubility of BODIPY-perylene conjugates in aqueous media, however, could limit the applications of these molecules, requiring structural modification to improve the water solubility.
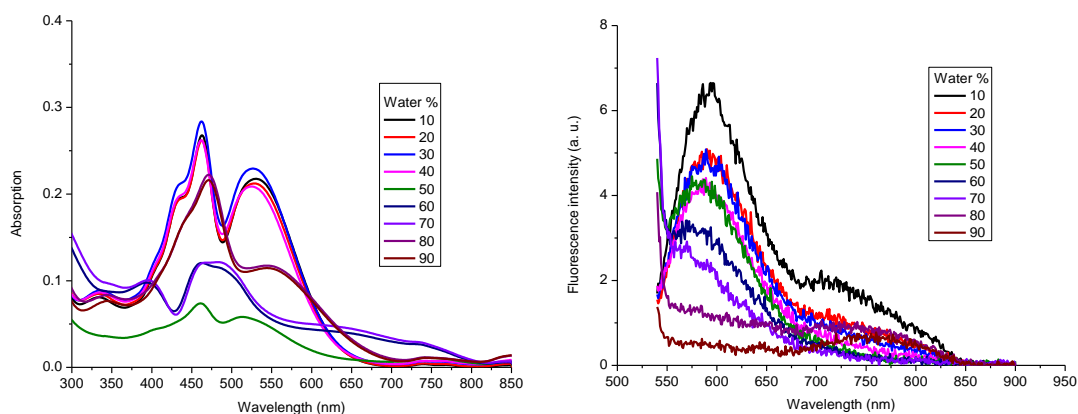
Figure 101 *Absorption (left) and emission (right) spectra of 8-DMB2P at 10µM in solutions with an increasing percentage of water in dioxane. Excitation at 530 nm, emission recorded using 5-5 nm slit widths. Percentage expressed in v/v.*

Addition of water, particularly in the case of 8-DMB2P, causes significant changes in both absorption and emission. This is likely, in strong part, due to aggregation effects. Therefore, it was of interest to compare the spectroscopy of the compounds at high water content solutions where aggregation is likely to be the most prevalent effect and compare the data with the spectroscopic properties of the crystalline materials. X-ray crystallography shows that MB2P crystals are formed by units containing two molecules in an antiparallel arrangement in such a way that the perylene unit of one molecule is interacting with the BODIPY core of the other molecule via hydrogen interactions with fluorine as the acceptor. These units form chains (Figure 102).
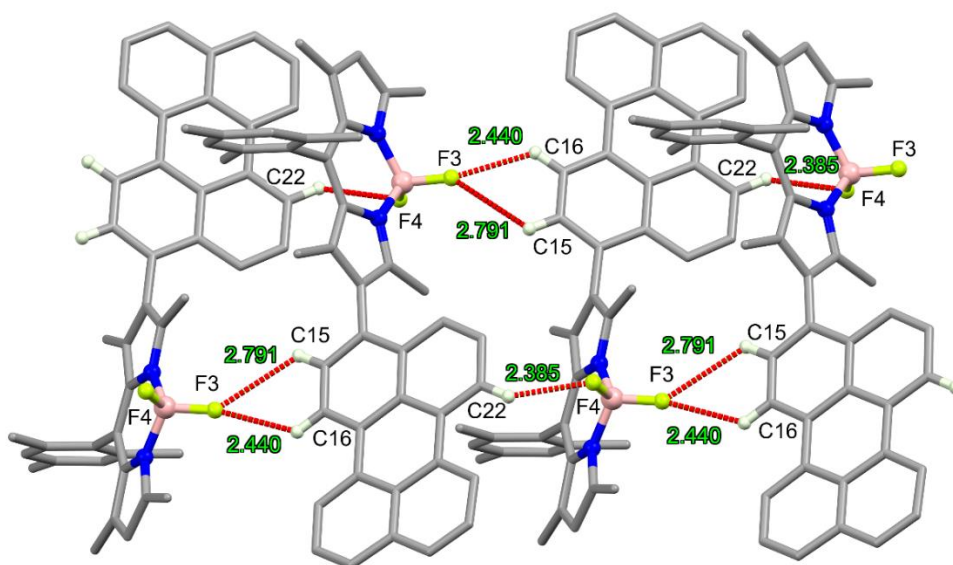
Figure 102 *(sp²) C–H-F hydrogen bonds linking MB2P molecules into chains showing H⋯F distances (Å). Hydrogen atoms not involved in H-bonding omitted.*

Interestingly, the emission maximum of crystalline MB2P (see next section) does not correspond to the emission maxima observed in dioxane/water solutions at 10 μM (Figure 103). Consequently, if the emission changes are due to aggregation, it is not resulting from the same crystalline form of the complex. This makes sense as intermolecular H-F interactions would not be expected to occur in aqueous media. Alternatively, it is possible that the aggregates formed are J-type or H-type, as this has been reported in literature for other BODIPYs in solution.[74]
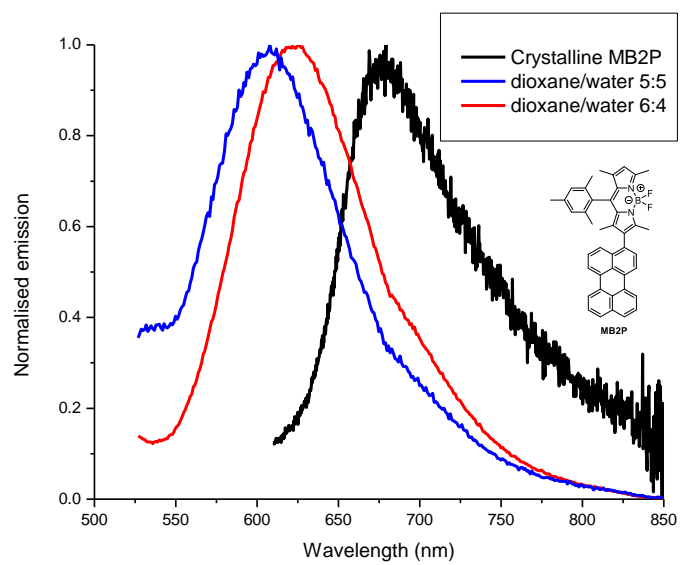
Figure 103 *Normalised emission of crystalline MB2P (black) and the same dye dissolved in solutions of 50% (blue) and 60% (red) water in dioxane.*

4.3.5 Solid state spectroscopy

Samples of B2P, B2PI, MB2P, 2-DMB2P, and 8-DMB2P were dissolved in test tubes containing a hexane:EtAcO solution (95:5). The tubes were partially covered to allow slow evaporation at room temperature. In the case of B2P, B2PI, and MB2P a good degree of crystallisation was observed, and the crystals formed were isolated and washed with hexane and their spectroscopic properties were studied. These crystals were prepared under different conditions than the ones used for single-crystal X-ray diffraction of the same molecules, that were prepared by slow vapor diffusion (see crystallography section in Chapters 2 and 3).

The wavelength that produces the maximum emission was determined with an emission map scanning every 5 nm from 520 nm to 600 nm. The emission spectra of B2P, B2PI, and MB2P are slightly red-shifted in the crystalline solids compared to the spectra in toluene solution, with emission maxima at ~675 nm in the solid-state vs ~640 nm, respectively. Based on the quantum yields, the fluorescence intensity of the crystalline samples follows the same trends as in solution, decreasing with iodination (B2PI) and increasing with restriction of rotation (MB2P) (Figure 104).
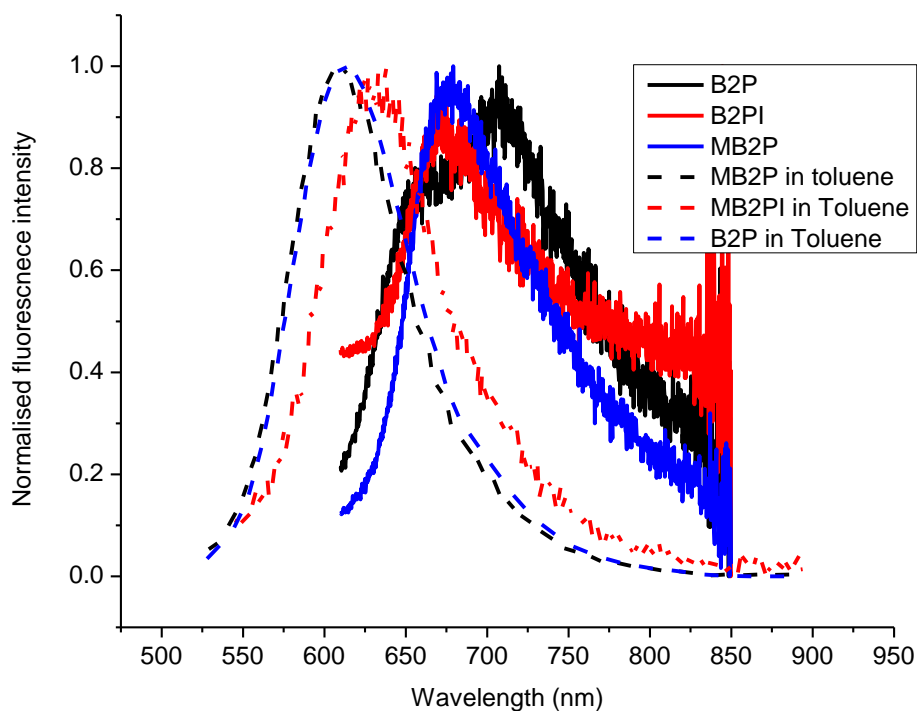
Figure 104 Normalised emission spectra of B2P (solid black), B2PI (solid red) and MB2P (solid blue) in the crystalline form., nm. And normalised emission spectra of B2P (dashed black), B2PI (dashed red) and MB2P (dashed blue) for comparison.

The quantum yields of the crystalline dyes can be found in Table 4. The quantum yields were recorded using both the direct and the indirect method with no difference found between resulting values (see Appendix C). The excitation was carried out at two wavelengths, one close to the one used to determine the quantum yield in solution (510 nm) and other at the maximum absorption of the crystalline solid (595 nm) determined by an emission map. The results follow the same trends as in solution; the iodinated dye presents a low quantum yield (0.8%) due to the presence of the heavy atom vs 8% for B2P, the non-iodinated molecule. MB2P, the most structurally rigid molecule shows the highest quantum yield due to the reduced number of degrees of freedom.

Table 4 Quantum yields of B2P, B2PI, and MB2P in the crystalline form.

	At 510nm	At 595nm
B2P	4.62±0.32	8.41±0.27
B2PI	0.95±0.02	0.81±0.03
MB2P	6.91±0.34	12.98±0.01

To understand whether the structural form of the crystals influenced the photophysical behaviour, crystals of B2P were ground with a metallic spatula inside a glass vial. Interestingly, grinding did influence the emission spectra with a substantial red-shift of the emission after grinding, from 668 nm in the crystalline sample to 702 nm for the strongly ground sample. With gentle grinding, the emission spectra seem to show features of both spectra, suggesting that there are two B2P forms present. B2P is not a very rigid molecule. As explained in Chapter 2, there is a conformational change in the excited state, and the BODIPY and perylene units become more coplanar. In the crystalline form the perylene and BODIPY are locked at a discrete angle of 74°, whereas the amorphous solid after grinding likely contains a range of orientations, reducing strain and energy of the charge transfer state.
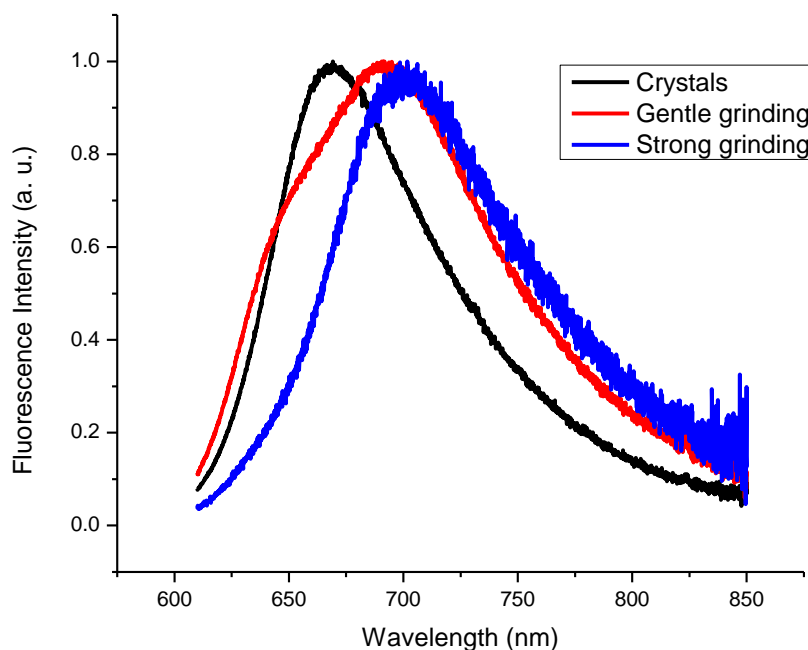
Figure 105 *Normalised emission spectra of B2P in the crystalline state (black)after a gentle grinding (red) and after a strong grinding (blue). Spectra were recorded using 595 nm light for excitation and 4-1 slit widths.*

The quantum yield analysis of the strongly ground sample was found to be 7.3% ±0.1, only 1% less than the crystalline form. These results suggest that intermolecular interactions in the crystalline state have a significant though small effect on the properties of B2P. In literature reports, J-agregates are responsible for the massive changes in emission maxima in the crystalline vs ground states. From crystallography, B2P does not form J-agregates in the crystalline state (see Chapter 2 and Appendix A). This is probably because B2P lacks the symmetry elements required to form J-agregates in which all the molecules interact with the surrounding molecules in the same way. The lack of symmetry of B2P also allows the inclusion of solvent molecules in the crystal structure which contributes to isolate molecules. The formation of J-aggregates responds to very precise symmetry requirements; only C2-symmetric BODIPYs seem to show a capacity to

185

form J-agregates in the crystalline state, but that capacity abruptly decreases with the loss of the symmetry axis even by minor modifications.[13] A good example can be seen even in a simple BODIPY like intermediate **3** (Chapter 2) in which the C2 axis is lost by the introduction of a bromine atom, much larger than a hydrogen atom certainly, but less bulky than perylene. For this molecule the formation of J-aggregates is already impossible (Figure 106).
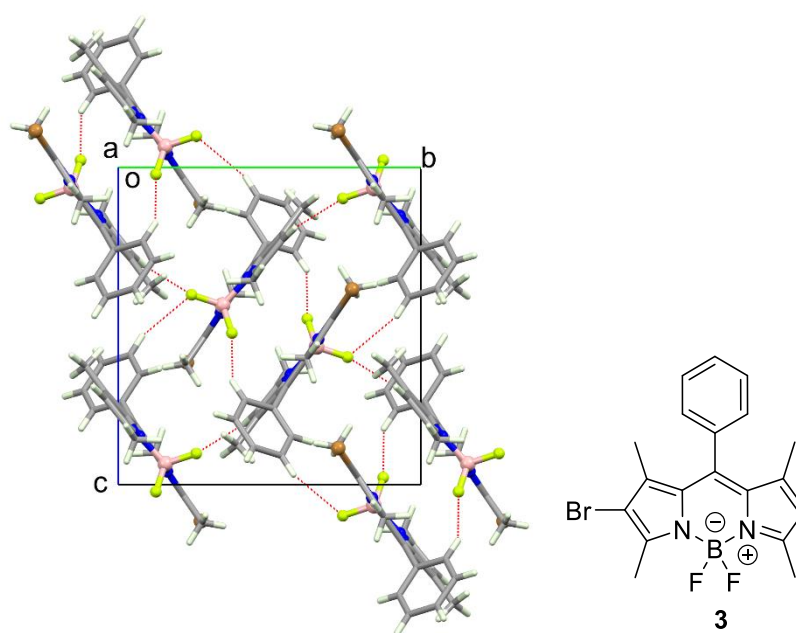
Figure 106 Unit cell packing of intermediate 3 (Chapter 2). Hydrogen atoms not involved with H-F interactions are omitted.

The emission of crystalline B2P was studied in the near infrared region in the hope of identifying phosphorescence from this species in the solid state. There is a prominent broad emission band centred at around 1325 nm. Emission spectra were recorded in the presence and absence of air, flushing the sample holder module with nitrogen for two minutes each time. The emission bands at 1325 show a strong oxygen dependence and are attributed to phosphorescence from the dyad.
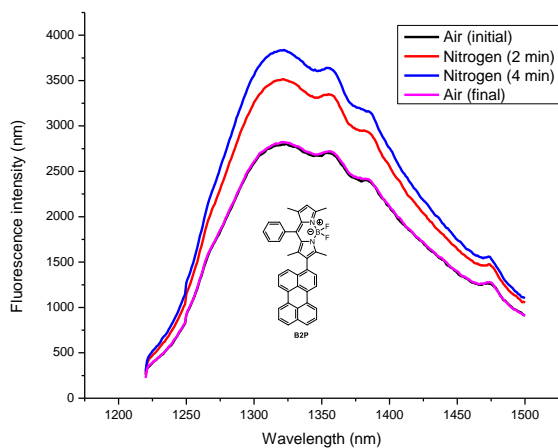
Figure 107 *Emission spectra of crystalline B2P in the 1222-1500 nm range.*

In the same conditions as above, the emission of crystalline B2PI, the iodinated derivative, is much less intense. An emission is similarly observed around 1350 nm but surprisingly, it is much weaker than that of B2P with a low signal to noise and weaker effect of oxygen on intensity .
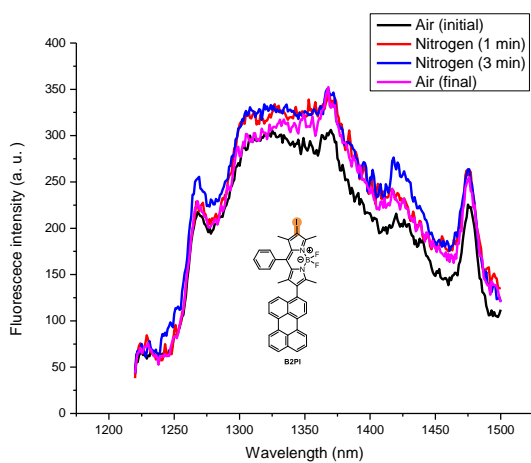
Figure 108 *Emission spectra of crystalline B2PI in the 1220-1500 nm range.*

4.3.6 Solid state properties of dimethylamino benzopyrrole-BF$_2$ complex

During attempts to prepare dimethylaminophenyl BODIPY from the corresponding ketopyrrole, a different BF$_2$ complex was isolated. The product was dissolved in DCM (10 mL) and then cyclohexane was added (60 mL), DCM was evaporated under vacuum, and then cyclohexane was slowly evaporated until crystals of the unexpected product dimethylaminobenzoylpyrole-BF$_2$ (DMAB-BF$_2$) were isolated (compound **2.9**, Chapter 3). The compound was characterised in solution and in the solid state. The emission maximum of the compound in toluene was 466 nm whereas in the crystalline form the emission maximum was well red-shifted to 652 nm (Figure 109 left). The molecule presented a remarkably high quantum yield in solution, dioxane= 86.7±0.9% and toluene = 83.6±1.3% with a lifetime of 2.1 ns in toluene, whereas the crystalline state quantum yield was 21.1±0.2 %.
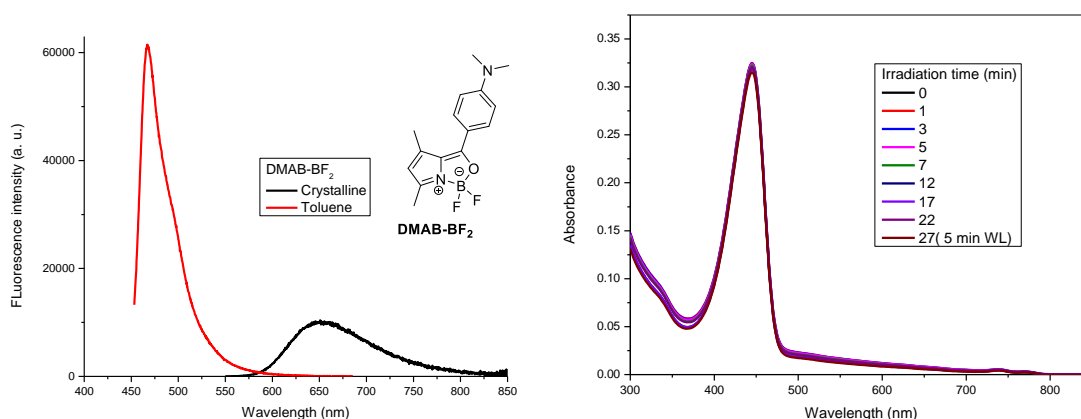
Figure 109 (Left)Emission spectra of DMAB-BF$_2$ in the crystalline (black) state and at 10µM in toluene solution (red). Photostability of DMAB-BF$_2$ under 440 nm irradiation and white light (WL) at 5µM in dioxane.

DMAB-BF$_2$ showed outstanding photostability when irradiated with 440 nm light and also with white light (Figure 109 right). However, after a few days at room temperature, the solutions started to lose their yellow colour. It is likely that

the complexation with BF_2 is reversible, but given the evidence it does not seem to be light-driven. The presence of oxygen, water, or acids in the solvents could affect the complexation. The solid magenta crystals were stable at room temperature over two years.

The large difference between emission maxima in solution and the crystalline state could be due to the packing of DMAB-BF_2 in the crystalline state. The extended structure shows CH-F interactions, the donors are the aromatic CHs whereas the acceptor is the florin atom attached to the boron atom. As every molecule has a donor and an acceptor, these weak interactions make the ensemble behave like a chain that could experience intermolecular charge transfer, an effect that according to some reports could move the emission to the red.[13]
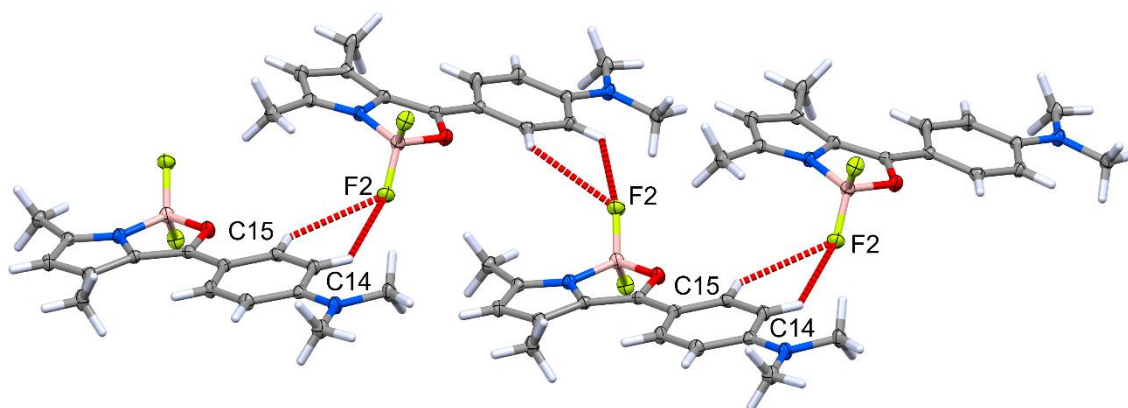
Figure 110 *CH-F interactions in DMAB-BF$_2$ (C- F distances 3.218 and 3.334 Å for C14 and C15, respectively).*

In order to prepare an iodinated derivative of DMAB-BF_2 and further shift the emission into the red, two different methods were tested. Ketopyrrole **2.8** was complexed with BF_3-Et_2O and DMAB-BF_2 was iodinated with NIS. The completion of both reactions was determined by TLC and NMR, but isolation of the product by column chromatography on silica gel was not possible. In both cases, only the

non-iodinated DMAB-BF₂ was isolated indicating that dehalogenation occurs very quickly.
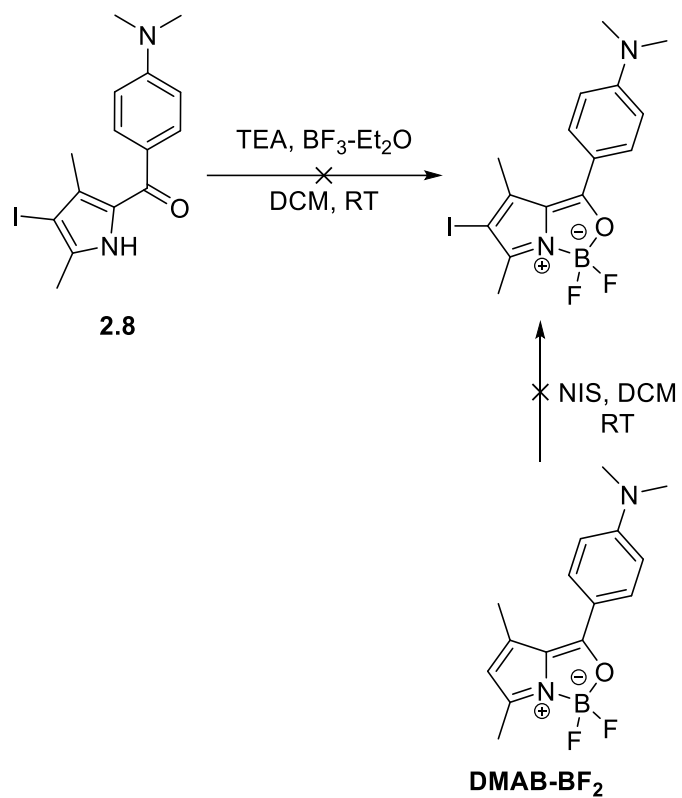
Figure 111 *Attempted reactions to prepare an iodinated derivative of DMAB-BF₂.*

4.3.7 Singlet oxygen and phototoxicity in cells

Given the triplet state formation was evident from TTA-UC, it was of interest to understand whether the excited states of the dyads lead to generation of singlet oxygen in solution. This was determined by the indirect method, which uses 1,3-diphenylisobenzofuran (DPBF) as an oxygen scavenger. The reaction of DPBF, a diene, with singlet oxygen, a dienophile, produces an endoperoxide. The observable effect is the reduction of the absorption of DPBF.[75]

In this experiment, the dyes were dissolved in organic solvents and mixed with a DPBF solution in such a way that final concentrations of the dyes were either 1 µM or 5 µM and the final concentration of the scavenger was 25 µM, which is in the range of concentrations reported in literature.[76–78] Literature reports indicate that DPBF has a high sensitivity that is diffusion-based; methanol/water solutions of this scavenger can detect up to 50% of the oxygen generated in comparison with, for example, 9,10-anthracenediyl-bis(methylene)dimalonic acid (ABDA), another singlet oxygen scavenger that, under the same conditions, can detect only 2% of the oxygen generated.[79]

In contrast to the TTA-UC experiments where both the iodinated and non-iodinated BODIPYs acted as triplet sensitizers, the generation of singlet oxygen was only observed in iodinated molecules B2PI (Figure 112 left) and MB2PI (Figure 112 right) using the DPBF method. In addition, consistent with TT-UC data, the singlet oxygen generation process was found to be very solvent dependent, and it was only observed in dioxane under the conditions studied. Other solvents with low dielectric constants were tested but no singlet oxygen was observed in toluene, hexane, or octanol. The mole fraction solubility of molecular oxygen available for some of these solvents at 20 °C and 1 atmosphere of

pressure are as follow: dioxane 5.20, toluene 9.2, hexane, 19.2.[80] From the solubility data it seems that the availability of oxygen is not responsible for the absence of singlet oxygen production in solvents such as hexane and toluene. The TTA-UC experiments in Chapter 2 supported the hypothesis that the formation of triplet states using BODIPY-perylene conjugates is very solvent dependent as TTA-UC only works in dioxane and toluene. In the case of DMSO, however, no singlet oxygen was detected due to the fact that this solvent is a singlet oxygen quencher. [81] Spectroscopic direct detection of singlet oxygen was not possible.
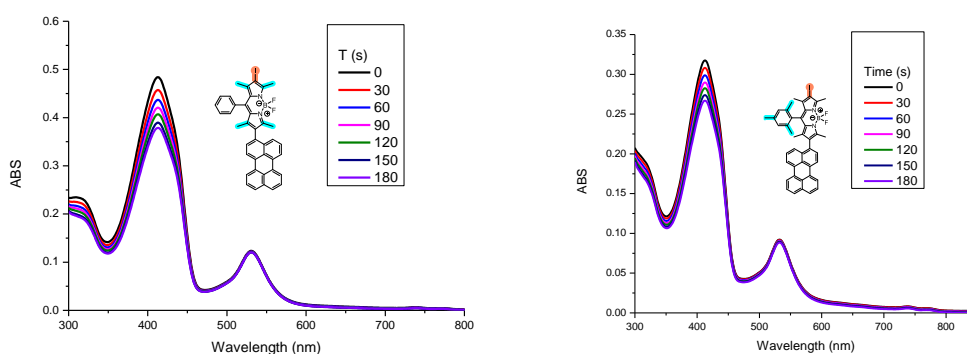
Figure 112 Singlet oxygen generation experiment using B2P (left) and MB2PI (right). Dye conc. = 1µM in dioxane. DPBF conc. = 25 µM. 520 nm light used for excitation.

Again, as it is evident that the dyads undergo triplet state formation and that, in some cases, they form singlet oxygen it was of interest to understand their uptake in cells and whether they show photocytotoxic effects. Cell studies were conducted by Rhianne Curley using B2P, B2PI, MB2P, and MB2PI. The cell line used as a model was MCF-7 a breast cancer line. The cells were incubated with the dye for 17 hours in the absence of light sources, and after this period, all of the cells were viable at all the concentrations tested. In fact, the four molecules showed an IC_{50} > 50µM which can be considered as non-toxic. After incubation, the cells were irradiated at a total dose of 17 ± 1.64 J/cm^2 (2 hours at 2.37 ± 0.23

mW/cm^2) using a 470 nm LED. As observed in Figure 113, B2PI and MB2PI were the most phototoxic molecules.

Confocal images of the B2P, B2PI, MB2P, and MB2PI infused cells were obtained to confirm the uptake of the dyes by the cells. The images show that the compounds are readily cell permeable and that the dyes are distributed mainly in the cytosol, where they appear to accumulate in lipid droplets, and are excluded from the nucleus (Figure 114).
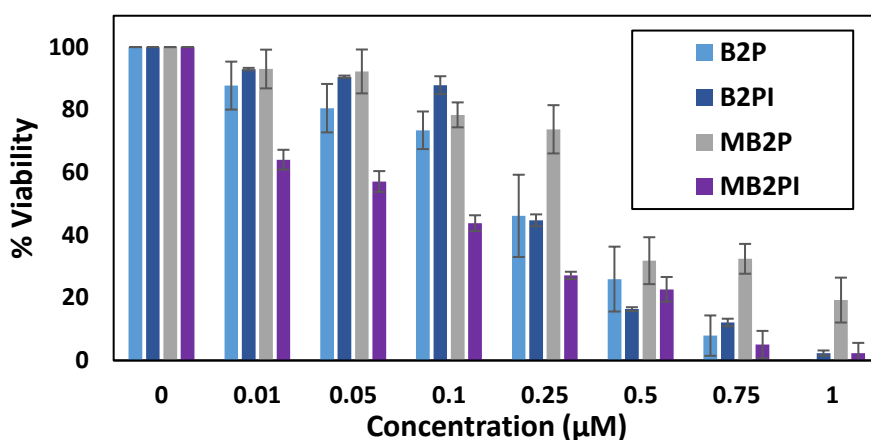
Figure 113 Phototoxicity assay of B2P, B2PI, MB2P and MB2PI in MCF-7 cells. Incubation time = 17 hours. Irradiating at a total dose of 17 ± 1.64 J/cm2 (2 hours at 2.37 ± 0.23 mW/cm2) using a 470 nm LED. Courtesy of Rhianne Curley.
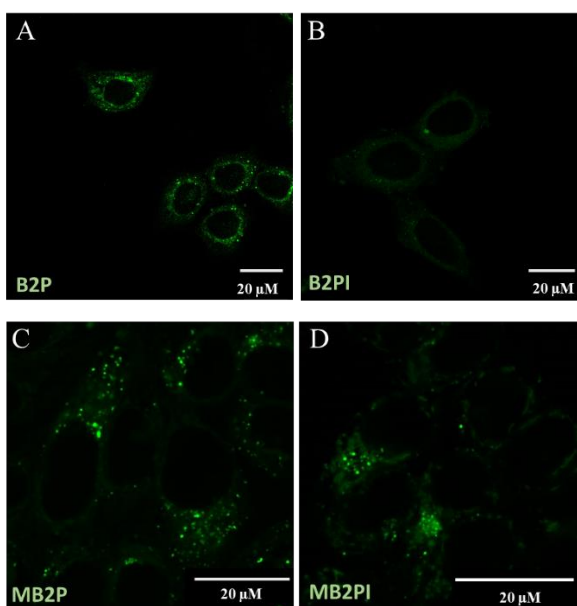
Figure 114 Confocal imaging of MCF-7 Cells with: B2P, B2PI (10 µM), and MB2P, MB2PI (30 µM), 40X, 17 h uptake.

4.4 Conclusions

The detailed photophysics of the families of BODIPY dyads were explored in this Chapter along with an unexpected product DMAB-BF$_2$. The BODIPY-perylene were evaluated as potential viscosity sensors in a castor oil/toluene system. B2P, 2-DMB2P, and MB2P showed a non-systematic relationship between viscosity and emission intensity. The fluorescence intensity decreases with increasing viscosity in solutions with low to medium viscosity, whereas in solutions with high viscosity, the emission intensity increases significantly. The changes at lower viscosity were tentatively attributed to the impact of solvent polarity which is overcome by rotational restriction at high viscosity. In spite of the non-systematic nature of the changes, the probes may be suitable viscosity sensors for high viscosity media where there are not changes in polarity. In the case of 8-DMB2P the fluorescence intensity increased systematically with viscosity following an exponential profile, though with some modification of emission maxima. The compound 8-DMB2P might be a more appropriate viscosity sensor but only in highly viscous media. The lifetime to viscosity relationship of the dyes was studied, and only 8-DMB2P was found to have a lifetime that consistently increases with increasing viscosity, although the changes are modest.

B2P, 2-DMB2P, MB2P, and 8-DMB2P were studied in a polar viscous system comprised of methanol and glycerol in different proportions. The dyes presented two emission bands, one at around 535 to 570 nm and one band at around 700-750 nm. For polar viscose media, the systems displayed an emission switch with viscosity. Solutions with 70% glycerol or less displayed only the short wavelength band, but in solutions with the highest viscosity (80% glycerol or

more), the 700 nm band was the most intense feature. This band was significantly red-shifted by up to 200 nm in some cases.

The temperature dependence of the charge transfer that generated the 700 nm emission band was studied in some high viscosity media. For two dyes, MB2P and 8-DMB2P, the increase in temperature only modified the intensity of the band but did not suppress it. In contrast, for B2P and 2-DMB2P, the band at 680 nm (B2P) and the band at 750 nm (2-DMB2P) were completely suppressed at temperatures ≥ to 50°C.

The compound 8-DMB2P could be a useful molecule. On one hand, the fluorescence of 8-DMB2P in methanol/glycerol solutions displays a marked switch in the emission bands in 90% glycerol. On the other hand, the fluorescence intensity of the dye consistently decreases with increasing percentage of water in dioxane/water solutions. This behaviour suggests that 8-DMB2P might be useful in biological applications as a polarity sensor.

Crystals of B2P, B2PI, and MB2P were prepared by slow evaporation of the solvent. The crystals showed a similar trend to that of the dyes in solution; thus the iodinated dye was the one with the lowest quantum yield, whereas the dye with the highest quantum yield was the most structurally rigid one. All of the dyes have a red-shifted emission in the crystal state compared with the dyes in solution.

A dimethylaminobenzoyl pyrrole complex of BF_2 was isolated and studied in the solid state and in solution. The emission was found to be largely red-shifted and the X-ray diffraction studies suggest that the properties of the dye might be due to the formation of J-aggregates in the crystalline sate.

The capacity of B2P, B2PI, MB2P, and MB2PI to generate singlet oxygen was tested by indirect detection using a singlet oxygen scavenger, DPBF, in a few nonpolar solvents. Under these conditions, only the iodinated molecules showed measurable singlet oxygen sensitisation in solution. The PDT potential of the four molecules was tested in MCF-7 cells. They were found to be non-toxic in the absence of irradiation, but all became toxic after exposure to a light source. Consistent with the singlet oxygen studies, the iodinated BODIPYs were the most phototoxic dyes.

4.5 Experimental section

4.5.1 Spectroscopy

Spectroscopical measurements. Glycerol, anhydrous toluene and castor oil (tested according to European pharmacopeia) were purchased from Merck and used as received. Solutions were prepared using 5 mL class B volumetric flasks. The spectroscopical measurements of the viscosity effect were done using a Jasco V670 spectrometer (absorption) using Hellma quartz fluorescence cuvettes with 1 cm path length and doing background measurements prior to each measurement. The scan rate was set to 1000 nm/min. Fluorescence emission spectra were obtained using a Varian Cary Eclipse fluorescence spectrophotometer. Lifetimes values were measured using a PicoQuant FluoTime 100 Compact FLS TCSPC system using a 450 nm pulsed laser source generated from a PicoQuant PDL800-B box. Lifetime decay plots were analysed using PicoQuant TimeHarp software. The quality of the fit to exponential decay kinetics was assessed from χ^2 values (where $\chi 2 < 1.3$) and visual inspection of residuals. Temperature dependent fluorescence emission measurements were recorded using the SC-25 heating module on an SF5 fluorimeter (Edinburgh Instruments). Solid state and solution quantum yield measurements were performed on the same instrument using the SC-30 integrating sphere module. The fluorescence intensity of the crystalline samples between 900 and 1500 nanometres was measured using an InGaS detector in the SC-5 module of the same instrument.

4.5.2 Crystallography

Single crystals of DMAB-BF$_2$ were prepared by slow evaporation of a concentrated DCM solution. The data were collected at 100(1)K on a Synergy, Dualflex, AtlasS2 diffractometer using CuKα radiation (λ = 1.54184 Å) and the

CrysAlis PRO 1.171.42.49 suite1. Using shelXle2 and Olex23, the structure was solved by dual space methods (SHELXT4) and refined on F^2 using all reflections (SHELXL-2019/25). All non-hydrogen atoms were refined using anisotropic atomic displacement parameters and hydrogen atoms were inserted at calculated positions using a riding model.

4.5.3 Cell studies.

MCF-7 breast cancer cells were incubated for 17 hours to allow uptake. BODIPYs were removed and replaced with phenol red free media (in 96 well plate, each concentration was performed in triplicate per plate). The irradiating was done at a total dose of 17 ± 1.64 J/cm^2 (2 hours at 2.37 ± 0.23 mW/cm^2) using a 470 nm LED (TeleOpto LEDA-X LED driver and array). Control plates were incubated in the dark during the irradiation period (2 h). After irradiation, the cells were incubated in the dark overnight to allow for cell recovery. Irradiation conditions were tested on untreated cells to confirm cells remained viable at this dose before any experiments were performed and each phototoxicity plate included untreated test wells for cell viability comparison. Viability was determined using the alamar blue assay. A 10% Resazurin-medium solution (alamarBlue, Invitrogen) was added to the wells and incubated for 5 h in the absence of light. Absorbance was measured using a BMG LABTECH CLARIOstar plate reader at 570 nm and 600 nm (corrected for background subtraction). In the presence of live cells the blue Resazurin solution is reduced to pink Resorufin.

4.6 References

[1]   K. Li, T.-B. Ren, S. Huan, L. Yuan, X.-B. Zhang, *J. Am. Chem. Soc.* **2021**, *143*, 21143–21160.

[2]   S. Banerjee, A. K. Both, M. Sarkar, *ACS Omega* **2018**, *3*, 15709–15724.

[3]   Q. Wu, T. Zhang, Q. Peng, D. Wang, Z. Shuai, *Phys. Chem. Chem. Phys.* **2014**, *16*, 5545–5552.

[4]   M. Wang, G. Zhang, D. Zhang, D. Zhu, B. Z. Tang, *J. Mater. Chem.* **2010**, *20*, 1858.

[5]   H. Tong, Y. Hong, Y. Dong, M. Häußler, J. W. Y. Lam, Z. Li, Z. Guo, Z. Guo, B. Z. Tang, *Chem. Commun.* **2006**, 3705–3707.

[6]   T. Schillmöller, P. N. Ruth, R. Herbst-Irmer, D. Stalke, *Chem. Eur. J.* **2020**, *26*, 17390–17398.

[7]   C. Wang, Z. Li, *Mater. Chem. Front.* **2017**, *1*, 2174–2194.

[8]   T. Mutai, H. Satou, K. Araki, *Nature Mater.* **2005**, *4*, 685–687.

[9]   S. Xu, Y. Duan, B. Liu, *Adv. Mater.* **2020**, *32*, 1903530.

[10]   C. Shi, Z. Guo, Y. Yan, S. Zhu, Y. Xie, Y. S. Zhao, W. Zhu, H. Tian, *ACS Appl. Mater. Interfaces* **2013**, *5*, 192–198.

[11]   Z. Liu, Z. Jiang, M. Yan, X. Wang, *Front. Chem.* **2019**, *7*, 712.

[12]   H. A. A. El-Ali, J. Jing, X. Zhang, *RSC Adv.* **2019**, *9*, 16246–16251.

[13]   C. Duan, Y. Zhou, G.-G. Shan, Y. Chen, W. Zhao, D. Yuan, L. Zeng, X. Huang, G. Niu, *J. Mater. Chem. C* **2019**, *7*, 3471–3478.

[14]   K. Shimizu, D. Kitagawa, S. Kobatake, *Dyes and Pigments* **2019**, *161*, 341–346.

[15]   T. T. Vu, M. Dvorko, E. Y. Schmidt, J.-F. Audibert, P. Retailleau, B. A. Trofimov, R. B. Pansu, G. Clavier, R. Méallet-Renault, *J. Phys. Chem. C* **2013**, *117*, 5373–5385.

[16] Z. Wang, J. Zhao, A. Barbon, A. Toffoletti, Y. Liu, Y. An, L. Xu, A. Karatay, H. G. Yaglioglu, E. A. Yildiz, M. Hayvali, *J. Am. Chem. Soc.* **2017**, *139*, 7831–7842.

[17] S. G. Awuah, J. Polreis, V. Biradar, Y. You, *Org. Lett.* **2011**, *13*, 3884–3887.

[18] J. Deckers, T. Cardeynaels, S. Doria, N. Tumanov, A. Lapini, A. Ethirajan, M. Ameloot, J. Wouters, M. Di Donato, B. Champagne, W. Maes, *J. Mater. Chem. C* **2022**, *10*, 9344–9355.

[19] N. Kiseleva, M. A. Filatov, J. C. Fischer, M. Kaiser, M. Jakoby, D. Busko, I. A. Howard, B. S. Richards, A. Turshatov, *Phys. Chem. Chem. Phys.* **2022**, *24*, 3568–3578.

[20] Q. Zhou, M. Zhou, Y. Wei, X. Zhou, S. Liu, S. Zhang, B. Zhang, *Phys. Chem. Chem. Phys.* **2017**, *19*, 1516–1525.

[21] B. Kim, B. Sui, X. Yue, S. Tang, M. G. Tichy, K. D. Belfield, *Eur. J. Org. Chem.* **2017**, *2017*, 25–28.

[22] R. A. Arellano-Reyes, A. Prabhakaran, R. C. E. Sia, J. Guthmuller, K. K. Jha, T. Yang, B. Dietzek-Ivanšić, V. McKee, T. E. Keyes, *Chem. Eur. J.* **2023**, *29*, e202300239.

[23] S.-L. Niu, G. Ulrich, P. Retailleau, J. Harrowfield, R. Ziessel, *Tetrahedron Lett.* **2009**, *50*, 3840–3844.

[24] M. C. Malacarne, M. B. Gariboldi, E. Caruso, *IJMS* **2022**, *23*, 10198.

[25] E. Caruso, M. Gariboldi, A. Sangion, P. Gramatica, S. Banfi, *J. Photochem. Photobiol. B.* **2017**, *167*, 269–281.

[26] C. S. Kue, A. Kamkaew, S. H. Voon, L. V. Kiew, L. Y. Chung, K. Burgess, H. B. Lee, *Sci. Rep.* **2016**, *6*, 37209.

[27] A. Kamkaew, K. Burgess, *J. Med. Chem.* **2013**, *56*, 7608–7614.

[28] C. S. Kue, A. Kamkaew, H. B. Lee, L. Y. Chung, L. V. Kiew, K. Burgess, *Mol. Pharmaceutics* **2015**, *12*, 212–222.

[29]   W. Pang, X.-F. Zhang, J. Zhou, C. Yu, E. Hao, L. Jiao, *Chem. Commun.* **2012**, *48*, 5437.

[30]   Y. Cakmak, S. Kolemen, S. Duman, Y. Dede, Y. Dolen, B. Kilic, Z. Kostereli, L. T. Yildirim, A. L. Dogan, D. Guc, E. U. Akkaya, *Angew. Chem. Int. Ed.* **2011**, *50*, 11937–11941.

[31]   X. Xiao, K. Ye, M. Imran, J. Zhao, *App. Sci.* **2022**, *12*, 9933.

[32]   J. Zhao, W. Wu, J. Sun, S. Guo, *Chem. Soc. Rev.* **2013**, *42*, 5323.

[33]   R. Youf, M. Müller, A. Balasini, F. Thétiot, M. Müller, A. Hascoët, U. Jonas, H. Schönherr, G. Lemercier, T. Montier, T. Le Gall, *Pharmaceutics* **2021**, *13*, 1995.

[34]   M. Tim, *J. Photochem. Photobiol. B.* **2015**, *150*, 2–10.

[35]   W. J. Peveler, S. Noimark, H. Al-Azawi, G. B. Hwang, C. R. Crick, E. Allan, J. B. Edel, A. P. Ivanov, A. J. MacRobert, I. P. Parkin, *ACS Appl. Mater. Interfaces* **2018**, *10*, 98–104.

[36]   B. Muz, P. de la Puente, F. Azab, A. K. Azab, *Hipoxia (Auckl.)* **2015**, 83-92.

[37]   L. Hong, J. Li, Y. Luo, T. Guo, C. Zhang, S. Ou, Y. Long, Z. Hu, *Biomolecules* **2022**, *12*, 81.

[38]   L. Wei, Z. Zhang, A. Kumar, S. Banerjee, H. Huang, *Chem. Eur. J.* **2022**, *28*, e202202233.

[39]   I. S. Turan, D. Yildiz, A. Turksoy, G. Gunaydin, E. U. Akkaya, *Angew. Chem. Int. Ed.* **2016**, *55*, 2875–2878.

[40]   J. Zhu, J. Zou, J. Zhang, Y. Sun, X. Dong, Q. Zhang, *J. Mater. Chem. B* **2019**, *7*, 3303–3309.

[41]   S. Toliautas, J. Dodonova, A. Žvirblis, I. Čiplys, A. Polita, A. Devižis, S. Tumkevičius, J. Šulskus, A. Vyšniauskas, *Chem. Eur. J.* **2019**, *25*, 10342–10349.

[42]   A. Vyšniauskas, I. López-Duarte, N. Duchemin, T.-T. Vu, Y. Wu, E. M. Budynina, Y. A. Volkova, E. Peña Cabrera, D. E. Ramírez-Ornelas, M. K. Kuimova, *Phys. Chem. Chem. Phys.* **2017**, *19*, 25252–25259.

[43]   A. Vyšniauskas, D. Ding, M. Qurashi, I. Boczarow, M. Balaz, H. L. Anderson, M. K. Kuimova. *Chem. Eur. J.* **2017**, *23*, 11001–11010.

[44]   W.-J. Shi, R. Chen, J. Yang, Y.-F. Wei, Y. Guo, Z.-Z. Wang, J. Yan, L. Niu, *Anal. Chem.* **2022**, *94*, 14707–14715.

[45]   Z. Yang, Y. He, J. H. Lee, W.-S. Chae, W. X. Ren, J. H. Lee, C. Kang, J. S. Kim, *Chem. Commun.* **2014**, *50*, 11672–11675.

[46]   N. Gupta, S. I. Reja, V. Bhalla, M. Gupta, G. Kaur, M. Kumar, *J. Mater. Chem. B* **2016**, *4*, 1968–1977.

[47]   D. Jurgutis, G. Jarockyte, V. Poderys, J. Dodonova-Vaitkuniene, S. Tumkevicius, A. Vysniauskas, R. Rotomskis, V. Karabanovas, *IJMS* **2022**, *23*, 5687.

[48]   A. Vyšniauskas, I. Lopez-Duarte, A. J. Thompson, J. A. Bull, M. K. Kuimova, *Methods Appl. Fluoresc.* **2018**, *6*, 034001.

[49]   E. Xochitiotzi-Flores, A. Jiménez-Sánchez, H. García-Ortega, N. Sánchez-Puig, M. Romero-Ávila, R. Santillan, N. Farfán, *New J. Chem.* **2016**, *40*, 4500–4512.

[50]   D. Martínez-Bourget, E. Rocha, P. Labra-Vázquez, R. Santillan, B. Ortiz-López, V. Ortiz-Navarrete, V. Maraval, R. Chauvin, N. Farfán, *Spectrochim. Acta A.* **2022**, *283*, 121704.

[51]   P. R. Aswathy, S. Sharma, N. P. Tripathi, S. Sengupta. *Chem. Eur. J.* **2019**, *25*, 14870–14880.

[52]   D. Su, C. Teoh, N. Gao, Q.-H. Xu, Y.-T. Chang, *Sensors* **2016**, *16*, 1397.

[53]   A. Polita, M. Stancikaitė, R. Žvirblis, K. Maleckaitė, J. Dodonova-Vaitkūnienė, S. Tumkevičius, A. P. Shivabalan, G. Valinčius, *RSC Adv.* **2023**, *13*, 19257–19264.

[54]   M. K. Kuimova, G. Yahioglu, J. A. Levitt, K. Suhling, *J. Am. Chem. Soc.* **2008**, *130*, 6672–6673.

[55]   L.-L. Li, K. Li, M.-Y. Li, L. Shi, Y.-H. Liu, H. Zhang, S.-L. Pan, N. Wang, Q. Zhou, X.-Q. Yu, *Anal. Chem.* **2018**, *90*, 5873–5878.

[56]   S.-C. Lee, J. Heo, H. C. Woo, J.-A. Lee, Y. H. Seo, C.-L. Lee, S. Kim, O.-P. Kwon, *Chem. Eur. J.* **2018**, *24*, 13706–13718.

[57]   M. A. Haidekker, E. A. Theodorakis, *Org. Biomol. Chem.* **2007**, *5*, 1669–1678.

[58]   H. Sunahara, Y. Urano, H. Kojima, T. Nagano, *J. Am. Chem. Soc.* **2007**, *129*, 5597–5604.

[59]   F. Song, Y. Xue, X. Wang, J. Wang, X. Xiong, X. Peng, *Chem. Res. Chin. Univ.* **2014**, *30*, 738–742.

[60]   X. Wu, C. Barner-Kowollik, *Chem. Sci.* **2023**, *14*, 12815–12849.

[61]   I. Kamińska, J. Ortyl, R. Popielarz, *Polymer Testing* **2016**, *55*, 310–317.

[62]   J. M. Nölle, C. Jüngst, A. Zumbusch, D. Wöll, *Polym. Chem.* **2014**, *5*, 2700–2703.

[63]   A. Prlj, L. Vannay, C. Corminboeuf, *Helv. Chim. Acta* **2017**, *100*, e1700093.

[64]   I. P. Gulyaev, O. P. Solonenko, *Exp Fluids* **2013**, *54*, 1432.

[65]   T. T. Vu, R. Méallet-Renault, G. Clavier, B. A. Trofimov, M. K. Kuimova, *J. Mater. Chem. C* **2016**, *4*, 2828–2833.

[66]   D. Dziuba, P. Jurkiewicz, M. Cebecauer, M. Hof, M. Hocek, *Angew. Chem. Int. Ed.* **2016**, *128*, 182–186.

[67]   Y.-F. Kang, W.-K. Chen, K.-X. Teng, L.-Y. Wang, X.-C. Xu, L.-Y. Niu, G. Cui, Q.-Z. Yang, *CCS Chem* **2022**, *4*, 3516–3528.

[68]   X. Wang, Z. Jiang, Z. Liang, T. Wang, Y. Chen, Z. Liu, *Sci. Adv.* **2022**, *8*, eadd5660.

[69]   K. Li, X. Duan, Z. Jiang, D. Ding, Y. Chen, G.-Q. Zhang, Z. Liu, *Nat. Commun.* **2021**, *12*, 2376.

[70]   R. Hu, E. Lager, A. Aguilar-Aguilar, J. Liu, J. W. Y. Lam, H. H. Y. Sung, I. D. Williams, Y. Zhong, K. S. Wong, E. Peña-Cabrera, B. Z. Tang, *J. Phys. Chem. C* **2009**, *113*, 15845–15853.

[71]   X. Qin, X. Yang, L. Du, M. Li, *RSC Med. Chem.* **2021**, *12*, 1826–1838.

[72]   S. Ludwanowski, A. Samanta, S. Loescher, C. Barner-Kowollik, A. Walther, *Adv. Sci.* **2021**, *8*, 2003740.

[73]   S. Ye, C.-H. Hsiung, Y. Tang, X. Zhang, *Acc. Chem. Res.* **2022**, *55*, 381–390.

[74]   D. Tian, F. Qi, H. Ma, X. Wang, Y. Pan, R. Chen, Z. Shen, Z. Liu, L. Huang, W. Huang, *Nat Commun* **2018**, *9*, 2688.

[75]   J. A. Howard, G. D. Mendenhall, *Can. J. Chem.* **1975**, *53*, 2199–2201.

[76]   X.-F. Zhang, X. Yang, *J. Phys. Chem. B* **2013**, *117*, 9050–9055.

[77]   W. Hu, R. Zhang, X.-F. Zhang, J. Liu, L. Luo, *Spectrochim. Acta A.* **2022**, *272*, 120965.

[78]   X.-F. Zhang, X. Yang, *J. Phys. Chem. B* **2013**, *117*, 5533–5539.

[79]   T. Entradas, S. Waldron, M. Volk, *J. Photochem. Photobiol. B.* **2020**, *204*, 111787.

[80]   R. Battino, T. R. Rettich, T. Tominaga, *J. Phys. Chem. Ref. Data.* **1983**, *12*, 163–178.

[81]   L. V. Lutkus, S. S. Rickenbach, T. M. McCormick, *J. Photochem. Photobiol. A.* **2019**, *378*, 131–135.

Chapter 5 Membrane, mitochondria, and NO sensors.

Overview

Fluorescent sensors have largely contributed to improve the understanding of cellular functions. However, there is still room for improvement, especially considering the selectivity of certain probes and the combination of more than one sensor in the same system. In this Chapter, three molecules with sensing potential were prepared and studied. A brief introduction of the literature advances in the area will be presented as introduction, the synthesis of the sensors will be discussed as well as their spectroscopic properties and applications. These probes are aimed at sensing cell membrane viscosity, mitochondrial function, and cellular levels of nitric oxide.

The eukaryotic cell membrane is a protective structure mainly formed by phospho- and sphingolipids, cholesterol, and proteins. This molecular barrier not only plays a key role regulating transport of nutrients and waste in and out the cell, but also plays important role in cell signalling and in cell-to-cell interactions. Many of these functions are regulated by internal and external chemical stimuli; however, given the fluidic nature of the membrane and mobility of its constituents, there is substantial evidence that viscosity of the membrane also has an important role in maintaining homeostasis.

Fluorescent probes have helped understand some of the mechanisms involving the macromolecular organisation of the membrane and the dynamics of the molecules imbedded in it. Nonetheless, many of the mechanisms regarding the relationship between viscosity and functionality are not yet fully understood, encouraging the development of new molecular probes that are suitable for phase

selection and can be used with methods such as confocal fluorescence, fluorescence lifetime and fluorescence correlation spectroscopy (FCS) techniques. In this Chapter a BODIPY-cholesterol conjugate, with potential as a membrane viscosity sensor, was prepared. The spectroscopic characterisation of the dye was carried out in pure solvents and in viscous solutions prepared from a castor oil toluene mixture. The lifetime response to changes in viscosity was also studied.

Another organelle that fulfils essential functions in the cells are the mitochondria. They are mainly known for being responsible for energy production in the form of adenosine triphosphate, but they also play a key role in signalling pathways, metabolism, and immune response. Dysfunction of the mitochondrial function can cause severe medical conditions such as diabetes and cancer, and that makes these organelles attractive therapeutic targets. Spectroscopic techniques including fluorescence and Raman imaging are helping to solidify our understanding of this organelles' functions. In this Chapter, a highly selective mitochondrial Raman reporter was developed. Structural modifications were completed to assure the dye had a functionality, i.e. an alkyne bond, that shows vibrational features in the so-called silent region of the Raman spectrum, namely the introduction of triple bonds. The specificity of the dye and its comparison with Raman standards was studied in cells.

Understanding cell organelles is important, but it is also important to know the individual molecules involved in the correct functioning of a cell. One of these molecules is nitric oxide. This very reactive molecule has been identified in skeletal muscle, blood vessels, and the brain. The correlation between nitric oxide production and diseases has been well established. However, studying this gas is challenging given its high diffusion rate and high reactivity. In this Chapter a

fluorescent chemical nitric oxide sensor was developed. The synthetic pathway to prepare the compound was optimised and the nitric oxide sensing properties of the molecule were studied in solution.

5.1 Membrane sensors

5.1.1 Lipid bilayer structure and functions

The eukaryotic cell membrane is a very complex and dynamic structure, it is formed mainly by sphingolipids, phospholipids, sterols, and a large number of proteins that form all the receptors and transmembrane channels. For comparison, half of the membrane's mass is lipid and half is proteins.[1] The cell plasma membrane is responsible for a number of functions, from the physical protection to the intracellular organelles to the regulation of the passive and active transport of nutrients and waste, in and out of the cell, respectively, and the communication with other cells and tissues.[1]

Most lipids of the cell membrane are amphipathic. Lipids have a charged polar head and long non-polar hydrocarbon chains whereas sterols have a polar hydroxy group and aliphatic rings fused together. These molecules can spontaneously form lipid bilayers in water. In a eukaryotic cell membrane, the lipid bilayer is formed with the polar groups on opposite sides of the membrane and with the non-polar chains pointing towards the inside of the membrane, and the 3-dimensional structure is stabilised by non-covalent interactions[2] (Figure 115)**Figure** . Cholesterol contributes toward membrane stability, rigidifying the membrane and increasing the melting point of the membrane if the temperature increases, and it also prevents aggregation of the lipids when the temperature decreases.[3,4]

The lipids of the cell membrane do not have a homogeneous composition, and proteins and lipids are not randomly distributed. Our understanding of the membrane's organisation has improved by taking into consideration the formation

of lipid rafts.[5] These structures are formed by sphingolipids and cholesterol in the external side of the cell, and phospholipids and cholesterol in the internal side, the lipids often surround a protein. Lipid rafts contain a higher amount of cholesterol compared to the rest of the lipid bilayer and they are assembled in the Golgi apparatus in mammals.[5,6] The lipid rafts belong to the liquid order domain (Lo), a fraction of the membrane characterised by the tight and orderly packaging of the lipids inside it. The fractions not belonging to a lipid raft are considered liquid disordered phase (Ld). Figure 115.
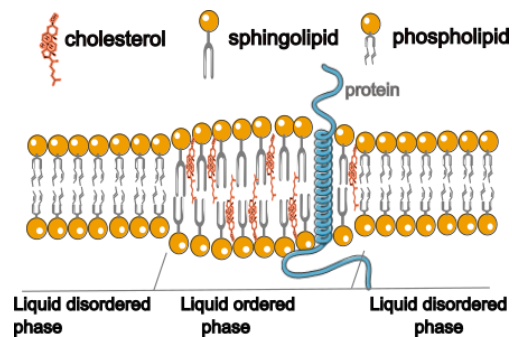

Figure 115 Schematic representation of a cell membrane indicating the main components of the liquid disordered phase (phospholipids) and the liquid ordered phase (sphingolipids and cholesterol).

Despite all existing research on membranes, a further understanding of this structure is desirable due to its involvement in disease conditions.[7] For example, some studies suggests that understanding the cholesterol homeostasis could be important to prevent or reduce the progression of neurodegenerative conditions.[6,8,9] Lipid raft domains have been identified as the starting contact point between some viruses and host cells. These viruses include respiratory diseases such as influenza and COVID-19,[10–14] and also viruses with a much higher mortality rate such as HIV and Ebola.[15–17]

5.1.2 Fluorescent probes for lipid membranes

Fluorescence is one of the main methods used to study the biophysical structure and chemical functions of the cell membrane over the last decades. For example, the use of 1-[6-(dimethylamino)naphthalen-2-yl]dodecan-1-one (Laurdan) has been widely applied to understand the phase behaviour of lipid membranes, i.e., the degree of lipid order or lipid disorder character of membranes and membrane sections.[18] The lipophilic hydrocarbon chain of Laurdan is responsible for its membrane selectivity. The emission maximum of Laurdan depends on the water molecules around it, that is to say, in the membrane. The water content of a membrane section depends itself on the lipid packing.[19–21] Cholesterol has also been used in a few other examples as a targeting unit as it allows the integration of fluorescent probes into the membrane without interfering with it. A suitable combination is the conjugation of BODIPY with cholesterol. In one example, researchers who conjugated the alkyl chain of cholesterol to BODIPY used this probe to study cholesterol trafficking in mammalian cells.[22,23] The Keyes research group has demonstrated the capacity of a 6-carbon linker between cholesterol and BODIPY to improve the selectivity of the probe for the liquid order domain, something that is difficult to achieve given the tight lipid packing of these membrane domains (Figure 116 BDP-Ahx-cholesterol), in this case, the linker was added via the cholesterol's hydroxyl group.[24] A promising approach is the use of cholesterol-based imidazolium salts (CHIM) that have shown very good cholesterol mimicking properties and have been used to study cholesterol trafficking in cells. Once the

CHIM molecule has been integrated into the membrane, it can be functionalised with fluorophores via click chemistry[25,26] (Figure 116).

Laurdan   **CHIM**   **BDP-Ahx-chol**
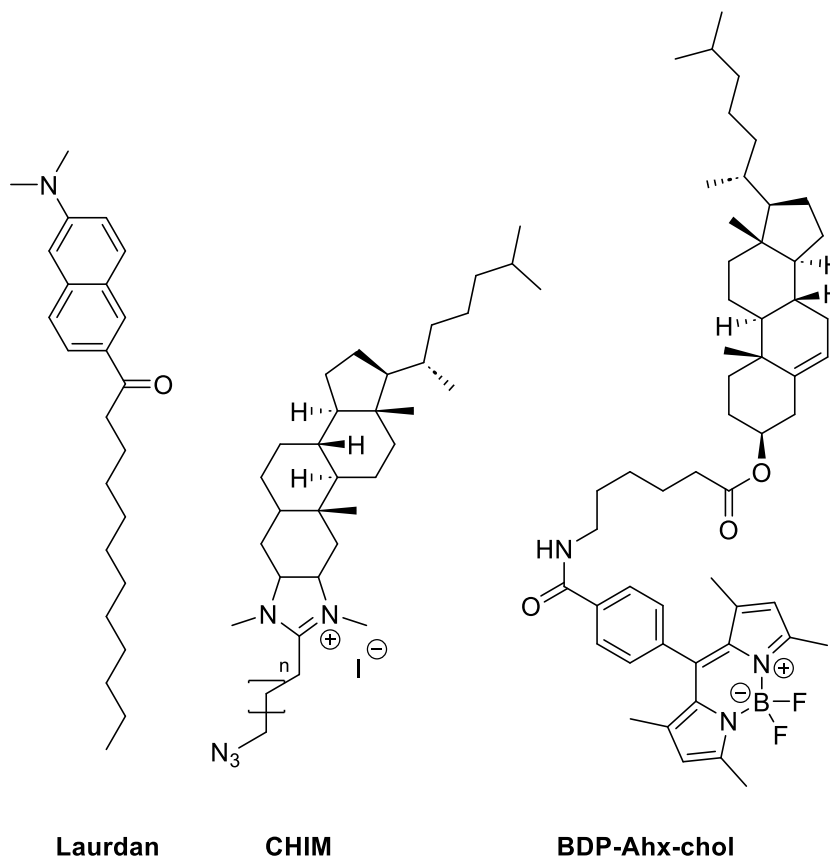
Figure 116 Left: Laurdan, a fluorescent probe used to determine the Lo/Ld character or a membrane. Centre: CHIM, an efficient cholesterol mimic. Right: BDP-Ahx-chol a Lo-specific probe. [25,26]

Another approach to prepare membrane probes is to integrate the fluorophore, very frequently BODIPY, into the structure of a fatty acid with 3 to 12 carbon atoms. The molecules produced in this fashion have been used to study fatty acid transport across the nuclear membrane.[27] Other molecules of this kind have been used to study lipid peroxidation with increasing popularity, [28–30] although some early studies demonstrated that the probe was not only overestimating, but also inhibiting lipid oxide damage[31] (Figure 117).
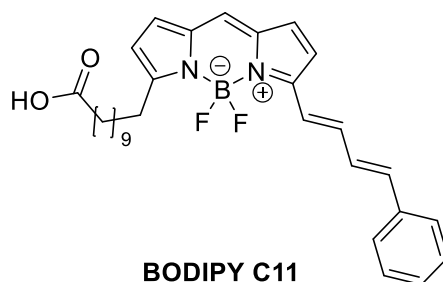
BODIPY C11

Figure 117 BODIPY C11 a dye commonly used to study oxidation of lipids in the membrane. [31]

The example of C11 gives us some hints into the desired properties of a dye. Given that the cell membrane is a complex environment, the presence of exogenous molecules can, in principle, cause a disruption to lipid packing. However, for both sensing and cell imaging, there are no standard protocols to determine the impact of dye labels on the membrane apart from the toxicity assays used in live cells.

The fluorescent membrane sensors that have been described so far can be classified based on their strategies to target the membrane, their sensing mechanism (chemical or biophysical), and on the optical response used for the sensing (lifetime- or emission-based).[32] The design of a fluorescent probe depends consequently on the cell membrane parameter that is to be studied, on the environment (*in vitro, in vivo*), the cell line, and the relationship between the probe and other cell structures present.

5.2 Mitochondrial sensors

The mitochondrion is a double-membraned organelle present in Eucaryotic cells, its functions include the production of energy, signalling and immune response.[33] Mitochondria are called the powerhouses of the cell since they generate most of the chemical energy in the form of adenosine triphosphate (ATP).[34]The production of energy is key to control the cell cycle, in fact low energy levels could even stop cell division.[35]Another function of the mitochondria can be found in the series of reactions that produces apoptosis. It has been observed that the fragmentation of mitochondria and the release of cytochrome C are essential to start the mechanisms leading to programmed cell death.[36,37] Finally, the mitochondria play also an essential role in the immune response, namely, the production of interferon and cytokines in response to a viral infection.[38,39]

5.2.1 Mitochondria and disease

As explained above, the good function of mitochondria ensures more than energy production. However, external and internal stimuli can modify the normal functions of these organelles. Even before the discovery of the genetical singularities of mitochondria and the elucidation of the complex metabolic pathways involved in the synthesis of ATP, deficient cell respiration was associated to cancer. In fact, cancer cells metabolise glucose by lactic fermentation even when oxygen is available, suggesting a disfunction of the mitochondrial activity in this type of cells.[40] It is known nowadays that mutations of certain enzymes inside the mitochondria can be the cause of cancer progression[41] and that proteins that stimulate mitochondrial biogenesis or the oxidative function of the mitochondria could be used as tumour suppressors.[41,42]

Recent reports have also demonstrated that hyperglycaemic or hyperlipidaemic conditions, such as those produced by obesity, increase the production of reactive oxygen species and induce morphological changes of the mitochondria altering their functions.[43,44] One striking example is the non-alcoholic fatty liver disease (NAFLD) in which mitochondria increase their activity in the short term, to overcome lipotoxicity, but fail to do so in the long term leading to liver fibrosis and liver failure.[45,46]
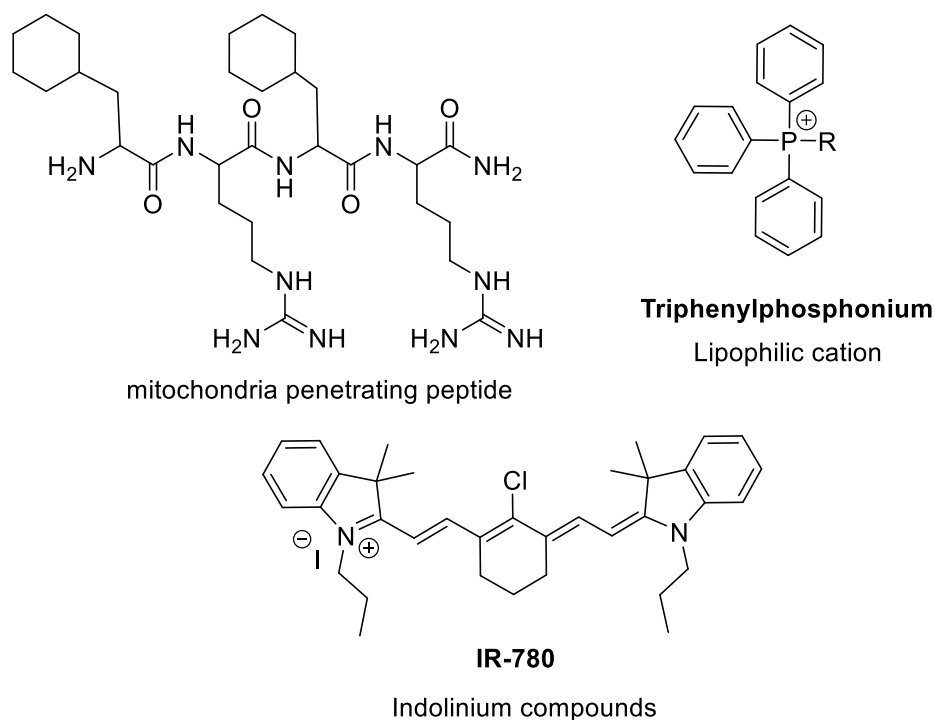
Mitochondrial dysfunction has been associated with diabetes at different stages. On one hand, it has been observed that the correct function of mitochondria is essential for the release of insulin, and any abnormality in the calcium signalling will affect this process.[47,48]On the other hand, insulin stimulates mitochondrial activity in adipocytes and skeletal and cardiac muscle. In those cells the metabolic activity of mitochondria is responsible for lipid oxidation, so any disfunction in slow turnover of the metabolic pathways leads to the accumulation of intermediates such as acylcarnitines and a general disfunction of the cell.[49,50]

Finally, dysfunctions in the oxidative phosphorylation system have been associated with schizophrenia. Neuron activity is highly dependent on ATP availability. Functional magnetic resonance imaging has revealed a bioenergetic disfunction in temporal, frontal, and prefrontal lobes in patients with schizophrenia.[51,52]The metabolism of dopamine, one of the main neurotransmitters, also requires the intervention of mitochondria. A high concentration of dopamine or mitochondrial defects results in the accumulation of toxic reactive metabolites.[53] As such, mitochondrial functions are directly linked to the pathogenesis of schizophrenia.[54]

5.2.2 Targeting mitochondria for drug delivery and cell imaging

Due to its participation in disease conditions, mitochondria have become an important therapeutic target particularly in oncological research. Some of the reported strategies to produce cancer cell death include depolarising the mitochondrial membrane, suppressing glycolysis, or changing the permeability of the mitochondrial membrane.[55,56] Selectively targeting the mitochondria is not an easy task, as reaching these organelles implies that a the therapeutic agent can be transported into the cell, resist cytoplasmic metabolism and cross the closely packed mitochondrial membrane.[57] The mitochondrial membrane of the cancer cells is generally hyperpolarised, with a potential of -220 mV, much more than the -160 mV observed in healthy cells. This feature facilitates the transfer of positively charged molecules across the membrane and their concentration in the mitochondrial matrix.[58]

The most widely applied mitochondrial targeting strategy is the conjugation of triphenylphosphonium (TPP) salts. Figure 118. The potential of TPP to accumulate in the mitochondria was observed during the study of oxidative phosphorylation. M. P. Murphy and coworkers extended its application by conjugating several molecules to TPP. There are abundant examples in the literature in which TPP salts were used to deliver therapeutic agents or fluorophores.[59,60] Other examples of targeting moieties include peptides with natural or non-natural amino acid residues,[61–63] pyridinium, or indolinium salts. One example of an indolinium salt is IR-780. This molecule and its derivatives have been extensively used for diagnosis and treatment in oncology research[64] (Figure 118).

Triphenylphosphonium
Lipophilic cation

mitochondria penetrating peptide

IR-780
Indolinium compounds

Figure 118 Common mitochondria-targeting motifs. Non-natural peptides and triphosphonium salts can be conjugated to drugs. Indolinium salts can act as diagnosis and therapeutic agents.

In the areas of fluorescence imaging, positively charged dyes have also been extensively used. The most common ones are probably the MitoTracker™ series. MitoTracker Red™, a xanthene derivative, is particularly useful; it is lipophilic therefore capable of diffusing through the cell and mitochondrial membrane, and it is positively charged which is the reason for their specificity. The fact that this dye they can covalently bond to cysteine residues inside the mitochondria makes it useful for studies requiring cell fixation.[65] Other dyes sharing the brand, MitoTracker DeepRed™ and MitoTracker Green™, are indolinium derivates, and they are used for specific functions, such as the combination with other dyes for multicolour imaging or staining mitochondria at a specific stages.[66]

When it comes to Raman imaging, TPP derivatives are the current gold standard probes. A common standard for imaging is mitoBADY, developed by Yamakoshi and coworkers.[67] The key functional feature of this dye is the presence

of a disubstituted 1,3-diyne. The Raman signal of the triple bond can be found in the "silent" region of the Raman spectra (1800-2800 cm^{-1}), a region where very few other functional groups vibrate, thus avoiding interference irrespective of the matrix under study. Using similar structural features, Wilson and coworkers developed a pH sensitive mitochondrial Raman reporter, Mitokyne[68] (Figure 119). It is important to study the effect of any mitochondria-targeting fluorophores, especially TPP-based trackers, as research has shown that some TPP conjugates inhibit electron transport chain and can cause proton leak. This action is potentially useful in targeted drug delivery but much less so in imaging techniques.[69–71]

The selectivity of this proves is still a challenge, as most of these compounds do not exclusively localise in the mitochondria, especially after incubation times longer than 30 min. Structural modification could be done to address this issue, for example combining these alkyne probes with peptides or with reactive moieties that bond covalently to the mitochondrial membrane or matrix.
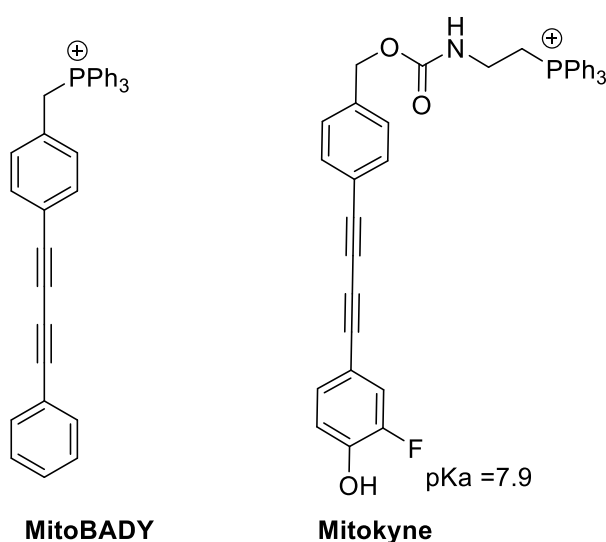

Figure 119 *MitoBady and Mitokyne, mitochondia-targeting Raman probes.*

5.3 Nitric oxide sensors

NO is a colourless and odourless gas, which is soluble in water and in organic solvents and can rapidly defuse through organic tissues. NO is produced in a number of biological structures by the NO synthases from L-arginine.[72] This highly reactive gas fulfils different functions in smooth muscle tonicity (vasculature) and inhibition of platelet formation,[73] immune response,[74,75]and neurotransmission.[76]

Sensing NO in cell environments poses a number of challenges. Firstly, the NO sensor has to distinguish between NO and other radicals. Secondly, NO easily oxidises to NO_2, so the sensing reaction must be quick. NO diffuses rapidly so it is very likely that any chemical sensor is always underestimating the actual concentration, an effect observed in other sensing techniques such as chemiluminescence and electrochemical detection.[77,78]

Chemical sensing requires the fast reaction of a sensing unit with NO. Some of the literature examples include 1,2-diamino groups, hydrazones, secondary amines, or dihydropyridines. The reaction of hydrazines and other primary amines with NO produced the break of the fluorophore-hydrazine bond. The reaction of 1,2-diamino groups with NO yields a triazole, and secondary amines react covalently with NO to form nitrosamides[79–83] (Figure 120).
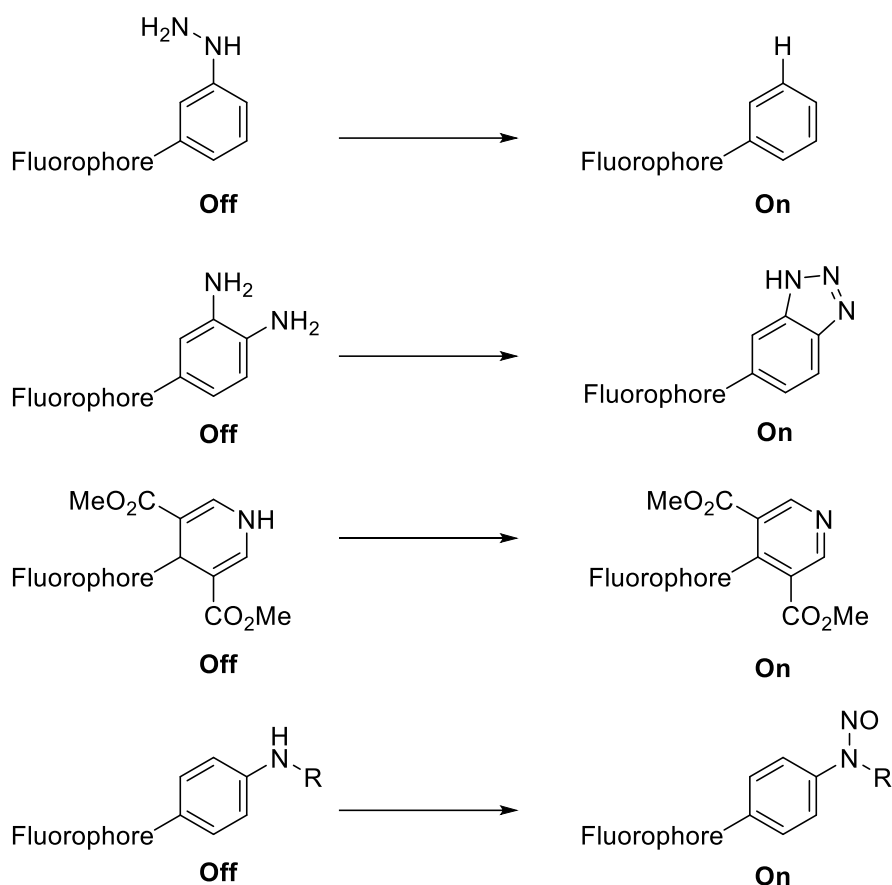
Figure 120 Common functional groups used in the sensing of nitric oxide. Off= low fluorescence On= high fluorescence.

In an ideal situation, the NO sensor should have a very low fluorescence intensity before reacting with NO. A good example is a thiourea derivative reported by Han and coworkers. The sensor is not fluorescent, but the reaction with NO produced a cyclisation reaction forming an oxadiazole that is highly fluorescent. This molecule was used to measure NO in zebra fish. However, the main drawback is that both the excitation and emission lights are in the blue side of the visible region, 436 nm and 470 nm respectively. Blue light produces strong fluorescence, but it has been observed that red or near infrared light have a better capacity to penetrate tissues making the measurements more accurate (Figure 121).[82]
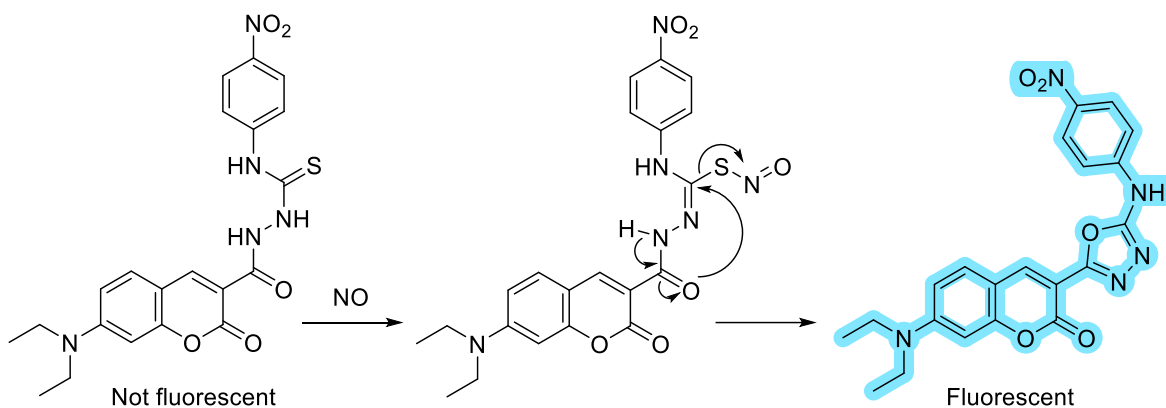
Figure 121 *Example of an off/on sensor for nitric oxide.*

The main challenge for NO sensors is achieving reversible sensing. This would allow continuous sensing in conditions where the concentrations of NO change. Chemicals probes involving the formation of a covalent bond are necessarily unsuitable and there are, to the best of my knowledge, no examples in literature. The use of metallic complexes that include NO as a reversible ligand or the combination with electrochemical techniques could be good alternatives.[84–86]

5.4 Results and discussion

In this Chapter, three sensors were developed as part of the LogicLab project. This EU-funded initiative aims to developed lipidic vesicles capable of delivering molecular sensors to endothelial cells. The goal is being able to sense more than one parameter, be it pH, nitric oxide, calcium, or viscosity, at the same time, and producing a detectable optical response. The molecules described in this Chapter were prepared and characterised and some of them were sent to other laboratories, which are members of the LogicLab consortium, for study.

The sensors include a BODIPY-cholesterol developed with the goal of sensing the viscosity of the cell membrane, a Raman probe for mitochondrial studies, and an NO sensor with potential applications in TTA-UC systems.

5.4.1 Membrane sensors
5.4.1.1 Synthesis and characterisation

The synthesis of symmetric BODIPY-cholesterol conjugates has been reported by our group.[24] The synthesis follows a three-step one-pot method to prepare the BODIPY unit followed by esterification with cholesterol. However, to improve the viscosity sensitivity of the dye and following literature reports on other viscosity sensors, a BODIPY-cholesterol with increase rotation was designed. The unsymmetric nature of the dye did not allow the use of the one-pot methodology so a different method was developed, and the is route summarized in Figure 122.

The first key intermediate is the methoxycarbonyl 2-benzoyl pyrrole **12**. The synthesis of this molecule was completed as described in Chapter 2, via the Vilsmeier-Haack reaction of the corresponding morpholine amide with pyrrole. The reaction, however, did not proceed at room temperature and reflux conditions were

necessary. This result can be explained by low reactivity of the morpholine amide. The first step includes the nucleophilic attack of this species to phosphorus oxychloride. The ester group being a powerful electron withdrawing group, the reaction will be much slower than with electron donating or electron neutral amides.
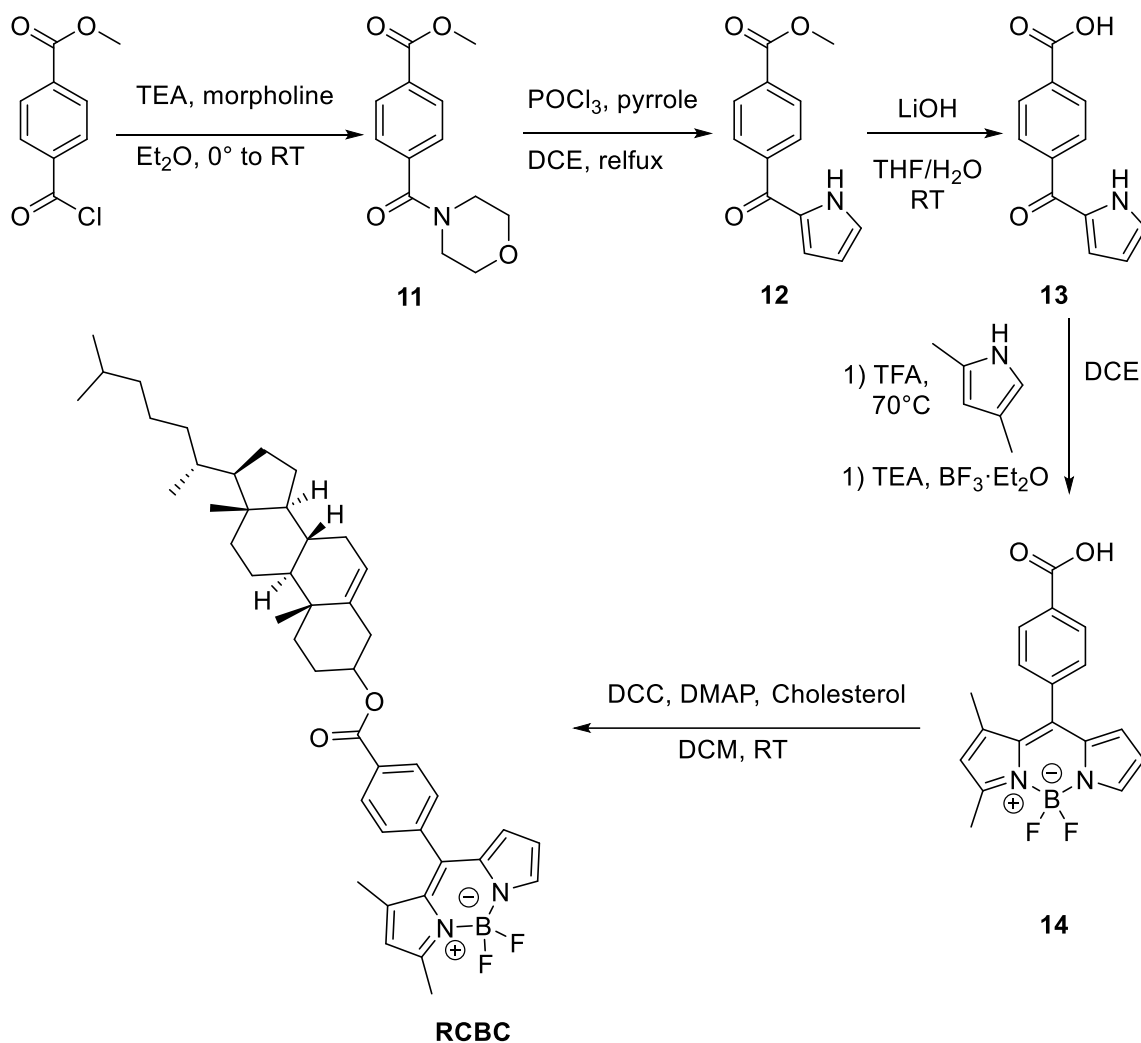

Figure 122 Synthetic pathway to prepare RCBC, a potential viscosity sensing probe.

The hydrolysis of the ester, **12,** was completed using standard conditions of LiOH in THF. The hydrolysis was carried out before the condensation to form the BODIPY core, as this fluorophore is not stable under basic conditions as observed throughout this thesis. The condensation of benzoyl-pyrrole **13** with one equivalent of 2,4-dimethylpyrrole did not occur at room temperature as in Chapter 2. Reflux was necessary to facilitate the nucleophilic attack of the pyrrole on the carbonyl

group. However, at high temperatures, 2,4-dimethylpyrrole reacts with TFA to form an acylated pyrrole (confirmed by X-ray diffraction, see Appendix D). So, addition of 0.5 to 1 extra equivalents of pyrrole was necessary as the reaction proceeded.

The esterification reaction was completed by two methods, Steglich conditions and via the acyl chloride prepared with oxalyl chloride and DMF. The product of the oxalyl chloride reaction was two different fluorescent species whereas the Steglich methodology yielded a much cleaner product.

Crystals of the resulting dye were prepared by dissolving a few milligrams in hot octanol. The solution was then cooled to room temperature and then put in the fridge for several days.[87] The crystal structure was solved by Prof. Vickie McKee. In the crystal structure two different conformations were found. One conformation shows orthogonality between BODIPY and the phenyl ring at the *meso* position. In the second conformation, both moieties are nearly in the same plane (Figure 123). The absence of a methyl group in position 7 of the BODIPY core surely allows the coplanar conformation, and the availability of the two conformers in the crystal structure speaks to its likely value as a rotamer for viscosity sensing.
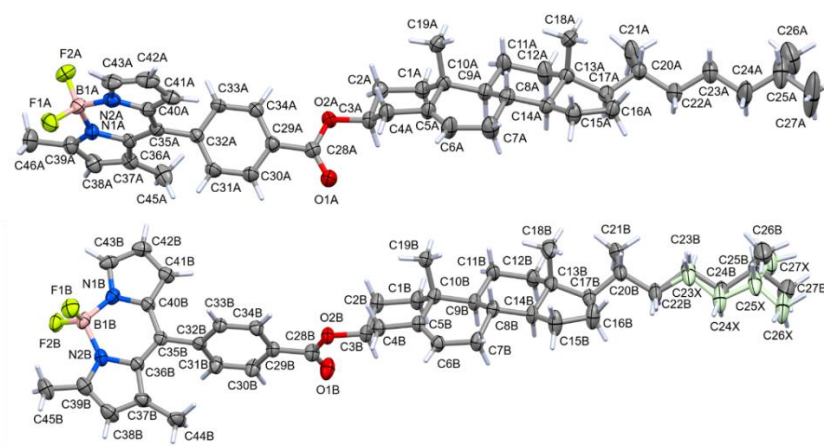
Figure 123 Crystal structure of 2 independent RCBC molecules with different conformations (50% probability ellipsoids). Molecule B has some disorder in the alkyl chain – minor component shown in green.

5.4.1.2 Spectroscopic studies

The absorption of **RCBC** shows significant solvent dependence. The absorbance cross section increases in the non-polar solvents, dioxane and cyclohexane, but is also high in polar protic solvents such as ethanol, whereas it decreases significantly in chloroform, a non-protic solvent (Figure 124). The reasons behind this behaviour are not simple to determine. Poor solubility of the dye or the formation of aggregates in chloroform is not likely to be the reason, the dye being very soluble in chlorinated solvents. The emission follows a more consistent trend. It is the highest in low polarity solvents and decreases as the dielectric constant of the solvent increases. It is worth noticing that polar solvents did not completely suppressed the emission as observed in charge transfer BODIPYs.[88]
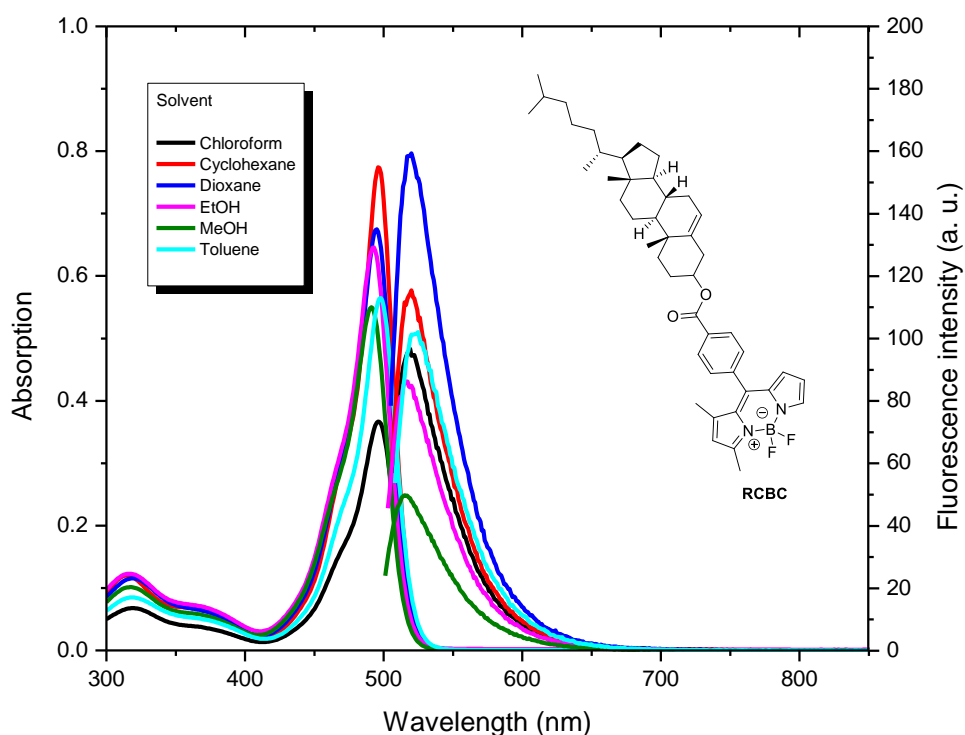
Figure 124 *Absorption (left) and emission (right) spectra od RCBC at 10 µM in different solvents, excitation at λ_{max} and slit widths of 5-5 nm.*

The lifetime of RCBC in dioxane and methanol shows two components. The first component τ1 is equal to 0.2 ns and is the one with the largest amplitude (~93%). τ2, is the longest component but it has the smallest amplitude (~7%). The fitting was made using a reconvolution model (Table 5). This behaviour suggests the presence of more than one emitting species in solution, which is not surprising given that the molecule has a high rotational freedom.

Table 5 Lifetime of RCBC in dioxane. The measurement was carried out trice. AVG = average, SD = standard deviation. IW = intensity-weighted average lifetime.

		DIOXANE			
	t_1	Amplitude (%)	t_2	Amplitude (%)	IW
	0.16	99.7	3.93	0.3	0.42
	0.16	99.7	4.04	0.3	0.42
	0.16	99.7	4.03	0.3	0.39
AVG	0.2		4.0		0.4
SD	0.0		0.0		0.0

5.4.1.3 Viscosity studies in castor oil-toluene

To understand the effect of viscosity on the absorbance and emission properties for the probe studies were carried out using the castor oil toluene system described in Chapter 3. The absorption remains essentially constant at all viscosities measured with a maximum absorbance at 500 nm. The emission maximum was also unaffected by the solvent mixture and is observed at 520 nm. This small Stokes shift is characteristic of BODIPYs π-π* fluorescence from the BODIPY core in such complexes without charge transfer transitions (Figure 125). The relationship between emission intensity at the λ_{max} and castor oil percentage follows a systematic trend with an exponential plot providing a good fitting such that this molecule could be used as an intensity-based viscosity sensor (Figure 126). BODIPY-cholesterol dyes have been reported, but there are only a few examples in which these dyes have been used as viscosity sensors.[24,89] In addition, in the literature examples, the

BODIPY core has been linked to cholesterol via an aliphatic chain so RCBC could be a complementary dye to study membrane viscosity.
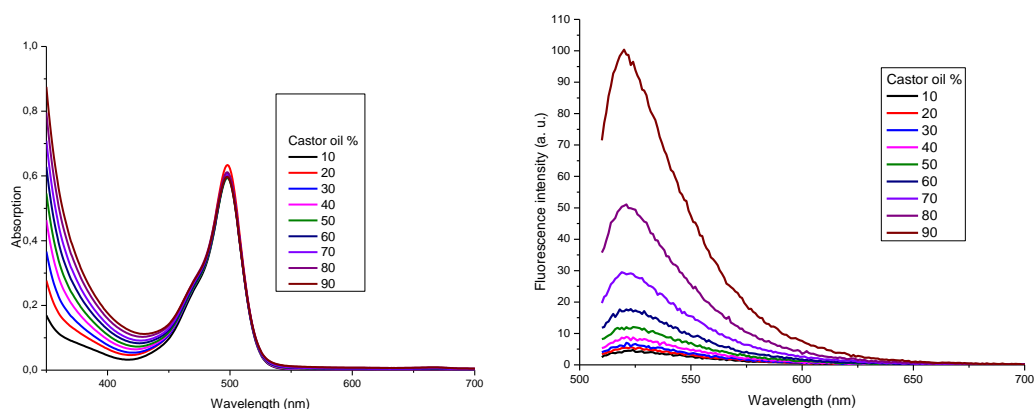
Figure 125 Absorption (left) and emission (right) spectra or RCBC in solutions of castor oil in different proportions in toluene at 10µM excitation at 500 nm, emission slit 2.5-2.5nm widths.
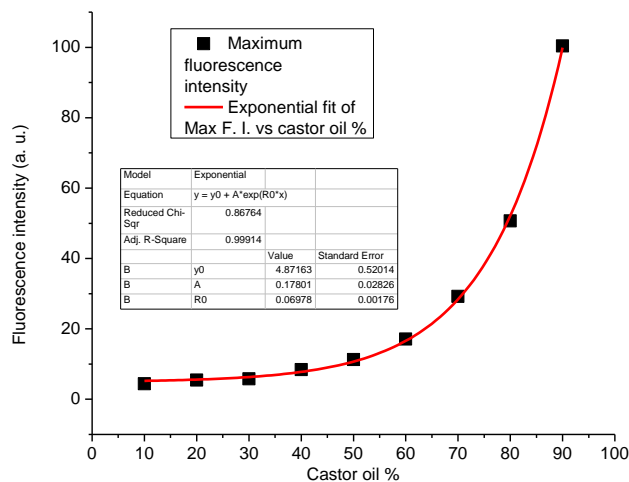
Figure 126 Maximum fluorescence intensity of RCBC at 520 nm vs castor oil percentage (black + square) and exponential fitting of the data (red). Equation of the fitting y = A1*exp(x/t1) + y0, R²=0.99857.

The lifetime of RCBC in castor oil toluene mixtures has a very complex behaviour and good reconvolution fittings were very difficult to obtain. The lifetime shows two components, which is not surprising given all the stable potential conformations in which the BODIPY and carboxyphenyl groups can be arranged. The first component, τ_1 has values between 2.2 ns and 0.6ns, and there is no clear systematic pattern as the castor oil percentages changes. The second component, τ_2, changes systematically from 13 ns to 2.5 ns as viscosity increases, but is not the

mayor component. This is reflected in the intensity weighted average lifetime which barely changes between 0.7 ns at 10% castor oil and 1.4 ns at 90% castor oil (Figure 127). The longer component, τ_2, does systematically decrease with the increase in viscosity, but it is the minor component. This behaviour is in opposition to other reported dyes in which the increase in viscosity systematically increases the lifetime.[90,91] With these results, it can be concluded that RCBC can be used exclusively as an intensity-based viscosity sensor. It would be interesting to modify the structure further with bulkier substituents in position 1 and 7 to modulate the rotation and try to produce a lifetime response to viscosity. In literature examples, another way to improve the viscosity sensitivity of BODIPYs is by increasing the electronegativity of the *meso* substituent, for example by adding nitro groups or triazine substituents.[92,93] However, following the synthetic strategy used to prepare RCBC, that cannot be easily carried out as any electron-withdrawing substituents will decrease the reactivity of the intermediate ketopyrroles as explained above.
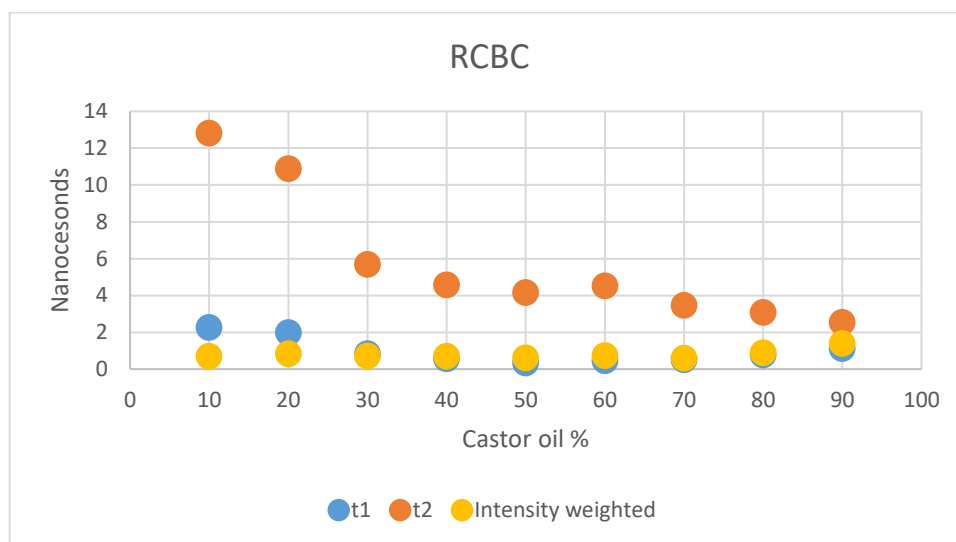
Figure 127 *Lifetime of RCBC in the castor oil toluene system at 10µM.*

5.4.1.4 Viscosity studies in methanol-glycerol.

As RCBC is a very lipophilic molecule, it is likely to distribute in regions with high lipid content in cells similar to other BODIPY-cholesterol conjugates.[24] Nonetheless, the viscosity experiment was also completed in mixtures of methanol and glycerol for comparison. The absorption shows a surprising behaviour, with minor changes in 10% to 30% glycerol (~0.5), but decreasing by slightly more than half in solutions from 40% to 60% glycerol (~1.5) and showing strong absorption changes. The absorption increases again in remains almost constant (~0.27) in solutions with 70% to 90% glycerol.

The fluorescence intensity of RCBC in methanol/glycerol mixtures shows a systematic increase from 10% to 70% and only starts decreasing in highly viscous solutions (80% glycerol and above), contrary to what was observed in the castor oil toluene system. This reduction in absorption is probably the effect of aggregation given that the dye is very lipophilic. There is a small bathochromic shift (~20 nm) going from 30% to 40% glycerol and above.
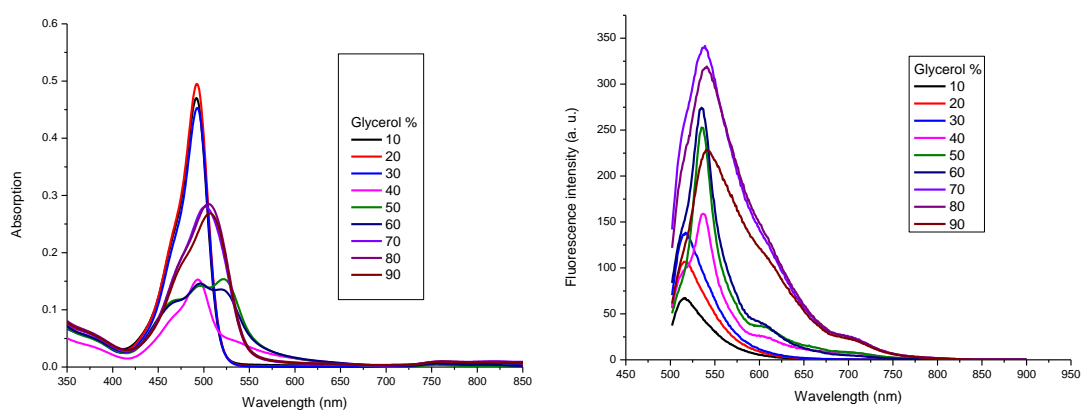
Figure 128 *Absorption (left) and emission (right) of RCBC at 10μM in solutions of methanol/glycerol in different proportions.*

Contrary to the exponential relationship between fluorescence intensity and castor oil percentage, the relationship between the fluorescence intensity and

228

glycerol percentage is complex. The relationship between fluorescence intensity and viscosity in cP is leaning towards a logarithmic function (Figure 129). In both cases 80% and 90% were not included in the calculations as the emission decreases in these solutions (this effect is likely due to both viscosity and polarity). The results of the mathematical analysis of the RCBC experiments in solution are only for comparison with the castor oil/toluene system. As explained above, the non-polar solvent is likely a better approximation of the behaviour of a lipophilic dye like RCBC in a cell environment. In fact, lipid bilayers present a dielectric constant of 2-3 whereas glycerol's is around 46.[94]
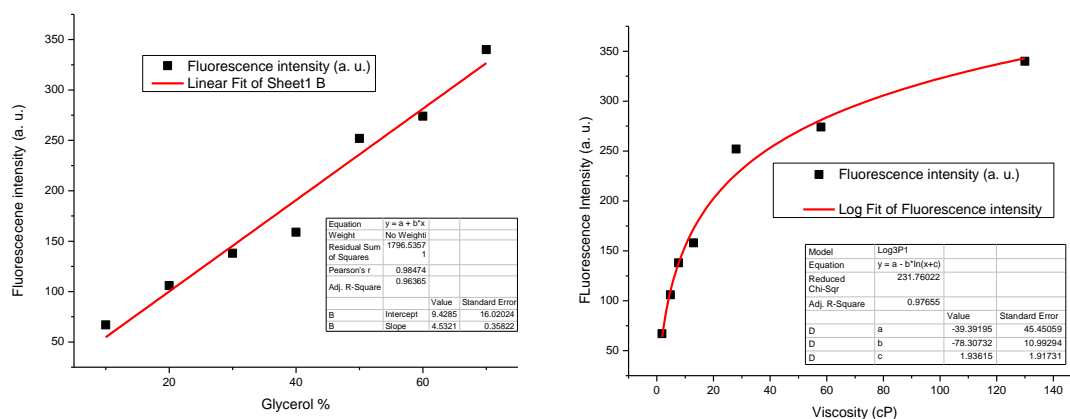
Figure 129 *(Left) Linear fitting of the fluorescence intensity vs glycerol percentage. y = a + b*x, R^2 = 0.9636. (Right) Logarithmic fitting of the fluorescence intensity vs viscosity in centipoises. y = a - b*ln(x+c), R^2 = 0.9765.*

5.4.2 Mitochondrial reporter for Raman imaging

The second custom probe targeted was a Raman reporter capable of participating in click chemistry reactions (Huisgen cycloaddition). The probe was originally aimed at reacting with 5-ethynyl-2′-deoxyuridine (EdU) after cell incubation with this nucleoside. The combination of EdU and a Raman probe is very useful for imaging of the cell nuclei. For that reason, both an azide and an alkyne group were added. The azide group will form the 1,2,3-triazole and the alkyne group will act as a Raman reporter. The alkyne group was not a terminal alkyne to avoid intermolecular reaction of the azide with the alkyne in other molecules of the same chemical species. However, before doing those experiments the Raman probe candidate was evaluated alone.

5.4.2.1 Synthesis

The full synthetic pathway for the Raman probe (RAR-BR) can be found in Figure 130. The synthesis started with the reaction of CBr_4 and PPh_3 with methyl-4-formylbenzoate to form a 1,1-dibromoalkene **15**. The palladium-catalysed reaction of this kind of substrate with terminal alkynes has been reported to yield the linear 1,3-diyne **16.1**.[95,96] However, in this case only, the 1,1-diynyl-1-alkene **16** was consistently observed and no linear alkyne was detected even when the temperature was increased to 100 °C and the reaction time extended to 16 h. The reason behind this reactivity is so far unclear as the reaction mechanism for this transformation is not fully understood. Some early literature studies of this transformation suggested that the products obtained highly depend on the phosphine ligand used. Using tri(2-furyl)phosphine yields mainly the homocoupling of the alkyne whereas using highly electron rich phosphines such as tris(4-methoxyphenyl)phosphine yields the Sonogashira cross-coupling product. In both

cases, the 1,1-diynyl-1-alkene is considered an undesirable minor product.[97] The hydrolysis step was readily completed using LiOH and the peptide coupling was done using HATU as the coupling reagent and 3-azidopropylamine as the nucleophile.
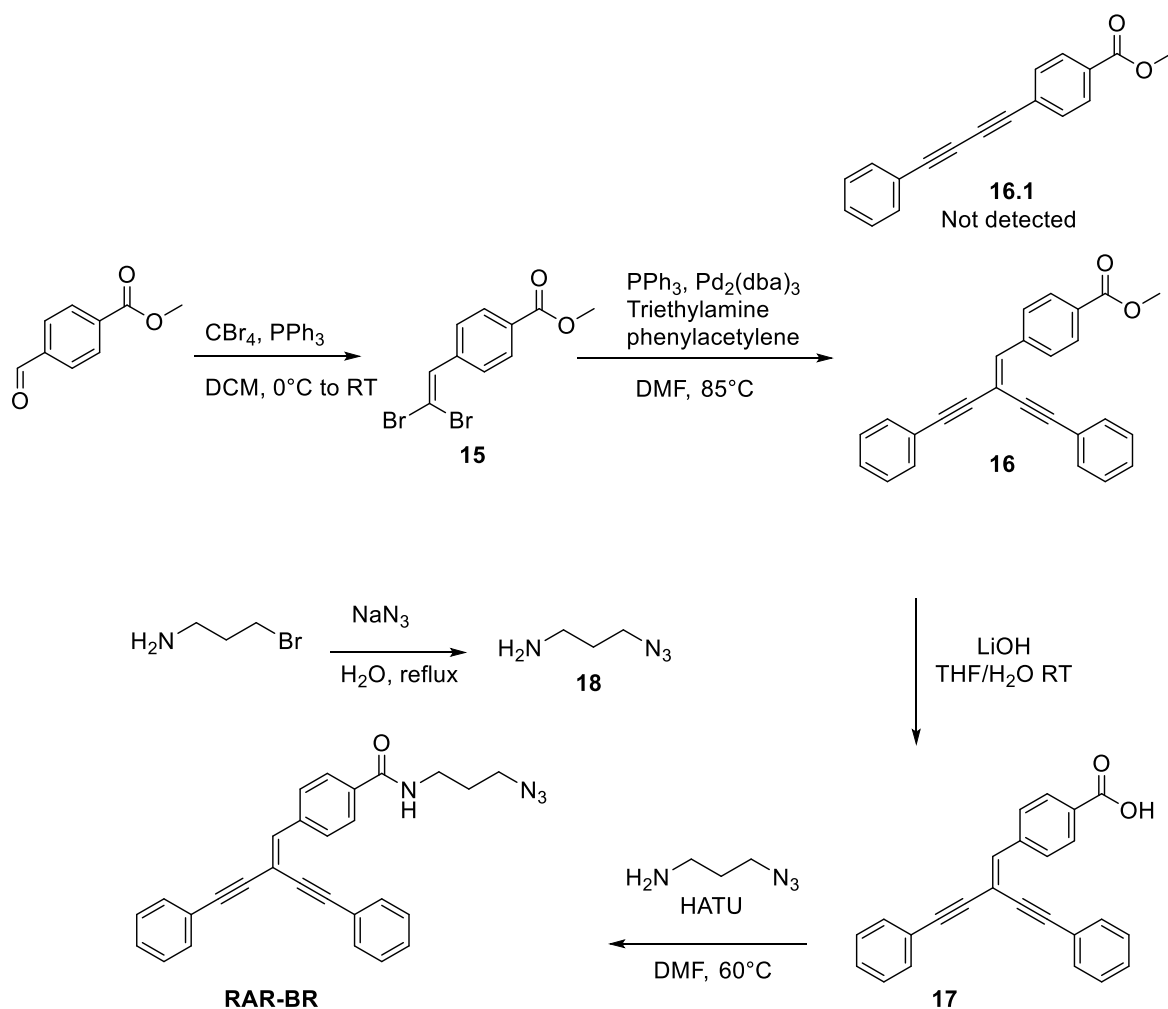
Figure 130 *Synthetic pathway to prepare RAR-BR, the Raman reporter possessing an azide and two alkyne groups.*

The NMR spectrum of the probe shows the presence of a trisubstituted double bond at 7.17 ppm and the relative integration indicates the presence of two phenyl rings corresponding to the two equivalents of phenylacetylene added to the 1,1-dibromoalkane during the palladium-catalysed coupling (Figure 131). It is important to point out that the NMR analysis of the crude product did not show any signals of the 1,3-diyne originally expected.
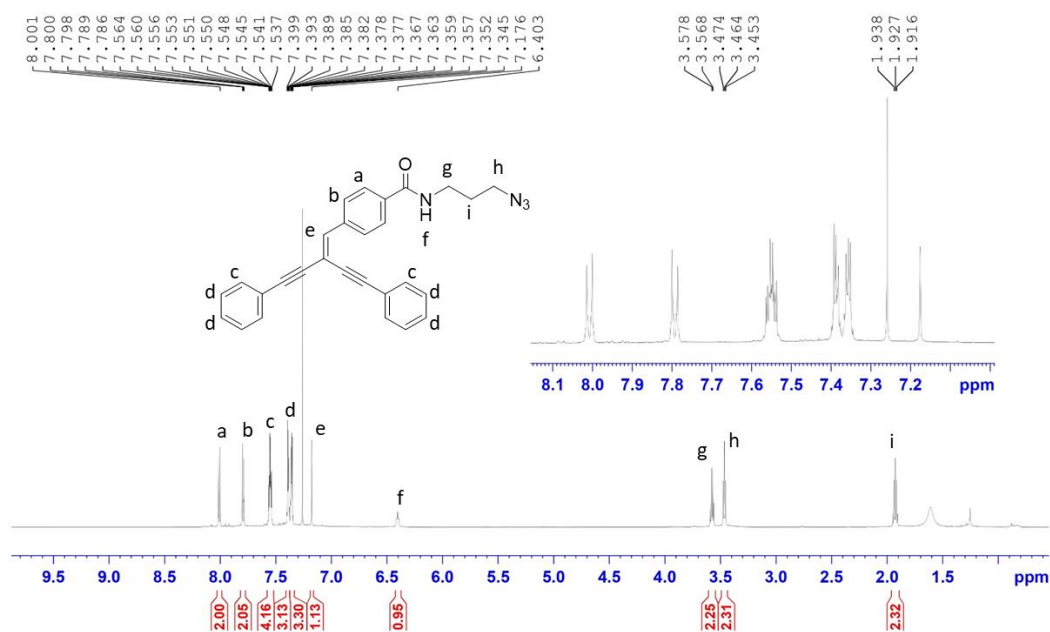
Figure 131 *^{1}H-NMR of the RCBC probe showing the assignment of every signal.*

5.4.2.2 Raman spectroscopy

The Raman spectroscopical characterisation in cells was completed by Anna Pieczara from the Jagiellonian Centre for Experimental Therapeutics (JCET), Jagiellonian University. The cells used were Human Aortic Endothelial Cells (HAEC).

The Raman profile of RAR-BR was first characterised to see whether it might be a suitable Raman marker. The Raman spectra of RAR-BR in DMSO is shown in Figure 132 (a), it shows two intense bands at 2212 cm^{-1} and 2198 cm^{-1}, corresponding to two non-conjugated Csp-Csp bonds. The commercially available probe used for comparison was MitoBADY. This commercial probe has a characteristic Raman band at 2220 cm^{-1}.

In the same concentrations (50, 100, 400 nM) RAR-BR showed a higher intensity than MitoBADY; consequently our novel probe showed better signal to

noise ratio than the standard, and improved the quality of the imaging as shown in Figure 132 (b). The analysis of both probes in a 1 µM solution of DMSO indicated a higher Raman cross section for the standard (MitoBADY) than for RAR-BR. This piece of evidence suggests that the superiority of RAR-BR over MitoBADY comes from a better mitochondrial selectivity rather than a higher cross-section.
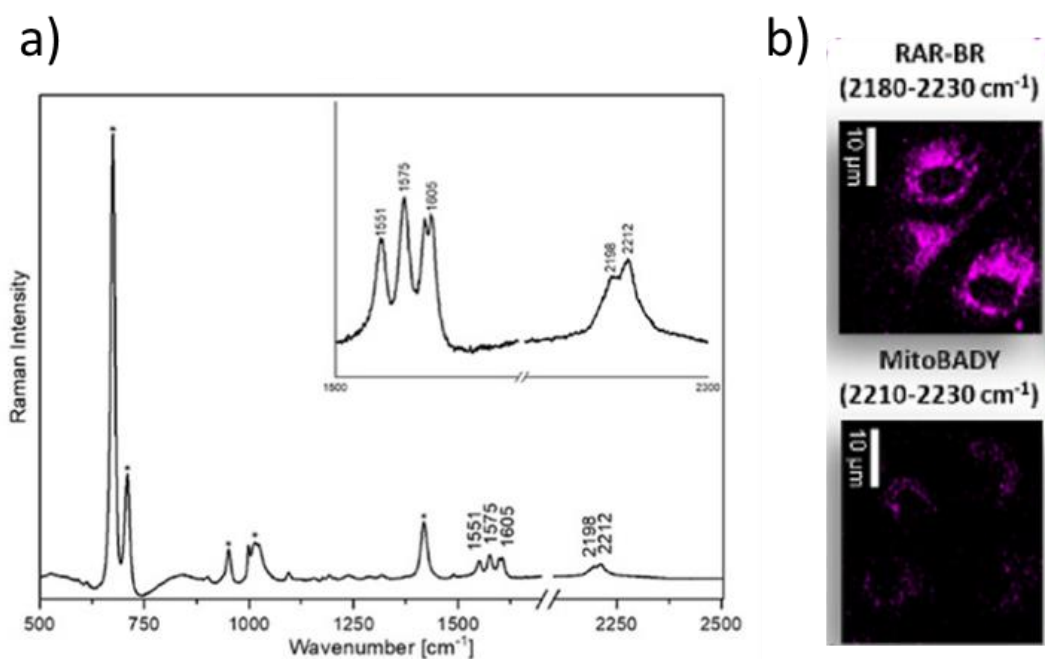
Figure 132 (a) Raman spectra of RAR-BR in DMSO. (b) Comparison of the Raman imaging using RAR-BR and MitoBADY at 400 µM with 30 minutes of incubation time. Image courtesy of Anna Pieczara.

The specificity of the probe for mitochondia was determined by incubating the HAEC with MitoSpy™ and MitoTracker™, two mitochondria-targeting dyes commercially available, and RAR-BR. After a short incubation time (30 min), fluorescence imaging was performed. The results show a high selectivity of RAR-BR for these mitochondria (Figure 133).
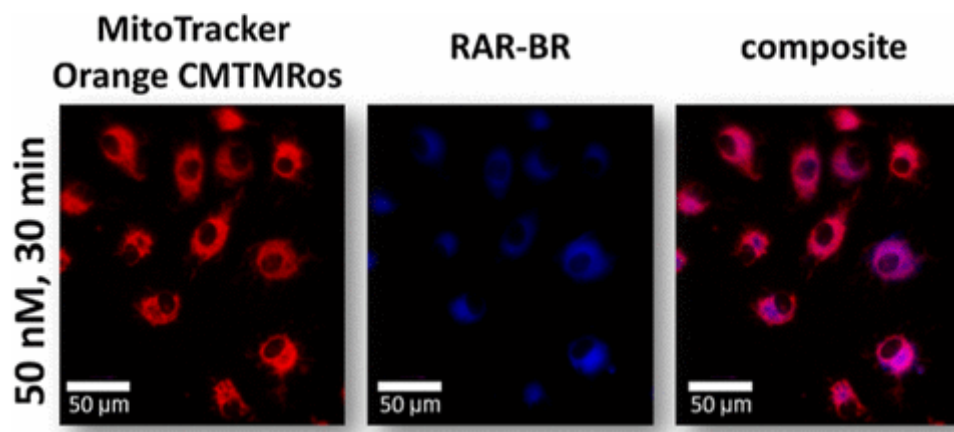
Figure 133 *Fluorescence imaging of live HAEC incubated with MitoTracker™ MitoSpy™ and RAR-BR at 50 nM for 30 min. Images were collected with a 40X objective. Image courtesy of Anna Pieczara.*

The results obtained in this project are very promising and they have been peer-reviewed and published.[98]

5.4.3 NO sensors

The third sensor prepared in this chapter was an NO sensor. As explain in the introduction NO plays a key role in the vascular function. The combination of a NO sensor and other functional dyes developed in this thesis was the final goal of the LogicLab project.

5.4.3.1 Synthesis

To prepare the NO sensor, two features were considered. First, the sensing unit chosen was an aromatic 1,2-diamine, as this motif is easy to synthesise and it has been extensively used for NO sensing.[99–102] The only inconvenience of this sensing moiety is that it is redox active, so stability might be a challenge.[103] The second aspect in the design of the NO probe was the introduction of a fluorophore capable of working as the annihilator in a TTA up-converting system. For that reason, perylene was used as the fluorophore. The idea behind this combination was preparing an up-converting system capable of sensing NO. In an ideal scenario, the combination of a TTA-UC sensitizer and the sensor will not produce an up-converted signal in the absence of NO. The up-converted photons would be observed only once the sensor has reacted with NO and becomes a perylene benzotriazole (Figure 134).

Sensitizer   **Sensor**   NO, O₂   **Annihilator**   **Sensitizer**

Unreacted sensor = absence of TTA-UC

Activation of TTA-UC after reaction of the sensor with NO.
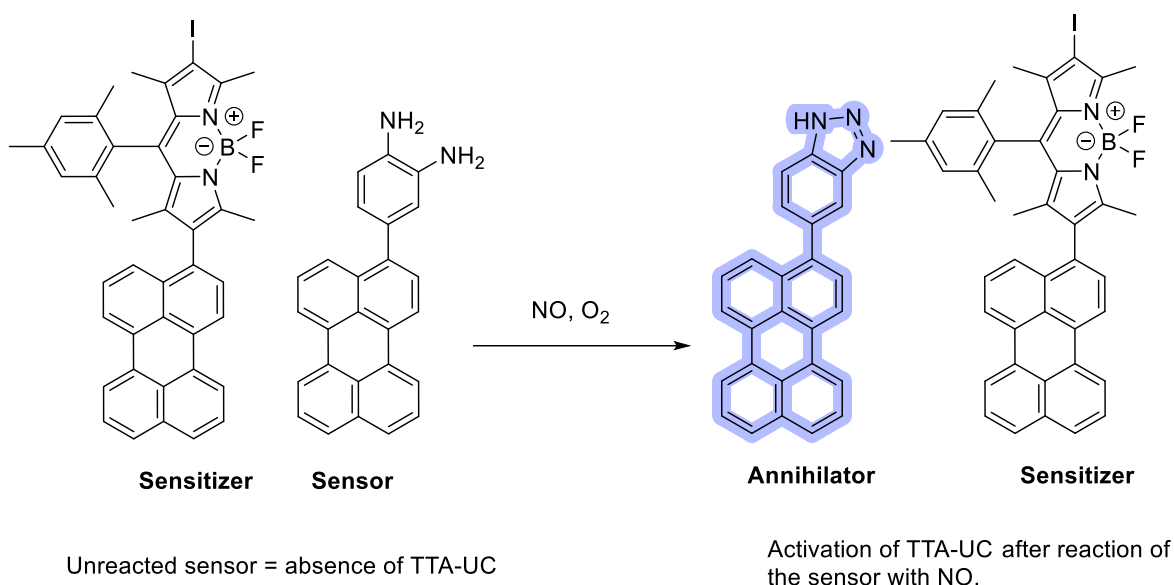
Figure 134 Rational behind NO sensing via TTA-UC using a diaminophenil perylene as the sensor/annnihilator and a BODIPY-perylene derivative as the sensitizer.

The synthesis of the NO sensor is described in Figure 135. The first step consisted of the protection of 4-bromodiaminobenzene with *t*-butoxycarbonyl (BOC) protecting groups. The reaction of this molecule with 3-perylene boronic acid pinacol ester yielded a product in moderate yield (35-44%), and the chromatographic separation was carried out using chloroform and cyclohexane as mobile phase. However, given the low stability of the perylene boronate explained in Chapters 2 and 3, an alternative synthetic approach was envisaged. The protected 4-bromodiaminobenzene was borylated under Miyaura conditions. This reaction consumed all the starting material and there was no need for chromatographic purification. The Suzuki-Miyaura cross-coupling reaction was performed in refluxing dioxane, and the yield obtained was higher than in the first approach (57-64%). The cleavage of the BOC groups was readily accomplished with TFA in dichloromethane. The final product was protected from light and stored at 4 °C to avoid degradation.
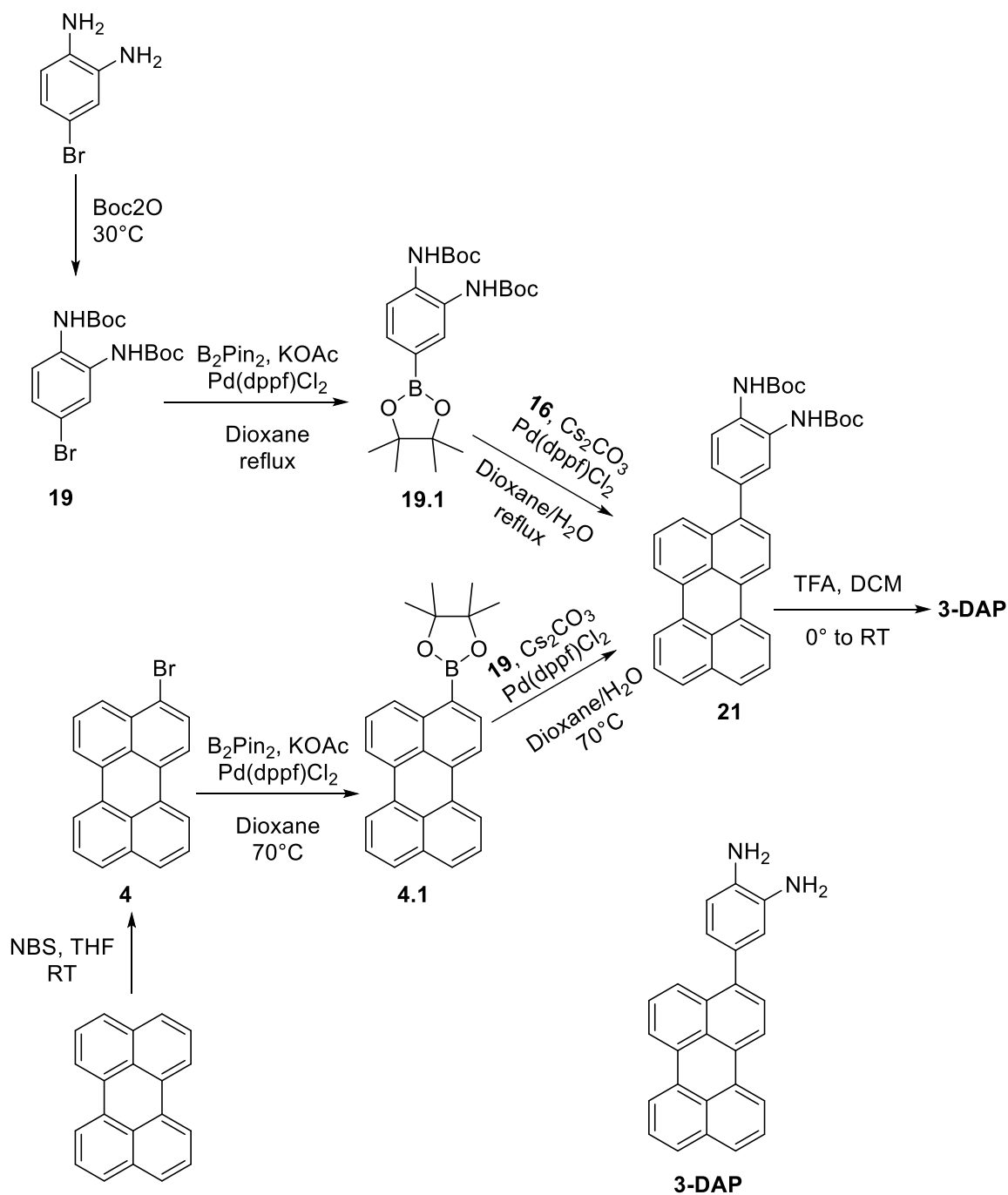
Figure 135 *Synthetic strategies applied to prepare 3-DAP, a potential NO sensor.*

5.4.3.2 Proof of concept

Preliminary capacity of 3-DAP to act as an NO sensor was tested in solution by Dr. Amrutha Prabhakaran. Thus, 3-DAP was dissolved in chloroform with increasing concentrations of diethylamino NONOate, an NO donor. As shown in Figure 136, the emission was observed to increase as the NONOate concentration

increases. However, the change in fluorescence intensity across the range of concentrations explored was modest and suggests that the dynamic range of the sensor is likely not large enough to use 3-DAP an intensity-based sensor. In addition, 3-DAP is already a very fluorescent molecule. A good sensor should be barely emissive until it meets the analyte.

Using 3-DAP as an intensity-based sensor present some challenges that could be addressed by the integration of the sensor in up-converted systems. However, assays using 3-DAP as an annihilator paired with any of the sensitizers prepared in Chapter 2 show that there is no up-conversion in the absence of nitric oxide.
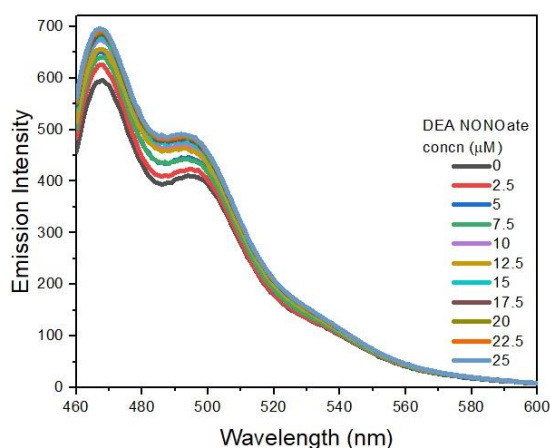
Figure 136 *Emission spectra of 3-DAP in chloroform with increasing concentrations diethylamine NONOate. Excitation at 450 nm, emission slit widths 2.5-5 nm.*

The reaction of NO with 3-DAP yields a triazole following the mechanism in Figure 137. As observed, the sensing reaction involves three different molecules, the sensor, nitric oxide, and molecular oxygen. This is a severe limitation, not only to 3-DAP, but to other sensors following the same mechanism, as any changes in the availability of any of the substrates will have an impact on the measurement.
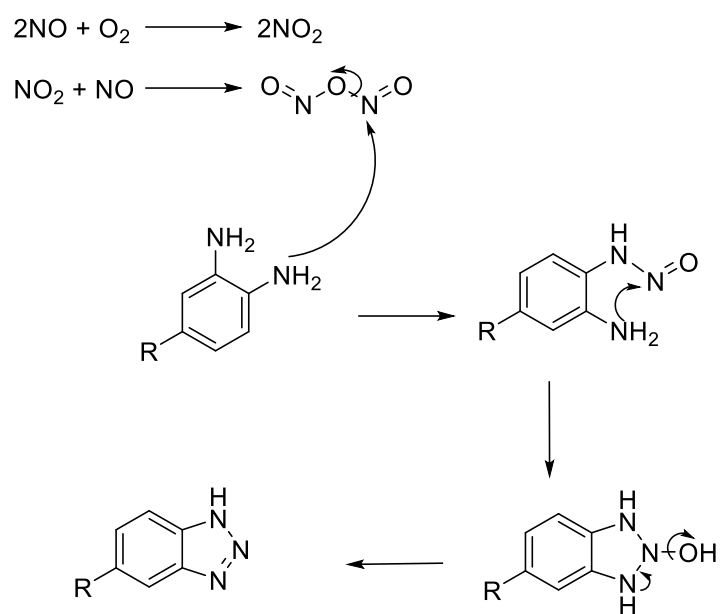
Figure 137 *Reaction mechanism of the NO sensing by vicinal diamino moieties.*

Experiments in liposomes and in cells are currently underway.

5.5 Conclusions

In this chapter three novel sensor molecules were developed as part of the collaborative programme in LogicLab for direct sensing or cell imaging probes or for integration into novel TTA-UC sensors. Firstly, a BODIPY-cholesterol dye, RCBC, was designed and prepared. Single crystals were grown, and the structure elucidated by X-ray diffraction. The photophysical properties of RCBC were studied in a non-polar castor oil toluene system. The results show an exponential relationship between castor oil percentage and fluorescence intensity. The intensity weighted lifetime of the dye, however, does not change systematically as the viscosity increases. Consequently, RCBC can be used only as an intensity-based sensor, which has limitations in the context of complex environments.

Secondly, a novel mitochondria-targeting Raman probe was designed and prepared, for intracellular mapping of mitochondrial function, RAR-BR. The molecule possesses two geminal triplet bonds that have Raman active bands in the silent region of the spectra. The high mitochondrial selectivity was determined by co-staining with commercially available dyes. The dye was found to have a higher preference to accumulate in mitochondria than the commercial Raman standard (MitoBADY). At the same concentrations, RAR-BR was found to be a brighter probe than the standard, increasing the quality of the imaging.

Finally, a potential nitric oxide sensor and annihilator for TTA-UC, 3-DAP, was prepared. The sensor included a 1,2-diaminophenyl moiety as the sensing unit attached to perylene. The capacity of the sensor to react with NO was observed in solution, but the molecule was found to be very fluorescent even in the absence of the analyte. This characteristic makes the sensor difficult to use in classical

fluorescence imaging. However, given that perylene is the fluorophore carrying the sensing moiety, 3-DAP could be used as an annihilator in TTA-UC sensing systems.

5.6 Experimental section

5.6.1 Synthesis of RCBC

Synthesis of **11.** In a 250 mL round bottom flask, 5 g of methyl 4-chlorocarbonyl benzoate (25.18 mmol) were dissolved in 50 mL of diethyl ether and cooled to 0°C in an ice water bath. Then, 3.5 mL of triethylamine (25 mmol. 1 eq.) and 2.2 mL of morpholine (25 mmol 1 eq.) were added dropwise. The reaction was stirred at room temperature overnight. The reaction was vacuum-filtered to remove triethylammonium chloride. The solids were rinsed with 300 mL of diethyl ether. The combined filtrate was concentrated under vacuum, washed in a separatory funnel with a saturated aqueous solution of ammonium chloride and then with a saturated aqueous solution of sodium carbonate. The organic phase was dried over magnesium sulphate and the solvent was evaporated under vacuum to yield an off-white solid in 95% yield. ^{1}H-NMR (600 MHz, DMSO-d$_6$) δ (ppm) 8.02-8.01 (m, 2H), 7.56-7.55 (m, 2H), 3.87 (s, 3H), 3.65-3.63 (d, 4H), 3.53, (s, 2H), 3.28 (s, 2H).

Synthesis of **12**. In a 50 mL round bottom flask, 1.5 g of **11** (6 mmol) were dissolved in 1.28 mL of POCl$_3$ (13.7 mmol, 2.3 eq.) at 40 °C. After dissolution, pyrrole (0.5 mL, 7 mmol, 1.2 eq.) were added to the flask dissolved in 10 mL of dichloroethane. The mixture was refluxed for 3 hours. The reaction was cooled to room temperature and quenched with a saturated aqueous solution of sodium carbonate (10 mL). Further solid sodium carbonate was added until the pH of the reaction was slightly basic (pH~8). The reaction was extracted with dichloromethane, the organic phases were combined, dried over magnesium

sulphate, and evaporated under vacuum. The product was purified by column chromatography using hexane/EtAcO (8:2), and the product was obtained as a red solid in 48 % yield.

^{1}H-NMR (600 MHz, CDCl$_3$) δ (ppm) 9.65 (br, 1H), 8.12-8.14(m, 2H), 7.94-7.93 (m, 2H), 7.18-7.17 (m, 1H), 6.87-6.86 (m, 1H), 6.37-6.36 (m, 1H), 3.97 (s, 3H). ^{13}C-NMR (150 MHz, CDCl$_3$), δ (ppm) 183.2, 166.2, 143.0, 132.2, 130.7, 129.7, 129.3, 127.6, 120.5, 111.1, 52.89.

Synthesis of **13**. In a 50 mL round bottom flask, 1.06 g (4.62 mmol) of **12** were dissolved in 8 mL of THF, lithium hydroxide monohydrate (970 mg, 23 mmol, 5 eq.) was dissolved in 2 mL of water and added to flask. The reaction was refluxed for 3 hours. The solution was cooled to room temperature and 20 mL of 1 M hydrochloric acid were added and the whole solution was poured onto ice. The precipitate was vacuum filtered and dried. The product was an off-white solid, the yield was quantitative, and no further purification was required.^{1}H-NMR (600 MHz, DMSO), δ (ppm) 13.24 (br s, 1H), 12.15 (s, 1H), 8.05-7.89 (m, 4H), 7.26 (m, 1H), 6.80 (m, 1H), 6.28 (m, 1H). ^{13}C-NMR (600 MHz, DMSO-d6), δ (ppm) 183.4, 167.2, 142.6, 133.7, 130.9(2C), 129.8(2C), 129.1, 127.5, 120.4, 111.0.

Synthesis of **14**. In a 50 mL round bottom flask, 400 mg of **13** (1.86 mmol) were dissolved in 10 mL of dichloroethane. 229 µL of 2,4-dimethylpyrrole (2.23 mmol, 1.2 eq.) were added and the reaction was refluxed for 3 hours adding 0.5 equivalents of 2,4-dimethylpyrrole every hour. The reaction was cooled to room temperature and 2 mL of triethylamine (15 mmol, 8 eq.) and 1.9 mL of BF$_3$ etherate (14.9 mmol, 8 eq.) were added. The reaction proceeded at room temperature overnight. Volatiles were removed under vacuum and the product was purified by column chromatography on silica gel using EtAcO:DCM (8:2) with 0.5% acetic acid. The

product was obtained as an orange solid in 27% yield. ^{1}H-NMR (600 MHz, DMSO-d6) δ (ppm) 13.28 (s, 1H), 8.11-8.09 (m, 2H), 7.78 (s, 1H), 7.62 (m, 2H), 6.45 (m, 2H), 6.39 (m, 2H), 2.56 (s, 3H), 1.51 (s, 3H). ^{13}C-NMR (150 MHz, DMSO-d_6) δ (ppm) 163.8, 159.7, 143.9, 138.9, 136.0, 134.4, 130.5, 129.6, 128.8, 126.5, 126.1, 123.6, 121.0, 113.6, 11.8, 11.7.

Synthesis of **RCBC**. In a 50 mL round bottom flask, 100 mg of **14** (0.294 mmol) and 136 mg of DCC (0.352 mmol, 1.2 eq.) were dissolved in 10 mL of DCM. After 30 min, 5.5 mg of DMAP (0.044 mmol, 0.15 eq.) and added and the reaction was stirred at RT for 1 hour. 182 mg of cholesterol (0.882 mmol, 3 eq.) were added, and the reaction was tarried at room temperature overnight. Solvents were evaporated under vacuum and the product was purified by column chromatography on silica gel using hexane/ethyl acetate (8:2). RCBC was isolated as a red solid in 77% yield. ^{1}H-NMR (600 MHz, CDCl3) δ (ppm) , 8.16 (d, J = 8.0 Hz, 2H), 7.68 (s, 1H), 7.44 (d, J = 8.0 Hz, 2H), 6.38-6.35 (m, 1H), 6.34-6.32 (m, 1H), 6.14 (s, 1H), 5.43 (d, J = 5 Hz, 1H), 4.94-4.86 (m, 1H), 2.62 (s, 3H), 2.49 (d, J = 8 Hz, 2H), 2.06-0.96 (br, m, 32H), 0.91 (d, J = 6.5 Hz, 3H), 0.86 (dd, J = 2.5, 6.5 Hz, 6H) 0.69 (s, 3H). ^{13}C-NMR (150 MHz, DMSO-d_6) δ (ppm) 165.4, 162.9, 147.0, 142.1, 139.7, 139.2, 138.6, 134.4, 133.4, 132.0, 129.8, 129.0, 127.0, 123.6, 123.1, 116.5, 75.3, 56.9, 56.3, 50.2, 42.5, 39.9, 39.7, 38.4, 37.2, 36.8, 36.3, 35.9, 32.1, 32.05, 28.4, 28.2, 28.1, 24.5, 24.0, 23.0, 22.7, 21.2, 19.5, 18.9, 15.4, 15.3,12.0. HR-MS (ESI) calculated for $C_{45}H_{58}BF_2N_2O_2$ (M-H): 707.4565, found: 707.4508, calculated for $C_{45}H_{59}BF_2N_2NaO_2$ (M+Na): 731.4530, found: 731.4461.

5.6.2 Synthesis of RAR-BR

Methyl 4-(2,2-dibromovinyl)benzoate (15). In a 100 mL round-bottom flask, carbon tetrabromide (2.02 g, 6.09mmol, 1 eq.) was dissolved in DCM and the solution cooled to 0 °C in an ice-water bath. Triphenylphosphine (3.20 g, 12.18 mmol, 2 eq.) was added slowly and the solution stirred for 20 minutes at that temperature. Methyl-4-formylbenzoate dissolved in 20 mL of DCM was then added slowly to the reaction mixture. The ice-water bath was removed, and the solution was stirred for 4 hours and allowed to reach room temperature. The solvent was evaporated, and the product purified by column chromatography using silica gel and cyclohexane:ethyl acetate (8:2) to afford **2** as a white solid in 74% yield. ^{1}H-NMR (600MHz, CDCl$_3$) δ ppm 8.03 (d, J = 8.0, 2H), 7.59 (d, J = 8.0, 2H), 7.52 (s, 1H), 3.92, (s, 3H).

Methyl 4-(4-phenyl-2-(phenylethynyl)but-1-en-3-yn-1-yl)benzoate (16). In a sealed tube, 856 mg of **1** (2.68 mmol) was dissolved in 3 mL of dry DMF, phenylacetylene (441 μL, 4.01 mmol, 1.5 eq.), triethylamine (1.12 mL, 8.08 mmol, 3 eq.), triphenylphosphine (28 mg, 0.1 mmol, 0.04 eq.), and Pd$_2$(dba)$_3$ (25 mg, 0.026 mmol, 0.01 eq.) were added. The mixture was stirred at 85 °C for 4 hours. After cooling to room temperature, the solution was diluted with ethyl acetate and washed with diluted hydrochloric acid (1M, 3 x 30 mL) and then with sodium hydroxide (1M, 3x 30 mL). The combined organic fractions were dried over magnesium sulphate and the solvent evaporate under vacuum. Then, 3 portions of 30 mL of heptane were added to fully remove DMF. The product was purified by column chromatography using silica gel and EtOAc:Cyclohexane (8:2 V/V) to afford **3** as a yellow solid in 67% yield. ^{1}H-NMR (600MHz, CDCl$_3$) δ ppm 8.06 (d, J = 8.5, 2H), 8.00 (d, J = 8.5, 2H), 7.58-7.52 (m, 4H), 7.41-7.37 (m, 3H), 7.37-7.33 (m, 3H), 7.18

(s, 1H), 3.93 (s, 3H). ^{13}C-NMR (150 MHz, CDCl$_3$) δ ppm 166.6, 141.5, 139.9, 131.8, 131.7, 130.0, 129.6, 129.1, 128.8, 128.7, 128.5, 128.3, 122.6, 122.5, 105.8, 95.6, 89.4, 88.9, 86.6, 52.1.

4-(4-phenyl-2-(phenylethynyl)but-1-en-3-yn-1-yl)benzoic acid (17). In a 50 mL round-bottom flask, 338 mg of 3 (0.932 mmol) were dissolved in 10 mL of THF. Lithium hydroxide monohydrate (78.27 mg, 1.87 mmol, 2 eq.) was dissolved in 1 mL of water and was added to the flask. The reaction was stirred at room temperature for 3 hours. The solution was acidified with HCl until pH 3 and poured onto ice. The product precipitated as a light-yellow solid and was filtered under vacuum. Intermediate **4** was obtained in quantitative yield and was pure enough to be used without purification in the next step. ^{1}H-NMR (600MHz, DMSO-d$_6$) δ ppm 13.09 (s, 1H), 8.10 (d, J = 8.5, 2H), 8.03 (d, J = 8.5, 2H), 7.66-7.622 (m, 2H), 7.60-7.56 (m, 2H), 7.51-7.43 (m, 7H).

3-azidopropan-1-amine (18). In a 100 mL round-bottom flask, 3-bromopropylamine hydrobromide (2 g, 9.14 mmol) was dissolved in 10 mL of water, sodium azide (2.97 g, 45.7 mmol, 5 eq.) was dissolved in 15 mL of water and added to the flask. The resulting solution was refluxed for 16 hours. The solution was allowed to cool to room temperature, 30 mL of a 1 M potassium hydroxide solution was added, and the solution was then transferred to a separatory funnel and extracted with diethyl ether (3 x 30 mL). The combined organic layers were dried over magnesium sulphate and the solvent evaporated to afford **18** as a viscous yellow oil in 89% yield. ^{1}H-NMR (600MHz, CDCl$_3$) δ ppm 3.37 (t, J = 7 Hz, 2H), 2.80 (t, J = & Hz, 2H), 1.72 (p, J = 7 Hz, 2H), 1.17 (br, 2H).

N-(3-azidopropyl)-4-(4-phenyl-2-(phenylethynyl)but-1-en-3-yn-1-yl)benzamide (RAR-BR). In a 25 mL Schlenk flask, 147 mg of **4** (0.421 mmol), 241

mg of HATU (0.532 mmol, 1.5 eq.), 106 mg of **1** (1.05 mmol, 2.5 eq.) and 3 drops of triethylamine were dissolved in 3 mL of DMF. The mixture was heated at 60 °C for 16 hours under inert atmosphere. The solvent was evaporated with heptane under vacuum and the product was purified by column chromatography using silica gel and cyclohexane:EtOAc (6:4) to afford a yellow solid in 71 %yield. ^{1}H-NMR (600MHz, CDCl$_3$) δ ppm 8.00 (d, J = 8.5, 2H), 7.79 (d, J = 8.5, 2H), 7.57-7.52 (m, 4H), 7.40-7.37 (m, 3H), 7.37-7.33 (m, 3H), 7.17 (s, 1H), 6.40 (s, 1H), 3.57(q, J = 6.5, 2H), 3.46 (t, J = 6.5, 2H), 1.92 (p, J = 6.5, 2H). ^{13}C-NMR (150 MHz, CDCl$_3$) δ ppm 167.1, 141.6, 138.9, 134.3, 131.9, 131.8, 129.2, 129.2, 128.8, 128.7, 128.5, 127.1, 122.8, 122.7, 105.5, 95.6, 89.5, 89.0, 86.7, 49.8, 38.0, 28.9. HR-MS (ESI) m/z: calculated for C$_{28}$H$_{23}$N$_4$O 431.1871 found 431.1816.

5.6.3 Synthesis of 3-DAP

3-Bromoperylene (4). Perylene (1 g, 3.86 mmol) was suspended in 50 mL of THF, 706 mg of freshly recrystallized NBS (3.96 mmol, 1 eq.) were added and the reaction stirred for 24 hours at room temperature. The solvent was evaporated, and the product was triturated in hot methanol (50 mL) for 1 hour to remove succinimide. The product was allowed to cool to room temperature, vacuum-filtered and was pure enough to be used as such without removing unreacted perylene.

Di-tert-butyl (4-(perylen-3-yl)-1,2-phenylene)dicarbamate (21). The compounds 3-bromoperylene (230 mg, 0.7 mmol), caesium carbonate (669 mg, 2.08 mmol, 3 eq.), di-tert-butyl(4-(4,4,5,5-tetramethyl-1,3,2-dioxaborolan-2-yl)-1,2-phenylene) dicarbamate (**19**) (362 mg, 0.83 mmol, 1.2 eq.) and Pd(dppf)Cl$_2$ (25 mg, 0.05 eq.) were refluxed in 10 mL of a dioxane/water mixture (9:1) for 16 hours. The solvent was evaporated under vacuum and the product was purified by column

chromatography using chloroform/cyclohexane (50/50) to yield a yellow solid in 68% yield.

^{1}H-NMR (CDCl$_3$, 600 MHz): δ (ppm) 8.25-8.11 (m, 4H), 7.77 (d, J = 8.0 Hz, 1H), 7.67 (d, J = 8.0 Hz, 2H), 7.66-7.62 (broad, 1H) 7.62-7.55 (broad, 1H), 7.47 (t, J = 8.0 Hz, 2H), 7.43-7.37 (m, 2H), 7.32-7.27 (m, 1H), 6.93 (broad, NH), 6.78 (broad, NH), 1.55 (s, 9H), 1.52 (s, 9H). 154.0. ^{13}C-NMR (CDCl$_3$, 150MHz): δ (ppm) 139.1, 138.0, 134.8, 133.0, 131.6, 131.5, 131.4, 130.8, 130.0, 129.1, 128.8, 127.91, 127.88, 127.3, 126.74, 126.69, 126.2, 125.9, 124.3, 120.49, 120.46, 120.3, 120.0, 81.2, 81.1, 28.5, 28.4. MS-ESI calculated for C$_{36}$H$_{35}$N$_2$O$_4$ [M+H] = 559.2596 found = 559.2591. Calculated for C$_{36}$H$_{34}$N$_2$NaO$_4$ [M+Na]+ = 581.2416 found 581.2411.

4-(perylen-3-yl)benzene-1,2-diamine (3-DAP). 210 mg of **21** were dissolved in 5 mL of dichloromethane at 0 °C, and 5 mL of trifluoroacetic acid were added dropwise and the solution stirred overnight at room temperature. The reaction was quenched with 30 mL of a saturated aqueous solution of sodium carbonate. The product was extracted with THF. The combined organic layers were dried over magnesium sulphate and evaporated under vacuum. The product was triturated in hot ethyl acetate for 15 minutes and then filtered to afford **3-DAP** as a dark yellow solid in 74% yield. ^{1}H-NMR (DMSO-d$_6$, 600 MHz): δ (ppm) 8.38-8.31 (m, 4H), 7.89 (d, J^β = 8.0 Hz, 1H), 7.77 (t, J = 9 Hz, 2H), 7.54 (td, J = 8.0, 1.5 Hz, 2H), 7.49 (t, J = 8 Hz, 1H), 7.35 (d, J = 7.5 Hz, 1H), 6.69 (d, J = 2.0 Hz, 1H), 6.65 (d, J = 8 Hz, 1H), 6.59 (dd, J = 8.0, 2.0 Hz, 1H), 4.67 (br, NH$_2$), 4.62 (br, NH$_2$). ^{13}C-NMR (DMSO-d$_6$, 150 MHz): δ (ppm) 134.9, 134.8, 134.3, 132.5, 130.84, 130.76, 130.6, 128.6, 128.5, 128.4, 127.9, 127.8, 127.4, 127.2, 127.01, 126.96, 126.9, 126.4, 120.7, 120.62, 120.57, 120.2, 118.8, 115.7, 114.28, 114.25. ESI-MS calculated for C$_{26}$H$_{19}$N$_2$ [M+H] = 359.1548, found = 359.1542.

5.7 References

[1]   P. L. Yeagle, in *The Membranes of Cells*, Elsevier, Berkeley. **2016**, pp. 1–25.

[2]   B. Alberts, Ed., *Mol. Biol. Cell.*, Garland Science, New York, **2002**.

[3]   J. Zhang, Q. Li, Y. Wu, D. Wang, L. Xu, Y. Zhang, S. Wang, T. Wang, F. Liu, M. Y. Zaky, S. Hou, S. Liu, K. Zou, H. Lei, L. Zou, Y. Zhang, H. Liu, *Cell. Commun. Signal.* **2019**, *17*, 15.

[4]   S. J. Singer, G. L. Nicolson, *Science* **1972**, *175*, 720–731.

[5]   K. Simons, R. Ehehalt, *J. Clin. Invest.* **2002**, *110*, 597–603.

[6]   L. Anchisi, S. Dessì, A. Pani, A. Mandas, *Front. Physio.* **2013**, *3*.

[7]   R. M. Zamora-Prieto, J. F. Maldonado-Serrano, W. González-Calderón, *Heliyon* **2023**, *9*, e21924.

[8]   W. Zhang, Y. Huang, X. Guo, M. Zhang, X. Yuan, H. Zu, *Acta Neuropathol. Commun.* **2023**, *11*, 102.

[9]   K. Reemst, J. Y. Broos, M. R. Abbink, C. Cimetti, M. Giera, G. Kooij, A. Korosi, *Front. Immunol.* **2022**, *13*, 967437.

[10]   P. Scheiffele, A. Rietveld, T. Wilk, K. Simons, *J. Biol. Chem.* **1999**, *274*, 2038–2044.

[11]   A. Petrich, S. Chiantia, *Viruses* **2023**, *15*, 1830.

[12]   P. Raut, B. Obeng, H. Waters, J. Zimmerberg, J. A. Gosse, S. T. Hess, *Viruses* **2022**, *14*, 2509.

[13]   A. M. Abdel-Megied, I. A. Monreal, L. Zhao, A. Apfel, H. C. Aguilar, J. W. Jones, *Anal. Bioanal. Chem.* **2023**, *415*, 5269–5279.

[14]   J. Zhang, A. Pekosz, R. A. Lamb, *J. Virol.* **2000**, *74*, 4634–4644.

[15]   C. Jin, B. Che, Z. Guo, C. Li, Y. Liu, W. Wu, S. Wang, D. Li, Z. Cui, M. Liang, *Biosaf. Health.* **2020**, *2*, 25–31.

[16]   Z. Liao, L. M. Cimakasky, R. Hampton, D. H. Nguyen, J. E. K. Hildreth, *AIDS Res. Hum.Retrov.* **2001**, *17*, 1009–1019.

[17]   Y. J. Gee, Y. L. Sea, S. K. Lal, *Rev. Med. Virol.* **2023**, *33*, e2413.

[18]   L. A. Bagatoll, T. Parasassi, G. D. Fidelio, E. Gratton, *Photochem. Photobiol.***1999**, *70*, 557–564.

[19]   H.-J. Kaiser, D. Lingwood, I. Levental, J. L. Sampaio, L. Kalvodova, L. Rajendran, K. Simons, *Proc. Natl. Acad. Sci. U.S.A.* **2009**, *106*, 16645–16650.

[20]   K. Gaus, T. Zech, T. Harder, *Mol. Membr. Biol.* **2006**, *23*, 41–48.

[21]   T. Parasassi, G. De Stasio, A. d'Ubaldo, E. Gratton, *Biophys. J.* **1990**, *57*, 1179–1186.

[22]   M. Hölttä-Vuori, R. Uronen, J. Repakova, E. Salonen, I. Vattulainen, P. Panula, Z. Li, R. Bittman, E. Ikonen, *Traffic* **2008**, *9*, 1839–1849.

[23]   D. Wüstner, L. Solanko, E. Sokol, O. Garvik, Z. Li, R. Bittman, T. Korte, A. Herrmann, *Chem. Phys. Lipids.* **2011**, *164*, 221–235.

[24]   D. O' Connor, A. Byrne, T. E. Keyes, *RSC Adv.* **2019**, *9*, 22805–22816.

[25]   L. Rakers, D. Grill, A. L. L. Matos, S. Wulff, D. Wang, J. Börgel, M. Körsgen, H. F. Arlinghaus, H.-J. Galla, V. Gerke, F. Glorius, *Cell Chem. Biol.* **2018**, *25*, 952-961.e12.

[26]   A. L. L. Matos, F. Keller, T. Wegner, C. E. C. del Castillo, D. Grill, S. Kudruk, A. Spang, F. Glorius, A. Heuer, V. Gerke, *Commun. Biol.* **2021**, *4*, 720.

[27]   A. Esteves, A. Knoll-Gellida, L. Canclini, M. C. Silvarrey, M. André, P. J. Babin, *J. Lipid Res.* **2016**, *57*, 219–232.

[28]   G. P. C. Drummen, L. C. M. van Liebergen, J. A. F. Op den Kamp, J. A. Post, *Free Radic. Biol. Med.* **2002**, *33*, 473–490.

[29]   R. J. Aitken, J. K. Wingate, G. N. De Iuliis, E. A. McLaughlin, *Mol. Hum. Reprod.* **2007**, *13*, 203–211.

[30]   Z. Dai, W. Zhang, L. Zhou, J. Huang, in *Ferroptosis* (Eds.: G. Kroemer, D. Tang), Springer US, New York, **2023**, pp. 61–72.

[31]   M. Macdonald, I. Murray, P. Axelsen, *Free Radic. Biol. Med.* **2007**, *42*, 1392–1397.

[32]   A. S. Klymchenko, *Acc. Chem. Res.* **2023**, *56*, 1–12.

[33]   H. M. McBride, M. Neuspiel, S. Wasiak, *Curr. Biol.* **2006**, *16*, R551–R560.

[34]   G. M. Cooper, *The Cell: A Molecular Approach,* Sinauer Associates, An Imprint Of Oxford University Press, Oxford, **2019**.

[35]   R. G. Jones, D. R. Plas, S. Kubek, M. Buzzai, J. Mu, Y. Xu, M. J. Birnbaum, C. B. Thompson, *Mol. Cell* **2005**, *18*, 283–293.

[36]   E. Bossy-Wetzel, M. J. Barsoum, A. Godzik, R. Schwarzenbacher, S. A. Lipton, *Curr. Opin. Cell Biol.* **2003**, *15*, 706–716.

[37]   R. J. Youle, M. Karbowski, *Nat. Rev. Mol. Cell. Biol.* **2005**, *6*, 657–663.

[38]   R. B. Seth, L. Sun, C.-K. Ea, Z. J. Chen, *Cell* **2005**, *122*, 669–682.

[39]   L.-G. Xu, Y.-Y. Wang, K.-J. Han, L.-Y. Li, Z. Zhai, H.-B. Shu, *Mol. Cell* **2005**, *19*, 727–740.

[40]   O. Warburg, F. Wind, E. Negelein, *Klein. Wochenschr.* **1926**, *5*, 829–832.

[41]   E. Gottlieb, I. P. M. Tomlinson, *Nat. Rev. Cancer.* **2005**, *5*, 857–866.

[42]   G. Lauria, R. Curcio, P. Lunetti, S. Tiziani, V. Coppola, V. Dolce, G. Fiermonte, A. Ahmed, *Cancers* **2023**, *15*, 411.

[43]   B. N. Whitley, E. A. Engelhart, S. Hoppins, *Mitochondrion* **2019**, *49*, 269–283.

[44]   T. Yu, J. L. Robotham, Y. Yoon, *Proc. Natl. Acad. Sci. U.S.A.* **2006**, *103*, 2653–2658.

[45]   J. S. Teodoro, A. P. Rolo, F. V. Duarte, A. M. Simões, C. M. Palmeira, *Mitochondrion* **2008**, *8*, 367–376.

[46]   C. A. Galloway, H. Lee, P. S. Brookes, Y. Yoon, *Am. J. Physiol. Gastrointest. Liver Physiol.* **2014**, *307*, G632–G641.

[47]   P. Maechler, E. D. Kennedy, T. Pozzan, C. B. Wollheim, *EMBO J.* **1997**, *16*, 3833–3841.

[48]   A. del Campo, V. Parra, C. Vásquez-Trincado, T. Gutiérrez, P. E. Morales, C. López-Crisosto, R. Bravo-Sagua, M. F. Navarro-Marquez, H. E. Verdejo, A. Contreras-Ferrat, R. Troncoso, M. Chiong, S. Lavandero, *Am. J. Physiol. Endocrinol. Metab.* **2014**, *306*, E1–E13.

[49]   D. J. Fazakerley, A. Y. Minard, J. R. Krycer, K. C. Thomas, J. Stöckli, Dylan. J. Harney, J. G. Burchfield, G. J. Maghzal, S. T. Caldwell, R. C. Hartley, R. Stocker, M. P. Murphy, D. E. James, *J. Biol. Chem.* **2018**, *293*, 7315–7328.

[50]   A. Diaz-Vegas, P. Sanchez-Aguilera, J. R. Krycer, P. E. Morales, M. Monsalves-Alvarez, M. Cifuentes, B. A. Rothermel, S. Lavandero, *Endocr. Rev.* **2020**, *41*, bnaa005.

[51]   F. Du, A. J. Cooper, T. Thida, S. Sehovic, S. E. Lukas, B. M. Cohen, X. Zhang, D. Öngür, *JAMA Psychiatry* **2014**, *71*, 19.

[52]   L. H. Fairley, A. Grimm, A. Eckert, *Cells* **2022**, *11*, 3603.

[53]   H. Xu, F. Yang, *Transl. Psychiatry* **2022**, *12*, 464.

[54]   M. O. Klein, D. S. Battagello, A. R. Cardoso, D. N. Hauser, J. C. Bittencourt, R. G. Correa, *Cell. Mol. Neurobiol.* **2019**, *39*, 31–59.

[55]   J. Teixeira, C. Oliveira, F. Cagide, R. Amorim, J. Garrido, F. Borges, P. J. Oliveira, *J. Enzyme Inhib. Med. Chem.* **2018**, *33*, 567–576.

[56]   A. Dilip, G. Cheng, J. Joseph, S. Kunnimalaiyaan, B. Kalyanaraman, M. Kunnimalaiyaan, T. C. Gamblin, *Anti-Cancer Drugs* **2013**, *24*, 881–888.

[57]   C. A. Mannella, *Biochim. Biophys. Acta.* **2006**, *1763*, 542–548.

[58]   L. D. Zorova, V. A. Popkov, E. Y. Plotnikov, D. N. Silachev, I. B. Pevzner, S. S. Jankauskas, V. A. Babenko, S. D. Zorov, A. V. Balakireva, M. Juhaszova, S. J. Sollott, D. B. Zorov, *Anal. Biochem.* **2018**, *552*, 50–59.

[59]   M. P. Murphy, *Trends Biotechnol.* **1997**, *15*, 326–330.

[60]   J. Zielonka, J. Joseph, A. Sikora, M. Hardy, O. Ouari, J. Vasquez-Vivar, G. Cheng, M. Lopez, B. Kalyanaraman, *Chem. Rev.* **2017**, *117*, 10043–10120.

[61]   K. S. Gkika, A. Byrne, T. E. Keyes, *Dalton Trans.* **2019**, *48*, 17461–17471.

[62]   A. Martin, A. Byrne, C. S. Burke, R. J. Forster, T. E. Keyes, *J. Am. Chem. Soc.* **2014**, *136*, 15300–15309.

[63]   C. S. Burke, A. Byrne, T. E. Keyes, *Angew. Chem. Int. Ed.* **2018**, *57*, 12420–12424.

[64]   C. Zhang, L. Long, C. Shi, *Adv. Therap.* **2018**, *1*, 1800069.

[65]   B. Chazotte, *Cold Spring Harb. Protoc.* **2011**, *2011*, pdb.prot5648.

[66]   K. Neikirk, A. G. Marshall, B. Kula, N. Smith, S. LeBlanc, A. Hinton, *Eur. J. Cell. Biol.* **2023**, *102*, 151371.

[67]   H. Yamakoshi, A. Palonpon, K. Dodo, J. Ando, S. Kawata, K. Fujita, M. Sodeoka, *Bioorg. Med. Chem. Lett.* **2015**, *25*, 664–667.

[68]   L. T. Wilson, W. J. Tipping, C. Wetherill, Z. Henley, K. Faulds, D. Graham, S. P. Mackay, N. C. O. Tomkinson, *Anal. Chem.* **2021**, *93*, 12786–12792.

[69]   L. S. Khailova, P. A. Nazarov, N. V. Sumbatyan, G. A. Korshunova, T. I. Rokitskaya, V. I. Dedukhova, Yu. N. Antonenko, V. P. Skulachev, *Biochem. Mosc.* **2015**, *80*, 1589–1597.

[70]   J. Trnka, M. Elkalaf, M. Anděl, *PLoS ONE* **2015**, *10*, e0121837.

[71]   C. Reily, T. Mitchell, B. K. Chacko, G. A. Benavides, M. P. Murphy, V. M. Darley-Usmar, *Redox Biol.* **2013**, *1*, 86–93.

[72]   G. Wilson, J. Garthwaite, in *Encyclopedia of Neuroscience*, Elsevier, Berkeley **2009**, pp. 1151–1156.

[73]   K. Chen, R. N. Pittman, A. S. Popel, *Antioxid. Redox. Signal.* **2008**, *10*, 1185–1198.

[74]   C. Bogdan, *Nat. Immunol.* **2001**, *2*, 907–916.

[75]   E. M. Palmieri, C. McGinity, D. A. Wink, D. W. McVicar, *Metabolites* **2020**, *10*, 429.

[76]   P. Picón-Pagès, J. Garcia-Buendia, F. J. Muñoz, *Biochim. Biophys. Acta.* **2019**, *1865*, 1949–1967.

[77]   R. Liu, Y. Ishibe, N. Okazaki, K. Kimura, *Br. J. Anaesth.* **2000**, *84*, 596–599.

[78]   L. Bellavia, D. B. Kim-Shapiro, S. B. King, *Future Sci. OA* **2015**, *1*, fso.15.36.

[79]   Y. Chen, *Nitric Oxide* **2020**, *98*, 1–19.

[80]   A. Beltrán, M. Isabel Burguete, D. R. Abánades, D. Pérez-Sala, S. V. Luis, F. Galindo, *Chem. Commun.* **2014**, *50*, 3579.

[81]   Y.-L. Fu, H. Li, X.-Z. Wei, Q.-H. Song, *J. Mater. Chem. B* **2019**, *7*, 3792–3795.

[82]   Q. Han, J. Liu, Q. Meng, Y.-L. Wang, H. Feng, Z. Zhang, Z. P. Xu, R. Zhang, *ACS Sens.* **2019**, *4*, 309–316.

[83]   H.-L. Wang, F.-T. Liu, A.-X. Ding, S.-F. Ma, L. He, L. Lin, Z.-L. Lu, *Spectrochim. Acta. A.* **2016**, *169*, 1–6.

[84]   W. Cha, M. E. Meyerhoff, *Langmuir* **2006**, *22*, 10830–10836.

[85]   T. Shioya, T. M. Swager, *Chem. Commun.* **2002**, 1364–1365.

[86]   S. A. Hilderbrand, M. H. Lim, S. J. Lippard, *J. Am. Chem. Soc.* **2004**, *126*, 4972–4978.

[87]   M. B. Al-Handawi, P. Commins, D. P. Karothu, G. Raj, L. Li, P. Naumov, *Chem. Eur. J* **2018**, *24*, 11493–11497.

[88]   R. A. Arellano-Reyes, A. Prabhakaran, R. C. E. Sia, J. Guthmuller, K. K. Jha, T. Yang, B. Dietzek-Ivanšić, V. McKee, T. E. Keyes, *Chem. Eur. J.* **2023**, *29*, e202300239.

[89]   M. R. Dent, I. López-Duarte, C. J. Dickson, N. D. Geoghegan, J. M. Cooper, I. R. Gould, R. Krams, J. A. Bull, N. J. Brooks, M. K. Kuimova, *Phys. Chem. Chem. Phys.* **2015**, *17*, 18393–18402.

[90]   K. K. Jha, A. Prabhakaran, L. Spantzel, R. C. Sia, I. Pérez, R. A. Arellano-Reyes, A. Elmanova, A. Dasgupta, C. Eggeling, M. Börsch, J. Guthmuller,

M. Presselt, T. E. Keyes, B. Dietzek-Ivanšić, *ChemPhotoChem* **2023**, *7*, e202300091.

[91]   W. Miao, C. Yu, E. Hao, L. Jiao, *Front. Chem.* **2019**, *7*, 825.

[92]   S. Toliautas, J. Dodonova, A. Žvirblis, I. Čiplys, A. Polita, A. Devižis, S. Tumkevičius, J. Šulskus, A. Vyšniauskas, *Chem. Eur. J.* **2019**, *25*, 10342–10349.

[93]   D. Su, C. Teoh, N. Gao, Q.-H. Xu, Y.-T. Chang, *Sensors* **2016**, *16*, 1397.

[94]   G. Gramse, A. Dols-Perez, M. A. Edwards, L. Fumagalli, G. Gomila, *Biophys. J.* **2013**, *104*, 1257–1262.

[95]   Q. Jin, X. Fan, C. Chen, L. Huang, J. Wang, X. Tang, *Anal. Chem.* **2019**, *91*, 3784–3789.

[96]   C. Ding, Y. Chen, H. Li, B. Wang, Q. Wei, H. Tang, S. Jia, Z. He, P. Wang, X. Zhou, *Chin. Chem. Lett.* **2019**, *30*, 1393–1396.

[97]   W. Shen, S. A. Thomas, *Org. Lett.* **2000**, *2*, 2857–2860.

[98]   A. Pieczara, R. A. Arellano Reyes, T. E. Keyes, P. Dawiec, M. Baranska, *ACS Sens.* **2024**, acssensors.3c02576.

[99]   S. Lepiller, V. Laurens, A. Bouchot, P. Herbomel, E. Solary, J. Chluba, *Free Radic. Biol. Med.* **2007**, *43*, 619–627.

[100]   H. Kojima, N. Nakatsubo, K. Kikuchi, S. Kawahara, Y. Kirino, H. Nagoshi, Y. Hirata, T. Nagano, *Anal. Chem.* **1998**, *70*, 2446–2453.

[101]   Y. Gao, Z. Wang, J. Wu, L. Lu, *Microchem. J.* **2023**, *190*, 108714.

[102]   M. J. Marín, P. Thomas, V. Fabregat, S. V. Luis, D. A. Russell, F. Galindo, *ChemBioChem* **2011**, *12*, 2471–2477.

[103]   D. L. J. Broere, R. Plessius, J. I. van der Vlugt, *Chem. Soc. Rev.* **2015**, *44*, 6886–6915.

Chapter 6 General conclusions and future work.

6.1 General conclusions

The thesis key objectives were the synthesis of novel fluorescent dyes for application as triplet-triplet annihilation up-conversion sensitizers, imaging, and viscosity sensors for the cytosol and cell membrane, and nitric oxide sensors. The application objectives reflect the goals of the LogicLab research consortium whose overall aim was to develop liposomal vesicles capable of sensing multiple cellular parameters at the same time. The molecules prepared in this thesis were developed to fulfil some of the molecular sensors required for that purpose. At the submission this thesis, the novel materials prepared herein are the focus of ongoing studies in cells, liposomes, and unilamellar vesicles by consortium members.

The main family of molecules prepared in this work are BODIPY-perylene conjugates. BODIPY was chosen for its high synthetic tuneability and because its derivatives tend to have high photostability, good extinction coefficients, and high quantum yields. Perylene was chosen because it has the capacity to act as sensitizer or as annihilator in TTA-UC systems, and this capacity can be modulated by introduction substituents capable or interacting electronically.

In Chapter 2, a synthetic strategy was developed to prepare non-symmetrically substituted tetramethyl phenyl BODIPYs possessing perylene as the main substituent at position 2. BODIPY-perylene conjugates possessing electron withdrawing groups, nitro- or difluorophenyl, were not stable enough to be isolated. The stable molecule, B2P, was isolated and structurally characterised by NMR, mass spectrometry and single crystal X-ray diffraction. A second molecule, B2PI, was prepared from B2P by electrophilic iodination. Both molecules were studied

using absorption and emission spectroscopic techniques. B2P and B2PI showed absorption bands with intensities independent of the solvent whereas the emission intensity was highly solvent-dependent. The fluorescence quantum yield was higher in solvents with low dielectric constants, e.g., dioxane, toluene and decreased in solvents with high dielectric constants, e.g., DMSO or methanol. The large Stokes shift (3500 cm^{-1}) and the solvent-dependence indicated that a charge transfer state is responsible for the emission. This hypothesis was confirmed by Raman spectroscopy in combination with DFT calculations and transient absorption studies. B2P and B2PI were found to be good sensitizers in TTA-UC systems using perylene as the annihilator. The process was found to be very highly solvent-dependent and only observed in dioxane and DMSO. Due to the presence of a heavy atom the iodinated derivative, B2PI, proved a better sensitizer than B2P.[1] The crystallographic analysis was performed by Prof. Vickie McKee. Computational calculations were carried out in collaboration with other members of the LogicLab group, Dr. Julien Guthmuller and Rengel Cane Sia, and the transient absorption studies in collaboration with Dr. Keshav Kumar Jha and Dr. Tingxiang Yang.[2,3]

In Chapter 3, a few different synthetic strategies were developed to functionalise BODIPY with perylene at position 2 varying the number of methyl groups on the main core. The resulting molecules, MB2P, 2-DMB2P, and 8-DMB2P, have different degrees of rotational freedom and were designed as potential viscosity sensors. The synthesis included the preparation of ketopyrroles as the starting point. These molecules were halogenated and then condensed with one equivalent of a pyrrole to produce non-symmetric monohalogenated BODIPYs. The functionalisation with perylene was performed via a Suzuki-Miyaura cross-coupling reaction which was optimised to work under mild conditions using a Buchwald

precatalyst. An iodinated derivative, MB2PI, was prepared from MB2P. All of the molecules were characterised by spectroscopic techniques. As observed for B2P and B2PI, the molecules have a solvent-independent absorption and solvent-dependent emission intensities. Large Stokes shifts (~3500 cm^{-1}) were also observed for these molecules. The absolute fluorescence quantum yield showed a relationship between rotational freedom and fluorescence intensity. MB2P, the most rotationally restricted molecule, showed the highest quantum yield, 37% in toluene. The quantum yield in the same solvent decreases in 2-DMB2P to 5% and it is the lowest, 2%, for 8-DMB2P, the molecule with the highest degree of rotational freedom.

In the synthesis of dimethylaminophenyl BODIPY, one unexpected BF$_2$ complex was isolated. The presence of this molecule explains the low reactivity of certain ketopyrroles in condensation reactions to form BODIPYs. Ketopyrroles with electron-donor substituents are good ligands, and they complex one equivalent of BF$_2$ instead of condensing with a pyrrole equivalent.

Efforts were made to prepare a BODIPY-perylene derivative with a double bond joining both fluorophores at position 2. The Mizoroki-Heck methodology afforded a mixture of α and β isomers which were difficult to separate. The Knoevenagel reaction was carried out as an alternative. This methodology allowed the formation of a double bond using one of the methyl substituents of the BODIPY and 3-formyl perylene. However, the products obtained by this method were very unstable and difficult to isolate. AGB3P was the only molecule isolated in a sufficient amount to be characterised by spectroscopic techniques. AGB3P shows solvent-dependent absorption and emission properties. The Stokes shift was between 504

and 1024 cm^{-1}, significantly smaller than the large values observed for BODIPY-perylene conjugates bearing perylene at position 2.

Single crystals of MB2P, DMAB-BF$_2$ were prepared, and their structures resolved by X-ray diffraction by Professor Vickie McKee and Dr. James McPherson. The ensemble of analyses helped confirm the structure of the molecules, the relative orientation of the fluorophores, and the formation or absence of interactions in the crystalline state.

In Chapter 4, B2P, MB2P, 2-DMB2P, and 8-DMB2P, dyes with different degrees of rotational freedom were studied as potential viscosity sensors. The dyes were studied in viscous solutions prepared by the combination of castor oil and toluene in different percentages. Three of the four dyes tested, B2P, MB2P and 2-DMB2P presented complex and non-systematic response to changes in viscosity. Solutions of low viscosity showed similar fluorescence intensity to solutions of high viscosity. The non-systematic response to viscosity, which is thought to be due to dielectric effects of the medium, makes the dyes unsuitable for intensity-based viscosity sensing. In contrast, 8-DMB2P, the dye with the highest degree of rotational freedom, shows a more consistent behaviour and it could be used as an intensity-based viscosity sensor in solutions of high viscosities (30% v/v castor oil and above). The relationship between fluorescence lifetime of all of the dyes and viscosity was also studied. The compound 8-DMB2P was also found to be the only dye whose lifetime systematically changes with the change in the viscosity of the medium. The rest of the dyes were unsuitable to be used as lifetime-based viscosity sensors as the changes in lifetime did not systematically change with viscosity. As the compounds show solvent dielectric dependence, as expected for charge transfer, the properties of B2P, MB2P, 2-DMB2P, and 8-DMB2P were also studied

in a polar viscous system comprised of varying ratios of methanol and glycerol. Interestingly, MB2P and 8-DMB2P presented a switch-like behaviour, their emission maxima changing from 580 nm to 660 nm in very viscous solutions, namely 80 and 90% glycerol.

From the viscosity studies, it can be concluded that, even though the charge transfer between perylene and BODIPY is an excellent way to promote the formation of triplet states and large Stokes shifts, its solvent dependence makes it challenging to use them as viscosity sensors in systems where changes in viscosity are accompanied by changes in dielectric constant. However, some of the dyes having a switch-like behaviour, MB2P and 8-DMB2P, could be used as sensors for polymerisation processes.

Crystals of B2P, B2PI, and MB2P were grown and their spectroscopic properties studied. The fluorescence quantum yield follows the same trends as in solution. The molecule with the highest restriction of rotation, MB2P, is the one with the highest quantum yield. Iodination (B2PI) or increase in rotational freedom (B2P) decrease the fluorescence. In the former case, the reduction in fluorescence is due to the population of the triplet state whereas in the latter case the reduction in fluorescence is due to the increased non-radiative relaxation. In the case B2P, a phosphorescence band was identified at 1325 nm, and the intensity of this band showed a strong oxygen sensitivity.

Crystals of B2P were ground and the powder analysed. The emission maximum changed from 668 nm in the crystalline sample to 702 nm for the strongly ground sample. The quantum yield of the ground sample was only reduced by 1% (from 8% to 7%) indicating that the crystalline arrangement does not contribute to

increase the emission intensity and it has an impact only on the maximum wavelength of emission.

DMAB-BF$_2$ was studied in solution and in the crystalline state. The crystalline emission is red-shifted compared to the solution in toluene, being 652 nm vs 466 nm, respectively. The molecule had a high fluorescence quantum yield in solution (83% in toluene) and a surprisingly high quantum yield in the solid state (20%). The extended crystal structure of this molecule revealed the presence of weak CH---F interactions that make the molecules in the crystals behave like a chain. This arrangement is likely to be the cause of the photophysical properties of the crystalline DMAB-BF$_2$.

In Chapter 5, three new potential optical sensor molecules were prepared. RCBC was a molecule developed to sense cell membrane viscosity, RAR-BR was developed as a Raman reporter to track mitochondria and 3-DAP was a sensor for nitric oxide.

The synthesis of RCBC involved the combination of a non-symmetric BODIPY, as the viscosity-sensitive fluorophore, and a cholesterol substituent as a membrane-targeting unit. Single crystals of RCBC were prepared, and their structures obtained by X-ray diffraction by Professor Vickie McKee. The analysis showed that BODIPY and the cholesteryl benzoate substituent can orient in more than one stable conformation. The moieties can be in a conformation close to orthogonality but also in a planar orientation. The spectroscopic characterisation of the dye was carried out and the molecule's potential as a viscosity sensor was determined in a castor oil-toluene system. RCBC was found to be a good candidate for intensity-based viscosity sensing. The lifetime of the dye, however, did not systematically change with viscosity, limiting the scope of applications of this dye.

The synthesis of RAR-BR was an unexpected result obtained in the synthesis of a Raman reporter capable of participating in click chemistry reactions. The synthetic pathway involved a palladium-catalysed coupling between 1,1-dibromoalkene and phenylacetylene. This reaction did not produce the 1,3-diyne expected and produced the 1,1-diyne instead. The structure of RCBC was confirmed by NMR, mass spectrometry and single crystal X-Ray diffraction. RAR-BR was tested as a Raman reporter in aortic endothelial cells. In the same concentrations RAR-BR was found to be a better Raman reporter than MitoBADY, the commercial standard to track mitochondria. The superior properties of RAR-BR were determined to be due to its higher mitochondrial selectivity rather than a higher Raman cross section than MitoBADY. The results were peer-reviewed and published.[4]

Finally, 3-DAP was developed as potential NO sensor. The synthesis involved the coupling of the sensing moiety (1,2-diaminobenzene) to perylene. The goal was trying to develop an NO sensor capable of being incorporated into TTA-UC systems. The capacity of 3-DAP to react with nitric oxide was tested in solution; however, the sensor presented a very hight emission intensity even in the absence of the analyte. The changes in fluorescence intensity observed after the reaction with NO were not large enough to distinguish between two NO concentrations with high precision. The TTA-UC test using 3-DAP as an annihilator and B2P or B2PI as the sensitizers were unsuccessful.

6.2 Future work

The molecules prepared in this project seem to have promising properties in areas such as TTA-UC and viscosity sensing. Some of the molecules prepared in this thesis are still being studied. The compound RCBC is being studied in cells, MB2P and MB2PI are being studied as TTA-UC sensitizers in all the solvents tested before, but also in chloroform. A manuscript about nitric oxide sensing using 3-DAP in solution and in liposomes is in preparation, and a manuscript including cell studies with B2P, B2PI, MB2P, and MB2PI is also in preparation.

However, there are also some projects started during this project which could not be concluded or were beyond the scope of the work. These projects aimed to further study the properties of the molecules prepared or try to address some of the issues encountered.

6.2.1 Crystallisation of BODIPY-perylene conjugates

To study further the properties of the BODIPY-perylene conjugates in the solid state, co-crystals of B2P, B2PI, MB2P, or MB2PI with perylene could be prepared. It would be interesting to explore the charge transfer properties in the crystalline state. Such arrays showed potential as organic semiconductors[5] or as "jumping crystals" that transform non-kinetic energy to kinetic energy.[6] Cocrystals of BODIPY-perylene conjugates could produce solid state TTA-UC and have applications in photovoltaics.[7]

There are some reports in literature of charge transfer in co-crystals of perylene and 7,7,8,8-tetracyanoquinodimethane derivatives. In this example, an intermolecular charge transfer was observed and tuned by modifying the proportion

of the crystals' constituents. The supramolecular structures prepared this way have potential in optoelectronics.[8] There are also examples in the literature involving perylene and acceptor 1,2,4,5-tetracyanobezene, that have been use as piezochromic materials[9] (Figure 138)**Figure** . So far, there are very few examples of BODIPY co-crystals.[10]
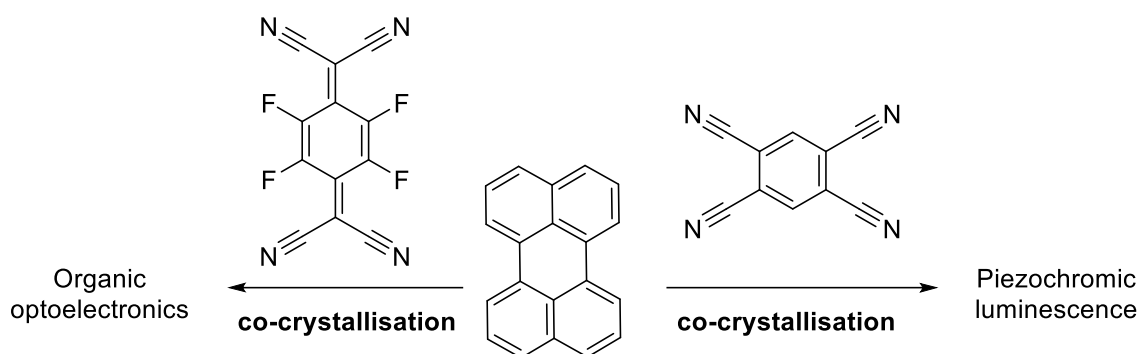
Figure 138 Molecules used for co-crystalisation with perylene and their potential applications

6.2.2 pH-sensitive BODIPY-perylene conjugates

To improve the sensing properties of BODIPY-perylene conjugates some new analogues could be prepared. Functionalisation with a basic or acidic functional groups could lead to dual pH and viscosity sensors. In this way two essential parameters of a biological system could be studied simultaneously.

One on the key intermediates for these derivatives has already been prepared in Chapter 3. The suggested synthetic pathway from BODIPY **3.7** can be found in Figure 139. The synthesis includes the borylation of the BODIPY's phenyl ring, this reaction is not in competition with the borylation at position 2 of the BODIPY core since both bromine atoms have a very different reactivity. Crossed reactions between molecules of the same borylated product are also not favoured due to steric hindrance, to the use of low temperatures for the borylation and to the use of a weak base such as potassium-2-ethylhexanoate.[11] The substitution of the pinacol ester

by an amino group can be achieved by a Chan-Lam coupling without the need of preparing the boronic acid.[12] The direct conversion of **3.7** to an amino-BODIPY could be also achieved by the Buchwald-Hartwig methodology, although some preliminary assays have suggested that BODIPYs are not stable enough in the basic conditions required for this transformation. In addition, given that the Buchwald-Hartwig reaction used highly reactive palladium catalyst, there is a risk of replacing the bromine atom at position 2 of the BODIPY core as well. So, choosing the right catalyst for this transformation is essential.
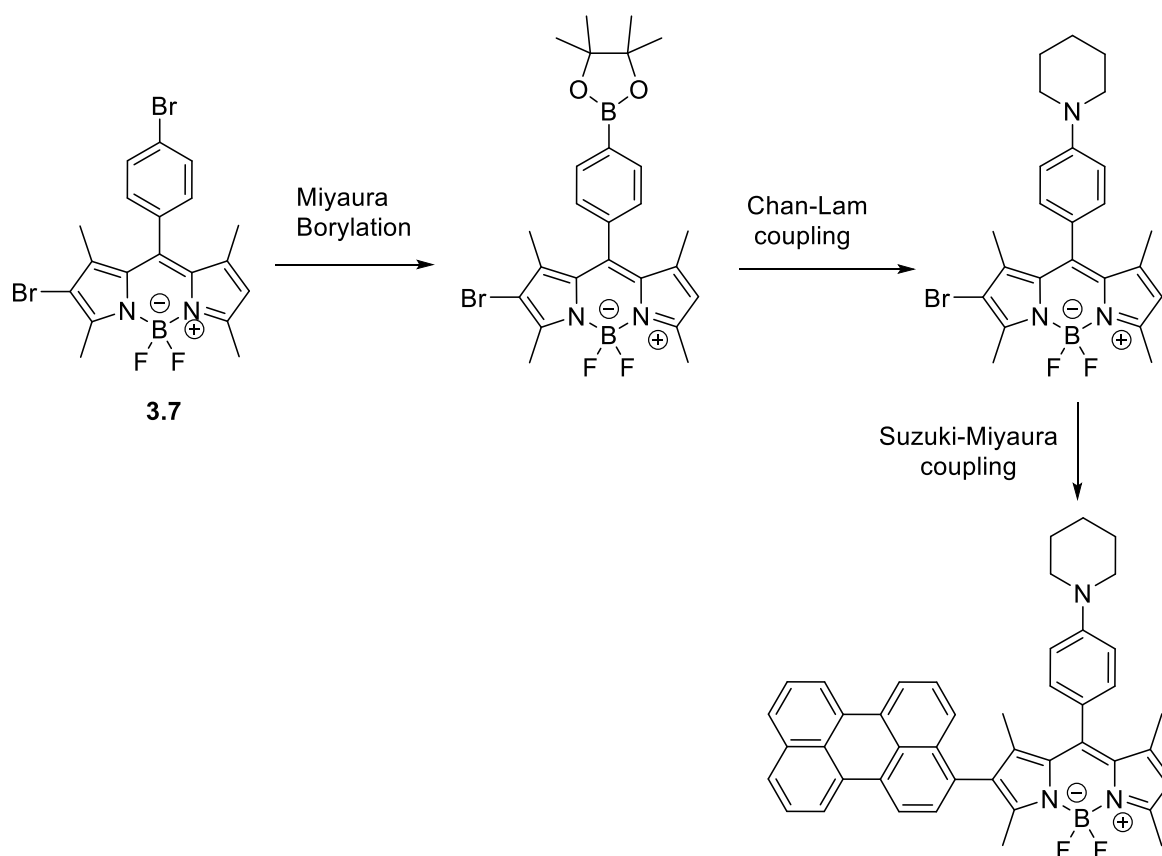
Figure 139 Suggested synthetic pathway to prepared BODIPY-perylene conjugates sensitive to pH.

The main challenges of this synthetic pathway are the difficulty to prepare the starting material, BODIPY **3.7**, as well as the low reactivity of the piperidine-BODIPY in the Suzuki-Miyaura conditions as observed with other BODIPYs bearing electron-donating groups in Chapter 3.

6.2.3 1,2-Diaminophenyl anthracene as an NO sensor

One of the main drawbacks observed in the sensing experiments concerning 3-DAP was the intrinsic high fluorescence of the senor even before reacting with NO. One way to address this issue could be using a fluorophore capable of participating in TTA-UC systems but presenting less fluorescence. One alternative could be an anthracene derivative. The compound 9,10-diphenyl anthracene is a well-known TTA-UC annihilator in organic and inorganic sensitized up-conversion systems.[13–15]

Some of the molecules have already been prepared. The starting material was 9-phenyl anthracene, which was then brominated with NBS. In a first approach, 9-phenyl anthracene was borylated (Miyaura) and then coupled to a Boc-protected diamino bromobenzene (Suzuki-Miyaura). In the second approach 9-phenyl anthracene was coupled to a Boc-protected diamino pinacol ester under Suzuki-Miyaura conditions. However, the last deprotection step is not easy to achieve given the high reactivity of the 1,2-diamino product.
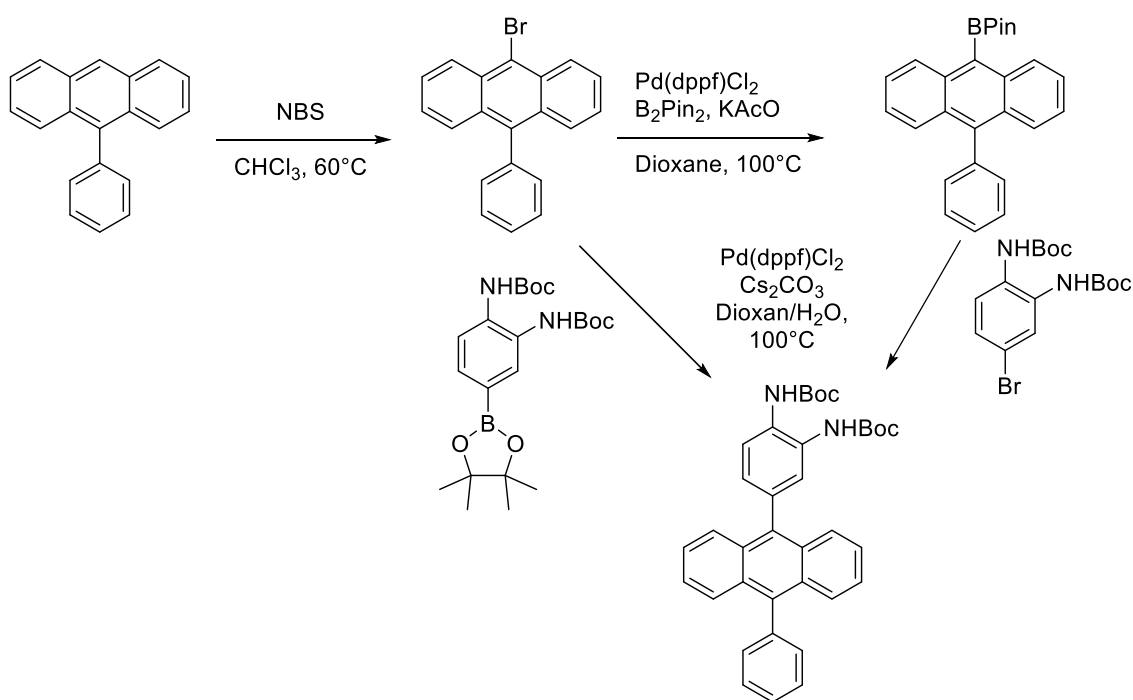
Figure 140 Synthesis of an anthracene-based NO sensor.

6.2.4 Palladium-BODIPY complexes

BODIPY-perylene conjugates were found to be good sensitisers for TTA-UC and the iodinated derivatives showed potential as singlet oxygen generators. However, both processes were very solvent-dependent. Introducing a metallic atom could improve the properties of the dyes. There are reports of stable BODIPY-palladium complexes that were successfully applied to singlet oxygen generation, photooxidation of sulphides and Suzuki-Miyaura cross coupling.[16] The BODIPY-palladium complexes are similar to the one in Figure 141. The molecules prepared in this way presented a very high reactivity but adding a perylene unit could help red-shift the absorption of the molecules. To the best of my knowledge there are no reported examples of BODIPYs including metallic atoms, other than palladium, such as nickel or including other phosphine ligands in this particular fashion.

The palladium-BODIPY complex synthesis was tested under the same conditions reported for simpler BODIPYs; however, only dehalogenated products have been obtained. These results suggest that oxidative addition is very efficient, but the conditions need to be modified to avoid the reductive elimination that causes dehalogenation (Figure 141).
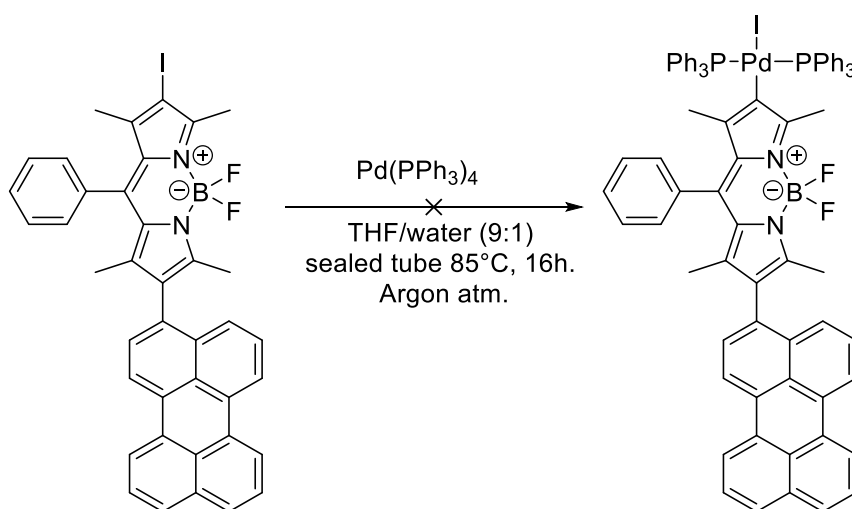
Figure 141 Conditions reaction to obtain palladium-BODIPY-perylene complexes. Only dehalogenation was observed.

6.2.5 BODIPY in polymeric matrixes

The good photostability and tuneability of BODIPYs makes them suitable for some photoelectronic applications, light emitting diodes, and solar cells.[17,18] For these applications, a common strategy consists of dissolving the dyes in a transparent polymeric matrix such as polymethyl methacrylate (PMMA) or polydimethylsiloxane (PDMS).

To test this concept, MB2P was dissolved in PDMS + curing agent (final concentration ~20 µM) the solution was degassed by sonication and deposited onto microscope glass slides. The slides were heated at 90 °C for 90 min and then cooled to room temperature. The polymer was detached from the slides and its emission spectrum recorded with a 515 nm excitation. The normalised emission spectrum was compared to MB2P in other solutions and in the crystalline state (Figure 142). The emission maximum was 587 nm, which is blue-shifted compared to the same dye in toluene, methanol/glycerol solution (1:9) or the crystalline state.
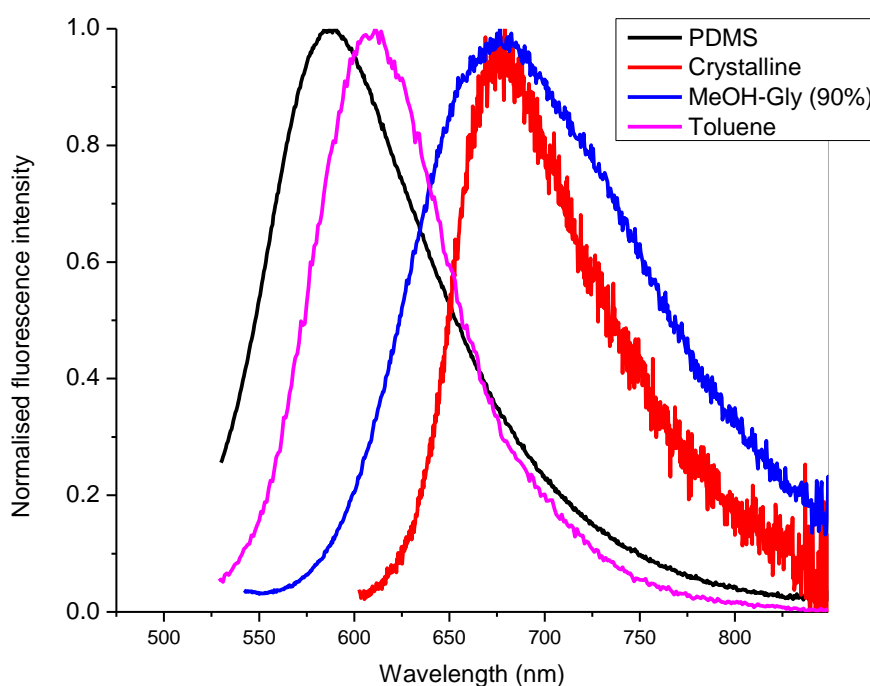
Figure 142 *Normalised spectra of MB2P in solid PDMS, toluene, Methanol-glycerol (1:9) and crystalline state.*

6.3 References

[1]   R. A. Arellano-Reyes, A. Prabhakaran, R. C. E. Sia, J. Guthmuller, K. K. Jha, T. Yang, B. Dietzek-Ivanšić, V. McKee, T. E. Keyes, *Chem. Eur. J.* **2023**, *29*, e202300239.

[2]   K. Kumar Jha, A. Prabhakaran, R. Cane Sia, R. A. Arellano Reyes, N. Kumar Sarangi, T. Yang, K. Kumar, S. Kupfer, J. Guthmuller, T. E. Keyes, B. Dietzek-Ivanšić, *ChemPhotoChem* **2023**, *7*, e202300073.

[3]   T. Yang, R. A. Arellano-Reyes, R. C. Curley, K. K. Jha, A. Chettri, T. E. Keyes, B. Dietzek-Ivanšić, *Chem. Eur. J.* **2023**, *29*, e202300224.

[4]   A. Pieczara, R. A. Arellano Reyes, T. E. Keyes, P. Dawiec, M. Baranska, *ACS Sens.* **2024**, acssensors.3c02576.

[5]   K. P. Goetz, H. F. Iqbal, E. G. Bittle, C. A. Hacker, S. Pookpanratana, O. D. Jurchescu, *Mater. Horiz.* **2022**, *9*, 271–280.

[6]   Y. Chen, J. Li, J. Gong, *ACS Materials Lett.* **2021**, *3*, 275–281.

[7]   V. Gray, K. Moth-Poulsen, B. Albinsson, M. Abrahamsson, *Coord. Chem. Rev.* **2018**, *362*, 54–71.

[8]   T. Salzillo, M. Masino, G. Kociok-Köhn, D. Di Nuzzo, E. Venuti, R. G. Della Valle, D. Vanossi, C. Fontanesi, A. Girlando, A. Brillante, E. Da Como, *Cryst. Growth Des.* **2016**, *16*, 3028–3036.

[9]   C. Zhai, X. Yin, S. Niu, M. Yao, S. Hu, J. Dong, Y. Shang, Z. Wang, Q. Li, B. Sundqvist, B. Liu, *Nat. Commun.* **2021**, *12*, 4084.

[10]   G. Gümüşgöz Çelik, B. Dedeoglu, A. G. Gürek, Y. Zorlu, M. M. Ayhan, *Cryst. Growth Des.* **2023**, *23*, 7285–7294.

[11]   S. Barroso, M. Joksch, P. Puylaert, S. Tin, S. J. Bell, L. Donnellan, S. Duguid, C. Muir, P. Zhao, V. Farina, D. N. Tran, J. G. de Vries, *J. Org. Chem.* **2021**, *86*, 103–109.

[12]   J. C. Vantourout, H. N. Miras, A. Isidro-Llobet, S. Sproules, A. J. B. Watson, *J. Am. Chem. Soc.* **2017**, *139*, 4769–4779.

[13]   C. Wang, F. Reichenauer, W. R. Kitzmann, C. Kerzig, K. Heinze, U. Resch-Genger, *Angew. Chem. Int. Ed.* **2022**, *61*, e202202238.

[14]   T. Serevičius, R. Komskis, P. Adomėnas, O. Adomėnienė, G. Kreiza, V. Jankauskas, K. Kazlauskas, A. Miasojedovas, V. Jankus, A. Monkman, S. Juršėnas, *J. Phys. Chem. C* **2017**, *121*, 8515–8524.

[15]   D. Dzebo, K. Börjesson, V. Gray, K. Moth-Poulsen, B. Albinsson, *J. Phys. Chem. C* **2016**, *120*, 23397–23406.

[16]   D. Wang, N. S. D. Solomon, I. Pernik, B. A. Messerle, S. T. Keaveney, *Aust. J. Chem.* **2020**, 73, 979–986.

[17]   B. M. Squeo, L. Ganzer, T. Virgili, M. Pasini, *Molecules* **2020**, *26*, 153.

[18]   H. Yuce, T. Guner, S. Dartar, B. U. Kaya, M. Emrullahoglu, M. M. Demir, *Dyes Pigm.* **2020**, *173*, 107932.

Appendix A

Supporting information for Chapter 2

Contents

A.1 Reagents, Instruments, and synthesis

All reagents and solvents were purchased from Merck Ireland and used as received unless otherwise stated. 1,4-dioxane used for TTA-UC experiments was anhydrous. NMR spectra were recorded on a 600 MHz Bruker spectrometer and analysed with Top Spin. Without exception ^{13}C-NMR spectra were recorded decoupled from hydrogen. Absorbance spectra were carried out using a Jasco V670 Spectrophotometer and all data was manipulated using Jasco Spectra Manager v2 software. Samples were analysed in Hellma quartz fluorescence cuvettes, with a path length of 1 cm, and spectral range of 300-900 nm unless otherwise stated. Background measurements were carried out at room temperature prior to each measurement. Fluorescence emission spectra were obtained using a Varian Cary Eclipse fluorescence spectrophotometer. The lifetime of the excited state was measured using a PicoQuant FluoTime 100 Compact FLS TCSPC system using a 450 nm pulsed laser source generated from a PicoQuant PDL800-B box. Lifetime decay plots were analysed using PicoQuant TimeHarp software. The goodness of each fit to exponential

decay kinetics was assessed from chi-squared values (where $\chi^2 < 1.3$) and visual inspection of residuals. Resonance Raman spectroscopy was carried out on a Horiba Labram HR confocal microscope, using a 10x objective with a 473 nm diode laser (5 µW) for resonance excitation and a dispersion grating with 1200 grooves/mm. The instrument was calibrated using a Si(100) wafer calibrated to its phonon peak at 520.7 cm^{-1} and the Rayleigh line before the measurement of the sample. The sample was dispersed 10% w/w in KBr to prevent burning and typically, an exposure time of 20 seconds per spectrum was used and 15 spectra were averaged for each sample. An exposure time of 4 s and accumulation for 6 s were typically used for spectral recording.

Synthesis of 3-bromoperylene

Perylene (1 g, 3.96 mmol) was dissolved in 60 mL of tetrahydrofuran, previously recrystallized N-bromosuccinimide was added (0.706 g, 396 mmol, 1 eq.). The mixture was stirred at room temperature for 24 hours. The solvent was evaporated under vacuum and the crude was triturated in methanol. No traces of succinimide were observed only traces of perylene, but the product was used without further purification.

Synthesis of (3-Perylenyl)boronic acid pinacol ester

1 g of 3-bromoperylene (3 mmol), potassium acetate (0.884 g, 9 mmol, 3 eq.), bis(pinacolato) diboron (0.838 g, 3.3 mmol, 1.1 eq.) and Pd(dppf)Cl$_2$ (0.066 g, 90 μmol, 0.03eq) were dissolved in anhydrous dioxane and heated at 70 degrees for 16 hours. The reaction was cooled to RT, filtered through a celite plug and the solvent was evaporated under vacuum. The product was purified by column chromatography (CHCl$_3$: cyclohexane, 8:2). The reaction yielded 0.691 g of a yellow powder, 45 % yield. ^{1}H-NMR (CDCl$_3$, 600 MHz): δ (ppm) 8.65 (d, ^3J = 8.4 Hz, 1H), 8.25-8.20 (m, 3H), 8.18 (d, ^3J = 6.0 Hz, 1H), 8.06 (d, ^3J = 6.0 Hz, 1H), 7.71-767 (m, 2H), 7.54 (t, ^3J = 7.2 Hz, 1H), 752-7.47 (m, 2H), 1.43 (s, 12H).

A.2 NMR and mass spectra

1.437

7.474
7.477
7.487
7.490
7.500
7.503
7.527
7.540
7.541
7.553
7.671
7.684
7.699
7.712
8.055
8.067
8.175
8.188
8.203
8.214
8.225
8.239
8.251
8.648
8.649
8.661
8.662

7.474
7.477
7.487
7.490
7.500
7.503
7.527
7.540
7.541
7.553
7.671
7.684
7.699
7.712
8.055
8.067
8.175
8.188
8.203
8.214
8.225
8.239
8.251
8.648

ppm

12.19

1.97
0.98
1.94
0.94
4.00
0.93
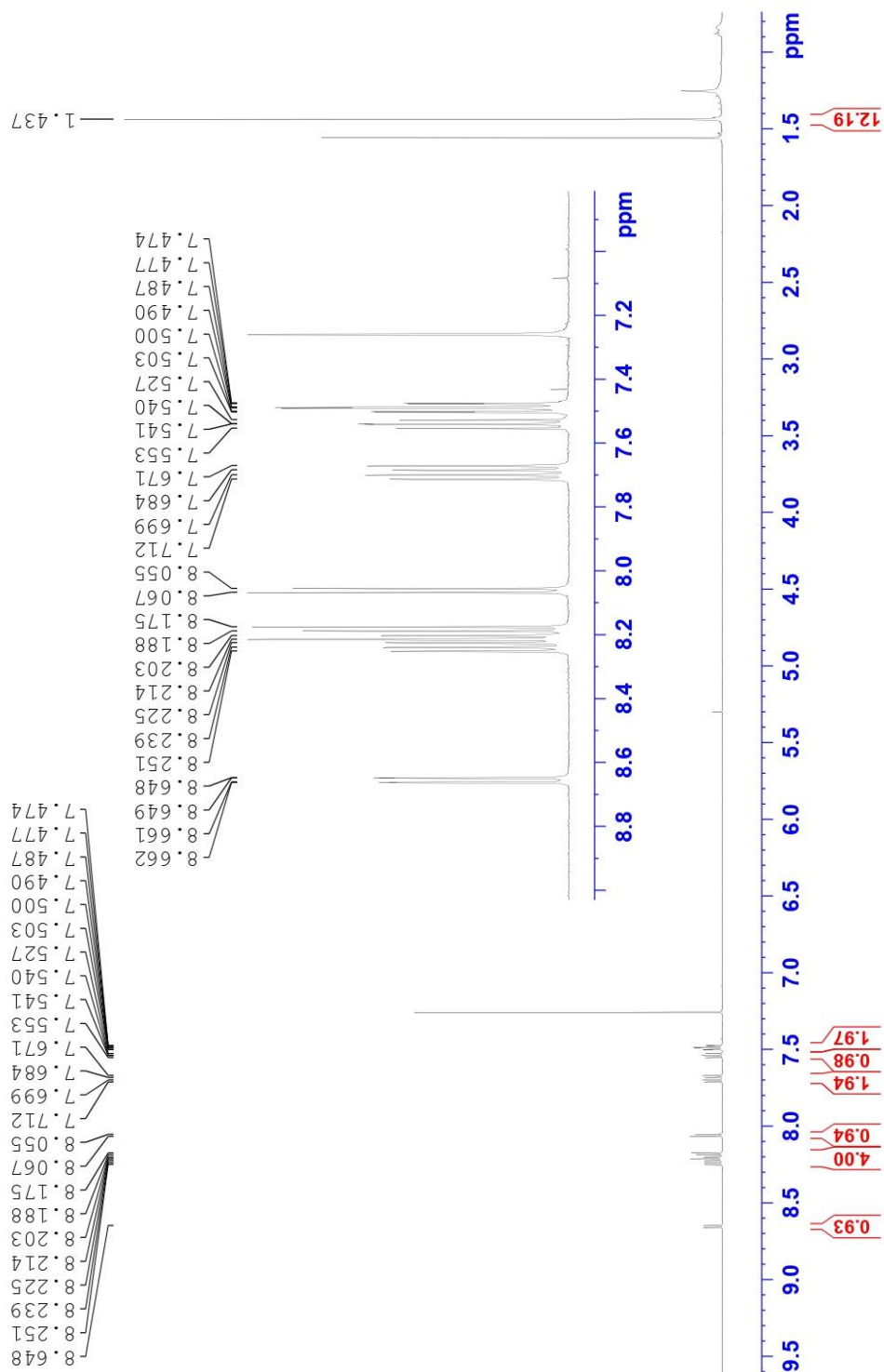
1. ^{1}H-NMR spectrum of (3-Perylenyl)boronic acid pinacol ester in CDCl$_3$ at 600 MHz

A4
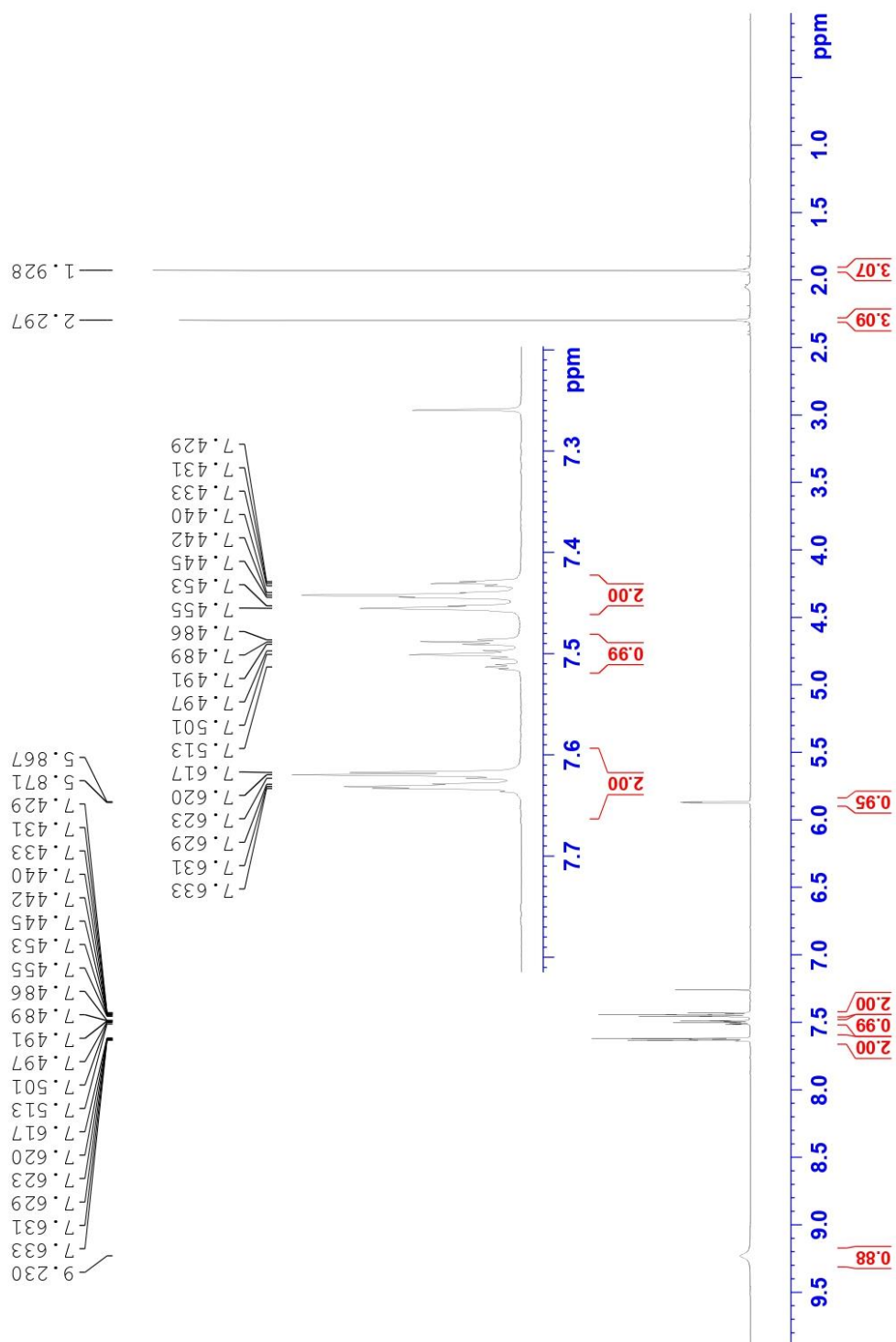
2. ^{1}H-NMR spectrum of 1 in CDCl$_3$ at 600 MHz
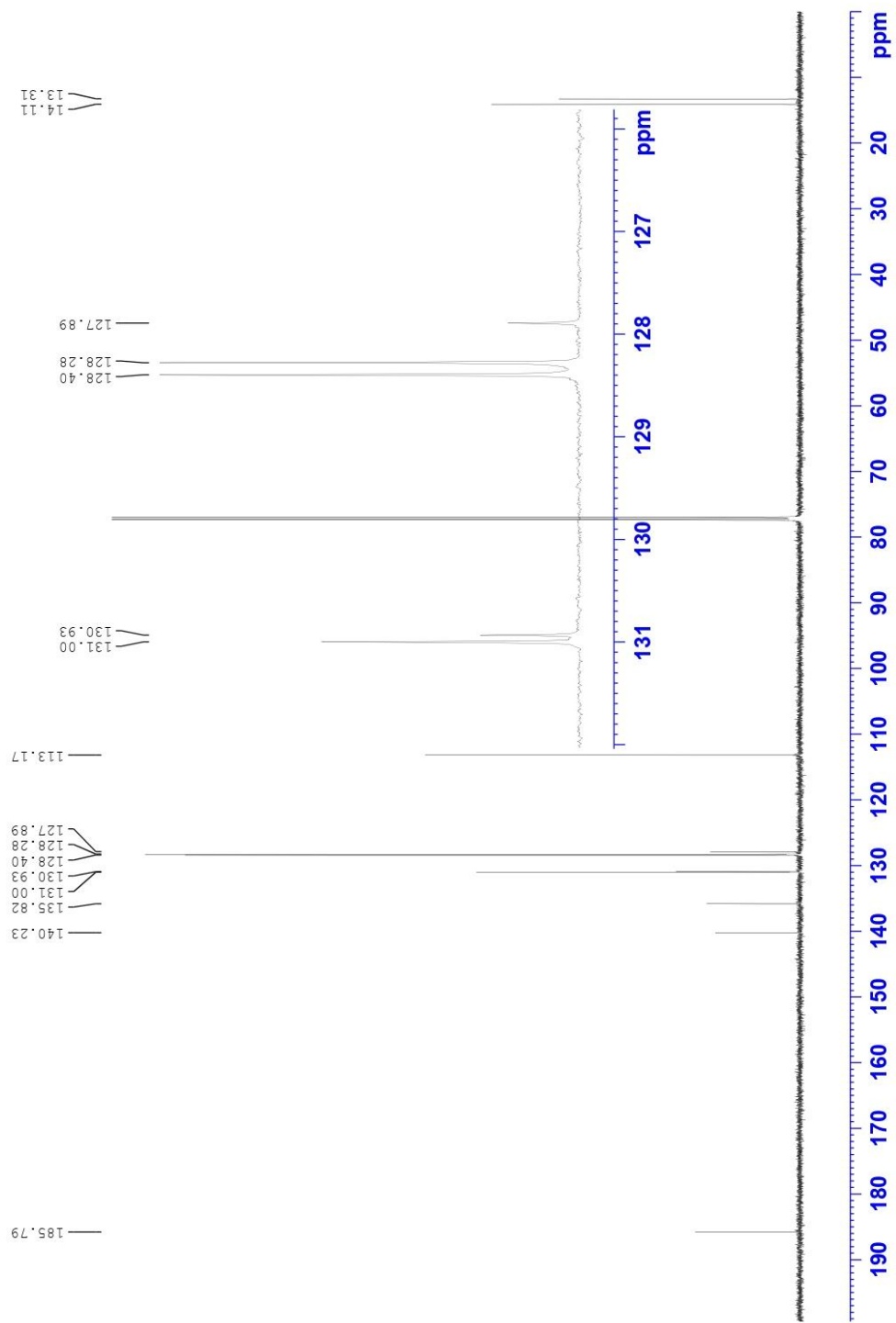
3. ^{13}C-NMR spectrum of 1 in CDCl$_3$ at 150 MHz

Meas. m/z	#	Ion Formula	m/z	err [mDa]	err [ppm]	rdb	N-Rule	e⁻ Conf	mSigma
200.106681	1	C13H14NO	200.106990	-0.3	-1.5	7.5	ok	even	5.4
222.089156	1	C13H13NNaO	222.088935	-0.2	-1.0	7.5	ok	even	9.8
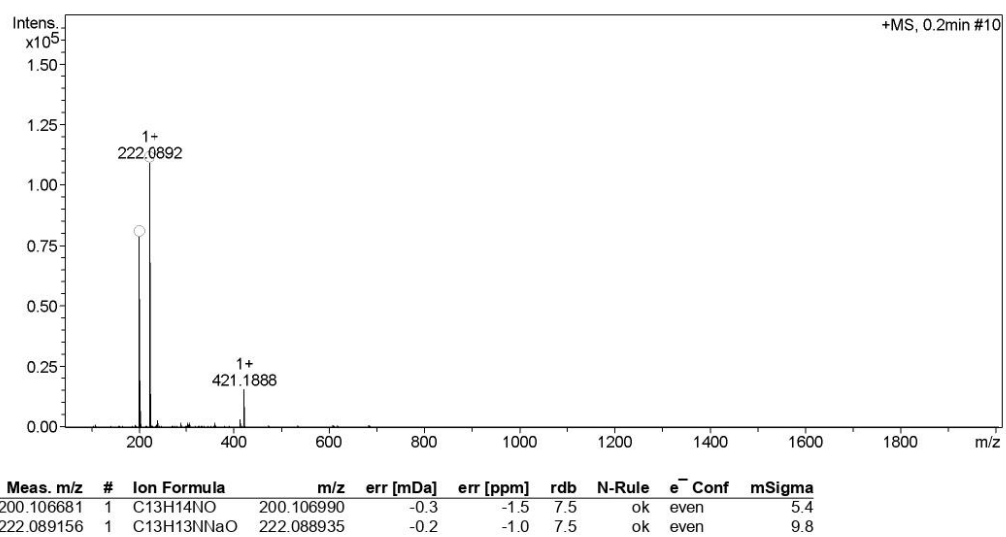
4. Mass spectrum of 1 using electrospray ionisation (ESI)
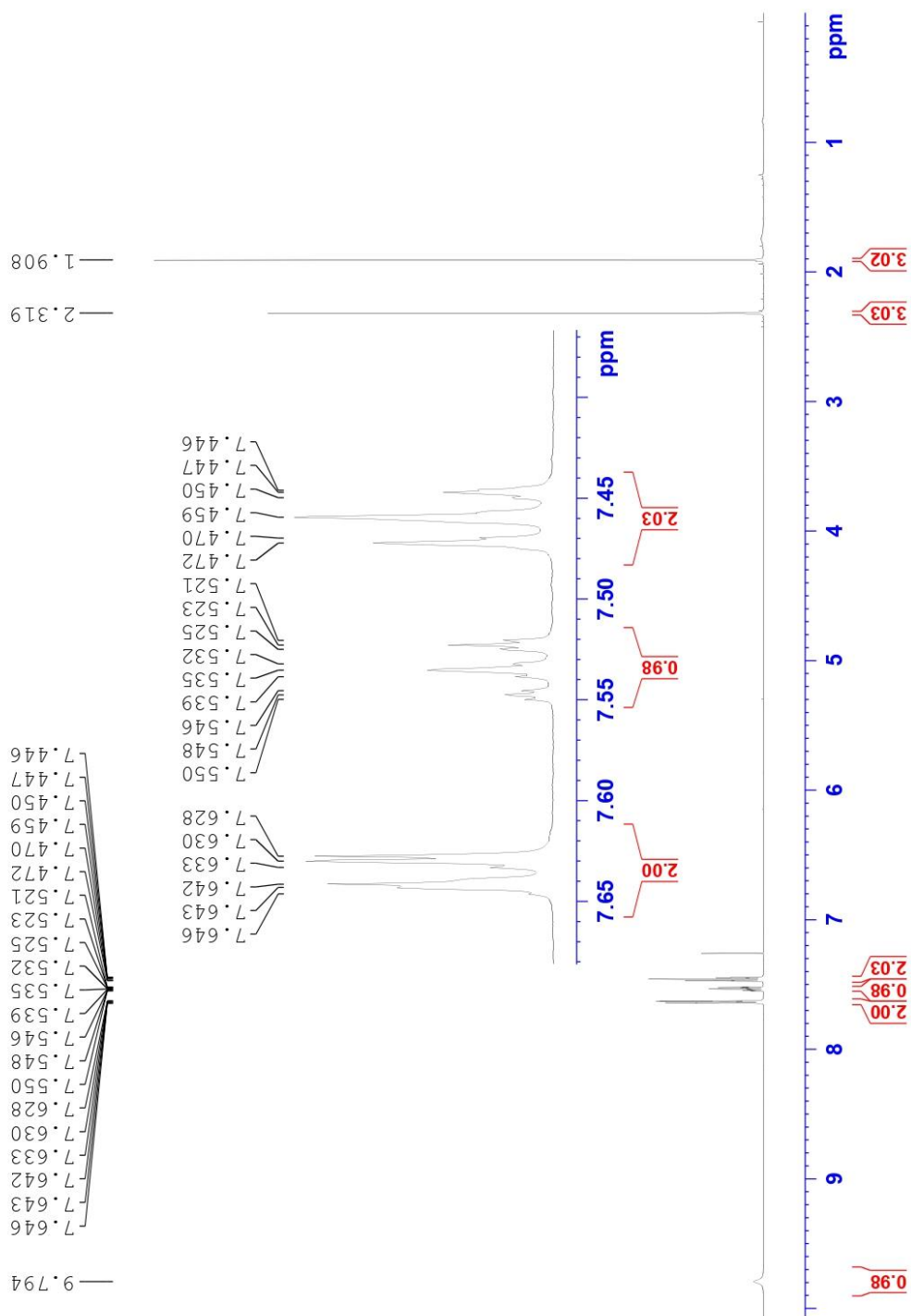
5. ^{1}H-NMR spectrum of 2 in CDCl$_3$ at 600 MHz
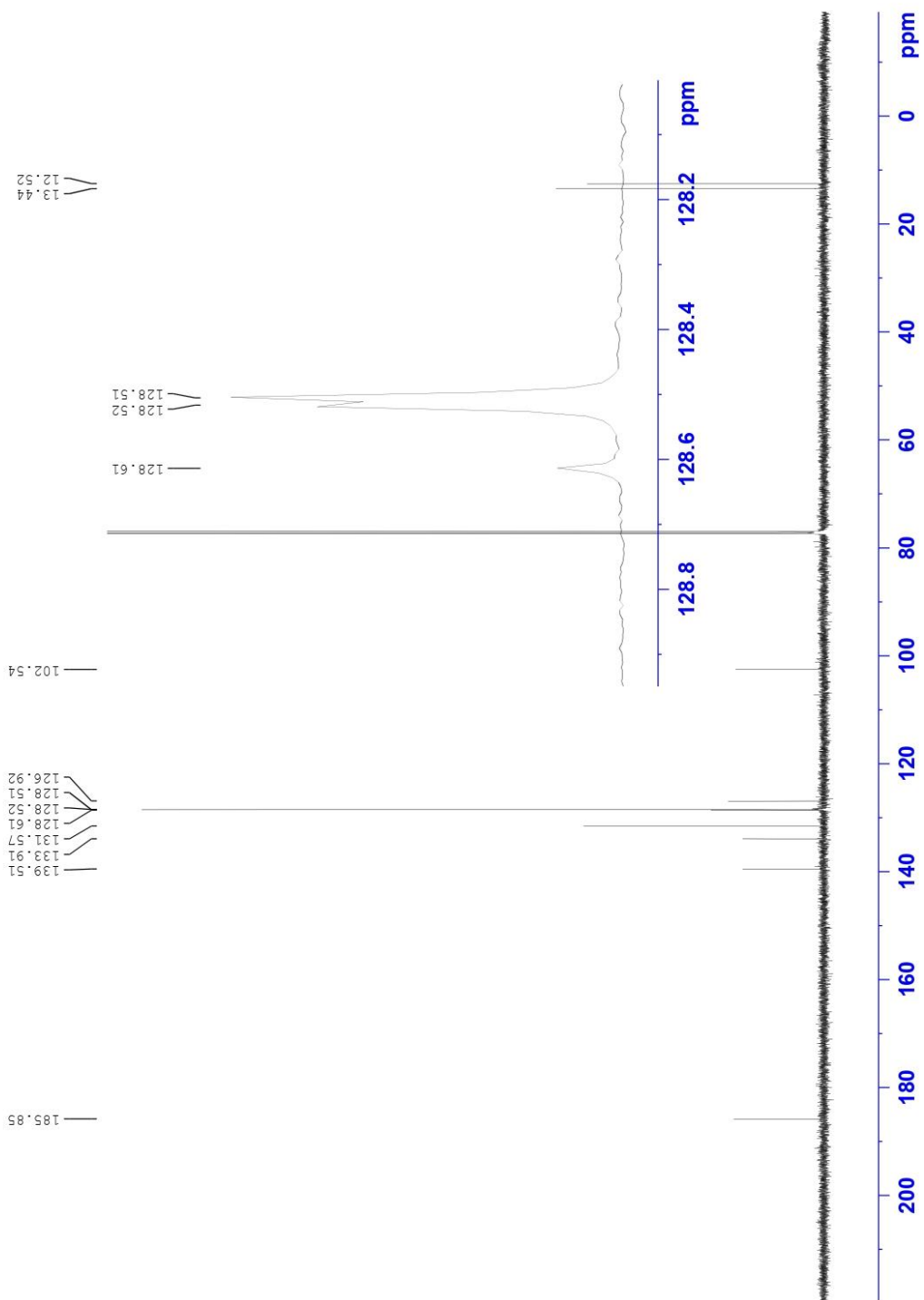
6. ^{13}C-NMR spectrum of 2 in CDCl$_3$ at 150 MHz

Meas. m/z	#	Ion Formula	m/z	err [mDa]	err [ppm]	rdb	N-Rule	e⁻ Conf	mSigma
278.017589	1	C13H13BrNO	278.017503	-0.1	-0.3	7.5	ok	even	27.7
300.000249	1	C13H12BrNNaO	299.999447	0.8	2.7	7.5	ok	even	25.7
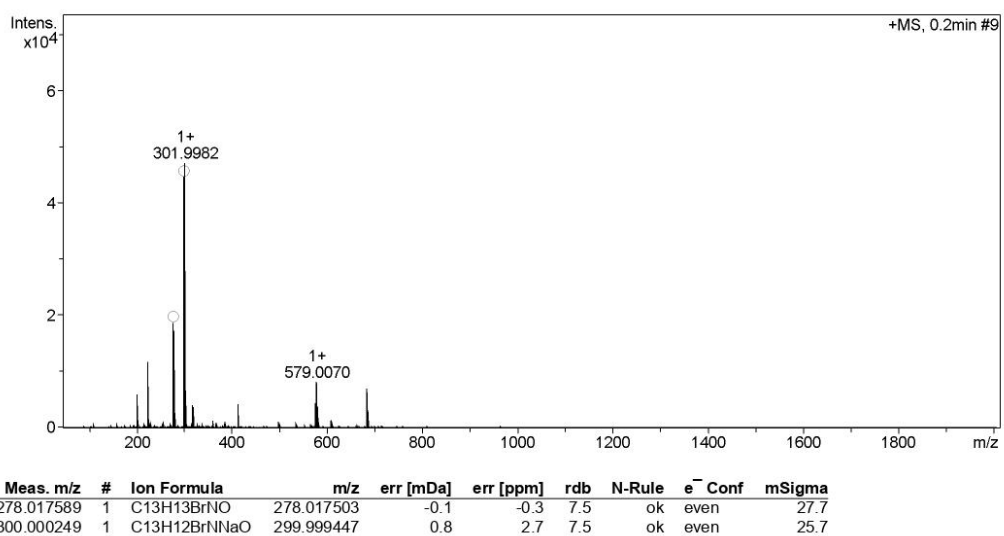
7. Mass spectrum of 2 using ESI
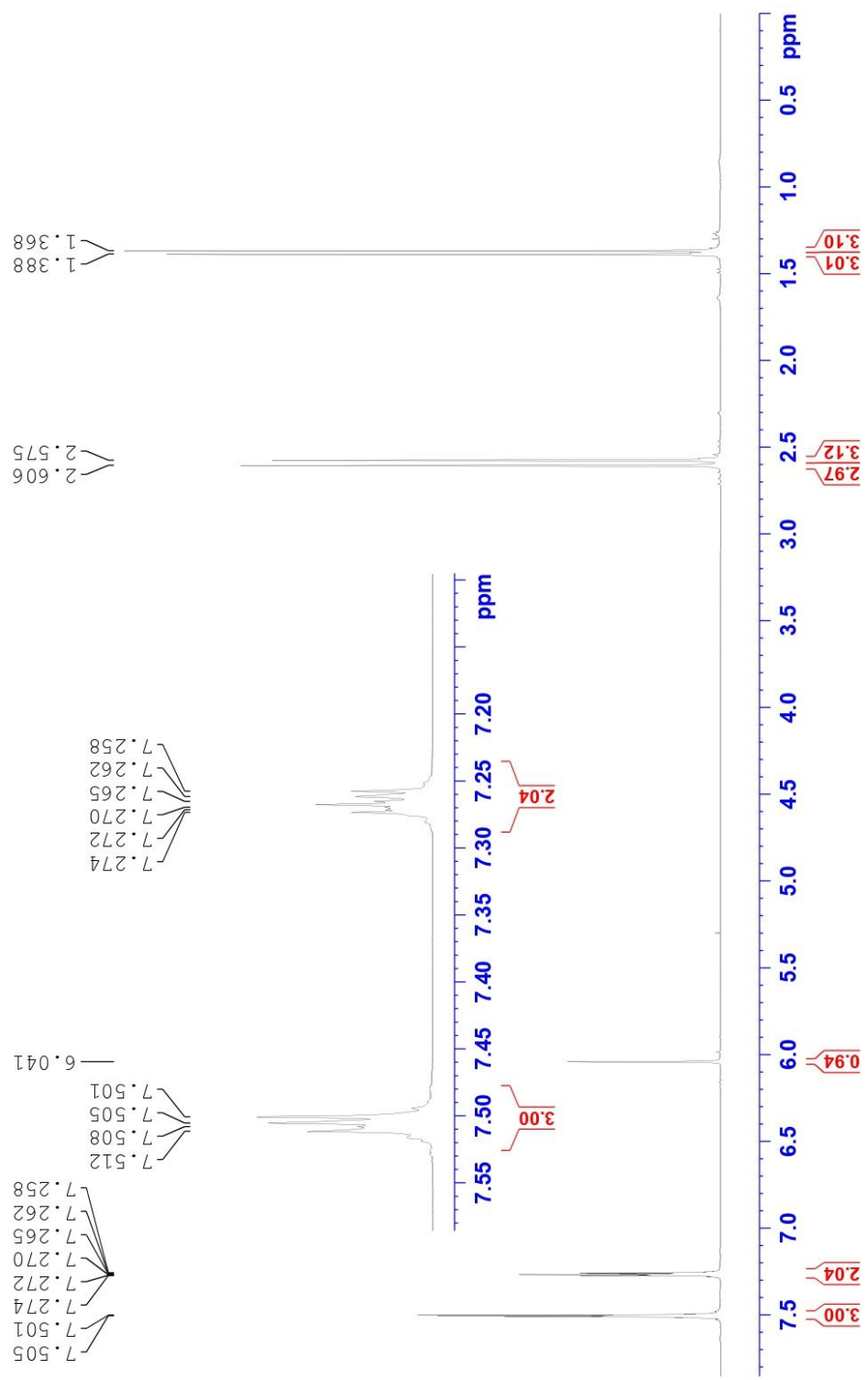
8. ^{1}H-NMR spectrum of 3 in CDCl$_3$ at 600 MHz
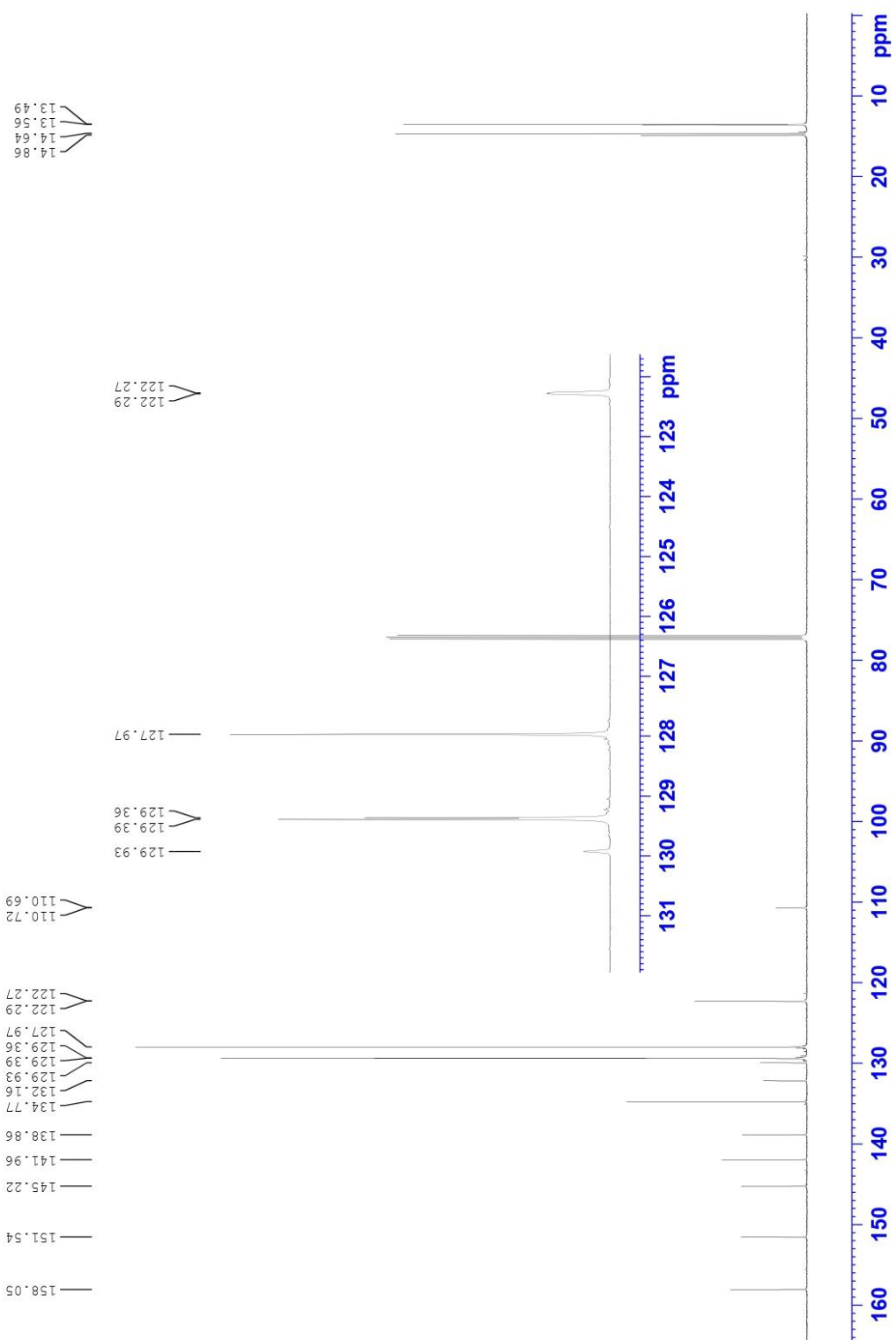
9. ^{13}C-NMR spectrum of 3 in CDCl$_3$ at 150 MHz

Meas. m/z	#	Ion Formula	m/z	err [mDa]	err [ppm]	rdb	N-Rule	e⁻ Conf	mSigma
425.060813	1	C19H18BBrF2N2Na	425.061013	-0.2	-0.5	10.5	ok	even	32.6
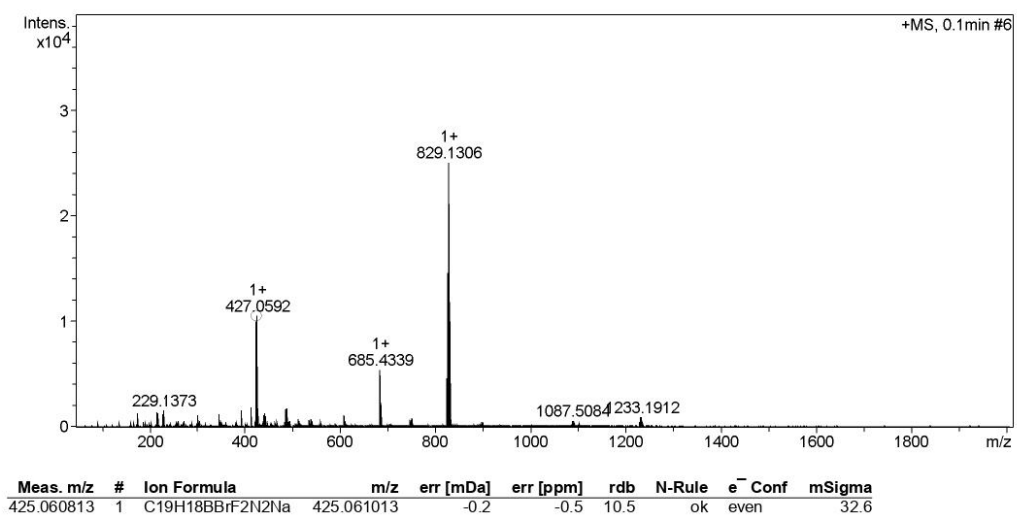
10. Mass spectrum of 3 using ESI.

A13
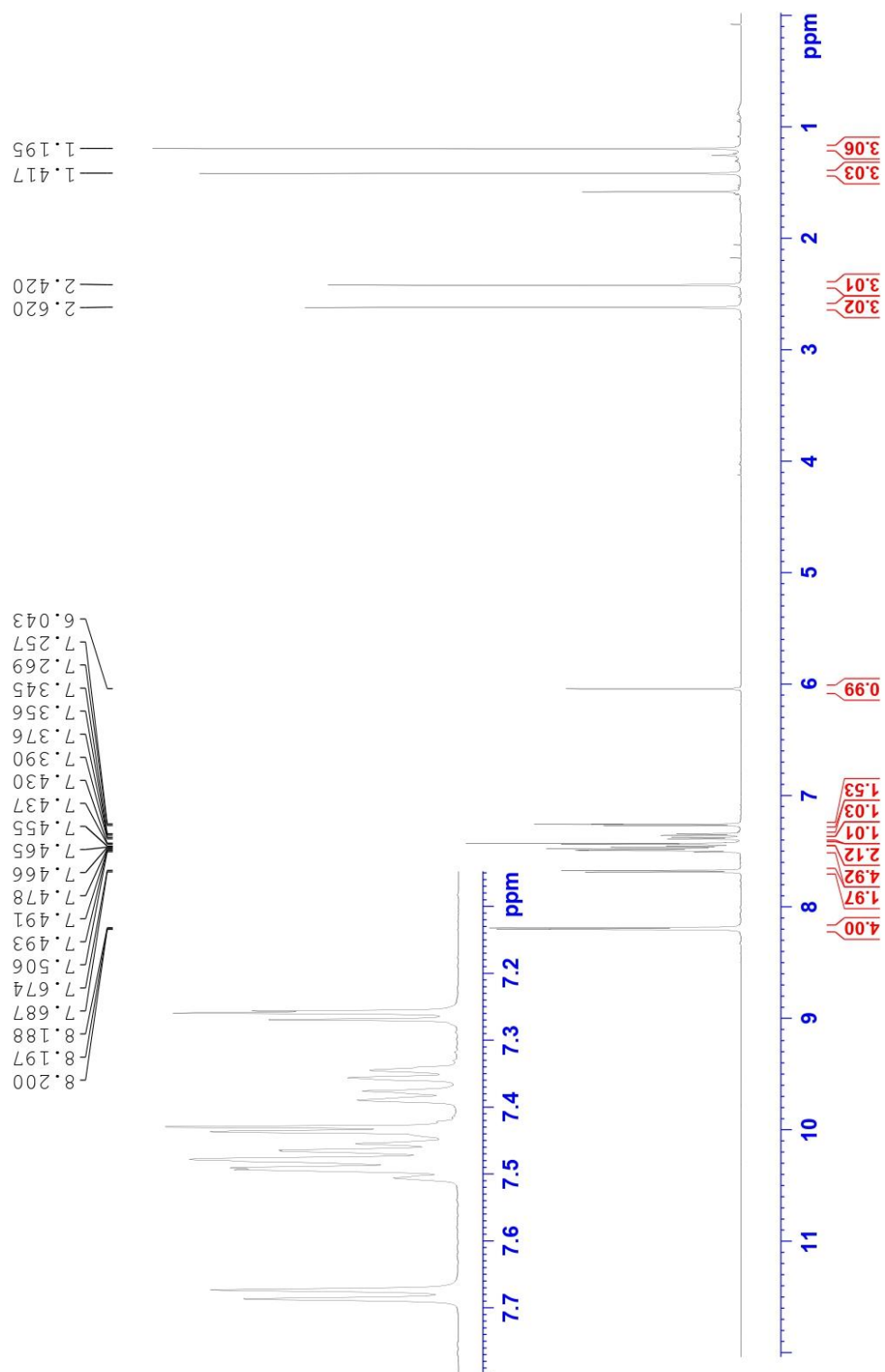
11. ^{1}H-NMR spectrum of B2P in CDCl$_3$ at 600 MHz.
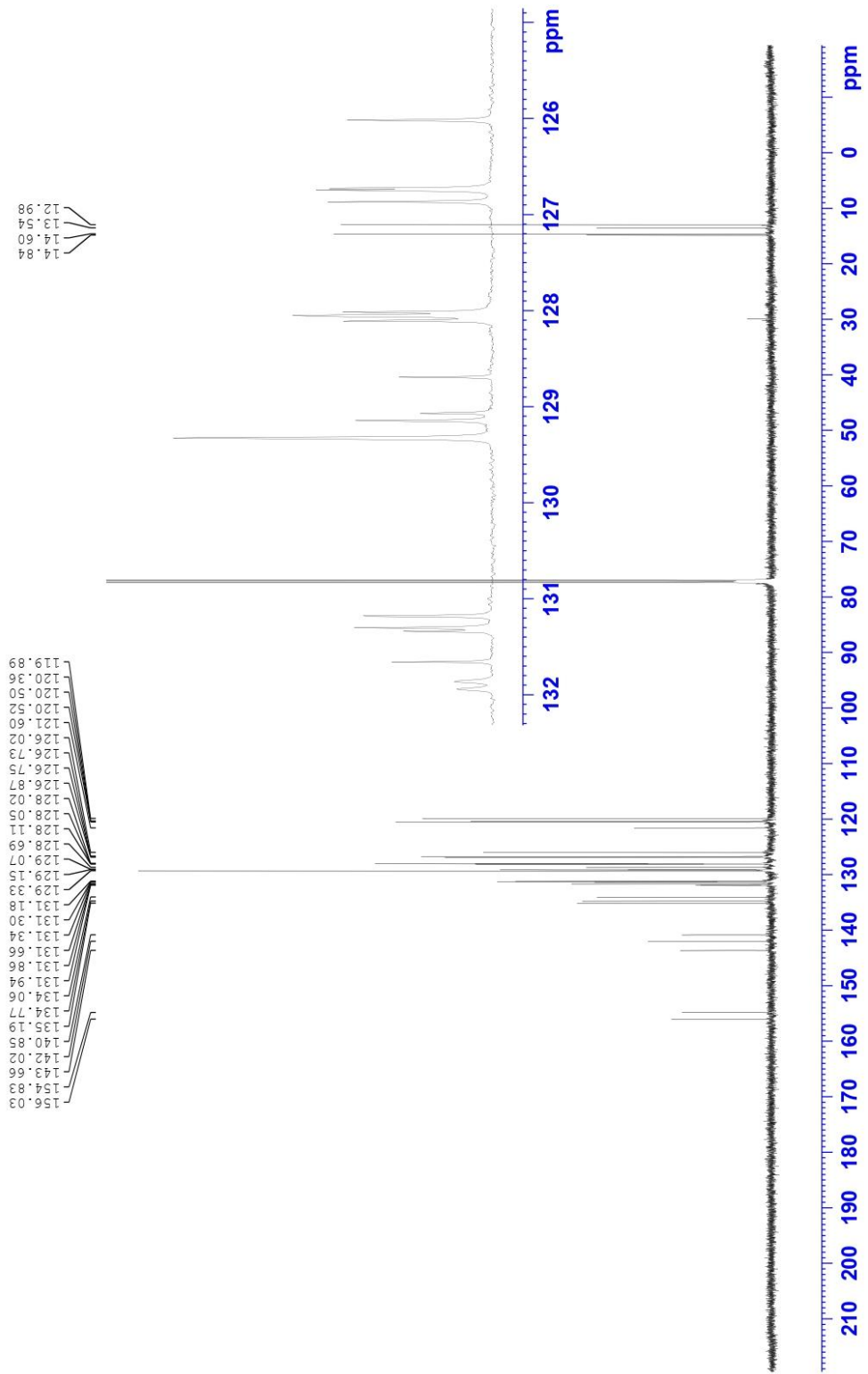
12. ^{13}C-NMR spectrum of B2P in CDCl$_3$ at 150 MHz.
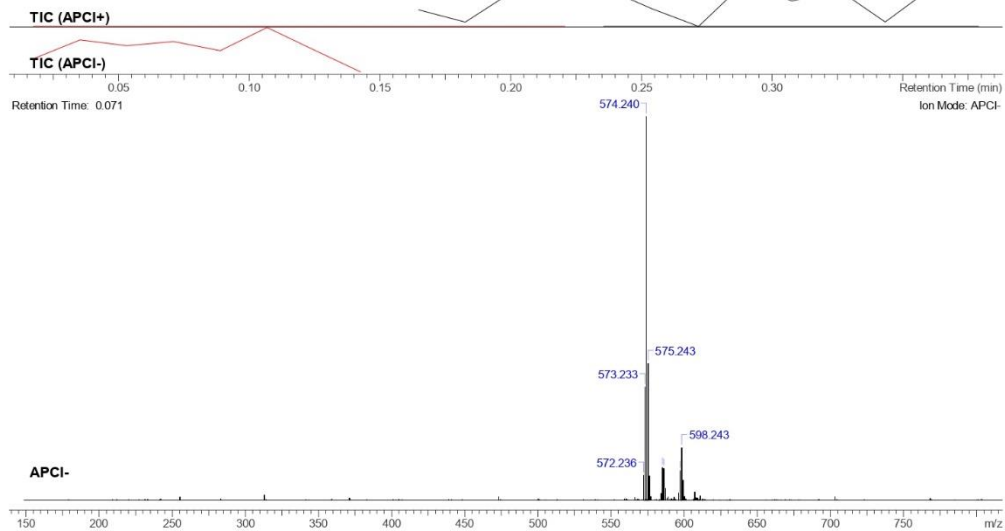
13. Mass spectrum of B2P using Atmospheric Pressure Chemical Ionisation (APCI).
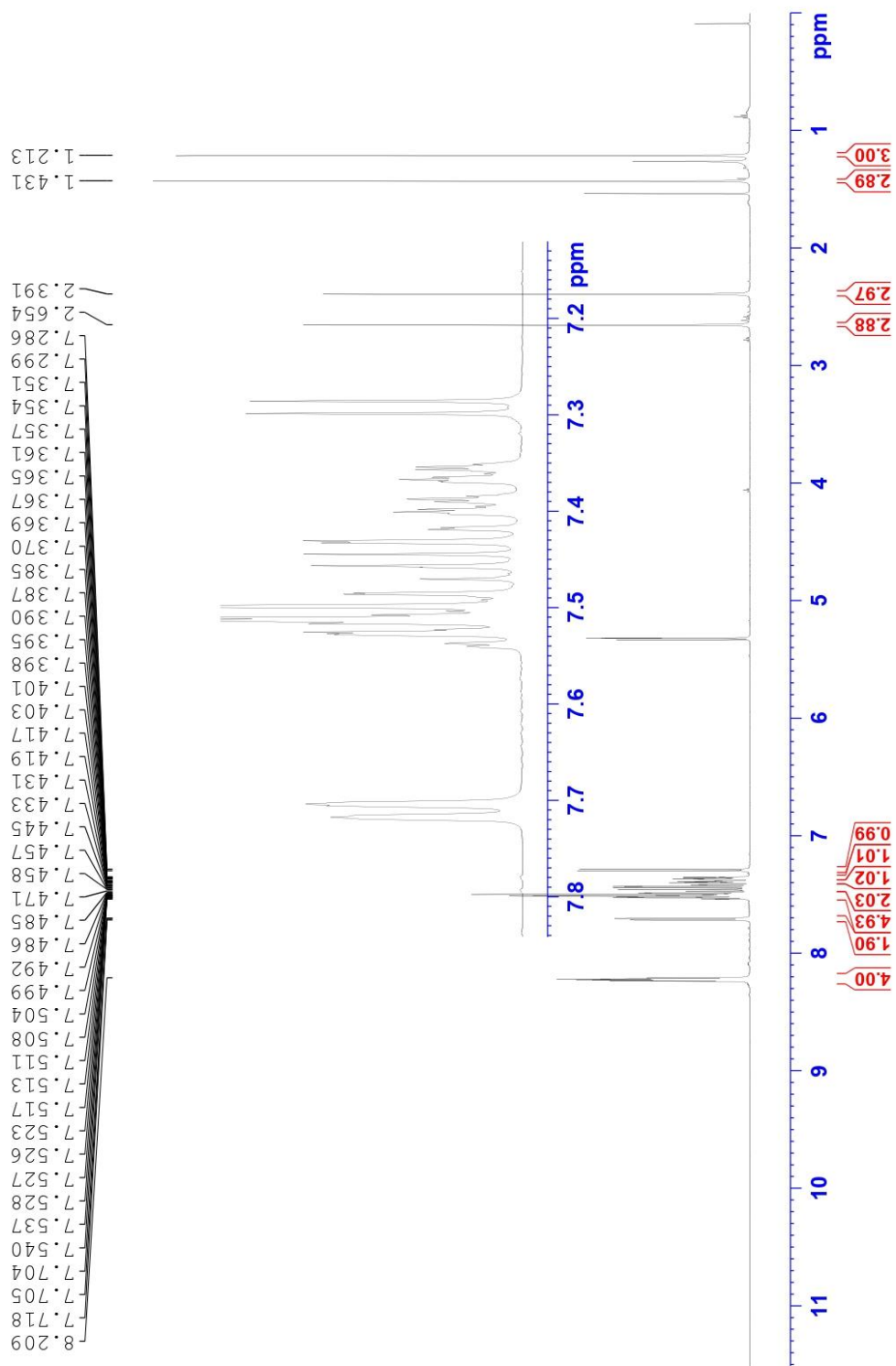
14. ^{1}H-NMR spectrum of B2PI in CD$_2$Cl$_2$ at 600 MHz

13.30
13.76
16.08
16.94

84.66

120.23
120.78
120.87
120.91
126.10
127.07
127.09
127.27
128.33
128.36
128.40
128.43
128.86
129.33
129.66
129.78
131.05
131.28
131.44
131.63
131.92
132.11
133.26
134.23
135.10
135.23
142.40
143.18
144.04
155.03
157.56
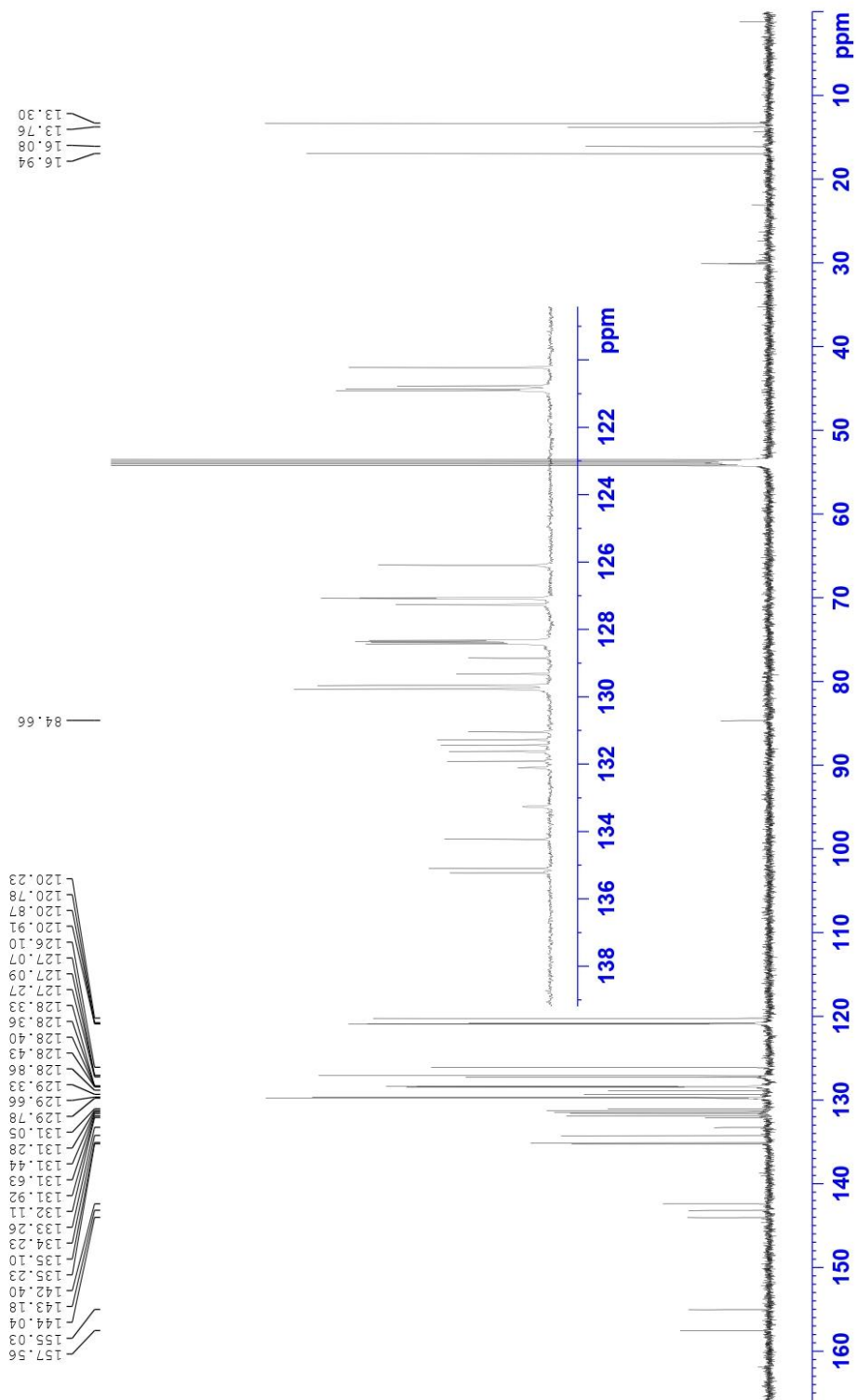
15. ^{13}C-NMR spectrum of B2PI in CD$_2$Cl$_2$ at 150 MHz
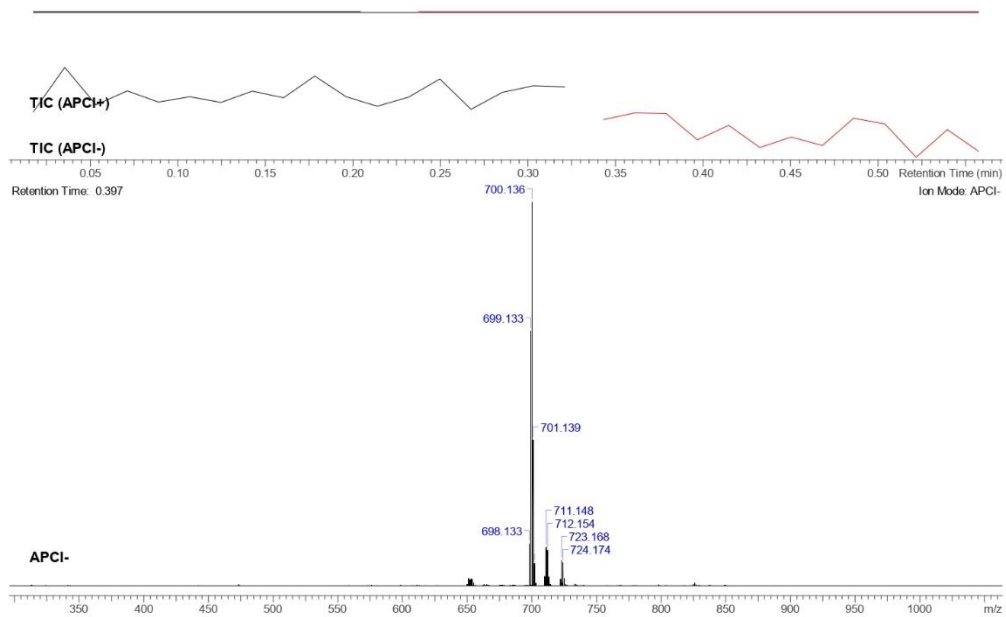
16. Mass spectrum of B2PI using APCI.

A.3 Photophysical data
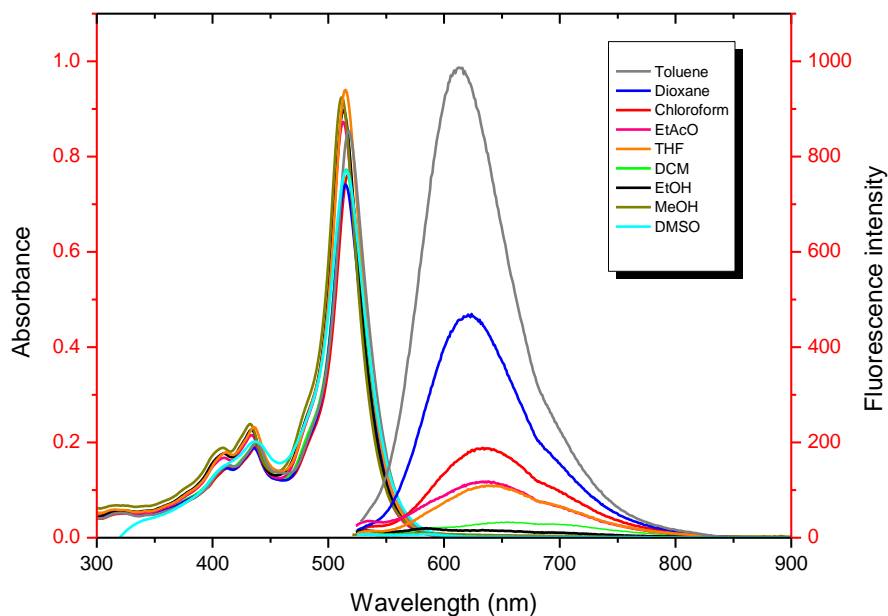
Figure A1 Absorption and emission spectra of B2P at 10 µM in different solvents, emission data recorded at 5-5 nm of slit width.
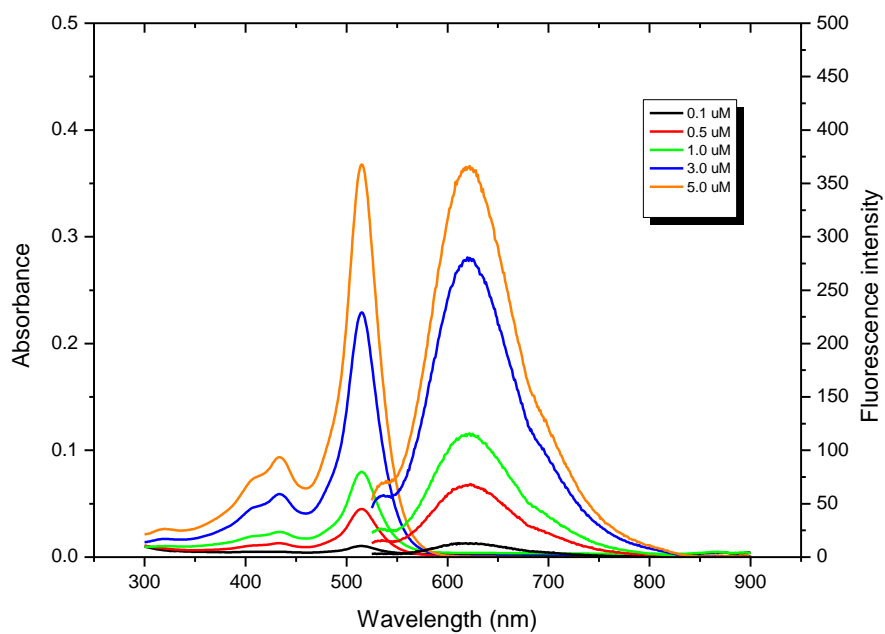
Figure A2 Concentration effect of B2P in 1,4-dioxane.
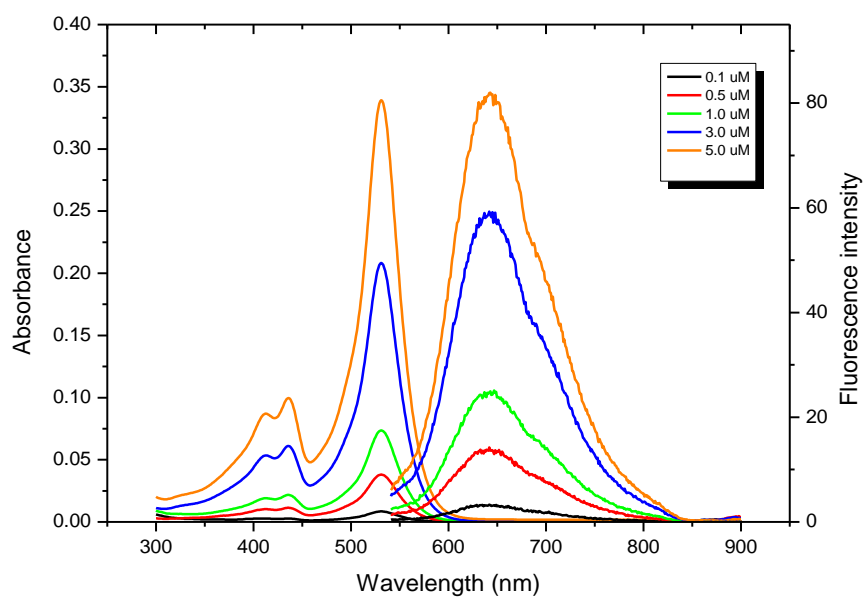
Figure A3 Concentration effect of B2PI in 1,4-dioxane.
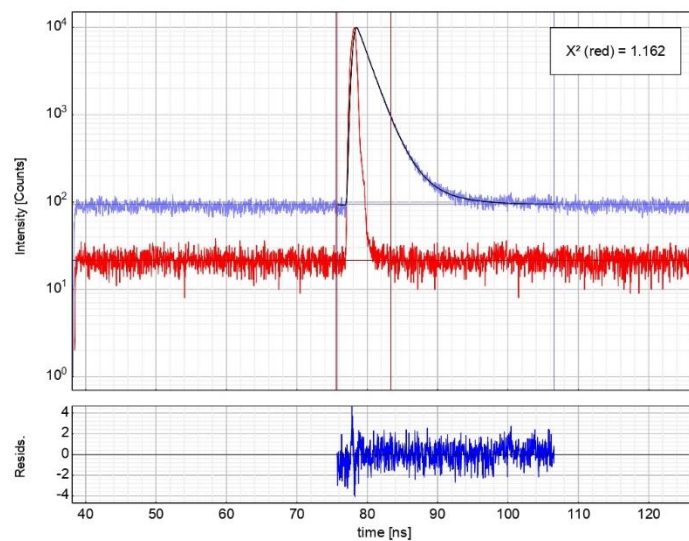
$$I(t) = \int\limits_{-\infty}^{t} IRF(t') \sum_{i=1}^{n} A_i\, e^{-\frac{t-t'}{\tau_i}}\, dt'$$

Figure A4 Example of TCSPC decay of an aerated solution of B2P at 0.1 µM in 1,4-dioxane.

A21
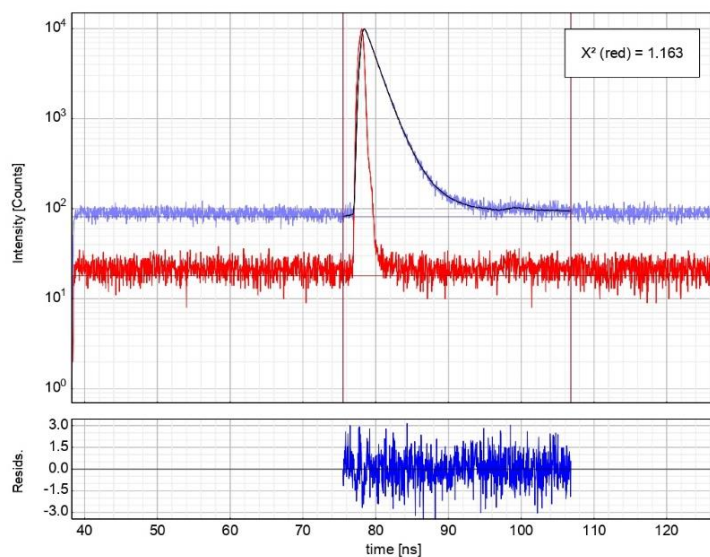
$$I(t) = \int\limits_{-\infty}^{t} IRF(t') \sum_{i=1}^{n} A_i\, e^{-\frac{t-t'}{\tau_i}}\, dt'$$

Figure A5 Example of TCSPC decay of a deaerated solution of B2P at 0.1 µM in 1,4-dioxane.
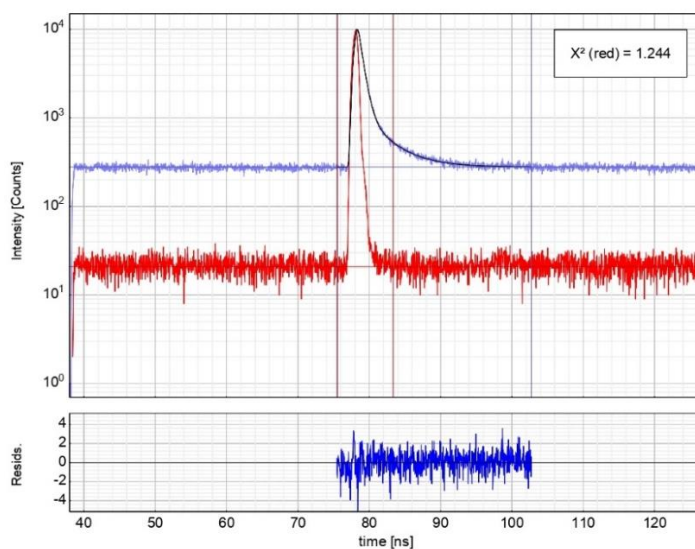
$$I(t) = \int\limits_{-\infty}^{t} IRF(t') \sum_{i=1}^{n} A_i\, e^{-\frac{t-t'}{\tau_i}}\, dt'$$

Figure A6 Example of TCSPC decay of an aerated solution of B2PI at 0.1 µM in 1,4-dioxane.

A22
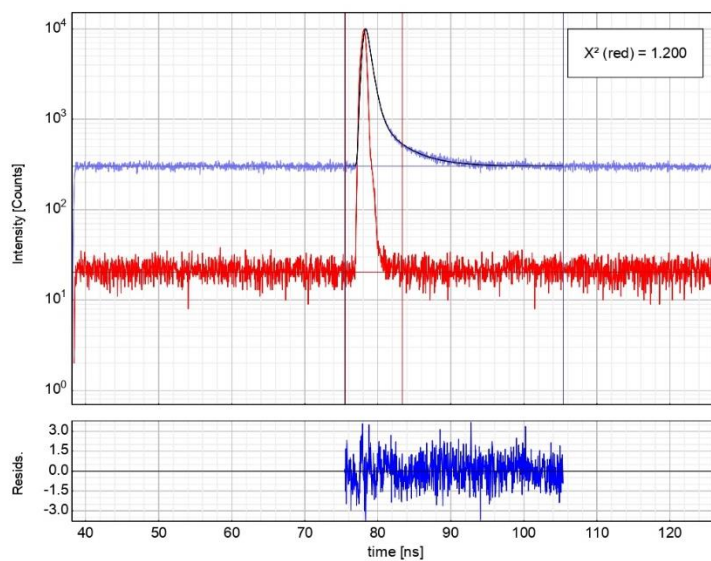
$$I(t) = \int\limits_{-\infty}^{t} IRF(t') \sum_{i=1}^{n} A_i \, e^{-\frac{t-t'}{\tau_i}} \, dt'$$

Figure A7 Example of TCSPC decay of a deaerated solution of B2PI at 0.1 µM in 1,4-dioxane.
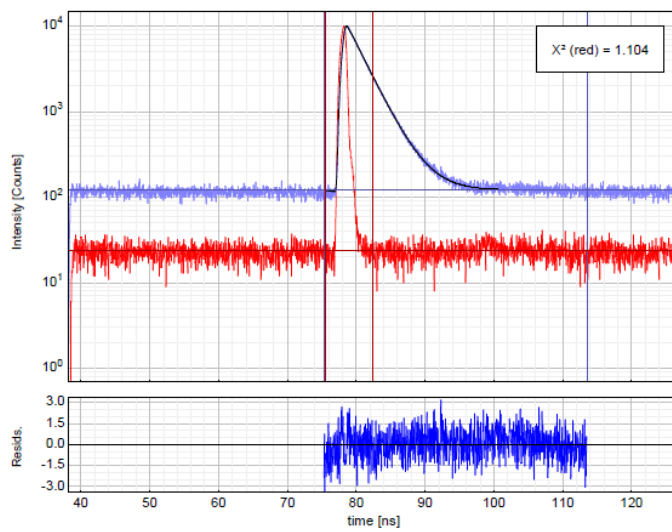
$$I(t) = \int\limits_{-\infty}^{t} IRF(t') \sum_{i=1}^{n} A_i \, e^{-\frac{t-t'}{\tau_i}} \, dt'$$

Figure A8 Example of TCSPC decay of a deaerated solution of B2P at 0.1 µM in toluene.

A23
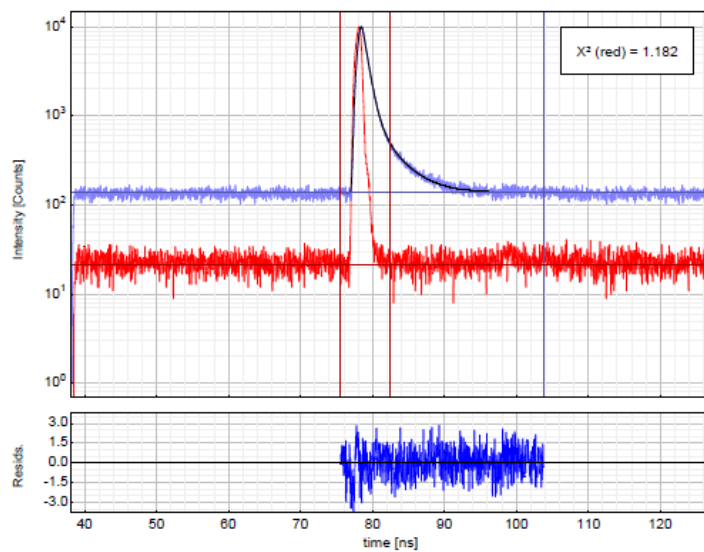
$$I(t) = \int\limits_{-\infty}^{t} IRF(t') \sum\limits_{i=1}^{n} A_i \, e^{-\frac{t-t'}{\tau_i}} \, dt'$$

Figure A9 Example of TCSPC decay of a deaerated solution of B2PI at 0.1 µM in toluene.
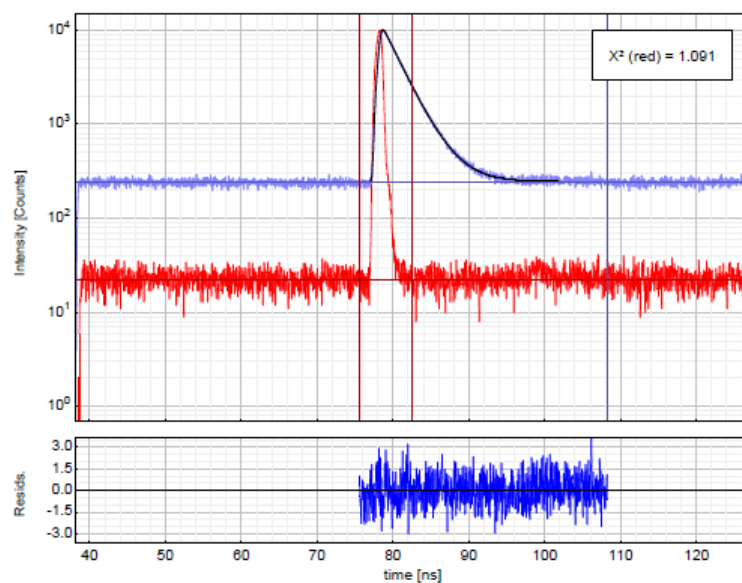
$$I(t) = \int\limits_{-\infty}^{t} IRF(t') \sum\limits_{i=1}^{n} A_i \, e^{-\frac{t-t'}{\tau_i}} \, dt'$$

Figure A10 Example of TCSPC decay of an aerated solution of B2P at 0.1 µM in toluene.

A24
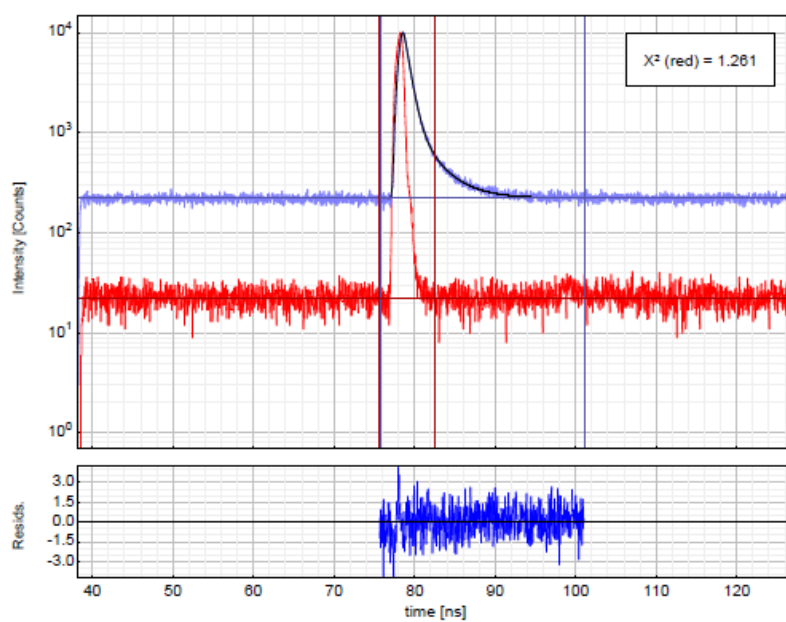
$$I(t) = \int\limits_{-\infty}^{t} IRF(t') \sum_{i=1}^{n} A_i \, e^{-\frac{t-t'}{\tau_i}} \, \mathrm{d}t'$$

Figure A11 Example of TCSPC decay of an aerated solution of B2PI at 0.1 µM in toluene.

A25
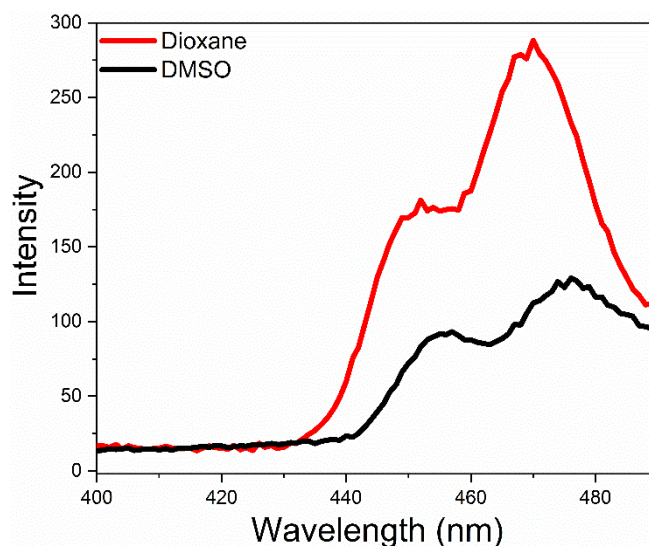
Figure A12 Up-converted emission from 5 µM B2P and 100 µM perylene in deaerated dioxane (red) and DMSO (black) at 10 nm slit width under 532 nm excitation.

Table A1 spectroscopic properties of B2P and B2PI in deaerated solutions. Air was removed by purging the solutions with argon for 15 minutes.

Compound	Deaerated			
	τ_1 (ns)	Amplitud (%)	T_2 (ns)	Amplitud (%)
Dioxane				
B2P	3.82 ± 0.32	4.8	1.75 ± 0.01	95.2
B2PI	3.54 ± 0.01	5.1	0.62 ± 0.01	94.9
Toluene				
B2P	2.61 ± 0.0	100	---	---
B2PI	3.10 ± 0.02	6.0	0.7± 0.01	94.0

A.4 Crystallography

A) B2P·[CH₃OH] $C_{39}H_{29}BF_2N_2$ [CH_3OH]

Crystal parameters, data collection and structure refinement details are summarised in Table A2.

References

Rigaku Oxford Diffraction, (2020), CrysAlisPro Software system, version 1.171.40.81a, Rigaku Corporation, Oxford, UK.

C.B. Hübschle, G.M. Sheldrick and B. Dittrich. *J. Appl. Cryst.*, 2011, **44**, 1281-1284.

O.V. Dolomanov, L.J. Bourhis, R.J. Gildea, J.A.K. Howard and H. Puschmann. *J. Appl. Cryst.*, 2009, **42**, 339-341

G.M. Sheldrick, *Acta Cryst.*, 2015, **A71**, 3-8.

A.L. Spek, (2015). *Acta Cryst.* C**71**, 9–18.
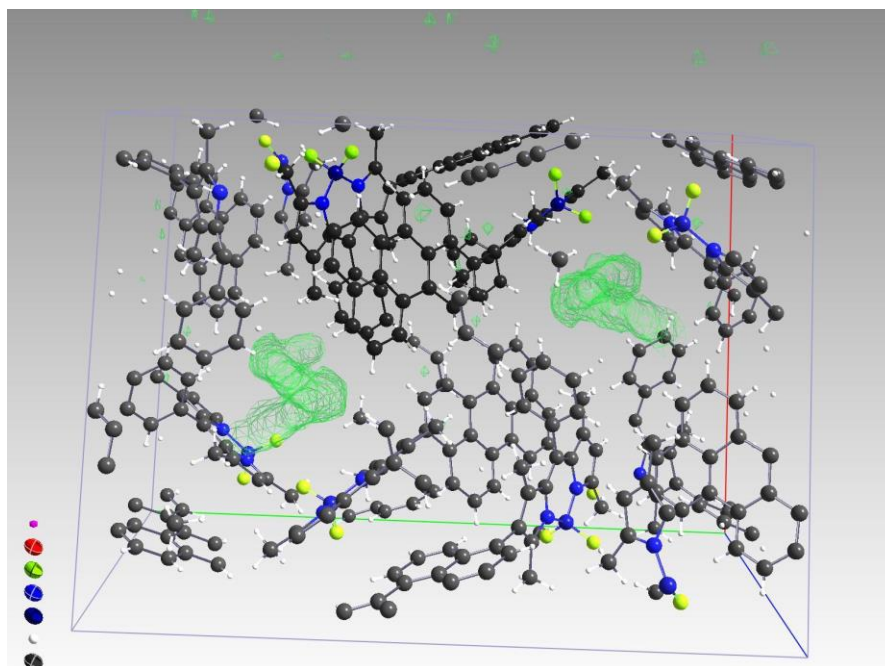
Figure A13 Diffuse electron density (green surface) due to disordered solvent – assigned to one molecule of MeOH per molecule.

Table A 2 **Crystal data and structure refinement for B2P·[CH₃OH]**

Empirical formula	$C_{40}H_{33}BN_2F_2O$
Formula weight	606.49
Temperature/K	100.01(10)
Crystal system	monoclinic
Space group	$P2_1/c$
a/Å	18.7924(6)
b/Å	26.3468(4)
c/Å	13.2543(3)
α/°	90
β/°	106.402(3)
γ/°	90
Volume/Å³	6295.4(3)
Z	8
ρ_{calc} g/cm³	1.280
μ/mm⁻¹	0.674
F(000)	2544.0
Crystal size/mm³	0.21 × 0.067 × 0.027
Radiation (Å)	Cu Kα (λ = 1.54184 Å)
2θ range for data collection/°	4.902 to 136.502
Index ranges	-22 ≤ h ≤ 22, -31 ≤ k ≤ 18, -15 ≤ l ≤ 15
Reflections collected	22736
Independent reflections	11407 [R_{int} = 0.0284, R_{sigma} = 0.0431]
Data/restraints/parameters	11407/0/801
Goodness-of-fit on F²	1.021
Final R indexes [I>=2σ (I)]	R1 = 0.0583, wR2 = 0.1434
Final R indexes [all data]	R1 = 0.0814, wR2 = 0.1595

Description

The asymmetric unit contains two independent B2P molecules and some disordered solvate. The two molecules (A and B) are very similar (Figs S14 & S15), although the ADPs of molecule B suggest a slight disorder; this has not been modelled. Additionally, the perylene moiety in molecule B is distinctly less planar than that of molecule A (Table A3). In each case the mean plane of the perylene group is rotated with respect to the mean plane of the BODIPY core, and the interplanar angles are 73.54(3)° and 74.512(4)° for molecules A and B, respectively.
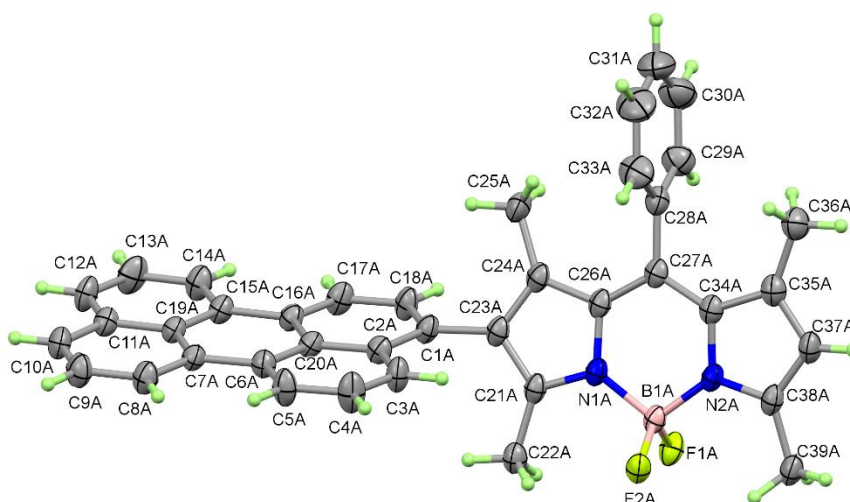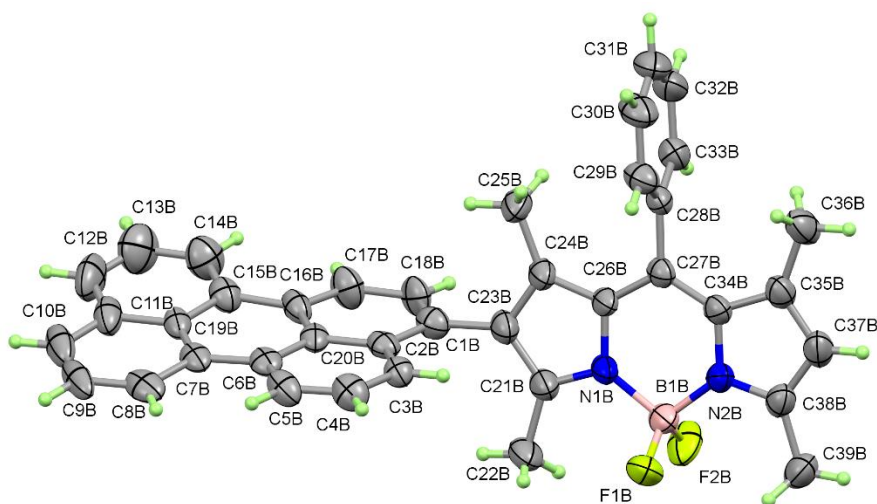
Figure A14 The two independent molecules in the asymmetric unit of B2P·[CH₃OH] showing the labelling scheme and 50% probability ellipsoids.
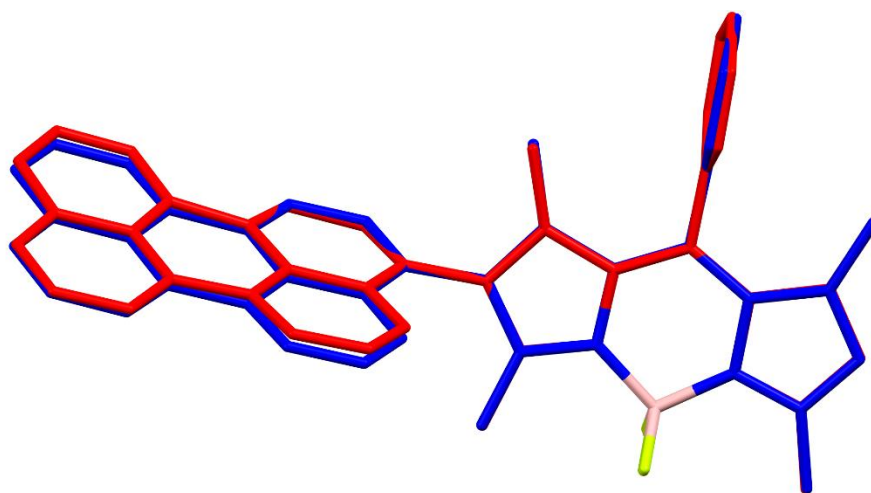
Figure A 15 Overlay of molecules A (blue) and B(red)

Molecule A is paired with a symmetry equivalent by inversion (symmetry operation 2-x, 1-y, -z) to generate π-stacked dimeric units, although the overlap is mostly confined to one edge of the perylene (Fig S16); this stacking does not extend further through the structure. There are no equivalent π-interactions involving molecule B.
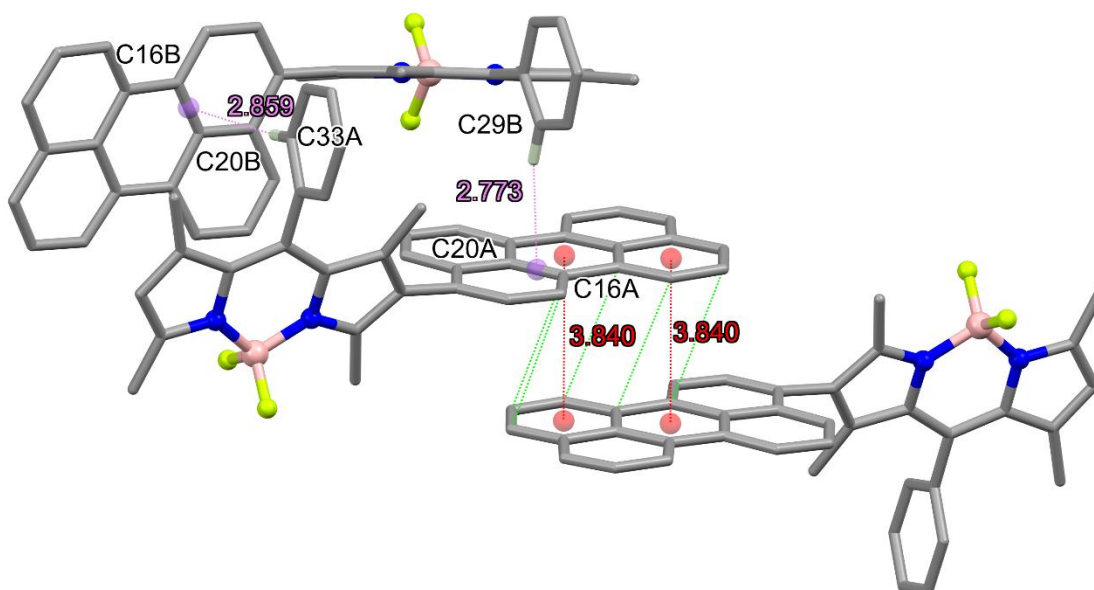
Figure A16 π-interactions showing centroid-centroid distances (Å) between molecule A and its symmetry equivalent under 2-x, 1-y, -z in red. The dashed green lines show C – C distances in the range 3.71-3.72 Å and the violet lines show C–H···π(bond centroid) interactions.

Molecules A and B are weakly linked via two C–H···π interactions and by a number of (sp^3)C –H ···F interactions (Table A3) linking the molecules in layers perpendicular to *b* (Table A3 and Fig A17).

Table A 3 **Hydrogen Bonds for B2P·[CH₃OH] .**

D	H	A	d(D-H)/Å	d(H-A)/Å	d(D-A)/Å	D-H-A/°
C22A	H22B	F2A	0.96	2.48	3.058(3)	118.9
C22A	H22B	F2B[1]	0.96	2.55	3.197(3)	125.2
C39A	H39A	F2A	0.96	2.44	3.133(3)	128.8
C37B	H37B	F1B[2]	0.93	2.41	3.215(3)	144.1
C39B	H39F	F2B	0.96	2.58	3.144(4)	117.9

[1] 2-x,1-y,1-z;   [2] x,½-y,-½+z
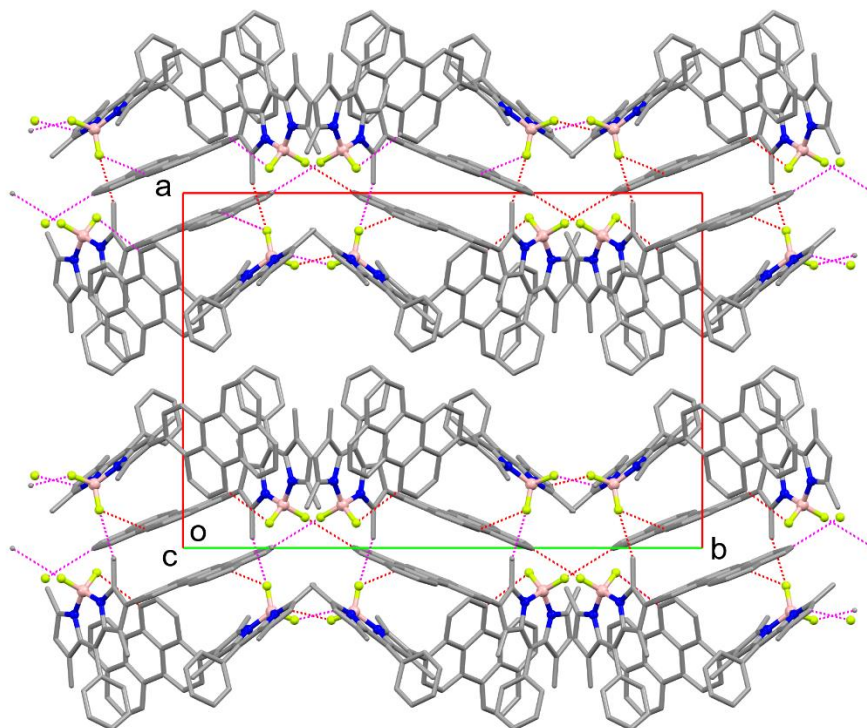
Figure A17 Unit cell packing viewed down the b axis. Dotted lines represent hydrogen bonds

Table A4 Least-squares planes (x,y,z in crystal coordinates) and deviations from them (* indicates atom used to define plane)

1.8440 (0.0104) x + 21.7839 (0.0052) y - 7.4094 (0.0035) z = 12.8094 (0.0111)

```
* -0.0250 (0.0016)  N1A
*  0.0262 (0.0016)  N2A
*  0.0622 (0.0018)  B1A
* -0.1042 (0.0017)  C21A
* -0.0449 (0.0017)  C23A          BODIPY of mol A
*  0.0882 (0.0017)  C24A
*  0.0621 (0.0019)  C26A
*  0.0185 (0.0017)  C27A
* -0.0371 (0.0019)  C34A
* -0.0847 (0.0018)  C35A
* -0.0135 (0.0019)  C37A
*  0.0522 (0.0018)  C38A
```

Rms deviation of fitted atoms =   0.0588

16.9883 (0.0022) x + 9.8545 (0.0072) y - 0.7502 (0.0040) z = 20.1561 (0.0023)

Angle to previous plane (with approximate esd) = 73.545 (0.035)

```
* -0.0006 (0.0021)  C1A
*  0.0106 (0.0021)  C2A
* -0.0327 (0.0023)  C3A
```

```
*  -0.0612 (0.0026)  C4A
*  -0.0335 (0.0025)  C5A
*   0.0201 (0.0022)  C6A
*   0.0324 (0.0021)  C7A
*   0.0533 (0.0023)  C8A
*   0.0372 (0.0023)  C9A                    perylene of mol A
*  -0.0051 (0.0022)  C10A
*  -0.0233 (0.0022)  C11A
*  -0.0563 (0.0024)  C12A
*  -0.0401 (0.0025)  C13A
*  -0.0042 (0.0024)  C14A
*   0.0147 (0.0022)  C15A
*   0.0422 (0.0021)  C16A
*   0.0401 (0.0023)  C17A
*   0.0064 (0.0022)  C18A
```

Rms deviation of fitted atoms =   0.0339

  14.5140 (0.0070) x + 16.6127 (0.0134) y - 1.9119 (0.0082) z = 16.7147 (0.0022)

Angle to previous plane (with approximate esd) = 18.201 (0.052)

```
*   0.0027 (0.0022)  N1B
*   0.0157 (0.0021)  N2B
*  -0.0031 (0.0027)  B1B
*   0.0272 (0.0025)  C21B
*  -0.0060 (0.0024)  C23B
*  -0.0256 (0.0023)  C24B              BODIPY of mol B
*  -0.0205 (0.0024)  C26B
*   0.0069 (0.0022)  C27B
*   0.0332 (0.0023)  C34B
*   0.0207 (0.0023)  C35B
*  -0.0277 (0.0025)  C37B
*  -0.0234 (0.0024)  C38B
```

Rms deviation of fitted atoms =   0.0204

- 2.0320 (0.0077) x + 17.0726 (0.0064) y - 9.1814 (0.0029) z = 2.0539 (0.0078)

Angle to previous plane (with approximate esd) = 74.512 (0.041)

```
*  -0.0847 (0.0025)  C1B
*  -0.0035 (0.0023)  C2B
*   0.1312 (0.0022)  C3B
*   0.2116 (0.0025)  C4B
*   0.1421 (0.0025)  C5B
*   0.0182 (0.0022)  C6B
*  -0.0550 (0.0022)  C7B
*  -0.1510 (0.0024)  C8B
*  -0.1849 (0.0026)  C9B                    perylene of mol B
*  -0.1098 (0.0028)  C10B
*  -0.0093 (0.0028)  C11B
```

* 0.1195 (0.0033) C12B
* 0.2156 (0.0037) C13B
* 0.1653 (0.0034) C14B
* 0.0301 (0.0027) C15B
* -0.0700 (0.0025) C16B
* -0.1763 (0.0031) C17B
* -0.1890 (0.0027) C18B

Rms deviation of fitted atoms =   0.1339

B) Compound 2 $C_{19}H_{18}N_2BF_2Br$**:**

This structure has been reported previously (CCDC number1819378, M.Gorbe, A.M. Costero, F. Sancenon, R. Martinez-Manez, R. Ballesteros-Cillero, L.E. Ochando, K. Chulvi, R. Gotor, S. Gil, *Dyes Pigm.* (2019), **160**, 198-207, doi:10.1016/j.dyepig.2018.08.007). The current version seems to have somewhat less disorder and hence an improved refinement.

Experimental

The data were collected at 100(1) K on a Synergy, Dualflex, AtlasS2 diffractometer using Cu$K\alpha$ radiation (λ = 1.54184 Å) and the *CrysAlis PRO* 1.171.40.29a suite[1]. Using SHELXLE[2] and Olex2[3] the structure was solved by dual space methods (SHELXT[4]) and refined on F^2 using all the reflections (SHELXL-2018/3[5]). All the non-hydrogen atoms were refined using anisotropic atomic displacement parameters and hydrogen atoms were inserted at calculated positions using a riding model. There is one significant residual peak in the electron density map (2.39 e Å^{-3} near C17); this is ascribed to the Br atom of a small disordered component (inverted and slightly translated relative to the main component which has not been modelled. Crystal parameters, data collection and structure refinement details are summarised in Table A5.

Rigaku Oxford Diffraction, (2018), CrysAlisPro Software system, version 1.171.40.81a, Rigaku Corporation, Oxford, UK.

C.B. Hübschle, G.M. Sheldrick and B. Dittrich. *J. Appl. Cryst.*, 2011, **44**, 1281-1284.

O.V. Dolomanov, L.J. Bourhis, R.J. Gildea, J.A.K. Howard & H. Puschmann. J. Appl. Cryst., 2009, **42**, 339-341

Table A 5 **Crystal data and structure refinement for 2.**

Empirical formula	$C_{19}H_{18}N_2BF_2Br$
Formula weight	403.07
Temperature/K	100.00(10)
Crystal system	monoclinic
Space group	$P2_1/n$
a/Å	10.9836(2)
b/Å	12.2567(3)
c/Å	12.9727(3)
α/°	90
β/°	97.381(2)
γ/°	90
Volume/Å^3	1731.95(7)
Z	4
ρ_{calc} g/cm^3	1.546
μ/mm^{-1}	3.442
F(000)	816.0
Crystal size/mm^3	0.133 × 0.095 × 0.028
Radiation (Å)	Cu Kα (λ = 1.54184 Å)
2θ range for data collection/°	9.944 to 149.922
Index ranges	-13 ≤ h ≤ 13, -14 ≤ k ≤ 15, -16 ≤ l ≤ 16
Reflections collected	48487
Independent reflections	3532 [R_{int} = 0.0561, R_{sigma} = 0.0195]
Data/restraints/parameters	3532/0/230
Goodness-of-fit on F^2	1.056
Final R indexes [I>=2σ (I)]	R_1 = 0.0400, wR_2 = 0.1071
Final R indexes [all data]	R_1 = 0.0423, wR_2 = 0.1093
Largest diff. peak/hole / e Å^{-3}	2.39/-0.49
CCDC number	2157530

Description
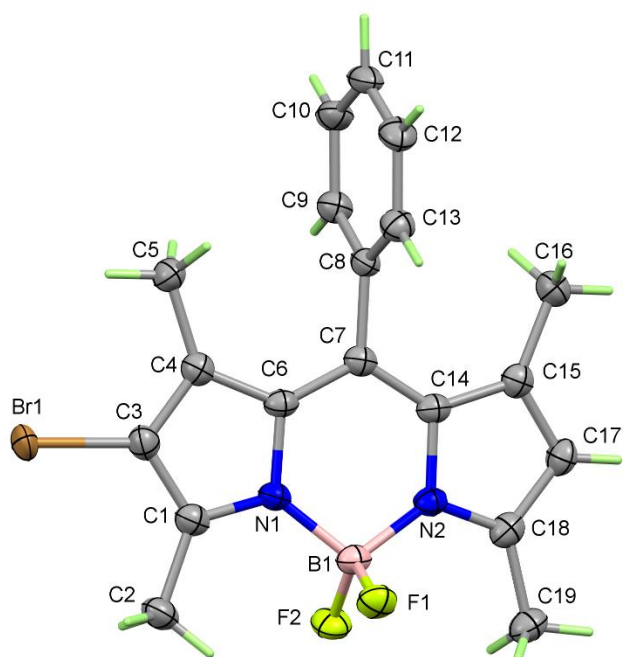
Figure A18 Asymmetric unit of 2 showing 50% probability displacement ellipsoids.

The molecule has the expected geometry (Fig S18), there are no very striking π-interactions but there are a few C-H ···· F H interactions (Fig S19). This results in herring-bone type packing (Fig A20)
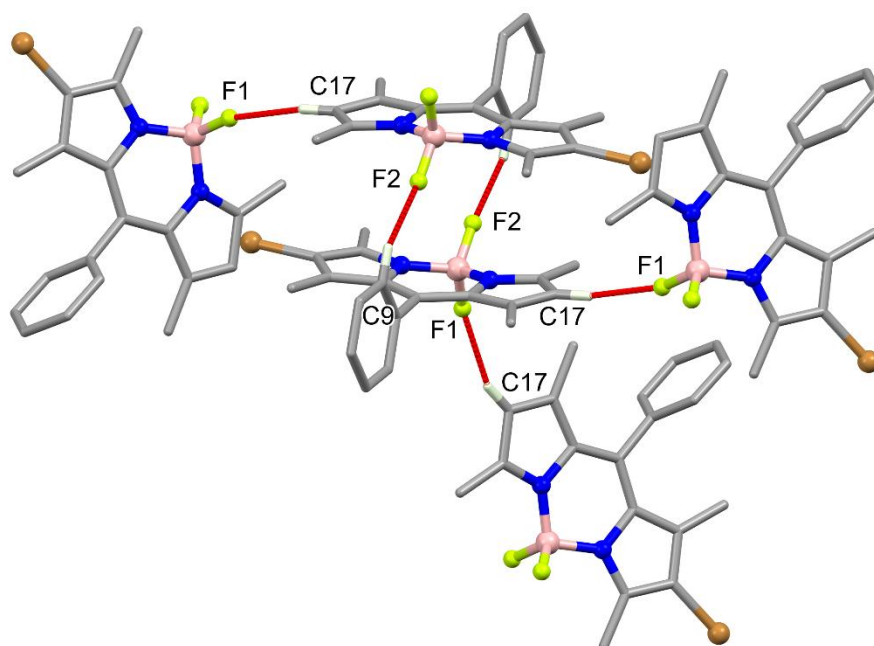
Figure A19 C-H ⋯ F H-bonds in 3. Hydrogen atoms not involved with H-bonds are omitted.
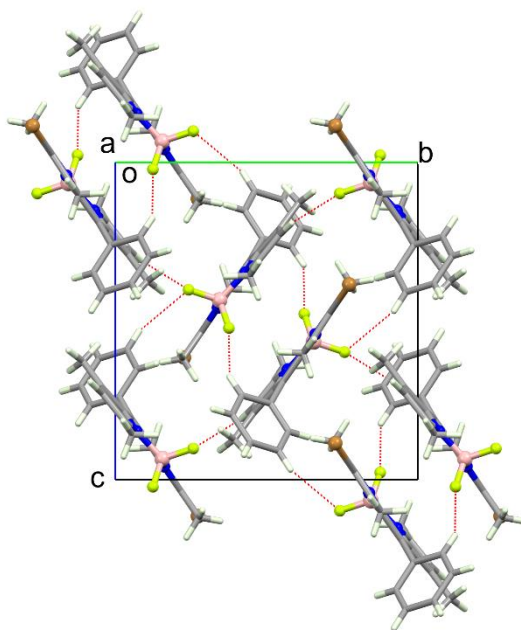
Figure A20 Unit cell packing for 3 viewed down the a axis.

A.5 Computational Studies

Table A 6 : Excited state properties of the three lowest singlet states of B2P and B2PI at the S_0 geometry. The orbital transitions, weights, vertical absorption energies (VA), wavelengths, oscillator strengths (f) and charge density differences (CDD) were calculated at the MN15/6-311++G(2d,p)/MWB46, PCM=1,4-Dioxane level of theory.
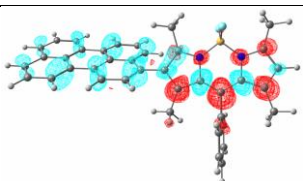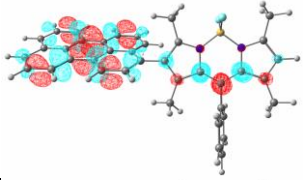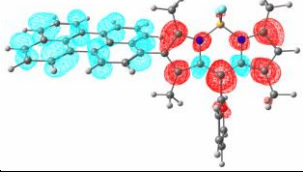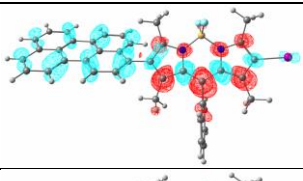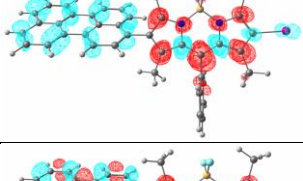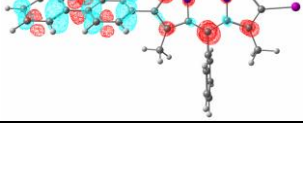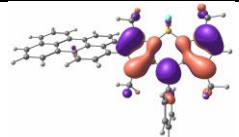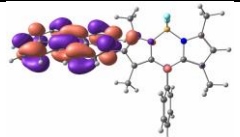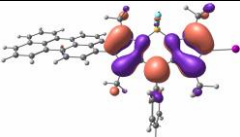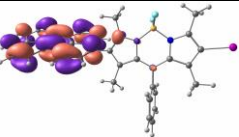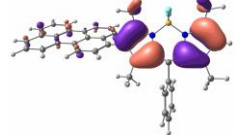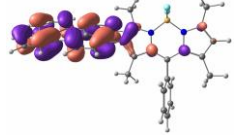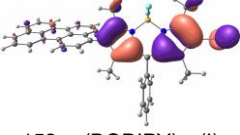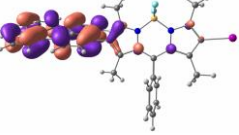
State	Transition	Weight (%)	VA (eV)	λ (nm)	f	CDD
B2P						
S_1	150 → 151 149 → 151	63 23	2.57	483	1.128	
S_2	150 → 152 149 → 151	81 15	2.92	425	0.087	
S_3	149 → 151 150 → 151	58 32	2.98	416	0.272	
B2PI						
S_1	153 → 154 152 → 154	64 25	2.51	493	1.126	
S_2	152 → 154 153 → 154	71 21	2.89	429	0.117	
S_3	153 → 155 153 → 154	85 11	2.91	426	0.346	

Table A 7 Frontier molecular orbitals of B2P and B2PI.

B2P		B2PI	
  151: π*(BODIPY) (LUMO)	 152: π*(Perylene) (LUMO+1)	 154: π*(BODIPY) (LUMO)	 155: π*(Perylene) (LUMO+1)
  149: π(BODIPY) (HOMO-1)	 150: π(Perylene) (HOMO)	 152: π(BODIPY),π(I) (HOMO-1)	 153: π(Perylene) (HOMO)

Figure A 21 Calculated RR spectrum (MN15/6-311++G(2d,p)/MWB46, PCM=1,4-Dioxane) of B2PI obtained within the short-time approximation (i.e. vertical gradients method) assuming resonance with the S_1 state (i.e. mixing of $\pi \rightarrow \pi^*$ excitation localized on the BODIPY fragment and of $\pi \rightarrow \pi^*$ excitation from the perylene fragment toward the BODIPY fragment).
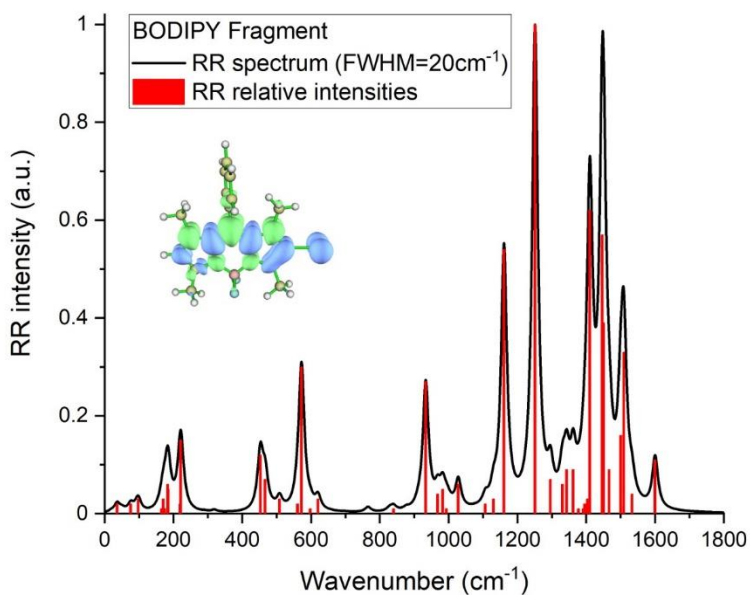
Figure A 22 Calculated RR spectrum (MN15/6-311++G(2d,p)/MWB46, PCM=1,4-Dioxane) of the BODIPY fragment obtained within the short-time approximation (i.e. vertical gradients method) assuming resonance with the S_1 state (i.e. $\pi \rightarrow \pi^*$ excitation localized on the BODIPY core).
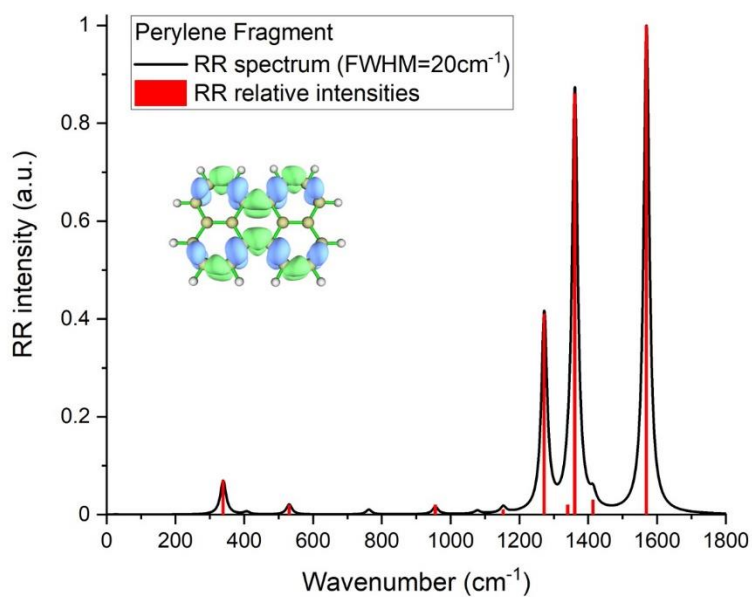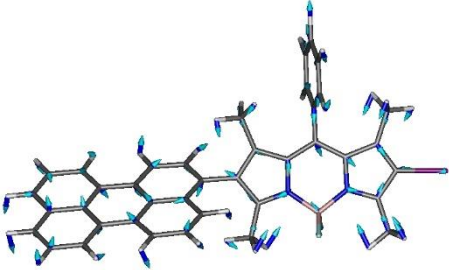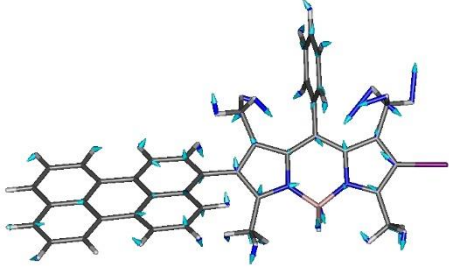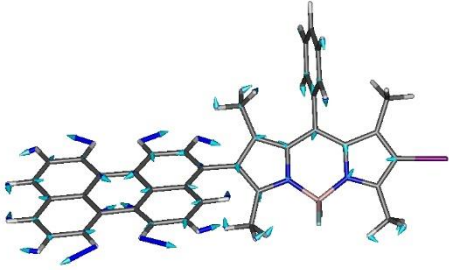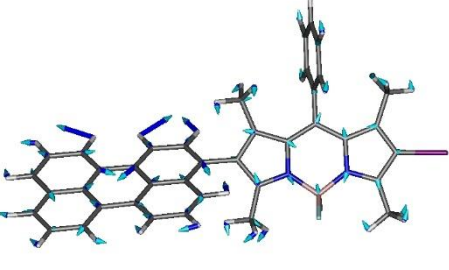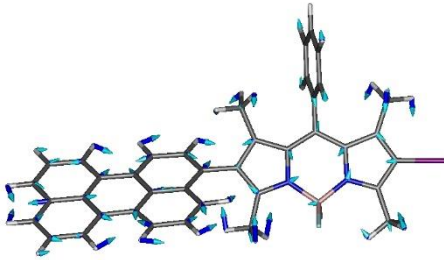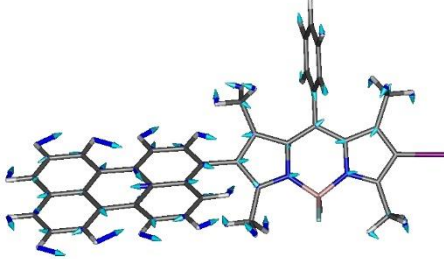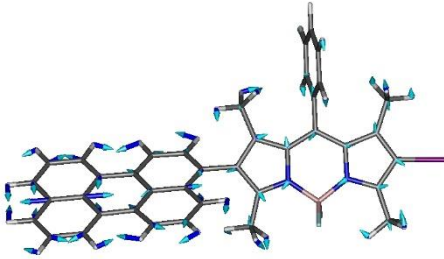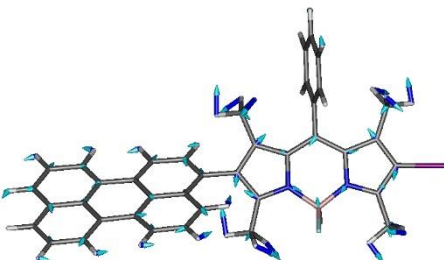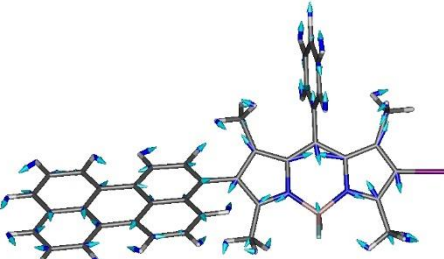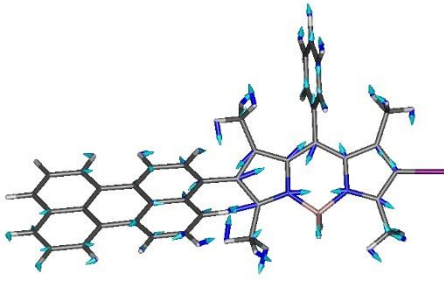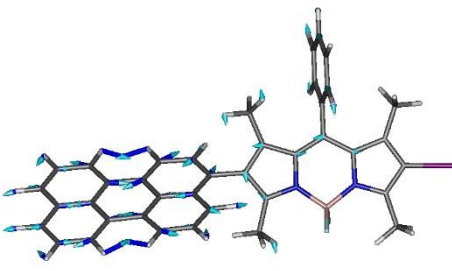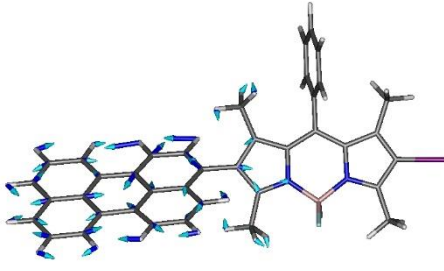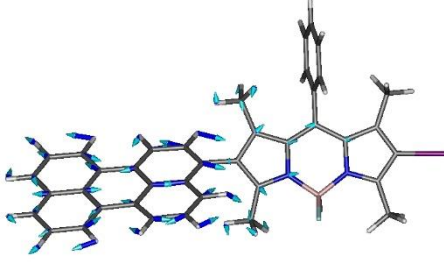
Figure A 23 Calculated RR spectrum (MN15/6-311++G(2d,p)/MWB46, PCM=1,4-Dioxane) of the perylene fragment obtained within the short-time approximation (i.e. vertical gradients method) assuming resonance with the S_1 state (i.e. $\pi \rightarrow \pi^*$ excitation localized on perylene).

Table A 8 Calculated vibrational frequencies and normal coordinates of the most Raman active modes of B2PI (MN15/6-311++G(2d,p)/MWB46, PCM=1,4-Dioxane). The frequencies were scaled by the factor 0.96. The relative RR intensities were obtained with the simplified Φ_e approximation including the contribution of the states S_1, S_2 and S_3. The assigned experimental frequencies are given in brackets.

Mode number	Freq. (cm^{-1})	Relative RR intensity	Normal mode
64	582.6 (*600.0*)	0.04	
108	982.0 (*958.1*)	0.07	
140	1270.7 (*1296.5*)	0.19	
141	1281.5 (*1296.5*)	0.20	

150	1344.5 (*1364.5*)	0.22	
151	1354.0 (*1364.5*)	0.25	
152	1358.3 (*1364.5*)	0.37	
166	1425.6	0.14	
173	1498.5	0.12	

177	1536.9	0.14	
178	1567.7 (*1567.0*)	1.00	
180	1579.7 (*1567.0*)	0.14	
182	1586.9 (*1567.0*)	0.48	

Appendix B

Supporting information for Chapter 3.

Contents

B. 1 Crystallography

Sample: MB2P·0.475(CHCl$_3$)   C$_{42}$H$_{35}$BF$_2$N$_2$·0.475(CHCl$_3$):

Experimental:

The data were collected at 100(1)K on a Synergy, Dualflex, AtlasS2 diffractometer using Cu$K\alpha$ radiation (λ = 1.54184 Å) and the *CrysAlis PRO* 1.171.40.67a suite[1]. Using SHELXLE[2] and Olex2[3] the structure was solved by dual space methods (SHELXT[4]) and refined on F^2 using all the reflections (SHELXL-2018/3[5]) using a range of restraints. All the non-hydrogen atoms were refined using anisotropic atomic displacement parameters, except for the carbon atoms of the overlapping, partial-occupancy chloroform solvate molecules and the 5% occupancy chlorine atoms. Hydrogen atoms were inserted at calculated positions using a riding model. The crystals diffracted poorly, and, despite a long collection time (*ca*. 80 hr), the data set is very weak and shows significant disorder. Consequently, the precision of the structure determination is reduced but the main features are clear. Crystal parameters, data collection and structure refinement details are summarised in Table B1.

References

1.   Rigaku Oxford Diffraction, (2019), CrysAlisPro Software system, version 1.171.40.67a, Rigaku Corporation, Oxford, UK.

2.   C.B. Hübschle, G.M. Sheldrick and B. Dittrich. *J. Appl. Cryst*., 2011, **44**, 1281-1284.

3.   O.V. Dolomanov, L.J. Bourhis, R.J. Gildea, J.A.K. Howard And H. Puschmann. J. Appl. Cryst., 2009, **42**, 339-341

4.   G.M. Sheldrick, Acta Cryst., 2015, **A71**, 3-8.

Table B1 Crystal data and structure refinement for MB2P·0.475(CHCl$_3$) **.**

Empirical formula	$C_{42.48}H_{35.48}BCl_{1.43}F_2N_2$
Formula weight	673.23
Temperature/K	100.01(11)
Crystal system	monoclinic
Space group	$P2_1/c$
a/Å	22.5919(8)
b/Å	12.5812(5)
c/Å	25.2321(9)
α/°	90
β/°	96.352(3)
γ/°	90
Volume/Å^3	7127.8(5)
Z	8
ρ_{calc} g/cm^3	1.255
μ/mm^{-1}	1.584
F(000)	2812.0
Crystal size/mm^3	0.609 × 0.043 × 0.032
Radiation (Å)	Cu Kα (λ = 1.54184 Å)
2θ range for data collection/°	7.05 to 133.202
Index ranges	-26 ≤ h ≤ 26, -14 ≤ k ≤ 10, -28 ≤ l ≤ 30
Reflections collected	52467
Independent reflections	12557 [R_{int} = 0.0886, R_{sigma} = 0.0612]
Data/restraints/parameters	12557/3043/1179
Goodness-of-fit on F^2	1.059
Final R indexes [I>=2σ (I)]	R1 = 0.1039, wR2 = 0.2897
Final R indexes [all data]	R1 = 0.1305, wR2 = 0.3148
Largest diff. peak/hole / e Å^{-3}	0.81/-0.40
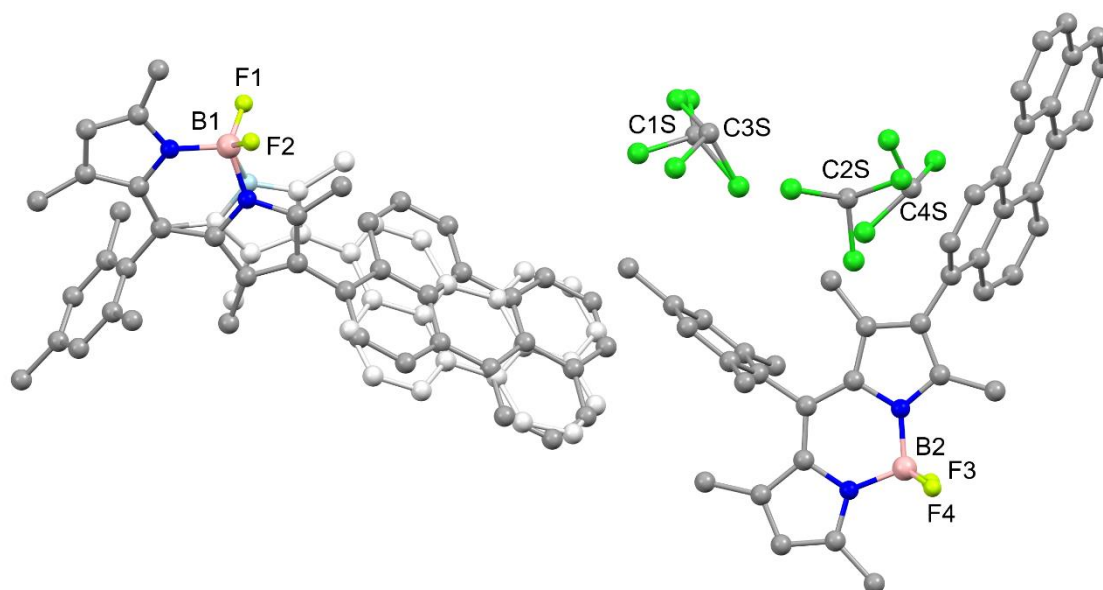
Figure B1. Asymmetric unit of MB2P·0.475(CHCl₃) *showing disorder in the mol1 (minor component shown in paler colours).*

The asymmetric unit (Fig S1) contains two independent $C_{42}H_{35}BF_2N_2$ molecules and some disordered chloroform solvate. In the molecule containing B1 (mol1), the perylene group is disordered by rotation of 180° about the C–C bond linking it to the BODIPY section, and the site occupancies refined to 0.74 and 0.26 for the major and minor components, respectively. A slight displacement of the linked 5-membered ring allows a close spatial overlap of the two perylene components (Figs S2 & S3). The same restraints were applied to all the perylene groups, to the disordered section of the BODIPY in mol 1, and to the chloroform molecules.
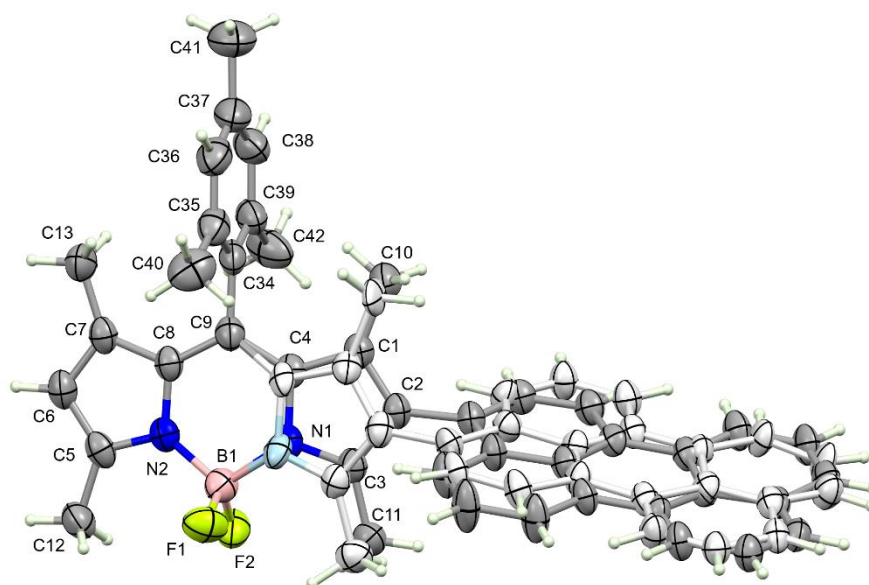
Figure B2. Disordered mol1 (50% probability ellipsoids) showing numbering scheme for the BODIPY section. Minor component shown in paler colours.
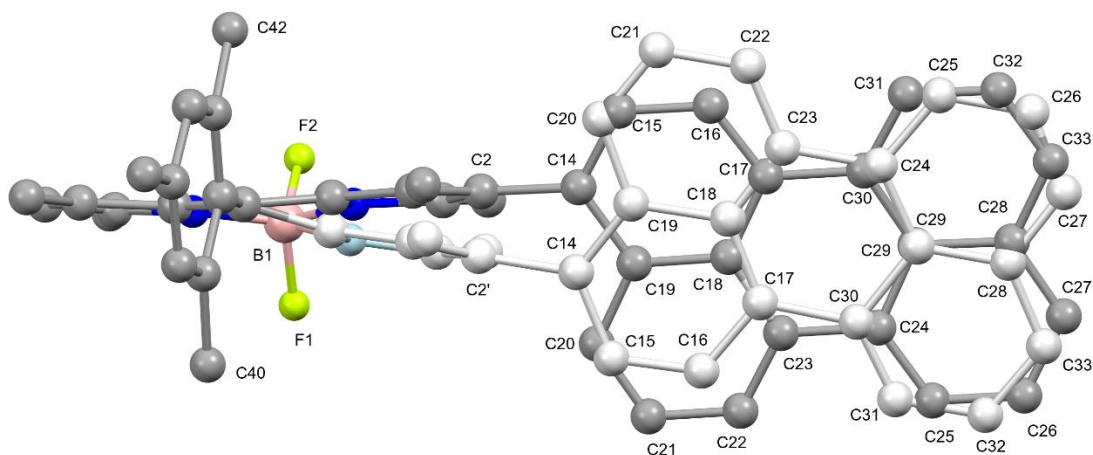
Figure B3. Disordered mol1 showing numbering scheme for the perylene sections. Minor component shown in paler colours.

The ADPs of the second molecule (mol2, containing B2) suggest a small amount of disorder in the perylene group (Fig S4) but this has not been modelled, given the low data quality and the more significant disorders elsewhere. The conformations of the two molecules are similar and the small differences (Fig S5) can

probably be ascribed to intermolecular interactions in the solid state. In each case the mean plane of the perylene group is rotated with respect to the mean plane of the BODIPY core, the interplanar angles are 69.8(1)° and 73.5(3)° for the major and minor components of mol1 and 73.23(6)° for mol2.
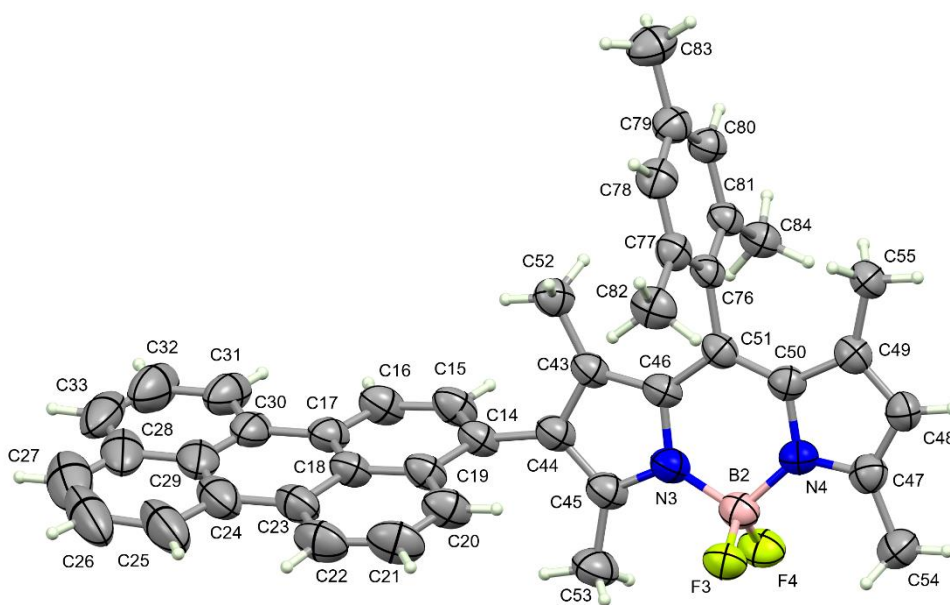
Figure B4. Mol 2 (50% probability ellipsoids) showing numbering scheme.
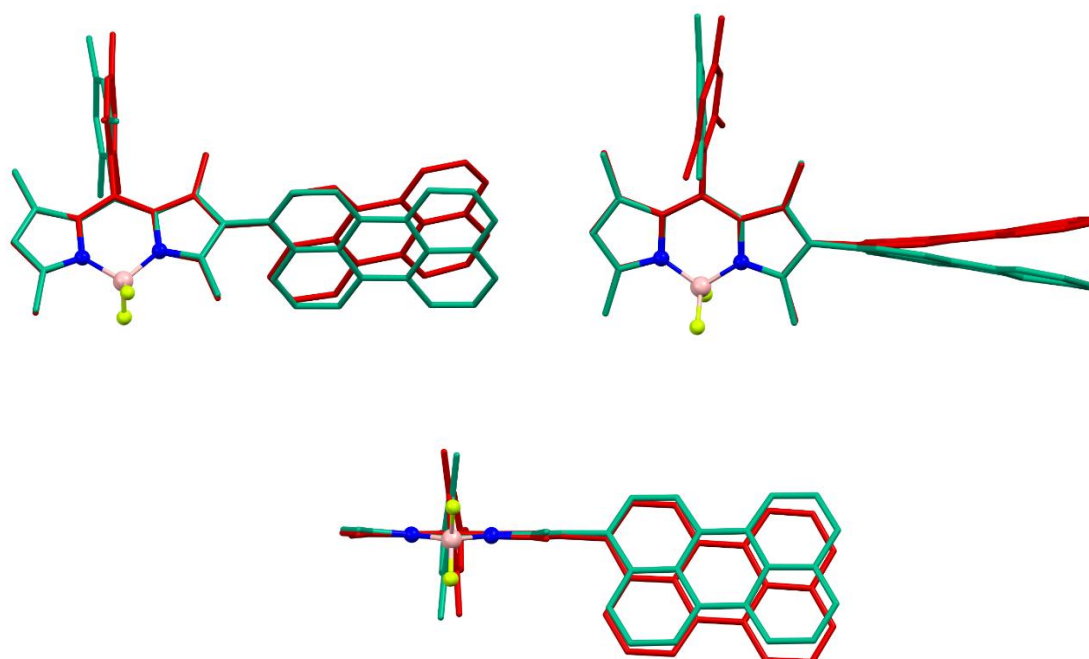
Figure B5. Overlays of mol1 (green) and mol2 (red), based on fitting the N and F atoms only. Only the major component of the disorder is shown for mol1 and it is inverted relative to the asymmetric unit coordinates (permitted in this centrosymmetric space group).

Mol1 is paired with a symmetry equivalent by inversion (symmetry operation 1-x, 1-y, 1-z) to generate π-stacked dimeric units; this stacking does not extend further through the structure (Fig B6). There are no equivalent π-interactions involving mol2 but there is a set of reasonably convincing (sp^2)C–H····F interactions linking the mol2 units into chains running parallel to the *b* axis (Fig B7).
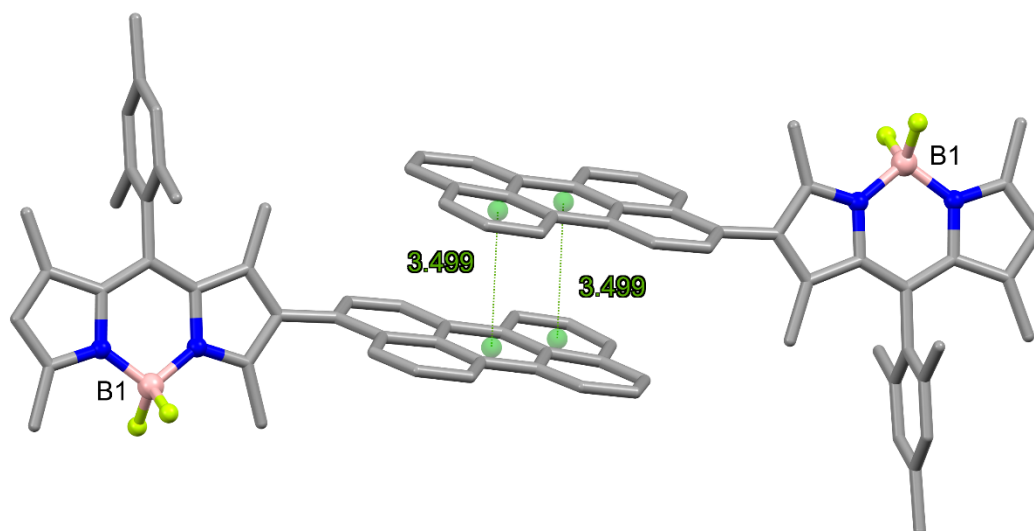
Figure B6. π-stacking showing centroid-centroid distances (Å) between mol1 and its symmetry equivalent under 1-x, 1-y, 1-z.

Examination of the unit cell packing (Fig S8 & S9) shows the solvate chloroform molecules lying in columns parallel to the b axis, the solvate was modelled over four overlapping sites with occupancies of 0.35, 0.40, 0.15 and 0.05 for the molecules cantered on C1S, C2S, C3S and C4S, respectively. The site occupancies were adjusted by hand to minimise the residual electron density in this region. Part-occupancy carbon atoms C1S, C2S and the 0.05 occupancy chlorine atoms were refined isotropically, while a fixed isotropic parameter was used for C3S and C4S.
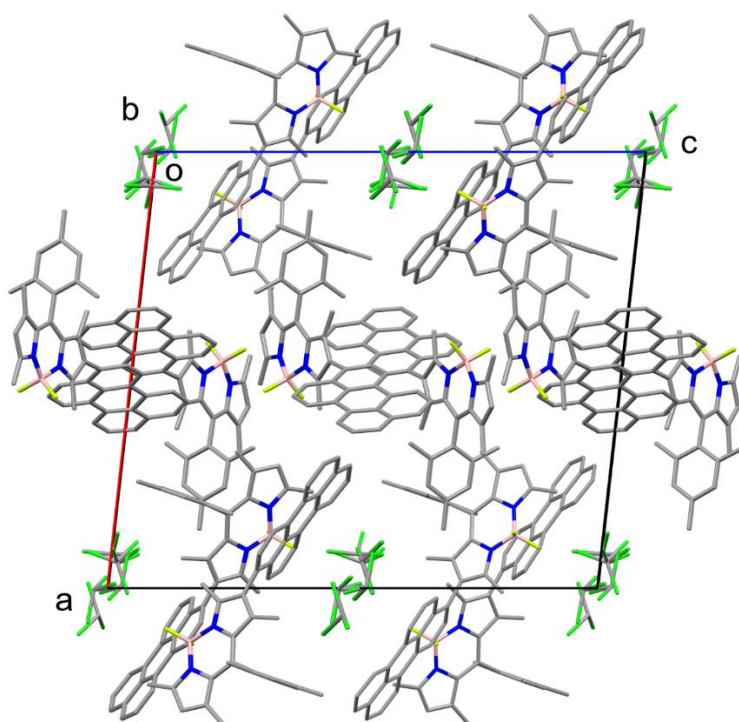
Figure B7. Unit cell packing viewed down the b axis. Perylene disorder and hydrogen atoms removed for clarity.
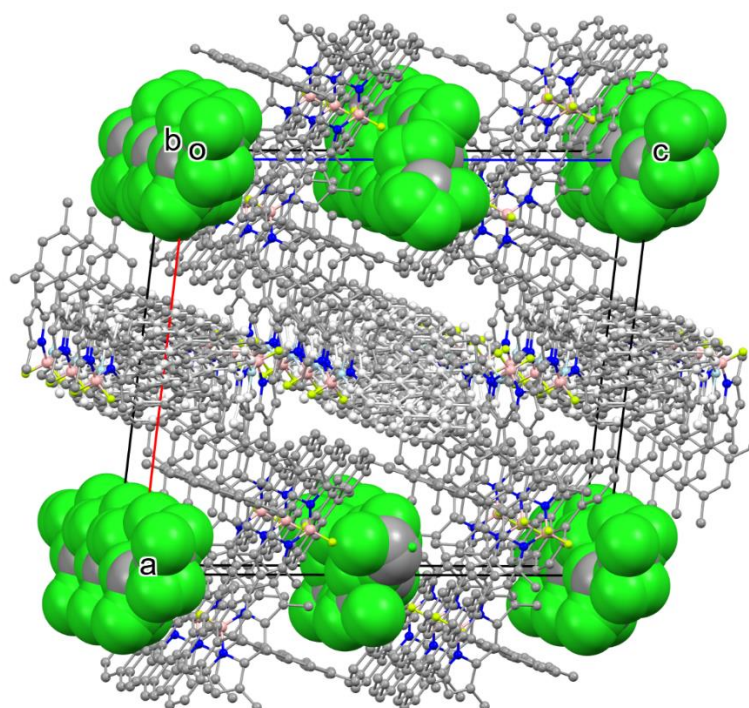
Figure B8. Unit cell packing showing partial-occupancy chloroform molecules (spacefill) in channels parallel to the b axis. Hydrogen atoms removed for clarity.

Least-squares planes (x,y,z in crystal coordinates) and deviations from them(* indicates atom used to define plane)

- 1.9685 (0.0239) x + 6.8107 (0.0081) y + 21.2147 (0.0106) z = 14.0095 (0.0140)

```
* -0.2028 (0.0049)  B1
* -0.0556 (0.0032)  N2
* -0.0277 (0.0056)  N1^a
*  0.0287 (0.0062)  C1^a
*  0.0556 (0.0055)  C2^a
*  0.0102 (0.0059)  C3^a                    mol1
* -0.0009 (0.0070)  C4^a                    major component BODIPY
*  0.0306 (0.0038)  C5
*  0.0775 (0.0039)  C6
*  0.0202 (0.0037)  C7
* -0.0541 (0.0037)  C8
* -0.1009 (0.0043)  C9
*  0.0235 (0.0065)  C10^a
*  0.0864 (0.0059)  C11^a
*  0.0687 (0.0045)  C12
*  0.0408 (0.0044)  C13
```

Rms deviation of fitted atoms = 0.0724

19.6313 (0.0155) x + 5.6019 (0.0147) y + 2.9914 (0.0351) z = 15.8318 (0.0122)

Angle to previous plane (with approximate esd) = <mark>69.759 (0.100)</mark>

```
*  0.0377 (0.0068)  C14_1^a                 interplanar angle
*  0.0012 (0.0160)  C15_1^a
* -0.0228 (0.0066)  C16_1^a
* -0.0166 (0.0085)  C17_1^a
*  0.0030 (0.0070)  C18_1^a
*  0.0079 (0.0064)  C19_1^a
*  0.0217 (0.0157)  C20_1^a
* -0.0146 (0.0083)  C21_1^a
* -0.0003 (0.0078)  C22_1^a
* -0.0088 (0.0077)  C23_1^a                 mol1
*  0.0083 (0.0083)  C24_1^a                 major component perylene
* -0.0346 (0.0083)  C25_1^a
* -0.0348 (0.0081)  C26_1^a
*  0.0349 (0.0094)  C27_1^a
*  0.0615 (0.0128)  C28_1^a
* -0.0212 (0.0474)  C29_1^a
*  0.0061 (0.0113)  C30_1^a
* -0.0525 (0.0101)  C31_1^a
* -0.0136 (0.0089)  C32_1^a
*  0.0377 (0.0102)  C33_1^a
```

Rms deviation of fitted atoms = 0.0277

- 1.7187 (0.0679) x + 5.1812 (0.0258) y + 22.9846 (0.0242) z = 12.4624 (0.0462)

Angle to previous plane (with approximate esd) = 71.734 (0.186)

* 0.1078 (0.0070) B1
* 0.0868 (0.0042) N2
* -0.0560 (0.0173) N1'^b
* 0.0014 (0.0177) C1'^b
* -0.0738 (0.0164) C2'^b   mol1
* -0.0707 (0.0166) C3'^b   minor component BODIPY
* 0.0330 (0.0190) C4'^b
* 0.0442 (0.0175) C10'^b
* 0.0343 (0.0153) C11'^b
* -0.0636 (0.0083) C12
* -0.0433 (0.0092) C13

Rms deviation of fitted atoms =   0.0624

 19.8223 (0.0424) x + 5.5667 (0.0440) y + 2.2004 (0.1001) z = 15.4728 (0.0386)

Angle to previous plane (with approximate esd) = <mark>73.510 (0.287)</mark>

* 0.0687 (0.0191) C14_2^b
* -0.0309 (0.0393) C15_2^b
* -0.0189 (0.0193) C16_2^b
* -0.0021 (0.0227) C17_2^b
* 0.0003 (0.0202) C18_2^b
* -0.0120 (0.0179) C19_2^b
* 0.0296 (0.0534) C20_2^b   mol1
* -0.0168 (0.0200) C21_2^b   minor component perylene
* -0.0283 (0.0189) C22_2^b
* -0.0204 (0.0270) C23_2^b
* -0.0572 (0.0377) C24_2^b
* -0.0378 (0.0293) C25_2^b
* 0.0553 (0.0289) C26_2^b
* 0.0247 (0.0377) C27_2^b
* -0.0413 (0.0444) C28_2^b
* 0.1278 (0.1428) C29_2^b
* -0.0135 (0.0295) C30_2^b
* 0.0139 (0.0281) C31_2^b
* -0.0216 (0.0245) C32_2^b
* -0.0193 (0.0270) C33_2^b

Rms deviation of fitted atoms =   0.0425

 5.2683 (0.0129) x + 10.4651 (0.0063) y + 11.9805 (0.0178) z = 16.0468 (0.0174)

Angle to previous plane (with approximate esd) = 48.237 (0.262)

* -0.0934 (0.0050) B2
* -0.0031 (0.0039) N3
* 0.0233 (0.0037) N4
* 0.0350 (0.0042) C43
* 0.0019 (0.0044) C44
* -0.0161 (0.0047) C45   mol2 BODIPY
* 0.0224 (0.0042) C46
* 0.0519 (0.0043) C47
* 0.0390 (0.0043) C48
* -0.0125 (0.0040) C49
* 0.0014 (0.0041) C50
* 0.0098 (0.0040) C51
* 0.0341 (0.0040) C52
* -0.0357 (0.0050) C53
* 0.0359 (0.0047) C54
* -0.0939 (0.0041) C55

Rms deviation of fitted atoms =   0.0420

 10.7093 (0.0112) x - 3.6436 (0.0101) y + 19.5288 (0.0097) z = 24.1375 (0.0106)

Angle to previous plane (with approximate esd) = <mark>73.233 (0.058)</mark>

* -0.0874 (0.0043) C14_3
* -0.0212 (0.0047) C15_3
* 0.0504 (0.0048) C16_3
* 0.0411 (0.0044) C17_3
* -0.0042 (0.0045) C18_3
* -0.0599 (0.0046) C19_3   mol2 perylene
* -0.0624 (0.0050) C20_3
* 0.0218 (0.0057) C21_3
* 0.1028 (0.0057) C22_3
* 0.0481 (0.0052) C23_3
* 0.0390 (0.0057) C24_3
* 0.0168 (0.0069) C25_3
* -0.0690 (0.0073) C26_3
* -0.0556 (0.0071) C27_3
* -0.0307 (0.0053) C28_3
* 0.0134 (0.0049) C29_3
* 0.0414 (0.0047) C30_3
* 0.0387 (0.0053) C31_3
* 0.0150 (0.0064) C32_3
* -0.0381 (0.0060) C33_3

Rms deviation of fitted atoms =   0.0494

B.2 Synthesis

(3,5-dimethyl-1H-pyrrol-2-yl)(4-methoxyphenyl)methanone **(1.3)** Prepared following general procedure **A** (chapter 2.4.2). Light yellow solid 67%. ^{1}H-NMR (CDCl$_3$, 600 MHz) δ (ppm) 8.79 (br, 1H), 7.66 (d, J = 9 Hz, 2H), 6.54 (d, J = 9 Hz, 2H), 5.84 (d, J = 3 Hz, 1H), 3.36 (s, 3H), 2.28 (s, 3H), 2.09 (s, 3H).

(4-bromophenyl)(3,5-dimethyl-1H-pyrrol-2-yl)methanone (1.4). Prepared following general procedure **A** (chapter 2.4.2). Light yellow solid 75%. ^{1}H-NMR (CDCl$_3$, 600 MHz) δ (ppm) 8.96 (br, 1H), 7.59 (d, J = 8.0 Hz, 2H), 7.51 (d, J = 8.0 Hz, 2H), 5.47 (s, 1H), 2.29 (s, 3H), 1.93 (s, 3H).

(3,5-dimethyl-1H-pyrrol-2-yl)(4-(dimethylamino)phenyl)methanone **(1.5)** Prepared following general procedure **A** (chapter 2.4.2). Yellow solid 63%. ^{1}H-NMR (CDCl$_3$, 600 MHz) δ (ppm) 8.86 (br, 1H), 7.65 (d, J = 9.0 Hz, 2H), 6.68 (d, J = 9.0 Hz, 2H), 5.94 (d, J = 3 Hz, 1H), 3.04 (s, 6H), 2.28 (s, 3H), 2.08 (s, 3H).

(4-bromo-3,5-dimethyl-1H-pyrrol-2-yl)(4-methoxyphenyl)methanone **(2.6).** Prepared following the same procedure to prepare molecule 2 (chapter 2.4.2). ^{1}H-NMR (CDCl$_3$, 600 MHz) δ (ppm) 9.18 (br, 1H), 7.66 (d, J = 9.0 Hz, 2H), 6.95 (d, J = 9.0 Hz, 2H), 3.87 (s, 3H), 2.30 (s, 3H), 1.98 (s, 3H).

(4-bromo-3,5-dimethyl-1H-pyrrol-2-yl)(4-bromophenyl)methanone **(2.7)**. Prepared following the same procedure to prepare molecule 2 (chapter 2.4.2). ^{1}H-NMR (CDCl$_3$, 600 MHz) δ (ppm) 9.23 (br, 1H), 7.60 (d, J = 8.0 Hz, 2H), 7.51 (d, J = 8.0 Hz, 2H), 2.31 (s, 3H), 1.92 (s, 3H).

BODIPY 3.6 In a 100 mL round-bottom flask 7.50 mg of ketopyrrole 2.6 (2.43 mmol) were dissolved in 10 mL of DCM, 2,4-dimethylpyrrole (0.3 mL, 2.92 mmol, 1.2 eq.) and 5 drops of TFA were added. The reaction was stirred at room temperature for 48 hours. After this time, starting material was still present so 1.1 eq. of pyrrole were added, and the reaction stirred at room temperature for 24 hours. Triethylamine (2 mL, 14.60 mmol, 6 eq.) and BF_3-etherate (2.4 mL, 19.47 mmol, 8 eq.) were added and the reaction stirred at room temperature overnight. The solvents were evaporated and the product was purified by column chromatography using silica gel and cyclohexane:EtAcO (1:9) to yield a dark red solid in 28% yield.

^{1}H-NMR (CDCl$_3$, 600 MHz) δ (ppm) 7.15 (d, J = 8.7 Hz, 2H), 7.02 (d, J = 8.7 Hz, 2H), 6.03 (s, 1H), 3.88 (s, 3H), 2.59 (s, 3H), 2.56 (s, 3H), 1.44 (s, 3H), 1.41 (s, 3H).

^{13}C-NMR (CDCl$_3$, 150 MHz), δ (ppm) 160.5, 157.9, 151.4, 145.3, 142.1, 138.9, 132.6, 130.4, 126.8, 122.2, 110.6, 77.6, 55.5, 14.93, 14.90, 13.8, 13.6. HR-MS (ESI-TOF) m/z calculated for $C_{20}H_{21}BBrF_2N_2O$ (M+H): 433.0893, found: 433.0913, Calculated for $C_{20}H_{20}BBrF_2N_2NaO$ 455.0712, found: 455.0744.

BODIPY 3.7 In a 100 mL round-bottom flask 1g of ketopyrrole 2.7 (2.80 mmol) was dissolved in 10 mL of DCM, 2,4-dimethylpyrrole (0.346 mL, 3.36 mmol, 1.2 eq.) and 5 drops of TFA were added and the reaction was stirred at room temperature for 24 hours. After this time TLC showed starting material still present in the flask, so 0.2 mL of pyrrole were added, and the reaction was heated at 40°C for 48 hours. Triethylamine (2.34 mL, 16.80 mmol, 6 eq.) and BF_3-etherate (2.77 mL, 21.40 mmol, 8 eq.) were added and the reaction stirred at room temperature overnight. Solvents were evaporated and the product was purified by column chromatography using silica gel and cyclohexane:EtAcO (1:9) to yield a dark red solid in 18% yield. ^{1}H-NMR (CDCl$_3$,

600 MHz) δ (ppm) 7.66 (d, J = 8.0 Hz, 2H), 7.16 (d, J = 8.0 Hz, 2H), 6.04 (s, 1H), 2.59 (s, 3H), 2.56 (s, 3H), 1.41 (s, 3H), 1.40 (s, 3H). ^{13}C-NMR (CDCl$_3$, 150 MHz), δ (ppm) 158.5, 152.1, 144.9, 140.3, 138.7, 133.7, 132.7, 131.9, 129.9, 129.7, 123.7, 122.5, 111.0, 15.0, 14.9, 13.9, 13.6. HR-MS (ESI-TOF) m/z calculated for $C_{19}H_{16}BBr_2F_2N_2$ (M-1): 478.9747 found: 478.9733. Calculated for $C_{19}H_{17}BBr_2F_2N_2Na$ (M+Na): 502.9717, found: 502.9637.

Optimised synthesis of **(3-Perylenyl)boronic acid pinacol ester (4.1).** 1 g of 3-bromoperylene (3.0 mmol), potassium 2-ethylhexanoate (1.10 g, 6.04 mmol, 2 eq.), bis(pinacolato)diboron (920 mg, 3.62 mmol, 1.2 eq.) and Pd(dppf)Cl$_2$ (0.066 g, 0.090 mmol 0.03 eq.) were dissolved in isopropyl acetate (30 mL) and stirred at 50 °C for 16 hours. The solvent was evaporated under vacuum. The product was purified by column chromatography (CHCl$_3$: cyclohexane, 5:5). **4.1** was obtained as a yellow solid in 61 % yield. ^{1}H-NMR (CDCl$_3$, 600 MHz): δ (ppm) 8.65 (d, J = 8.4 Hz, 1H), 8.25-8.20 (m, 3H), 8.18 (d, J = 6.0 Hz, 1H), 8.06 (d, J = 6.0 Hz, 1H), 7.71-767 (m, 2H), 7.54 (t, ^3J = 7.2 Hz, 1H), 752-7.47 (m, 2H), 1.43 (s, 12H).

BODIPY 6. In a sealed tube, 100 mg of BODIPY 3 (0.248 mmol), Pd(dppf)Cl$_2$ (9 mg, 0.012 mmol, 0.05 eq.), and bis(tributyltin) (0.138 mL, 0.272 mmol, 1.1 eq.) were dissolved in dry toluene. The tube was sealed and heated at 100 °C for 16 hours. The solvents were evaporated, and the product purified by column chromatography. The product was obtained as a red solid in 35 % yield. ^{1}H-NMR (CDCl$_3$, 600 MHz) δ (ppm) 7.51-7.42 (m, 6H), 7.36-7.29 (m, 2H), 7.25-7.20 (m, 2H), 5.98 (s, 2H), 2.56 (s, 6H), 2.35 (s, 6H), 1.36 (s, 6H), 1.11 (s, 6H).

BODIPY 7. In a sealed tube, 115 mg of BODIPY 3 (0.285 mmol), Vinyl tributyltin (0.172 mL, 0.570 mmol, 2 eq.) and Pd(PPh3)4 (16.5 mg, 0.014 mmol, 0.05 eq.) were dissolved in 2mL of toluene. The reaction was heated at 100 °C for 5 hours. Solvents were evaporated under vacuum and the product was purified by column chromatography using cyclohexane/EtAcO (9:1). The product was obtained as a red solid in 87% yield. ^{1}H-NMR (CDCl$_3$, 600 MHz) δ (ppm) 7.52-7.45 (m, 3H), 7.3-7.26 (m, 2H), 6.46 (dd, J = 17.9, 11.6 Hz, 1H), 5.98 (s, 1H), 5.30 (dd, J = 11.6, 1.6 Hz, 1H), 5.26 (dd, J =, 17.9, 1.6 Hz, 1H), 2.63 (s, 3H), 2.56 (s, 3H), 1.36 (s, 3H), 1.36 (s, 3H).^{13}C-NMR (CDCl$_3$, 150 MHz), δ (ppm) 155.8, 154.7, 143.4, 141.9, 139.1, 135.3, 131.8, 131.0, 129.3, 129.1, 128.2, 127.9, 121.5, 117.0, 14.7, 14.6, 13.9, 13.8, 12.7.

B.3 NMR and mass spectra
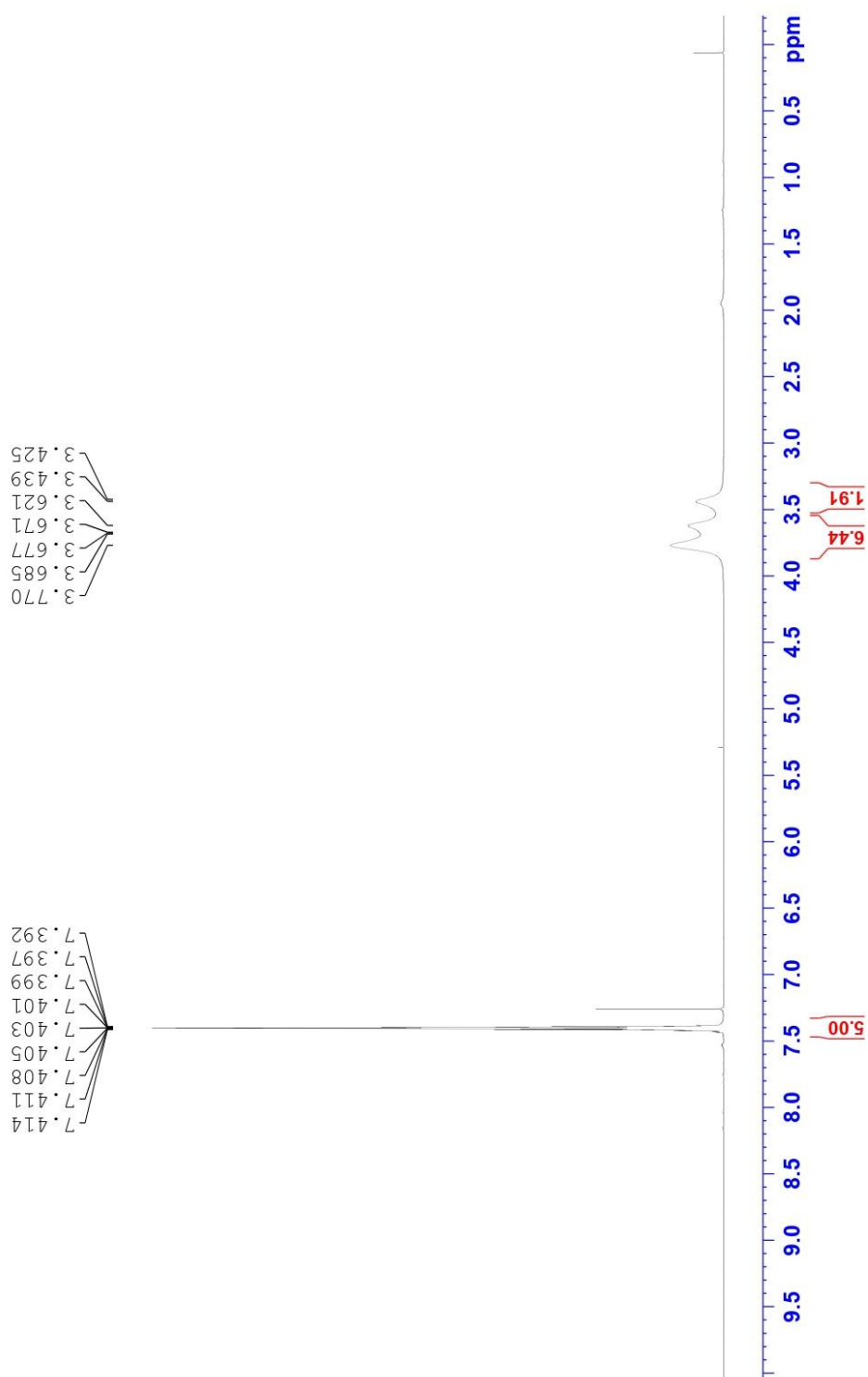
Figure B9 ^{1}H-NMR spectrum of morpholino(phenyl)methanone in CDCl$_3$ at 600 MHz.

6.884
6.886
6.888
6.891
7.129
7.132
7.134
7.137
7.489
7.492
7.499
7.501
7.512
7.515
7.517
7.579
7.582
7.584
7.591
7.594
7.597
7.604
7.606
7.608
7.874
7.876
7.879
7.888
7.890
7.893
9.703
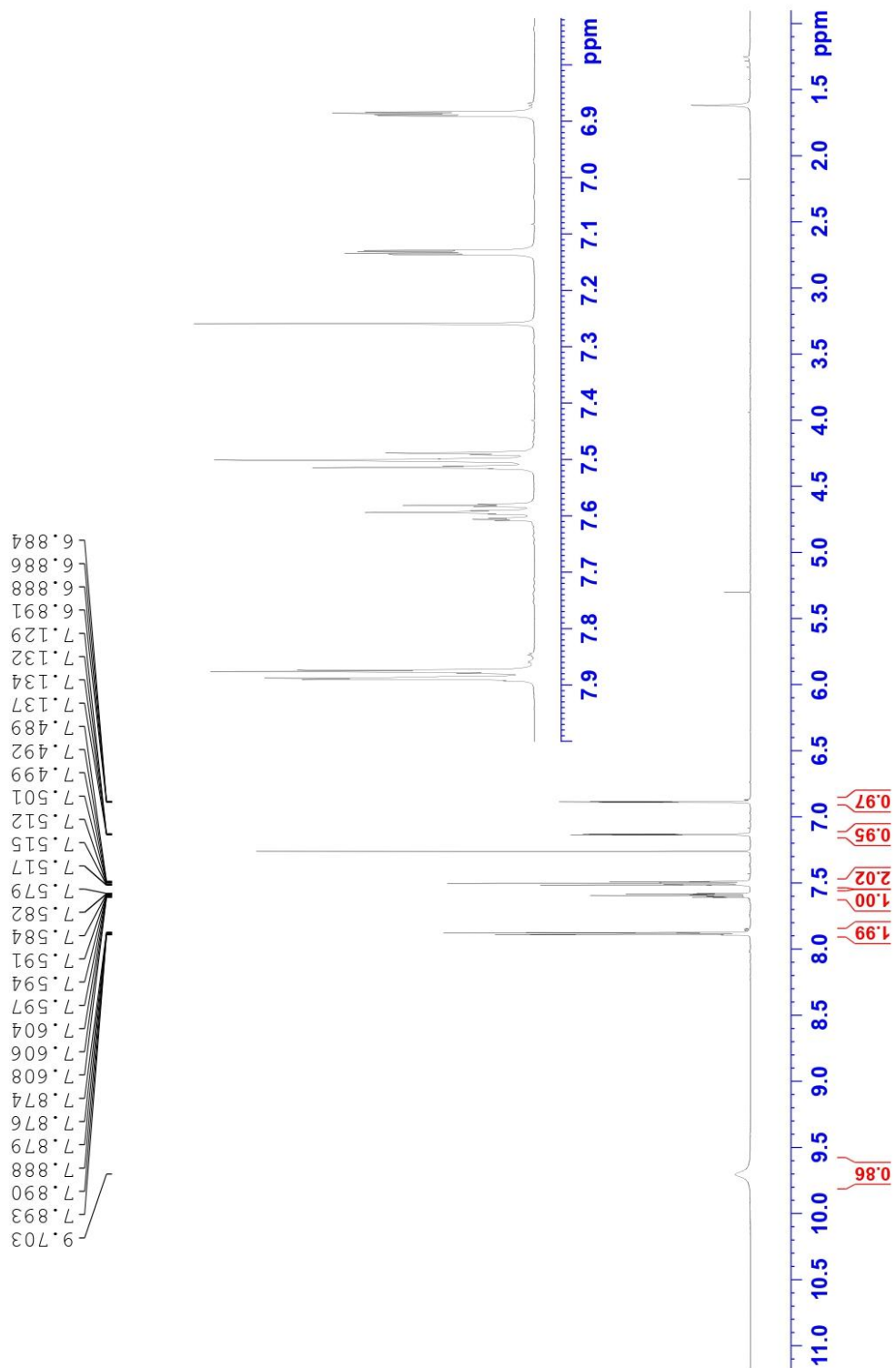
Figure B10 ^{1}H-NMR spectrum of 1.6 in CDCl$_3$ at 600 MHz.
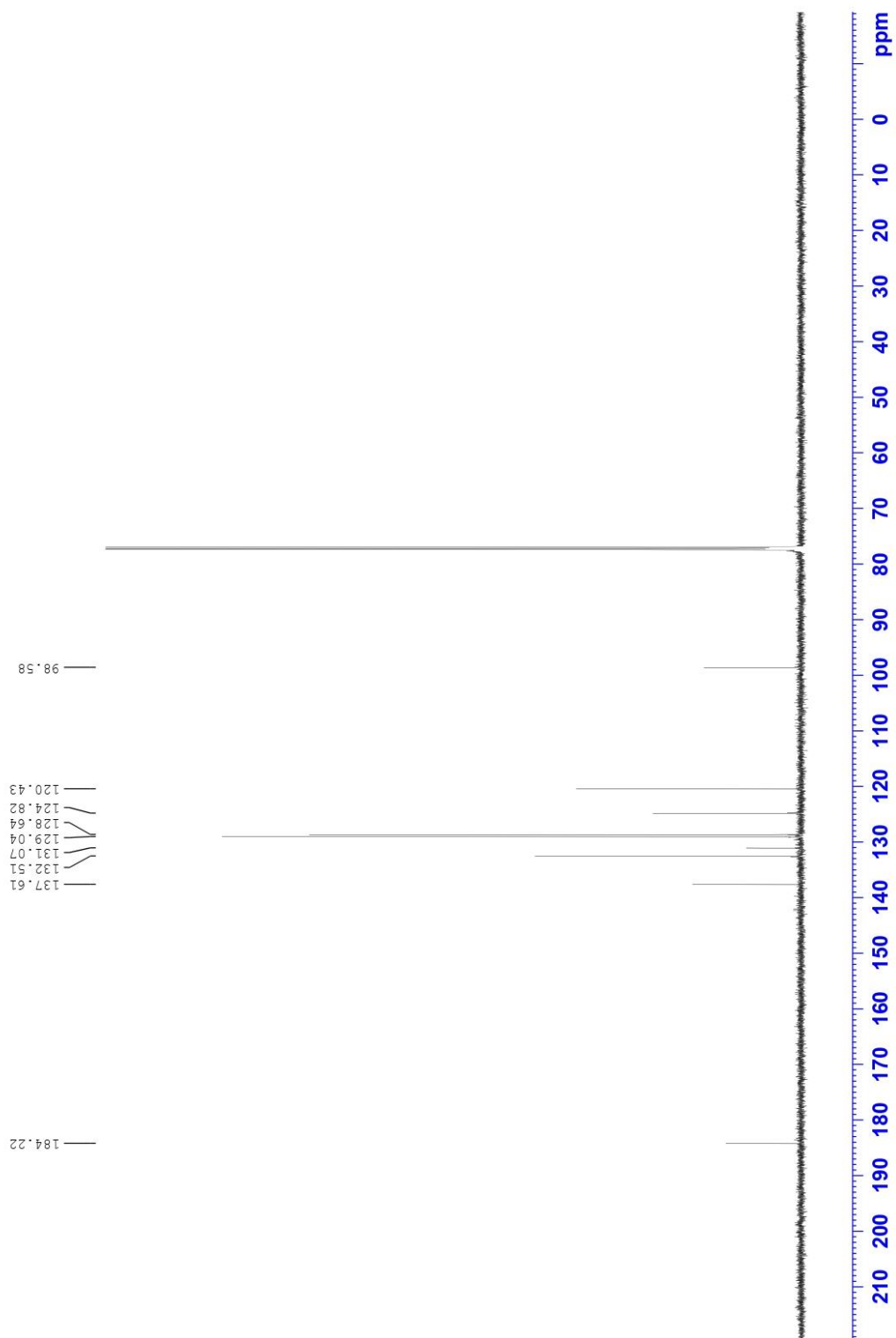
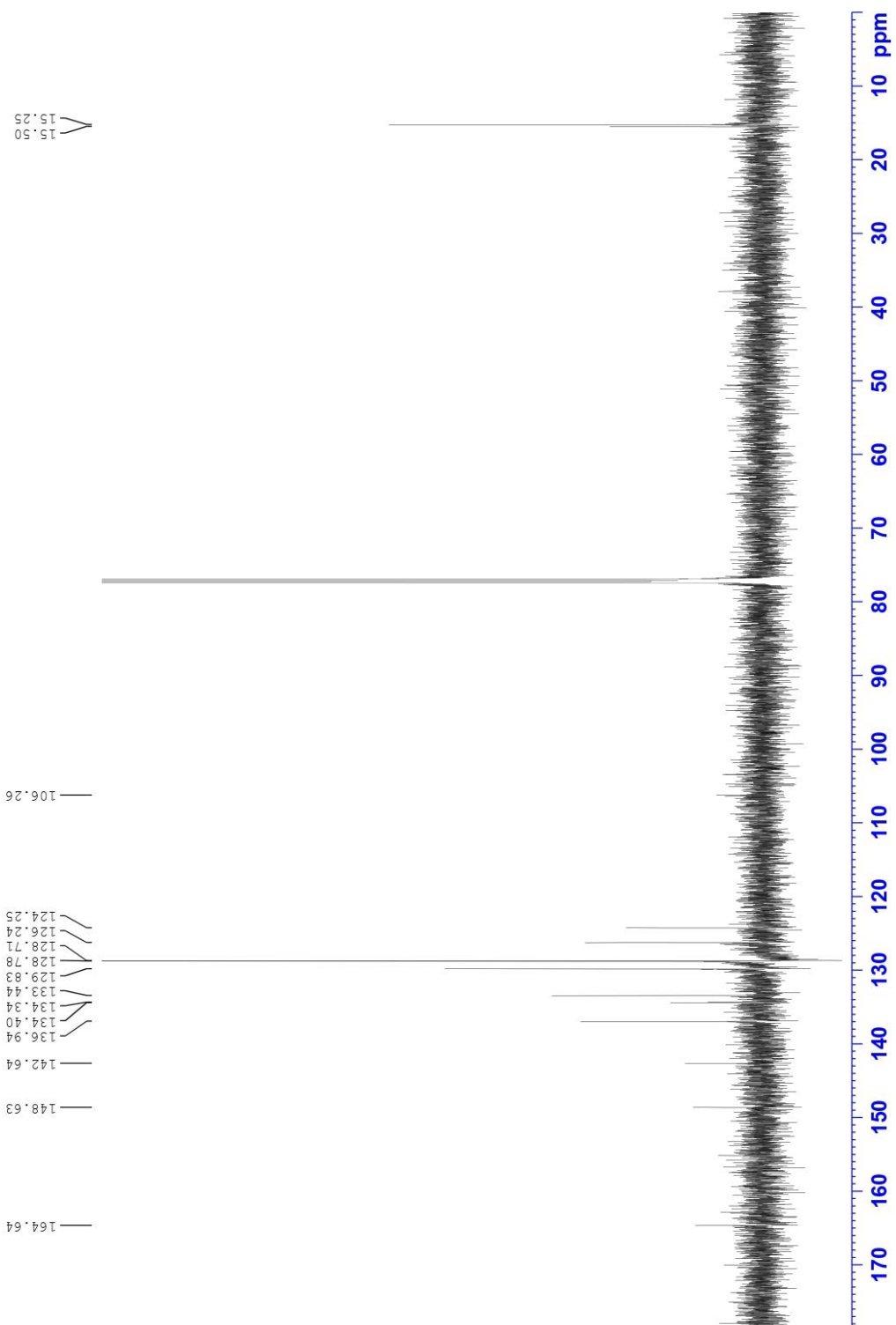Figure B10.1 ^{13}C-NMR spectrum of 1.6 in CDCl$_3$ at 150 MHz.
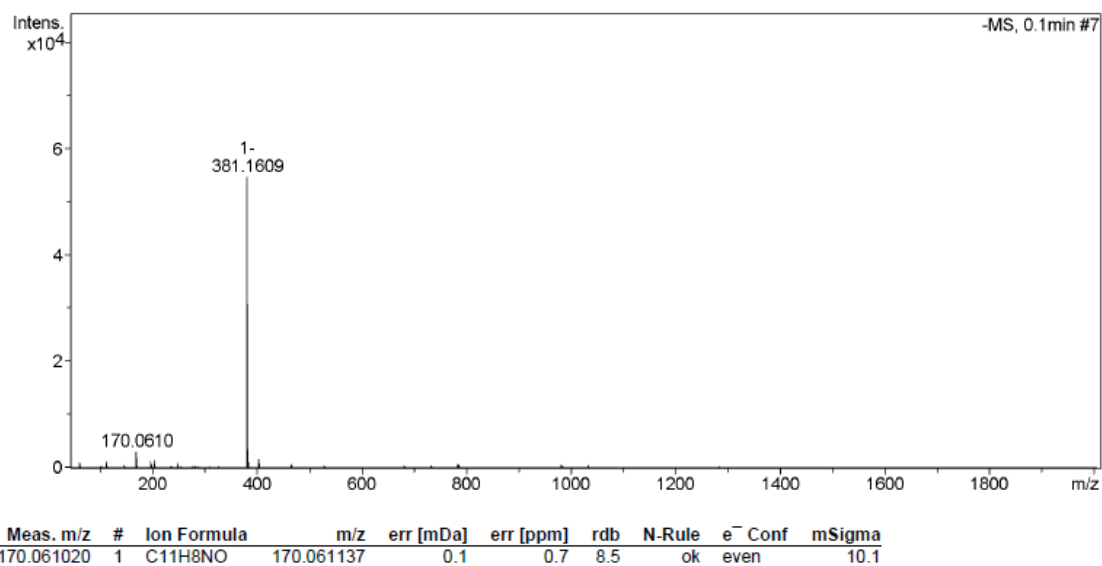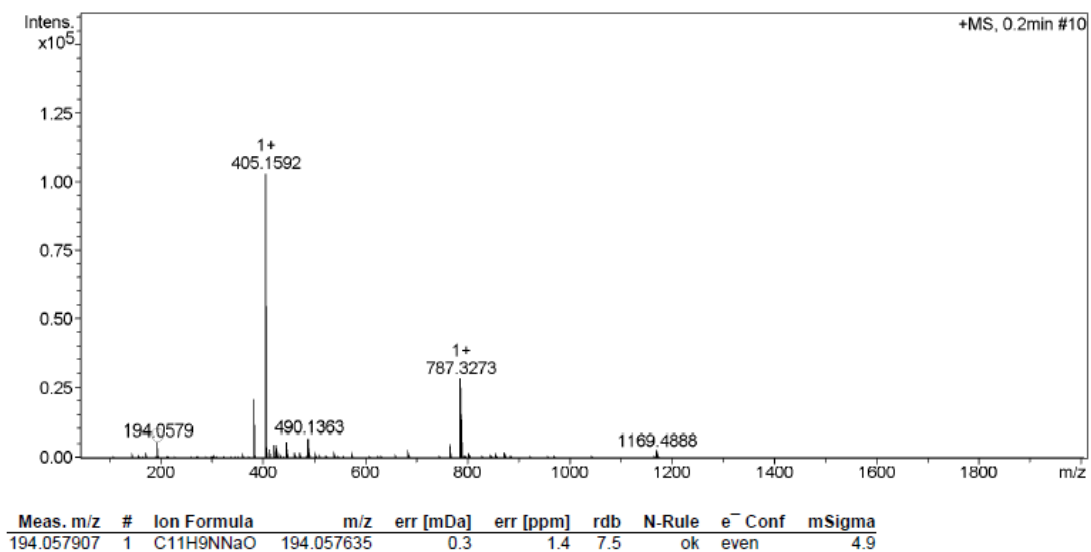
Figure B11 HR-MS (ESI-TOF) positive and negative scans of 1.6.

6.884
6.886
6.888
6.891
7.129
7.132
7.134
7.137
7.489
7.492
7.499
7.501
7.512
7.515
7.517
7.579
7.582
7.584
7.591
7.594
7.597
7.604
7.606
7.608
7.874
7.876
7.879
7.888
7.890
7.893
9.703
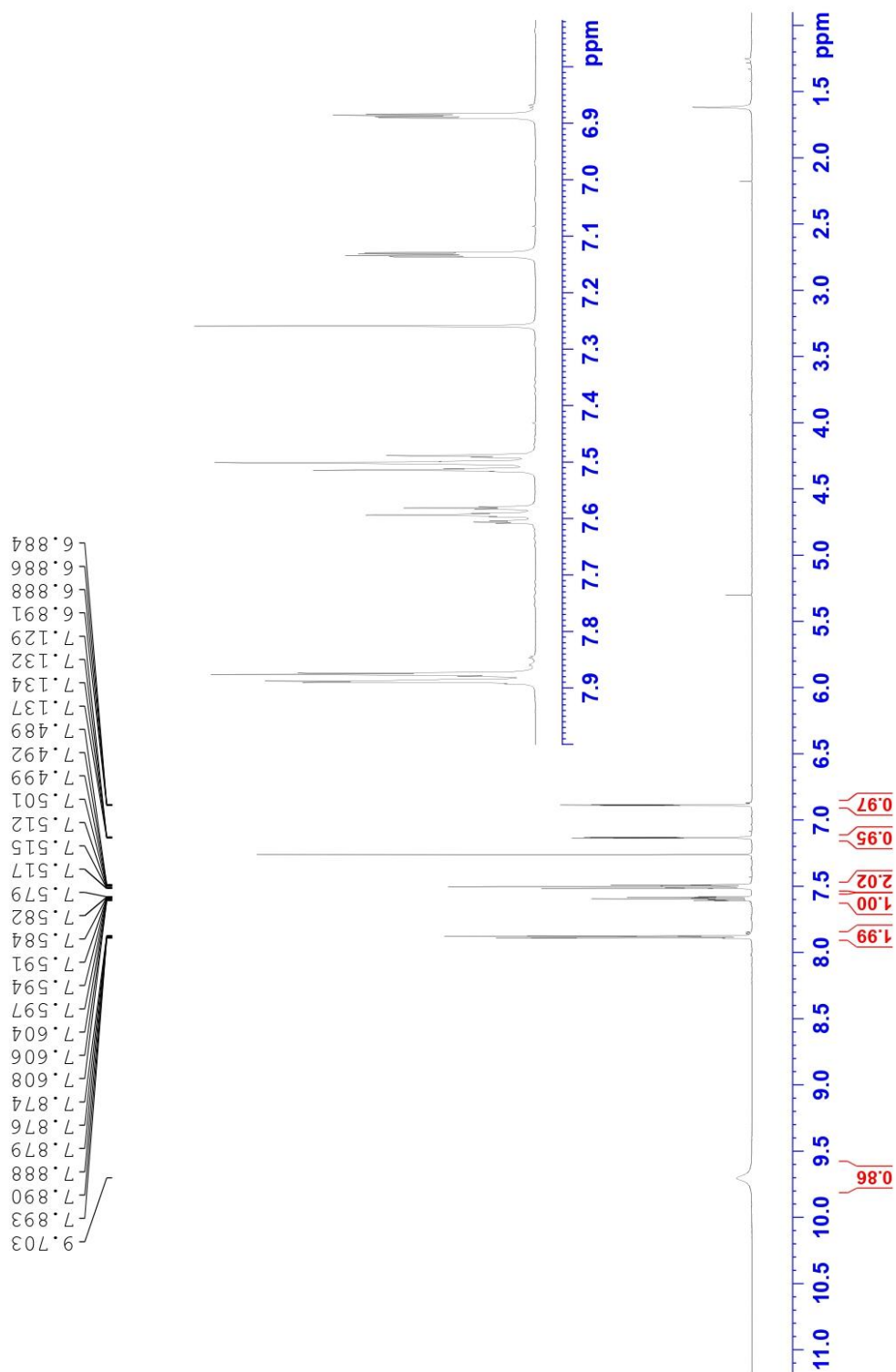
Figure B12 ^{1}H-NMR spectrum of 2.4 in CDCl$_3$ at 600 MHz.
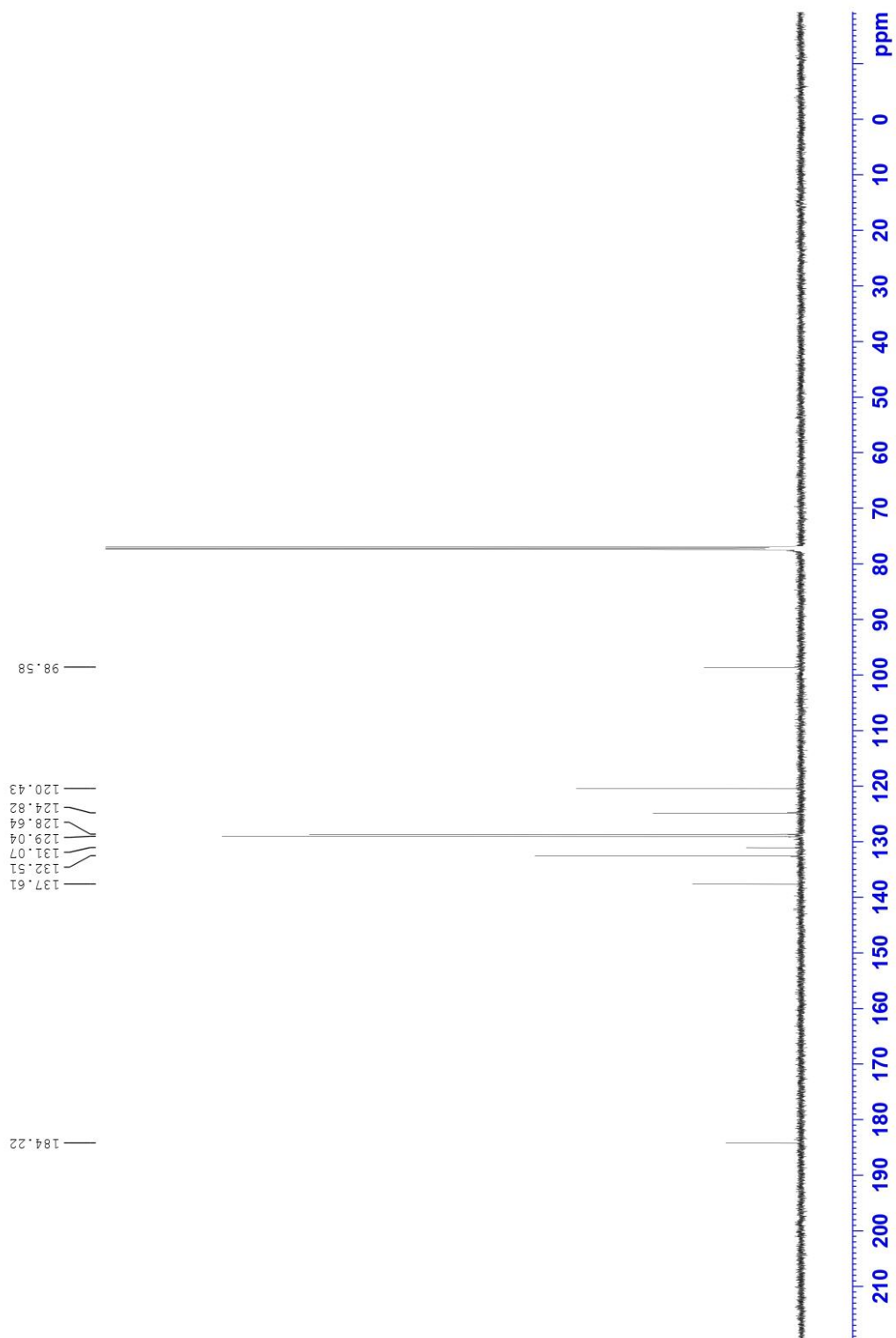
Figure B13 ^{13}C-NMR spectrum of 1.6 in CDCl$_3$ at 150 MHz.

98.58

120.43
124.82
128.64
129.04
131.07
132.51
137.61

184.22
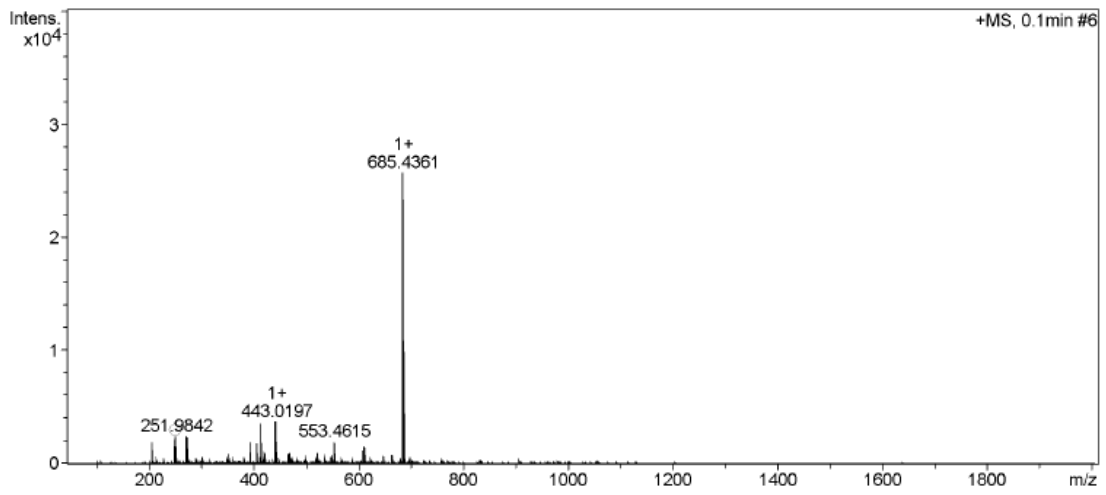
Meas. m/z	#	Ion Formula	m/z	err [mDa]	err [ppm]	rdb	N-Rule	e⁻ Conf	mSigma
249.986822	1	C11H9BrNO	249.986202	0.6	2.5	7.5	ok	even	15.8
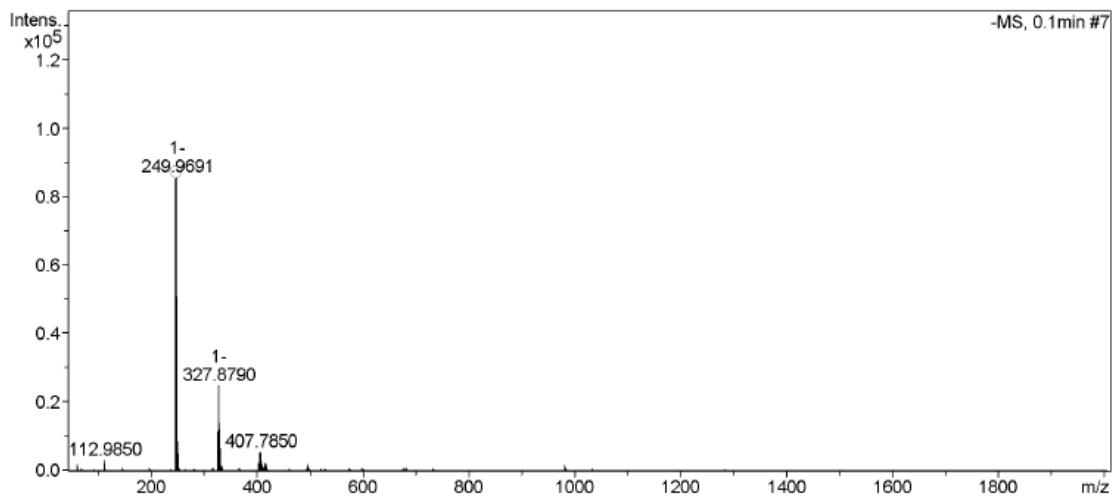
Meas. m/z	#	Ion Formula	m/z	err [mDa]	err [ppm]	rdb	N-Rule	e⁻ Conf	mSigma
247.971303	1	C11H7BrNO	247.971650	0.3	1.4	8.5	ok	even	13.0

Figure B14 HR-MS (ESI-TOF) positive and negative scans of 2.4.
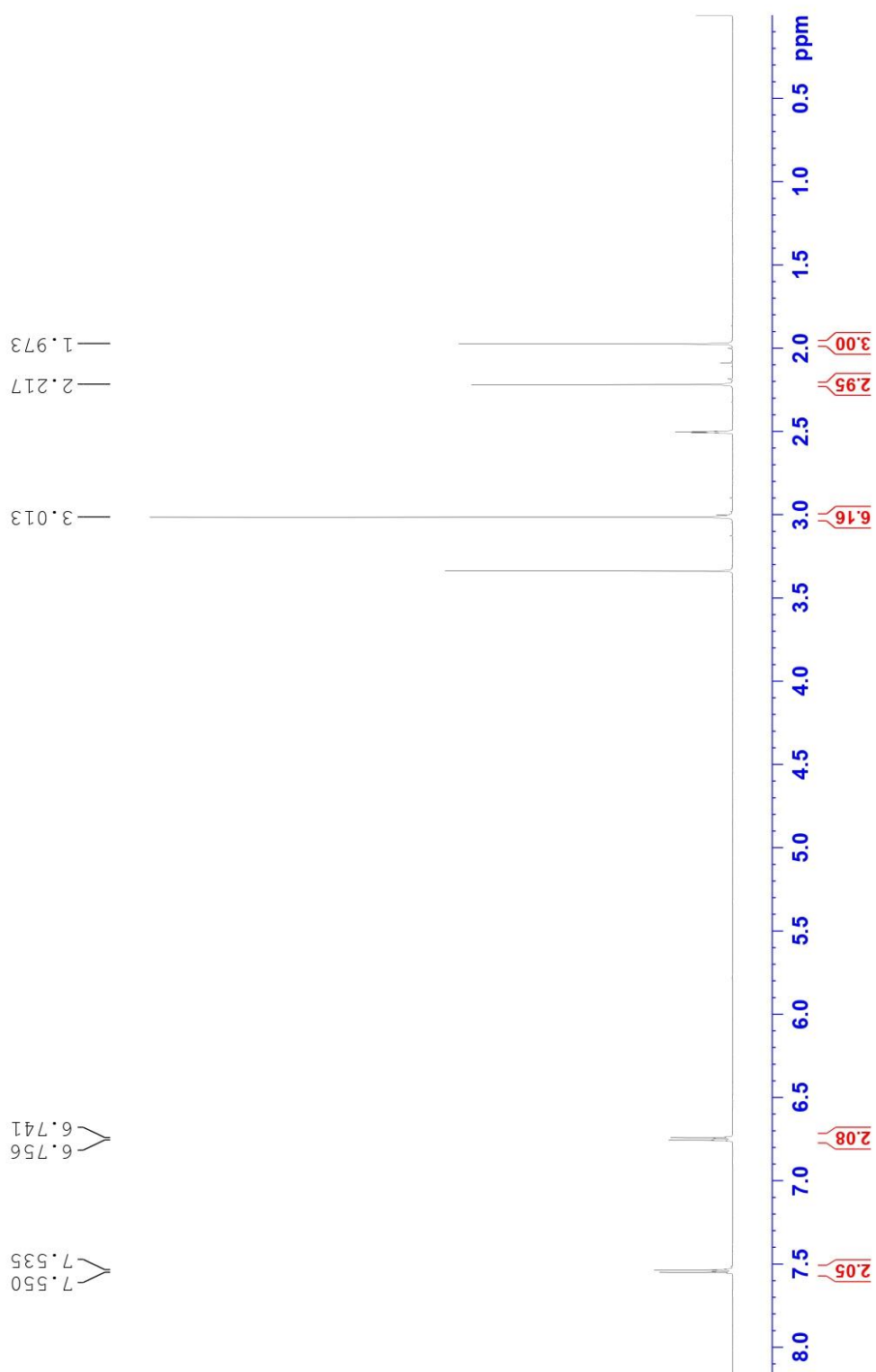
Figure B15 ^{1}H-NMR spectrum of 2.8 in DMSO-d$_6$ at 600 MHz.
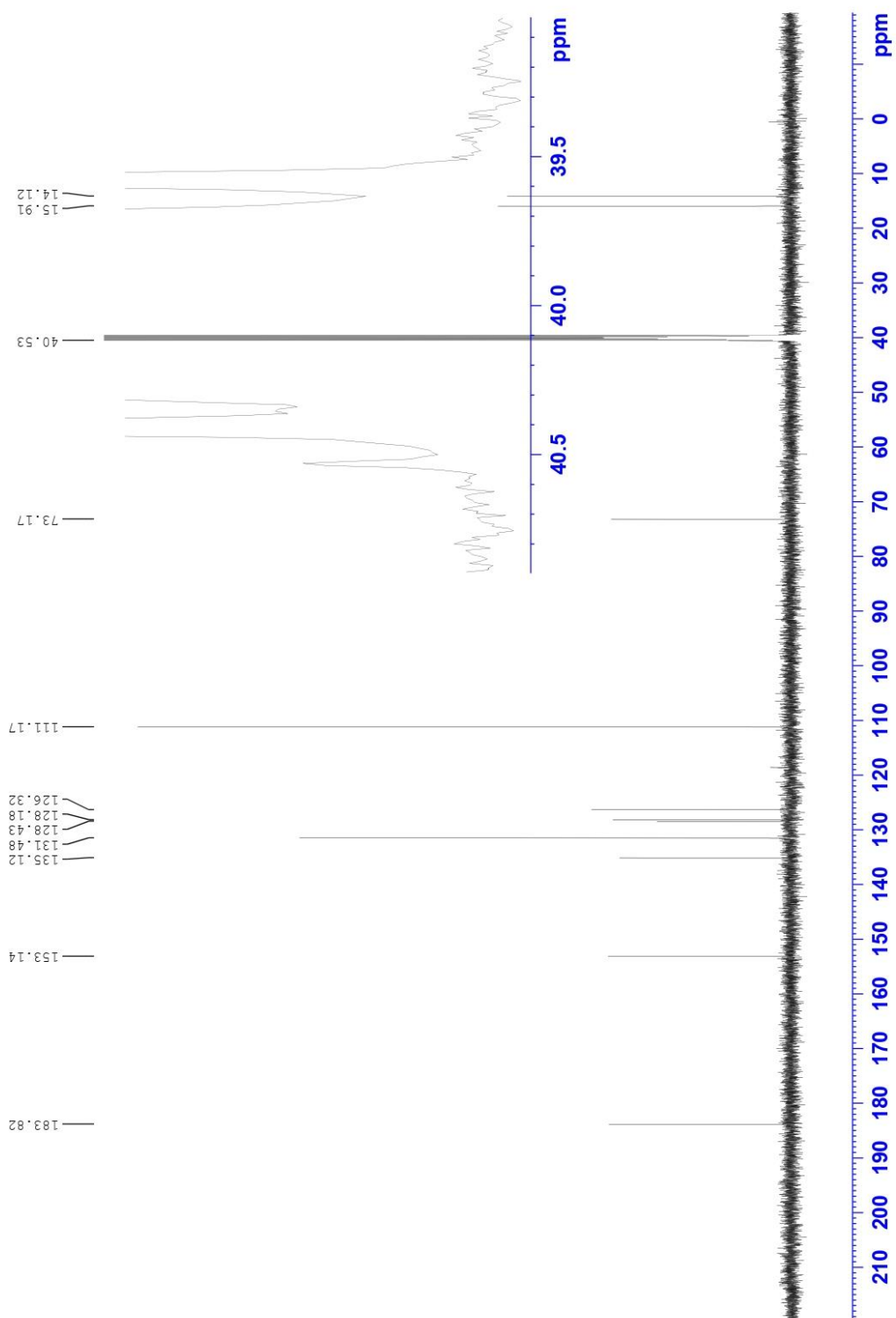
Figure B16 ^{13}C-NMR spectrum of 2.8 in DMSO-d_6 at 150 MHz.

2.308
2.422

3.148

6.307

6.914
6.926
6.929

7.958
7.974

ppm
1.0
1.5
2.0
3.00
3.05
2.5
3.0
6.08
3.5
4.0
4.5
5.0
5.5
6.0
0.96
6.5
2.07
7.0
7.5
2.04
8.0
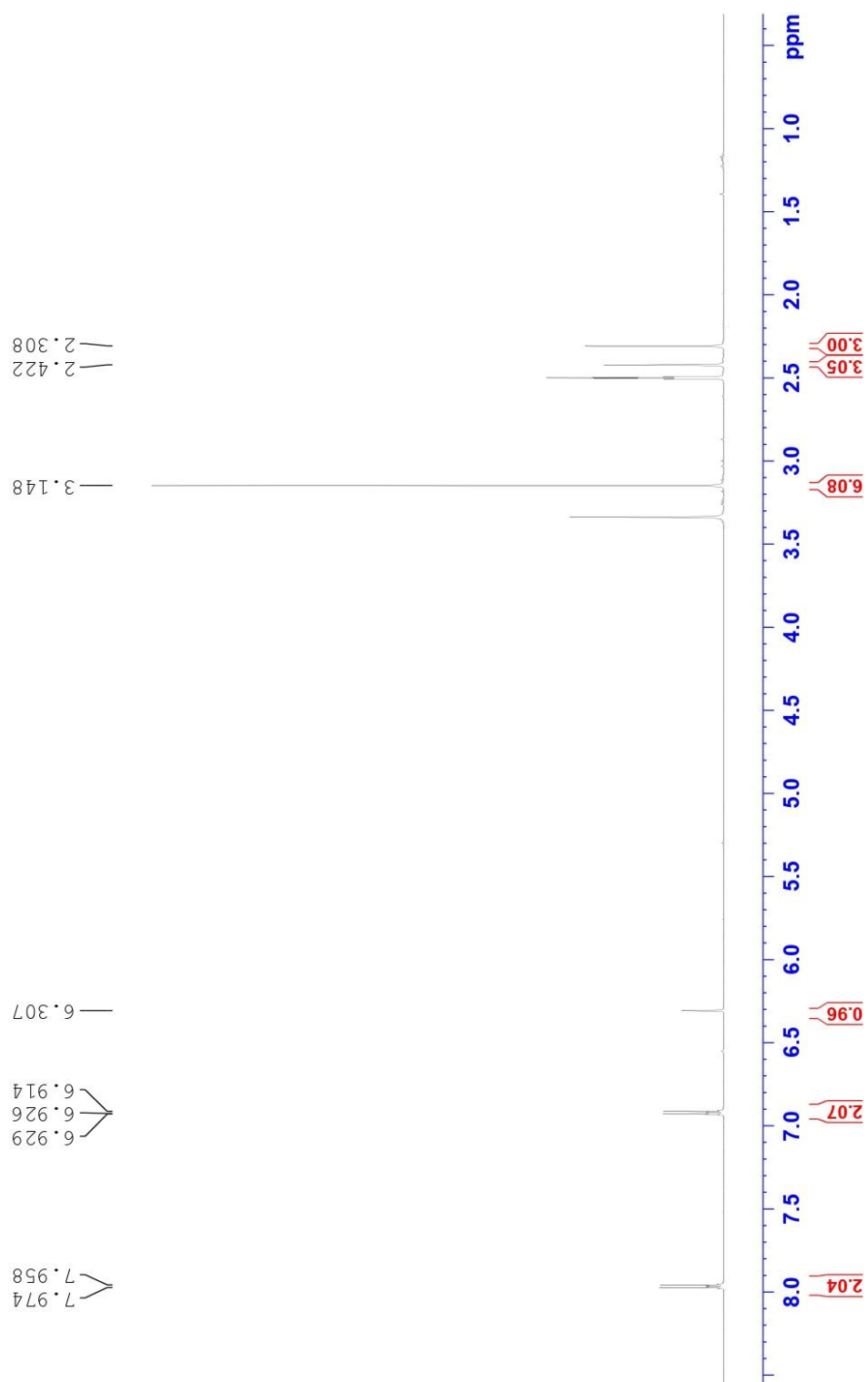
Figure B17 ^{1}H-NMR spectrum of DMAB-BF$_2$ in DMSO-d$_6$ at 600 MHz

13.49
16.01
112.20
114.04
122.29
130.63
133.80
134.30
138.39
147.62
155.44
173.55

ppm
0 10 20 30 40 50 60 70 80 90 100 110 120 130 140 150 160 170 180 190 200 210
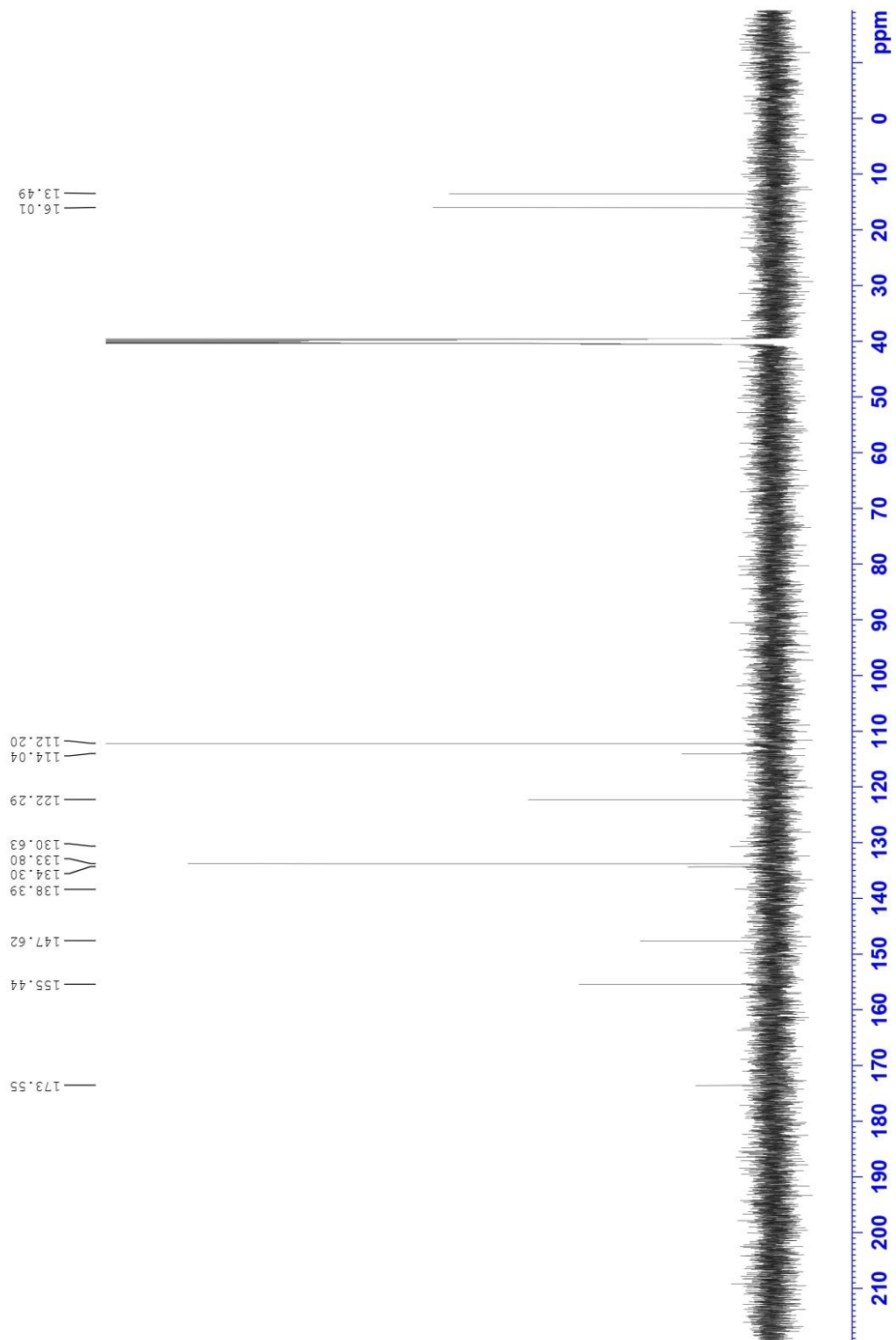
Figure B18 ^{13}C-NMR spectrum of DMAB-BF$_2$ in DMSO-d$_6$ at 150 MHz
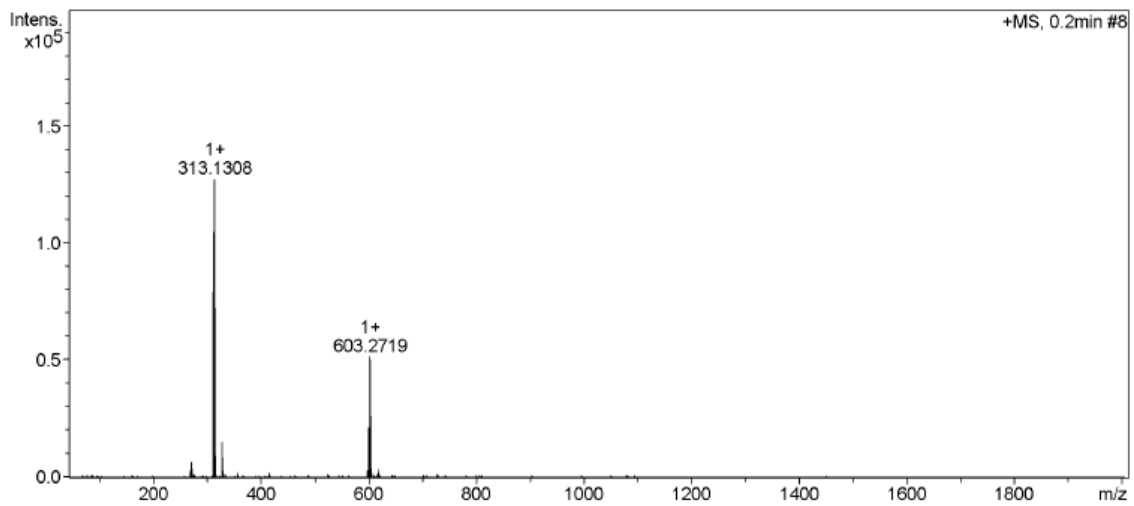
Figure B19 HR-MS (ESI-TOF) positive scan of DMAB-BF$_2$.
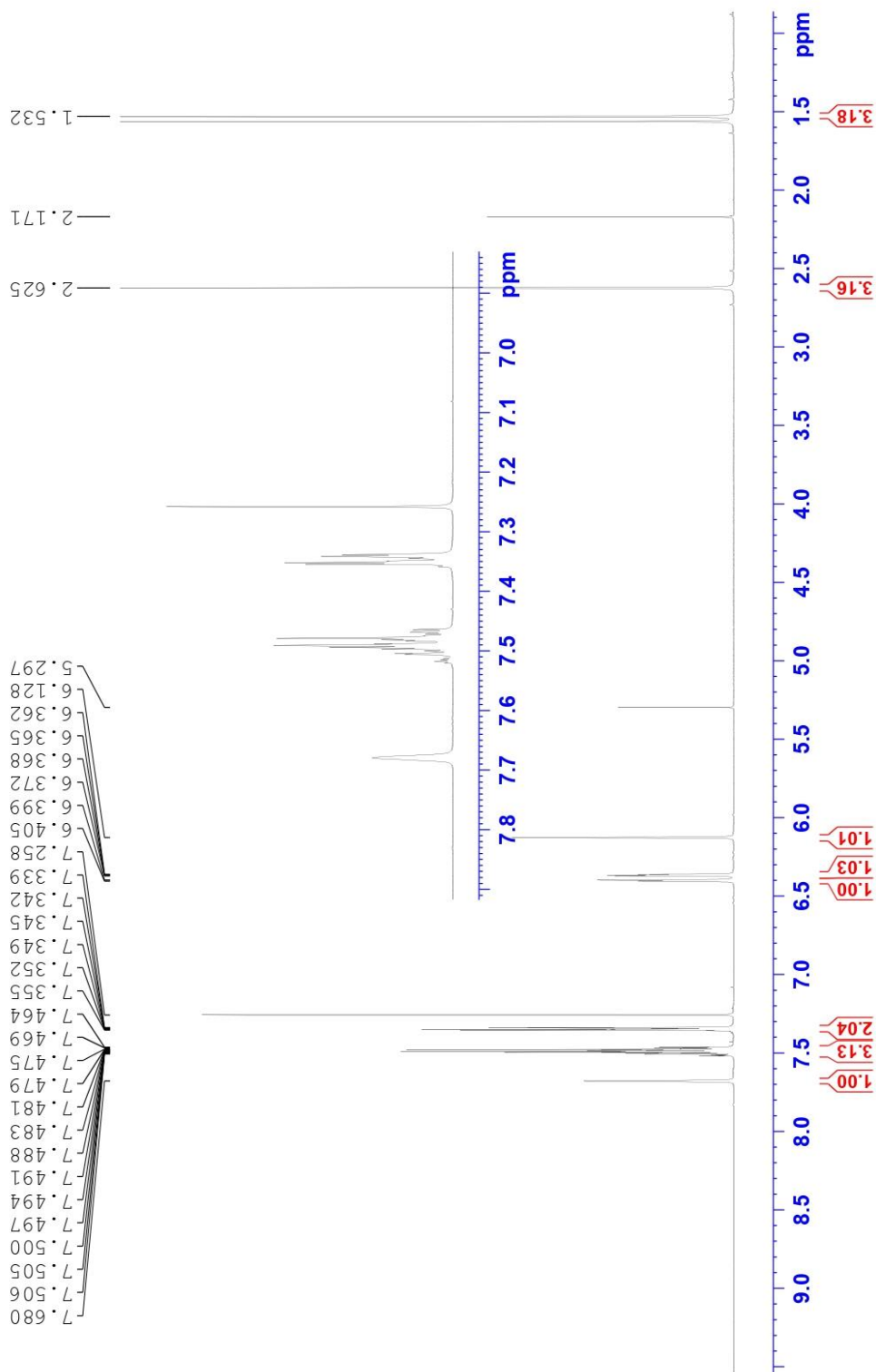
Figure B20 ^{1}H-NMR spectrum of 1.7 in CDCl$_3$ at 600 MHz
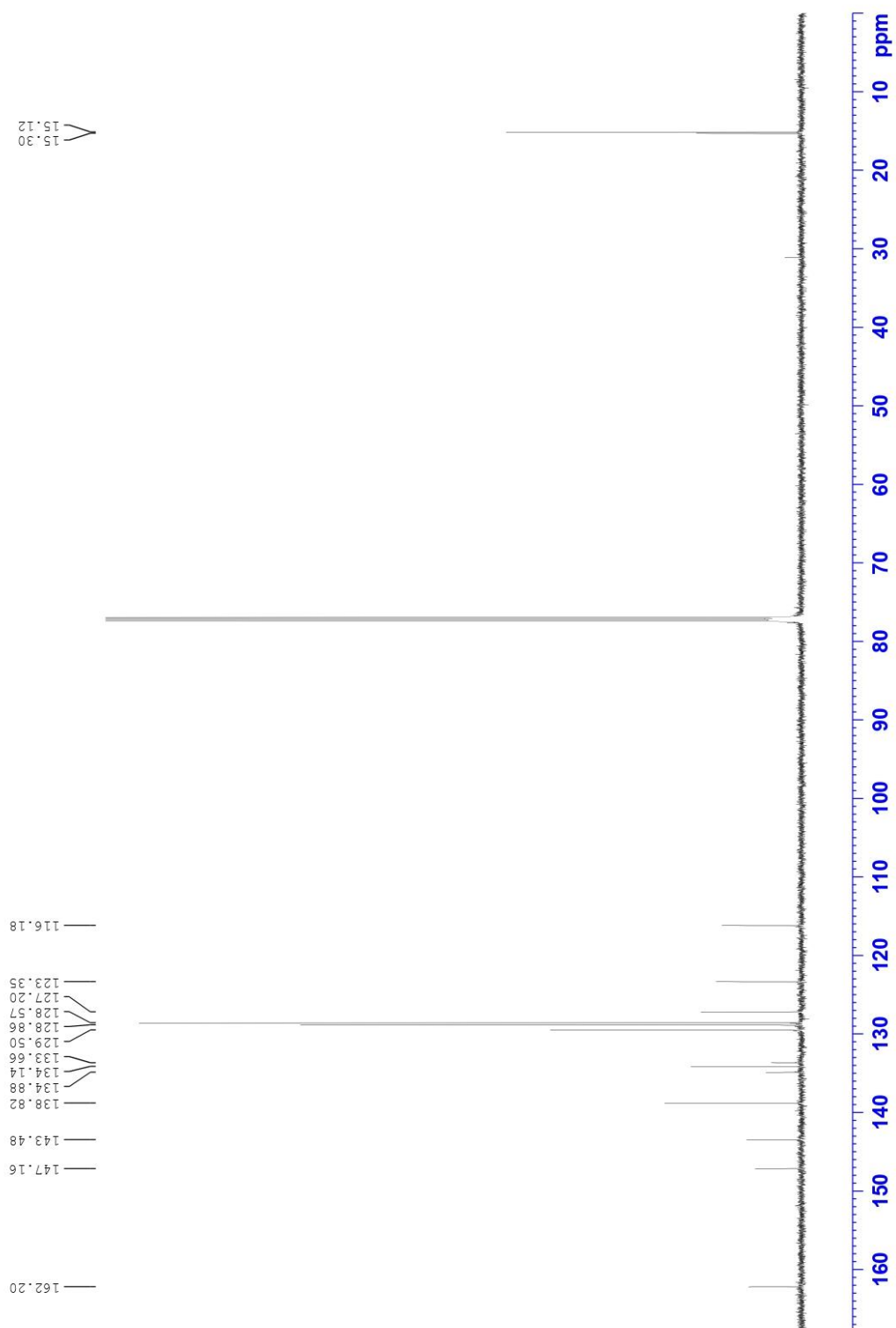
Figure B21 ^{13}C-NMR spectrum of 1.7 in CDCl$_3$ at 150 MHz.

Meas. m/z	#	Ion Formula	m/z	err [mDa]	err [ppm]	rdb	N-Rule	e⁻ Conf	mSigma
319.119140	1	C17H15BF2N2Na	319.119166	0.0	0.1	10.5	ok	even	11.3

Meas. m/z	#	Ion Formula	m/z	err [mDa]	err [ppm]	rdb	N-Rule	e⁻ Conf	mSigma
295.122498	1	C17H14BF2N2	295.122668	-0.2	-0.6	11.5	ok	even	29.6
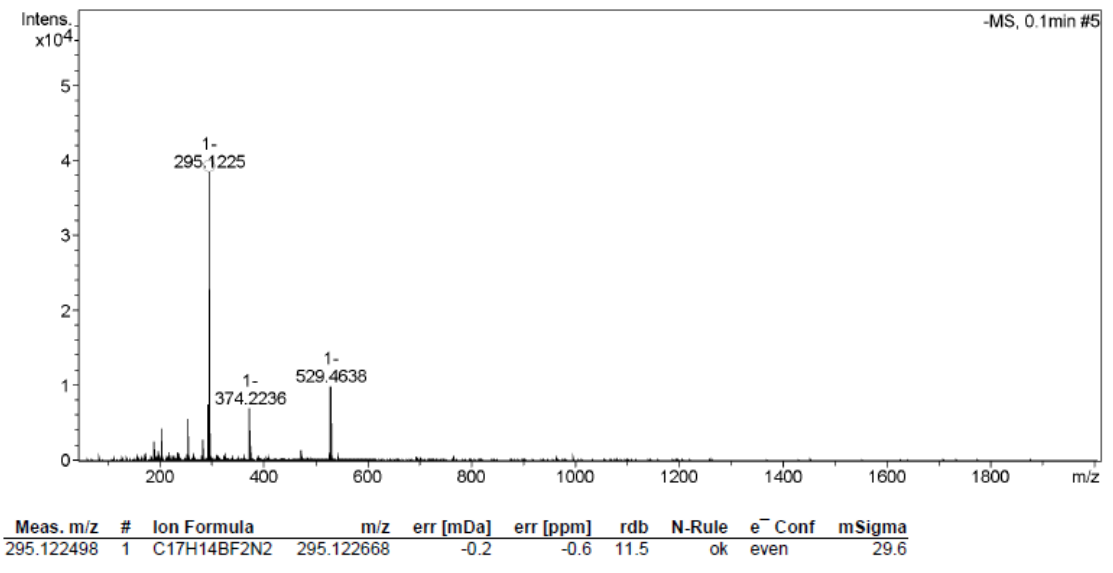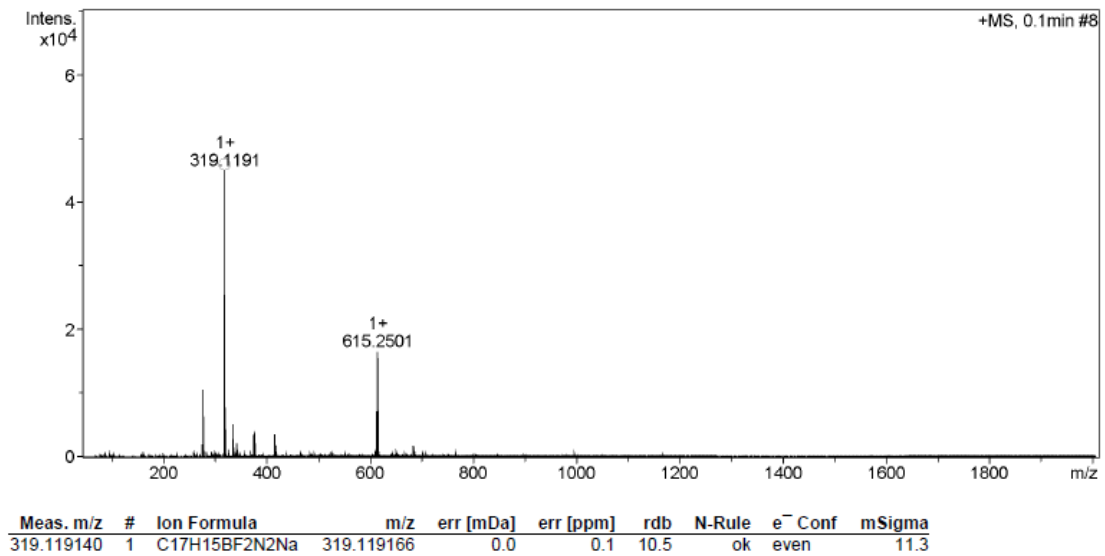
Figure B22 HR-MS (ESI-TOF) positive and negative scans of 1.7.
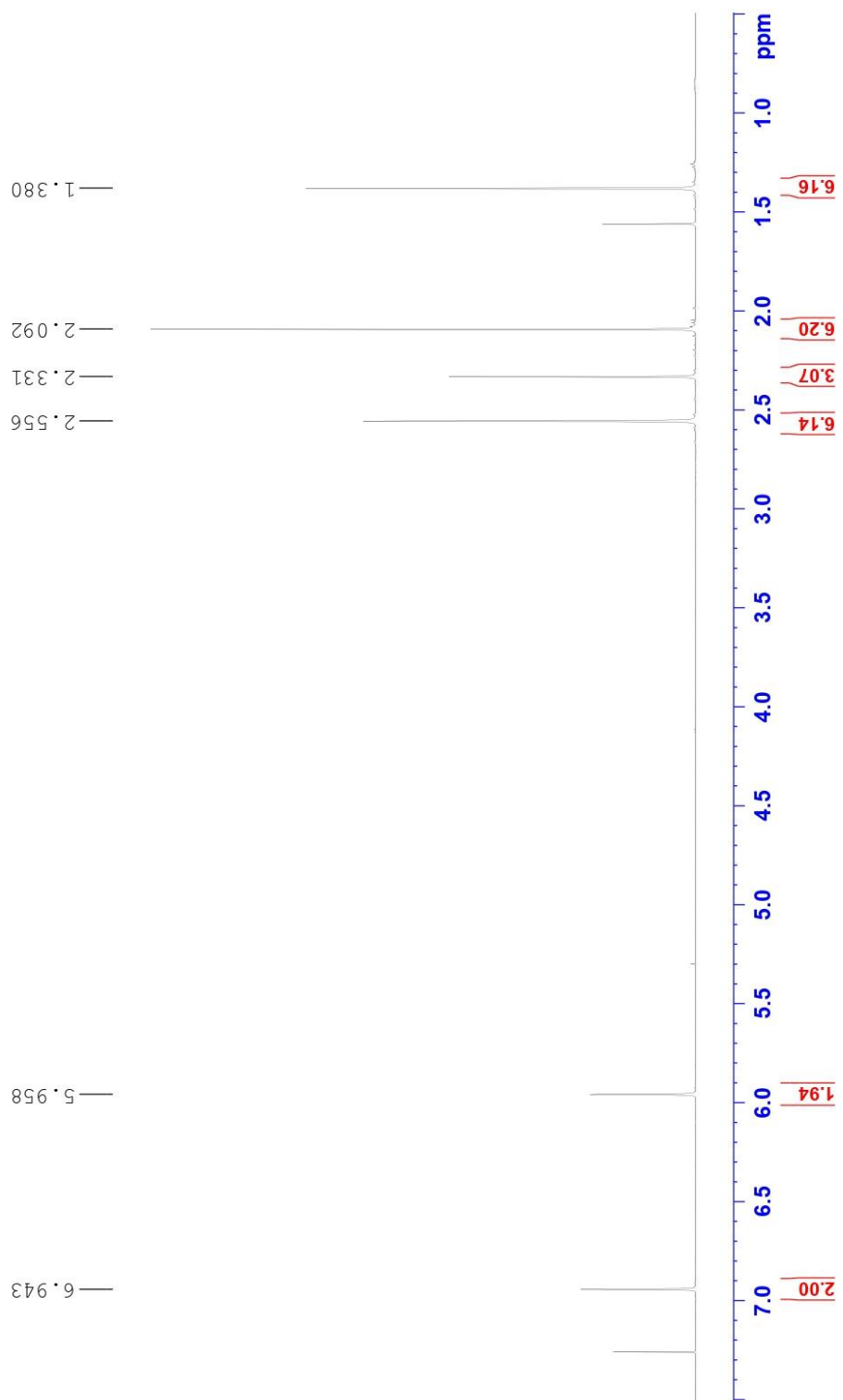
Figure B23 ^{1}H-NMR spectrum of 1.9 in CDCl$_3$ at 600 MHz.

Peaks: 1.380, 2.092, 2.331, 2.556, 5.958, 6.943

Integrations: 6.16, 6.20, 3.07, 6.14, 1.94, 2.00
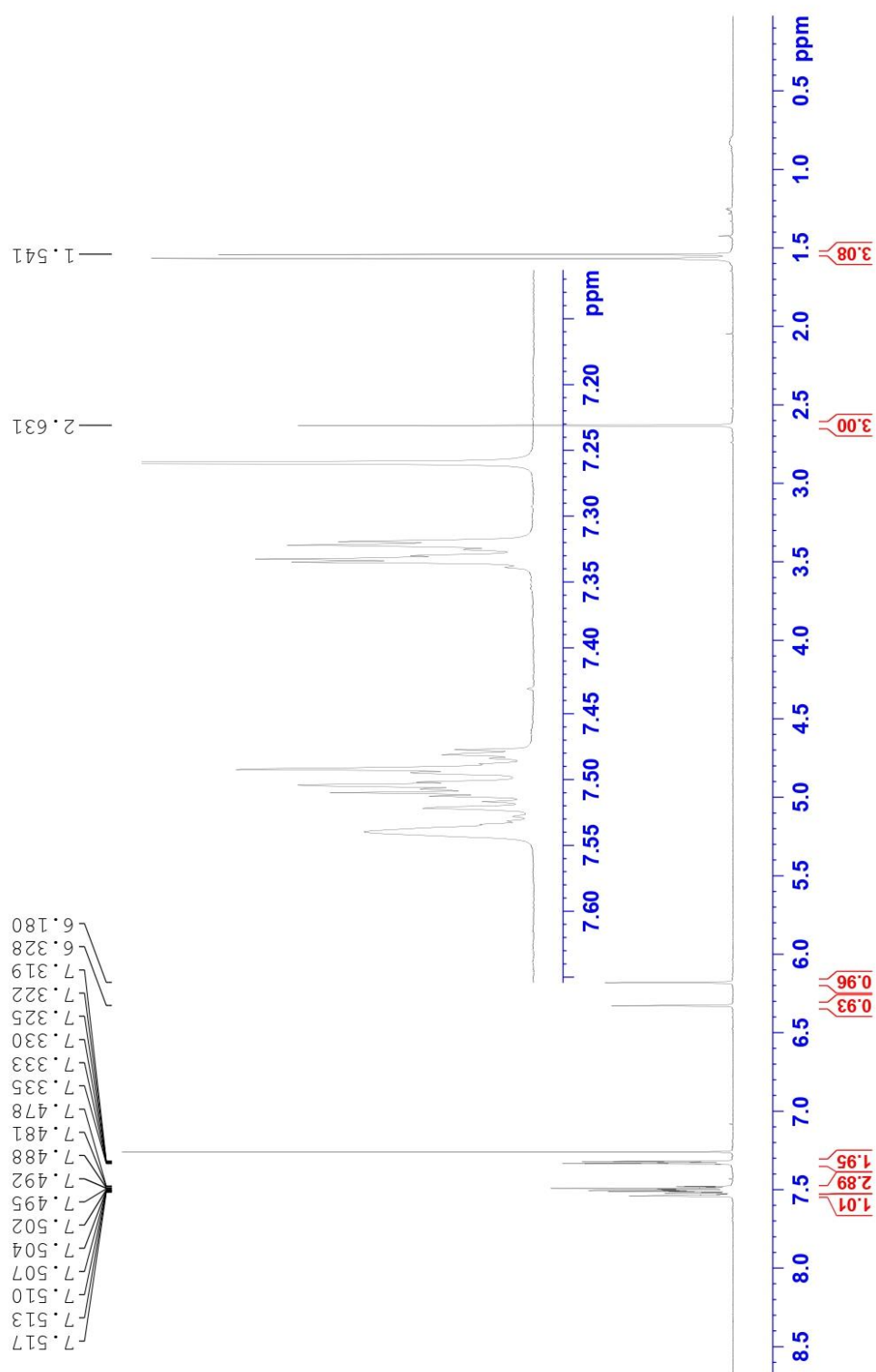
Figure B24 ^{1}H-NMR spectrum of 3.4 in CDCl$_3$ at 600 MHz

Figure B25 ^{13}C-NMR spectrum of 3.4 in CDCl$_3$ at 150 MHz

Meas. m/z	#	Ion Formula	m/z	err [mDa]	err [ppm]	rdb	N-Rule	e⁻ Conf	mSigma
397.029750	1	C17H14BBrF2N2Na	397.029678	0.1	0.2	10.5	ok	even	20.0

Meas. m/z	#	Ion Formula	m/z	err [mDa]	err [ppm]	rdb	N-Rule	e⁻ Conf	mSigma
373.032399	1	C17H13BBrF2N2	373.033180	0.8	2.1	11.5	ok	even	27.1
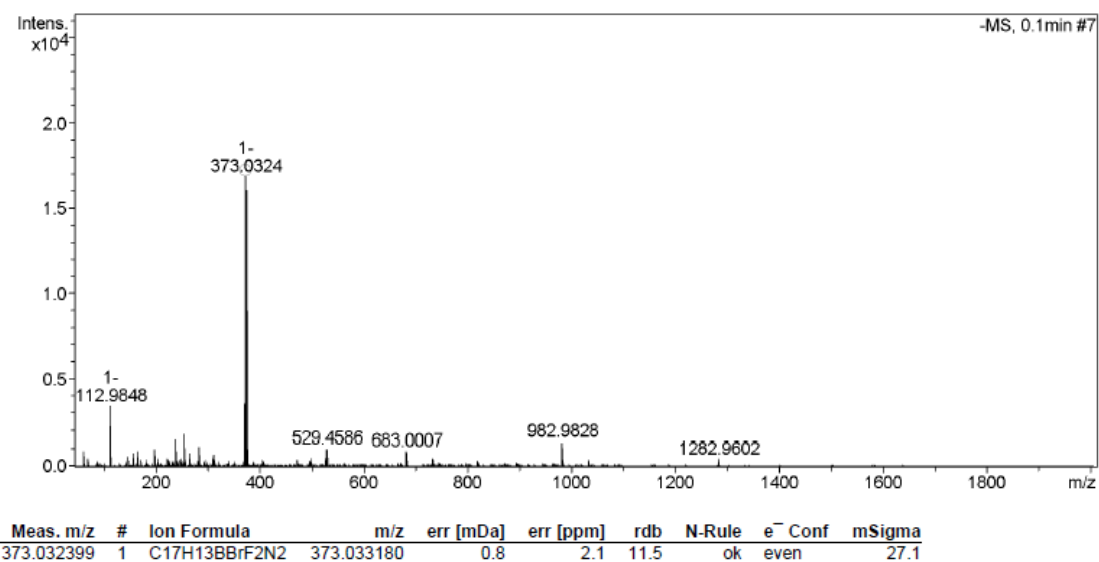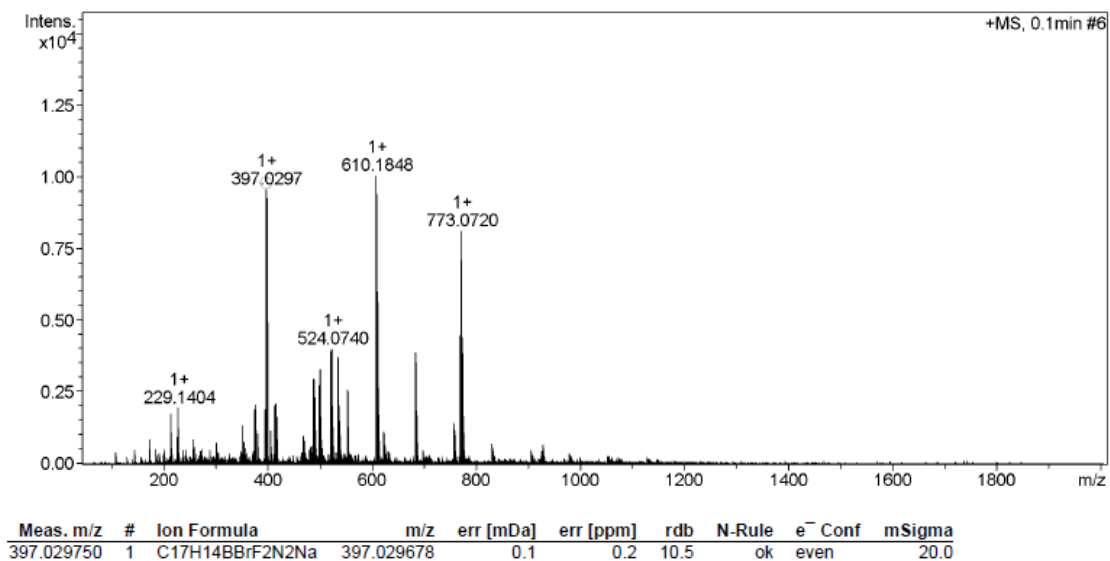
Figure B26 HR-MS (ESI-TOF) positive and negative scans of 3.4.
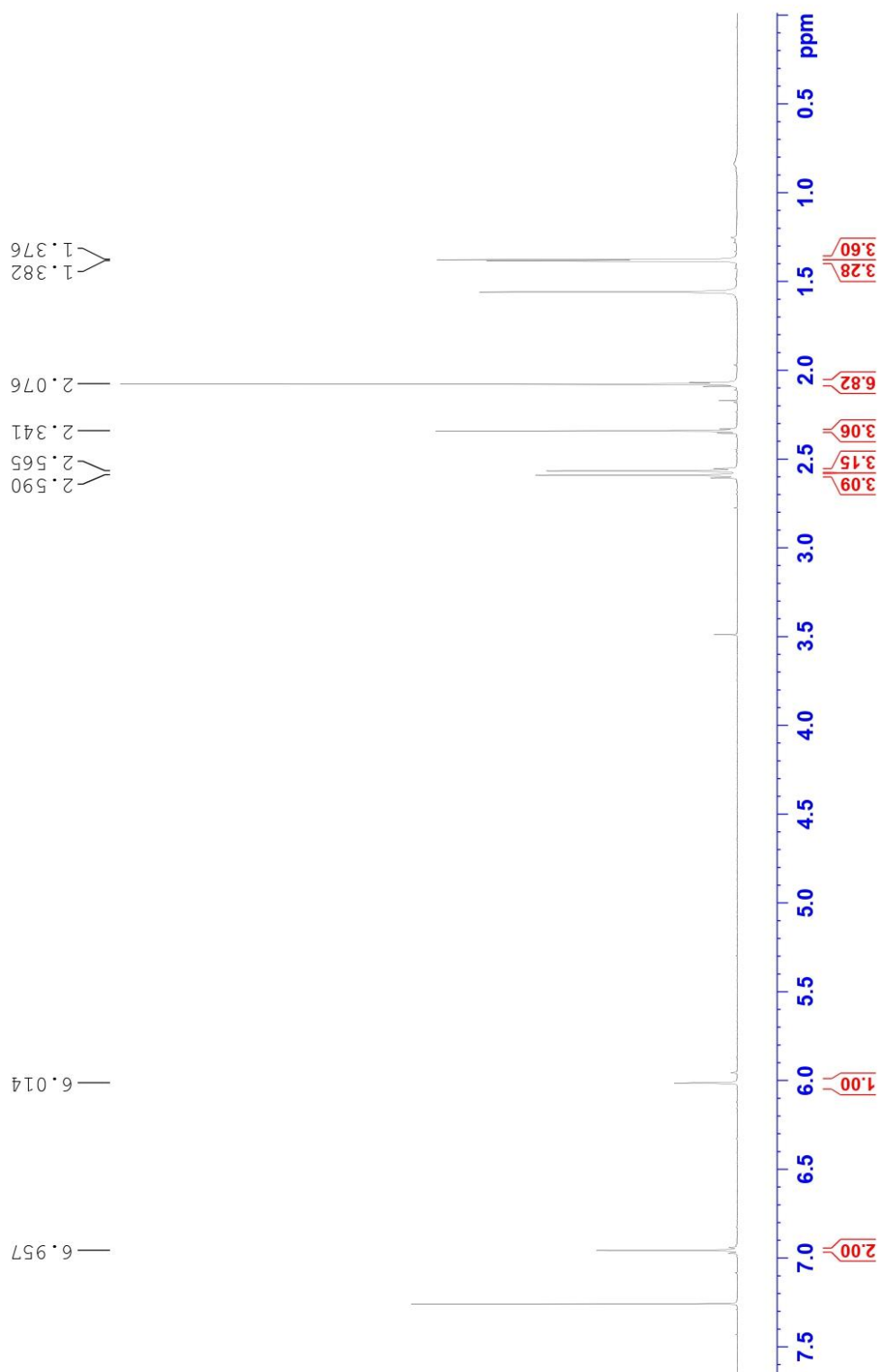
Figure B27 ^{1}H-NMR spectrum of 3.8 in CDCl$_3$ at 600 MHz.
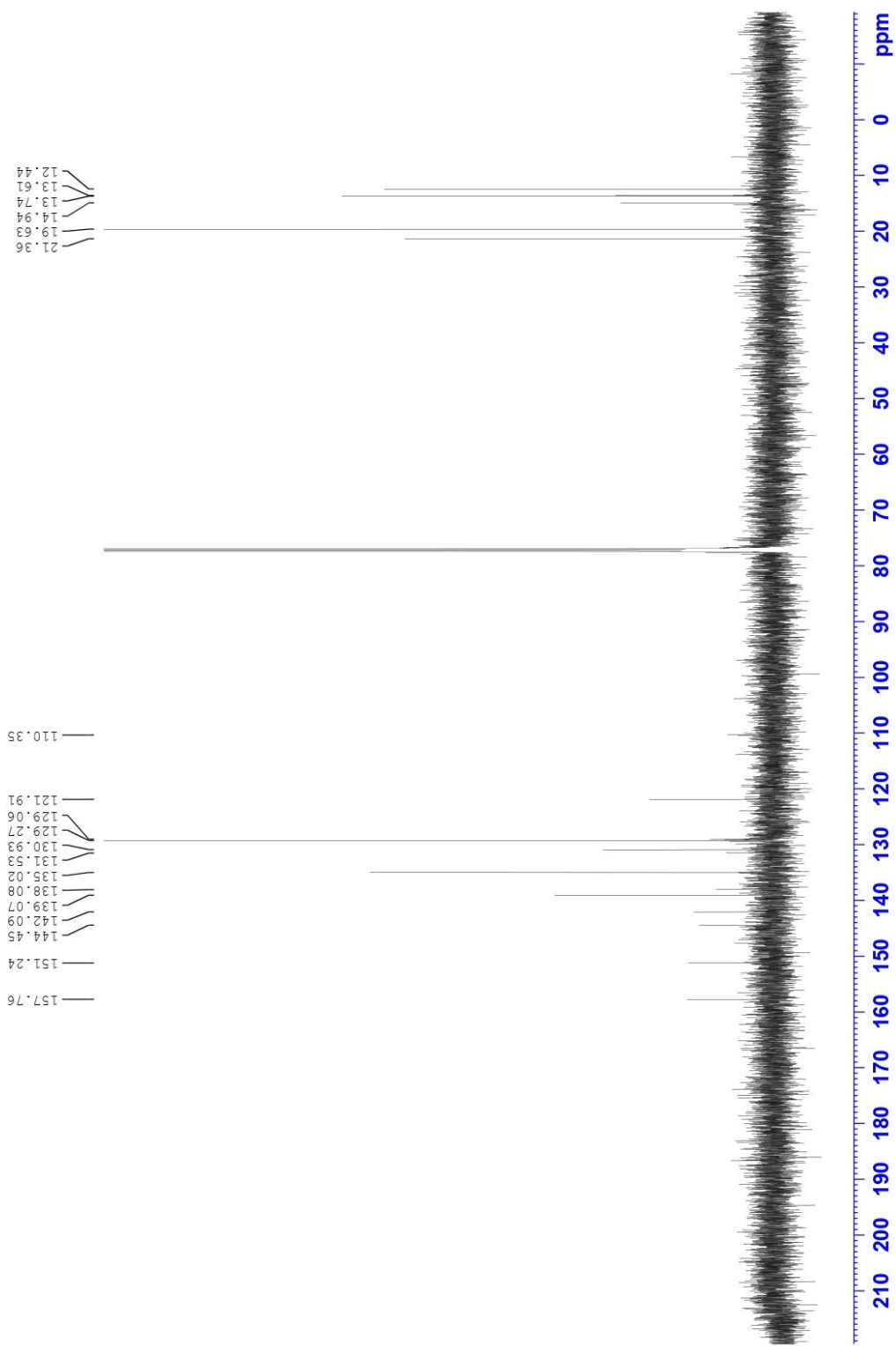
Figure B28 ^{13}C-NMR spectrum of 3.8 in CDCl$_3$ at 150 MHz.

Peak labels: 12.44, 13.61, 13.74, 14.94, 19.63, 21.36, 110.35, 121.91, 129.06, 129.27, 130.93, 131.53, 135.02, 138.08, 139.07, 142.09, 144.45, 151.24, 157.76

Meas. m/z	#	Ion Formula	m/z	err [mDa]	err [ppm]	rdb	N-Rule	e⁻ Conf	mSigma
467.108163	1	C22H24BBrF2N2Na	467.108015	-0.1	-0.3	10.5	ok	even	42.6
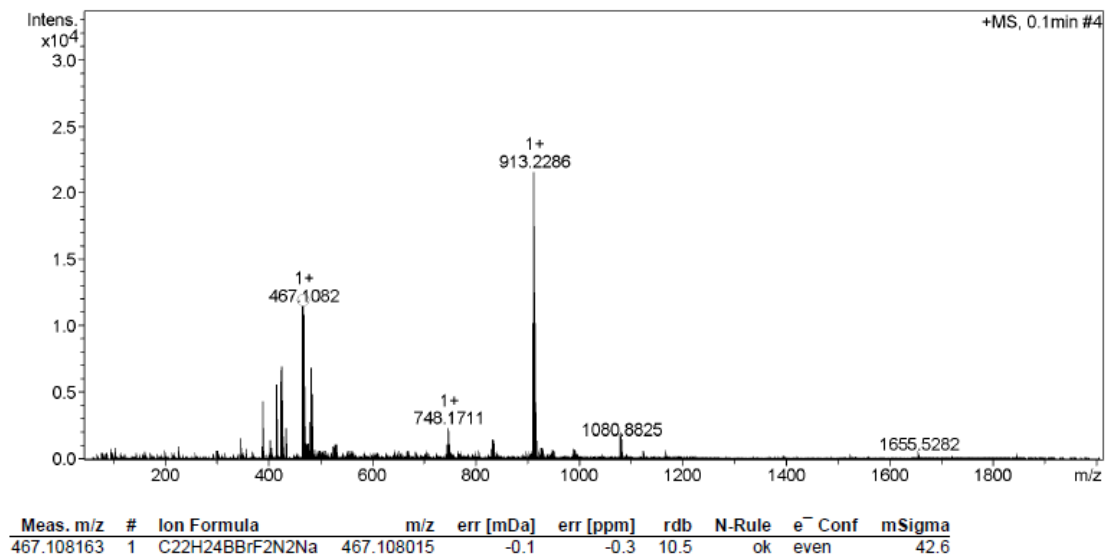
Figure B29 HR-MS (ESI-TOF) positive scan of 3.8.

1.520

2.671

6.411
6.414
6.417
6.420
6.488
6.495
7.334
7.336
7.348
7.486
7.498
7.510
7.524
7.536
7.747

3.10

3.19

2.01

3.18

0.99

1.00
0.97

2.01
3.18

0.99

ppm

7.1 7.2 7.3 7.4 7.5 7.6 7.7 7.8

0.5 ppm 1.0 1.5 2.0 2.5 3.0 3.5 4.0 4.5 5.0 5.5 6.0 6.5 7.0 7.5 8.0
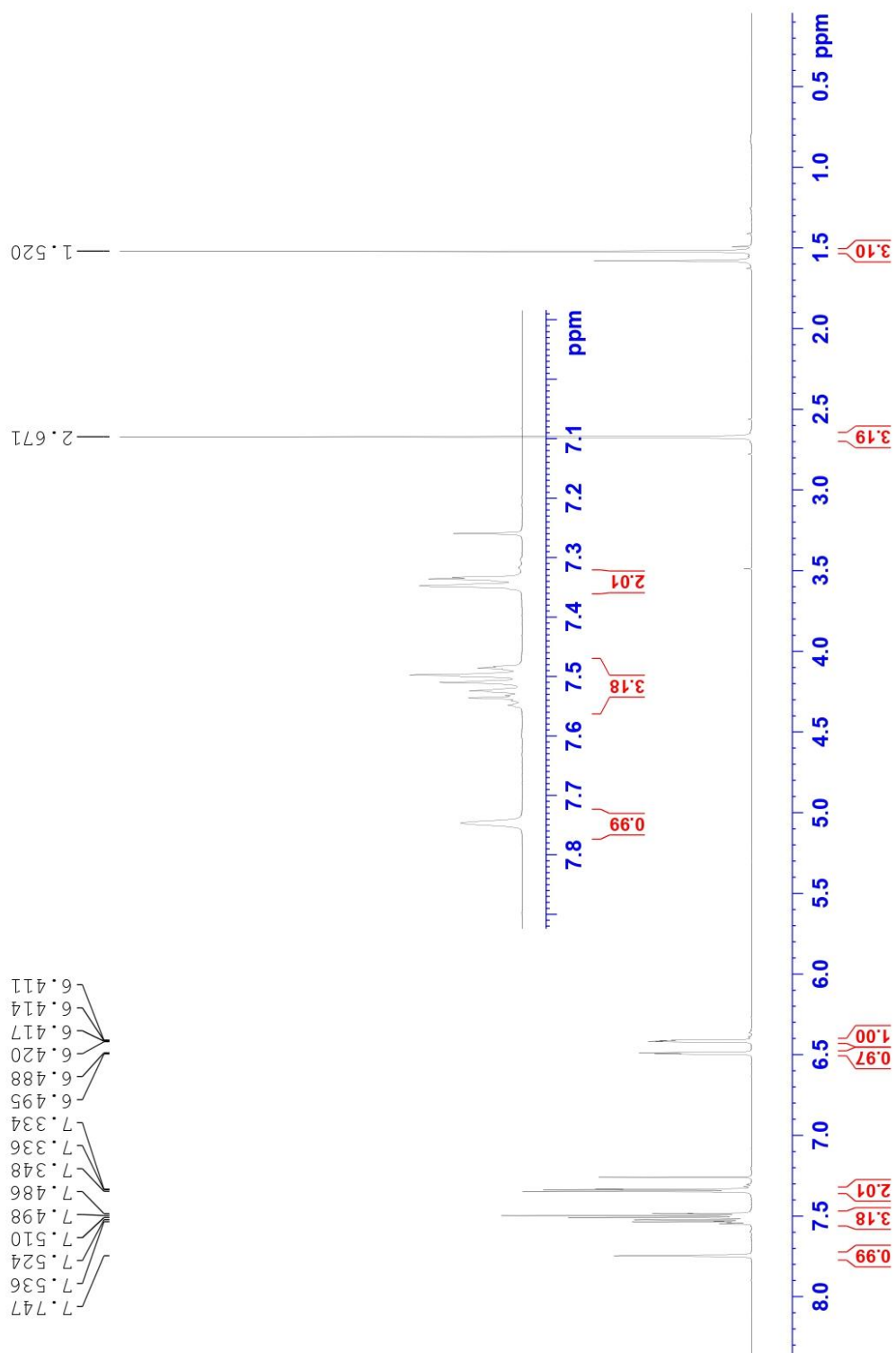
Figure B30 ^{1}H-NMR spectrum of 3.9 in CDCl$_3$ at 600 MHz

14.222
14.438

113.268
117.056
128.661
128.823
128.980
129.821
131.895
133.859
135.047
140.670
142.880
144.134
158.434

126
127
128
129
130
131
ppm

0
20
40
60
80
100
120
140
160
180
200
ppm
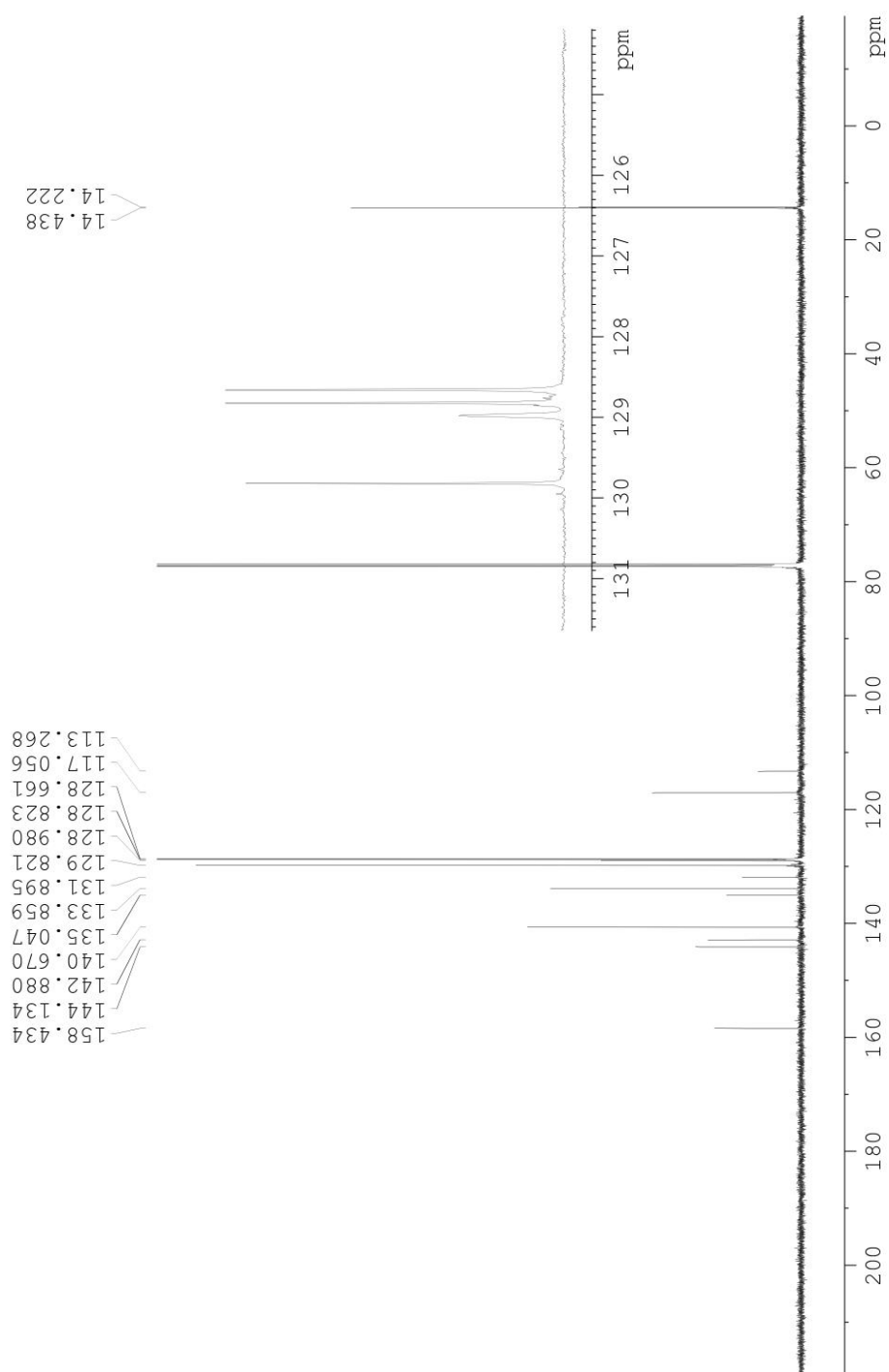
Figure B31 ^{13}C-NMR spectrum of 3.9 in CDCl$_3$ at 150 MHz

Meas. m/z	#	Ion Formula	m/z	err [ppm]	mSigma	# mSigma	Score	rdb	e⁻ Conf	N-Rule
397.0305	1	C17H14BBrF2N2Na	397.0294	-2.1	19.9	1	100.00	10.5	even	ok
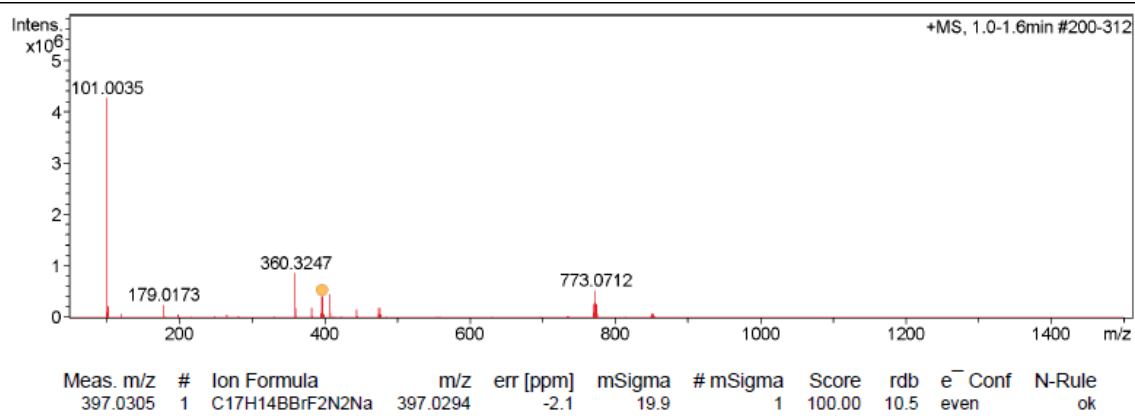
Figure B32 HR-MS (ESI-TOF) positive scan of 3.9.
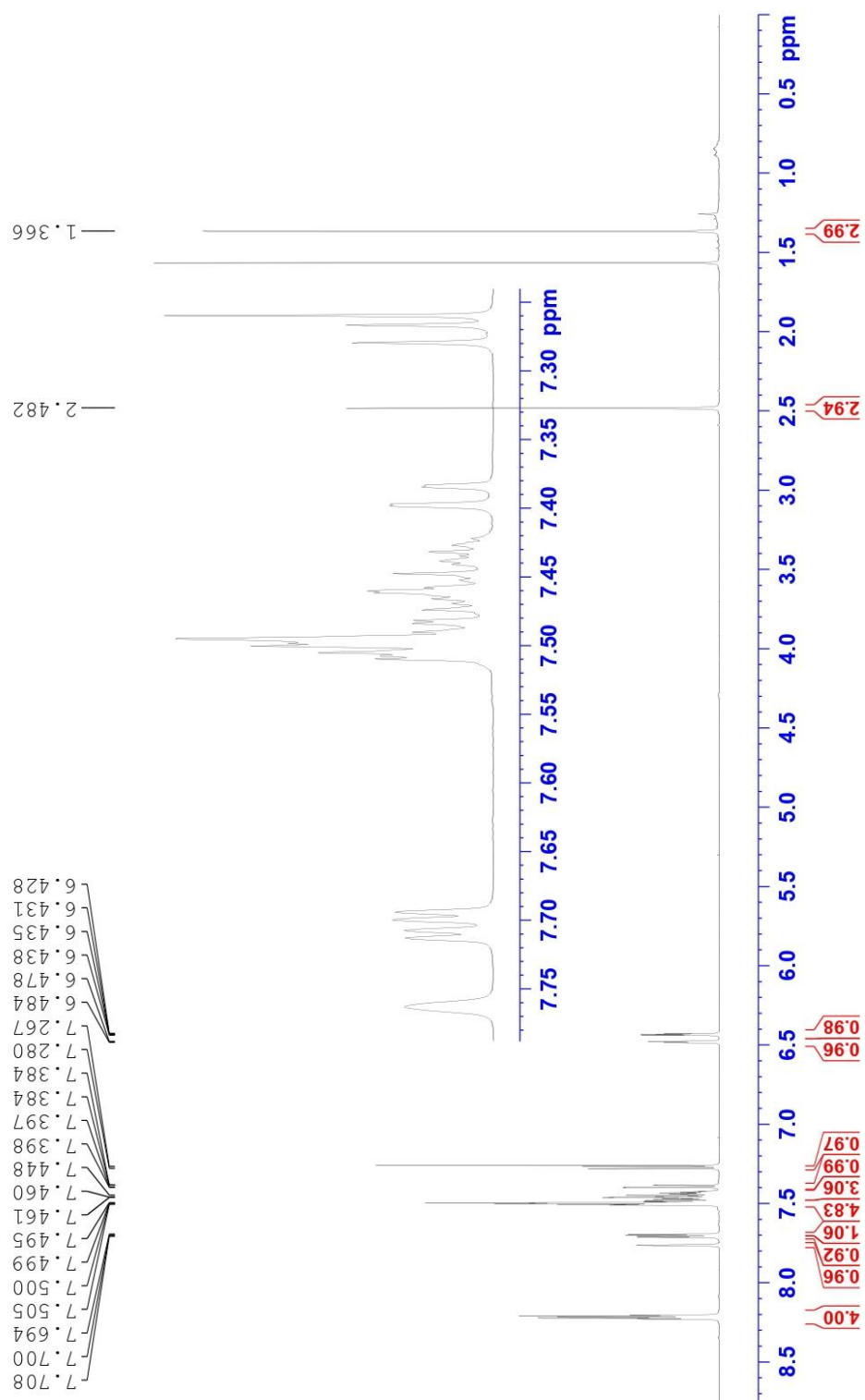
Figure B33 ^{1}H-NMR spectrum of 2-DMB2P in CDCl$_3$ at 600 MHz
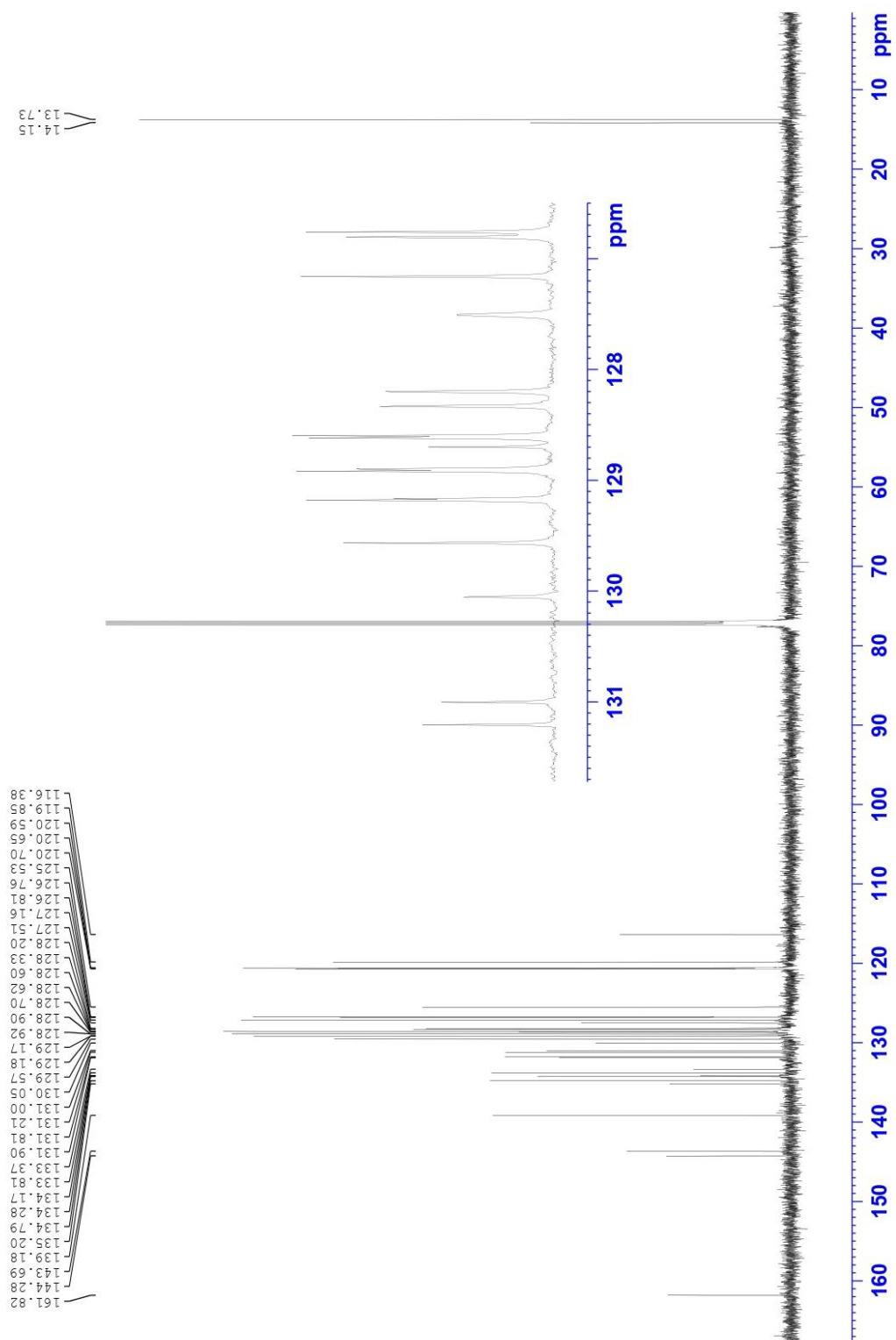
Figure B34 ^{13}C-NMR spectrum of 2-DMB2P in CDCl$_3$ at 150 MHz

Meas. m/z	#	Ion Formula	m/z	err [ppm]	mSigma	# mSigma	Score	rdb	e⁻ Conf	N-Rule
569.2098	1	C37H25BF2N2Na	569.1971	-21.2	12.9	1	100.00	25.5	even	ok

Meas. m/z	#	Ion Formula	m/z	err [ppm]	mSigma	# mSigma	Score	rdb	e⁻ Conf	N-Rule
545.2059	1	C37H24BF2N2	545.2006	-8.6	18.4	1	100.00	26.5	even	ok
577.1973	1	C38H28BF2N2O	577.2268	52.3	28.0	1	100.00	25.5	even	ok
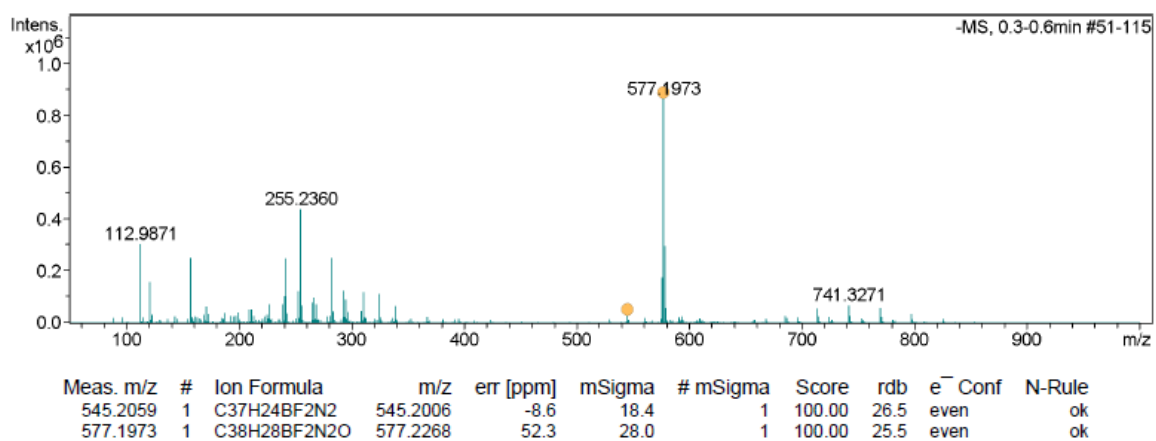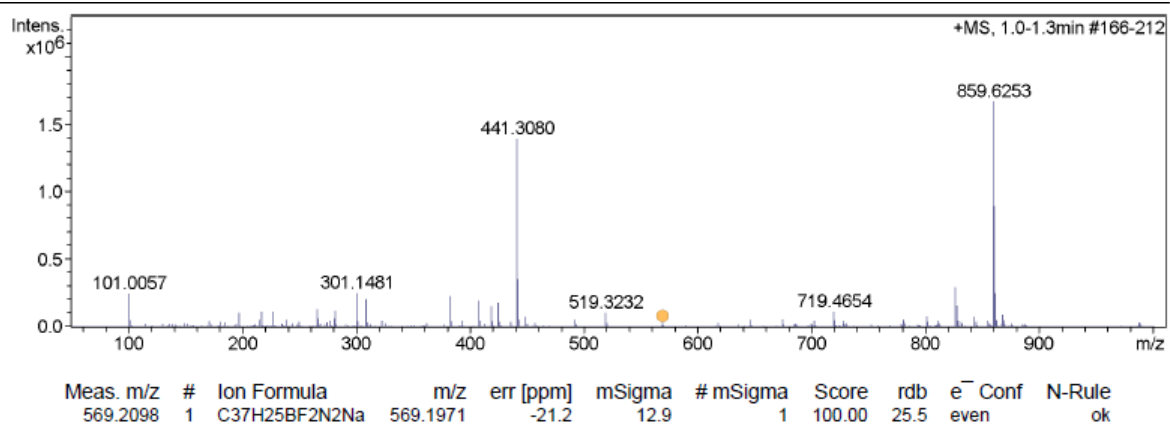
Figure B35 HR-MS (ESI-TOF) positive and negative scans of 2-DMB2P.
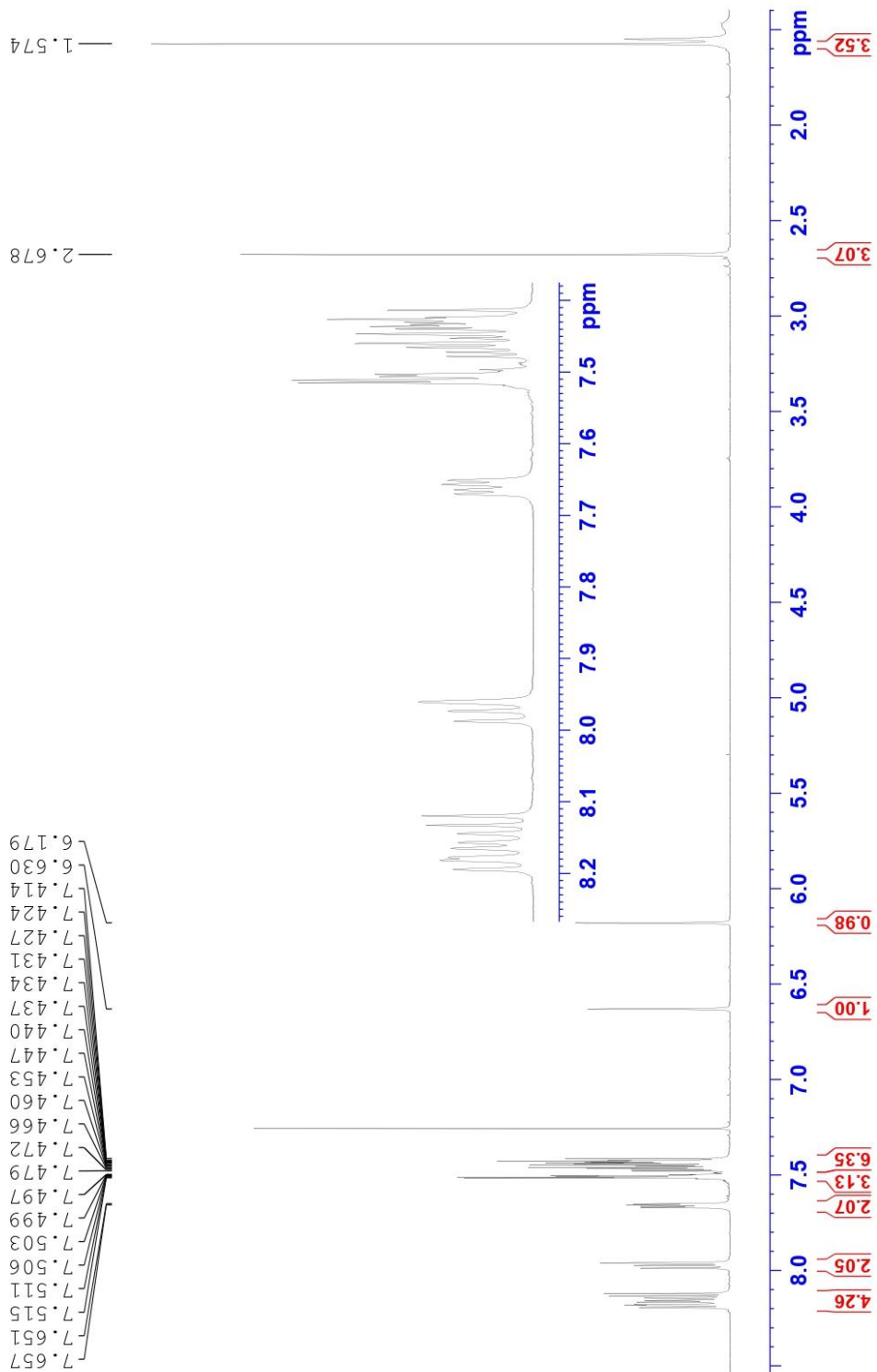
Figure B36 ^{1}H-NMR spectrum of 8-DMB2P in CDCl$_3$ at 600 MHz
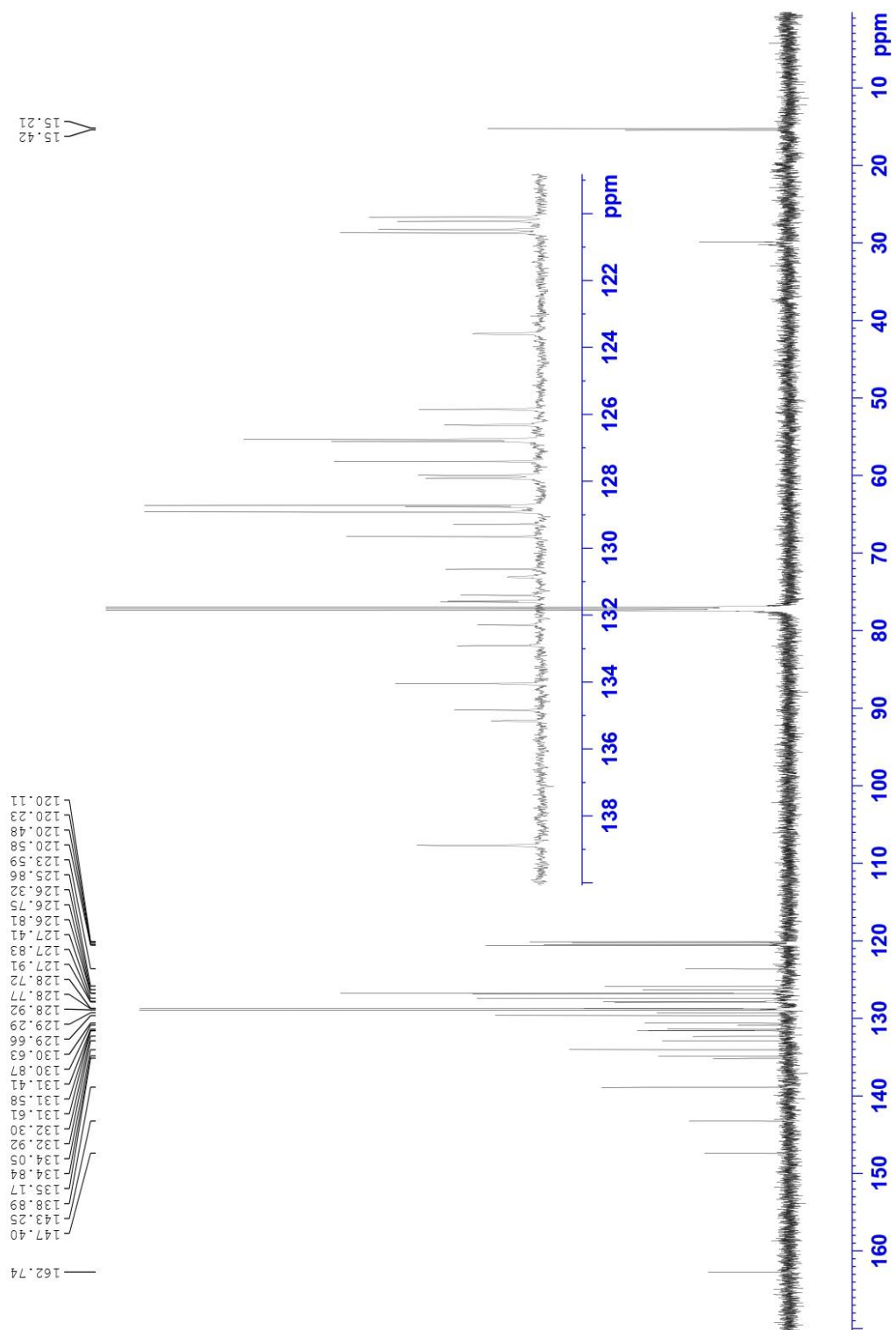
Figure B37 ^{13}C-NMR spectrum of 8-DMB2P in CDCl$_3$ at 150 MHz
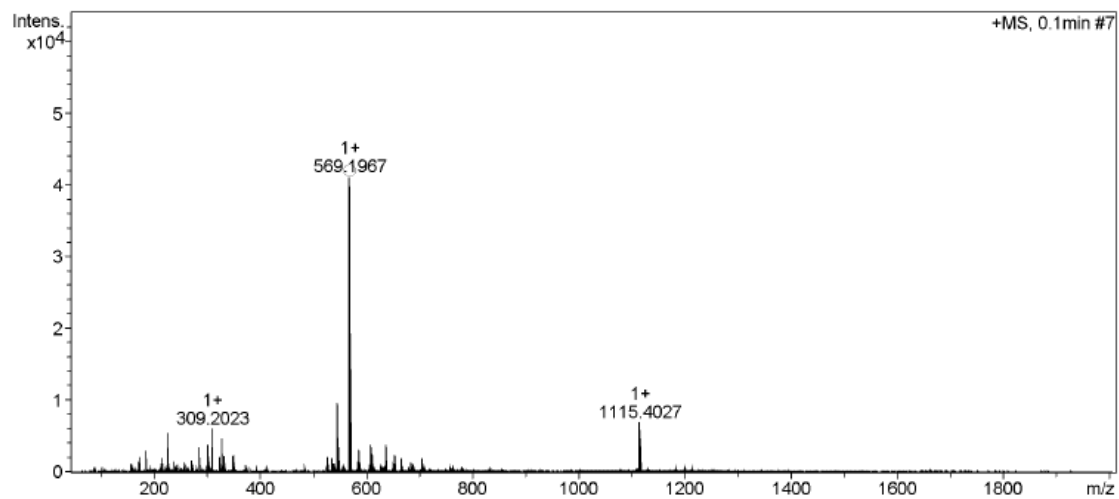
Meas. m/z	#	Ion Formula	m/z	err [mDa]	err [ppm]	rdb	N-Rule	e⁻ Conf	mSigma
569.196742	1	C37H25BF2N2Na	569.197744	1.0	1.8	25.5	ok	even	20.4
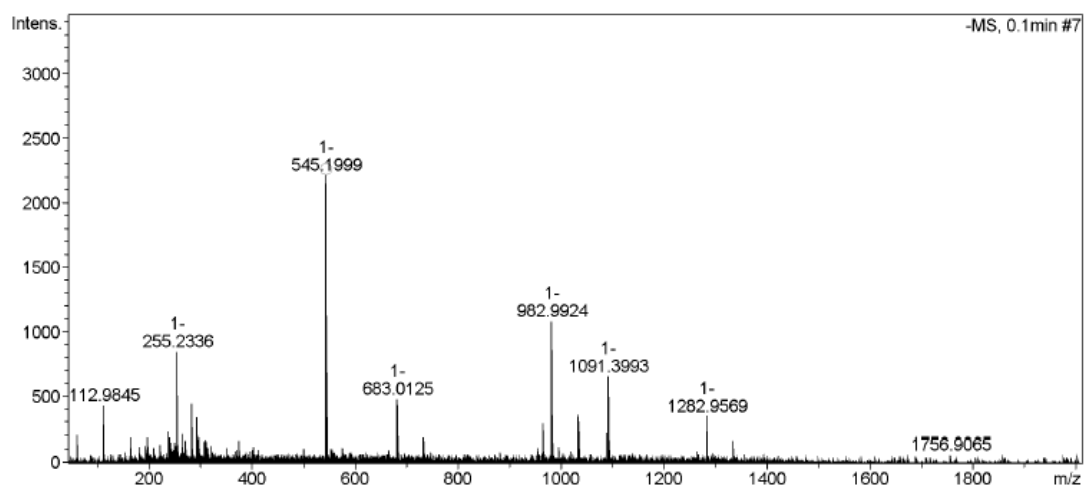
Meas. m/z	#	Ion Formula	m/z	err [mDa]	err [ppm]	rdb	N-Rule	e⁻ Conf	mSigma
545.199944	1	C37H24BF2N2	545.201247	-1.3	-2.4	26.5	ok	even	35.8

Figure B38 HR-MS (ESI-TOF) positive and negative scans of 8-DMB2P.
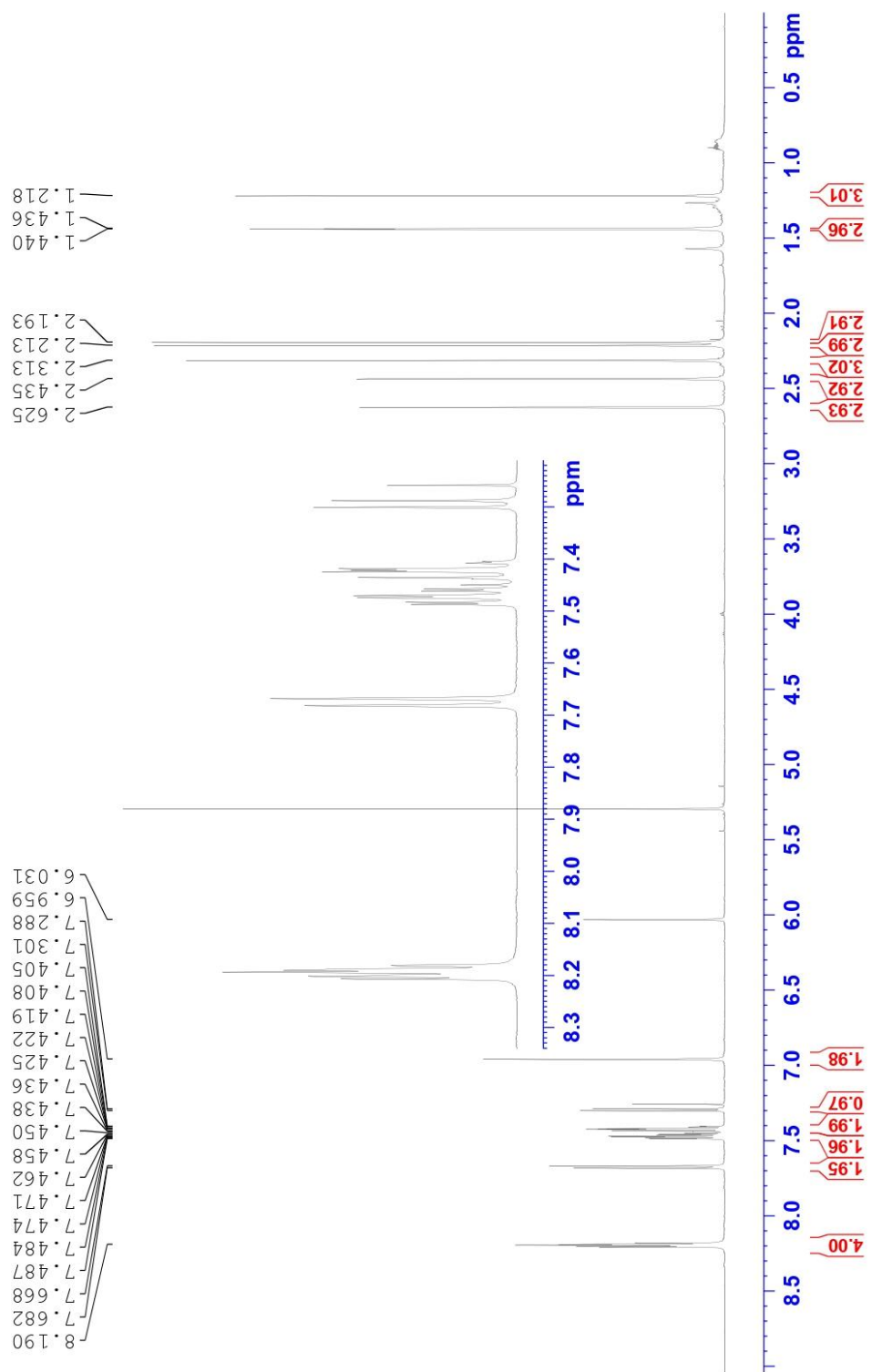
Figure B39 ^{1}H-NMR spectrum of MB2P in CDCl$_3$ at 600 MHz
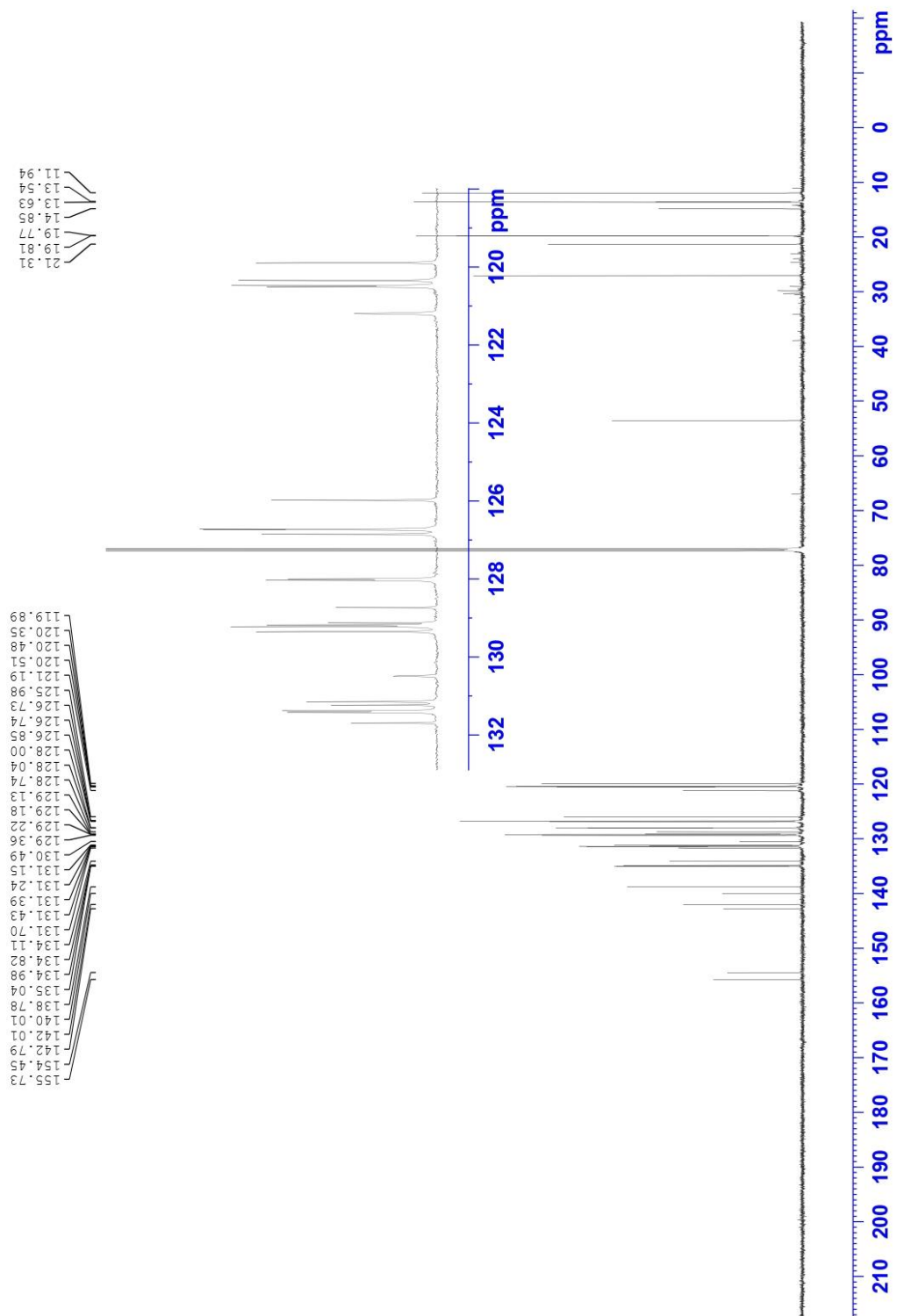
Figure B40 ^{13}C-NMR spectrum of MB2P in CDCl$_3$ at 150 MHz
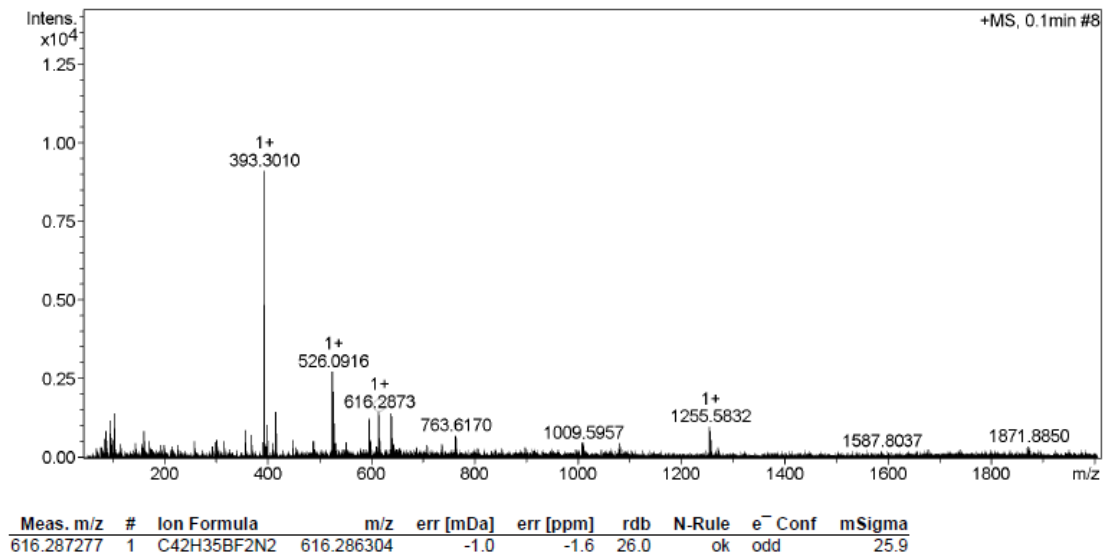
Figure B41 HR-MS (ESI-TOF) positive scan of MB2P.
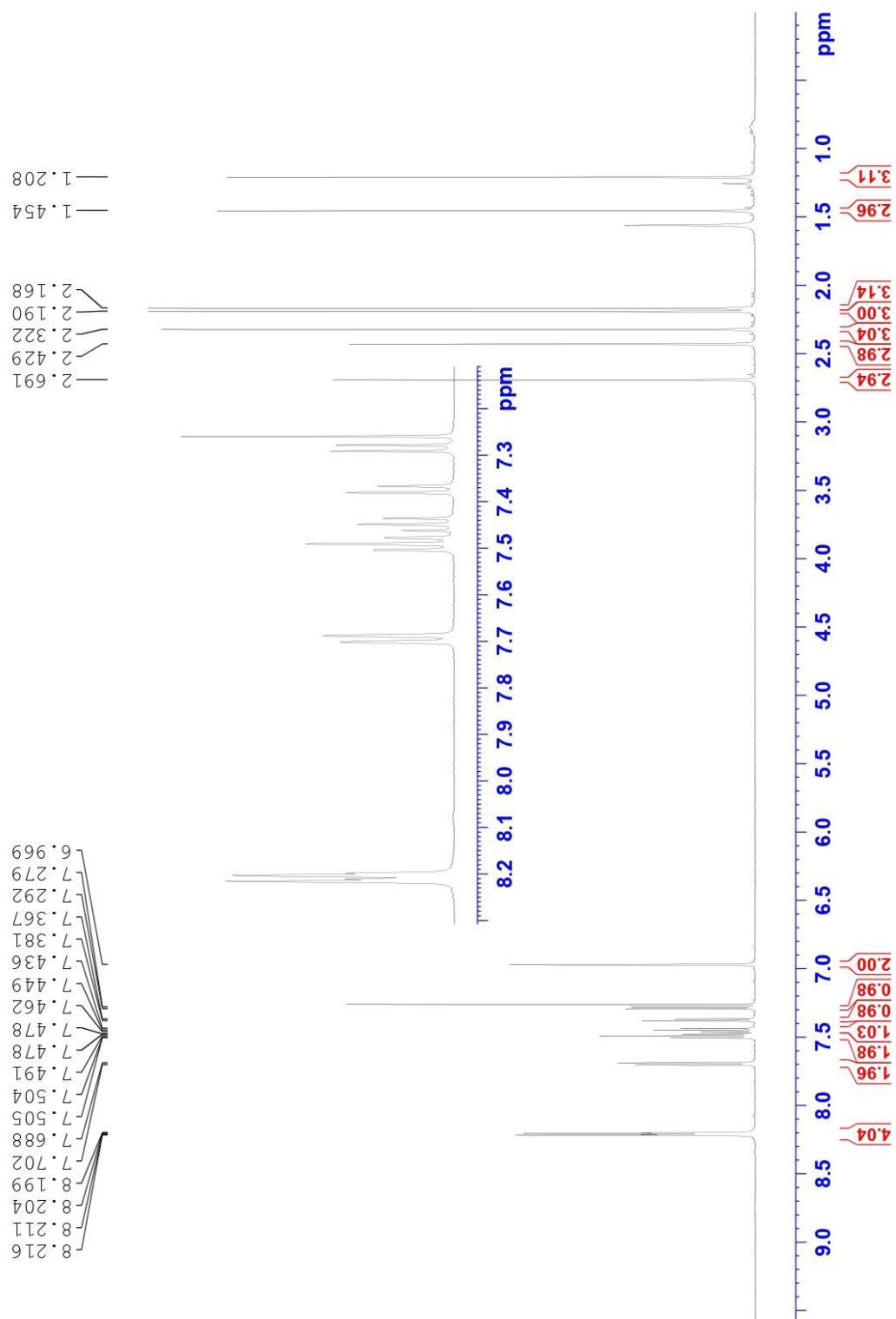
Figure B42 ^{1}H-NMR spectrum of MB2PI in CDCl$_3$ at 600 MHz
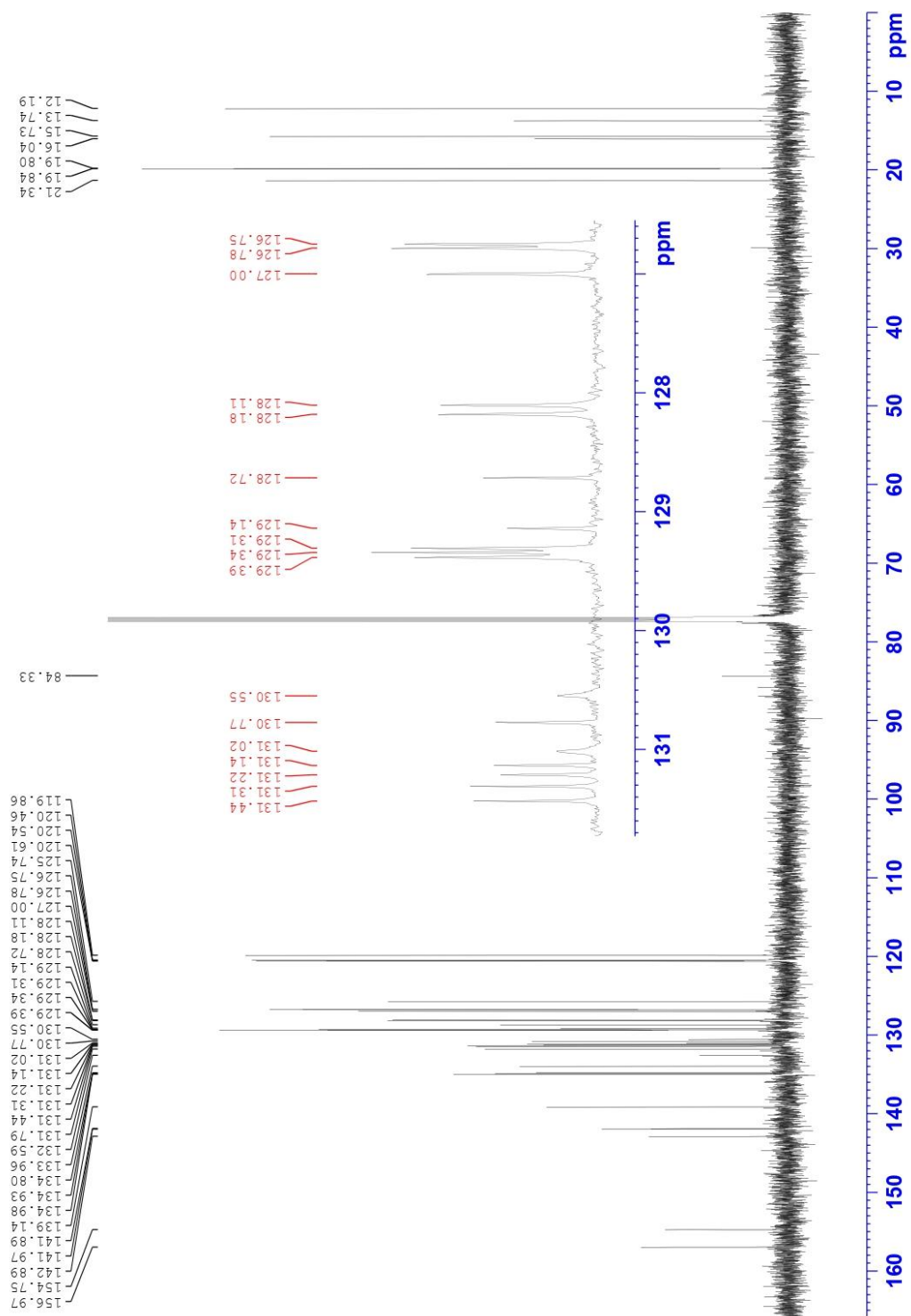
Figure B43 ^{13}C-NMR spectrum of MB2PI in CDCl$_3$ at 150 MHz.

Meas. m/z	#	Ion Formula	m/z	err [mDa]	err [ppm]	rdb	N-Rule	e⁻ Conf	mSigma
742.181927	1	C42H34BF2IN2	742.182952	-1.0	-1.4	26.0	ok	odd	15.6

Meas. m/z	#	Ion Formula	m/z	err [mDa]	err [ppm]	rdb	N-Rule	e⁻ Conf	mSigma
741.174473	1	C42H33BF2IN2	741.176224	-1.8	-2.4	26.5	ok	even	29.9
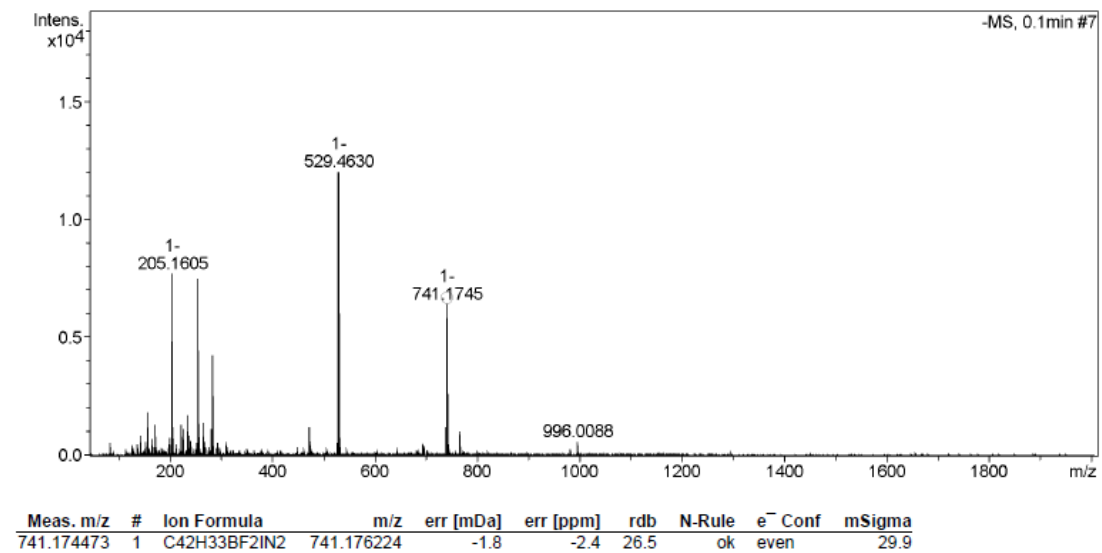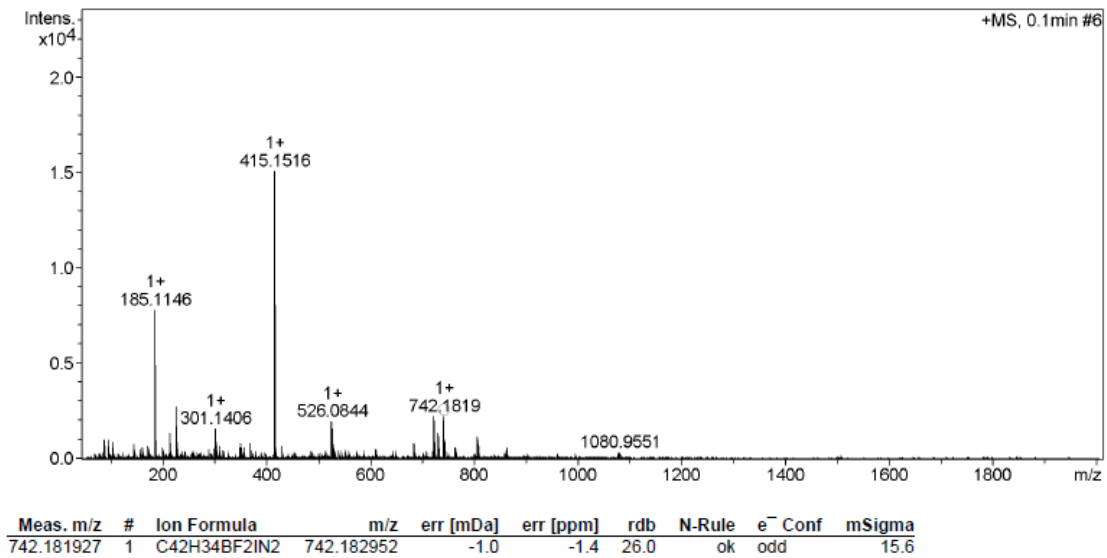
Figure B44 HR-MS (ESI-TOF) positive and negative scans of MB2PI.
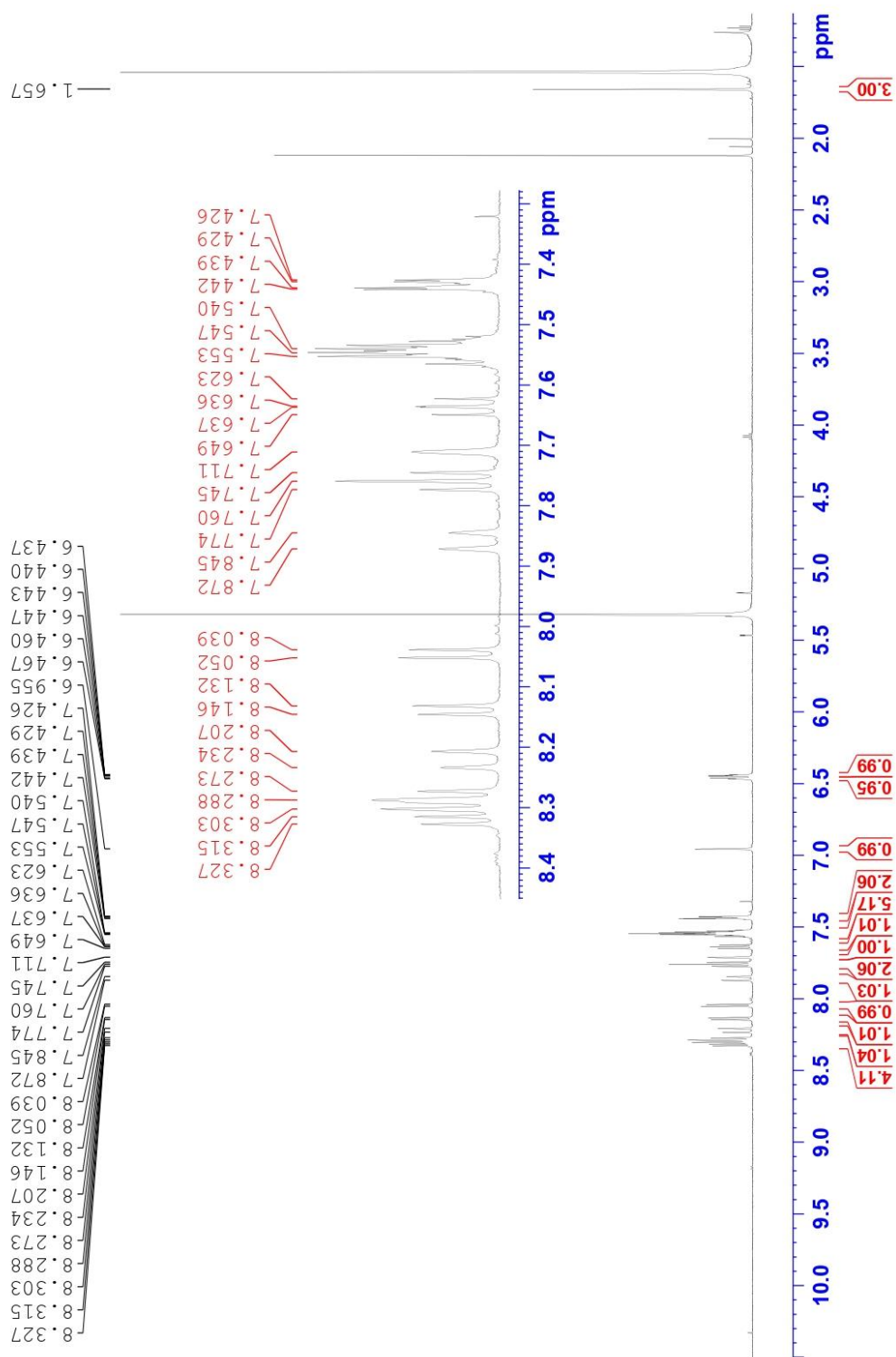
Figure B45 ^{1}H-NMR spectrum of AGB3P in CDCl$_3$ at 600 MHz

Meas. m/z	#	Ion Formula	m/z	err [mDa]	err [ppm]	rdb	N-Rule	e⁻ Conf	mSigma
559.214934	1	C38H26BF2N2	559.215816	-0.9	-1.6	26.5	ok	even	19.6
581.197340	1	C38H25BF2N2Na	581.197760	-0.4	-0.7	26.5	ok	even	21.1
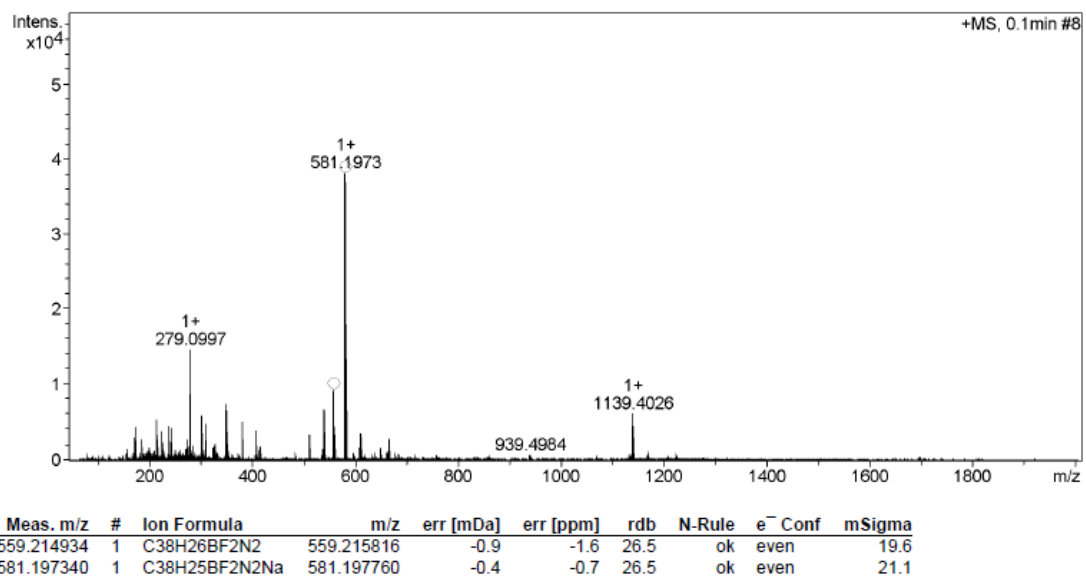
Figure B47 HR-MS (ESI-TOF) positive scan of AGB3P.
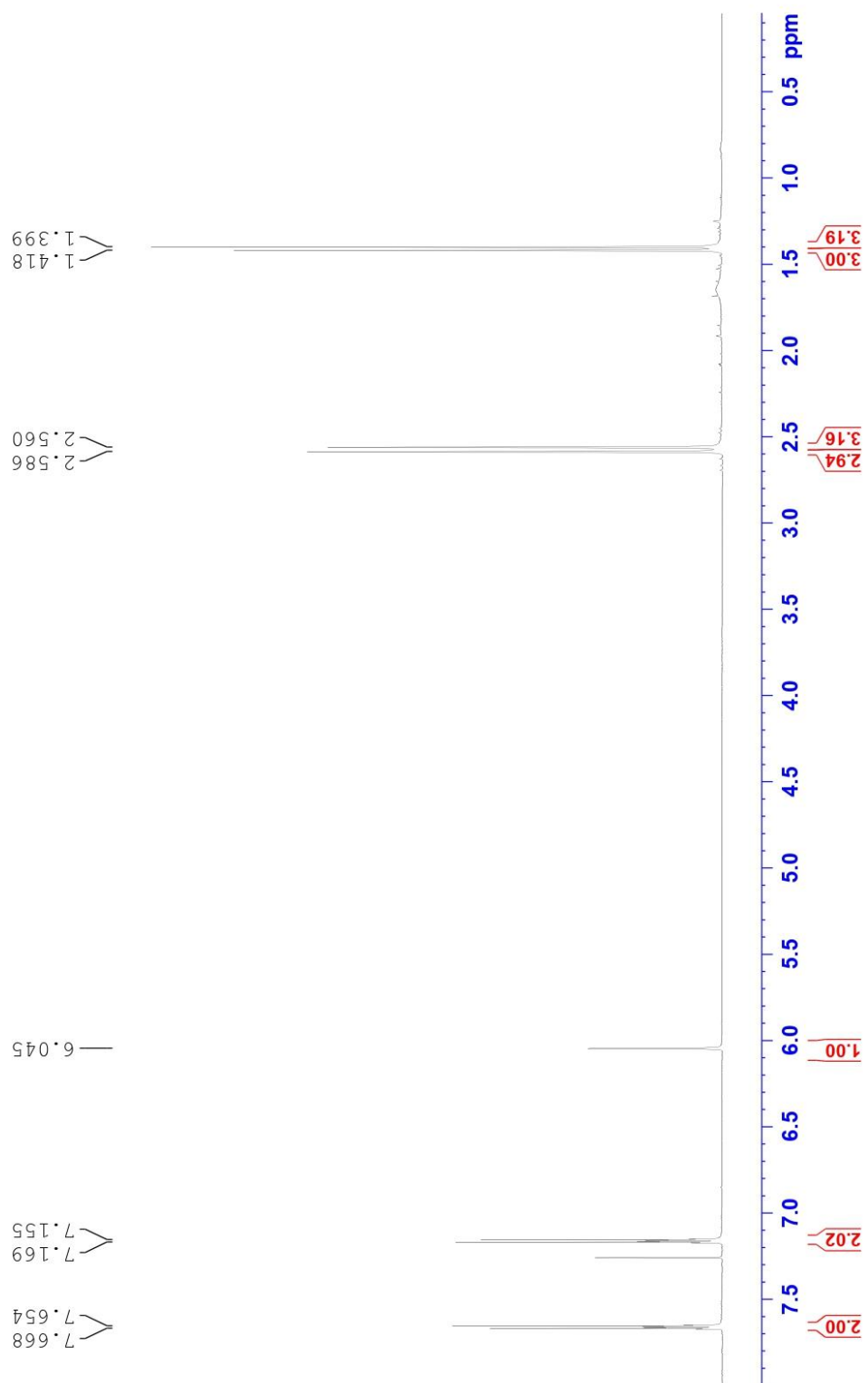
Figure B48 ^{1}H-NMR spectrum of BODIPY 3.7 in CDCl$_3$ at 600 MHz.

13.63
13.85
14.93
14.99

110.99

122.55
123.73
129.69
129.86
131.94
132.74
133.73
138.69
140.25
144.94

152.10

158.52

ppm
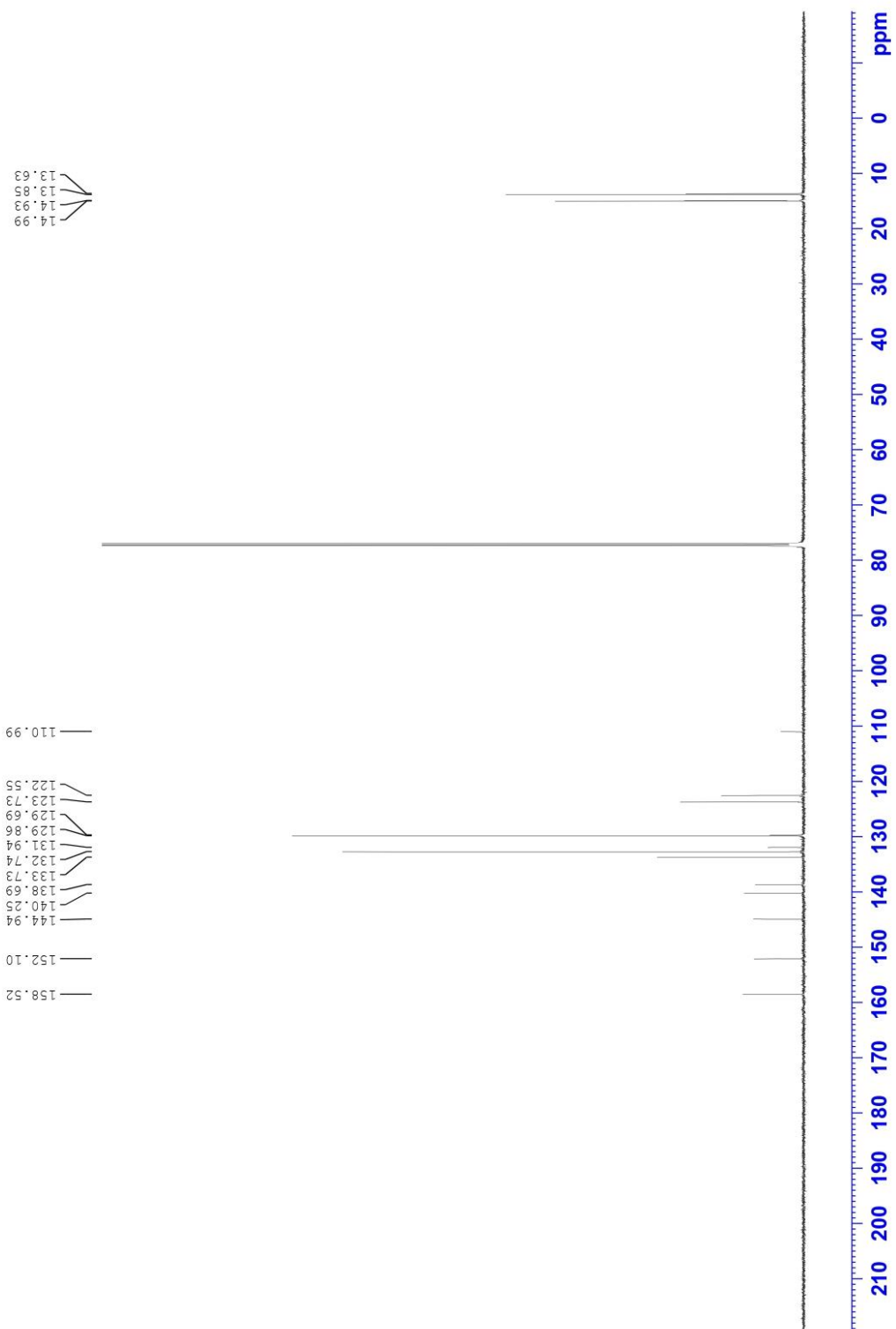
Figure B49 ^{13}C-NMR spectrum of BODIPY 3.7 in CDCl$_3$ at 150 MHz.

Meas. m/z	#	Ion Formula	m/z	err [ppm]	mSigma	# mSigma	Score	rdb	e⁻ Conf	N-Rule
478.9733	1	C19H16BBr2F2N2	478.9747	3.5	24.2	1	100.00	11.5	even	ok

Meas. m/z	#	Ion Formula	m/z	err [ppm]	mSigma	# mSigma	Score	rdb	e⁻ Conf	N-Rule
502.9637	1	C19H17BBr2F2N2Na	502.9712	15.6	17.8	1	100.00	10.5	even	ok
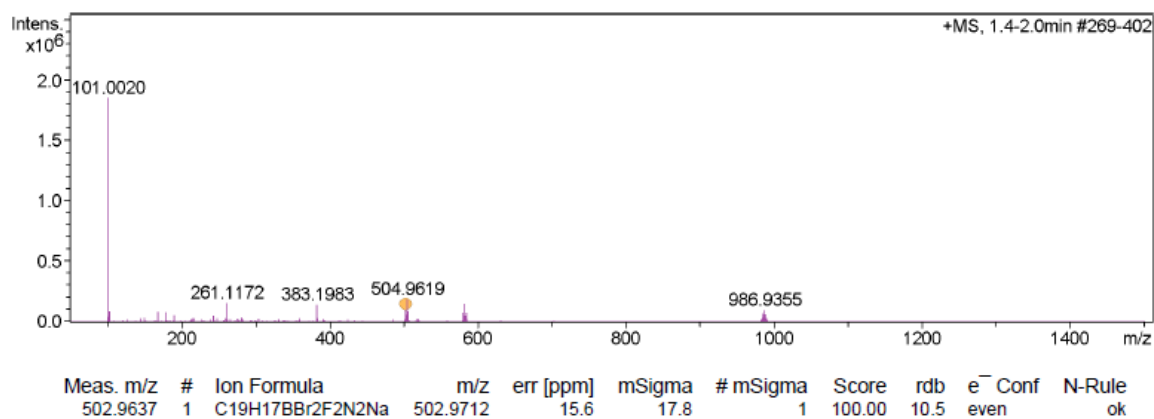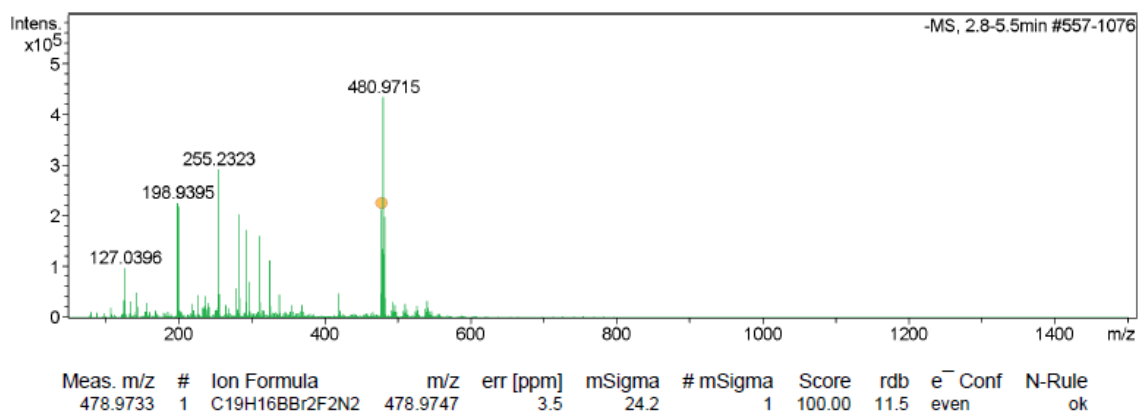
Figure B50 HR-MS (ESI-TOF) positive and negative scan of 3.7.
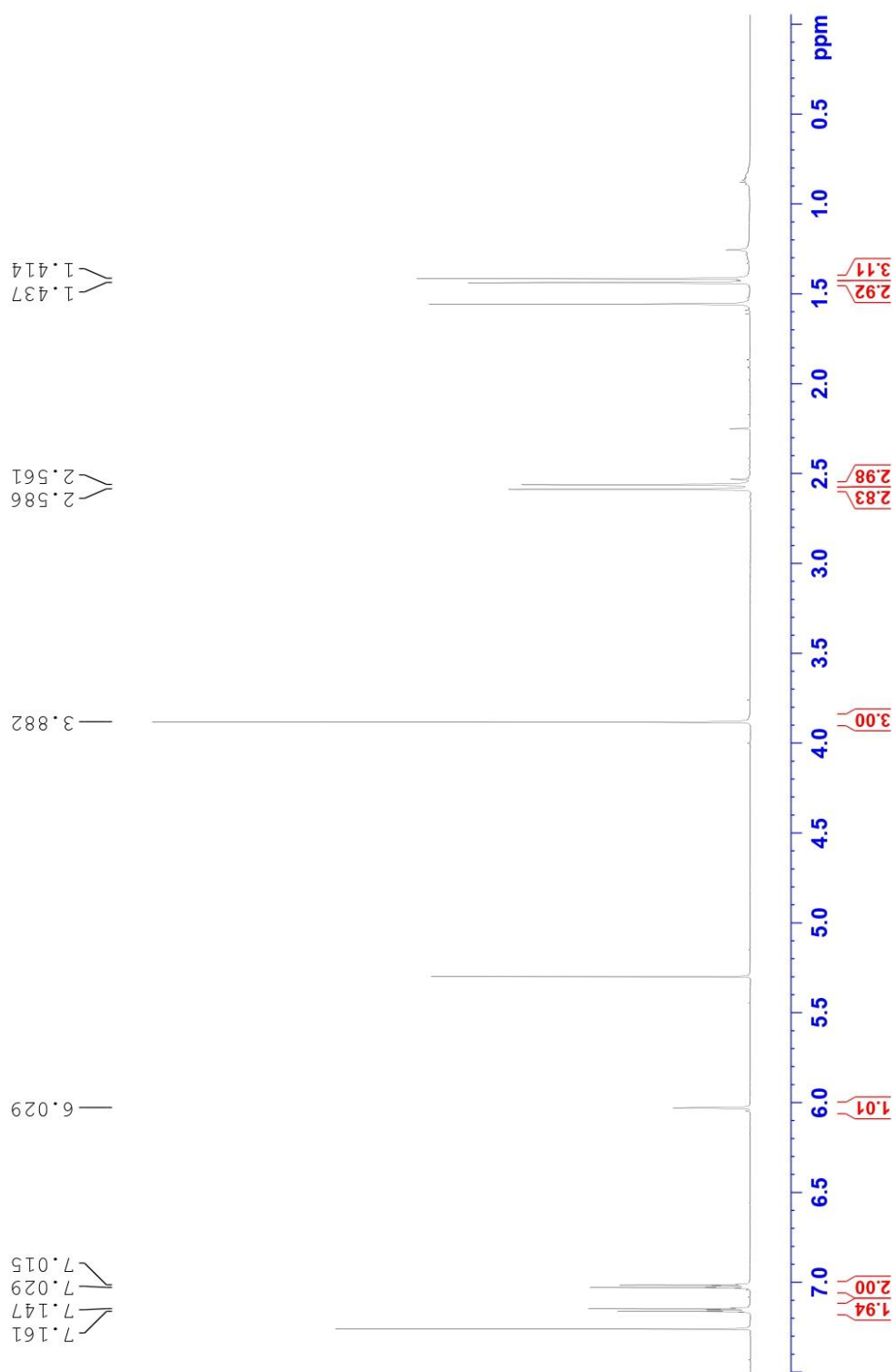
Figure B51 ^{1}H-NMR spectrum of BODIPY 3.6 in CDCl$_3$ at 600 MHz.
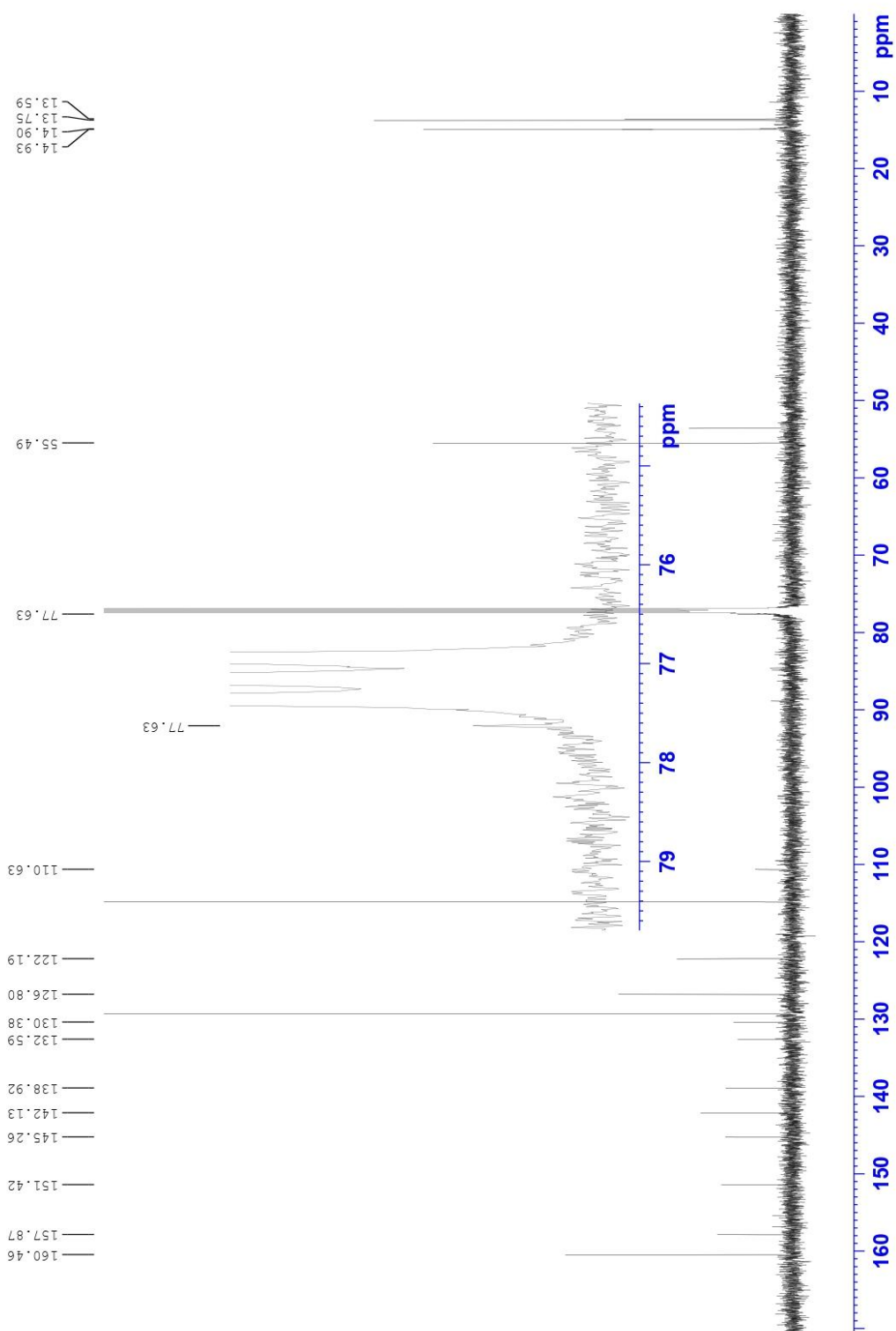
Figure B52 ^{13}C-NMR spectrum of BODIPY 3.6 in CDCl$_3$ at 150 MHz.

Meas. m/z	#	Ion Formula	m/z	err [ppm]	mSigma	# mSigma	Score	rdb	e⁻ Conf	N-Rule
433.0913	1	C20H21BBrF2N2O	433.0893	-3.8	19.5	1	100.00	10.5	even	ok
455.0744	1	C20H20BBrF2N2NaO	455.0712	-6.2	24.3	1	100.00	10.5	even	ok
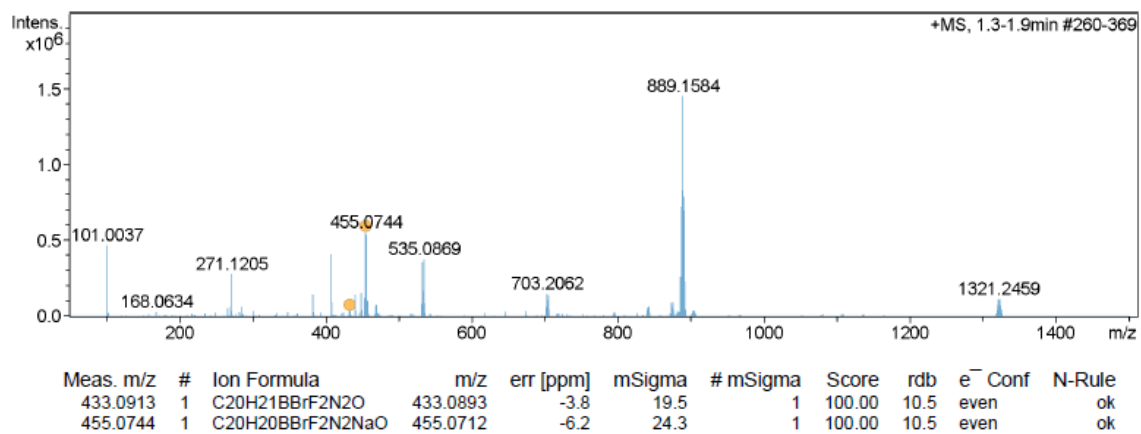
Figure B53 HR-MS (ESI-TOF) positive scan of 3.6.

B.4 Spectroscopy
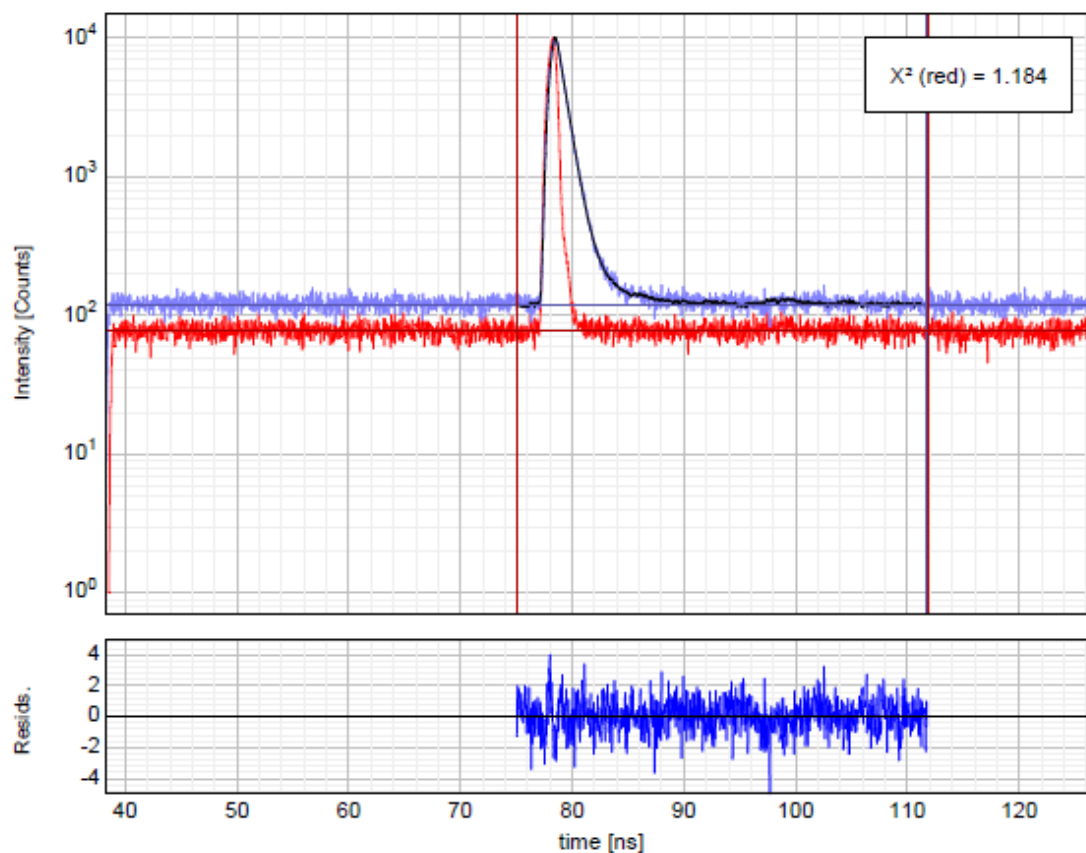
$$I(t) = \int_{-\infty}^{t} IRF(t') \sum_{i=1}^{n} A_i\, e^{-\frac{t-t'}{\tau_i}}\, dt'$$

Parameter	Value	Conf. Lower	Conf. Upper	Conf. Estimation
A_1 [Cnts]	315.2	-48.8	+48.8	Fitting
τ_1 [ns]	3.203	-0.336	+0.336	Fitting
A_2 [Cnts]	28759	-298	+298	Fitting
τ_2 [ns]	0.78758	-0.00629	+0.00629	Fitting
Bkgr. Dec [Cnts]	120.39	-2.08	+2.08	Fitting
Bkgr. IRF [Cnts]	77.6	---	---	<none>
Shift IRF [ns]	0.31312	-0.00513	+0.00513	Fitting
A Scat [Cnts]	112480	-4560	+4560	Fitting

Figure B54 Example of a lifetime decay of 2-DMB2P in toluene.
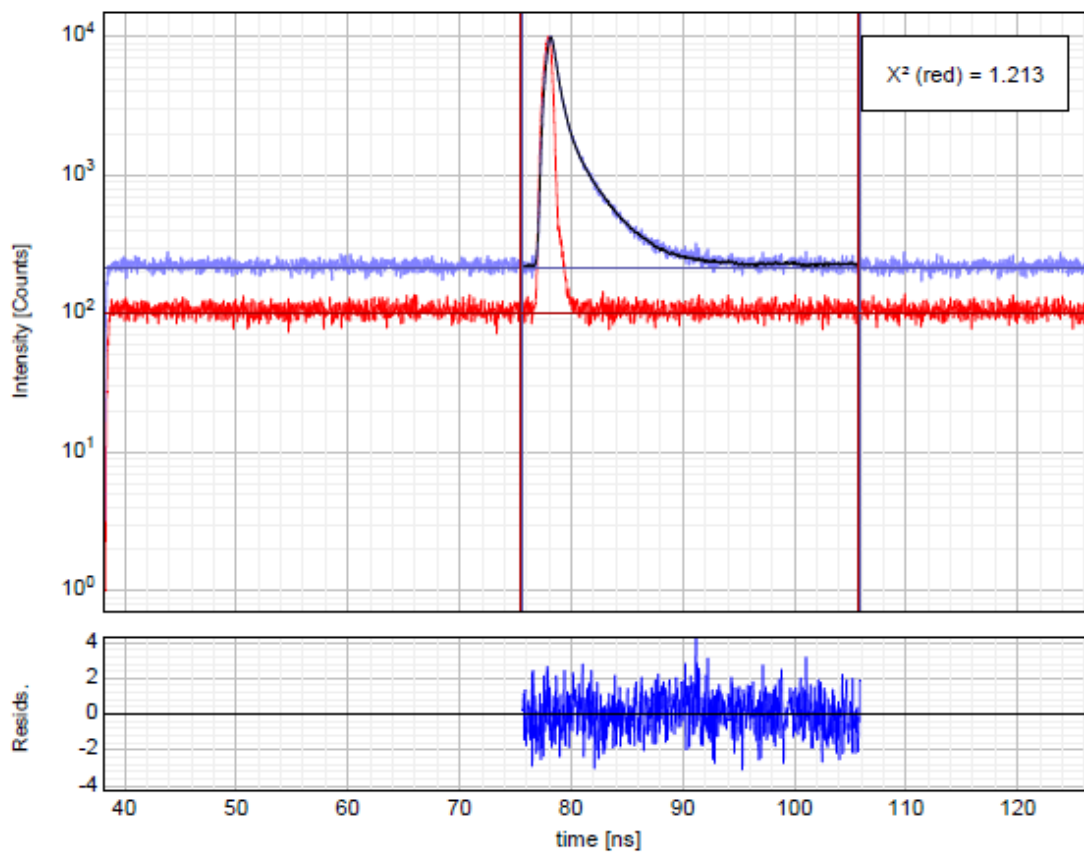
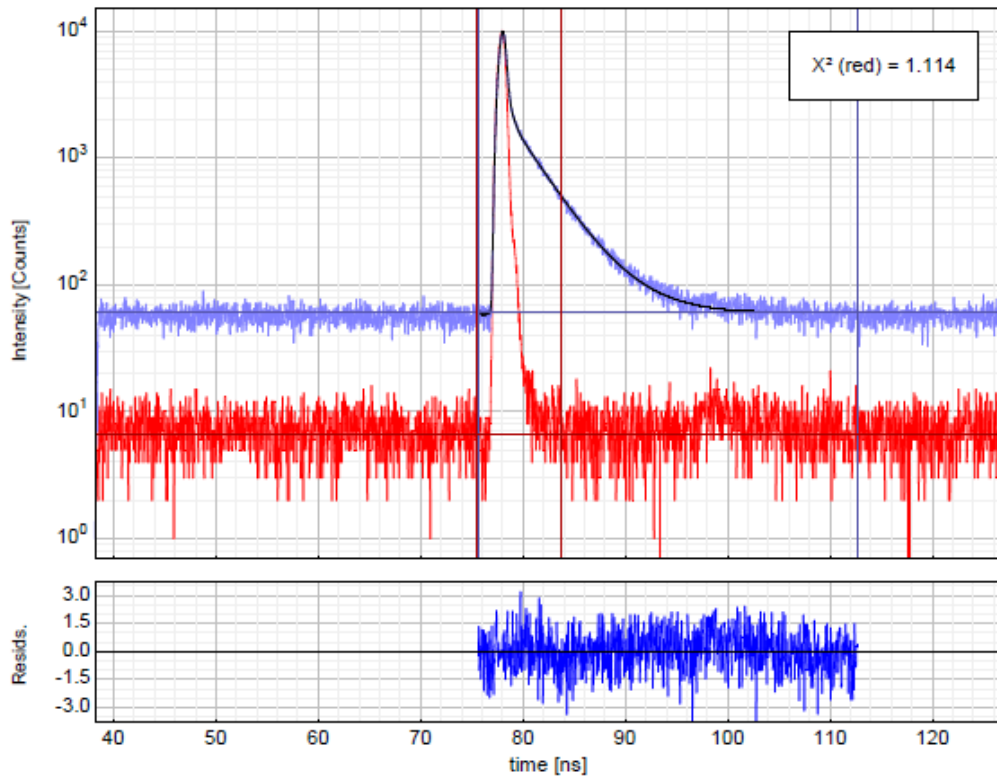$$I(t) = \int\limits_{-\infty}^{t} IRF(t') \sum_{i=1}^{n} A_i\, e^{-\frac{t-t'}{\tau_i}}\, dt'$$

Parameter	Value	Conf. Lower	Conf. Upper	Conf. Estimation
A_1 [Cnts]	6344.7	-92.7	+92.7	Fitting
τ_1 [ns]	2.6628	-0.0298	+0.0298	Fitting
A_2 [Cnts]	30662	-472	+472	Fitting
τ_2 [ns]	0.51514	-0.00737	+0.00737	Fitting
Bkgr. Dec [Cnts]	213.07	-3.06	+3.06	Fitting
Bkgr. IRF [Cnts]	100.0	---	---	<none>
Shift IRF [ns]	0.14047	-0.00491	+0.00491	Fitting
A Scat [Cnts]	116810	-4830	+4830	Fitting

Figure B55 Example of a lifetime decay of 8-DMB2P in toluene.
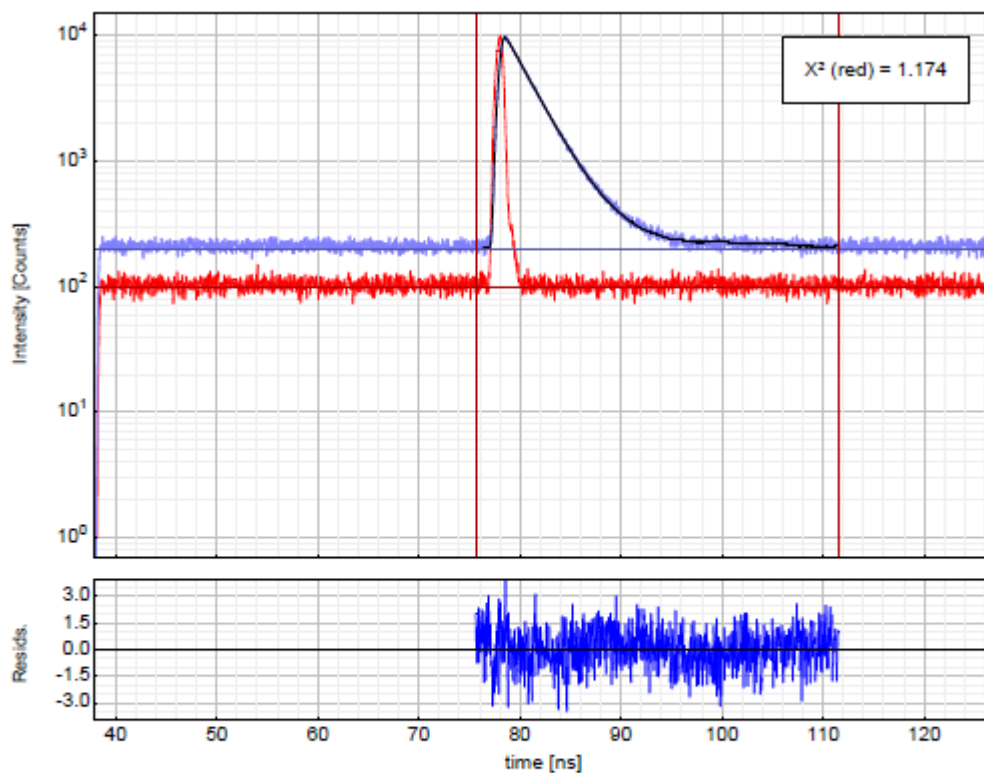
$$I(t) = \int_{-\infty}^{t} IRF(t') \sum_{i=1}^{n} A_i \, e^{-\frac{t-t'}{\tau_i}} \, dt'$$

Parameter	Value	Conf. Lower	Conf. Upper	Conf. Estimation
A$_1$ [Cnts]	26038	-149	+149	Fitting
τ_1 [ns]	2.8091	-0.0132	+0.0132	Fitting
Bkgr. Dec [Cnts]	198.20	-3.08	+3.08	Fitting
Bkgr. IRF [Cnts]	100.0	---	---	<none>
Shift IRF [ns]	0.07838	-0.00628	+0.00628	Fitting

Average Lifetime:

$\tau_{Av.1}$=2.8091 ns (intensity weighted)

$\tau_{Av.2}$=2.8091 ns (amplitude weighted)

Figure B56 Example of a lifetime decay of MB2P in toluene.
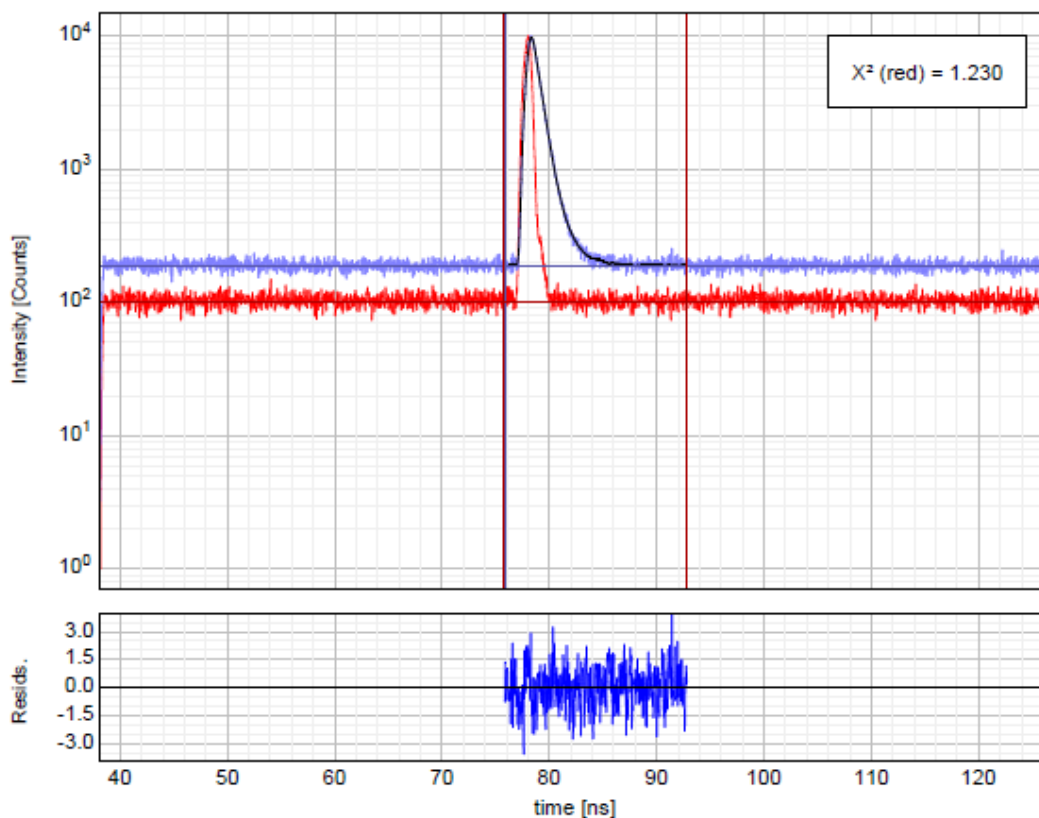
$$I(t) = \int\limits_{-\infty}^{t} IRF(t') \sum_{i=1}^{n} A_i\, e^{-\frac{t-t'}{\tau_i}}\, dt'$$

Parameter	Value	Conf. Lower	Conf. Upper	Conf. Estimation
A_1 [Cnts]	1398.8	-94.3	+94.3	Fitting
τ_1 [ns]	1.7792	-0.0768	+0.0768	Fitting
A_2 [Cnts]	40132	-267	+267	Fitting
τ_2 [ns]	0.71380	-0.00398	+0.00398	Fitting
Bkgr. Dec [Cnts]	185.31	-2.84	+2.84	Fitting
Bkgr. IRF [Cnts]	100.0	---	---	<none>
Shift IRF [ns]	0.07365	-0.00379	+0.00379	Fitting

Average Lifetime:

$\tau_{Av.1}$=0.7990 ns (intensity weighted)

$\tau_{Av.2}$=0.7497 ns (amplitude weighted)

Figure B57 Example of a lifetime decay of MB2PI un toluene.

$$I(t) = \int\limits_{-\infty}^{t} IRF(t') \sum_{i=1}^{n} A_i\, e^{-\frac{t-t'}{\tau_i}}\, dt'$$

Parameter	Value	Conf. Lower	Conf. Upper	Conf. Estimation
A_1 [Cnts]	9165	-472	+472	Fitting
τ_1 [ns]	0.2505	-0.0112	+0.0112	Fitting
A_2 [Cnts]	2590.4	-33.9	+33.9	Fitting
τ_2 [ns]	3.4160	-0.0341	+0.0341	Fitting
Bkgr. Dec [Cnts]	60.16	-1.64	+1.64	Fitting
Bkgr. IRF [Cnts]	6.6	---	---	<none>
Shift IRF [ns]	0.06218	-0.00438	+0.00438	Fitting
A Scat [Cnts]	167590	-2800	+2800	Fitting

Average Lifetime:

$\tau_{Av.1}$=2.7639 ns (intensity weighted)

$\tau_{Av.2}$=0.9480 ns (amplitude weighted)

Figure B58 Example of a lifetime decay of AGB3P un toluene.

Appendix C

Supporting information for Chapter 4

Contents

C.1 Lifetime decays of the viscosity experiment in toluene/castor oil
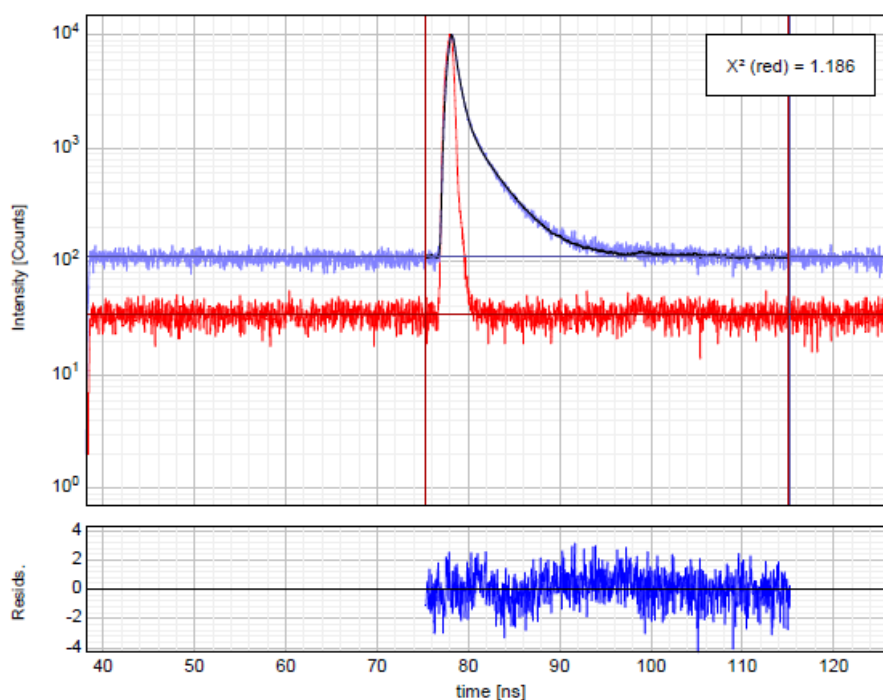
$$I(t) = \int_{-\infty}^{t} IRF(t') \sum_{i=1}^{n} A_i \, e^{-\frac{t-t'}{\tau_i}} \, dt'$$

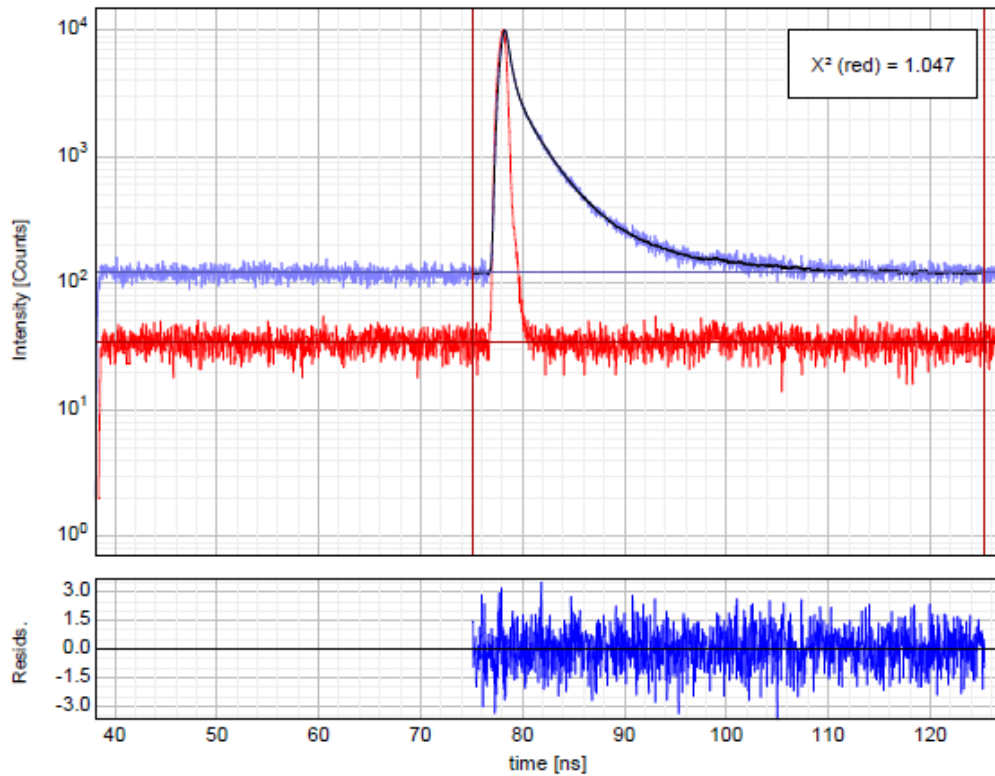| Parameter	Value	Conf. Lower	Conf. Upper	Conf. Estimation
A_1 [Cnts]	3149.3	-52.5	+52.5	Fitting
τ_1 [ns]	3.2170	-0.0392	+0.0392	Fitting
A_2 [Cnts]	17753	-316	+316	Fitting
τ_2 [ns]	0.56637	-0.00899	+0.00899	Fitting
Bkgr. Dec [Cnts]	110.19	-2.15	+2.15	Fitting
Bkgr. IRF [Cnts]	34.0	---	---	<none>
Shift IRF [ns]	0.13385	-0.00552	+0.00552	Fitting
A Scat [Cnts]	115220	-3670	+3670	Fitting

Figure C1 Example of lifetime decay of 8-DMB2P in toluene castor oil (90:10).
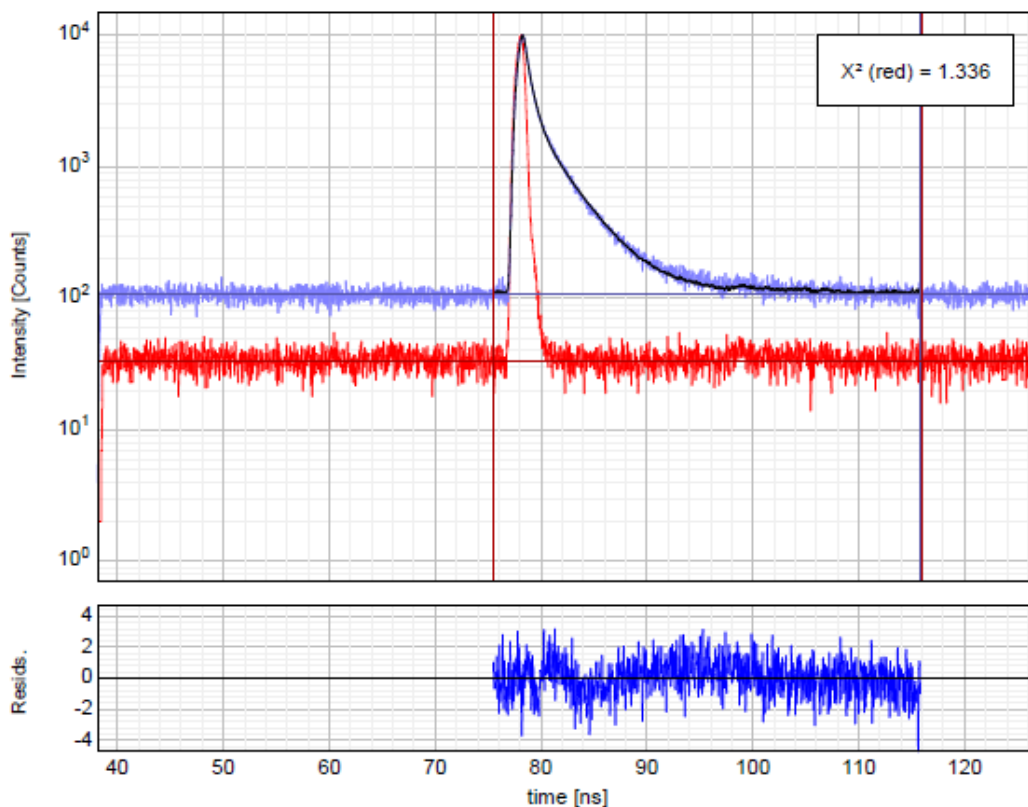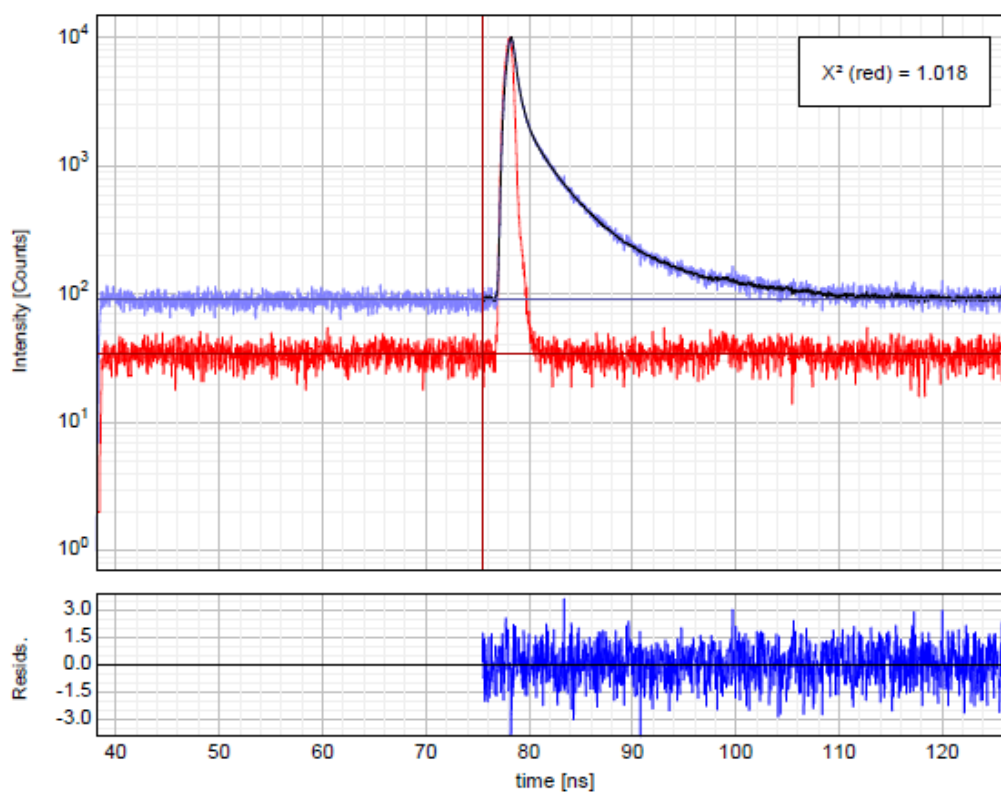
$$I(t) = \int_{-\infty}^{t} IRF(t') \sum_{i=1}^{n} A_i \, e^{-\frac{t-t'}{\tau_i}} \, dt'$$

Parameter	Value	Conf. Lower	Conf. Upper	Conf. Estimation
A_1 [Cnts]	3846.1	-58.6	+58.6	Fitting
τ_1 [ns]	3.3027	-0.0371	+0.0371	Fitting
A_2 [Cnts]	14673	-326	+326	Fitting
τ_2 [ns]	0.5942	-0.0119	+0.0119	Fitting
Bkgr. Dec [Cnts]	109.54	-2.32	+2.32	Fitting
Bkgr. IRF [Cnts]	33.0	---	---	<none>
Shift IRF [ns]	0.20878	-0.00579	+0.00579	Fitting
A Scat [Cnts]	135840	-3980	+3980	Fitting

Figure C2 Example of lifetime decay of 8-DMB2P in toluene castor oil (80:20).
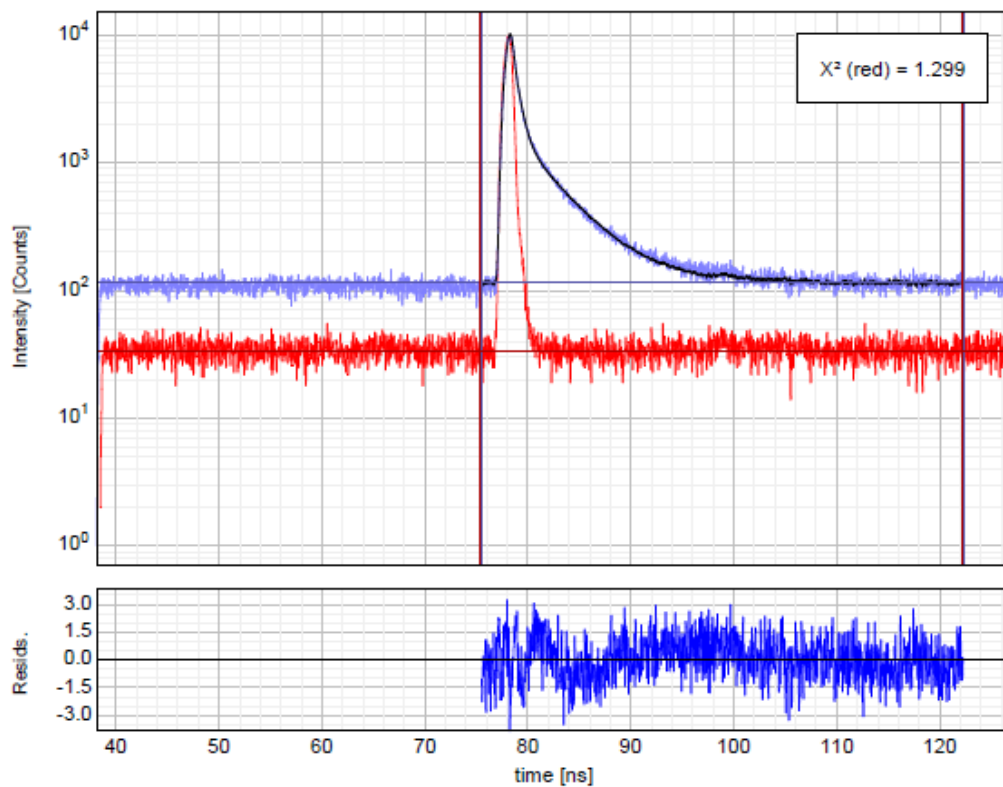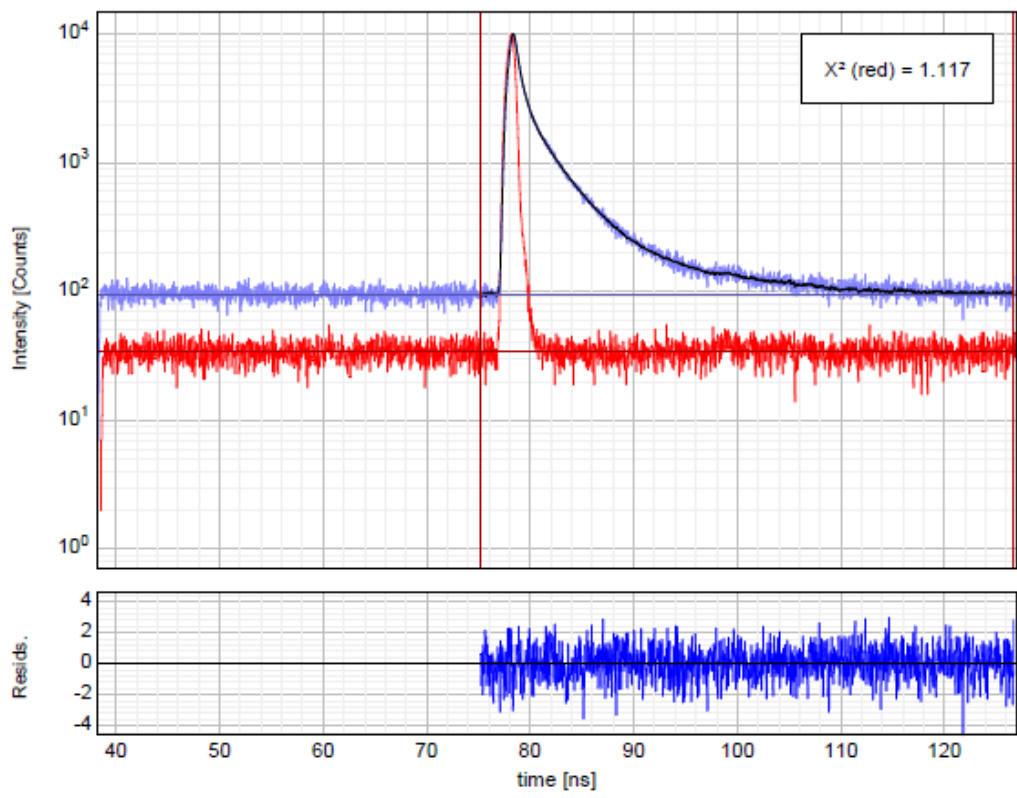
$$I(t) = \int\limits_{-\infty}^{t} IRF(t') \sum_{i=1}^{n} A_i \, e^{-\frac{t-t'}{\tau_i}} \, dt'$$

Parameter	Value	Conf. Lower	Conf. Upper	Conf. Estimation
A_1 [Cnts]	2404.4	-45.1	+45.1	Fitting
τ_1 [ns]	4.1320	-0.0602	+0.0602	Fitting
A_2 [Cnts]	15280	-355	+355	Fitting
τ_2 [ns]	0.5551	-0.0111	+0.0111	Fitting
Bkgr. Dec [Cnts]	114.44	-2.28	+2.28	Fitting
Bkgr. IRF [Cnts]	34.0	---	---	<none>
Shift IRF [ns]	0.26924	-0.00590	+0.00590	Fitting
A Scat [Cnts]	163310	-4320	+4320	Fitting

Figure C3 Example of lifetime decay of 8-DMB2P in toluene castor oil (70:30).

C3
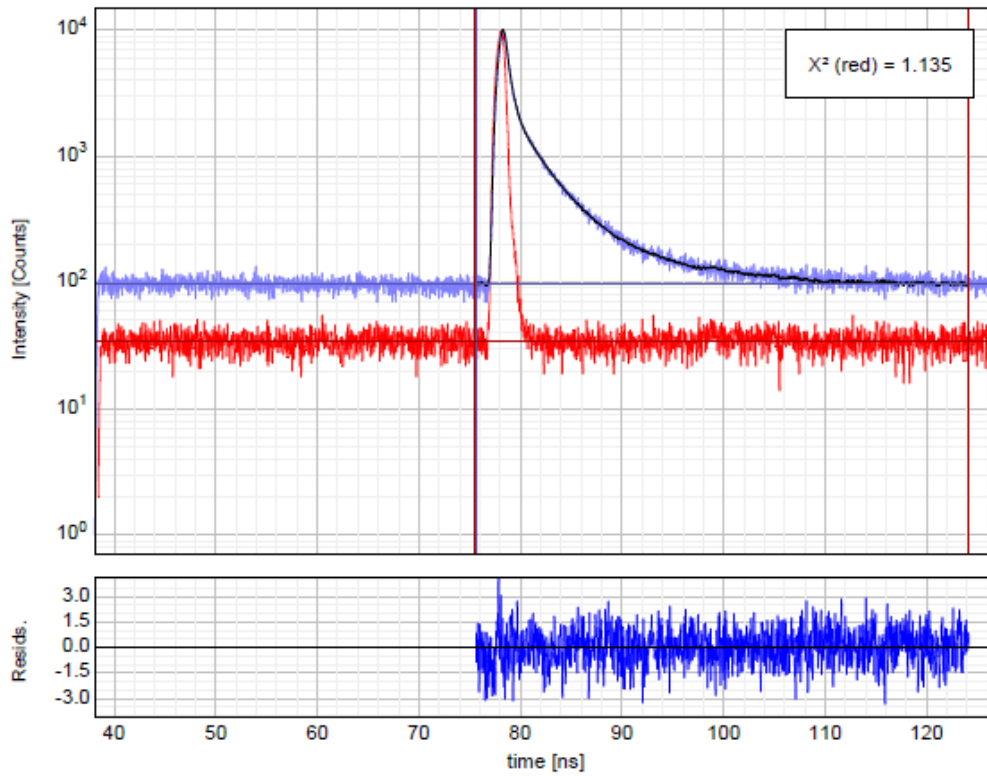
$$I(t) = \int\limits_{-\infty}^{t} IRF(t') \sum_{i=1}^{n} A_i\, e^{-\frac{t-t'}{\tau_i}}\, dt'$$

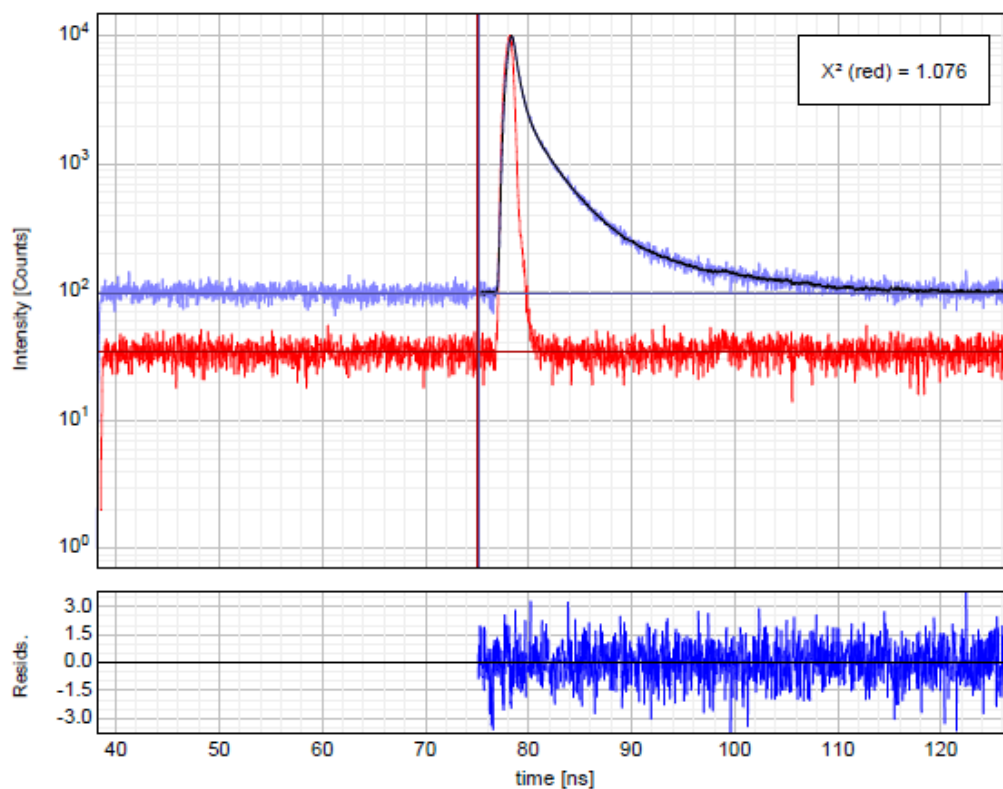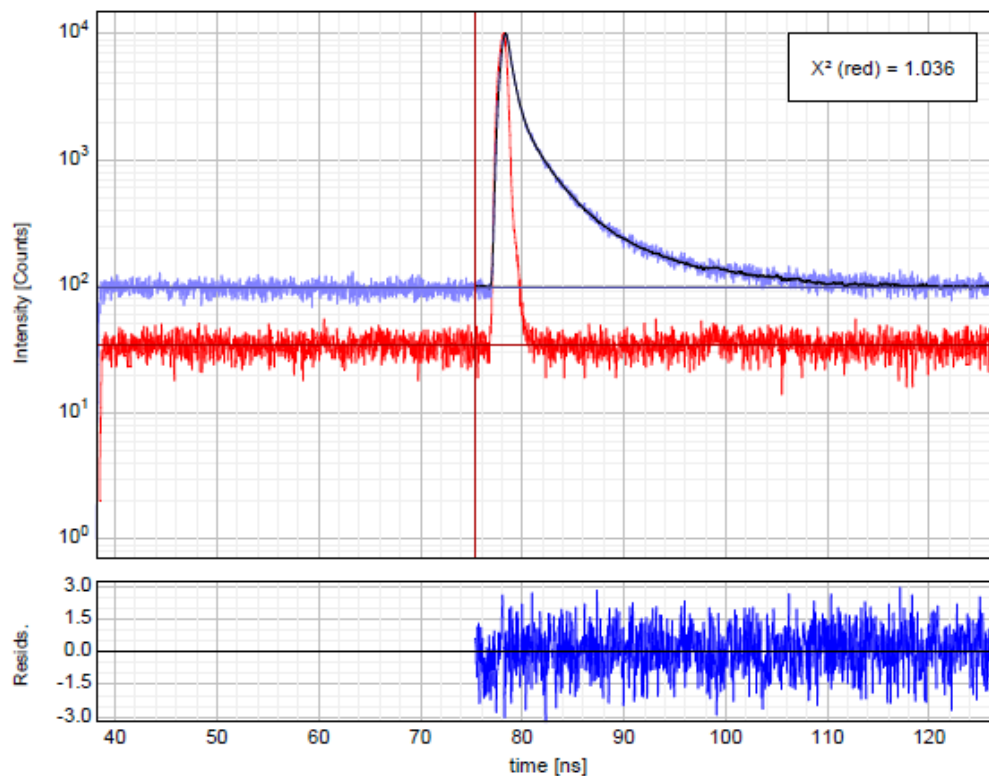| Parameter	Value	Conf. Lower	Conf. Upper	Conf. Estimation
A_1 [Cnts]	731.7	-26.0	+26.0	Fitting
τ_1 [ns]	6.869	-0.184	+0.184	Fitting
A_2 [Cnts]	3337.7	-73.6	+73.6	Fitting
τ_2 [ns]	2.6038	-0.0451	+0.0451	Fitting
A_3 [Cnts]	22419	-478	+478	Fitting
τ_3 [ns]	0.39014	-0.00771	+0.00771	Fitting
Bkgr. Dec [Cnts]	97.25	-2.04	+2.04	Fitting
Bkgr. IRF [Cnts]	34.0	---	---	<none>
Shift IRF [ns]	0.24159	-0.00578	+0.00578	Fitting
A Scat [Cnts]	101270	-3970	+3970	Fitting

Figure C4 Example of lifetime decay of 8-DMB2P in toluene castor oil (60:40).

C4

$$I(t) = \int_{-\infty}^{t} IRF(t') \sum_{i=1}^{n} A_i\, e^{-\frac{t-t'}{\tau_i}}\, dt'$$

Parameter	Value	Conf. Lower	Conf. Upper	Conf. Estimation
A_1 [Cnts]	1046.3	-31.8	+31.8	Fitting
τ_1 [ns]	6.193	-0.140	+0.140	Fitting
A_2 [Cnts]	5059.1	-87.7	+87.7	Fitting
τ_2 [ns]	2.3957	-0.0333	+0.0333	Fitting
A_3 [Cnts]	17916	-464	+464	Fitting
τ_3 [ns]	0.39976	-0.00998	+0.00998	Fitting
Bkgr. Dec [Cnts]	121.37	-2.14	+2.14	Fitting
Bkgr. IRF [Cnts]	34.0	---	---	<none>
Shift IRF [ns]	0.20659	-0.00591	+0.00591	Fitting
A Scat [Cnts]	100900	-3860	+3860	Fitting

Figure C5 Example of lifetime decay of 8-DMB2P in toluene castor oil (50:50).

C5

$$I(t) = \int\limits_{-\infty}^{t} IRF(t') \sum_{i=1}^{n} A_i \, e^{-\frac{t-t'}{\tau_i}} \, dt'$$

Parameter	Value	Conf. Lower	Conf. Upper	Conf. Estimation
A_1 [Cnts]	973.0	-26.9	+26.9	Fitting
τ_1 [ns]	6.686	-0.138	+0.138	Fitting
A_2 [Cnts]	3316.0	-75.9	+75.9	Fitting
τ_2 [ns]	2.5143	-0.0459	+0.0459	Fitting
A_3 [Cnts]	16713	-417	+417	Fitting
τ_3 [ns]	0.4397	-0.0100	+0.0100	Fitting
Bkgr. Dec [Cnts]	92.32	-1.89	+1.89	Fitting
Bkgr. IRF [Cnts]	34.0	---	---	<none>
Shift IRF [ns]	0.22840	-0.00560	+0.00560	Fitting
A Scat [Cnts]	137100	-3930	+3930	Fitting

Figure C6 Example of lifetime decay of 8-DMB2P in toluene castor oil (40:60).

$$I(t) = \int_{-\infty}^{t} IRF(t') \sum_{i=1}^{n} A_i \, e^{-\frac{t-t'}{\tau_i}} \, dt'$$

Parameter	Value	Conf. Lower	Conf. Upper	Conf. Estimation
A_1 [Cnts]	550.3	-23.2	+23.2	Fitting
τ_1 [ns]	8.347	-0.259	+0.259	Fitting
A_2 [Cnts]	4439.3	-75.5	+75.5	Fitting
τ_2 [ns]	2.8415	-0.0376	+0.0376	Fitting
A_3 [Cnts]	14915	-396	+396	Fitting
τ_3 [ns]	0.4993	-0.0124	+0.0124	Fitting
Bkgr. Dec [Cnts]	95.59	-2.02	+2.02	Fitting
Bkgr. IRF [Cnts]	34.0	---	---	<none>
Shift IRF [ns]	0.31323	-0.00597	+0.00597	Fitting
A Scat [Cnts]	128010	-4090	+4090	Fitting

Figure C7 Example of lifetime decay of 8-DMB2P in toluene castor oil (30:70).

$$I(t) = \int\limits_{-\infty}^{t} IRF(t') \sum_{i=1}^{n} A_i \, e^{-\frac{t-t'}{\tau_i}} \, dt'$$

Parameter	Value	Conf. Lower	Conf. Upper	Conf. Estimation
A_1 [Cnts]	586.3	-21.9	+21.9	Fitting
τ_1 [ns]	8.541	-0.245	+0.245	Fitting
A_2 [Cnts]	4096.0	-75.1	+75.1	Fitting
τ_2 [ns]	2.7532	-0.0395	+0.0395	Fitting
A_3 [Cnts]	18604	-405	+405	Fitting
τ_3 [ns]	0.47946	-0.00979	+0.00979	Fitting
Bkgr. Dec [Cnts]	98.72	-2.02	+2.02	Fitting
Bkgr. IRF [Cnts]	34.0	---	---	<none>
Shift IRF [ns]	0.30425	-0.00609	+0.00609	Fitting
A Scat [Cnts]	100470	-3960	+3960	Fitting

Figure C8 Example of lifetime decay of 8-DMB2P in toluene castor oil (20:80).

$$I(t) = \int_{-\infty}^{t} IRF(t') \sum_{i=1}^{n} A_i \, e^{-\frac{t-t'}{\tau_i}} \, dt'$$

Parameter	Value	Conf. Lower	Conf. Upper	Conf. Estimation
A_1 [Cnts]	830.7	-25.2	+25.2	Fitting
τ_1 [ns]	7.185	-0.166	+0.166	Fitting
A_2 [Cnts]	3754.2	-82.3	+82.3	Fitting
τ_2 [ns]	2.4342	-0.0415	+0.0415	Fitting
A_3 [Cnts]	19739	-374	+374	Fitting
τ_3 [ns]	0.51106	-0.00911	+0.00911	Fitting
Bkgr. Dec [Cnts]	98.17	-1.96	+1.96	Fitting
Bkgr. IRF [Cnts]	34.0	---	---	<none>
Shift IRF [ns]	0.27709	-0.00598	+0.00598	Fitting
A Scat [Cnts]	80630	-3800	+3800	Fitting

Figure C9 Example of lifetime decay of 8-DMB2P in toluene castor oil (10:90).

C.2 Excitation spectrum of crystalline solids
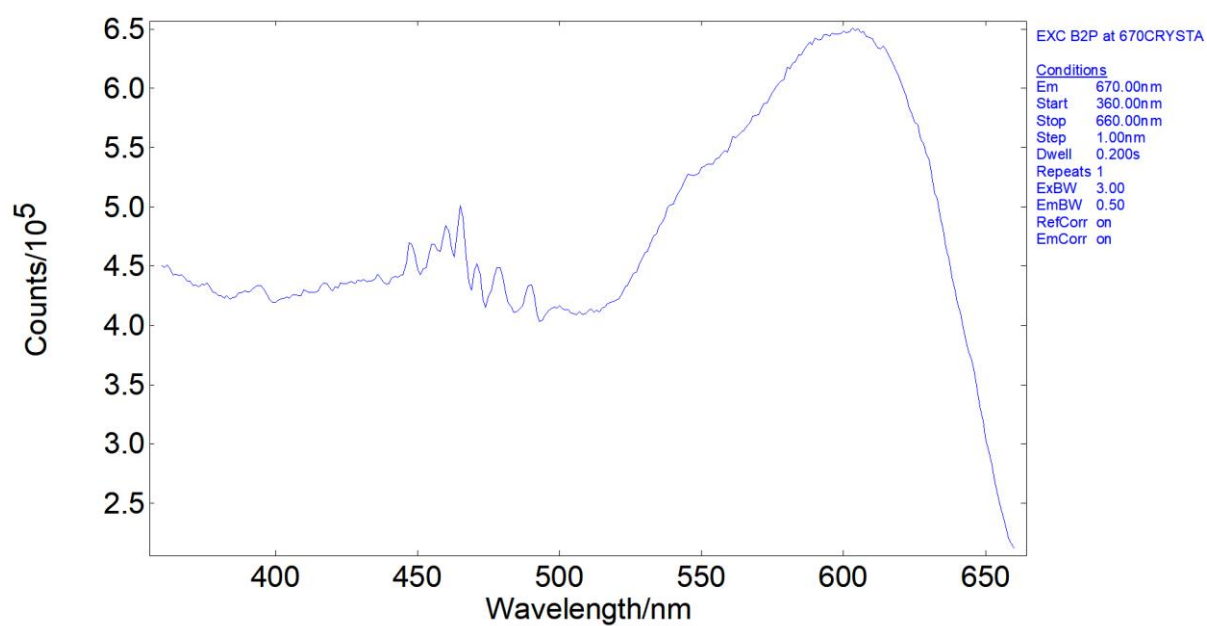
Figure C10 Excitation spectrum of crystalline B2P.

Appendix D

Supporting information of chapter 5

Contents

D.1 NMR and mass spectra of RCBC
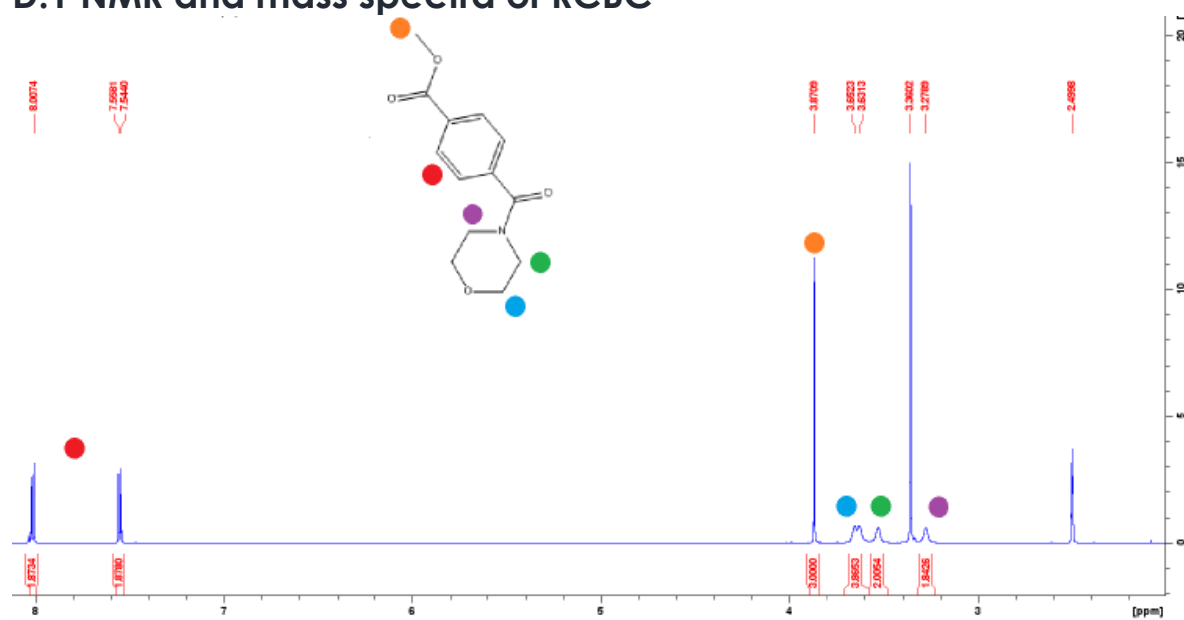
Figure D1 ^{1}H-NMR spectrum of 11 in DMSO-d$_6$ at 600 MHz.
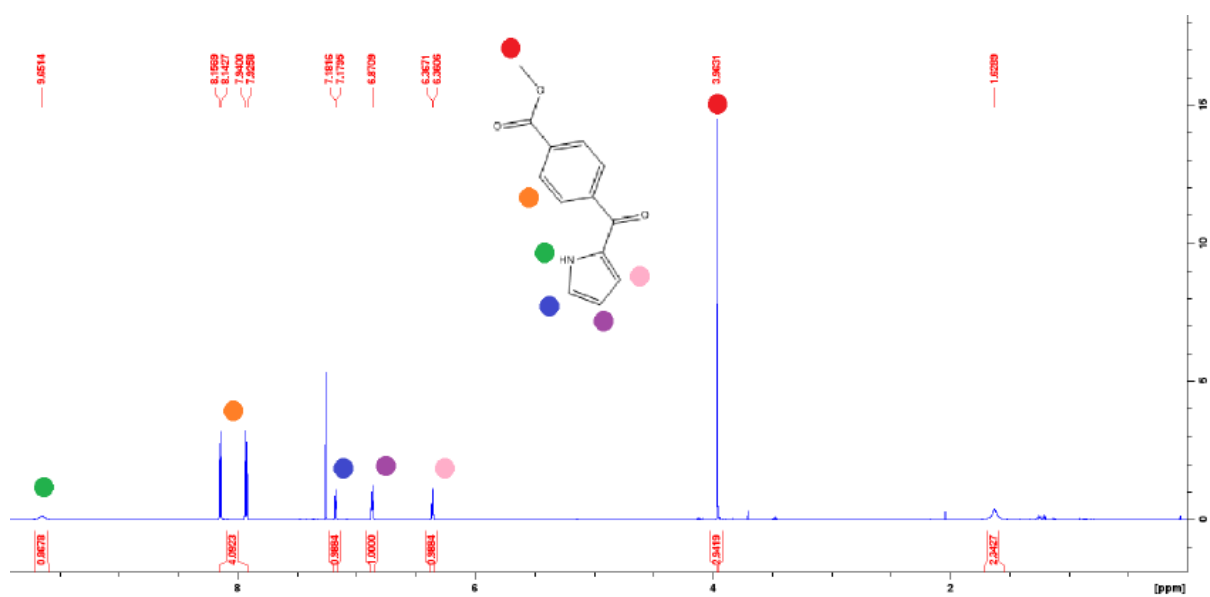
Figure D2 ^{1}H-NMR spectrum of 12 in CDCl$_3$ at 600 MHz.
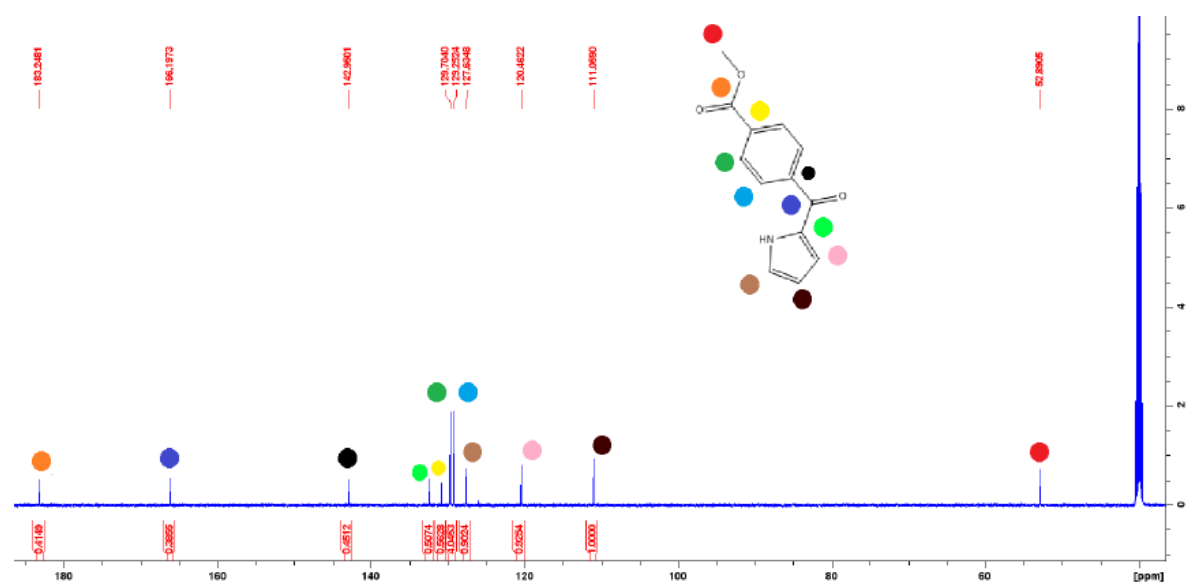
Figure D3 ^{13}C-NMR spectrum of 12 in CDCl$_3$ at 150 MHz.
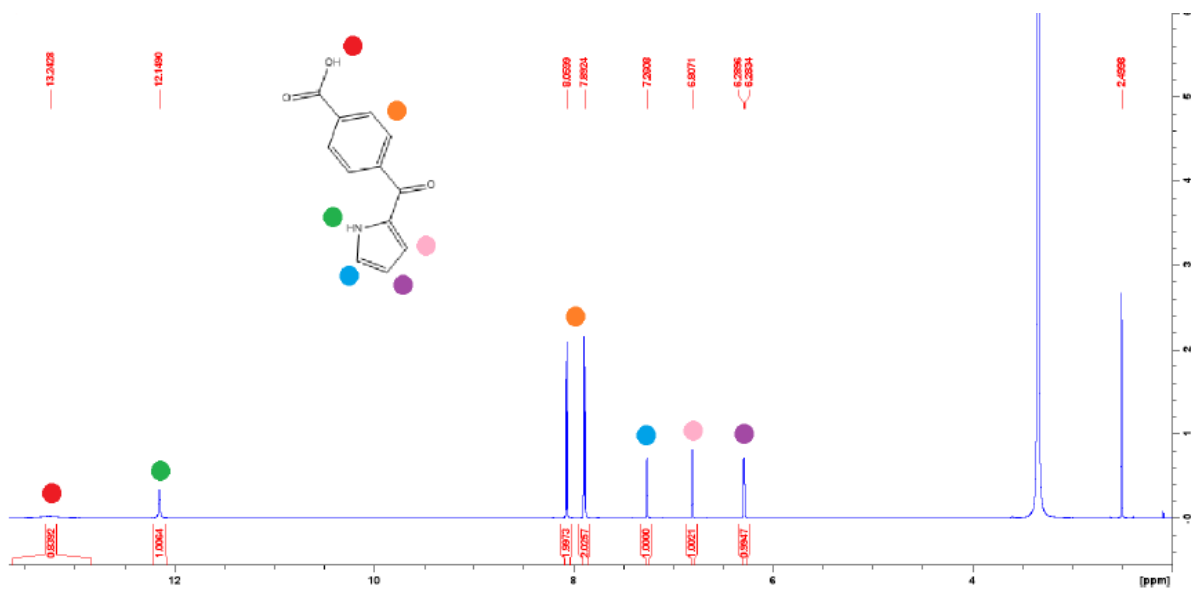
Figure D4 ^{1}H-NMR spectrum of 13 in DMSO-d$_6$ at 600 MHz.
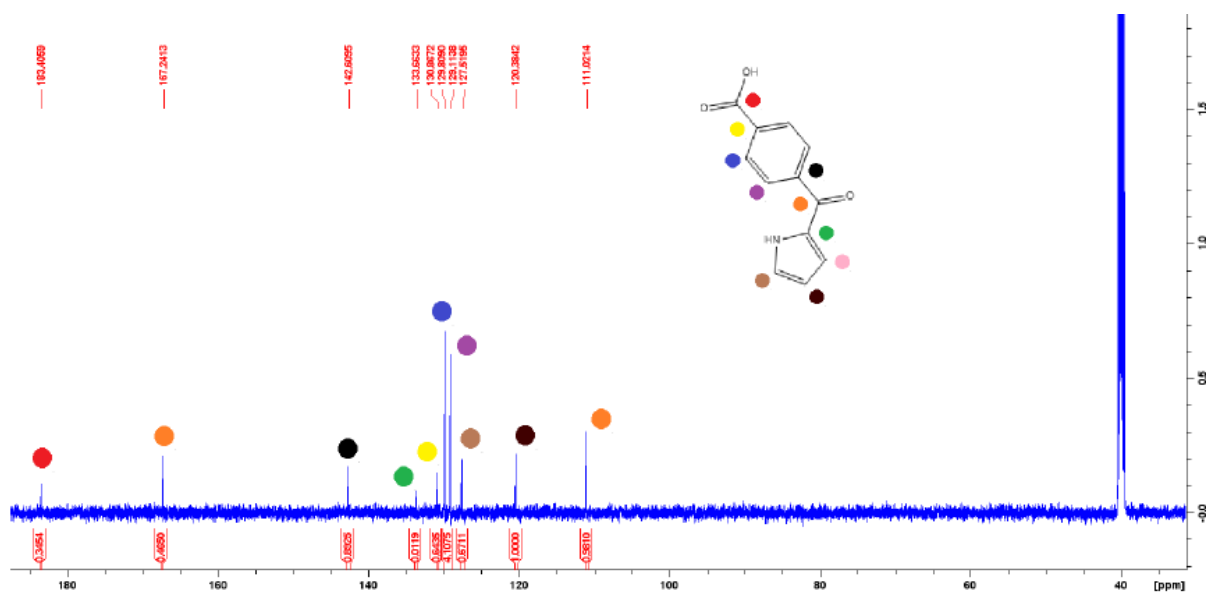
Figure D5 ^{13}C-NMR spectrum of 13in CDCl$_3$ at 150 MHz.
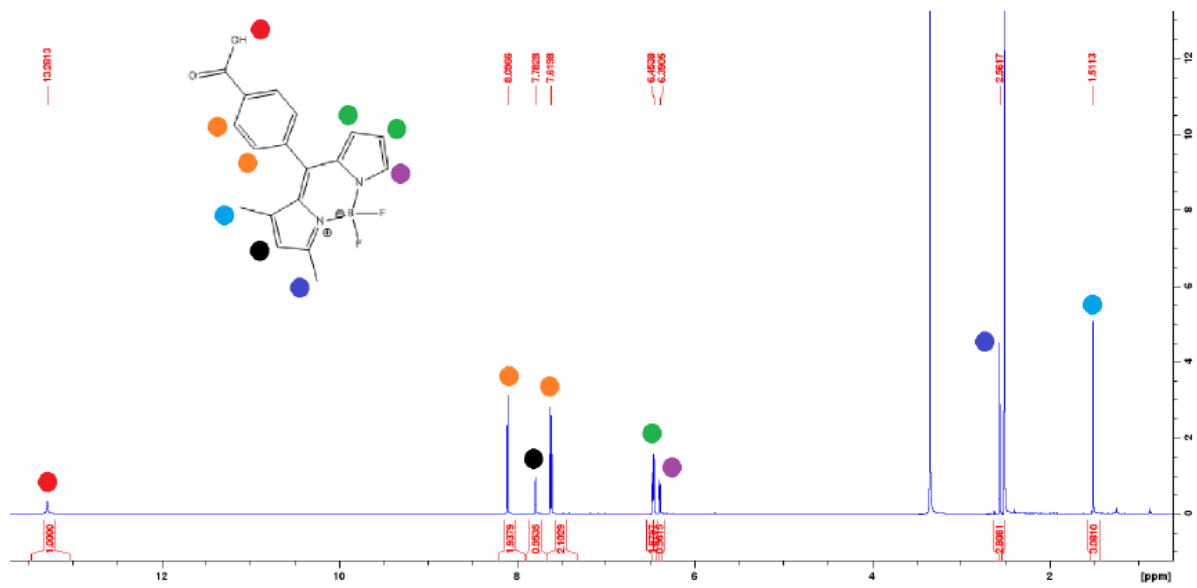
Figure D6 ^{1}H-NMR spectrum of 14 in DMSO-d$_6$ at 600 MHz.

14.71
14.85

116.63

123.97
126.63
129.12
129.46
131.81
132.60
133.49
137.37
138.95
141.94

146.90

162.74

166.80
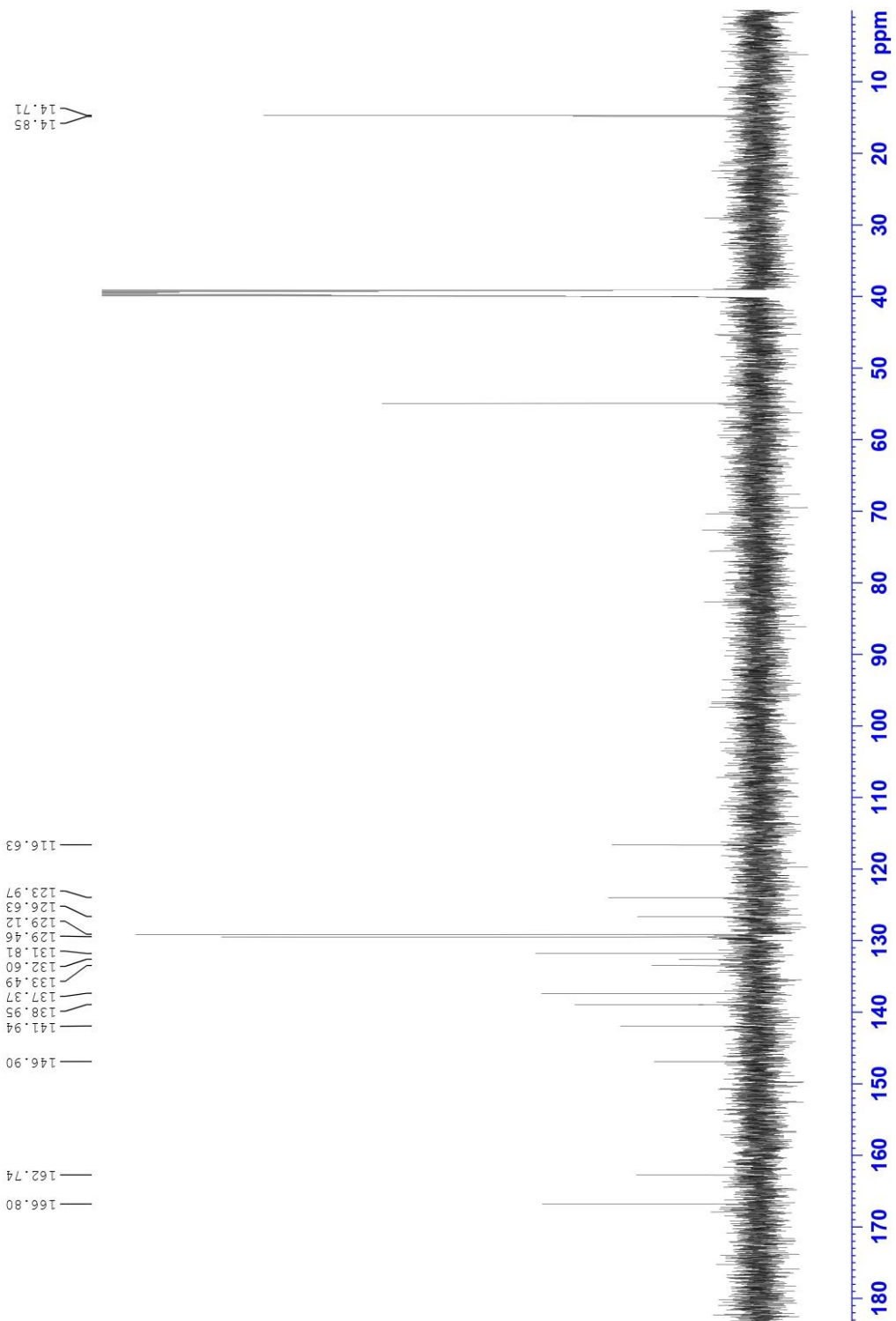
Figure D7 ^{13}C-NMR spectrum of 14 in DMSO-d$_6$ at 150 MHz.
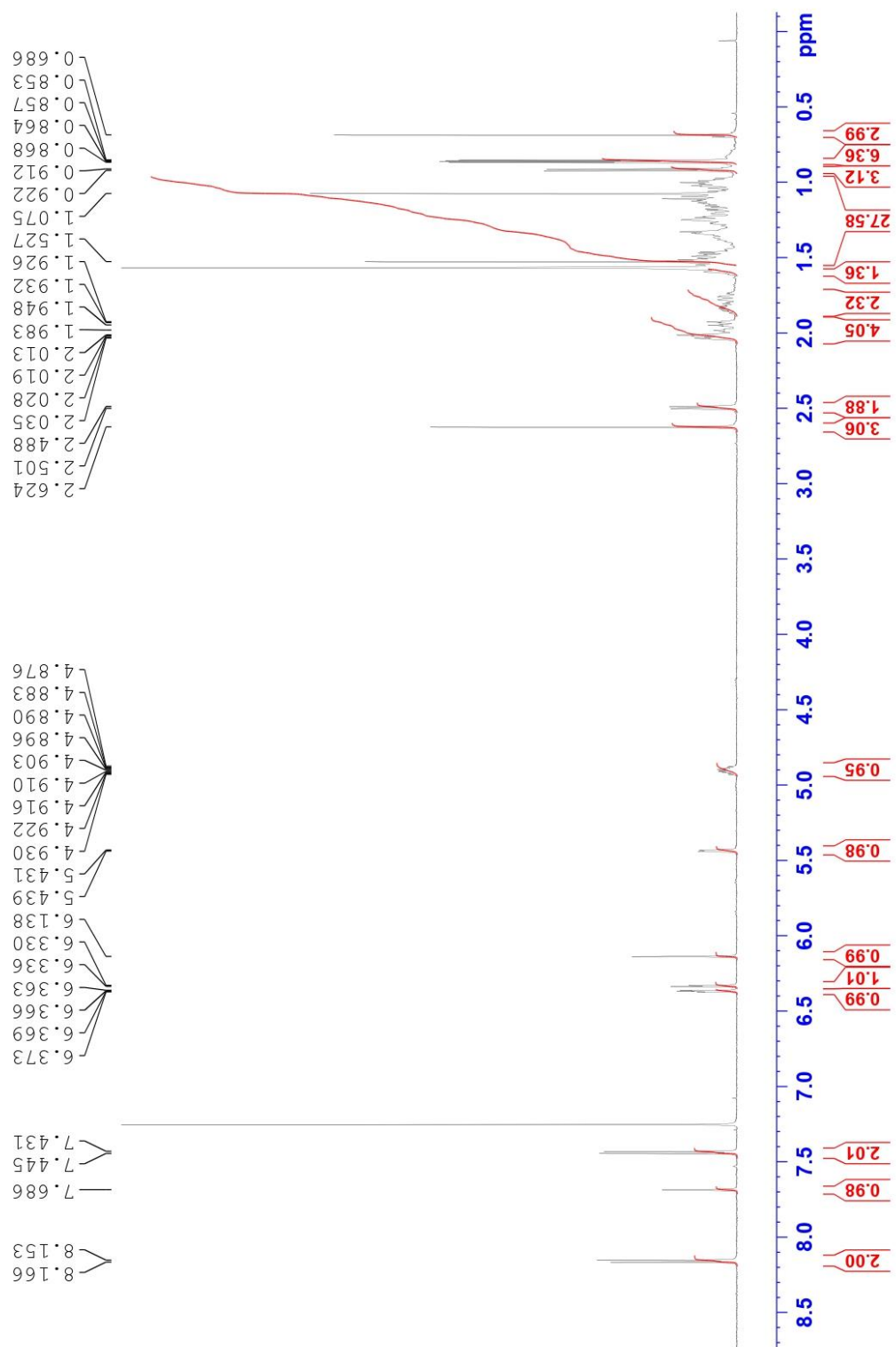
Figure D8 ^{1}H-NMR spectrum of RCBC in CDCl$_3$ at 600 MHz.
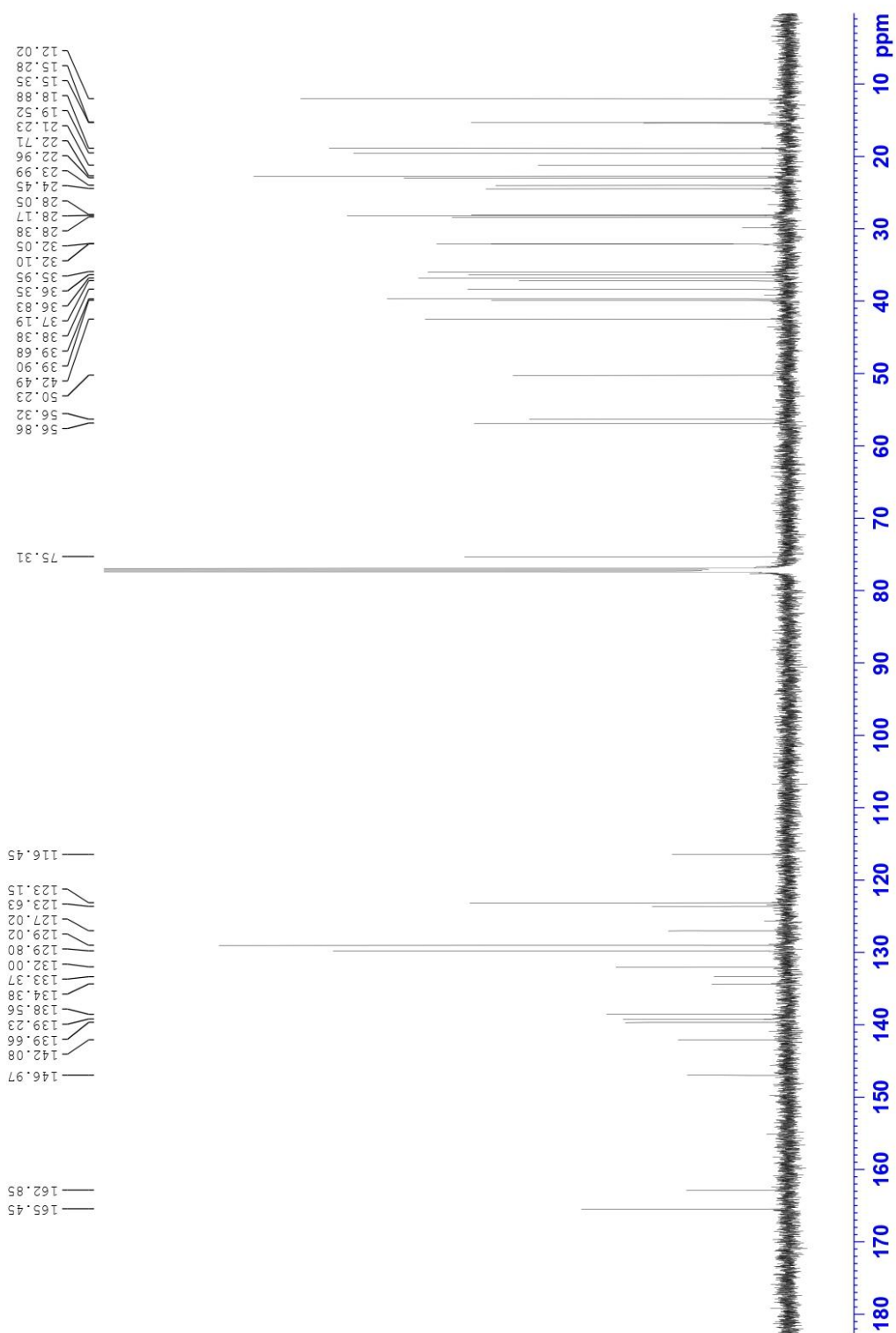
Figure D9 ^{13}C-NMR spectrum of RCBC in CDCl$_3$ at 150 MHz.
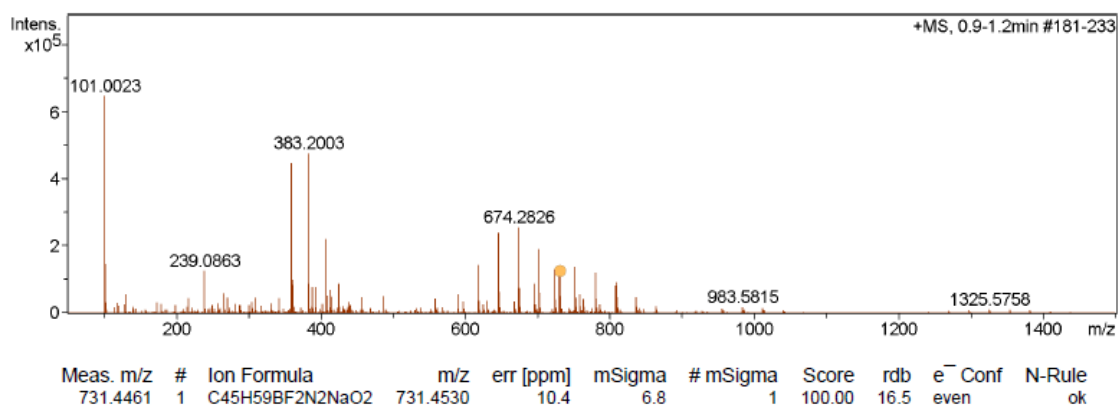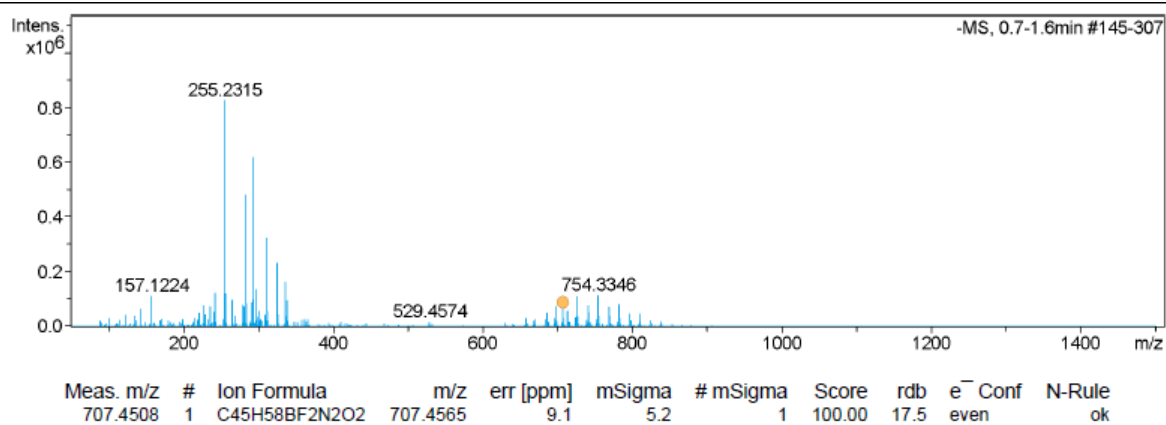
Figure D10 HR-MS (ESI-TOF) positive and negative scans of RCBC.

D.2 NMR and mass spectra of RAR-BR

3.921

7.521
7.591
7.604
8.023
8.026
8.034
8.037

ppm
0.92
1.92

0.92
1.92

1.92

1.92

3.00

ppm
2.0
2.5
3.0
3.5
4.0
4.5
5.0
5.5
6.0
6.5
7.0
7.5
8.0
8.5
9.0
9.5
10.0
10.5
11.0

ppm
7.6
7.7
7.8
7.9
8.0
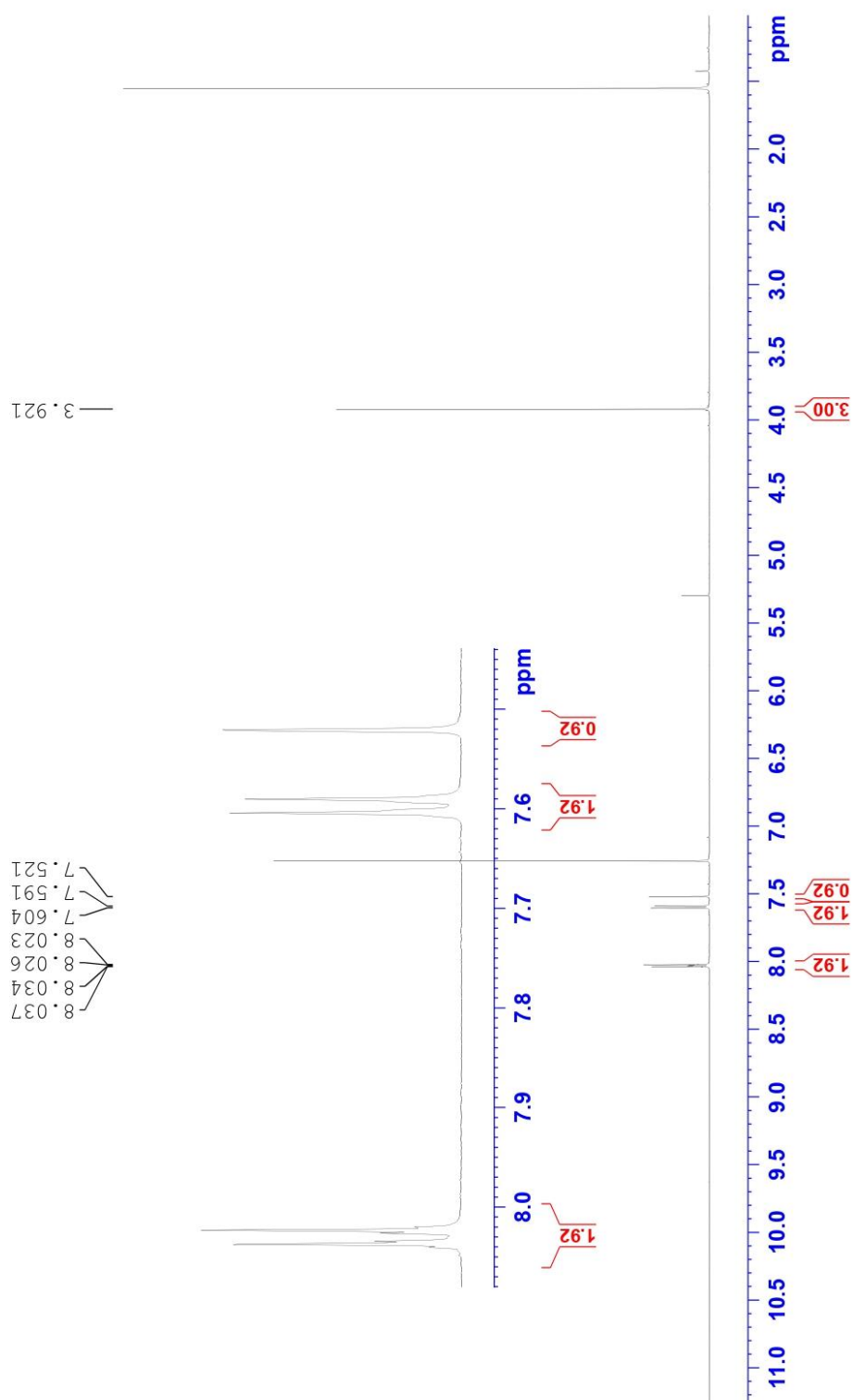
Figure D11 ^{1}H-NMR spectrum of 15 in CDCl$_3$ at 600 MHz.

Figure D12 ¹H-NMR spectrum of 16 in CDCl₃ at 600 MHz.
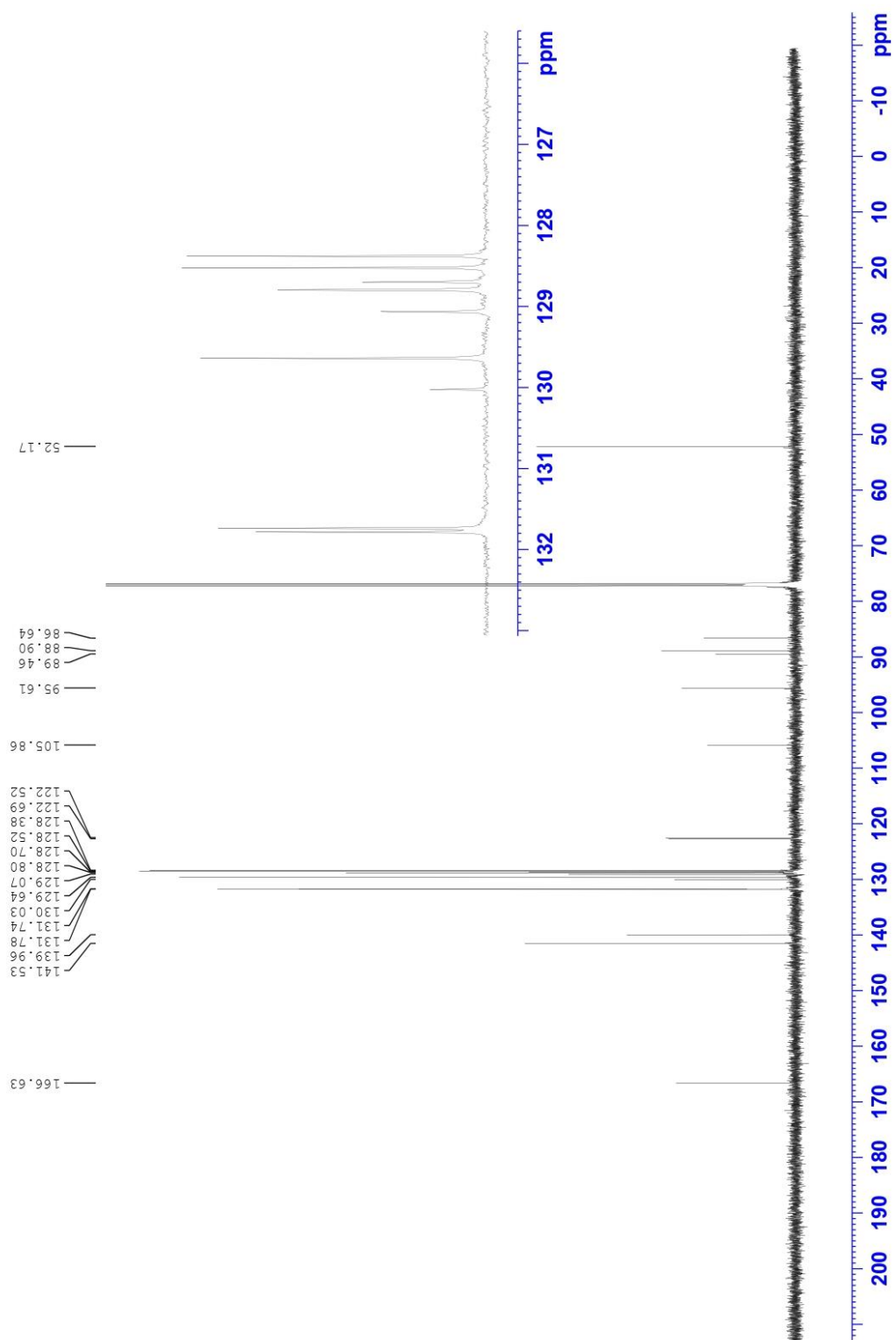
Figure D13 ^{13}C-NMR spectrum of 16 in CDCl$_3$ at 150 MHz.
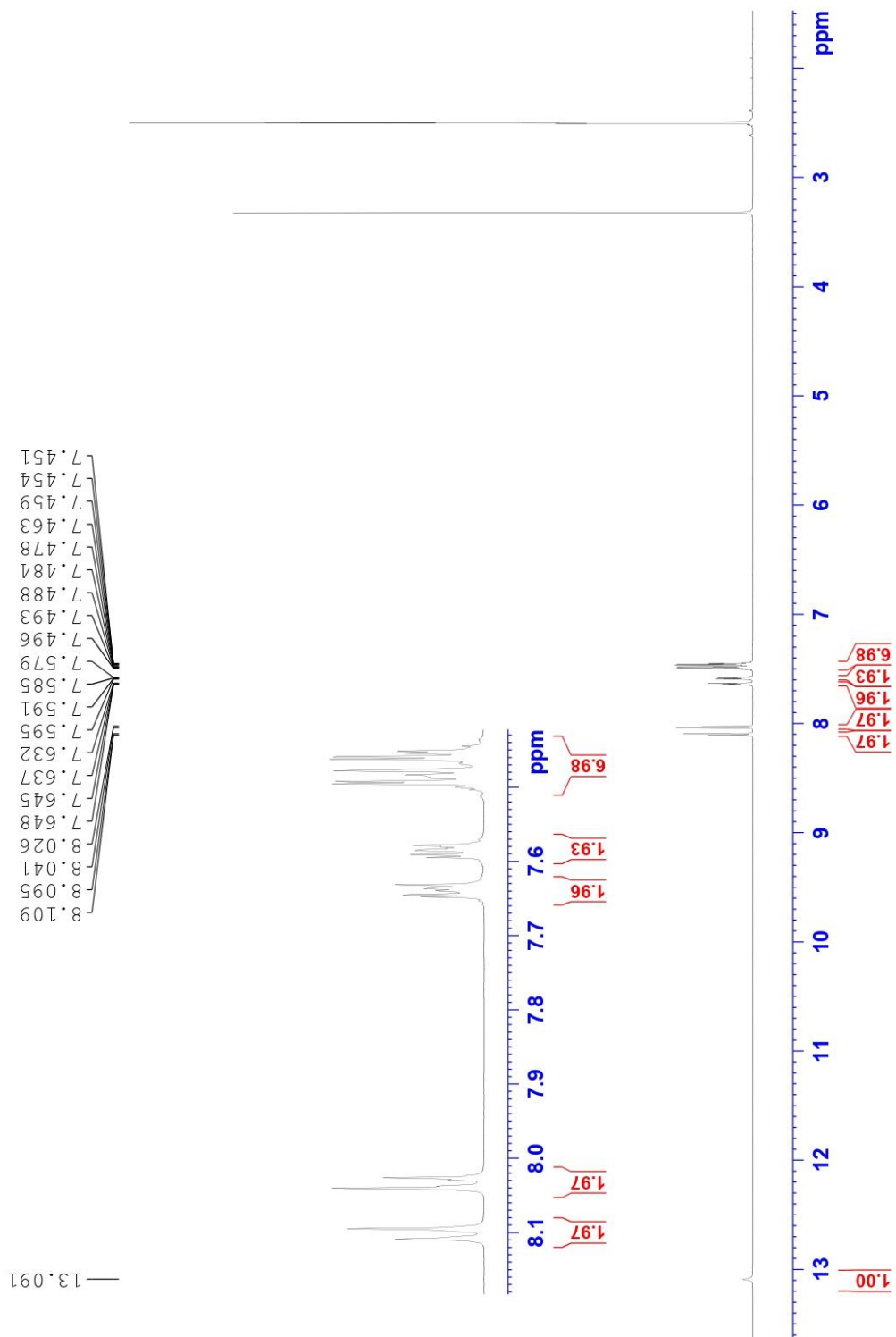
Figure D14 ^{1}H-NMR spectrum of 17 in DMSO-d$_6$ at 600 MHz.

7.451
7.454
7.459
7.463
7.478
7.484
7.488
7.493
7.496
7.579
7.585
7.591
7.595
7.632
7.637
7.645
7.648
8.026
8.041
8.095
8.109

13.091

6.98
7.93
7.96
1.97
1.97

6.98
1.93
1.96
1.97
1.97
1.00
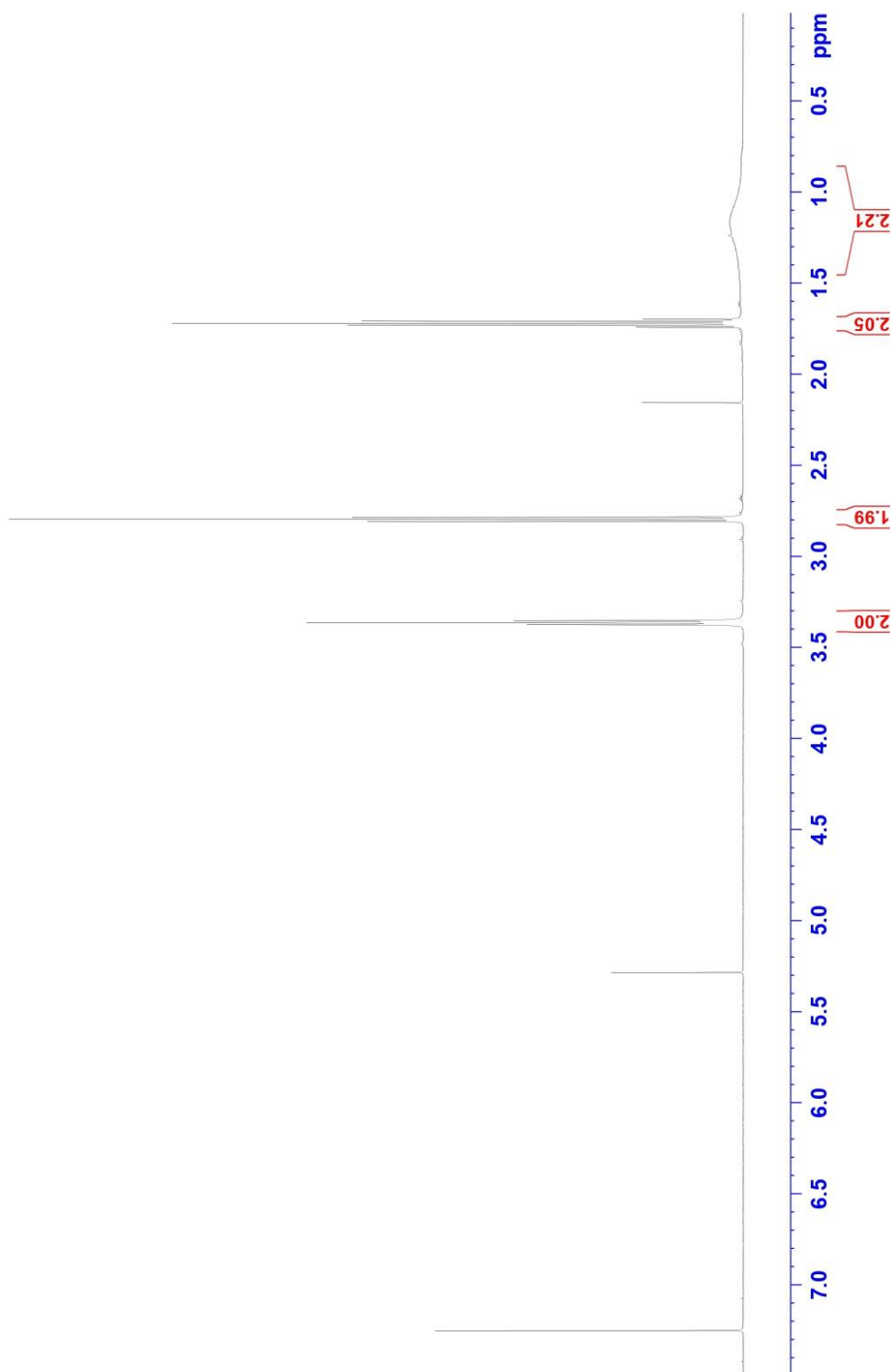
Figure D15 ^{1}H-NMR spectrum of 18 in CDCl$_3$ at 600 MHz.
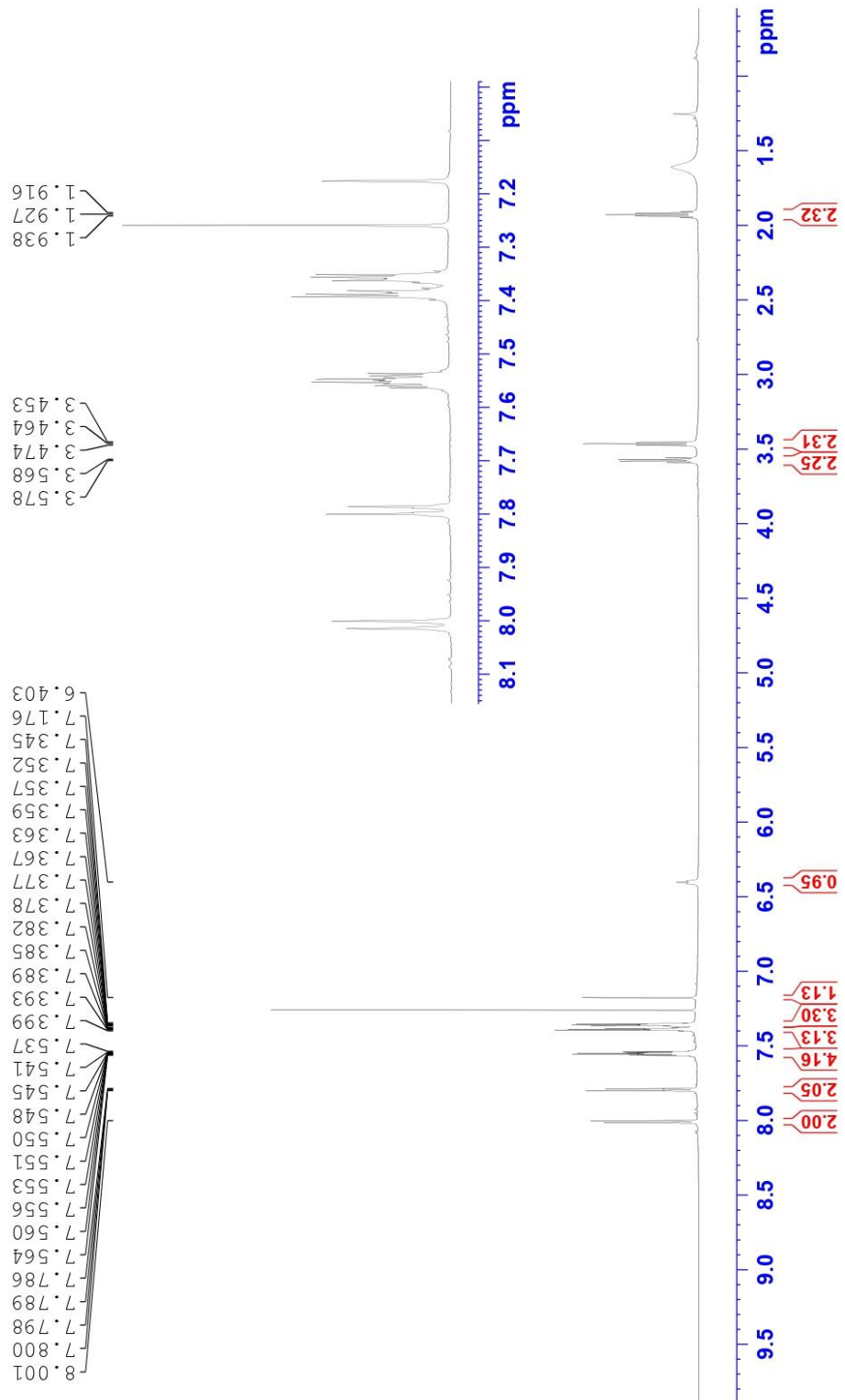
Figure D12 ^{1}H-NMR spectrum of RAR-BR in CDCl$_3$ at 600 MHz.
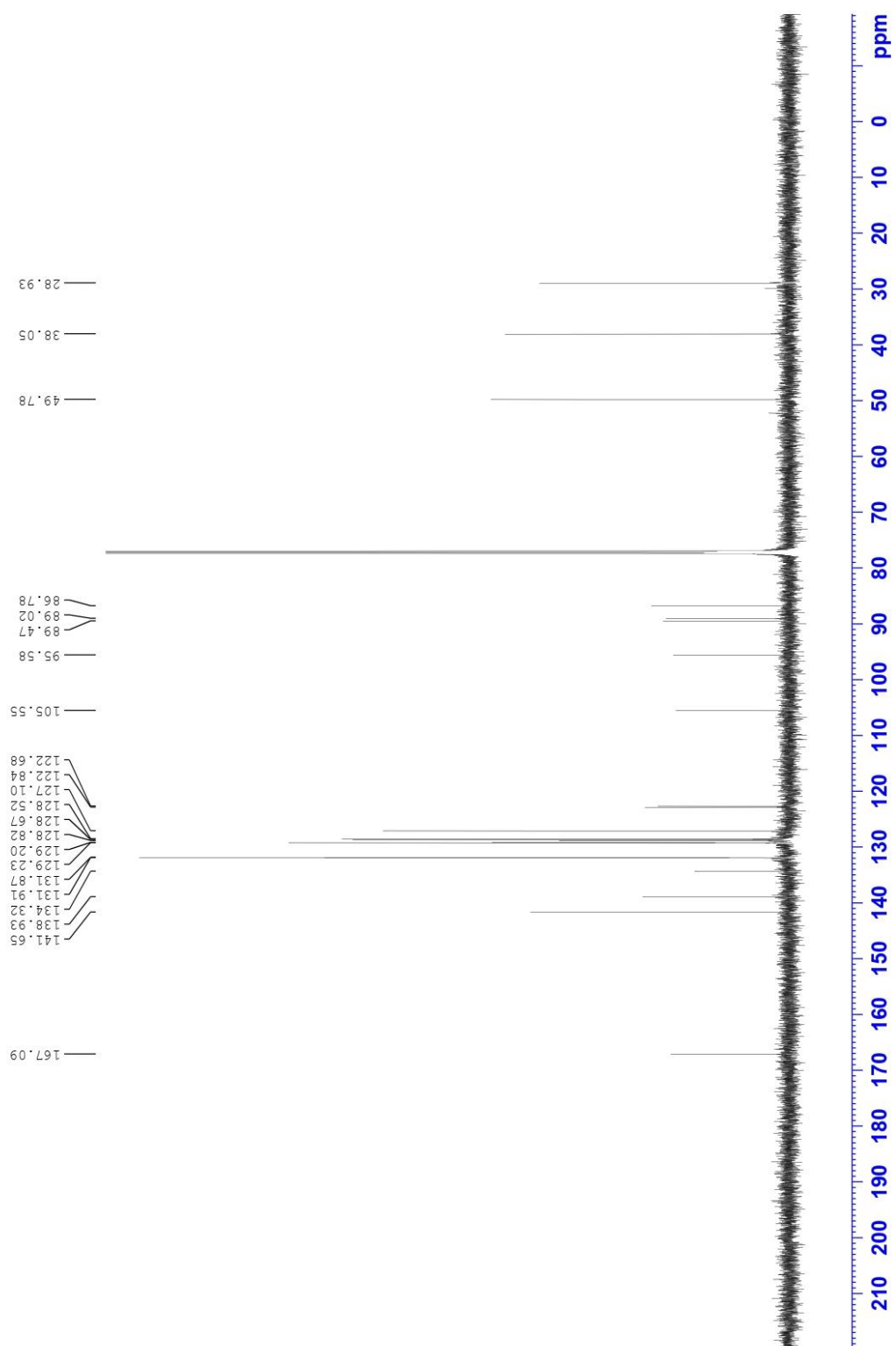
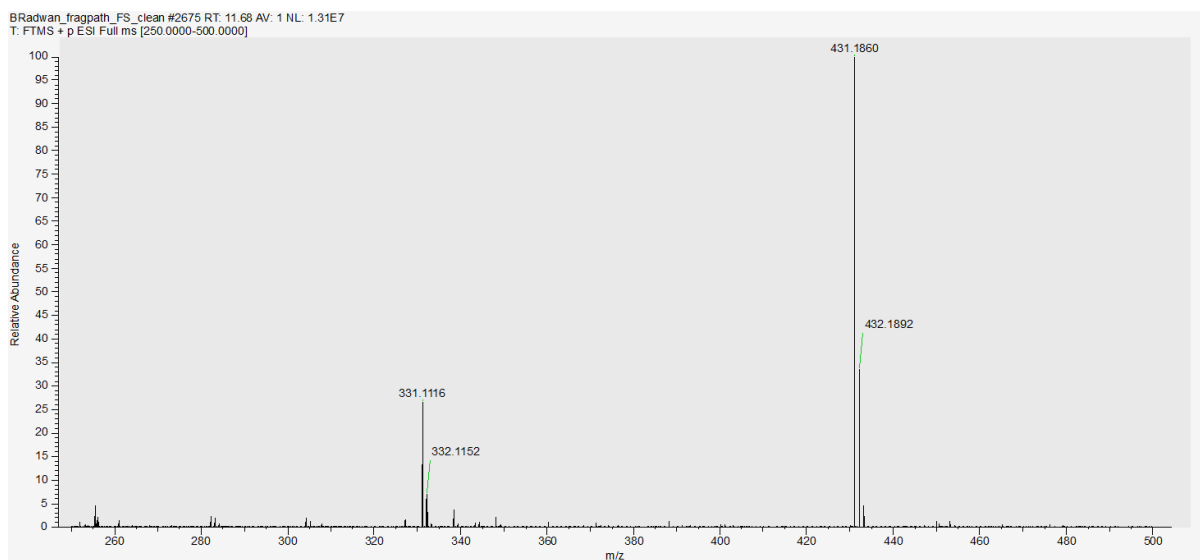Figure D13 ^{13}C-NMR spectrum of RAR-BR in CDCl$_3$ at 150 MHz.

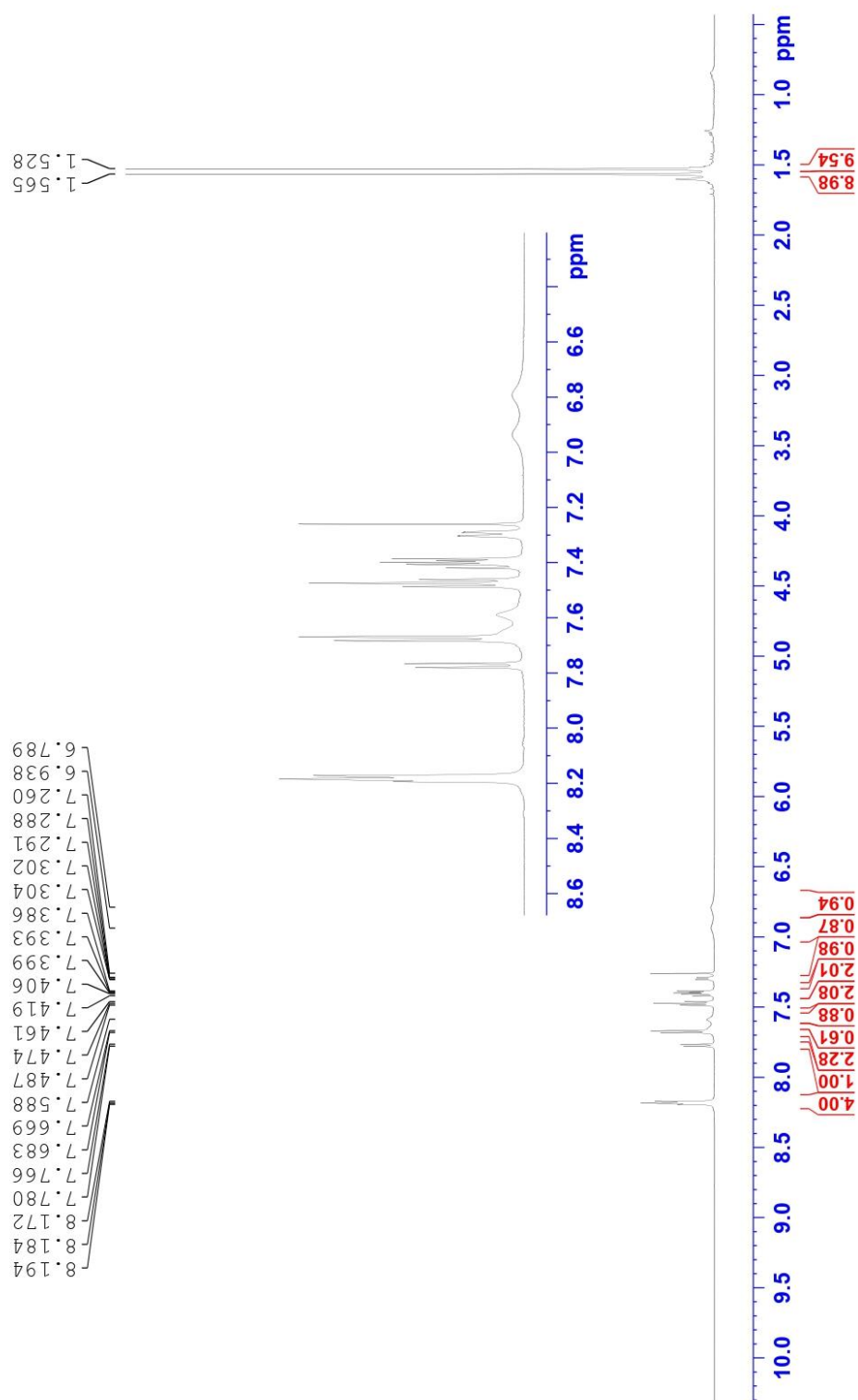Figure D14 Mass spectrum of RCBC (ESI)

D.3 NMR and mass spectra of 3-DAP

Figure D15 ^{1}H-NMR spectrum of 21 in CDCl$_3$ at 600 MHz.

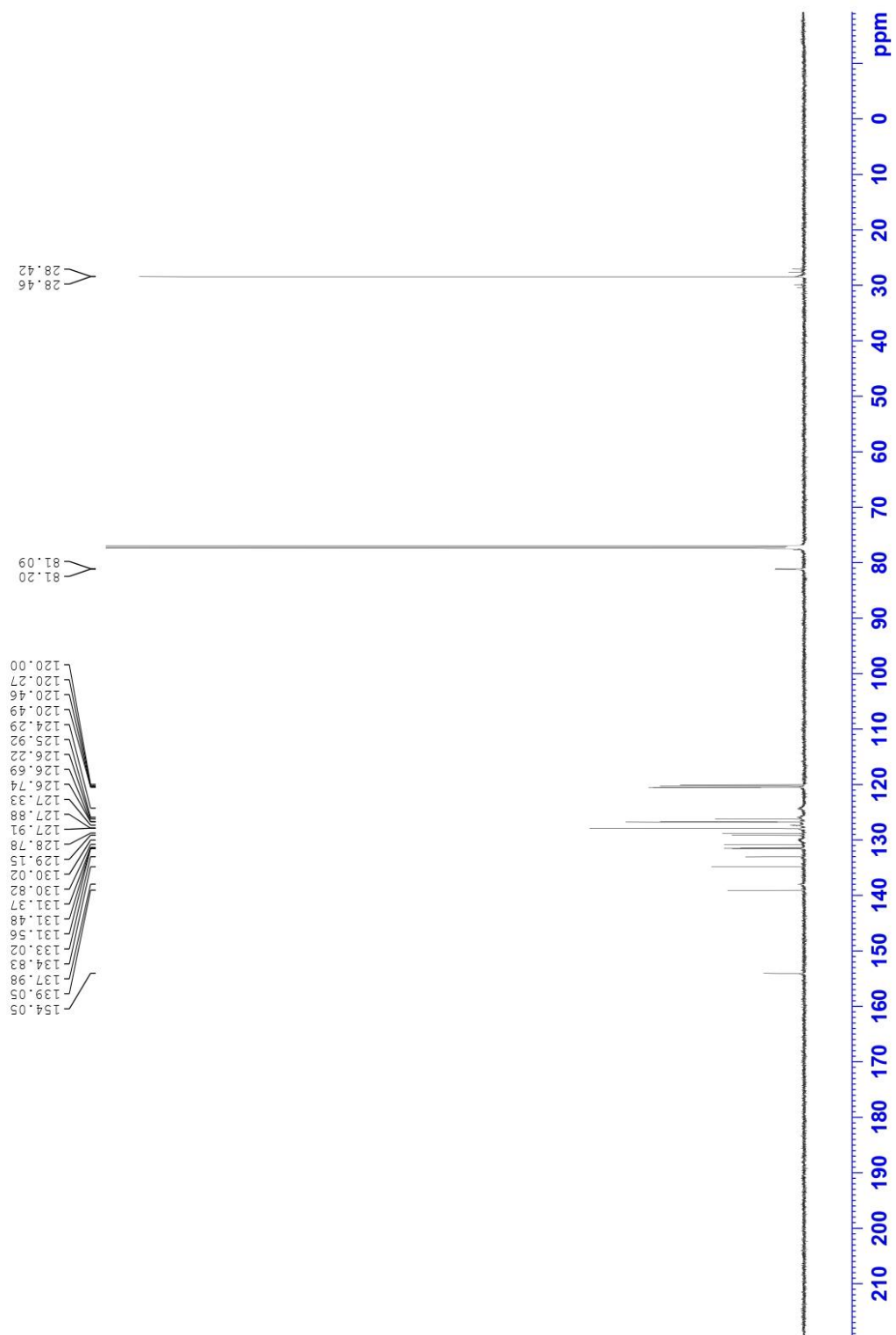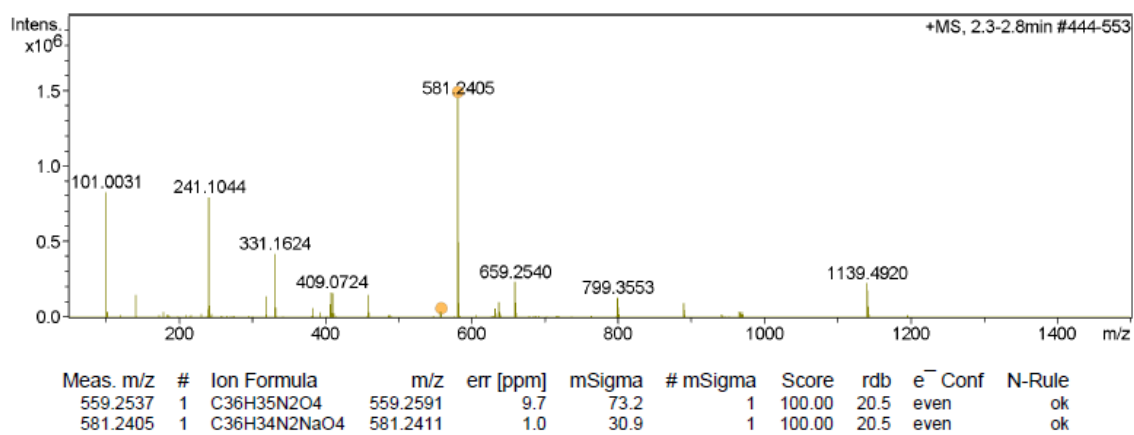Figure D16 ^{13}C-NMR spectrum of 21 in CDCl$_3$ at 150 MHz.

Meas. m/z	#	Ion Formula	m/z	err [ppm]	mSigma	# mSigma	Score	rdb	e⁻ Conf	N-Rule
557.2426	1	C36H33N2O4	557.2446	3.5	24.3	1	100.00	21.5	even	ok

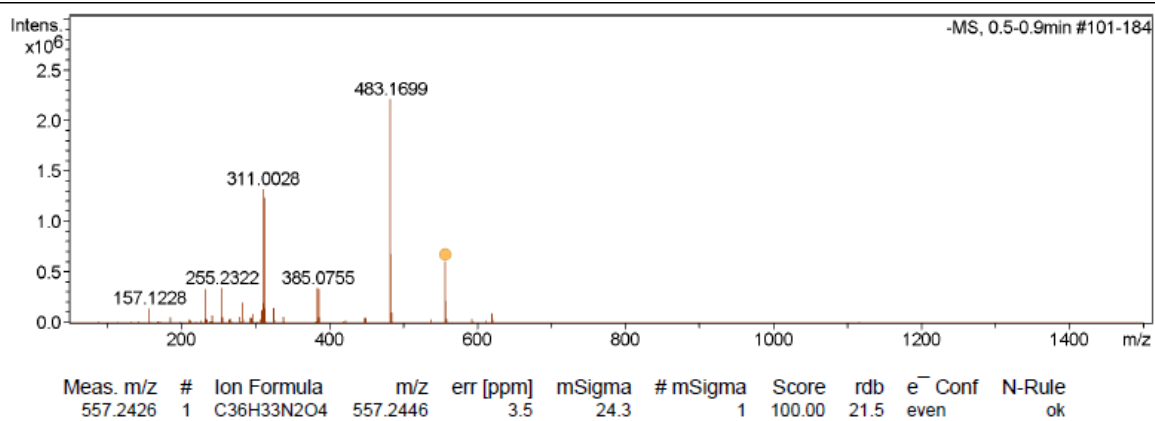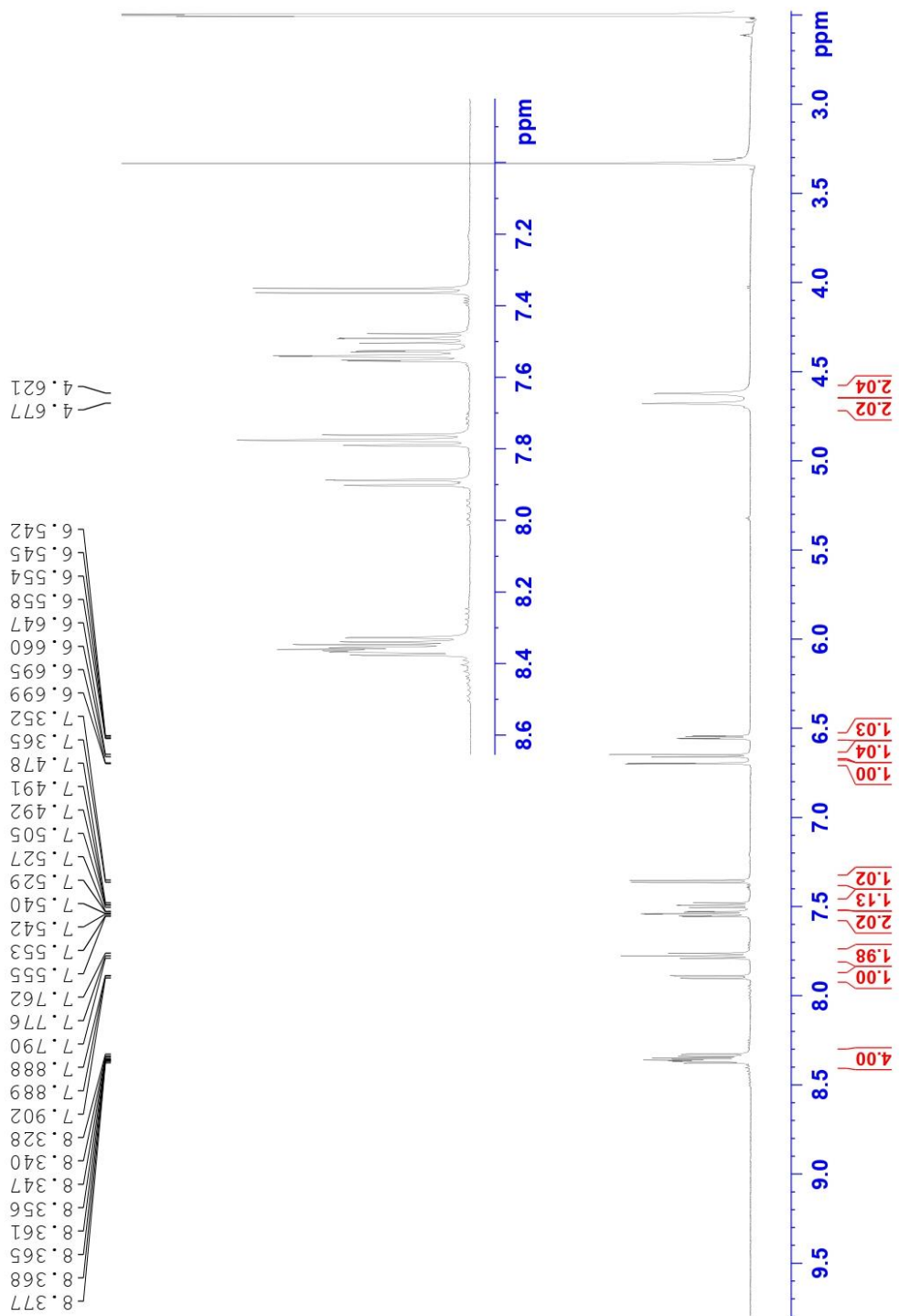| Meas. m/z	#	Ion Formula	m/z	err [ppm]	mSigma	# mSigma	Score	rdb	e⁻ Conf	N-Rule
559.2537	1	C36H35N2O4	559.2591	9.7	73.2	1	100.00	20.5	even	ok
581.2405	1	C36H34N2NaO4	581.2411	1.0	30.9	1	100.00	20.5	even	ok

Figure D14 HR-MS (ESI-TOF) positive and negative scans of 21.
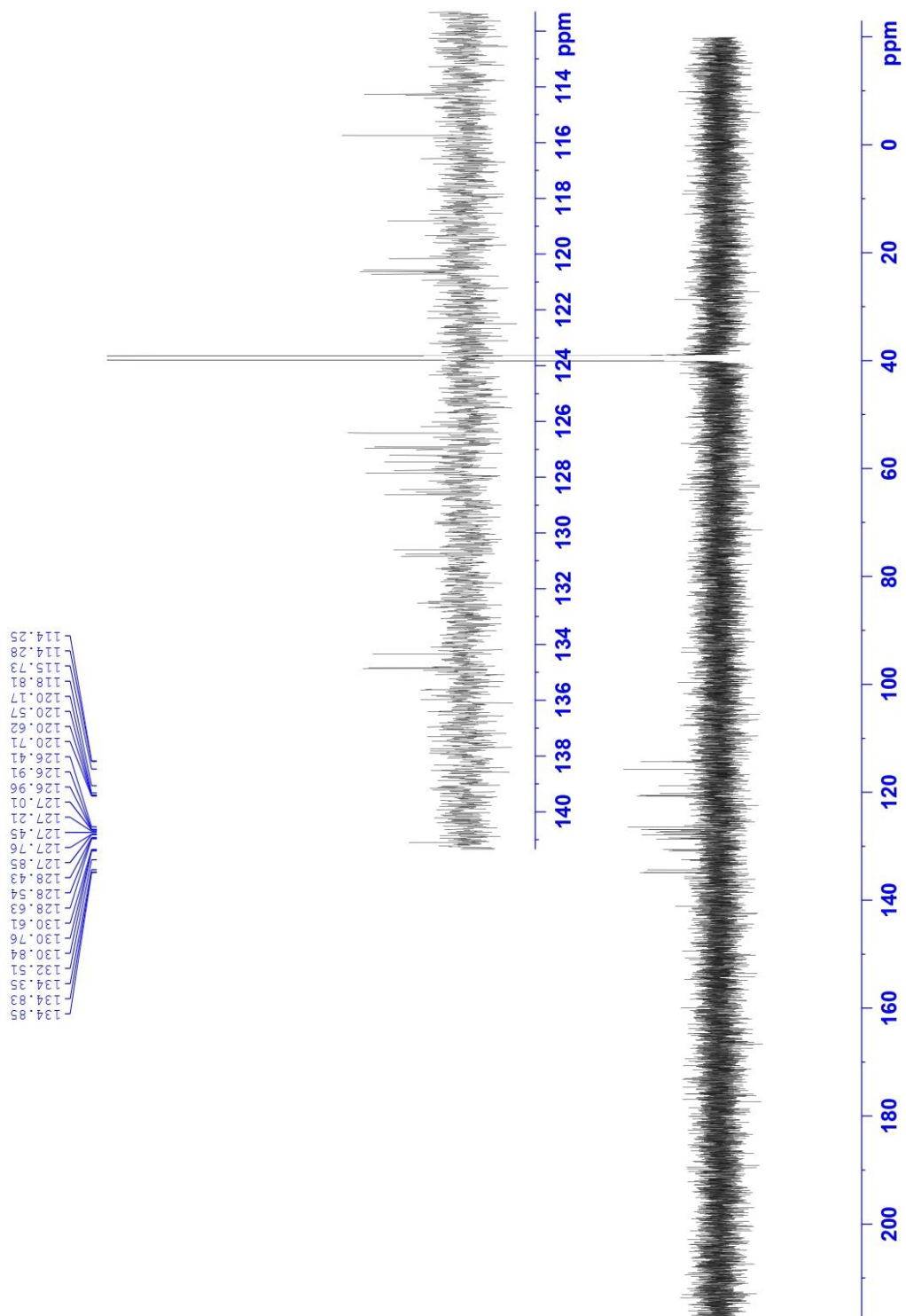
Figure D15 ^{1}H-NMR spectrum of 3-DAP in DMSO-d$_6$ at 600 MHz.

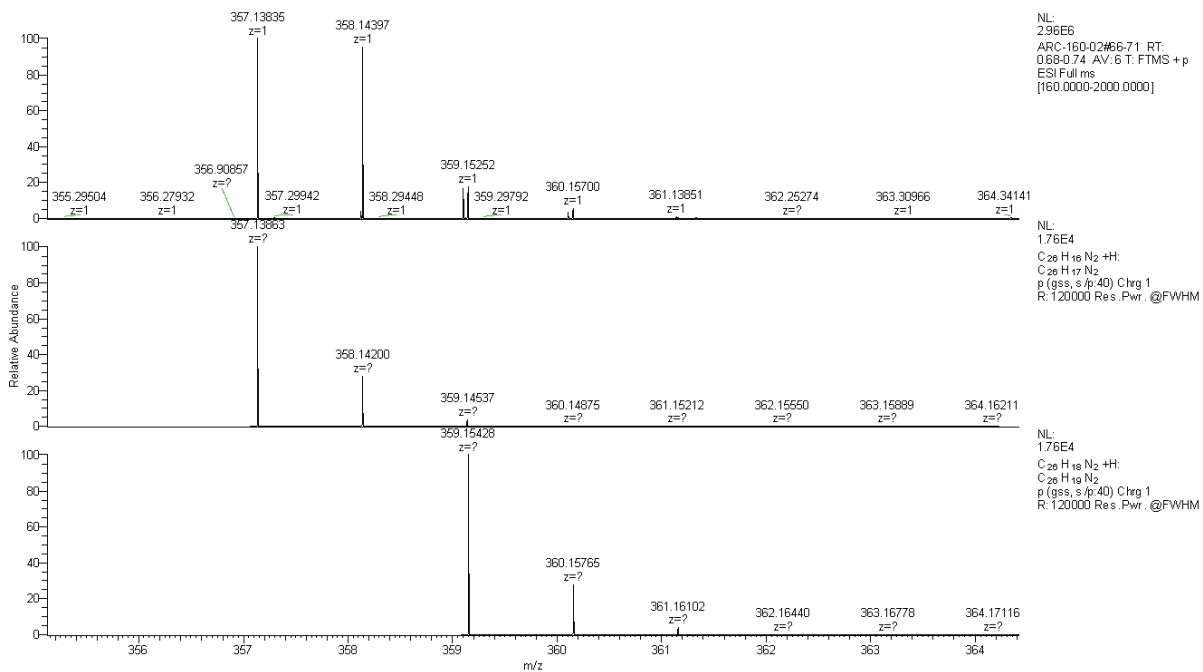Figure D16 ^{13}C-NMR spectrum of 3-DAP in DMSO-d_6 at 150 MHz.

Figure D14 HR-MS (ESI-TOF) scans of 3-DAP.
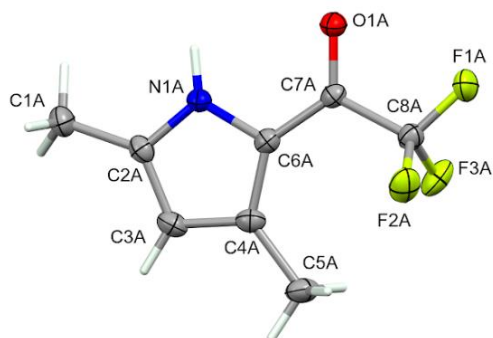
D. 3 Crystallography

Figure D17 Crystal structure of 1-(3,5-dimethyl-1H-pyrrol-2-yl)-2,2,2-trifluoroethan-1-one. Isolated as a by product in the condensation reactions to form BODIPYs from ketopyrroles.
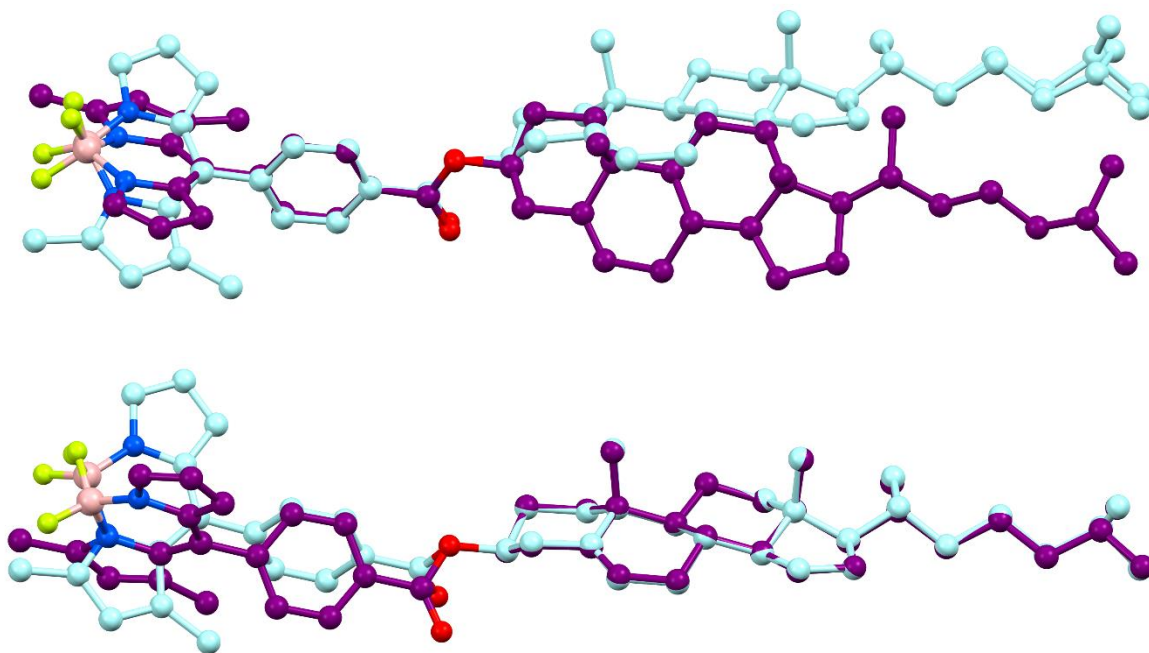

Figure D18 Overlays of the two molecules to emphasise the differences (molecule A in purple). Top is fitted on the boron and benzoate; bottom is fitted on the cholesterol.
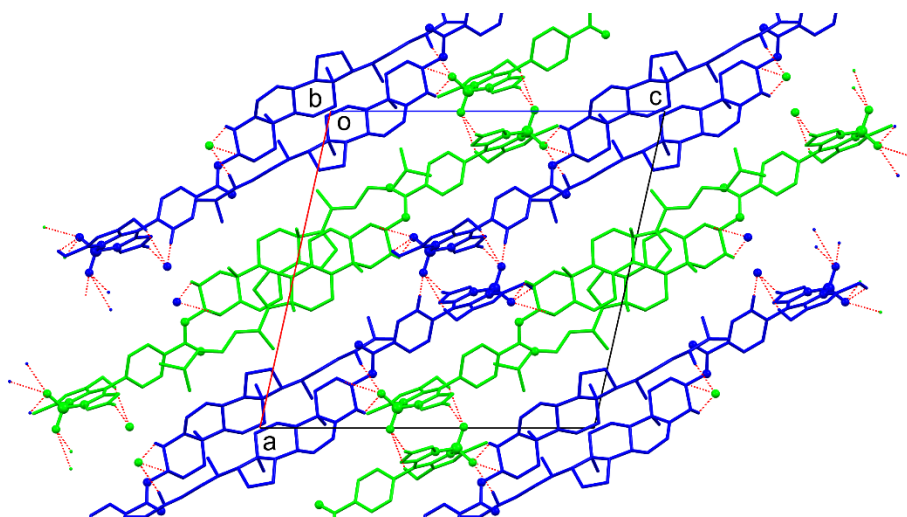
Figure D18 Unit cell packing viewed down the *b* axis showing C-H····F interactions molecule A in green, molecule B in blue.
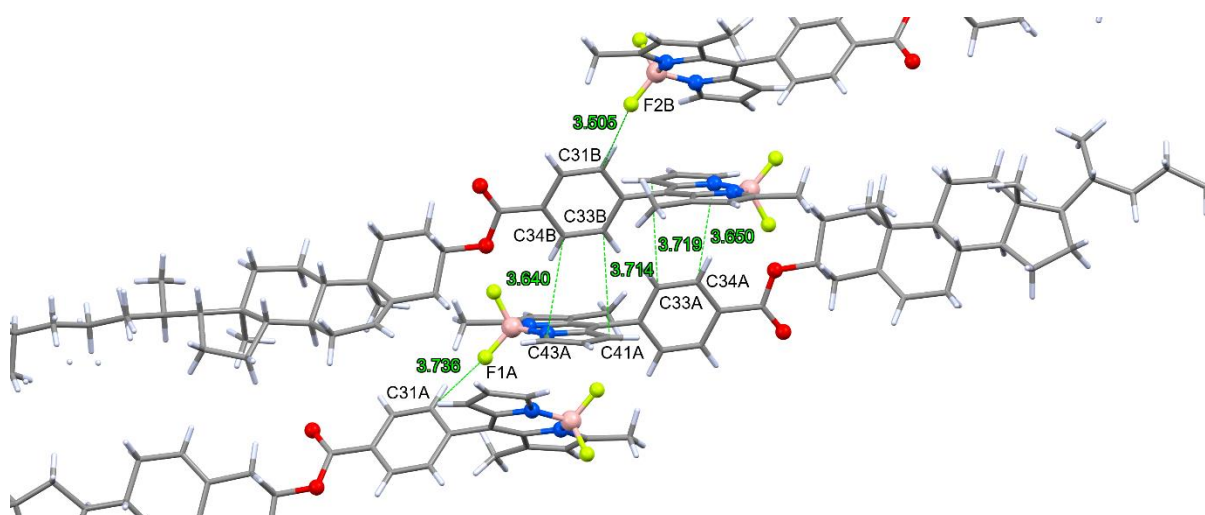

Figure D20 C-H····π interactions between A and B molecules

Experimental

The data were collected at 100(1)K on a Synergy, Dualflex, AtlasS2 diffractometer using Cu*K*α radiation (λ = 1.54184 Å) and the *CrysAlis PRO* 1.171.42.49 suite[1]. Using shelXle[2] and Olex2[3] the structure was solved by dual space methods (SHELXT[4]) and refined on F^2 using all the reflections (SHELXL-2019/2[5]). All the non-hydrogen atoms were refined using anisotropic atomic displacement

parameters and hydrogen atoms were inserted at calculated positions using a riding model. The asymmetric unit contains two independent molecules (A & B) with different conformations. Disorder in the alkyl chain of molecule B was modelled with 60:40% site occupancy of two overlapping orientations and some restraints were applied. There is also a slight disorder in the isopropyl group of molecule A but no attempt was made to model this. Crystal parameters, data collection and structure refinement details are summarised in Table 1.

Table D1 Crystal data and structure refinement for CN-BDP-Ch.

Identification code	CN-BDP-Ch
Empirical formula	$C_{45}H_{59}BN_2O_2F_2$
Formula weight	708.75
Temperature/K	100.01(10)
Crystal system	monoclinic
Space group	$P2_1$
a/Å	19.8601(5)
b/Å	10.0230(2)
c/Å	20.4738(6)
α/°	90
β/°	102.616(2)
γ/°	90
Volume/Å^3	3977.07(18)
Z	4
ρ_{calc} g/cm^3	1.184
μ/mm^{-1}	0.611
F(000)	1528.0
Crystal size/mm^3	0.15 × 0.09 × 0.03
Radiation (Å)	Cu Kα (λ = 1.54184)
2θ range for data collection/°	5.616 to 136.498
Index ranges	-21 ≤ h ≤ 23, -11 ≤ k ≤ 12, -24 ≤ l ≤ 24
Reflections collected	43100
Independent reflections	14458 [R_{int} = 0.0386, R_{sigma} = 0.0375]
Data/restraints/parameters	14458/460/998
Goodness-of-fit on F^2	1.041
Final R indexes [I>=2σ (I)]	R1 = 0.0566, wR2 = 0.1413
Final R indexes [all data]	R1 = 0.0656, wR2 = 0.1479
Largest diff. peak/hole / e Å^{-3}	0.60/-0.35
Flack parameter	-0.05(8)

Computing details

Data collection: *CrysAlis PRO* 1.171.42.49 (Rigaku OD, 2022); cell refinement: *CrysAlis PRO* 1.171.42.49 (Rigaku OD, 2022); data reduction: *CrysAlis PRO* 1.171.42.49 (Rigaku OD, 2022); program(s) used to solve structure: SHELXT 2018/2(Sheldrick 2015); program(s) used to refine structure: *SHELXL2019*/2 (Sheldrick, 2015a); molecular graphics: *Mercury* (Macrae at al., 2008); software used to prepare material for publication: Olex2 (Dolomanov *et al.* 2009), *publCIF* (Westrip, 2010).

References

Dolomanov, O. V., Bourhis, L. J., Gildea, R. J., Howard, J. A. K. and Puschmann, H. (2009). *J. Appl. Cryst.* **42**, 339–341.

Hübschle, C. B., Sheldrick, G. M. & Dittrich, B. (2011). *J. Appl. Cryst.* **44**, 1281–1284.

Macrae, C. F., Bruno, I. J., Chisholm, J. A., Edgington, P. R., McCabe, P., Pidcock, E., Rodriguez-Monge, L., Taylor, R., van de Streek, J. & Wood, P. A. (2008). *J. Appl. Cryst.* **41**, 466–470.

Rigaku Oxford Diffraction, (2018). *CrysAlis PRO* Software system, Rigaku Corporation, Oxford, UK.

Sheldrick, G. M. (2015). *Acta Cryst.* A**71**, 3–8.

Westrip, S. P. (2010). *J. Appl. Cryst.* **43**, 920–925.

Vista[n] tus hombros el verdor lozano,
joven, con que tu ciencia te laurea;
y puesto en ello dignamente, sea
índice de tus méritos ufano.

Corone tu discurso soberano
la que blanda tus sientes lisonjea
insignia literaria, en quien se emplea
el flamante sepulcro de un gusano.

¡Oh, qué enseñanza llevan escondida
honrosos los halagos de tu suerte,
donde despierta la atención dormida!,

pues ese verde honor, si bien se advierte,
mientras más brinda gustos a la vida,
más ofrece recuerdos a la muerte.

Sor Juana Inés de la Cruz, Segundo Volumen, 1692.